Atomic Layer Deposition of Transition Metal Oxide Coatings for Oxygen Catalysis at the Air Electrode in Zn-Air Batteries

by

Matthew Roy Labbe

A thesis submitted in partial fulfillment of the requirements for the degree of

Doctor of Philosophy

in

Materials Engineering

Department of Chemical and Materials Engineering

University of Alberta

Abstract

Energy storage is a critical step in fully adopting renewable energy, such as wind and solar, and eliminating carbon emissions from fossil fuel use. Electrochemical batteries are a versatile energy storage system and, as the ubiquitous battery of today, Li-ion batteries (LIBs) have begun to penetrate the market for grid-level energy storage. Coupled with the rising demand in electric vehicles and their associated battery requirements, there is a quest for new battery technologies that are more sustainable than the flammable, resource-limited, and expensive LIB. Zn-air batteries (ZABs) are one possible alternative chemistry, boasting higher theoretical energy density and safer operation than LIBs. Furthermore, Zn is inexpensive and abundant and the secondary reactant, oxygen, is freely available. Yet, ZABs are plagued by rechargeability issues at both the Zn and air electrodes. Specifically, the air electrode suffers from poor oxygen reaction kinetics and instability during cycling. One particular issue is flooding of electrolyte into the air electrode, which disrupts the necessary balance of oxygen, electrolyte, and electrons for the electrochemical reactions.

The objective of this work was to develop catalysts for the air electrode in ZABs that improve the oxygen reaction kinetics during discharge and recharge and to apply them on the air electrode such that they provide stable cycling performance. Precious metal-based catalysts (*e.g.*, Pt or RuO_2) display good catalytic activity for the oxygen reactions but are impractical for widespread adoption of ZABs. Instead, this work focuses on readily abundant transition metal oxide catalysts using the elements of Mn, Fe, Zn, and O. Using atomic layer deposition (ALD), these transition metal oxide catalysts are deposited onto, and within, ZAB air electrodes. The uniform and conformal nature of ALD coatings ensures that the porosity of the air electrode is preserved, the amount of catalyzed reaction sites is maximized, and the distribution of catalytic material is well

dispersed throughout the thickness and porosity of the electrode. These attributes improve the utilization of catalyst material and mitigate the effects of flooding on ZAB performance.

The first study in this work developed an ALD process to deposit Fe oxide (FeO_x) coatings on the air electrode in ZABs, which was shown to be a saturating and conformal ALD process using atomic force microscopy and *in situ* spectroscopic ellipsometry (SE). Electron microscopy and energy dispersive X-ray analysis revealed that a thin film of FeO_x encased the carbon particles of the air electrode and distributed the catalyst more than 10 μm within the air electrode porosity. Using half cell electrochemical testing, the FeO_x coating showed promise as a catalyst towards the recharge reaction at the air electrode.

The second study further analyzed the morphology and growth characteristics of the FeO_x ALD process on the carbon air electrode surface. Instead of the anticipated pinhole-free layer-by-layer growth signature to ALD, a series of island layers were revealed by electron microscopy. Pinholes between coalesced islands were visible and appropriate modelling of SE data determined that six layers of islands formed over a period of 650 ALD cycles.

The third study in this work combined the FeO_x ALD process developed in this thesis with a previously developed Mn oxide (MnO_x) ALD process from earlier work in our group. Based on electron diffraction and X-ray photoelectron spectroscopy, the optimized ALD supercycle process deposited spinel-type $(Mn,Fe)_3O_4$ coatings on the carbon particles of the air electrode. This catalyst layer showed bifunctional activity towards both the charge and discharge reactions in half cell and full cell electrochemical testing. In full cell ZAB cycling, the ALD coating maintained stable performance for 600 h (1565 cycles) at 10 mA cm^{-2}. The retention of bifunctional energy efficiency after cycling was 84% for the ALD coating and only 66% for a precious metal comparison under the same cycling conditions.

For the fourth study, an ALD process for Zn oxide was integrated with the other three ALD processes for FeO_x, MnO_x, and $(Mn,Fe)_3O_4$. Mixed oxide films were successfully developed and deposited on ZAB air electrodes, however, they did not generally improve ZAB performance compared with their non-Zn counterparts aside from some improvement for the FeO_x coating after Zn addition.

Preface

This thesis focuses on the deposition, characterization, and electrochemical evaluation of thin film metal oxide coatings, prepared by atomic layer deposition, for the air electrode in rechargeable Zn-air batteries. The research presented in Chapters 3, 4, 5 and 6, as well as in Appendices A and B, are all my original work.

Chapters 3 and 5 were done in collaboration with Dr. Michael P. Clark. Dr. Clark helped devise the atomic layer deposition processes in Chapters 3 and 5.

Chapter 3 also featured collaborations with Drs. Anqiang He and Zahra Abedi. Dr. He performed atomic force microscopy analysis and aided with X-ray photoelectron spectroscopy interpretation. Dr. Abedi performed pore size analysis and field emission scanning electron microscopy of the gas diffusion layer material.

Dr. Ken Cadien provided access to the atomic layer deposition facility and was consulted on synthesis and analysis. He is listed as a co-author for the publications of Chapters 3, 4, and 5.

All atomic layer depositions, electrochemical analyses, and battery tests were conducted by myself. Dr. Douglas G. Ivey performed all transmission electron microscopy, while I conducted most of the scanning electron microscopy. Analysis of characterization data was conducted primarily by myself with the assistance of Dr. Douglas G. Ivey.

All original manuscript drafts were written by myself and all figures were created by myself. Dr. Douglas G. Ivey was the main editor for all sections of this thesis.

Versions of Chapters 3, 4, and 5, as well as Appendices A and B, have been published as:

Chapter 3: M. Labbe, M. P. Clark, Z. Abedi, A. He, K. Cadien, and D. G. Ivey, "Atomic layer deposition of iron oxide on a porous carbon substrate via ethylferrocene and an oxygen plasma," *Surf. Coatings Technol.*, vol. 421, p. 127390, 2021.

Chapter 4: M. Labbe, K. Cadien, and D. G. Ivey, "Growth of Multiple Island Layers during Iron Oxide Atomic Layer Deposition: An Electron Microscopy and Spectroscopic Ellipsometry Investigation," *J. Phys. Chem. C*, vol. 126, no. 46, pp. 19883–19894, 2022.

Chapter 5: M. Labbe, M. P. Clark, K. Cadien, and D. G. Ivey, "Bifunctional Mn-Fe Oxide Catalysts for Zn-Air Battery Air Electrodes Fabricated Through Atomic Layer Deposition," *Batter. Supercaps*, in-press, e202400133, 2024.

Appendix A: M. Labbe and D. G. Ivey, "Catalyst Integration within the Air Electrode in Secondary Zn-air Batteries," *J. Phys. Energy*, vol. 6, no. 3, p. 032002, 2024.

Appendix B: M. Labbe and D. G. Ivey, "Experimental Concerns of Current Collector Interference and Electrolyte Creep During Zinc-Air Battery Testing," *J. Electrochem. Soc.*, vol. 170, no. 9, p. 090515, 2023.

For all chapters published: the Supporting Information, not typically included in the published article itself but available online, has been appended to the end of each chapter. The Supporting Information contains additional characterization or results that augment the discussion and are referred to within the main text.

Reuse permissions for all the images in this thesis that have been reproduced or adapted from the literature have been obtained from the publishers and are available upon reasonable request from the author of this thesis.

In addition to the above publications that comprise this thesis, I have also contributed to several publications for various members of my research group:

1. J. Cui, M. Labbe, H.-J. J. Chung, and D. G. Ivey, "Low-temperature tolerant poly(acrylic acid) (PAA) gel polymer electrolytes for rechargeable zinc–air batteries," *J. Mater. Chem. A*, vol. 11, no. 26, pp. 13971–13983, 2023.
2. Y. He, D. Aasen, A. McDougall, H. Yu, M. Labbe, C. Ni, S. Milliken, D. G. Ivey, and J. G. C. Veinot, "Hollow Mesoporous Carbon Nanospheres Decorated with Metal Oxide Nanoparticles as Efficient Earth-Abundant Zinc-Air Battery Catalysts," *ChemElectroChem*, vol. 8, no. 8, pp. 1455–1463, Apr. 2021.
3. Y. He, D. Aasen, H. Yu, M. Labbe, D. G. Ivey, and J. G. C. Veinot, "Mn_3O_4 nanoparticle-decorated hollow mesoporous carbon spheres as an efficient catalyst for oxygen reduction reaction in Zn–air batteries," *Nanoscale Adv.*, vol. 2, no. 8, pp. 3367–3374, 2020.

4. T. N. T. Tran, D. Aasen, D. Zhalmuratova, M. Labbe, H. J. Chung, and D. G. Ivey, "Compositional Effects of Gel Polymer Electrolyte and Battery Design for Zinc-Air Batteries," *Batter. Supercaps*, vol. 3, no. 9, pp. 917–927, 2020.

My contributions to (1) involved asssiting with the electrochemical testing, ultraviolet-visible spectroscopy testing, and the interpretation of the results for electrolytes that use a KI additive. My contributions to (2) included performing linear sweep voltammetry and Zn-air battery rate tests for some samples. My contributions to (3) were similar, where I performed linear sweep voltammetry and Zn-air battery rate, power, and cycling tests for some samples. In addition, I also performed rotating disk electrode voltammetry and analyzed the results to determine electron transfer numbers. My contributions to (4) were assisting with conductivity measurements and discussions regarding electrochemical testing.

Dedication

To everyone in my life who instilled, supported, and enabled my thirst for knowledge.

Acknowledgements

I would like to thank scholarly funding support from the Natural Sciences and Engineering Research Council of Canada and Future Energy Systems at the University of Alberta. I would also like to acknowledge various awards from the University of Alberta, the Department of Chemical and Materials Engineering, the Graduate Student Association, and the Faculty of Graduate and Postdoctoral Studies.

I would like to thank my family and friends for their unwavering support: you believed in me even at times when I didn't believe in myself.

I would like to thank all the colleagues and friends throughout the years who enriched my graduate school experience. Thank you to Mr. Shiraz Merali and Dr. Beth Sterling Lee for your teaching support and collaboration. Thank you to Ry Karl and Tamara Kazoun for the enjoyable teaching atmosphere we created.

I would like to thank all the members of Dr. Ken Cadien's research group who I had the pleasure of collaborating with, including Dr. Alex Ma and Eric Milburn. Special thanks to Dr. Triratna Muneshwar for your advise and guidance on atomic layer deposition and to Dr. Elham Rafie Borujeny for your assistance with the deposition system.

I would like to thank the many members of Dr. Douglas G. Ivey's research group who I had the pleasure of interacting with throughout my graduate school experience. Thank you to the international scholars of Liuqin Lai, Dr. Josiel M. Costa, Yi Shen, and Maosen Zhao for providing enjoyable cultural and academic experiences. Thank you Drs. Ming Xiong and Elaheh Davari for your brief but memorable encounters. Thank you to Dr. Anqiang He for all your help with materials characterization and analysis. Thank you to Dr. Wendy Tran, Dr. Zahra Abedi, Dr. Desirée Leistenschneider, Dr. Jay He, Alexander McDougall, Ken Hou, Hang Hu, Carolina Rodriguez Baez, and Arsalan Khan for your stimulating scholarly and non-scholarly discussions, both in and out of the lab. I would also like to extend my gratitude to Arjun Dhiman, Drew Aasen, and Mark Cui for your friendship in addition to group collaboration. I truly valued each and every conversation we had. Lastly, thank you to Dr. Michael P. Clark, my mentor and collaborator for much of my graduate work. Most of my knowledge on atomic layer deposition

and Zn-air batteries is because of you, and I hope that I took your pioneering research in a fruitful direction.

I would like to extend a thanks to any other colleagues, acquaintances, or collaborators who I forgot to mention but made a positive impact on my experience as a graduate student.

Finally, I would like to thank the members of my supervisory committee: Thank you Dr. Xiaolei Wang for your time and kinds words of encouragement. Thank you Dr. Ken Cadien for sharing your vast knowledge of atomic layer deposition and microfabrication with me. I also loved your stories whenever we finished talking research. And last, but certainly not least, thank you Dr. Douglas G. Ivey for your supervision and involvement in my graduate student experience. You are an exemplary member of the scientific community, with sound judgement and reasonable compromise. Your wealth of knowledge is magnificent, and your perspective on life is aspirational. All too often during my graduate student experience I would get caught up in my own thinking, blowing everything out of proportion. But every time I left your office, I felt 1000% better than when I walked in. And for that, I am eternally grateful and happy that you were my graduate advisor.

Table of Contents

List of Tables

List of Figures

Glossary of Terms

Term	Definition
2D	2-dimensional
3D	3-dimensional
ABS	acrylonitrile butadiene styrene
ADF	annular dark field
AES	Auger electron spectroscopy
AFM	atomic force microscopy
ALD	atomic layer deposition
BET	Brunauer–Emmett–Teller
BF	bright field
BL	backing layer
CBED	convergent beam electron diffraction
CC	current collector
CF	carbon fiber
CMO	$CoMn_2O_4$
CNT	carbon nanotube
CPC	coverage per cycle
CV	cyclic voltammetry
CVD	chemical vapour deposition
$(EtCp)_2Mn$	bis(ethylcyclopentadienyl)manganese
DEZ	diethylzinc
DF	dark field
EDX	energy dispersive X-ray
EF	ethyl(biscyclopentadienyl)iron, or ethylferrocene
EMA	effective medium approximation
EV	electric vehicle
FG	forming gas
FIB	focused ion beam
f_S	surface fraction
f_V	volume fraction
FWHM	full-width half-maximum
GDL	gas diffusion layer
GPC	growth per cycle
GPE	gel polymer electrolyte
HAADF	high angle annular dark field
HCC	hollow carbon cubes
HER	hydrogen evolution reaction
HMC	hollow mesoporous carbon

HRTEM	high resolution transmission electron microscopy
η	overpotential
IUPAC	Internation Union of Pure and Applied Chemistry
LEIS	low energy ion scattering
LIB	Li-ion battery
LSV	linear sweep voltammetry
$\{M\}O_x$	elemental oxide, where {M} = Mn, Fe, Ni, Zn, and Si
MPL	microporous layer
MSE	mean-squared-error
N-CNT	nitrogen-doped carbon nanotube
Ni-MH	Ni metal hydride
OER	oxygen evolution reaction
ORR	oxygen reduction reaction
PAA	poly(acrylic acid)
PDF	powder diffraction file
PEM	proton-exchange-membrane
PLD	pulsed layer deposition
PTFE	polytetrafluoroethylene
PVD	physical vapour deposition
QCM	quartz crystal microbalance
QSDFT	quenched solid density functional theory
RMS	root-mean square
RTIL	room temperature ionic liquid
SAD	selected area diffraction
SE	spectroscopic ellipsometry
SEM	scanning electron microscopy
SHE	standard hydrogen electrode
SPM	scanning probe microscopy
SSA	specific surface area
STEM	scanning transmission electron microscopy
STM	scanning tunneling microscopy
TBF	tert-butylferrocene
TEM	transmission electron microscopy
TOFSIMS	time-of-flight secondary ion-mass spectroscopy
WDX	wavelength dispersive X-ray
XPS	X-ray photoelectron spectroscopy
XRD	X-ray diffraction
XRF	X-ray fluorescence
ZAB	Zn-air battery

1. Introduction

According to the Canadian Interagency Forest Fire Centre, nearly 12 million hectares of area in Canada were burned from wildfires in the year 2023, roughly 1.6 times more than any other year on record.[1] As well, 2023 was the hottest year in the 174-year observational record, with an average global temperature 1.45 °C above pre-industrial levels.[2,3] In fact, the 10 warmest years on record have all occurred during the last decade (2014-2023).[4] A consensus among scientists is that anthropogenic (human caused) climate change, due in large part from the emission of CO_2, is the main driving force for recent global warming events.[5] Contributions from the energy and transportation sectors comprise over 65% of the total global emissions of CO_2.[6] To decarbonize the energy sector, renewable energy sources are required. The two most prominent renewable energy sources in Alberta, wind and solar, are both intermittent and do not produce energy on-demand.[7] Energy storage serves to bridge the gap between these sporadic energy sources and the requirements of on-demand energy in the power grid.[8,9] Technologies to store renewable energy include pumped hydroelectric storage, compressed air storage, mechanical flywheels, and electrochemical batteries, among others.[10] Pumped hydroelectric storage comprises over 90% of the world's current energy storage capacity, where large reservoirs of water are pumped to higher elevation to store vast amounts of gravitational potential energy. However, appropriate geographical conditions are required to implement this technology and, in addition to long construction times and high initial costs, reduces the practicality of pumped hydroelectric storage as a universal energy storage solution.[8] Compressed air storage, where energy is stored by compressing air into underground salt caverns, is also geographically restricted.[10] Mechanical flywheels store rotational kinetic energy which provides fast response times and long service life but suffer from severe self discharge such that they cannot be used to store energy long term.[11] Electrochemical batteries, where energy is stored in chemical bonds within the battery material,[11] are easily built, compact, and scalable.[8,12] As a result, electrochemical batteries are rapidly emerging as a prominent energy storage technology.[8,13] Moreover, electrochemical batteries are the largest hurdle to electric vehicle (EV) implementation, which is currently the most popular method to decarbonize the transportation sector.[14,15] Therefore, advances in rechargeable electrochemical batteries can provide a large impact in reducing global CO_2 emissions from both the energy and transportation sectors and help suppress further progression of climate change.

Devised in 1800, the voltaic pile is the first known instance of an electrochemical battery.[16] It featured Ag and Zn metal plates sandwiched between pieces of cloth or cardboard soaked in a salt solution.[17,18] Since then, advancements in primary (discharge only) batteries lead to the development of alkaline Zn-MnO_2 batteries, which are used currently to power small electronics such as remotes, flashlights, and smoke detectors.[19] The Pb-acid battery, developed in 1859, represents one of the first successful secondary (rechargeable) electrochemical batteries.[19–22] It features Pb-based electrodes submerged in sulfuric acid with notable applications including emergency power, electric golf carts, and starting, lighting, and ignition in internal combustion engine vehicles.[8,19] The main advantages of a Pb-acid battery include low cost and good cycle life,[19] however, it has a low energy density and the use of Pb is being phased out in most industries.[19,20] For portable electronics, Ni-Cd batteries were more appropriate rechargeable batteries than Pb-acid batteries,[21–23] owing to their higher energy density and sealed construction.[19] These were replaced by Ni metal hydride (Ni-MH) batteries due to their higher energy density and an avoidance of Cd metal.[8,19,20,22] Yet, Ni-MH batteries still lacked sufficient energy and power densities for high energy requirements.[19] Researched throughout the 1960s to 1990s,[21,24] Li-ion batteries (LIBs) were first commercialized by Sony in 1991.[25] The higher energy density of LIBs can power more energy intensive devices and,[11] coupled with advancements in electronic miniaturization, is responsible for the revolution in portable electronics such as laptops and cell phones.[12,22,26–28] While they are currently the most employed secondary battery chemistry due to their high energy density and high energy efficiency,[29,30] LIBs still suffer from safety concerns and relatively high costs.[19,21,25,28] Also, their application in EVs has highlighted concerns over the availability of Li and Co resources, both of which are common components in LIBs.[30,31] Using oxygen as a component of the cell reaction, metal-air batteries can provide very high energy densities.[19,32] Zn-air batteries (ZABs) are among the most promising of the metal-air batteries,[8] with practical application as remote power sources and hearing aid batteries.[8,19] Table 1.1 compares the energy density, cycle life, efficiency, and cost of various battery chemistries.

Table 1.1. Comparison of energy density, cycle life, efficiency, and cost for different electrochemical battery chemistries. Zn-MnO_2 batteries are generally non-rechargeable and do not have a reported cycle life or energy efficiency.

Chemistry	Energy Density ($Wh\ kg^{-1}$)	Cycle Life (cycles)	Efficiency (%)	Cost ($\$USD\ kWh^{-1}$)
Zn-MnO_2[16,19]	154	-	-	15
Pb-acid[33,34]	40	2000	85	150
Ni-MH[16,34,35]	110	1000	80	200
LIB[25,33,34]	180	2500	90	1300
ZAB[21,34]	230	300	60	120

While promising for electrochemical energy storage, several phenomena limit the energy efficiency and cycle life of ZABs. The energy efficiency is hampered by large overpotentials at both the Zn and air electrodes.[36] Figure 1.1 schematically shows the voltage loss during discharge (shown in red) and the required overvoltage during recharge (shown in blue) that occurs at either electrode. The air electrode requires the largest amount of overpotential and represents the largest source of energy loss in ZABs.[8,37] As well, flooding of the electrolyte into the air electrode during extended battery cycling compromises the three phase boundary area between oxygen, electrolyte, and electrons necessary during operation,[38,39] leading to additional degradation in ZAB performance and poor cycle life.[40] The addition of electrocatalysts at the air electrode can improve the performance of ZABs and reduce energy loss.[38,39] Precious metal-based catalysts, such as Pt or RuO_2, while effective at catalyzing the oxygen reactions at the air electrode, continue to impeded practical widespread application of ZABs.[8,39] Air electrode catalysts can also be created from more abundant materials, such as non-precious metal oxides or carbon-based materials.[8,36,37,41] First row transition metals oxides have been widely studied,[36,42] and are relatively simple yet effective oxygen catalysts. Whereas Co is relatively abundant but extraction is limited,[31,43] Fe and Mn are already produced in large quantities worldwide for the steel industry.[44,45] Therefore, the use of Fe and Mn oxides as catalysts in ZABs would likely not be a socioeconomic issue, particularly since Fe and Mn are the 2nd and 8th most abundant metals in the Earth, respectively.[46] The catalytic shortcomings of one metal oxide material can be

alleviated by developing mixed transition metal oxide catalysts, which feature synergistic benefits from integrating multiple transition metal elements together.[36,37,42]

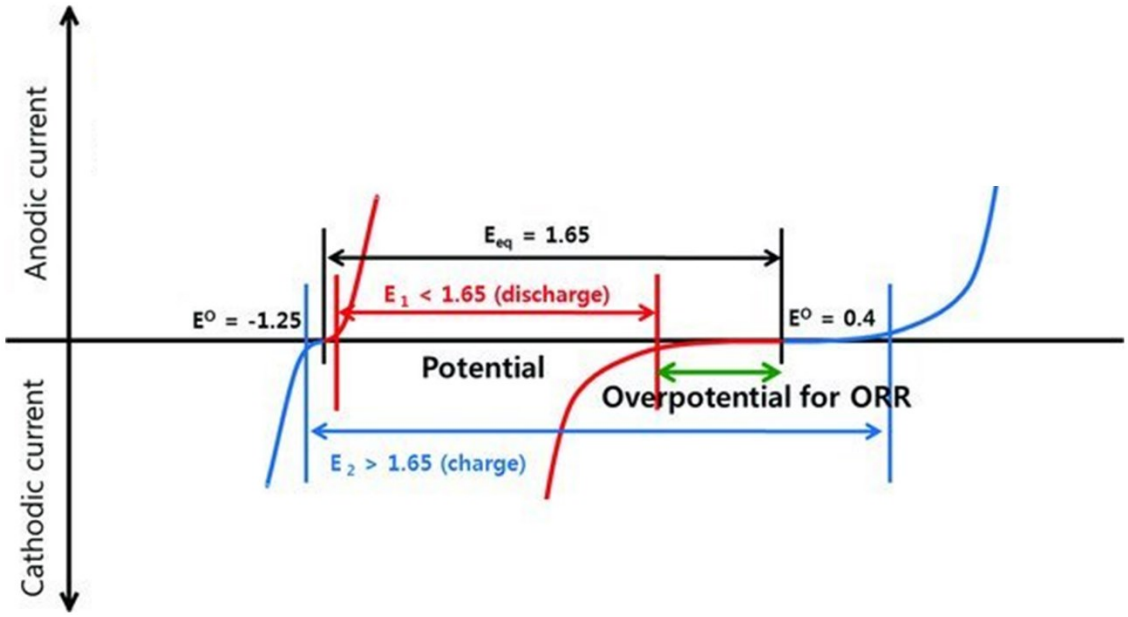

Figure 1.1. Schematic illustration of overpotentials during discharge (shown in red) and charge (shown in blue) for ZABs. The equilibrium operating voltage for a ZAB is 1.65 V, whereas the practical operating voltage is much lower or much greater during discharge or charge, respectively. The overpotential for the oxygen reaction during discharge (oxygen reduction reaction, or ORR) is highlighted by the green arrow. Adapted with permission from Ref.[38]. Copyright 2011 John Wiley and Sons.

Nanostructuring can enhance the performance of electrocatalysts through modifications in the activity of the material and by increasing the number of available active sites.[47,48] Atomic layer deposition (ALD) is a method that is ideally suited for developing nanostructured catalytic thin films on the air electrode of ZABs.[49–51] Based on alternating exposures of a precursor and reactant gas,[52] ALD produces thin films layer-by-layer at the atomic scale.[53] For ZABs, ALD can take advantage of the porous nature of the air electrode to deposit catalytic films throughout the air electrode thickness.[54] This maximizes the surface area for reaction and also enhances the three-phase boundary area required for the oxygen reactions at the air electrode. With the use of ALD supercycles,[55] mixed transition metal oxide films can be directly deposited on the air electrode of ZABs to create durable and bifunctionally active electrocatalysts.

This thesis aims to develop ALD recipes to deposit catalytically active thin films of Fe oxide (FeO_x), Mn-Fe oxide, and Zn-Mn-Fe oxide. These will be used at the air electrode of ZABs to improve the energy efficiency and cycling stability. Chapter 2 provides an overview of ZAB and ALD fundamentals as well as a review of the literature for ZAB and ALD applications of Mn, Fe, and Zn oxides. Fundamentals of the various characterization techniques employed in this thesis are also provided in Chapter 2. Chapter 3 explores ALD of FeO_x using a novel Fe precursor, with the FeO_x film characterized on a porous carbon substrate commonly employed as the air electrode in ZABs. Chapter 4 features an investigation of the FeO_x ALD film on both carbon and Si surfaces, revealing an uncharacteristic growth mode of successive island formation. Chapter 5 involves the integration of Mn oxide and FeO_x ALD processes into a single supercycle deposition, which yields bifunctionally active catalytic films for the air electrode in ZABs. Chapter 6 explores Zn-based oxide catalysts, deposited via ALD, with the aim of improving cycling stability in ZABs. In Chapter 7, the major conclusions from this work are provided along with future recommendations for ALD coatings in ZABs. Appendix A features a review on catalyst loading methods for the air electrode in ZABs, including ALD, with an emphasis on cycling stability. Appendix B discusses experimental concerns and implications when testing practical ZABs.

2. Literature Review

2.1 Electrochemically Rechargeable Zn-Air Batteries

The energy density of metal-air batteries is among the highest of the available chemistries for electrochemical batteries. Their energy density can be even higher if the weight contribution from O_2 at the air electrode is ignored, since O_2 simply exists in the ambient air and is available for reaction.[32,39] Li-air batteries have the highest theoretical energy density of any metal-air battery (11 680 Wh kg^{-1}), on par with gasoline (12 222 Wh kg^{-1}) (Figure 2.1).[56,57] However, safety issues and other shortcomings have impeded their development. Al-air, Fe-air, and Zn-air batteries are all popular choices because of their earth-abundant metal electrodes and compatibility with aqueous electrolytes, reducing safety concerns.[32,38] Zn-air batteries (ZABs) are often recognized as the most promising of these technologies, with commercial ZABs employed in hearing aids and remote power systems.[16,32,37] Yet, these are all primary ZABs, which can only be discharged. A secondary ZAB, which can be electrically recharged by reversing the electrochemical reactions within the battery, are required for energy storage applications in the power grid or as energy sources in electric vehicles (EVs).[16] The required components of a secondary ZAB include a reversible air electrode, a reversible Zn electrode, and an electrolyte.[32] Sometimes a separator is added to electrically isolate the air and Zn electrodes from each other to prevent short circuits.[36] An alternative way to effectively recharge ZABs is by way of mechanical recharging, where the spent Zn electrode is replaced with a new one and the electrolyte is refreshed, thereby resetting the cell components.[16,32] Zn metal can then be recovered from the discharged battery components at a secondary location,[16] ideally using renewable energy. A major downside to this mechanical recharging, which is akin to refuelling a conventional gas-powdered vehicle, is the requirement of a network of refueling stations for EV implementation.[58]

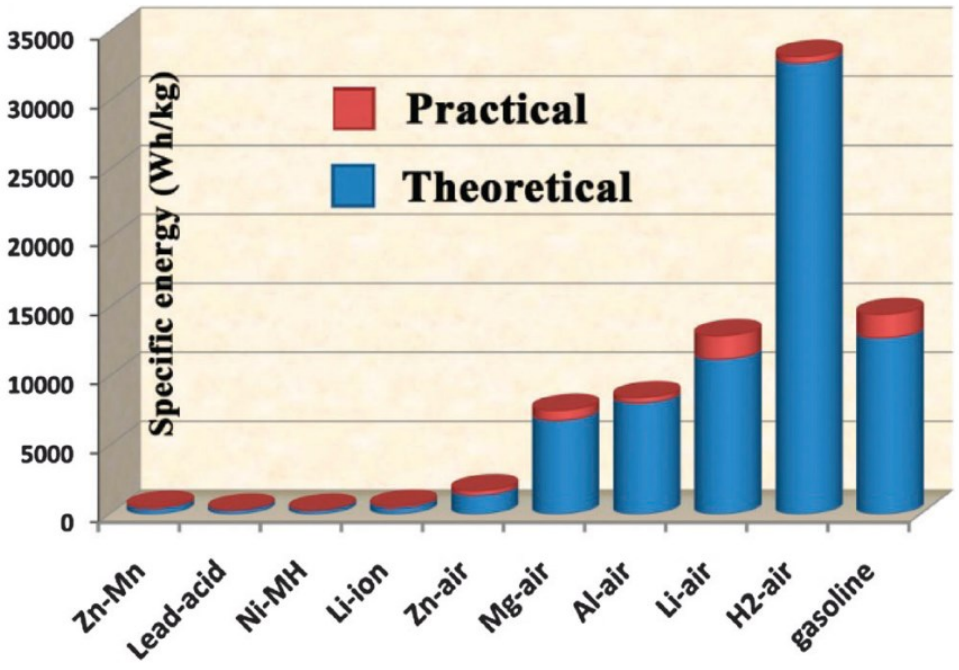

Figure 2.1. Gravimetric energy densities for some traditional battery chemistries and some promising metal-air batteries, compared with H_2-air fuel cells and gasoline. Theoretical values are calculated on the basis of thermodynamics of active materials. Reused with permission from Ref.[37]. Copyright 2011 Royal Society of Chemistry.

2.1.1 Air Electrode

The air electrode in a ZAB consists of three major components: the gas diffusion layer (GDL), the current collector, and the catalyst layer.[36,59] The requirements of the air electrode in ZABs are not so different from proton-exchange-membrane (PEM) fuel cells, so that GDLs designed for PEM fuel cells are often directly applied to ZAB applications. In fact, the commercial GDL used experimentally throughout this thesis was purchased from the Fuel Cell Store (SGL Carbon, Sigracet 39BC/39BB). When the catalyst layer is combined with the GDL and current collector, the construction is sometimes referred to as a gas diffusion electrode. The three components must be well joined to maintain mechanical strength for long-term use, while reducing interfacial electrical resistance.[36]

2.1.1.1 Gas Diffusion Layer

The GDL must be highly porous to allow exchange of O_2 gas between the cell and the outside environment, yet hydrophobic to prevent liquid electrolyte from leaking out of the cell.[32,36,38,40,60]

Hydrophobicity is usually achieved by a hydrophobic polymer coating, particularly polytetrafluoroethylene (PTFE).[32,36,40,54,60,61] Electrically conductive GDLs may also act as the current collector, so that thin, porous carbon paper or cloth, as well as metal foams, are common GDL materials.[36,37,60] A downside to carbon-based air electrodes is carbon corrosion, particularly during charging in an alkaline environment.[62] The corrosion results in a loss of surface area for electrochemical reaction, uneven current distribution on the electrode, and leakage of the electrolyte.[32,60] Stainless steel, Ti, and Ni are among the most popular metal foams for air electrodes, which exhibit improved resistance to the corrosive environment due to surface passivation layers.[32,36,60,63] Since electrically conductive GDLs are common practice, the term GDL is more commonly used to refer to a combined gas diffusion and current collector layer. This is how the term GDL is used in the remainder of this thesis. Thus, the GDL commonly serves as the support for the catalyst layer.[32,38,60] The support for the catalyst layer must have a high surface area since the process of catalysis is a surface phenomenon and increasing surface area increases the number of active catalytic sites.[37] To bridge the high surface area demands of the catalyst layer and the high porosity requirements for gas diffusion, carbon-based air electrodes feature both microporous and macroporous layers.[32,36,37,39] The macroporous layer, sometimes called the backing layer, is a carbon paper material with large pores to enable gas diffusion, while the microporous layer is a blend of graphitic carbon particles and a PTFE binder, applied to the backing layer to form a high surface area scaffolding for good catalyst distribution.[32,36,39,40,60,63,64]

The oxygen reduction reaction (ORR) necessary for ZAB discharge requires the presence of gaseous O_2, a solid electrode for electron transfer, and liquid water (Equation 2.1).[32,39,58,65] The electrochemical reaction occurs only at regions where all three phases co-exist, so the three-phase boundary area must be maximized in the air electrode.[37,54] An electrochemical catalyst improves the electron transfer steps during ORR and should also be in intimate contact with the other phases, coating as much electrode surface area as possible. Therefore, the electrolyte must absorb into the catalyst layer to create three-phase regions that make use of the catalyst. However, too much electrolyte penetration into the gas diffusion layer prevents gaseous O_2 from reaching the catalyst layer, a process known as flooding (a schematic of flooding can be found in Figure 2.2 and in Appendix A).[37,39,40,63] Flooding can lead to an increase in ohmic resistance and results in a loss of power density and efficiency, due in part to the low O_2 solubility in the

electrolyte.[39,58,61] Furthermore, the humidity of atmospheric air may lead to electrolyte evaporation or electrode flooding, and well balanced hydrophobicity and hydrophilicity can assist with water management at the air electrode.[58] Thus, the interior facing electrode is made hydrophilic to encourage electrolyte infiltration and hydroxyl ion mass transfer, while the exterior facing electrode side is coated with a hydrophobic layer to prevent excess flooding and facilitate O_2 mass transfer.[32,36,37,40,58,60]

$$O_2 + 2H_2O + 4e^- \rightarrow 4OH^- \qquad E^o_{red} = +0.401\ \text{V vs. SHE} \qquad (2.1)$$

The use of O_2 as a reactant allows for an open cell construction, so that air can naturally enter/leave the cell. However, CO_2 in the air may interact with the electrolyte, neutralizing the alkaline environment and precipitating carbonates that block the pores of the air electrode.[37,39,62] An O_2 selective membrane can be used to mitigate this issue.[37] The air electrode does not inherently contain any of the required reactants for the oxygen half-reaction and, thus, capacity is not limited by this electrode.[38] Accordingly, the air electrode should be as thin and lightweight as possible to provide ample space for the capacity limiting Zn electrode.[37,59] Furthermore, thinner electrodes reduce electrical resistance and improve gas permeability, but at the cost of poor mechanical properties.[32,58] For flexible battery designs, a thicker air electrode may be necessary to avoid brittle electrode behaviour.[32]

2.1.1.1.1 Electrocatalyst Loading on GDL

The oxygen electrocatalyst employed must be uniformly distributed onto the high surface area substrate without filling porosity.[32,36] One method of catalyst loading is to create an ink with the catalyst, adding a conductive filler and binder if necessary, and spray-coating or drop-casting the ink onto the substrate.[32,36,38,60] Polymeric binders may increase interfacial resistance and block active catalytic sites, while carbon binders are not as stable in an oxidizing or alkaline environment.[32,36] Another method of catalyst loading is to directly synthesize the electrocatalyst on the porous substrate.[36,39] Electrodeposition, hydrothermal methods, pyrolysis techniques, and chemical vapour deposition (CVD) are common means of synthesis and electrodes with directly-integrated catalysts generally perform better in laboratory tests.[32,36] Lastly, a hybrid method of loading catalysts onto the air electrode substrate has been identified. In hybrid loading techniques, catalyst particles are synthesized on conductive nanomaterials and subsequently introduced into the GDL. While the method is technically indirect, since the GDL is not the

catalyst substrate, the integration of the catalyst loaded nanomaterial into the GDL is effective and thorough for hybrid methods, leading to similar benefits as direct deposition methods such as good adhesion and excellent catalyst distribution throughout the thickness of the GDL. A review of indirect, direct, and hybrid loading techniques employed in the ZAB literature, particularly as it pertains to cycling stability, has been recently published in *Journal of Physics: Energy* and a version can also be found in Appendix A.

Since the GDL must be gas permeable for O_2 exchange between the cell and exterior environment, a gas-based deposition technique would be suitable for loading catalyst material throughout the GDL structure. Sufficient loading of catalyst material deep within the microporous layer of GDL is important to reduce the impact of flooding and ensure catalytic reaction sites are available for the three-phase reaction of ORR (Figure 2.2).[54] While CVD is a well known example of vapour-based deposition, the chemical reactions that yield film growth occur in both the vapour phase and on the substrate surface.[66] A specialized form of CVD known as atomic layer deposition (ALD) isolates only surface-based chemical reactions to grow coatings, eliminating gas-phase reactions or thermal decomposition of precursors. As a result, the conformality, or step-coverage, of coatings via ALD is superior to traditional CVD.[66] Thus, ALD is ideally suited for high aspect ratio substrates, such as the high surface area microporous layer of GDL, and maximizes the surface area of the deposited catalyst film (Figure 2.2). The technique of ALD is reviewed in Section 2.2.

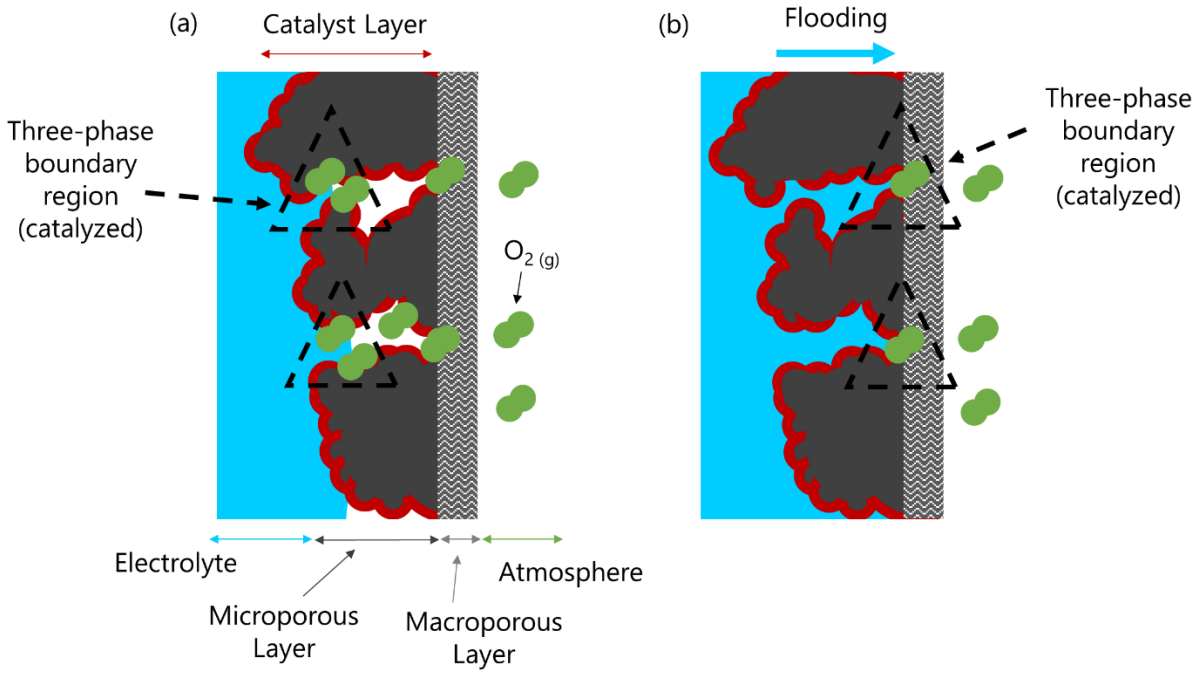

Figure 2.2. (a) Illustration of a carbon paper-based GDL substrate with an ALD coating as the catalyst layer, which maximizes the surface area of the deposited catalyst. (b) During flooding of the air electrode, an ALD coating that coats the entire microporous layer ensures that the migrated three phase region is still catalyzed.

When concerned with bifunctional air electrodes, the requirements of the charge and discharge reactions differ and often do not occur at the same location within the air electrode. For example, ORR during discharge requires a three-phase boundary area which includes O_2, accessible via the outside environment. Thus, ORR is likely to occur at regions closer to the air side of the GDL, where the electrode material is mildly hydrophobic to ensure a supply of gaseous O_2 reactant. The oxygen evolution reaction (OER; reverse direction of Equation 2.1) during recharge, on the other hand, is a two-phase reaction requiring only the liquid electrolyte and current collector. Therefore, OER is more likely to occur at regions closer to the electrolyte side of GDL, which is more hydrophilic and facilitates some degree of flooding to increase the two-phase area for reaction.[54,61,62] A multilayered structure for the oxygen reaction catalysts, with an ORR active catalyst at the air side of GDL and an OER active catalyst at the electrolyte side of GDL, may benefit bifunctional performance.[36,40,67] A layered catalyst coating on GDL is explored in Chapter 5.

2.1.1.2 Oxygen Electrochemistry

During ZAB discharge in an alkaline electrolyte, the Zn electrode reaction consumes hydroxide ions to form zincate ions and, eventually, ZnO.[36] To compensate for this, and to balance the overall cell reaction so that only a metal oxide is produced, hydroxide ions must be created by the oxygen discharge reaction at the air electrode (Equation 2.1).[65] However, the high strength of the O=O double bond in O_2 impedes the direct four-electron process shown in Equation 2.1.[58,65,68] Accordingly, a partial reduction of O_2 occurs for the two-electron process, illustrated in Equation 2.2, yielding peroxide.[69] Unlike hydrogen peroxide (H_2O_2), the peroxide ion (HO_2^-) is stable in high pH environments because it of its pKa value of 11.6.[70] The Henderson-Hasselback equation dictates that at a pH above the pKa value, the conjugate base is found in a much greater concentration.[71] Peroxide may then undergo further reduction as outlined by Equation 2.3, or a dissociation reaction, as shown in Equation 2.4.[65,69] Either way, four hydroxide ions are created to balance the overall metal-air reaction, similar to Equation 2.1.

$$O_2 + 2H_2O + 4e^- \rightarrow 4OH^- \qquad E^o_{red} = +0.401\ \text{V vs. SHE} \qquad (2.1)$$

$$O_2 + H_2O + 2e^- \rightarrow HO_2^- + OH^- \qquad E^o_{red} = -0.076\ \text{V vs. SHE} \qquad (2.2)$$

$$HO_2^- + H_2O + 2e^- \rightarrow 3OH^- \qquad E^o_{red} = +0.878\ \text{V vs. SHE} \qquad (2.3)$$

$$2HO_2^- \rightarrow 2OH^- + O_2 \qquad (2.4)$$

Note that Equations 2.2 and 2.3 combined are equivalent to Equation 2.1. Half cell potentials are not directly additive. Calculation of the combined half cell potential requires calculating the Gibbs free energies of each half reaction since electrons are present as a reactant in both half cell reactions.[72,73] Equation 2.2 and half of Equation 2.4 combined also yield the same chemical reaction as Equation 2.1 but, without the secondary electron transfer step (Equation 2.3), they are not electrochemically equivalent reactions. Since these two-electron transfer processes may appear to be a four-electron process overall, they have been dubbed serial 2 x $2e^-$ pathways. Particularly on surfaces that catalytically increase the peroxide decomposition rate, differentiation between the four-electron and the serial 2 x $2e^-$ pathway is nearly impossible.[37,68] The higher energy efficiency of the four-electron pathway makes it a much more desirable outcome, in addition to the fact that a peroxide intermediate is known to be corrosive towards carbon electrodes.[36,37] However, both reaction pathways usually occur simultaneously, with the

fraction of each dependent on the catalytic surface.[37] It has been established that the four-electron pathway dominates on noble metal surfaces, especially Pt, and that the two-electron pathway is more abundant on carbonaceous materials.[37,39,62,69] Transition metals and their oxides are speculated to have a mixture of both pathways, which is highly dependent on their crystal structure, composition, and electronic structure.[37,39]

When it is time to recharge a ZAB, the Zn and oxygen reactions run in reverse. A peroxide intermediate appears only during the discharge reaction of oxygen reduction and, thus, oxygen evolution during ZAB recharge does not occur via a serial 2 x $2e^-$ pathway.[65] Accordingly, the reverse of the direct four-electron pathway (reverse direction in Equation 2.1) is understood to represent OER.

2.1.1.2.1 Electrocatalysts

The net energy difference between a reaction's products and reactants, the free energy of reaction as it is known, determines whether the forward or reverse direction is thermodynamically favoured. To create the products of a reaction, the reactants must undergo electronic and configuration changes within and between species. This process occurs via a high energy, thermodynamically unstable, transition state. If the reactants have insufficient energy to create this transition state, the reactant complex dissolves back into the original reactants. However, if the reactants have sufficient energy to obtain the transition state, then the thermodynamically preferred outcome is for this transient state to separate into two new complexes, known as the products. This is, of course, assuming the reaction is spontaneous in the forward direction. The energy minimum for this process is called the activation energy.[74] An analogy for the process is the movement of a interstitial atom in a crystal lattice. To move from one interstitial site into a neighboring one, the interstitial atom must cross between two atoms bound together in the lattice. This bond can be modeled as being a spring that connects both lattice atoms. The interstitial atom must push the two lattice atoms away from each other to make enough room for itself to travel across. Once the interstitial atom is across, the two lattice atoms return to their original position and, in the case of spontaneous reactions, the overall energy of the system has been reduced. The energy necessary for the interstitial atom to extend the spring and push the lattice atoms apart is the activation energy for the process.

The role of a catalyst is to provide a surface for less energy intensive intermediates to form, each of which have an activation barrier lower than that of the original transition state. A sequence of these short-lived intermediates will eventually result in the same products as the original reaction pathway. In this case, the largest energy barrier of all the intermediates will determine the rate of reaction and is known as the rate-determining step.[74] A visualization of catalysis is shown in Figure 2.3, with two intermediates in this example.

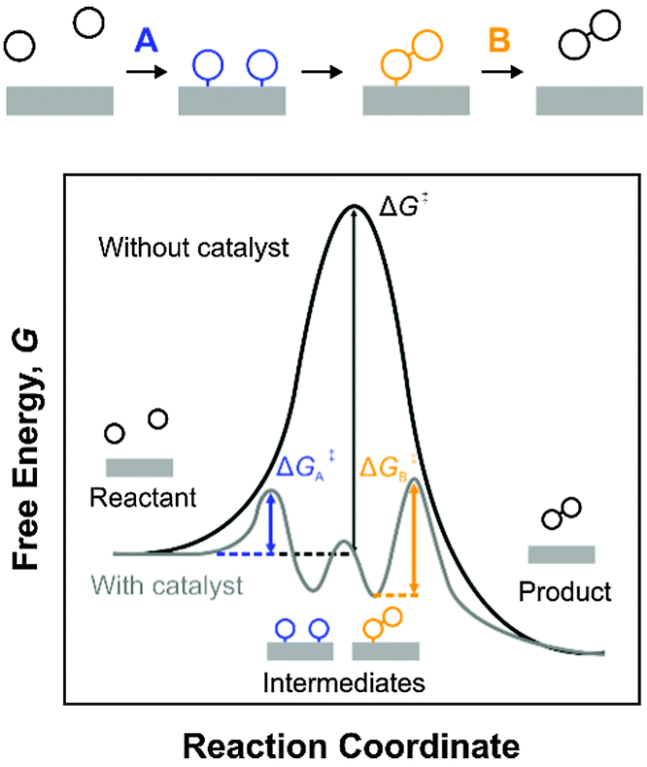

Figure 2.3. Illustration of the free energy profile along a reaction process. $\Delta G^{\ddagger}$ is the activation barrier without a catalyst, $\Delta G_A^{\ddagger}$ is the activation energy for the formation of the first intermediate (process A), and $\Delta G_B^{\ddagger}$ is the activation energy for the conversion of the second intermediate into the product (process B). Reused with permission from Ref.[74]. Copyright 2015 Royal Society of Chemistry.

One of the biggest shortcomings for ZABs is the slow reaction kinetics at the air electrode and the resultant low energy efficiency. Catalysts, however, can be incorporated to facilitate the oxygen reactions and improve the performance of ZABs. Catalysts for the discharge reaction (forward direction of Equation 2.1) are, unfortunately, often not applicable as catalysts for the recharge reaction (reverse direction of Equation 2.1). The quest for a bifunctional oxygen

catalyst, active towards both ORR and OER, is a key research area in ZABs and is the main focus of this thesis.[39]

Using density functional theory, Wang and Balbuena calculated that Pt has a higher potential to catalyze ORR than any other individual metal.[75] As well, it is known that ORR on a Pt surface occurs almost exclusively via the favorable four-electron process.[76] Therefore, Pt is widely regarded as the best electrocatalyst for ORR and represents the benchmark for comparison for all other experimental catalysts.[37] However, Pt's widespread use has been impeded by high cost and scarcity.[68] Furthermore, although Pt is praised for its ORR activity, when subjected to OER, a stable oxide layer forms and its resulting OER activity is poor.[58,62] The catalytic material of choice for OER lies in periodic groups left of Pt, *i.e.*, Ru and Ir or specifically their oxides. These precious metal oxides have been established as highly OER active and display good electrical conductivity.[77] Similar to Pt, however, Ru and Ir oxides are not good bifunctional catalysts, demonstrating very little ORR activity.[77] However, combining both Pt and RuO_2 can create a composite electrocatalyst with both ORR active material (Pt) and OER active material (RuO_2). In principle, the materials would work together to yield a bifunctional catalyst, capable of catalyzing both ORR and OER in a ZAB.[78] Unfortunately, a lack material compatibility between the two catalysts prevents the development of an effective or reliable composite catalyst.[32] In addition, since they are precious metals, high costs deter their widespread use and more affordable, earth-abundant materials are being sought as bifunctional oxygen catalysts.[79]

Carbon-based materials can be found in a variety of different chemistries or morphologies including graphene, mesoporous carbon, quantum dots, and carbon nanotubes, in addition to the typical carbon black.[39,58] The main factors in catalytic activity are surface functionality and surface area.[39] Mesoporous/microporous carbon is favorable over standard carbon black because of the increased number of active surface sites and improved mass transport.[39] Carbon nanotubes and graphene are an even larger improvement in terms of ORR performance because of their enhanced surface area and high electrical conductivity.[32] Nonetheless, pristine carbon materials have inherently poor ORR performance, with a notable two-electron pathway. However, chemical modification of the surface, usually via heteroatom doping, can improve ORR activity.[58] The most common addition is nitrogen, which yields pyrrolic, pyridinic and graphitic C-N bonds that increase the number of active catalytic sites.[39] Unfortunately, carbon-based

catalysts are still fairly inactive for OER and experience carbon corrosion during the high oxidative potentials of OER.[32]

2.1.1.2.1.1 Single Metal Transition Metal Oxides

The variety of oxidation states and crystal structures for Mn oxide (MnO_x) makes it a good candidate material for oxygen reaction catalysis.[36,58] The more commonly found chemistries of MnO_x include MnO, Mn_3O_4, Mn_2O_3 and MnO_2, corresponding to oxidation states of +2, +2/+3, +3, and +4, respectively.[37] Furthermore, MnO_2 can exist in five crystal structures, known as α, β, γ, δ, and λ; most reports consider α-MnO_2 as the most active towards ORR.[32,37,39] At the same time, this plethora of different MnO_x structures complicates the understanding of the catalytic mechanism during ORR or OER. MnO_x has been found to be highly active towards peroxide decomposition and/or reduction, making it increasingly difficult to distinguish the true catalytic mechanism.[37] Therefore, for ORR, both the direct four-electron and serial 2 x $2e^-$ pathways have been proposed for MnO_x.[37] Nonetheless, redox transitions between the different valence states occurring in MnO_x are often cited as a key component of the reduction process.[37]

There have been a handful of reports on Fe containing catalysts devoted to ORR; most of them utilize a nitrogen-doped nanostructured carbon support that contributes to much of the ORR activity.[80–85] On the other hand, the OER ability of Fe oxide (FeO_x) has been scarcely studied.[42] Despite this, many high performing OER catalysts employ Fe to some degree, suggesting that Fe may improve a catalyst's OER performance.[86–89] A study by Smith *et al.* concluded that while FeO_x is a poor OER catalyst, the addition of Fe into mixed metal oxides stabilizes higher oxidation states and results in the improvement of overall catalytic ability.[90] Scarr briefly investigated OER on an Fe surface but found no significant advantage or disadvantage over Ni or Pt.[91] Lyons and Brandon also investigated OER on FeO_x surfaces, but found them inferior to Co or Ni counterparts.[92] A review by Osgood *et al.* interpreted these last two reports as an illustration that FeO_x's inferior activity could be structurally based and that appropriate synthesis could develop an FeO_x that performs on par with other better known OER catalysts.[42]

There are four known crystallographic polymorphs of Fe(III) oxide: α-Fe_2O_3 (hematite), β-Fe_2O_3, γ-Fe_2O_3 (maghemite), and ε-Fe_2O_3. α-Fe_2O_3 is the most thermodynamically stable phase, to which all other phases eventually convert at elevated temperature.[93] The magnetic behaviour of γ-Fe_2O_3 and ε-Fe_2O_3 has been well studied for their superparamagnetism and high room-

temperature coercivity, respectively.[93] α-Fe_2O_3 has been applied recently as a photoanode for solar water splitting,[94] while β-Fe_2O_3 is an uncommon phase without any notable applications.[93] The catalytic ability of different FeO_x phases for ORR and OER has only recently been explored. In one study, Kwong *et al.* report that γ-Fe_2O_3 exhibits appreciable OER activity, while α-Fe_2O_3 does not.[95] Karunagaran *et al.* examined the ORR performance of α-Fe_2O_3 and γ-Fe_2O_3, in addition to Fe_3O_4 (magnetite) and α-FeOOH (goethite). They concluded that the ferrimagnetic crystal phases of γ-Fe_2O_3 and Fe_3O_4 exhibit superior ORR performance over the anti-ferrimagnetic phases of α-Fe_2O_3 and α-FeOOH. The authors attribute the improved ORR performance of the ferrimagnetic phases to their inverse spinel structure, magnetic properties, and higher electrical conductivity.[96] In another study, Wan *et al.* synthesized a mixed α-Fe_2O_3/Fe_3O_4 composite through controlled partial reduction of α-Fe_2O_3, which exhibited superior ORR performance compared to either FeO_x phase used separately.[97]

2.1.1.2.1.2 Mixed Transition Metal Oxides

When doping Mn, Co, and Cu into Fe_3O_4, Zhu *et al.* found that Mn provided the largest ORR improvement.[98] Zhu *et al.* did not explore OER performance; however, it has been shown by others that combining multiple transition metals or their oxides enables the mixing of both ORR and OER active sites to yield bifunctional activity.[36,37,99,100] In one such report, $MnFe_2O_4$/Fe nanoparticles were prepared onto nitrogen-doped mesoporous hollow carbon nanospheres. This material exhibited extraordinarily good bifunctional performance, on par with Pt and RuO_2 for ORR and OER, respectively.[101] Another report found that transition metal-based trimetallic oxides provided improvements in OER activity compared with bimetallic oxides, with comparable ORR activity. Furthermore, these trimetallic oxides exhibited excellent cycling stability in ZABs.[102] Low amounts of Fe doping (~ 3 at% Fe) in MnO_x nanorods was found to be beneficial in terms of both ORR and OER activity, with an overall bifunctional catalyst that was stable throughout 200 min of charge-discharge cycling in an assembled ZAB.[103]

While not always considered a transition metal,[104] Zn has also been added to transition metal oxide catalysts to provide improvements in catalytic activity. As a bifunctional catalyst, $ZnCo_2O_4$ was employed in ZABs, often supported onto nanostructured carbon, with ORR and OER performance comparable to precious metal benchmarks.[105–108] It was reported that the addition of Zn promotes higher oxidation states for the other transition metals, thereby improving OER

performance.[105,109] This has been demonstrated by a number of studies on the OER capabilities of $ZnCo_2O_4$.[110–112] Furthermore, Aasen *et al.* studied the addition of Zn into bimetallic and trimetallic oxides and concluded that Zn promoted higher oxidation states for the other metallic components, which for the most part, resulted in improved ORR and OER performance.[109] In general, the ability of transition metals to form multiple oxidation states improves their stability, particularly as bifunctional catalysts, because they can more easily tolerate the alternating conditions of oxidation and reduction at the air electrode.[42]

2.1.2 Zn Electrode

The most commonly used metal for battery electrodes is Zn, due in part to its abundance and low resistivity, and because it is inexpensive and non-toxic.[32,39,58,113,114] Other favourable qualities of Zn include being the most relatively stable electropositive metal without significant corrosion in aqueous and alkaline media and good electrochemical reversibility in alkaline environments.[58,113] Since ZABs derive O_2 from the exterior environment, Zn plays a significant role in the total energy capacity.[32,36] The ideal Zn electrode would have a long cycle life with high capacity retention over many charge and discharge cycles, have a high Zn utilization and high Coulombic efficiency, and be made such that there is a large proportion of usable active Zn material.[32,36] There is, however, performance loss at the Zn electrode, which is attributed to any or all of the following: shape change, passivation, and hydrogen evolution.[32,36,115,116] While several different strategies can be employed to combat each of these performance reducing effects,[36] the use of a circulating electrolyte has been found to be very beneficial in alleviating dendrites, shape change, and passivation.[32,113,115,117] A flowing electrolyte does, however, complicate overall battery design.[113]

The anodic reaction of a Zn electrode is useful in many energy storage system that utilize Zn, such as Ni-Zn, Ag-Zn, and ZABs.[118,119] Despite the use of a Zn anode in alkaline environments dating back to the 1930s,[19] the precise reaction mechanism of Zn dissolution in an alkaline electrolyte has still not been conclusively determined. A major confounding issue is the effect of supersaturation. In a report dating back to 1955, it was established that the concentration of zincate species in alkaline solutions, arising from oxidation of a Zn electrode, can exceed that of a saturated solution prepared by dissolving ZnO in concentrated KOH.[120] Furthermore, the

supersaturation concentration is time-dependent, where additional oxidation of the Zn electrode can further supersaturate the electrolyte.[121]

One understanding of the Zn electrode during battery discharge is represented by Equations 2.5-2.7.[73,120,122,123] First, the solid Zn electrode reacts with hydroxide ions, the highly concentrated species present in the electrolyte, to create solid Zn hydroxide, $Zn(OH)_2$. The Zn hydroxide then reacts further with hydroxide ions to yield zincate, $Zn(OH)_4^{2-}$, which acts as the main Zn species dissolved in solution. After prolonged battery discharge, the electrolyte will become saturated with zincate ions and ZnO will precipitate, generally nucleating on the surface of the Zn electrode.[32]

$$Zn + 2OH^- \rightarrow Zn(OH)_2 + 2e^- \qquad E^o_{red} = -1.249\ \text{V vs. SHE} \tag{2.5}$$

$$Zn(OH)_2 + 2OH^- \rightarrow Zn(OH)_4^{2-} \tag{2.6}$$

$$Zn(OH)_4^{2-} \rightarrow ZnO + H_2O + 2OH^- \tag{2.7}$$

A popular alternative to the two step formation of zincate (Equations 2.5 and 2.6) is the direct formation of the zincate species in a one step reaction (Equation 2.8).[73,120] Moreover, the direct formation of ZnO itself, without a zincate intermediate (Equation 2.9), has also been proposed by some researchers.[32,73,124]

$$Zn + 4OH^- \rightarrow Zn(OH)_4^{2-} + 2e^- \qquad E^o_{red} = -1.199\ \text{V vs. SHE} \tag{2.8}$$

$$Zn + 2OH^- \rightarrow ZnO + H_2O + 2e^- \qquad E^o_{red} = -1.260\ \text{V vs. SHE} \tag{2.9}$$

Note that in combination with the ZnO formation reaction (Equation 2.7), all three different Zn electrode processes (Equations 2.5-2.7, Equations 2.8 and 2.7, or Equation 2.9) have the same net total chemical reaction: 1 mole of metallic Zn reacts with 2 moles of hydroxide ions to yield 1 mole of ZnO, 1 mole of H_2O, and 2 moles of electrons (*i.e.*, Equation 2.9). However, the electrochemical half cell potential of these three different Zn electrode processes are not exactly the same. The 3-step formation of ZnO (Equations 2.5-2.7) provides a half cell potential of -1.249 V vs. SHE, the 2-step formation of ZnO (Equations 2.8 and 2.7) provides a half cell potential of -1.199 V vs. SHE, and the 1-step formation of ZnO (Equation 2.9) provides a half cell potential of -1.260 V vs. SHE. Thus, the true potential of the Zn electrode in an alkaline environment has not been unanimously decided. The spontaneous ZnO formation step (Equation

2.7) has been disputed by some researchers who claim that the decomposition reaction is second order vs. the supersaturating species, which is incompatible with the one-step process of Equation 2.7.[125] In fact, a whole range of theories from multiple researchers throughout the 20th century have been proposed to explain the behaviour of a Zn electrode in an alkaline environment.[118,126–132] For the purposes of this thesis, however, the reaction scheme proposed by Equations 2.5-2.7 is accepted as the Zn electrode process. Thus, the electrode potential of the Zn electrode in a ZAB is reported as -1.249 V vs. SHE in this work.

The high solubility of Zn ions in the electrolyte is thought to enable concentration gradients in the proximity of the Zn electrode so that during recharge, non-uniform re-deposition of Zn occurs.[32,36,58,113,115,117] This uneven Zn deposition can cause densification of the electrode and pore collapse, but may also result in dendritic growth.[32,36] Dendrites are tree-like structures that project from the Zn electrode and may grow long enough to make electrical contact between both electrodes, short circuiting the cell and causing failure.[32,36,61,115,117] Furthermore, the high zincate concentrations in the electrolyte can cause spontaneously precipitation of ZnO onto the Zn electrode.[32,36,115] This insulating layer of ZnO increases the resistance of the electrode and may block access to active sites on the Zn electrode and prevent species migration.[32,38,115,133] A common strategy to avoid spontaneous Zn electrode dissolution is to purposefully saturate the electrolyte with dissolved ZnO.[32,36] The goal is to precipitate ZnO very early during discharge and avoid zincate migration.

In the pH 14 electrolyte typically utilized in ZABs, the hydrogen evolution reaction (HER; Equation 2.10) can occur.[65] The potential of HER (-0.828 V vs. SHE) is more electropositive than the Zn electrode (-1.249 V vs. SHE) and results in spontaneous Zn dissolution to enable HER at the Zn electrode. This phenomenon is known as Zn self-discharge or Zn corrosion and is demonstrated by Equation 2.11.[32,36,38,114] The resulting H_2 gas can create additional resistance in the electrolyte and electrode interface, produce convection in the electrolyte, and may rupture sealed batteries.[38,39,115,133,134] As well, when recharging, electrons will be lost to HER as opposed to Zn reduction, lowering the Coulombic efficiency of the cell.[32,36,115]

$$2H_2O + 2e^- \rightarrow H_2 + 2OH^- \qquad E^o_{red} = -0.828\ \text{V vs. SHE} \qquad (2.10)$$

$$Zn + H_2O \rightarrow H_2 + ZnO \qquad (2.11)$$

2.1.3 Electrolyte

Aqueous electrolytes are the most prominent ionic conducting media for ZABs, due in part to their non-flammability, low toxicity, low cost, and high ionic conductivity.[32,135] Alkaline electrolytes are preferred over acidic or neutral electrolytes because they reduce the overpotential at the Zn electrode, have a high solubility of Zn species, and provide a wide range of stable catalysts for the air electrode.[32,36,135] KOH is widely regarded as the best alkaline salt for aqueous electrolytes because of faster O_2 diffusion, a larger temperature window, and higher ionic conductivity compared with other hydroxide salts such as NaOH or LiOH.[32,36,39,58,135,136] The concentration of KOH electrolytes is usually within the range of 6-7 M (26-30 wt%), since this composition exhibits the best ionic conductivity to ensure sufficient hydroxide ion transport through a separator.[32,38,39,58,113,136–138] One major downfall of alkaline electrolytes is the precipitation of carbonates in the air electrode as a result of reactions with CO_2.[32,36,62,135,139] Precipitation of K_2CO_3, according to Equations 2.12-2.14, blocks the pores of the air electrode, reducing O_2 access to catalytic sites.[32,37,39,62,135,138] The corrosion of carbon air electrodes in highly alkaline electrolytes can also be a source of carbonates, as predicted by Equation 2.15.[39,65] The best strategies to avoid carbonates is to use purified air, have an O_2 selective membrane, or employ CO_2 absorbents such as soda lime.[39,139]

$$CO_2 + OH^- \rightarrow HCO_3^- \tag{2.12}$$

$$HCO_3^- + OH^- \rightarrow CO_3^{2-} + H_2O \tag{2.13}$$

$$CO_3^{2-} + 2K^+ \rightarrow K_2CO_3 \tag{2.14}$$

$$C + 6OH^- \rightarrow CO_3^{2-} + 3H_2O + 4e^- \qquad E^o_{red} = -0.765\ \text{V vs. SHE} \tag{2.15}$$

Flexible battery designs necessitate the use of solid-state electrolytes, such as gel polymer electrolytes (GPEs). These are created when a solvent is used to swell polymer chains, which retain the solvent molecules and ions. Alkaline gel electrolytes may be created by using aqueous alkaline solvents, such as KOH dissolved in water.[32,36,136,140] Poly(acrylic acid) (PAA) has shown great promise as a GPE for ZABs.[141] Compared with other potential GPEs, PAA exhibits some of the highest conductivities, which approach the values associated with an aqueous electrolyte.[136,142]

Disadvantages to aqueous systems include evaporation and moisture control, a narrow electrochemical stability window, low thermodynamic stability of the Zn electrode, and short shelf life.[135] Organic electrolytes, which are non-aqueous mixtures of organic molecules and solvents that are ionically conductive, are attractive alternatives to aqueous electrolytes because the Zn electrode does not corrode.[135,143] On the other hand, the performance at the air electrode is not as good in organic electrolytes.[135] Organic electrolytes avoid HER, dendrite formation, water management, and carbonate precipitation; they can operate in a higher temperature window, and have a large electrochemical window.[135] Their main limitations include volatility, flammability, and toxicity.[135,144] Organic electrolytes have been well studied for Li-based battery systems, but have only received limited attention for Zn-based systems.[135]

An alternative category of non-aqueous electrolytes are room temperature ionic liquids (RTILs).[135] Composed exclusively of ions, these salts have melting temperatures at or below room temperature.[32,36,116,135,136,145] Large, complex organic or inorganic cations and anions form together to yield a RTIL.[135] The wide selection of cation and anion choices makes RTILs very diverse, with tunable characteristics.[136,144,146] RTILs are attractive for their low vapour pressure, high thermal stability, relatively high ionic conductivity compared to other non-aqueous options, and wide electrochemical stability window.[32,36,115,116,135,144] Furthermore, the Zn electrode is generally free of dendrites and Zn corrosion is suppressed. Overall, however, the high viscosity and low conductivity of RTILs result in poor reaction kinetics at both the Zn and air electrode.[36,39,58] [32,136] The higher temperature stability may enable operation at elevated temperatures, which may lead to better reaction kinetics.[32] Other disadvantages of ILs include the necessity for high purity, environmentally harmful synthesis, and high cost.[36,135,146] Another class of ionic liquids are molten salts, particularly molten carbonates, which operate at much higher temperatures than other electrolytes. One example is $Li_{0.87}Na_{0.63}K_{0.50}CO_3$ combined with KOH at 550 °C.[147] In general, elevated temperatures require additional insulation, reducing gravimetric performance, and cause corrosion of the air electrode.[61] Despite these consequences, molten salt electrolytes avoid carbonate precipitation, dendrite formation, and HER. Additionally, the elevated temperature accelerates reaction kinetics and allows for the use of established non-precious metal catalysts based on Ni or Fe.[39,61]

2.1.4 Separator

A separator acts to reduce mixing of the electrolyte near the anode with the electrolyte near the cathode, while still allowing the transfer of required current carrying ions.[39,148,149] Furthermore, a separator prevents electrical contact between the anode and cathode that would otherwise result in a cell short circuit. In this sense, the separator must be strong enough to resist penetration by growing Zn dendrites.[32,36,39,58] In addition, the pore size of the separator should prevent passage of zincate ions. Most commercial separators are designed for Li-ion cells and have pore sizes large enough for zincate transfer.[32,36,38,39,58,149] This causes a saturation of zincate at the air electrode, which precipitates ZnO onto the air electrode and reduces battery performance.[32,148–150] ZABs typically employ separators made from non-woven polymers such as polyethylene, polypropylene, or polyamide.[36,39,58]

2.1.5 ZAB Cell Design

The air electrode is exposed to a wide potential range due to the overpotentials associated with the oxygen reactions. Combined with the highly alkaline electrolyte, the air electrode and all its components must be stable in this environment to maintain long cycle life.[32,36,38] Some reports have used decoupled air electrodes, where OER occurs on an independent electrode from the ORR electrode.[40,62,86,113,151,152] The ORR electrode is not exposed to the oxidizing conditions of OER, leading to improved cycling stability; however, this approach complicates battery design and reduces energy and power density.[32,40,60,62,136] Another variable in ZAB cell design is whether the air electrode is horizontal or vertical with respect to the electrolyte and Zn electrode. For example, a vertical arrangement for the air electrode, where the electrolyte is positioned horizontally beside the electrode, imposes a hydrostatic pressure on the GDL. Even with a hydrophobic treatment, this pressure can accelerate the flooding of the air electrode and even potentially lead to physical rupture of the carbon paper electrode.[151] A horizontal arrangement for the air electrode, where the electrolyte sits vertically below the electrode, does not experience the hydrostatic pressure and may improve cycle life and durability of the air electrode.[151,153] On the other hand, evaporation and other sources of electrolyte loss can cause a break in ionic conduction between the air and Zn electrodes, terminating battery operation entirely.[32] This critical error in design means that most ZABs in the literature are of the vertical arrangement, including the cells employed in this work (refer to Appendix B for a schematic of the custom

made ZAB cells in this work). Note that the cell design(s) employed in this work have a large distance between the air and Zn electrodes such that short circuits from Zn dendrite growth are avoided and, thus, a separator is unnecessary and not included.[151]

The carbon paper GDL, while conductive on its own, is often paired with a metal or metal foam current collector because the stiffness of carbon paper results in breakage and loss of electrical contact when directly connected to electrochemical workstations. This additional current collector introduces complications to the cell design, one of which is interference of the metal oxide layer towards the catalysis of ORR/OER. An analysis of this issue, in addition to corrosion of the Zn electrode due to environmental conditions, is presented in Appendix B.

2.2 Atomic Layer Deposition

Self-limiting solid-vapour chemical reactions are the hallmark of a growth mechanism known as ALD.[154–156] This sequential deposition technique is well known for its extraordinary conformality and uniformity, with digital control of angstrom-level thicknesses.[155] The use of vapour phase reactants allows for conformal coatings of even the most complex substrates.[156] While ALD is used extensively in the semiconductor industry for conformal pinhole-free thin films, other applications of ALD include organic light-emitting diode displays, corrosion-resistance coatings, and nanostructured catalysts.[52,156]

2.2.1 Growth Mechanism

The growth of a monolayer in ALD occurs over four steps (Figure 2.4): precursor dose, purge, reactant dose, and a second purge. The first step introduces the vapours of a compound featuring a metal cation, which chemically adsorbs to the surface of the substrate, typically through an exchange reaction with surface groups such as hydroxide.[52] The purge step removes excess unreacted precursor vapours as well as the by-products of adsorption. The reactant, often water vapour or plasma radicals, is then introduced to the surface to react with the adsorbed precursors.[52] The goal is to remove the non-metallic ligands from the surface so that the resulting film is a compound formed from the metal cation of the precursor and the anion of the reactant.[157,158] Finally, a second purge step removes excess reactant and by-products and prevents gas-phase reactions between the precursor and reactant to avoid non-conformal CVD behaviour.[52,159]

The four steps are repeated until a desired thickness is reached. Since surface reactions are necessary for growth, only one monolayer of material can be deposited per cycle.[53,154,156,159] This enables ALD to produce very conformal and pinhole-free surface films.[156] Complete monolayer formation is rarely achievable, however, since steric hindrance restricts precursor adsorption on all areas of the surface and because not all surface sites are reactive to chemisorption with the precursor.[160,161] The increase in thickness of an ALD film accrued over one cycle is dubbed growth per cycle, or GPC. For a saturating mechanism, the GPC plateaus to a constant value while increasing dose or purging time (Figure 2.4). With GPC values generally on the order of 1 Å cycle^{-1}, one of ALD's limitations is the slow deposition rate compared with other thin film techniques.[52,160]

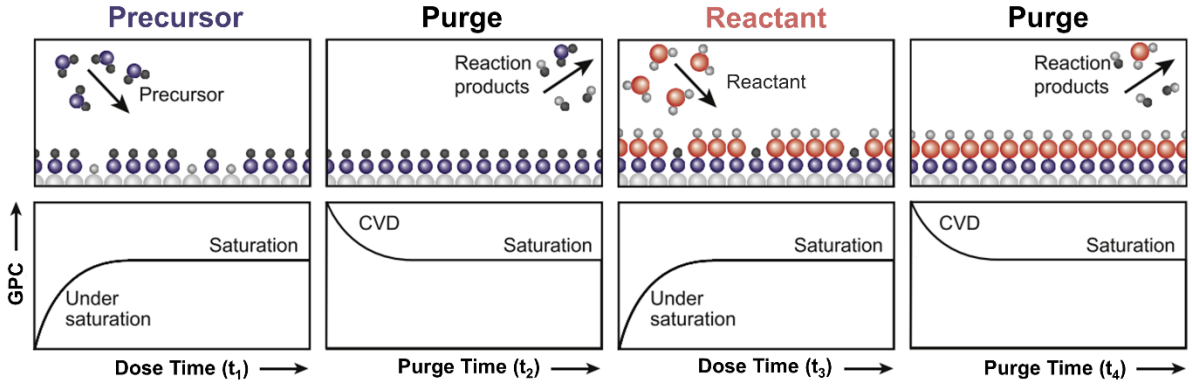

Figure 2.4. Schematic representation of the four steps in a generic ALD cycle. The precursor and reactant exposure steps are self-limiting such that the process ends when all available surface sites are occupied. These exposures are separated by purge steps. The lower panels show the GPC as a function of step time. Sufficient dose times result in saturated growth, while insufficient dose times exhibit incomplete saturation. For insufficient purging, a CVD component from mixing of the precursor and reactant is obtained. Adapted with permission from Ref.[158] Copyright 2015 Elsevier.

An ALD process begins with deposition on a bare substrate or a previously deposited film. Once a significantly thick layer of film is created, subsequent cycles deposit onto the film material itself. Often, the initial surface and the depositing film are chemically different, such that adsorption rates and reaction mechanisms differ between the two. As such, the growth rate is usually dynamic, eventually reaching a linear GPC after a sufficient amount of film has been

deposited.[160] An initially lower GPC, shown in Figure 2.5 by the blue curve, is known as substrate inhibited growth, where the initial surface has a limited number of reactive species as compared with the film material.[154,158] Substrate enhanced growth has also been found, where the number of reactive sites on the starting material is greater than that of the ALD film, shown in Figure 2.5 by the red curve.[154] In an ideal case, where deposition on the initial substrate and the subsequent film is very similar, a constant GPC is displayed, as shown in Figure 2.5 by the yellow curve.[158,160]

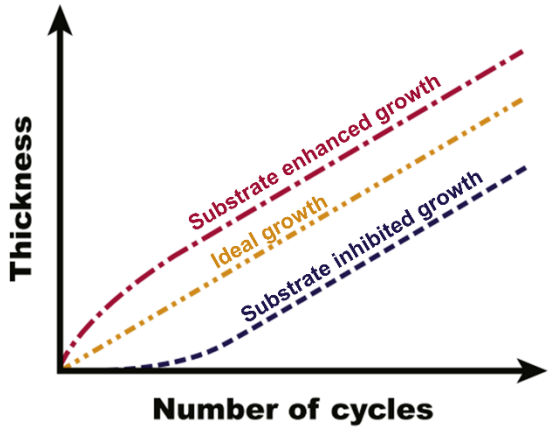

Figure 2.5. Monitoring of film thickness as a function of number of cycles during an ALD process. Substrate enhanced growth is concave downwards during the first few cycles, substrate inhibited growth is concave upwards during the first few cycles, and an ideal growth case exhibits a constant GPC throughout. Adapted with permission from Ref.[158] Copyright 2015 Elsevier.

The physical form of the growing film also varies with the surface energy difference of the substrate and growing material. When the substrate material has a higher surface energy than the growing film, it is preferential that the substrate is completely covered with the lower energy film. Once covered, subsequent deposition occurs on the new film and the coating is deposited layer by layer. This is also known as the Frank-van der Merwe growth mode (Figure 2.6a). In another situation, when the substrate material has a lower surface energy than the growing film, it is preferential that as much of the lower energy substrate material remains uncovered, and the higher surface energy depositing material agglomerates into islands. Subsequent deposition will occur on the high energy islands and continue to preserve the exposed substrate surface as much as possible. Eventually, however, the growing islands will coalesce, resulting in a completely

covered substrate with a fairly rough film topography. This island growth is also known as the Volmer-Weber growth mode (Figure 2.6b). The layer-by-layer and island growth modes generally do not account for interfacial energy and stress within the growing film. A third growth mode, known as the island-layer or Stranski-Krastonov growth mode, is a combination of the two simplistic growth modes (Figure 2.6c). Initially, while the film is very thin and internal stress contributions are minimal, the growth occurs via layer-by-layer growth. As the film grows thicker, however, contributions from stress due to lattice mismatch between the substrate and growing film cause the film to break up into isolated particles. While this arrangement increases the overall surface area and the energy of the film, the reduction of internal stress is greater and the deposit continues to grow as islands.[162–164] The island growth mode, with a low energy substrate, is analogous to substrate inhibited growth, with fewer nucleation sites for ALD. Thus, in most cases, ALD films showing substrate inhibited growth also display an island growth mode.[154] Once the islands coalesce, deposition is generally anticipated to occur via the layer-by-layer growth mode. This can be understood as the inverse of the Stranski-Krastonov growth mode, with initial island growth and subsequent layer-by-layer growth. As will be shown in Chapter 4, ALD of FeO_x in this work does not follow this growth process. Instead, multiple layers of islands nucleate one after another, even after coalescence of the previous island layer.

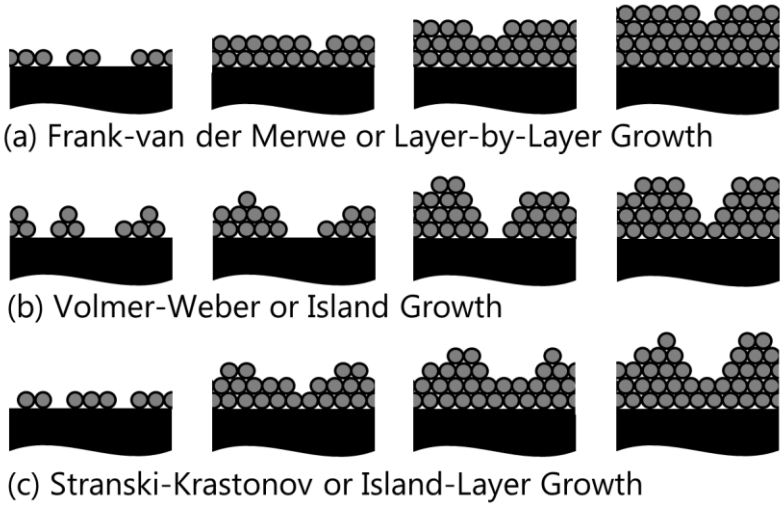

Figure 2.6. Three modes of initial thin film growth. (a) Frank-van der Merwe or layer-by-layer of growth, (b) Volmer-Weber or island growth, and (c) Stranski-Krastonov or island-layer growth. Adapted with permission from Ref.[162]. Copyright 2004 World Scientific Publishing.

2.2.2 ALD Precursor Chemistry

The vast majority of precursors used in ALD are inorganic coordination complexes, where the metal cation of the desired film is encapsulated by sacrificial ligands, which may be either organic or inorganic in nature.[157,158] The well-known trimethylaluminum is an example with organic ligands, whereas titanium(IV) chloride contains inorganic chloride ligands.[52] These ligands provide sufficient volatility and they also greatly impact the chemical characteristics of the precursor. As a rule of thumb, heavier, symmetrical molecules have lower volatility than lighter, asymmetric compounds.[158] There are numerous requirements for a functional ALD precursor, most notably volatility and reactivity towards surface groups. A vapour pressure of at least 0.1 Torr is required for most ALD systems and this is often achieved by heating the precursor.[155,160] Additionally, the precursor must not react with itself and it must have a decomposition temperature higher than the working temperature. As well, the by-products of the precursor and reactant should be volatile and neither adsorb to, nor etch, the growing film. Furthermore, smaller size precursors may reduce steric hindrance that inhibits full surface coverage. While not requirements, there are other favourable precursor attributes including low toxicity, low environmental impact, low cost, simple synthesis, and ease of handling. Liquid

precursors are generally easier to handle, while solid precursors may be more troublesome to vapourize.[158,160,165]

A non-metal reactant is generally a hydride (*e.g.*, H_2O), molecular species (*e.g.*, O_2), or a plasma-activated species (*e.g.*, O plasma radicals).[52] The obvious critical requirement for the reactant is that it reacts with surface adsorbed precursor molecules to create the desired film composition. Depending on the choice of precursor and substrate temperature, some reactants are ineffective in producing film growth and more reactive, unstable reactants are required to enable ALD.[158] When employing a plasma co-reactant, the process is also known as plasma-enhanced atomic layer deposition.[166] This is because plasma species contribute additional energy to the reaction process. ALD processes that are sufficiently reactive with temperature alone are dubbed thermal ALD.[156,158,167] Due to the short lifetime of the plasma radicals, the post-plasma purging step may be omitted, improving overall cycle times.[160] In addition, an ALD process that successfully utilizes H_2O as a reactant may sometimes use ozone (O_3) or an O plasma instead. The energy enhanced reactants can lower operating temperatures and purging times can be shortened. Water is well known to adsorb on the reactor walls and lines and on oxide films, so that extended purging times are required.[155,158,160] On the other hand, O_3 and O plasma reactants may be too oxidizing, damaging the depositing film or original substrate.[160]

2.2.3 ALD Reactor Design

Reactors for ALD may operate at pressures anywhere between atmospheric and utrahigh vacuum (10^{-9} Torr).[155,156,158,168] There are generally two categories of ALD reactors: inert gas flow reactors and high vacuum reactors.[155,156] The fact that ALD does not require a homogenous precursor flux allows for a variety of reactor shapes and designs.[155,160] Flow-type reactors are generally favoured, especially for production, since they allow for much more rapid pulses and purging of precursors and reactants.[155,156] Furthermore, high vacuum reactors limit the amount of collisions precursor molecules experience with the substrate. Flow-type reactors, operating at higher pressures (~1 Torr), have more precursor collisions which improve reaction rates, thereby decreasing the length of pulse times required to reach saturation, in addition to improving precursor utilization.[155,156] On the other hand, high vacuum reactors, also known as static-pulsing systems, have long residence times for the precursor and reactant gases, improving deposition of high aspect ratio structures, as well as increasing precursor utilization efficiency.[156,160] For

maximizing ALD throughput, batch reactors may be employed, where several substrates are coated at once.[156,158,160] The larger volume and reduced gas diffusion require longer dose and purge times, but the benefit of depositing on multiple samples results in an overall increase in efficiency.[156,158,160] The constant purging of an ALD reaction vessel may be avoided entirely by employing a spatial ALD design.[158] In this system, the dose and purge steps are separated by physical space within the reaction chamber, so that a substrate experiences each step sequentially as it commutes across the different reaction zones.[158,160] Alternately, the inlet may be mobile while the substrate is fixed.[158] While the throughput of the system is limited by technical specifics of the reactor, ALD can approach a continuous process with this design.[158] A similar design involves a rotating substrate, which cyclically enters a different reactant stream; however, only for one sample.[53,156]

Another consideration in ALD reactors is the heating of reactor walls, as well as the temperature of delivery lines; longer purge times may be necessary for adsorbed precursors on cold spots in the reactor or lines.[155 156 160] Hot wall reactors have a similar temperature to that of the substrate, while cold wall reactors operate with wall temperatures at, or slightly above, room temperature.[156] The trade-off with hot walled reactors is that precursor and reactant fluxes will result in deposition on the reactor walls, requiring regular cleaning. Warm wall reactors employ an intermediate temperature, high enough for rapid desorption but low enough to prevent deposition.[160]

If the vapour pressure of a precursor is higher than that of the ALD operating pressure, no additional equipment or transport gas is required for precursor molecules to enter the reaction chamber.[155 156] However, low vapour pressure precursors typically require the use of a bubbler, a specialized equipment that feeds an inert gas into the container of the precursor, carrying the precursor vapours with the inert gas flow and delivering them into the reaction chamber.[156] An alternative design for a bubbler is a pulsed precursor delivery system, colloquially referred to as a poor man's bubbler. Using only the original precursor ampoule, an inert gas is forced into the ampoule with the precursor, a dwell time is elapsed, and then the ampoule valve is opened, releasing the mixture of inert gas and entrained precursor vapours.[157,169] This pulsed precursor delivery system was employed for the Mn precursor in this work. The Fe and Zn precursors had sufficient volatility and were used directly with the ALD system.

2.2.3.1 In Situ *Film Characterization*

Since the growth rate exhibited by an ALD process is not always constant (Section 2.2.1), *in situ* techniques to determine the growth rate are powerful tools to accurately predict the amount of cycles necessary for a given thickness.[167]. Spectroscopic ellipsometry (SE) and quartz-crystal microbalance (QCM) are two of the most popular *in situ* growth characterization techniques employed in ALD for determining GPC.[52,160] Additionally, mass spectroscopy can be implemented *in situ* to monitor reaction processes occurring during ALD.[155,160]

SE can be used as a non-destructive technique to probe film thicknesses and to extract various optical constants over a wide range of photon energies.[167] The sensitivity of SE allows, in principle, the detection of changes in the thickness of surface layers less than a monolayer and is thus well-suited for *in situ* ALD.[167] The basis of SE is the measurement of polarization changes that occur when a beam of light is reflected from a surface, such as the growing ALD film. Physical information of the sample is then extracted through model-based analysis of the experimental data, including the complex dielectric function and film thickness. Ellipsometer models generally employ a two layer model, *i.e.*, the substrate and the ALD film, while additional layers may be added for more complex films that exhibit interfacial layers or relatively large surface roughness.[167] Most layer models assume a uniform, planar film when calculating model parameters. However, an effective medium approximation (EMA) model can be used to represent either surface roughness or island layers on the surface. In this model, the optical properties of the layer are approximated by a secondary phase contained within a matrix. The secondary phase has the optical properties of one material, while the matrix has the optical properties of a different material, often those of a vacuum to simulate voids when modelling islands or roughness. The model calculates the effective electrical and optical properties of the mixed layer through a mathematical combination of the two phases, with a defined volume fraction of each phase.[170–173] The mathematical functions range from a simple linear combination of the two phases to more involved models as proposed by Bruggman or Maxwell and Garnet.[170,174,175] In Chapter 4, a Bruggman EMA is employed to model the growth of multiple islands layers during ALD of FeO_x.

When operating as a piezoelectric, there is a well-defined relationship between a quartz crystal's resonance oscillation frequency and its mass, which can include the mass of a surface film. This

is the basis of QCM. The changes in oscillation frequency of the quartz are interpreted and used to dynamically measure the mass of the thin film, which can be converted to a thickness value by using a predicted density for the growing film.[155] However, the assumptions made in the predicted density value may lead to errors in thickness measurements.[176] Another issue with QCM is its sensitivity to temperature variations. Thus, a constant temperature must be maintained or else the variations must be predictable to allow for a calculated subtraction from measured frequency changes.[155] Furthermore, the quartz substrate used in QCM may differ from the actual substrate of interest within the reactor in terms of temperature and surface chemistry and, thus, is not completely reliable.[52]

2.2.4 MnO_x ALD Applications

It has been widely reported that an H_2O reactant is sufficient to obtain self-saturating ALD growth of MnO_x from bis(ethylcyclopentadienyl)manganese, or simply $Mn(EtCp)_2$ (Figure 2.7a).[177–185] The use of higher energy oxygen reactants, such as O_3, has mixed results. In one study, an O_3 reactant with $(EtCp)_2Mn$ leads to a quasi-ALD process, dubbed self-limited multilayer deposition, with an anomalously large GPC, which is higher than theoretical.[186] On the other hand, another report suggests that O_3 is incompatible with $Mn(EtCp)_2$ and that H_2O is the only effective oxygen source.[187] Nevertheless, a paper recently published by our group disputes self-limiting ALD growth of MnO_x from $(EtCp)_2Mn$ and H_2O.[157] This study found that a forming gas (FG) plasma step is necessary to initiate true ALD growth of MnO_x using H_2O. This was demonstrated on a porous carbon substrate, where an H_2O-only reactant resulted in significant loss in surface area.[157] In a following investigation, the addition of an O plasma, as opposed to FG, resulted in inferior surface coverage and an unstable MnO_x film.[54]

2.2.5 FeO_x ALD Applications

The birth of organometallic chemistry as a separate branch of science has been largely attributed to the discovery and study of bis(cyclopentadienyl)iron, better known as ferrocene.[188,189] Described as being a sandwich of two cyclopentadienyl rings between Fe, this molecule has also served as the go-to Fe precursor in ALD.[190] Numerous reports have used ferrocene to grow FeO_x films, mainly Fe_2O_3. Some reports also used ferrocene to grow other Fe-containing ALD films.[191,192] The drawbacks of ferrocene include its poor reactivity, yielding slow growth rates, and the fact that it is a solid precursor. As previously mentioned, solid precursors generally

require higher temperatures to generate sufficient volatility. One report also found that ferrocene is an unattractive precursor because it may condense in vacuum systems and cause damage.[176] The most common oxygen reactant used in conjunction with ferrocene is O_3.[191,193,202,194–201] An O plasma may also be used, or even molecular O_2 if the substrate temperate exceeds 300 °C.[203–207]

To increase the volatility of ferrocene, an organic side group can be attached to one of the cyclopentadienyl rings. These ferrocene derivatives are usually liquid at room temperature.[158,208,209] The addition of a dimethylaminomethyl side group yields N,N-(dimethylaminomethyl)ferrocene, which is a commercially available Fe precursor with limited study in literature, possibly because the nitrogen containing bulky side group may increase steric hindrance and potentially contaminate oxide films.[165,210] Tert-butylferrocene has a much smaller, carbon-based butyl ligand attached to one of the cyclopentadienyl rings. This commercially available Fe precursor has been used more than other ferrocene derivatives.[211–214] The addition of an ethyl branch to ferrocene yields an even smaller ferrocene derivative known as ethylferrocene (EF) (Figure 2.7b). EF is also commercially available and at a much lower cost than tert-butylferrocene, but has yet to be applied in an ALD setting. One report has used EF in combination with air to yield CVD of FeO_x, but all other references to EF in the literature are as a gaseous detector.[215–219] One of the most attractive features of EF is that it is air stable, greatly simplifying handling and reducing associated costs. A summary of selected FeO_x ALD research from the literature is shown in Table 2.1. Some CVD cases have also been included because of interest in the respective precursor.

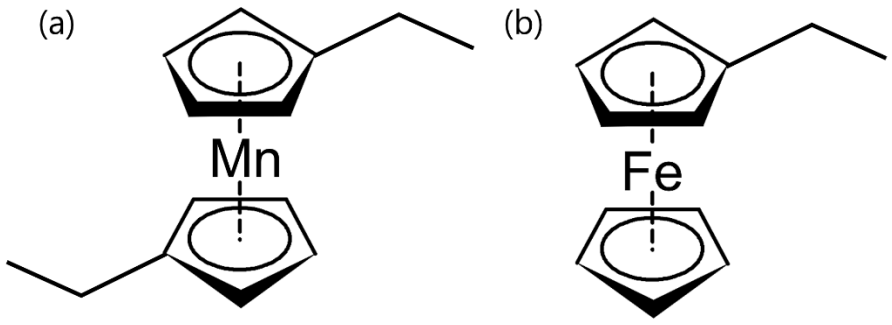

Figure 2.7. Molecular structure of (a) $Mn(EtCp)_2$, and (b) EF.

Table 2.1. Selected examples of ALD studies involving Fe precursors reported in the literature.

Ref.	Fe Precursor	Ampule T (°C)	Reactant	Product	Substrate	Substrate T (°C)	GPC (nm cycle^{-1})	Comments
[193]	$Fe(Cp)_2$	80	O_3	Fe_2O_3	Si	100	0.03	Precursor bubbler. H_2O reactant did not yield growth. H_2O_2 and O_2 reactants resulted in slow and undesirable growth.
						200	0.14	
[220]	$Fe(Cp)_2$	---	O_3	Fe_2O_3	SiO_2	400	0.07-0.12	$Fe(Cp)_2$ was ineffective at temperatures below 400 °C.
	dmamF					350	0.092	FG annealing led to partial reduction of Fe_2O_3 into Fe_3O_4.
						450	0.7	
[221,222]	$Fe(Cp)_2$	90	O_3	Fe_2O_3	Al_2O_3	200	---	400 °C H_2/Ar annealing step yielded Fe_3O_4.
	$[Fe(O'tBu)_3]_2$	100	H_2O			140	0.026	Homemade precursor. Static pulsing mode. 400 °C annealing in H_2/Ar resulted in Fe_3O_4.
[211]	nBF	80	O_2	Fe_2O_3	Si	400	4 nm min^{-1}	Metal-organic chemical vapour deposition. Precursor bubbler.
						500	50 nm min^{-1}	
[213]	TBF	65	O Plasma	Fe_2O_3	SiO_2	150	0.1	Static pulsing mode. No purge gas. Post-ALD annealing in H_2/He at 650 °C resulted in metallic Fe.
						300	0.12	
[223]	TBF	80	O_3	Fe_2O_3	Si	220	0.18	Precursor bubbler. Static pulsing mode. Excessive O_3 exposure (60 s) resulted in an anomalous GPC of 0.4 nm cycle^{-1}.
[215]	EF	150	air	FeO_x	Al_2O_3	300	---	CVD
[224]	$FeCl_3$	175	H_2O	Fe_2O_3	Si	225	0.04	Static pulsing mode. Precursor bubbler.
						250	0.06	
[176]	$Fe(amd)_2$	120	H_2O	FeO_x	Al_2O_3 (QCM)	150	0.055	$Fe(Cp)_2$ damaged vacuum pump.
			O_2				0.012	
			H_2O	Fe_2O_3	Si (SE)		0.047	500 °C annealing in air resulted in Fe_2O_3.
[225]	$Fe(thd)_3$	114	O_3	Fe_2O_3	Soda-lime-glass	186	0.013	Homemade precursor.
					Si		0.014	
[226]	$Fe(acac)_3$	60	O_2	Fe_2O_3	YSZ	150	---	No carrier gas for precursor pulse. Static pulsing mode.

Abbreviations: **$Fe(Cp)_2$** is ferrocene, **dmamF** is N,N-(dimethylaminomethyl)ferrocene, **$[Fe(O'tBu)_3]_2$** is iron(III)tert-butoxide, **nBF** is n-butylferrocene, **TBF** is tert-butylferrocene, **$FeCl_3$** is iron(III) chloride, **$Fe(amd)_2$** is bis(N,N'-di-tert-butylacetamidinato)iron(II), **$Fe(thd)_3$** is tris(2,2,6,6-tetramethyl-3,5-heptanedionate)iron(III), **$Fe(acac)_3$** is tris(acetylacetonate)iron(III), **YSZ** is Y-stabilized ZrO_2.

2.2.6 ZnO_x ALD Applications

The development of a synthesis technique to deposit thin films of ZnS for electroluminescent thin film displays is often quoted as the birth of ALD (or atomic layer epitaxy as it was known then).[53] Since then, many other compounds of Zn have been created with ALD, including Zn oxide (ZnO_x).[154] The properties of ZnO_x make it an ideal candidate for thin-film transistors, buffer layers in solar cells, and even light-emitting diodes.[227] Furthermore, since recent developments of ALD have been geared towards the semiconductor industry, and because of the conformality and thickness control associated with ALD, reports on ALD of ZnO_x are plentiful.[156] The first explored precursor in ZnO_x ALD was Zn acetate, coupled with an H_2O co-reactant.[227,228] Other potential Zn precursors include elemental Zn or $ZnCl_2$, but these yield relatively slow deposition rates and require extremely high temperatures.[227] The most common Zn precursor in ALD is diethylzinc (DEZ), which readily reacts with H_2O to yield an oxide film. Dimethylzinc is a similar precursor but is less widely used.[227] An O plasma can also be employed to create ZnO_x films, with reportedly fewer oxygen vacancies and smaller crystallite size.[227]

2.2.7 ALD Supercycles

To deposit a mixed transition metal oxide film, two or more binary ALD processes for a transition metal oxide can be combined to form an ALD supercycle.[158] Depending on how frequently the ALD process is switched between each material, a doped, multilayer, or homogenously mixed film can be deposited. For example, binary ALD processes for ZnO_x, MnO_x, and FeO_x are repeated for u subcycles, v subcycles, and w subcycles, respectively (Figure 2.8). The bilayer period is the cumulative amount of subcycles performed over one supercycle ($u + v + w$). The total number of times this one supercycle is repeated (n) determines the final overall film thickness. Large bilayer periods, with large subcycle values, result in distinct layers of individual oxides. Smaller bilayer periods, with smaller subcycle values, generally yield homogenous films, with diffusion of elements at the nanoscale producing an overall mixed oxide composition. However, frequently alternating between different ALD processes is sometimes undesirable because each repetition causes nucleation effects on the GPC (*e.g.*, substrate inhibited growth).[55] To avoid this, larger subcycle values can be used to deposit thicker layers and then the final film can be annealed to disperse the individual subcycle layers, although this

does not always yield the desired homogenous film.[55,229,230] The ratio of *u*:*v*:*w* subcycles determines the cycle ratio of the supercycle process and the composition of the final film. Employing a small cycle ratio for one ALD process results in a doped film, with low amounts of that material in the final composition. Equal cycle ratios do not, however, necessarily translate into equal amounts of each constituent material since each binary ALD process has a different GPC. Furthermore, the growth of one material on another material can introduce new nucleation effects or precursor ligand interactions that were not identified in the binary ALD process, further convoluting the ALD supercycle process.[55]

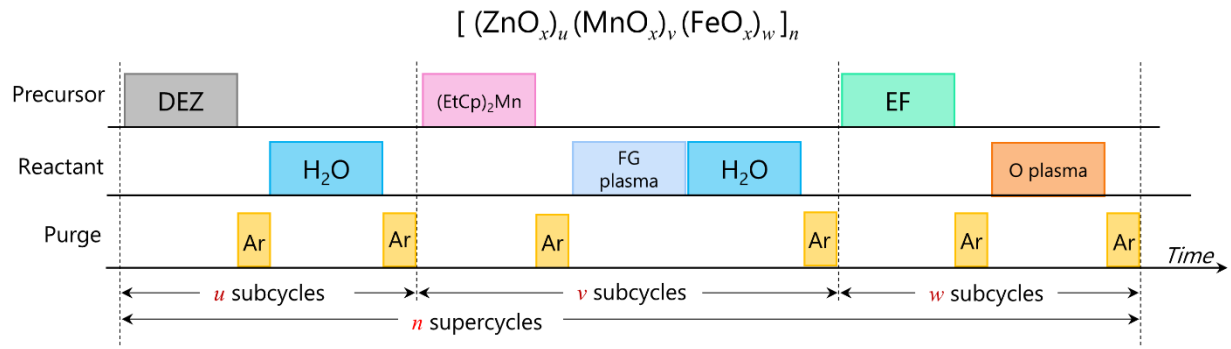

Figure 2.8. Schematic of a $ZnMn_xFe_yO_z$ supercycle deposition process. Adapted with permission from Ref.[158]. Copyright 2015 Elsevier.

Like most cases of ALD, the applications for ALD supercycles have been primarily for designing new materials in the semiconductor industry,[55] particularly high κ dielectrics,[231–235] buffer layers,[236–238] and diffusion barriers.[239–242] In addition, supercycles of transition metal oxides are most commonly investigated for their magnetic properties.[191,243–245] However, ALD supercycles have also been applied towards Li-ion battery (LIB) development,[246] such as cathode materials,[247,248] solid state electrolytes.[55,249,250] and protective coatings.[251,252] As well, ALD supercycles of transition metal oxides have been used to create catalysts for the water splitting reaction,[253–255] which is a research area related to metal air batteries through the common use of OER.[256–258]

2.3 Materials Characterization

The size, shape, elemental composition, and other material properties of the deposited catalyst films and modified air electrodes are probed through a variety of materials characterization

techniques. Imaging of catalyst coatings is primarily conducted using electron microscopy, while chemical composition is measured using both electron and photon-based techniques.

2.3.1 Scanning Electron Microscopy

A scanning electron microscope (SEM) directs a beam of high energy electrons onto the surface of a sample of interest. The electrons are generated either from a superheated W filament (thermionic source) or via an electron tunneling effect (field emission source).[259] For thermionic sources, an electrical current is used to reach temperatures in excess of 2500 K, where the thermal energy allows conduction electrons to escape the metal surface. LaB_6 can also be used as a filament material, which requires a lower operating temperature than W because of its lower surface work function. For field emission sources, a fine tipped W crystal (~100 nm tip radius) is subjected to an electric field and the effective field strength at the tip is so great that electrons can tunnel their way out of the tip without requiring the same thermal energy as thermionic sources.[259,260] In either case, the generated electrons are accelerated towards the sample surface, using potential differences on the order of 20 kV, and are focused into a narrow beam using a series of magnetic lenses.[260] The electron source, lenses, and sample are all contained within a low pressure vacuum ($<10^{-4}$ Torr) to reduce to chances of the accelerating electrons colliding with atoms that exist in the space between the source and the sample.[260–262]

When the beam of electrons reaches the sample, multiple events can occur (Figure 2.9). If an incident electron interacts with the electron cloud of an atom within the sample, the incident electron can be inelastically scattered, meaning it transfers some of its energy to an electron within the sample.[259] Loosely bound conduction electrons in the sample do not require significant amounts of energy to escape atomic orbit and they will eject from the sample with low energies. These electrons, known as secondary electrons, are collected by a detector within the SEM to form secondary electron images which provide topographical contrast of the sample surface with a large depth of field.[163,260] The topographical contrast arises because surfaces that are directly in-line with the detector yield a large signal and appear bright in the image, while electrons emitted by surfaces not facing the detector will be sparsely collected and the corresponding low signal will manifest into a dark area in the image. This trajectory effect provides most of the topographical contrast. In addition, edges or raised surfaces on the sample will facilitate the release of secondary electrons more so than flat surfaces and result in a greater

amount of signal. This is known as the electron number effect and causes certain areas, such as spherical edges or cavities, to appear bright in SEM images.[260] The incident beam electrons can also be elastically scattered, where most of the initial electron energy is preserved. Elastic scattering occurs due to interactions with the nuclei of atoms within the sample.[259] Both electron scattering processes within the sample can alter the trajectory of the incident electrons such that they are ejected back out of the sample. These so-called backscattered electrons are collected by a detector directly above the sample surface and form backscattered electron images. Since higher atomic number elements have larger nuclei and electron clouds, they are more likely to scatter the incident electrons. Therefore, SEM images formed using backscattered electrons provides atomic number, or compositional, contrast.[259] Lastly, if an incident beam electron transfers its energy to a strongly bound electron within the sample, which exists in an inner electron shell of the atom, the vacancy left by this ejected atom causes an unstable atomic state. As a result, an electron in a higher electron orbital will drop down to fill the vacancy and stabilize the atom. In doing so, the electron sheds energy, either in the form of electromagnetic radiation or the ejection of another electron. The former produces an X-ray with an energy value that is unique to that atom and that electron movement (characteristic X-ray), while the latter emits an Auger electron with an energy value that is also unique to that particular atom.[259] Both of these effects can be used to characterize the elemental composition of the sample, as discussed in Sections 2.3.4 and 2.3.5, respectively. The term *scanning* in SEM originates from the fact that the incident beam of electrons is scanned across a sample surface to create backscattered electrons, secondary electrons, X-rays, and Auger electrons from every area of a sample surface.[260]

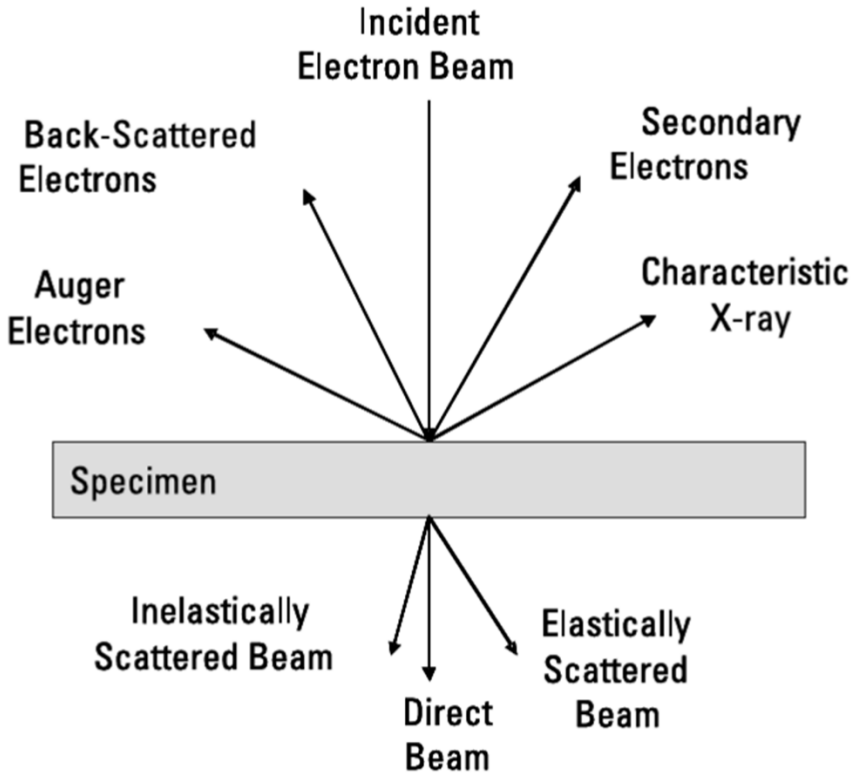

Figure 2.9. Schematic of the various signal types generated from an incident electron beam. The transmitted beams below the specimen are discussed in Section 2.3.2. Adapted with permission from Ref.[163]. Copyright 2009 Artech House.

The imaging resolution of an SEM is generally on the order of 5 nm.[259] Resolution is in a sense the size of area investigated by the electron probe when stationary. This is the physical limit of the distance between two objects that can be discerned. Finer imaging resolution enables resolving greater surface detail and allows for clear images at higher magnification. Imaging resolution in an SEM is governed by the electron probe size and the interaction volume within the sample (Figure 2.10). Field emission electron sources generate smaller probes than thermionic sources and, as a result, provide superior resolution.[261] Another method to reduce electron probe size is to reduce the working distance, a common practice when imaging at high magnifications. However, reducing the working distance sacrifices the depth of field.[260] The interaction volume in the sample is a function of the accelerating voltage, with higher voltages increasing the volume of interaction and, thus, decreasing the imaging resolution. Furthermore, secondary electrons have much less kinetic energy than backscattered electrons, leading to a

smaller interaction volume within the sample (Figure 2.10). Thus, images formed from secondary electrons generally have better imaging resolution than backscattered electron images.[260]

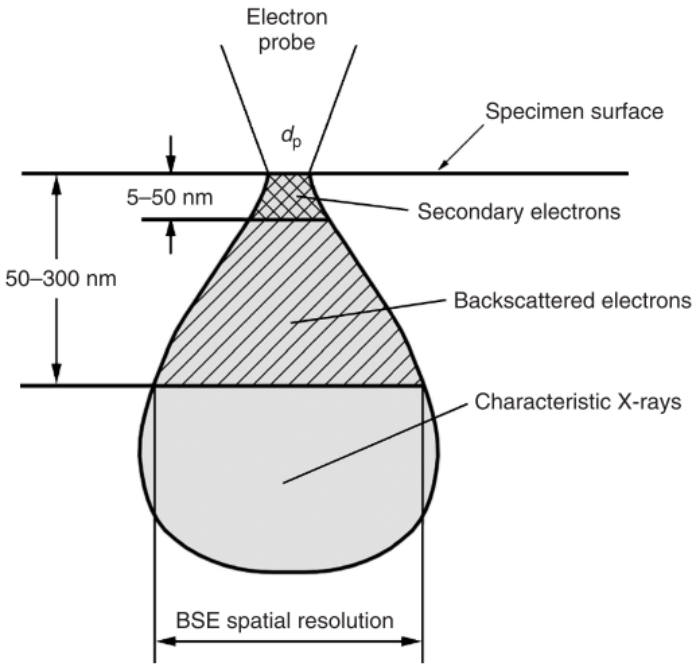

Figure 2.10. Illustration of the interaction volume for an incident electron beam in a bulk sample during SEM. Low energy secondary electrons can only escape from the upper most surface of the sample while the higher energy backscattered electrons can originate from a much wider and deeper area in the sample. X-rays can originate from an even larger area than backscattered electrons. Reused with permission from Ref.[260]. Copyright 2013 John Wiley and Sons.

Contamination describes the common occurrence of a dark region that develops at high magnification in electron microscopy. Hydrocarbons either on the sample surface or within the vacuum chamber are rapidly decomposed by the high energy electron beam and leave behind a residue of carbon. At high magnification in an SEM, the electron beam is scanned across a relatively small area at a faster rate than lower magnifications, thereby increasing the surface's exposure rate to the electron beam and depositing carbon at a faster rate. Charging is a phenomenon in SEM where an excess of electrons is built up on a non-conductive surface, creating a charged surface. This charged surface causes image distortion and artifacts because it

irregularly deflects incident electrons from the electron beam. A thin conductive coating, often carbon or Au, can be used to mitigate charging in nonconductive samples.[260,261]

2.3.2 Transmission Electron Microscopy

A transmission electron microscope (TEM) operates similar to a light microscope, with the key distinction that electrons are used instead of visible light. The wavelength of electrons, when treated as a wave, are orders of magnitude shorter than visible light, and this affords extraordinary fine resolution, with a theoretical minimum of 0.1 nm.[260] As with SEM, an electron source, electromagnetic lenses, and a high vacuum environment are required for TEM.[262] The term *transmission* in TEM indicates that, unlike in SEM, the electrons penetrate through the sample and are detected on the opposite side (Figure 2.9). Thus, the initial energy of the electrons must be sufficient to allow electrons to pass through the sample and, therefore, the accelerating voltage for the electron beam is about 10 times larger than for SEM, on the order of 200 kV.[260] Since the energy of an electron is inversely proportional to its wavelength, with shorter wavelengths enabling finer resolutions, a TEM has much finer resolution than an SEM (typically 0.3 nm).[262] In addition to the increased accelerating voltage, TEM samples must be electron transparent. This is achieved by ensuring the thickness of a sample is less than 100 nm, or even thinner for high atomic mass samples. Alternatively, a carbon-coated Cu mesh can act as a support to suspend very small specimens for viewing.[260] Most TEM work in this thesis involves the suspension of ALD coated GDL particles on a carbon coated Cu TEM grid.

Contrast in TEM images is created by deflection of the incident electron beam by the sample, either through mass-density contrast or diffraction contrast. Mass-density contrast is a function of the sample's density and thickness and both factors lead to contrast in TEM images. The mechanism of electron deflection in mass-density contrast is based upon collisions with atomic nuclei in the sample, which scatter the electrons away from the incident beam. The other mechanism for deflecting electrons is diffraction, similar to X-ray diffraction (XRD) explored in Section 2.3.3. The high energy electrons behave like waves and interfere with one another and with periodic structures in the sample, such as crystal lattices. This results in the collective deflection of electrons from the incident beam.[260] For TEM imaging in bright field (BF) mode, the undeflected transmitted beam of electrons is used. Accordingly, both mass-density effects and diffraction produce contrast in BF images. For imaging in dark field (DF) mode, a beam of

diffracted electrons is used. As explained further in Section 2.3.3, electron diffraction results in several different beams of collectively deflected electrons. A TEM operating in diffraction mode produces a reciprocal lattice pattern, with each point on the pattern representing diffraction from a particular lattice plane in the sample. Using only one point from this pattern, a DF image is created, representing the electrons that were deflected due to diffraction from that particular lattice plane. Bright and dark field imaging in visible light microscopy is a one-to-one correlation (*i.e.*, negatives of each other). In TEM, however, DF images can be acquired from any number of diffraction spots in the reciprocal lattice pattern, while BF involves the diffraction from all lattice planes simultaneously. Thus, BF and DF images are not completely complimentary in TEM.[260] High resolution transmission electron microscopy (HRTEM) operates on an entirely separate contrast mechanism than standard TEM. Mass-density and diffraction contrast are considered amplitude contrast since the signal intensity, or amplitude, is employed. Conversely, a difference in phase for electron waves can be employed for phase contrast in HRTEM. A periodic structure will produce a phase shift between the transmitted and diffracted electron beam. Consolidating the transmitted and diffracted beams together results in an interference pattern with periodic dark-bright changes in the HRTEM image.[260]

Scanning transmission electron microscopy (STEM) is a hybrid between conventional TEM and SEM, with signal acquired from *transmission* through the specimen. Traditional TEMs create an image similar to light microscopy, where all pixels of the image are acquired simultaneously. STEM, however, collects an image pixel by pixel, by scanning the electron beam across the surface as in SEM. In other words, STEM collects the information of an image in series, while TEM collects information in a parallel fashion.[263] Another important difference between traditional TEM and STEM is the position of the many electromagnetic lenses. In the latter case, there is ample room to fit additional detectors after the sample, in particular those for energy dispersive X-ray (EDX) analysis, discussed later in Section 2.3.4. Field emission electron sources are essential for STEM because they can provide high electron current, enabling the use of EDX analysis, yet maintain a fine probe size necessary for high resolution. The higher vacuum requirements of the field emission source usually correlates to higher expense for STEM relative to conventional TEM.[263] Contamination is also an issue in STEM, exacerbated by the higher energy electrons compared with SEM.[263]

Similar to BF and DF imaging in conventional TEM, BF and annular dark field (ADF) images can be formed in STEM, based on whether the undeflected or deflected beam is used, respectively (Figure 2.11).[262] The term *annular* dark field reflects the shape of the detectors used in STEM, which form an annulus around the undeflected transmitted beam.[263] Unlike conventional TEM, STEM ADF images use all diffracted beams of electrons simultaneously.[262] In ADF images, diffraction contrast dominates. On the other hand, high angle annular dark field (HAADF) images (Figure 2.11) exhibit very little diffraction contrast since high angle deflection occurs mostly through Rutherford scattering, where atomic nuclei are responsible for electron scattering. Accordingly, atomic number contrast is dominant for HAADF images, also called Z-contrast images.[262,263]

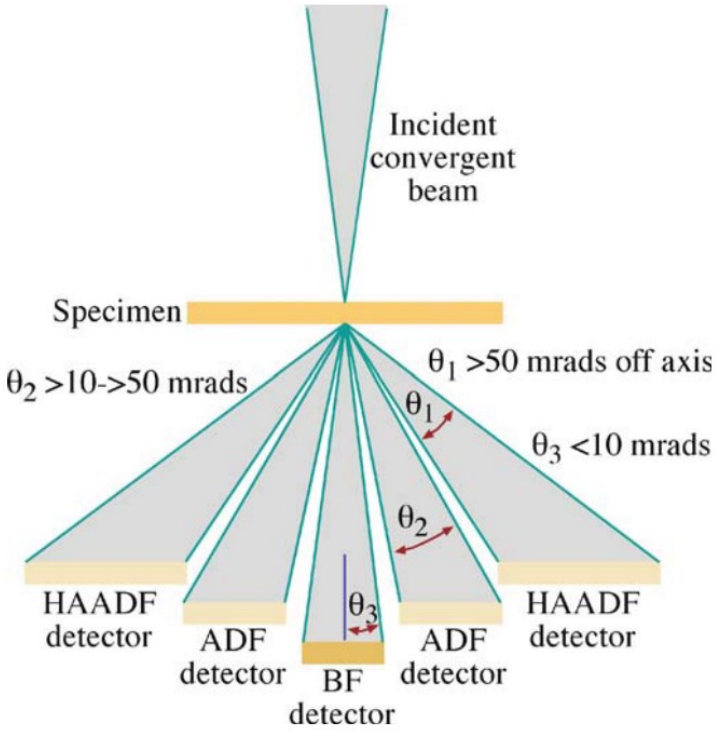

Figure 2.11. Schematic of the detectors used for imaging in STEM. Reused with permission from ref.[262]. Copyright 2009 Springer.

For both SEM and STEM (*i.e.*, scanning systems), magnification arises from the difference between the area scanned and area displayed.[263] Given a constant screen size, higher magnification is achieved by scanning a smaller area of the sample. Therefore, magnification can increased by simply scanning through smaller and smaller areas. The resolution of the image,

that is, the smallest discernable distance between points, is ultimately the limiting factor to achieving high quality images at high magnification.[262] Furthermore, a numerical magnification value is meaningless when images are transferred to another display (such as in a presentation). The dimensions of the screen originally used to calculate the magnification, which is simply a ratio of the sample dimensions to the display dimensions, are not the same for a different display and thus the numerical value is invalid. Therefore, the scale bar, often in the bottom left corner of the image, is the true determination of the magnification in the image. This scale bar, with a length fixed relative to the image length, can be compared with the size of objects in the image to estimate physical dimensions.[261]

One of the strongest attributes of STEM, or essentially any scanning technique, is the ability to create maps. Mapping refers to the creation of a two dimensional image that showcases the distribution of signal across a surface. Mapping of an EDX signal for a particular element is the most well-known example but, in principle, all STEM images are maps of their corresponding signal type. Taking EDX analysis as an example (Section 2.3.4), the development of a map begins with defining the detection window, which is the range of X-ray energies that will result in a signal. This window is often restricted to the energy range of a particular element, so that the map is a construction of all regions that emit X-rays of that element. As the electron probe is scanned across the surface, the signal acquired is correlated to the point of origin, *mapping* signal values to locations on the plane. With modern computing power, all possible windows can be scanned simultaneously, so that maps of different elements can be acquired at the same time. Furthermore, any other signals of interest (*e.g.*, BF or HAADF) can be recorded during the scan, so that any STEM image can be effectively considered a map.[263] Maps are a very powerful technique that are intuitive to understand. Elemental maps are more easily interpreted by a non-specialized audience as compared with EDX spectra or bodies of text.[263]

2.3.3 X-ray and Electron Diffraction

Due to the wave-particle duality of matter, electrons can experience diffraction and interference just like light waves. Therefore, the fundamentals of XRD are also applicable for electron diffraction in TEM.[260] For any two waves with the same wavelength, constructive interference occurs when the peaks and valleys of the two waves overlap so that the amplitude of the resulting wave is the sum of the two interfering waves. In a crystalline material, the periodic

arrangement of atomic planes can cause the constructive interference of waves that have a wavelength on the same order as the atomic spacing.[163] Bragg's Law (Equation 2.16) describes the conditions for constructive interference in diffraction, where n represents a positive integer, λ is the wavelength of the incoming wave, d is the atomic spacing of the crystal, and θ is the incident angle of the incoming wave. Since the wavelength and incident angle are controlled variables, d values that cause constructive interference are easily calculated, providing the planar spacings, or d-spacings, of a material.[260]

$$n\lambda = 2d \sin\theta \tag{2.16}$$

In XRD, the angle of diffraction (2θ) is varied while the intensity of diffracted X-rays are recorded. A plot of intensity versus 2θ is then created, which acts as a sort of fingerprint for a particular crystal structure. The location and relative intensity of diffraction peaks is compared with standard XRD patterns for bulk powder samples (power diffraction files, or PDFs) to analyze a sample's crystal structure.[163] Samples will rarely match PDFs perfectly, as there will always be deviation due to instrumentation differences and other factors discussed below.[260] Therefore, other characterization techniques should be used in addition to XRD to determine the elemental composition and reduce the number of possible crystal structures. While it is generally understood that the intensity of diffraction peaks from a particular phase in a mixed-phase compound is linked to its weight fraction in the material, quantitative XRD is complicated and may yield unreliable results. For thin film samples, the bulk substrate often dominates the XRD pattern due to the relatively large penetration depth of XRD (~10 μm). Glancing angle XRD, or grazing-incidence XRD, employs much smaller incident angles relative to the sample surface, reducing the penetration depth by up to an order of magnitude and reducing contributions from the substrate.[264,265]

When examining an XRD pattern, several phenomena should be taken into account. Preferential crystal orientation may cause the intensity of some XRD peaks to be favourably larger than others, obscuring direct comparisons between samples or PDFs. A smaller crystallite size results in wider XRD peaks. This is because of incomplete deconstructive interference, arising from a range of simultaneous incident angles from the XRD apparatus and a lack of complimentary planes in small crystal sizes.[260] Ideally, a single crystal produces an XRD pattern with vertical lines while an amorphous (non-crystalline) structure yields one broad peak. Lastly, any

phenomona that alters the d-spacing of a crystal structure can modify the XRD pattern.[260] Some common examples include: residual stress, where a tensile or compressive stress expands or contracts the lattice spacing, respectively, to alter the 2θ values; and intercalation of ions in LIBs, which increases d-spacings to lower 2θ values.

Diffraction, for both X-rays and electrons, operates in reciprocal space. A high level understanding of this reciprocal space is that crystallographic planes that satisfy Bragg's Law correspond to a single point in the reciprocal space. Diffraction from a single crystal yields an array of regularly spaced points in the reciprocal space with each point representing a plane that provides constructive interference.[260] A TEM operating in diffraction mode uses the electrons deflected from the incident beam due to crystal lattice diffraction to produce a reciprocal lattice pattern. A selected area of the specimen is examined in diffraction mode, often a single crystalline grain to simplify the diffraction pattern, but not necessarily only single crystals. This technique is called selected area diffraction (SAD), or selected area electron diffraction. An SAD pattern has periodic spots of intensity representing constructive interference from specific planes in the sample, with a high intensity point in the center of the pattern for the undeflected beam of electrons.[260]

Like XRD, SAD in TEM can be used to identify crystal structures, with the added benefit of a narrow spatial resolution. Furthermore, electron diffraction yields much higher intensities than XRD (several magnitudes of order in some cases) and does not require a large amount of sample, which is ideal for nanomaterials.[162] The diffraction angle in TEM is small enough that the approximation $sin\ \theta \approx \theta$ is valid and, considering the geometric relationship that exists in TEM, Bragg's Law can be transformed into Equation 2.17, where λ represents the wavelength of the electrons used in TEM, d is the crystallographic spacing of the diffraction plane, R is the distance between the central undeflected beam of electrons and a diffraction spot, and L is the camera length of the TEM. Since L does not bear physical significance, λL is often described as the camera constant.[260] The camera constant is calibrated for a particular TEM and its operating conditions.

$$\lambda L = Rd \tag{2.17}$$

Indexing an electron diffraction pattern means to identify the Miller indices (*hkl*) of the lattice planes that produce the spots in SAD. The distance between the central spot and any diffraction spot (R) is measured and, using the camera constant (λL), the d-spacing is easily calculated from Equation 2.17.[260] In a process similar to XRD, the d-spacings of planes that exhibit constructive interference in SAD are matched with PDFs to identify the crystal structure of the specimen. The Miller index (*hkl*) of each spot is based on the d-spacings provided in the PDF for specific planes in the crystal.

The SAD pattern for polycrystalline samples will generally appear as rings as opposed to individual spots (Figure 2.12). This is because each crystallite within the material will produce a spot pattern, but the random orientation of all the combined crystals will produce a series of spots that manifests into concentric rings. In other words, the SAD pattern is rotated about the transmitted electron beam for crystals of different orientation. Since not all possible orientations are likely found in an area examined in TEM, the ring patterns are typically broken, with incomplete circles (Figure 2.12).[260] In a similar manner to the appearance of a single broad peak for amorphous materials in XRD, an electron diffraction pattern for an amorphous sample produces wide, diffuse rings (Figure 2.12).[262] Nanocrystalline materials, which have grain sizes of less than 100 nm, also display diffuse rings, with larger grains producing less diffuse rings and more spots instead (Figure 2.12).[262] Another technique, known as convergent beam electron diffraction or CBED, utilizes a fine, focused electron probe permitting single crystal diffraction from nanocrystalline materials.[262]

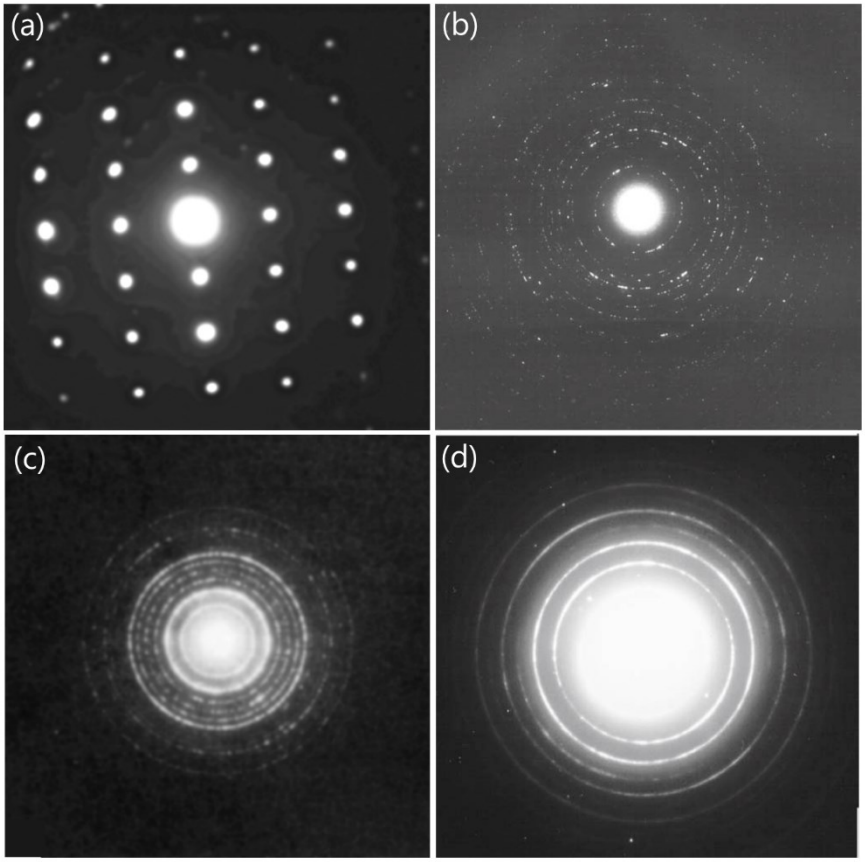

Figure 2.12. Examples of SAD patterns in TEM for materials of various crystallinity. (a) A single crystal material, (b) a polycrystalline material with large grain size, (c) a polycrystalline material with small grain size, and (d) an amorphous or nanocrystalline material. Adapted with permission from Refs.[260,262]. Copyright 2013 John Wiley and Sons. Copyright 2009 Springer.

2.3.4 Energy Dispersive X-ray Analysis

As mentioned in Section 2.3.1, inelastic scattering of an incident electron causes an inner shell electron to be ejected from an atom. A similar phenomenon can occur with a high energy photon, such as an X-ray. In either case, the incoming high energy photon or electron will have enough momentum to knock out an inner shell electron from an atom within the sample. The state of a missing inner shell electron with filled outer shell electrons is unstable and the atom quickly transfers to a lower energy state. To do so, one of the outer electrons drops down into the vacancy. However, in order to exist in this lower energy state, the high energy electron must shed some energy, usually as a photon. This high energy photon can escape the atom and be detected as a characteristic X-ray (Figure 2.13a) or the X-ray may be internally converted prior

to leaving the atom and result in the ejection of an Auger electron (Figure 2.13b). The energy of the characteristic X-ray is a factor of the energy of the orbital transition and the atomic number of the element. Auger electrons are also characteristics of the electron orbital transition and are discussed further in Section 2.3.5.

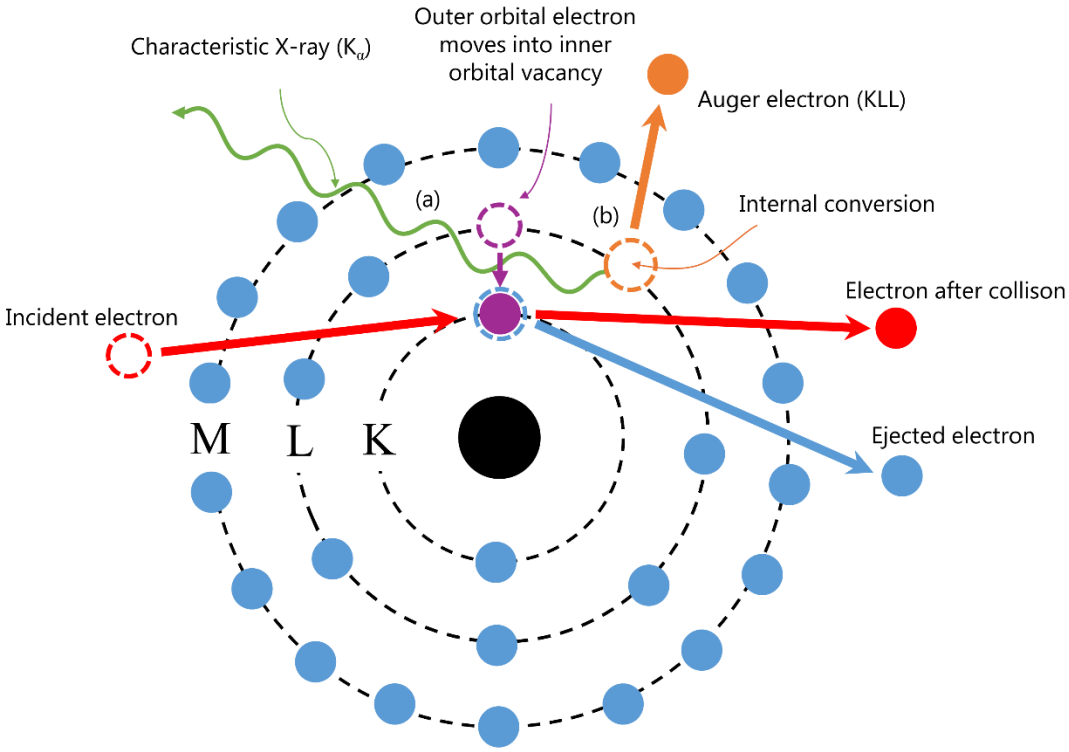

Figure 2.13. Inelastic scattering of an incident electron produces an unstable vacancy in the inner electron shell of an atom. An outer shell electron fills the vacancy by shedding its excess energy via (a) generation of a characteristic X-ray or (b) generation of an Auger electron. Adapted with permission from Ref.[260]. Copyright 2013 John Wiley and Sons.

As per quantum mechanics, each electron in an atom exists in a specific state or energy level. These states are classified via a series of quantum numbers: *n, l, m,* and *s*. No two electrons in one atom can have the same four quantum numbers. These are effectively the coordinates of the electron's location within the electron cloud. The principal quantum number (n) defines the electron orbital level or shell. Using an archaic system, this is also described with the letters K, L, M, *etc*.[262] The first orbital level (closest to the nucleus) is $n = 1$ or the K shell. The orbital angular-moment quantum number (l) is used to describe a subshell, which exists from 0 to (n-1). Another archaic system is used to describe the orbital angular-moment quantum number with the

letters s, p, d, f, *etc*., where s is the first subshell ($l = 0$).[266] The magnetic quantum number (m) describes an energy state within a subshell, with values ranging from $-l$ to 0 and from 0 to $+l$. Lastly, the spin magnetic quantum number (s) is used to characterize whether an electron is in a spin up or spin down state, represented by +½ or -½, respectively. An additional descriptor of an electron is the total angular momentum (J), which is the sum of $l+s$.[260,266]

When describing a characteristic X-ray, the Siegbahn notation is often used. The orbital level of the initial electron vacancy from the collision is used to classify the characteristic X-ray, with an additional classification based on the intensity, or likelihood, of the X-ray, which depends on the original orbital level of the replacement electron. Generally, α represents a transition of one orbital (*e.g.*, L to K) while β represents a transition of two orbitals (*e.g.*, M to K). For example, an electron from the L shell that replaces a K shell vacancy is labelled as a Kα X-ray (Figure 2.13a). [260] Further classification based on the subshell yields $K\alpha_1$ and $K\alpha_2$, where the former has a higher intensity.[260] The fluorescent yield is used to describe the chance a characteristic X-ray will be emitted from the excitation process, as opposed to an Auger electron. The fluorescent yield for atomic number elements of less than 4 (H, He, and Li) is zero and the fluorescent yield increases with atomic number.[260] Therefore, the analysis of lighter elements is difficult with EDX spectroscopy. Furthermore, the fluorescent yield is higher for K X-rays compared to L X-rays, meaning the X-ray intensities for K X-rays will be much larger than for L X-rays of the same element.[260] As well, K X-rays have the highest energy, followed by L and then M, because electrons are more tightly bound when they are closer to the nucleus.[262] In addition, higher atomic number elements, with more protons and more strongly bound electrons, generate higher energy X-rays.[262]

Characteristic X-rays can be emitted by a sample when impinged by a high energy beam, whether photons or electrons. In X-ray fluorescence (XRF), an initial beam of X-rays causes excitation of the atoms in the sample, which then produce characteristic X-rays through the process described above. The term *fluorescence* is used to describe the secondary emission of electromagnetic radiation due to incident electromagnetic radiation.[260,262] In electron microscopy (SEM and TEM), the incident beam of electrons also causes characteristic X-ray generation. In all cases, the analysis of the characteristics X-rays emitted by a sample can be done either using wavelengths or energies. The former is called wavelength dispersive X-ray (WDX) spectroscopy

while the latter is called energy dispersive X-ray (EDX) spectroscopy. WDX spectroscopy provides better energy resolution than EDX spectroscopy, which reduces peak overlap between elements in the spectra compared with EDX spectroscopy.[260] On the other hand, EDX spectroscopy is simpler and results in relatively fast detection. Due to its compactness, EDX spectroscopy is almost exclusively used in SEM and TEM systems as opposed to WDX spectroscopy.[260]

Since SEM and STEM operate based on a focused beam of electrons, the region of investigation for EDX analysis can be microscopic and precise. XRF, on the other hand, is used for an overall elemental analysis of a sample.[260] The incident electrons in an SEM penetrate deep into the specimen so that characteristic X-rays detected during EDX analysis arise from a larger interaction volume than simply the probe area (Figure 2.10). In fact, the lateral size can be significantly larger than the probe size. The depth of interaction volume is approximately the same as the lateral size, therefore this needs to be considered during EDX analysis in SEM.[260] In TEM, the spatial resolution of EDX spectroscopy is not much larger than the probe size because thin samples limit the spread of the interaction volume. Therefore, spatial resolution in TEM is much better (~10 nm or even less) compared with SEM (~1 μm).[262] As discussed in Section 2.3.2, EDX mapping refers to acquiring an EDX spectrum at every point on the sample surface as the electron probe is scanned. Energy windows are defined for elements of interest and a dot map of intensity is generated for each element.[262] Point analysis and line scans can also be performed using EDX analysis in electron microscopy.[260]

For reliable quantitative EDX analysis, the use of standards is required. An EDX spectroscopy standard contains a known amount of the element of interest and is measured using the same instrumental operating conditions as the sample for quantitative EDX analysis. Furthermore, matrix effects from the sample and the standard differ and are accounted for using the ZAF correction, which incorporates the atomic number effect (Z), absorption of X-rays (A), and X-ray fluorescence (F).[260] Standardless quantitative EDX analysis, sometimes referred to as semi-quantitative EDX analysis, should be used cautiously since large errors can occur for samples with low energy lines (<3 keV) or multiple X-ray families (K, L, *etc.*).[260] Furthermore, ZAF correction assumes a flat, bulk elemental sample, so that nanosized and uneven samples are less reliable.[260] The detection limit for EDX analysis in a TEM is in the range of 0.1 to 1 wt%, while

the detection limit is slightly better for EDX spectroscopy in an SEM due to the larger volume for analysis.[262] Overall, EDX spectroscopy results should be analyzed carefully, especially when the software automates peak identification,[261] elemental compositions are near the detection limit, or when trying to quantify carbon, since multiple phenomenon in electron microscopy can generate spurious carbon.

2.3.5 X-ray Photoelectron Spectroscopy

The photoelectric effect describes the emission of an electron from an atom as a result of interactions with an incident photon. In the same sense that inelastic scattering from an incident electron can remove an inner shell electron, a high energy X-ray photon can provide sufficient energy to an inner shell electron that it escapes atomic orbit. Using the kinetic energy of the detected photoelectron (ϵ_k), the binding energy of the electron's original position (ϵ_B) can be calculated with Equation 2.18,[260] where hv is the energy of the incident X-ray and Φ is the work function of the material surface (*i.e.*, the energy necessary to free an electron from the material's surface).[266,267]

$$\epsilon_B = hv - \epsilon_K - \Phi \tag{2.18}$$

The binding energy is characteristic of a particular electron position in a particular element, not unlike characteristic X-rays in EDX analysis, and can also be used for compositional analysis. Photoelectrons can be ejected from different electron orbital shells and subshells and this is reflected in a spectrum of photoelectron intensity versus binding energy.[260] The labelling of photoelectrons follows a similar principal to characteristic X-rays, so that the quantum mechanical background from Section 2.3.4 is necessary for X-ray photoelectron spectroscopy (XPS). Peaks are first labelled by the elemental symbol, followed by the electron shell number (n), and then the subshell letter (s, p, d, *etc.*). However, due to spin-orbit coupling, one more label is required. Spin-orbit coupling is a quantum mechanical phenomenon based on the electron orbit around the nucleus and the two states of spin up and spin down for an electron. Thus, a subshell (or orbital angular-moment (l)) manifests as a doublet of l+½ and l-½. This phenomenon is best described by the total angular moment (J) and is used to label the two peaks that appear for subshells other than s.[260,266] An example is Figure 3.8d in Chapter 3, which features both Fe $2p_{1/2}$ and Fe $2p_{3/2}$ peaks. In quantum mechanics, the s subshell has no orbital angular moment ($l = 0$) and, therefore, does not display spin-orbit coupling.[266]

In addition to photoelectrons, Auger electrons can show up in photoelectron spectra. This occurs when an inner-shell electron vacancy is filled by an outer-shell electron, where the dissipation of energy manifests into an Auger electron instead of a characteristic X-ray (Figure 2.13b in Section 2.3.4).[260] The nomenclature for describing Auger electrons is best explained using Equation 2.19, which approximates the kinetic energy (ϵ_K) of the Auger electron. An inner-shell electron is ejected from the atom by a high energy photon or electron, which provided sufficient energy to overcome the binding energy (ϵ_{BV}) leaving behind an electron vacancy. This unstable arrangement is resolved by the substitution of an outer-shell electron into the vacancy, which had a binding energy of ϵ_{BS}. Finally, the energy difference between the outer-shell and inner-shell positions during this transition ($\epsilon_{BV} - \epsilon_{BS}$) stimulates the ejection of an Auger electron, which overcame its own energy barrier (ϵ_{BA}). The orbital letters (n) for the inner, outer, and Auger electron positions, respectively, are combined to label Auger electrons, with the elemental symbol also included. For example, the Auger electron from Figure 2.13b in Section 2.3.4 arises from a K shell vacancy, an L shell substitution, and an L shell Auger emission. Therefore, this Auger electron is labelled as KLL, or for an O atom, O_{KLL}.[260]

$$\epsilon_K \approx \epsilon_{BV} - \epsilon_{BS} - \epsilon_{BA} \tag{2.19}$$

Photoelectrons and Auger electrons are generated with relatively low energies. Therefore, scattering events on the way out of the sample causes detected electrons to originate from only the surface level of the material (~10 nm). Photons for EDX spectroscopy, on the other hand, are less susceptible to energy loss as they exit the sample and the EDX spectroscopy signal can originate from several microns from the surface (Figure 2.10 in Section 2.3.1). This causes XPS to be classified as a surface characterization technique.[260–262] A common addition to XPS systems is an Ar ion gun, used to clean the surface of adsorbed hydrocarbons or oxide layers, which are undesirable for a surface sensitive technique. Furthermore, the ion gun can be used to mill away the surface atoms so that a depth profile can be created, where an XPS spectrum is obtained after each successive layer of material is removed.[260]

The incident X-rays for XPS are generated from high energy electron bombardment of a metal anode, typically Al or Mg, and the high intensity Kα X-rays are used. XPS systems are often described by their excitation source, *e.g.*, a spectrometer with Al Kα radiation.[260] The kinetic energy of Auger electrons is characteristic of the energy transitions involved (Equation 2.19), so

in contrast to photoelectrons, their kinetic energy does not change with ionization source. For photoelectrons, the kinetic energy is a function of *hv* (Equation 2.18), which changes for different X-ray sources. However, the binding energy, calculated using Equation 2.18, is often plotted in XPS which accounts for the energy difference in the excitation source. Therefore, Auger peaks appear to shift with different X-ray sources.[260,268] The detected intensity of electrons is plotted against the calculated binding energies in an XPS spectrum.[260] Three peak types are used in characterization: core level photoelectrons, valence level photoelectrons, and Auger electrons. Core level photoelectrons are the primary means of elemental characterization in XPS, while valence level peaks occur at lower binding energies (0-20 eV) and are more important for studying the electronic structure. Auger peaks may also be used for chemical analysis, although this was not the initial intention of XPS. Auger electron spectroscopy (AES) is a dedicated technique where incident electrons (not photons) stimulate Auger electron emission. These are collected and analyzed in a similar fashion to XPS in plots of signal intensity versus electron kinetic energy. The use of an electron source, however, causes significant background signal in an AES spectrum because of the generation of backscattered electrons and secondary electrons (recall Section 2.3.1). The derivative of the AES spectrum is commonly employed to eliminate the background.

In an XPS spectrum, the background increases step-wise with binding energy as a result of inelastic scattering of photoelectrons in the material and because X-ray sources are often not completely monochromatic.[260] Several phenomenon complicate XPS spectra and additional peaks not due to core or valence level photoelectrons, or Auger electrons, are conventionally called satellite peaks.[260] A non-monochromatic radiation source generates small additional peaks at lower binder energies due to minor amounts of higher energy X-rays in addition to the intended Kα X-rays.[268,269] Shake up satellite peaks are common for transition metals with unpaired electrons in the 3d orbital. An escaping photoelectron can excite (*shake up*) a valence electron to a higher energy state, reducing the total energy of the original photoelectron. This will manifest into a secondary core-level peak at a slightly higher binding energy than the main peak (recall Equation 2.18: ϵ_K has a negative coefficient and, therefore, a lower ϵ_K manifests into a higher ϵ_B).[260] An additional complication with XPS spectra is multiplet splitting of core-level peaks, which occurs for compounds with unpaired valence electrons.[260] When an inner-shell vacancy is created in photoionization, the outer-shell unpaired electron can couple with the

newly unpaired inner-shell electron to yield a series of final states that is expressed in the XPS spectrum as asymmetric and broad core-level peaks.[268,270] Lastly, plasmon loss, arising from the collective vibration of conduction electrons due to interactions with the escaping photoelectron, creates additional peaks in an XPS spectrum, typically for metal samples. This process removes a characteristic amount of energy from photoelectrons and presents as additional peaks in the spectrum at higher binding energies.[260,268,269]

The XPS spectrometer and sample surface can alter peak positions and, therefore, calibration of the spectrum is common place. The C 1s peak is the most well-known guide to calibrate an XPS spectrum since most samples have adventitious carbon deposited from the atmosphere. The main C 1s peak is generally accepted to occur at ~285 eV and spectra are shifted to match this. Identifying core level peaks is the basic objective of XPS analysis, however, the chemical shift of elements (*i.e.*, changes to the electron density due to chemical bonding) must also be considered during analysis. For example, C-C bonds exhibit a C 1s XPS peak at a different binding energy than C=O bonds.[260,268] Databases of binding energy values attributed to particular chemical species can assist in the analysis of XPS spectra, in addition to values reported in the XPS literature.[260,268] If chemical shifts in binding energy are small, two distinctly different peaks can overlap and complicate peak identification. Deconvolution of peaks is often performed with the aid of computer software, which can be used to determine the proportion of individual peaks lying within a peak overlap.[260] The relative proportion of constituent peaks within a deconvoluted peak can be used to estimate the chemical state of the sample. This is commonly performed for multiplet splitting of transition metals that have more than one oxidation state, where the weighted average of components for each oxidation state is used to calculate an average oxidation state for the element.[102,109,270] Furthermore, the shift in doublet spacing for spin-orbit coupling in 2p regions is a commonly employed technique to estimate the chemical state of transition metals.[271,272] Lastly, a survey scan over the range of binding energies for photoelectrons of all elements of interest in the sample is usually obtained. Quantitative analysis of elemental composition in XPS can then be conducted on this survey scan in a similar manner to quantitative analysis in EDX analysis, where the relative peak intensities for each element are compared. [260] A sensitivity factor must be included in quantitative analysis, which accounts for the relative emission of photoelectrons for each element.[273] Like EDX analysis, quantitative

analysis in XPS should be used with caution, as sensitivity factors can vary with sample or instrument.[260]

2.3.6 Atomic Force Microscopy

The surface topography of a sample can be examined using scanning probe microscopy (SPM), which, as the name suggests, scans a probe across the surface to generate an image. The use of near-field interactions in SPM, as opposed to far-field interactions in optical or electron microscopes, avoids the diffraction limit and enables true imaging of surface atoms, with lateral and vertical resolutions on the order of 0.1 nm.[260] Scanning tunneling microscopy (STM) takes advantage of quantum tunneling to generate a current between a W wire and a conductive sample. This tunneling current is between 10 pA and 10 nA and a change in probe-to-sample distance of only 0.1 nm results in magnitudes of order decay in the current, enabling atomic resolution. However, the tunneling current is sensitive to surface chemistry, such as adsorbed molecules, and the surface profile from STM is not necessarily the true surface topography of the sample as a result.[260] Atomic force microscopy (AFM) does not use tunneling currents so that samples do not need to be conductive. Instead, AFM employs a Si-based probe mounted onto a cantilever spring, which is deflected by near-field forces between the probe tip and sample surface. Near-field forces include: short-range forces (overlapping of electron clouds); van der Waals forces (dipole-dipole interactions); electrostatic forces (charge interactions); and capillary forces (surface tension of water vapour).[260] Operating modes for AFM can be categorized as either static or dynamic modes. In the former, the cantilever is deflected by a fixed, constant value and this deflection is maintained throughout scanning. The latter introduces oscillation to the cantilever at a designated frequency, and the amplitude of oscillation is maintained during scanning. All static modes are contact type, since the cantilever tip physically touches the sample surface. Dynamic modes, with cantilever oscillations, can be either contact or noncontact. One particular dynamic mode, intermittent contact mode, better known as tapping mode, reduces potential damage to the sample and can also provide chemical and physical information about the surface in addition to topography.[260]

2.3.7 Gas Physisorption

Gas molecules will naturally adsorb onto a surface to lower the free energy of the surface structure, which is more energetic because of the lower coordination number for surface atoms.

Physisorption is a readily reversible process governed primarily by the partial pressure of the adsorbing gas. Chemisorption, on the other hand, involves chemical bonds with surface atoms and generally requires elevated temperatures to release the adsorbed adatoms.[162,274] Chemisorption is an important process in ALD, as discussed in Section 2.2. Physisorption can be used to measure the surface area and pore sizes of surface structures and materials, particularly nanomaterials.[162] As the partial pressure of an adsorbing gas is increased at a constant temperature, several predictable mechanisms occur and are measured by an isotherm, which is a plot of the volume of adsorbed species as a function of partial pressure. First, a monolayer of adsorbed species occurs at lower partial pressures, which can be used to calculate the surface area of the sample if an estimate of the area occupied by one adsorbing species is known. Increases in the partial pressure results in multilayer formations. Assuming capillary condensation when pores are filled, the pore volume and size distribution can be calculated from the isotherm.[162] This is normally carried out using BET analysis (named after the researchers of Brunauer, Emmett, and Teller who originally proposed this methodology).[274,275] The adsorption species is most commonly N_2, while Ar and CO_2 are used in other circumstances. According to the International Union of Pure and Applied Chemistry (IUPAC), *micropores* have widths of 2 nm or less, *mesopores* are between 2 nm and 50 nm wide, while pores above 50 nm in width are called *macropores*.[274] Based on this definition, the microporous layer of the GDL (Section 2.1.1.1) is actually a mesoprous layer since a pore width of 20-50 nm is quoted by the manufacturer.[64]

2.4 Electrochemical Characterization

Electrochemistry is often defined as the branch of chemistry that investigates the relationship between electrical and chemical changes in a system.[276] ZABs operate on the same principle as all other batteries wherein chemically stored energy is converted into electrical energy. To probe the electrochemical characteristics of ZABs and their catalysts, several electrochemical techniques may be employed. These techniques can broadly be categorized as either half cell or full cell methods, based on whether just the air electrode is investigated or the whole ZAB is used, respectively. All electrochemical techniques involve the manipulation of the applied potential at a working electrode and the recording of the resulting current between the working electrode and a counter electrode. A reference electrode is required to measure and manipulate

the potential at the working electrode since the electrochemical potential at an electrode is not a physically absolute value but rather a difference between two electrodes.[276] A potentiostat is an experimental instrument that uses electrical feedback loops to perform the potential modulation and make current measurements.[276]

2.4.1 Half Cell

The term *half cell* is used to describe an experimental setup that isolates the *half cell* reactions that occur at a single electrode. In this setup, known as the three-electrode setup, there are three distinctly different electrodes: the working electrode, the counter electrode, and the reference electrode. The working electrode is where the current and potential values are measured/manipulated; the counter electrode serves as the electron source or electron sink for current flow at the working electrode; and the reference electrode is the standard to which the potential at the working electrode is measured.[277]

The counter electrode can be any convenient electrode material because the potential at this electrode is not typically measured or of concern. It is advisable to choose a counter electrode that does not produce any by-products that can interfere with the working electrode.[276] A Pt wire is a popular choice because of its high conductivity, high chemical stability, and tendency to cause the water splitting reaction, which is a relatively inconsequential electrochemical process.[278,279] Furthermore, the surface area of the counter electrode should always be larger than the working electrode so that the current of the overall three-electrode cell is not limited by the counter electrode but rather by the working electrode (*i.e.*, the current density at the counter electrode is low and the potential at this electrode is not beyond the capabilities of the potentiostat).[277] Therefore, a coiled Pt wire is common and is employed as the counter electrode in all half cell tests in this thesis.

Reference electrodes should have a stable and reliable half cell potential so that measurements are accurately made at the working electrode. Several different chemistries yield a reproducible half cell potential, even with small amounts of current flow, and are used as common reference electrodes. A few of these include the standard calomel electrode, the Ag/AgCl electrode, and the Hg/HgO electrode.[276,277] However, each reference electrode yields a different half cell potential for the same working electrode, so that half cell potentials must be reported *versus* a reference electrode. When tabulated in handbooks, however, standard half cell potentials (E^0) are

reported with respect to the standard hydrogen electrode (SHE), which is a theoretical electrode that, by definition, has a half cell potential of 0 V.[72,280] A standard half cell potential refers to the equilibrium half cell potential when all species are in their thermodynamic standard states and before any current flow disrupts the electrochemical equilibrium at the electrode (*i.e.*, polarization, explained further in Section 2.4.2).[276] Furthermore, the standard half cell potentials are provided in the reduction direction of the half cell reaction.[276]

Experimentally, an H_2 reference electrode is not convenient and, as such, a different reference electrode is used. Experimental half cell potentials can then be converted to SHE based on the half cell potential of the reference electrode with respect to SHE (Equation 2.20).[276,281] In this thesis, the Hg/HgO electrode is employed because it is reliable and chemically stable in a strongly alkaline electrolyte (such as that used in ZABs). Therefore, for half cell tests in this thesis, the potential at the working electrode is reported with respect to the Hg/HgO electrode, which itself is 0.098 V vs. SHE.[282] The standard half cell potential for reactions previously mentioned in Chapter 2, which were obtained from handbooks, are all reported vs. SHE.

$$E_{cell}(\text{vs. SHE}) = E_{cell}(\text{vs.}\,ref) + E_{ref}(\text{vs. SHE}) \tag{2.20}$$

When applied to ZAB research, the half cell configuration uses a piece of catalyst loaded GDL as the working electrode. This enables the study of ORR and OER at the air electrode. Since oxygen is a required reactant for ORR, the electrolyte used in half cell is saturated with O_2 gas. This electrolyte is often 1 M KOH, as opposed to 6 M KOH employed in practical ZABs, because of the higher O_2 solubility in 1 M KOH.[283] The potentiostats employed for half cell testing in this thesis are BioLogic VSP and SP-300 electrochemical workstations. They are operated using EC-Lab software, which contains a vast library of electrochemical techniques. One technique, called current interrupt, measures the internal resistance of the cell by disconnecting the counter electrode while a constant current is applied. The instantaneous drop in voltage is related to potential loss due to resistance in the cell.[284] This technique is performed before all half cell tests in this thesis to measure the resistance of the cell configuration and compensate for the resulting potentials losses (iR). In other words, all reported half cell potentials in this work are iR corrected.

Two main techniques are carried out in half cell configurations in this thesis. Cyclic voltammetry (CV) is used to electrochemically condition the electrode surface in the electrolyte and to

improve the wetting at the interface of the electrolyte and the hydrophobic GDL. In CV, the potential of the working electrode is scanned from an open circuit value to a specified reduction potential using a fixed scan rate, usually 20 mV s^{-1}. The potential is then scanned back to a specified end point (sometimes extending into an oxidative potential) and the potential scan is repeated. Once the working electrode is properly conditioned, a single sweep to the specified reduction potential is performed at a reduced scan rate (5 mV s^{-1}) to carefully examine the ORR kinetics at the working electrode. This single sweep is called linear sweep voltammetry (LSV).[72,276] This process is repeated for a specified oxidation potential to examine the OER kinetics at the working electrode. Analysis of the ORR process is conducted first, since the oxidative potentials required for substantial OER current lead to carbon corrosion of the GDL working electrode.[32]

To quantitatively compare the electrochemical response of different samples during LSV, an onset potential is defined in this thesis as the potential required to obtain 10 mA cm^{-2} of current between the working and counter electrodes. The current density will be -10 mA cm^{-2} when reduction potentials are applied. A plot of the LSV current density versus applied potential for ORR and OER is shown in Figure 2.14a. When multiple samples are plotted together, as in Figure 2.14a, it is difficult to distinguish exact values and quantitatively compare samples. Therefore, the onset potentials measured in Figure 2.14a are plotted as a bar chart in Figure 2.14b. In this plot, the horizontal axis crosses through the standard equilibrium potential for OER/ORR (+0.303 V vs. Hg/HgO) and the overpotential (η) can be visualized as the distance from this axis, with ORR overpotentials below the horizontal axis and OER overpotentials above.[92] These half cell bar charts are employed in Chapters 5 and 6, particularly during optimization of the ALD supercycle recipes.

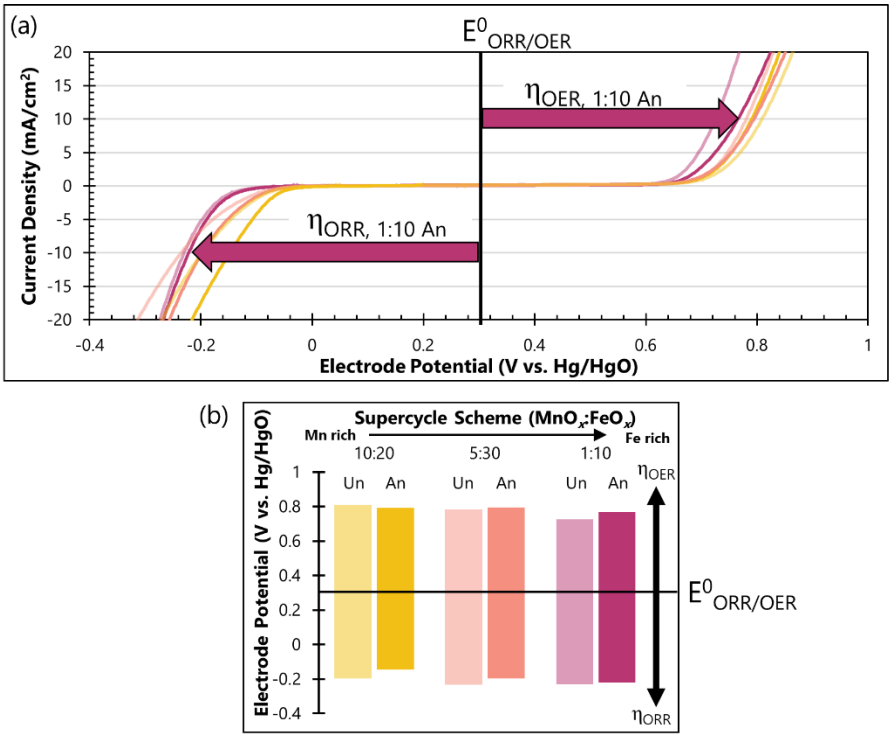

Figure 2.14. Example ZAB half cell LSV data for (a) a plot of current density versus potential, and (b) a bar chart of onset potentials defined at |10| mA cm^{-2}.

2.4.2 Full Cell

In this thesis, the term *full cell* describes a two-electrode setup where the counter and reference electrodes are the same electrode.[276] In the case of a ZAB, the Zn electrode experiences reduction and oxidation reactions mentioned in Section 2.1.2, meaning current passes through this electrode and it is, therefore, the counter electrode. In addition, potential values at the air electrode (working electrode) are measured relative to the Zn electrode making it the reference electrode in a two-electrode setup. Since the potentials measured at the working electrode are equivalent to the overall cell voltage, and not the half cell potentials of the working electrode, the term *full cell* is used.

Experimental full cell tests in this thesis employ catalyst loaded GDL as the working electrode and a piece of Zn foil as the combined counter and reference electrode. Oxygen species diffuse into the air electrode naturally, without forced convection, compared with the O_2 saturated environment in half cell. All full cell potentials reported in this thesis are versus Zn/Zn^{++} in an alkaline environment. As mentioned in Section 2.1.2, the true potential of this electrode is

somewhat uncertain, but in this thesis, a value of -1.249 V vs. SHE is assigned to the Zn electrode. Based on the equilibrium potential of ORR/OER (+0.401 V vs. SHE), a ZAB has a theoretical operating voltage of 1.650 V. Note that a reference to a standard electrode is not required for the overall cell voltage, since the potential value in this case is itself a potential difference between two electrodes.[276] The electrolyte employed in full cell tests is an aqueous mixture of 6 M KOH and 0.25 M ZnO. The addition of ZnO is intended to improve cyclability at the Zn electrode, as explained in Section 2.1.2. As mentioned in Section 2.1.5 and in Appendix B, a 3D printed cell, using acrylonitrile butadiene styrene (ABS) filament, is used to maintain a reproducible configuration for the air electrode, Zn electrode, and electrolyte volume.

The primary technique employed using the full cell configuration is programmed current reversal chronopotentiometry, better known as rate testing.[276] In this technique, the current density of the working electrode is maintained at a specified value for an elapsed period of time and then increased and held for another dwell period. This is repeated over a range of current density values. Then, the current density is reversed to the same magnitudes and hold periods, but of opposite sign. Chronopotentiometry describes the measurement of potential over a period of time, so the potential is plotted against time in these experiments. To investigate the discharge and charge performance of a ZAB with an experimental air electrode catalyst, the cell is maintained at specified current densities for 10 min intervals while the operating potential is recorded. Discharge data is collected before charge data due to the same reason as in half cell, *i.e.*, the oxidative potentials during charge can cause carbon corrosion of the air electrode. Figure 2.15a shows the discharge and charge potentials when the cell is maintained at 2, 5, 10 and 20 mA cm^{-2} current densities. Similar to half cell, the full cell results of rate testing are difficult to distinguish and make quantitative comparison between different catalyst samples difficult when plotted as potential versus time (with four different current densities over a period of 40 min). Therefore, the cell potentials during charge and discharge, at a current density of |20| mA cm^{-2}, are plotted as a bar graph for each catalyst (Figure 2.15b). As with Figure 2.14b, the overpotential can be visualized as the distance from the horizontal axis. However, in this case, it is the overpotential of the entire cell. It should be noted that the polarization of the Zn electrode is also factored into the overall cell voltage during charge and discharge, but this effect is assumed to be constant for all samples so that a direct comparison can be made for the air electrode. The horizontal axis passes through the standard potential of a ZAB (1.65 V).

Therefore, a negative overpotential is required to induce ORR in discharge. Likewise, a positive overpotential is applied to maintain OER during charge. These full cell bar charts are employed in Chapters 5 and 6, particularly during optimization of the ALD supercycle recipes.

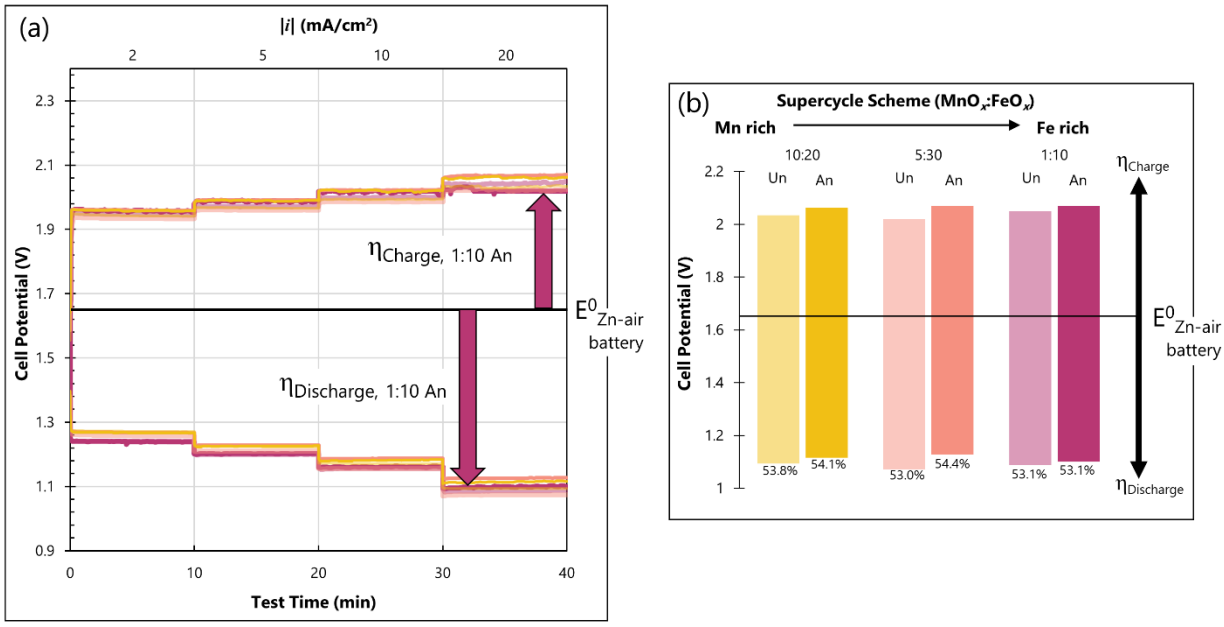

Figure 2.15. Example ZAB full cell rate test data for (a) a plot of cell potential versus test time, and (b) a bar chart of operating voltages at |20| mA cm^{-2}.

Energy efficiency can be defined, generally, as the output energy divided by the input energy (Equation 2.21).[57]

$$\varepsilon = \frac{\epsilon_{Output}}{\epsilon_{Input}} \tag{2.21}$$

The volt, as define in the SI units of measurement, is the potential difference associated with a current of 1 A resulting in the power dissipation of 1 W (*i.e.*, V=W/A).[285] Therefore, the product of a battery's voltage and current is the battery's power. The integral of this power over the time period of operation yields the energy of the battery's operation (Equation 2.22), where a constant current technique has a current value that is constant as a function of time.[286]

$$\epsilon = \int_{t_f}^{t_i} E(t) \cdot I(t) \cdot dt \approx I \cdot \int_{t_f}^{t_i} E(t) \cdot dt \tag{2.22}$$

Using the definition of energy efficiency above (Equation 2.21), the energy efficiency of a battery is energy of discharge (output) divided by the energy of charge (input) (Equation 2.23).

$$\varepsilon = \frac{\epsilon_{output}}{\epsilon_{input}} = \frac{\epsilon_{discharge}}{\epsilon_{charge}} \approx \frac{I_{discharge} \cdot \int_{t_f}^{t_i} E(t)_{discharge} \cdot dt_{discharge}}{I_{charge} \cdot \int_{t_f}^{t_i} E_{charge} \cdot dt_{charge}} \quad (2.23)$$

If the currents for discharge and charge are identical then the current values cancel in Equation 2.23. If a flat voltage profile with respect to time is assumed, which is generally the case in rate testing (Figure 2.15a), and the time duration of both charge and discharge is the same, then Equation 2.23 simplifies such that the energy efficiency is the discharge potential divided by the charge potential (Equation 2.24).[286]

$$\varepsilon \approx \frac{E_{discharge} \cdot \int_{t_f}^{t_i} \cdot dt_{discharge}}{E_{charge} \cdot \int_{t_f}^{t_i} \cdot dt_{charge}} = \frac{E_{discharge} \cdot t_{discharge}}{E_{charge} \cdot t_{charge}} = \frac{E_{discharge}}{E_{charge}} \quad (2.24)$$

Also included in Figure 2.15b are the energy efficiency values for each catalyst, which is calculated as the discharge potential divided by the charge potential and multiplied by 100%.

The highest performing catalyst samples are further studied in full cell using discharge polarization and long term cycling. Discharge polarization is a galvanodynamic technique, meaning the current density is not static. As the current density is increased, the potential at the working electrode is recorded. A plot of potential versus current density (Figure 2.16) has three polarization regimes: activation, ohmic, and mass transport. Polarization describes the increase in potential difference at the working electrode compared with the equilibrium value (*i.e.*, overpotential).[276,287] At low current densities, the potential increase (*i.e.*, increase in magnitude) is required to overcome the activation barrier of ORR (the discharge reaction at the air electrode).[32,36] At moderate current densities higher than the activation region, the ohmic resistance of the cell forces an increase in potential with current (Ohm's law: V=IR).[266] These ohmic losses are primarily limitations of the electrolyte's ionic conductivity and the interfacial resistance of the electrode surfaces in the electrolyte. Lastly, at high current densities, the potential value is dramatically increased as mass transport limitations to the electrode restrict the current density at the electrode surface. Within these polarization plots, the power density of the electrode can be determined by calculating the product of potential and current density.[32,36] The maximum value is known as the peak power density and describes the battery's ability to deliver energy at a fast rate, an important consideration for real world applications.

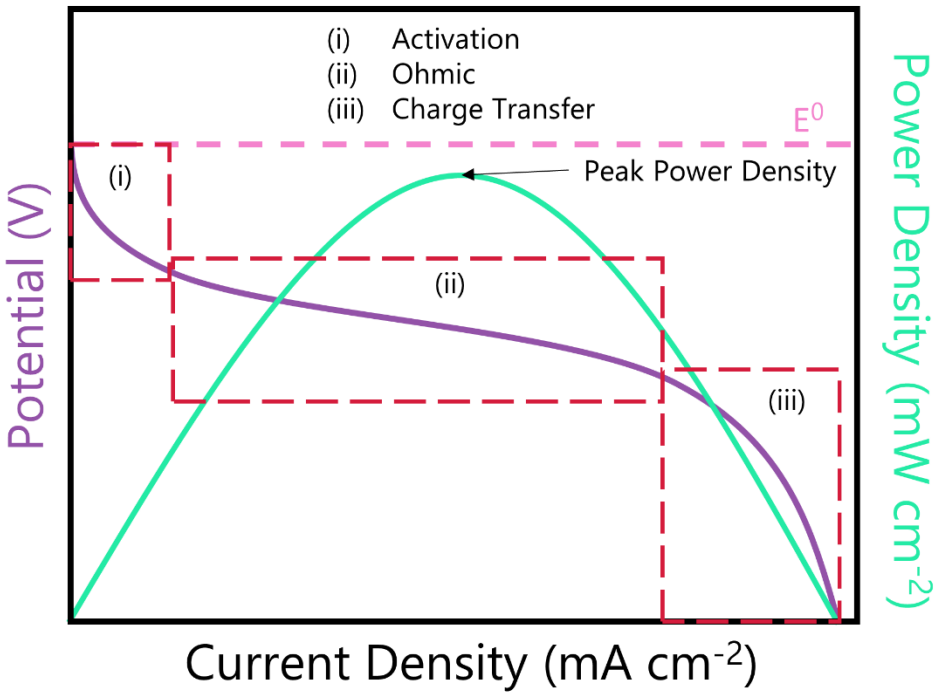

Figure 2.16. Simplified schematic of discharge polarization at the air electrode with three polarization regions identified. Also shown is the power density, which is the product of potential and current density. Adapted with permission from Ref.[288]. Copyright 2024 Elsevier.

Lastly, the use of cyclic chronopotentiometry testing for an extended period of time is known as long term cycling.[276] This involves repeating a rate test for a single current density many times over. This technique is also known as galvanostatic cycling, where galvanostatic simply refers to a constant current (*i.e.*, constant current cycling). The purpose of galvanostatic cycling is to accelerate the charge-discharge process experienced by a ZAB to probe its durability over many cycles of charge and discharge.[32,36] Several variables can be manipulated in this technique, including the current density, hold time, number of cycles, and cutoff voltage.[32,36] A cutoff voltage refers to the maximum voltage the battery will experience during cycling, at which point the current density is reduced to prevent voltages beyond the cutoff. Oftentimes, this essentially marks the failure of the battery/air electrode. Throughout the ZAB literature, multiple different values are used for each of these variables, making it difficult to compare cycling results between different studies.[32,36] In our research group, chosen somewhat arbitrary, cycling tests employ a current density of |10| mA cm^{-2} for 10 min periods. Additionally, a 5 min rest period is added between steps to reduce overheating at the air electrode.[289,290] A 1 min rest period yields identical

performance to a 5 min rest period; therefore, the rest period is reduce to 1 min for cycles beyond 200 in this thesis. For the first 200 cycles, a 5 min rest period ensures the cycling conditions are the same as previous investigations in our research group. In past work, a cycling test was terminated after 200 cycles regardless of the battery's performance. For the present work, cycling tests were prolonged until battery failure. Failure occurred when either the GDL air electrode was physically damaged (refer to Section 2.1.5) or the Zn electrode broke due to environmental corrosion, as explained in Appendix B.

An additional technique that can be employed in full cell is electrochemical impedance spectroscopy, which probes the resistance of the cell at various frequencies of alternating current. Since resistance phenomena respond differently in various frequency regimes, the contributions of different resistance mechanisms towards the overall resistance can be modelled and calculated.[276,287,291] The charge transfer resistance represents the kinetics of the ORR/OER process, while the electrolyte and electrode-electrolyte interfacial resistances are important for reducing the overall resistance of the cell, particular for batteries with solid state electrolytes, which have lower conductivity and inferior interfaces with the electrodes.[32]

3. Atomic Layer Deposition of Fe Oxide on a Porous Carbon Substrate via Ethylferrocene and an O Plasma

A version of this chapter has been published in a peer-reviewed journal:

M. Labbe, M. P. Clark, Z. Abedi, A. He, K. Cadien, and D. G. Ivey, "Atomic layer deposition of iron oxide on a porous carbon substrate via ethylferrocene and an oxygen plasma," *Surf. Coatings Technol.*, vol. 421, p. 127390, 2021.

3.1 Introduction

Atomic layer deposited (ALD) thin films are highly conformal and ideally exhibit a growth rate that is independent of time and flux intensity. Instead, the film thickness is determined by the number of reaction cycles.[53] ALD relies on self-saturating reactions between gaseous species and a substrate surface. During ALD, a precursor molecule chemically adsorbs (chemisorbs) onto a surface by forming chemical bonds with the substrate species. A fixed number of surface sites are active towards this bond formation and when all potential active sites are occupied, the surface is said to be saturated. Once saturated, additional exposure of the precursor does not result in additional chemisorbed species on the surface.[52,155] The formation of a full monolayer of chemisorbed species is rarely achievable, however, because not all surface sites are active towards chemisorption and because of steric hindrance effects of the precursor molecules.[160] The substrate surface is then exposed to a non-metal co-reactant, which react with the chemisorbed precursor species to form the desired compound. Four distinct stages occur during one cycle of ALD: precursor dose (t_1), precursor purging (t_2), reactant dose (t_3), and reactant purging (t_4). The gas purge steps (t_2 and t_4) are required to prevent gas phase reactions between the precursor and reactant which would otherwise create non-conformal CVD behaviour.[52,158] The repetition of an ALD cycle will produce another layer and this can be repeated until a desired thickness is reached.[155]

When selecting a precursor for ALD, some key considerations include sufficient volatility, reactivity with co-reactants, and a high decomposition temperature. Furthermore, low toxicity, low cost, and easy to handle precursors are beneficial.[158] Insufficient volatility may be overcome by the use of a bubbler or inert carrier gas pressurization, known as a boost.[157,292] A high

decomposition temperature is desirable to avoid CVD behaviour, which does not yield conformal films and may block porosity of a porous substrate.[160] Easy to handle precursors are generally liquid at room temperature, facilitating simple transfer and storage. Solid precursors may be difficult to volatilize and, more importantly, may damage ALD systems.[157,176]

ALD of Fe-based films is often achieved by the use of the solid precursor bis(cyclopentadienyl)iron, better known as ferrocene. In order to grow Fe oxide (FeO_x) from the very stable ferrocene molecule, a highly reactive oxygen-containing co-reactant is required. Both ozone (O_3) and O plasma fulfill this role, yet the use of O_3 is much more widespread.[193–195,198] Others have claimed FeO_x growth using O_2 gas as a reactant, with substrate temperatures in excess of 300 °C.[204,207] Other Fe precursors explored in the literature include bis(N,N'-di-tert-butylacetamidinato)iron(II),[176,293] iron(III)tert-butoxide,[229,294] and tris(2,2,6,6-tetramethyl-3,5-heptanedionate)iron(III).[295] These precursors are typically lab-synthesized directly for ALD use and exist in the solid state.[225,296–299] Iron(III) chloride has also seen use in ALD and is readily reactive with a water co-reactant.[224,300] The halide ligand, however, is known to contaminate films, and the volatile HCl by-product may damage the ALD reactor or the deposited film.[158] N,N-(dimethylaminomethyl)ferrocene is another alternative Fe precursor, with commercial availability.[301] This ferrocene derivative has a dimethylaminomethyl side group grafted to just one of the cyclopentadienyl rings that sandwiches the Fe atom. It has been reported that asymmetric compounds are more volatile and, as a result, this precursor exists in the liquid state.[158] While this precursor is attractive for ALD, the nitrogen-containing bulky side group may increase steric hindrance and possibly contaminate oxide films.[165]

Tert-butylferrocene (TBF) and ethylferrocene (EF) are two very similar ferrocene derivatives that are also commercially available and exist in the liquid state.[208,209] The only difference between these two molecules is the size of the side group that introduces the volatility of ferrocene; TBF contains a butyl (4 carbon) side group, while EF has an ethyl (2 carbon) side group (Figure 3.1). There have been multiple accounts of using TBF in ALD to synthesize FeO_x films,[213,223] but to the authors' knowledge, no one has implemented EF for ALD. There is, however, one report on the CVD of FeO_x using EF, with atmospheric air as the oxygen source.[215] In addition to the novelty, EF is a more favourable ALD precursor because the smaller ethyl side group should cause less steric hinderance. Moreover, EF costs significantly less than TBF.[208,209]

One of the most attractive features of EF is that it is air stable, greatly simplifying handling and reducing associated costs.

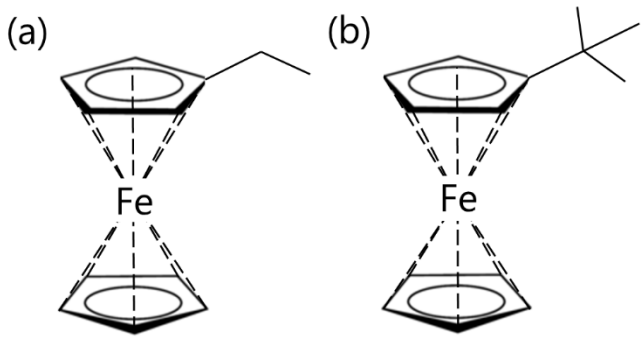

Figure 3.1. Molecular structure of (a) ethylferrocene and (b) tert-butylferrocene.

Iron(III) oxide, also known as hematite or more commonly, rust, is an earth-abundant material with recent applications in renewable energy. It has seen use as a photoanode for solar water splitting,[94] where nanostructured FeO_x enables the dissociation of water into H_2 and O_2 gas, the former being a key component in practical fuel cell use.[302] Alternatively, FeO_x may be applied to the electrochemical catalysis of the oxygen evolution reaction (OER), which is half of the water splitting reaction. Incorporating FeO_x with other transition metal oxides has demonstrated promising catalytic activity in order to replace precious metal oxides such as IrO_2 or RuO_2, which are regarded as the most efficient OER catalysts.[89] The OER plays a key role in metal-air batteries, which combine the closed-system aspects of a traditional battery with the open-system features of a fuel cell. The result is a very high theoretical energy density from abundant and inexpensive materials.[19] The OER is a requirement for charging a metal-air battery, while the reverse reaction, the oxygen reduction reaction (ORR), is necessary for discharge. Without catalysts, significant losses occur in secondary Zn-air batteries (ZABs) due to the slow kinetics of both the forward and reverse oxygen reactions.[39]

During the development of earth-abundant transition metal oxide catalysts for ZABs, nanostructuring is often emphasized as providing a significant boost to catalytic activity.[32] Additionally, the air electrode of a ZABs is often made of highly porous carbon, which serves as the support for catalyst loading. The conformal nature of ALD allows for uniform coverage of high aspect ratio surfaces, including porous substrates.[49] Thus, ALD is an attractive technique to

create nanostructured transition metals oxide catalysts for ZABs. Furthermore, conformal coating of the porous air electrode through ALD may improve catalyst distribution deep within the porosity. This in turn improves the cycling stability of a ZAB by alleviating the issues caused by electrolyte flooding.[54] ALD also provides added benefits over other synthesis techniques, such as precise control over catalyst layer thickness and lower impurity levels as compared to chemical vapour deposition (CVD).[52]

Herein, the development of an ALD recipe to deposit FeO_x using the novel precursor of EF, enabled by an O plasma reactant, is reported. Development of the process is done using single crystal Si as the substrate. The FeO_x film is then grown on carbon gas diffusion layers (GDL) as a potential catalyst for the OER reaction. To protect the delicate carbon-based substrate, a Mn oxide (MnO_x) sublayer is added to the ALD process. The deposited film is characterized through several materials techniques, and an elevated temperature heat treatment is explored. Preliminary electrochemical testing for application in a ZAB is also performed.

3.2 Experimental

3.2.1 ALD Process

A continuous flow ALD reactor (Kurt J. Lesker ALD 150L) operating at ~1 Torr with ultra high purity Ar gas (99.999%, Praxair) was used for all depositions. EF (98%, STREM Chemicals, Inc.) was used as the Fe precursor and was maintained at 80 °C. Although this temperature reportedly only yields a vapour pressure of 0.2 Torr, a bubbler was not required for sufficient precursor dose.[216] Precursor valve and transportation lines to the ALD reactor were kept at 100 °C and 110 °C, respectively. A 600 W inductively coupled remote plasma system provided an O plasma as the primary reactant (99.993% O_2, Praxair). A forming gas (FG: 5% H_2, balance N_2, Praxair) plasma, an H plasma (5% H_2, balance Ar, Praxair), as well as distilled water (held at ~22 °C) or O_2 gas flow without plasma, were also investigated as reactants. Si(100) substrates with the native oxide layer were used in the saturation study. Si substrates experienced a 30 s O plasma pre-clean prior to deposition. The substrate temperature ranged from 50 °C to 300 °C. *In situ* spectroscopic ellipsometry (SE) (Woolam M-2000DI) was used to monitor film thickness during depositions.[303]

For application as a ZAB catalyst, FeO_x films were deposited on a carbon gas diffusion layer (GDL; SIGRACET® 39BC, SGL Carbon) substrate. Si wafer pieces were also placed in the reactor to monitor film growth *in situ* via SE. All depositions with the carbon substrate experienced a 60 s O plasma treatment prior to deposition. In previous studies in our group of ALD-coated GDL using MnO_x, 40 nm thick films were deposited on GDL for use in electrochemical testing.[157] However, considering the growth rate for FeO_x in this work (0.1 Å $cycle^{-1}$), depositing a 40 nm film was deemed impractical. ALD films of 10 nm were used throughout this study. Furthermore, the highly reactive O plasma required to enable ALD from EF is likely to etch the carbon substrate during direct deposition, damaging the electrode.[54] Therefore, a thin layer of MnO_x was deposited prior to FeO_x ALD whenever the carbon substrate was utilized; the saturation study did not involve this MnO_x sublayer. The MnO_x ALD process has been developed previously in our group and does not damage the GDL substrate since no O plasma is required. Instead, a forming gas plasma followed by a distilled water pulse enabled MnO_x growth.[157] MnO_x depositions were carried out in the same reactor, using a procedure outlined in previous work.[157] Bis(ethylcyclopentadienyl)manganese ($(EtCp)_2Mn$, 98%, STREM Chemicals, Inc.) was used as the precursor and heated to 80 °C; valve and transportation lines were 100 °C and 110 °C, respectively. A vapour boost method was employed for $(EtCp)_2Mn$, wherein inert Ar gas was pushed into the ampoule and allowed to equilibrate with the precursor vapours and released into the reactor. The Ar gas effectively carried $(EtCp)_2Mn$ vapours out of the ampoule and into the reactor, which enabled the use of a low vapour pressure precursor without requiring a bubbler.[292]

Approximately 1 nm of MnO_x was first deposited onto the carbon substrate as a protective coating, followed by 9 nm of FeO_x at a substrate temperature of 150 °C. A schematic of the ALD process on the GDL samples is provided in Figure 3.2. The MnO_x sublayer was not considered electrochemically active and samples are simply referred to as FeO_x. ALD of the MnO_x sublayer followed the timing scheme of 3/2/20/20/2/30 as reported by Clark *et al.*[157] and explained in Figure 3.2, while FeO_x depositions on the carbon substrate utilized the optimized timing scheme of 3/20/15/5 as reported in this work. Substrate temperatures of 50 °C and 300 °C were also used to deposit the MnO_x – FeO_x dual layers. In an attempt to induce crystallinity and remove impurities from the ALD process, a 300 °C annealing heat treatment in air was applied for 30 minutes to select samples.[157] These are designated as An (*e.g.*, FeO_x – An). Samples without this

annealing step were used as-deposited (unannealed) from the ALD reactor and designated Un (*e.g.*, FeO_x – Un).

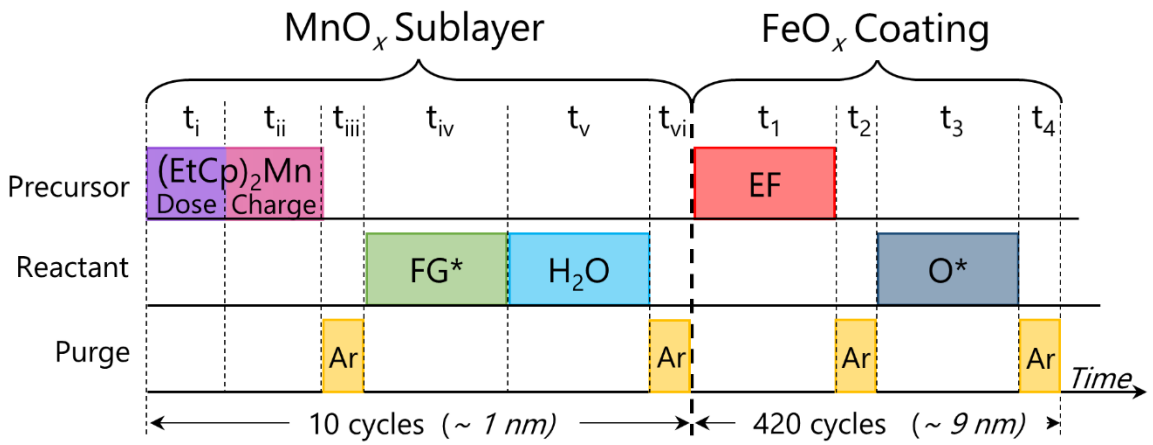

Figure 3.2. Schematic of ALD process for depositions on GDL. t_i, t_{ii}, t_{iii}, t_{iv}, t_v, and t_{vi} are the ALD timings (in seconds) for the MnO_x process (3/2/20/20/2/30). The vapour boost technique is comprised of t_i and t_{ii}, t_{iii} is the precursor purge, t_{iv} and t_v are the co-reactants, and t_{vi} is the reactant purge.[157] t_1, t_2, t_3, and t_4 are the ALD timings (in seconds) for the FeO_x process (3/20/15/5) as explained in Section 3.1. FG* and O* denote the FG and O plasma reactants, respectively.

3.2.2 Materials Characterization

The specific surface area (SSA) and pore size distribution of the microporous layer (MPL) of the GDL were obtained through N_2 physical adsorption/desorption at 77 K using an Autosorb-iQ-XR system. Samples were outgassed at 130°C for 4 h prior to the measurements. Quenched solid density functional theory (QSDFT) and Brunauer–Emmett–Teller (BET) methods were used to calculate the SSA. Pore size distribution was calculated from the adsorption curve using the QSDFT method, assuming slit and cylindrical pores, and the total pore volume was determined at a relative pressure (P/P_0, P = the equilibrium pressure and P_0 = the saturation vapor pressure of N_2 at 77 K) of 0.95. Atomic force microscopy (AFM) images and surface roughness of deposits on Si were obtained using a Bruker Dimension Icon AFM, operating in tapping mode in air. Root-mean-square (RMS) roughness values reported are the average of three values taken over different areas. A Zeiss Sigma 300 VP field emission scanning electron microscope (FE-SEM),

operating at an accelerating voltage of 10 kV, was used to obtain secondary electron images of ALD-coated GDL. A Tescan Vega3 scanning electron microscope (SEM), equipped with an Oxford Instruments energy dispersive X-ray (EDX) spectrometer, was used to image cross sectional samples and obtain EDX linescans, respectively. Cross sectional samples were prepared by fracturing unannealed ALD-coated GDL electrodes after cooling in liquid nitrogen. EDX linescans were repeated for at least five different regions per sample and showed overlapping spectra; the presented results are representative of each sample. Transmission/scanning transmission electron microscopy (TEM/STEM) and EDX analysis were conducted using a JEOL JEM-ARM200CF at an accelerating voltage of 200 kV. Sample preparation included scraping off surface material (ALD-coated GDL particles) from the microporous layer of the GDL and dispersing in ethanol before drop-casting directly onto carbon coated TEM grids. X-ray photoelectron spectroscopy (XPS) was performed with a Kratos AXIS Ultra spectrometer using monochromatic Al Kα (126 W, 1486.7 eV), operating at pass energy of 160 eV and 20 eV for the survey and high resolution scans, respectively. Shirley type background subtraction was used for all spectra.[270,304,305] All peak fitting utilized a 70%/30% Gaussian/Lorentzian product formula for line shape.[270] Spectra were calibrated using the main C 1s peak fit to a binding energy of 285.0 eV.[102]

3.2.3 Electrochemical Characterization

Electrochemical characterization was performed using a Biologic VSP-300 potentiostat. Linear sweep voltammetry (LSV) at a scan rate of 5 mV s^{-1}, as well as cyclic voltammetry (CV) at a scan rate of 20 mV s^{-1}, were conducted in a three-electrode cell with 1 M KOH at room temperature (~22 °C), saturated with either ultra high purity O_2 (99.993%, Praxair) or high purity Ar (99.998%, Praxair) flowing at 40 standard cubic centimeters per minute. A Hg/HgO reference electrode was employed, along with a Pt coil counter electrode. All LSV and CV potentials are versus Hg/HgO (+0.098 V vs. SHE) and all measurements were internal resistance corrected. The working electrodes were GDL coated with the designated ALD film. A Pt-Ru-C standard, for comparison, was prepared by spray coating a mixture of 40 wt% Pt-20 wt% Ru-balance carbon black powder (Alfa Aesar), H_2O, isopropyl alcohol, Nafion™ and polytetrafluoroethylene (PTFE) onto GDL (mass loading of 404 μg Pt cm^{-2} and 202 μg Ru cm^{-2}).

3.3 Results and Discussion

3.3.1 Saturation Curves

FeO_x growth using EF and an O plasma co-reactant was measured *in situ* via SE. Substrate-enhanced growth is observed for depositions directly on Si(100) from cycles 0 to 100, with a growth per cycle (GPC) of 0.17 Å cycle^{-1} (Figure S3.1a). A second linear region is established after 200 cycles, and this is deemed the saturating growth regime. GPC values calculated from this second linear region (Figure S3.1a) were used to construct Figure 3.3, which shows the GPC of the FeO_x ALD process when the various ALD timings ($t_1/t_2/t_3/t_4$) are modified. This saturation study was conducted on Si(100) substrates at a temperature of 150°C. The optimized timing scheme (3/20/15/5) was repeated three times to yield a saturating GPC of 0.09 ± 0.01 Å cycle^{-1} for the FeO_x process.

Saturation is thought to occur when all available active surface sites are occupied by a precursor molecule.[49] Therefore, under saturating conditions, the growth per cycle should remain constant despite an increase in precursor dose.[53,160] According to Figure 3.3a, 1 s of EF dose is sufficient to attain saturating behaviour. However, a dose time of 3 s is selected hereafter to ensure that saturating behaviour can still be obtained when other deposition parameters are manipulated; in this way, the EF dose time will not limit the extent of saturating behaviour for the remainder of the saturation study. Since ALD invokes self-saturating surface reactions, excess precursor does not affect film growth.[160] Furthermore, increasing the EF dose time may facilitate deposition into high surface area substrates, which is ultimately the end goal of this work.[306] In addition, extending the EF dose time from 1 s to 3 s only represents a 5% increase in total cycle time. The EF purge is more sensitive to time variation. As shown in Figure 3.3b, at least 20 s of inert gas purge is required to remove non-chemisorbed precursor molecules from the ALD chamber and maintain a constant GPC. The higher GPC values for purge times less than 20 s (Figure 3.3b) are attributed to non-conformal CVD-type deposition between EF and oxygen radicals as a result of insufficient purging.[52,158] Figure 3.3c demonstrates that a 15 s exposure to O plasma is required to fully react with all chemisorbed Fe precursor molecules. Less than 15 s of O plasma results in non-reacted Fe precursor molecules adsorbed to the surface, which prevent attachment of additional precursor molecules for the next cycle, lowering the GPC.[52,158] Since there is a fixed amount of chemisorbed molecules that can interact with the O plasma, increasing the reactant

dose past 15 s does not affect the saturating GPC, as shown in Figure 3.3c. The growth rate is essentially insensitive to variations in plasma purge time (Figure 3.3d), so that 5 s is sufficient to ensure a saturating mechanism. This result is in agreement with the understanding that plasma radicals have a short lifetime when the plasma source is removed, and necessary plasma purge times are very short or sometimes non-existent.[160]

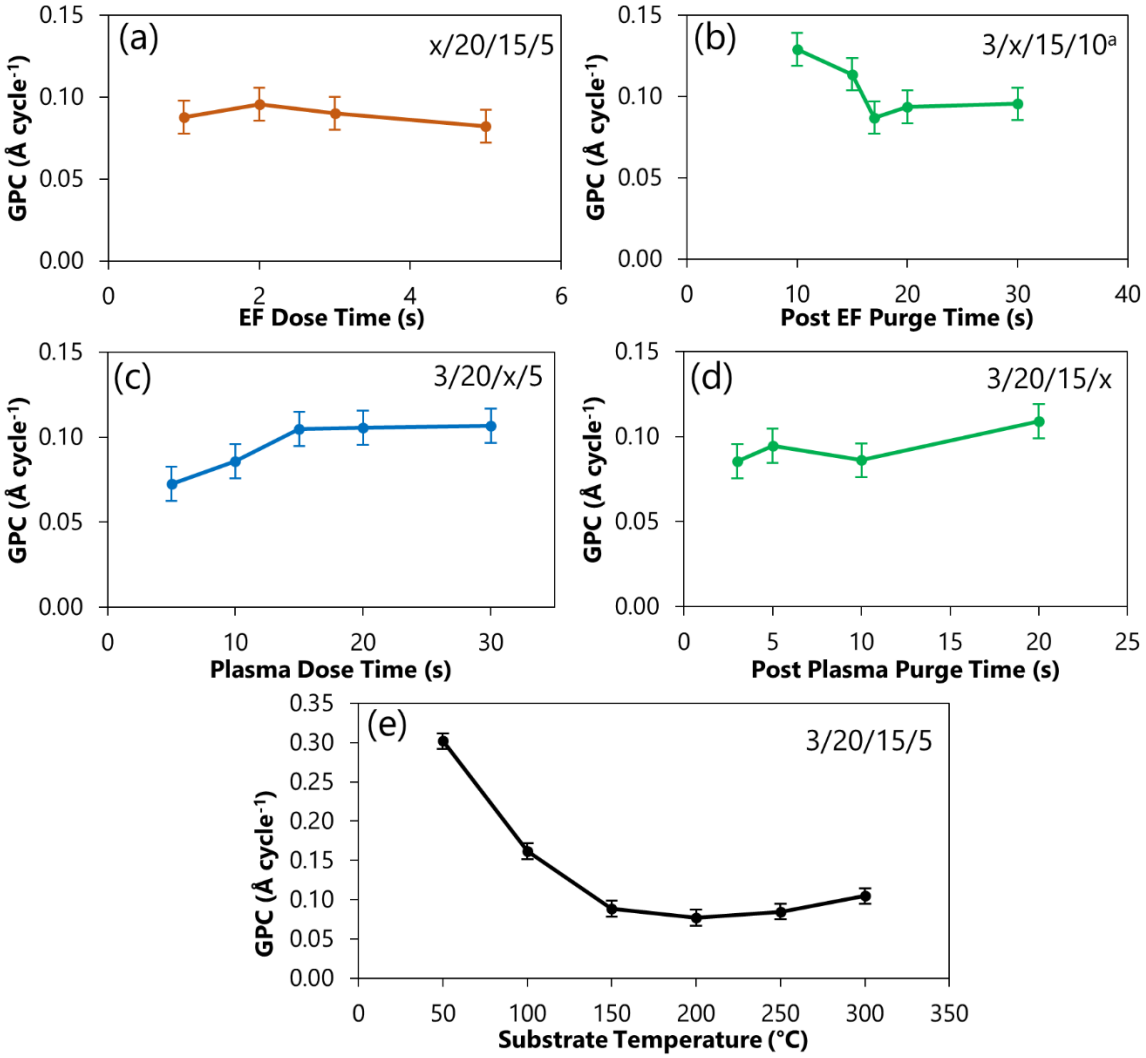

Figure 3.3. (a-d) Saturation curves for EF at 150 °C. GPC vs. (a) EF dose time, (b) post-EF purge time, (c) O plasma dose time, and (d) post-O plasma purge time. The labels for each figure show the ALD timing values ($t_1/t_2/t_3/t_4$), where t_1 is the EF dose time, t_2 is the EF purge time, t_3 is the plasma dose time, and t_4 is the plasma purge time. [a] A post-plasma purge time of 10 s was utilized, but (d) illustrates that both 5 s and 10 s are saturating. (e) GPC as a function of substrate temperature, with the label showing ALD timing values ($t_1/t_2/t_3/t_4$).

There exists a so-called ALD window where saturating ALD behaviour occurs over a range of substrate temperatures. Using the optimized timing scheme determined from Figures 3.3a-3.3d, the substrate temperature was varied and GPC recorded. Figure 3.3e provides an illustration of this ALD window, which exists from 150 °C to 250 °C. A large increase in GPC is observed for T<150 °C, which can be attributed to precursor condensation and CVD behaviour.[158,160] Additionally, it has been speculated that at reduced temperatures, the desorption kinetics for the precursor molecules is reduced. Therefore, longer purge times are necessary to prevent CVD behaviour from non-chemisorbed species.[157] On the other hand, the EF precursor decomposes in the range of 300 °C so that at T>250 °C precursor decomposition begins and CVD growth is exhibited.[215] While this increases the growth rate, it can eliminate the conformal nature that is characteristic of ALD.

3.3.2 EF Reactivity

The ALD films in this work are ultimately designed for use on a carbon-based substrate and, as such, there were concerns that an O plasma may cause carbon etching, thereby reducing the electrochemical performance of the electrode.[160,166] Thus, other reactants aside from the O plasma were also considered. A previous study found that an FG plasma, followed by a water pulse, yielded favourable deposition behaviour from a similar cyclopentadienyl-based precursor during MnO_x deposition.[157] When coupled with EF, an FG plasma reactant alone produced a GPC value half that of an O plasma (Figure S3.2b). Furthermore, a subsequent water pulse to deposit an oxide film did not improve the GPC (Figure S3.2c). Using only distilled water as a reactant yielded zero growth, as did O_2 gas without any RF plasma. H plasma, generated from a 5% H_2-95% Ar gas mixture, was also employed as a reactant but the growth rate was similar to that of the plasma (Figure S3.2d). All the alternative reactants had lower growth rates than the O plasma and were not pursued any further.

The poor growth behaviour from the alternative reactants is likely due to ethylferrocene's chemical stability. One of EF's attractive properties as an ALD precursor is that it is air stable, reducing the cost of handling and improving safety.[216] At the same time, this property causes EF to be fairly unreactive with most reactants. The stability of EF stems from the ferrocene molecule from which it is derived. The cyclopentadienyl rings that sandwich Fe create Fe-C bonds that complete the 18-electron rule. In organometallic chemistry, the most stable organometallic

complex is one that satisfies the 18-electron rule.[189] Thus, extraordinary reactive species are required to break the Fe-C bonds and form new Fe-O bonds.[158] O plasma radicals, along with O_3, are among the most reactive ALD reactants, which enable the growth of FeO_x from ferrocene.[165,307] The ethyl group in EF is thought to primarily provide volatility and not reactivity.[158] Thus, an O plasma is still required to enable appreciable growth from EF.

Since alternative co-reactants were deemed unsuccessful, a MnO_x sublayer was deposited on the carbon GDL substrates prior to FeO_x growth. The MnO_x layer shielded the carbon substrate from the highly oxidizing environment of the O plasma utilized during FeO_x deposition. Figure S3.1b presents the growth characteristics of the MnO_x – FeO_x dual layer electrode. The substrate-enhanced growth rate for the FeO_x process is amplified with a MnO_x sublayer, doubling in value. Furthermore, the saturating GPC is increased by 70%. The overall increase in growth rate is attributed to preferred growth of FeO_x on a MnO_x surface as opposed to a Si oxide (SiO_x) surface. This modification to the saturating GPC based on a different starting substrate has been noticed for other ALD chemistries as well.[308,309] For Ni oxide (NiO_x) deposition on a tungsten substrate, Song *et al.* have attributed an increase in saturating GPC to tungsten species that are continuously carried onto the growing film surface layer. As a result, the preferred growth of NiO_x on a tungsten-based surface increased the saturating GPC relative to a Pt or Ru substrate which propagates a NiO_x surface during ALD growth.[310] In the current work, however, no MnO_x substrate species were detected during XPS analysis, ruling out this possible mechanism. A thorough explanation of the enhanced saturating GPC from a MnO_x sublayer is not available at this time.

In this work, EF exhibits a low saturating GPC of 0.1 Å cycle^{-1} at a substrate temperature of 150 °C. A similar Fe precursor, TBF, demonstrated a saturating GPC of 0.2 Å cycle^{-1} at 150 °C, as reported by Ramachandran *et al.*, when combined with an O plasma reactant.[213] Both ferrocene derivatives satisfy the 18-electron rule and have similar vapour pressures.[213,216] The extension of the cyclopentadienyl ligand from an ethyl group to a butyl group is not expected to increase the reactivity of the metal center. On the other hand, Ramachandran *et al.* used a static flow ALD system, where the precursor is pulsed into the ALD chamber and allowed to sit without inert gas flow.[213] For this study, a continuous flow ALD system is used, where inert gas flows during the precursor pulse step. This difference in ALD design is likely responsible for the

discrepancy in GPC values reported. As shown by Muneshwar and Cadien, the processes associated with chemisorption free up previously blocked active sites for additional chemisorption of precursor molecules.[311] However, with a continuous flow design, precursor molecules only have a short window of opportunity to adsorb onto the substrate surface before they are swept away by the flow gas. Thus, the additional surface sites created by chemisorption cannot be utilized by traditional continuous flow operation. Furthermore, desorption of precursor molecules may occur during the relatively long precursor purge time and the desorbed molecules are immediately escorted away from the substrate surface by the flow gas, leaving behind an unused surface site. Muneshwar and Cadien found that pulsing the precursor dose improved GPC since the additional active sites from chemisorption/desorption could be utilized by the next precursor pulse. This improvement in GPC was larger for bulky precursor molecules.[311] In a static flow ALD system, the precursor molecules are allowed to remain at the substrate surface for an extended amount of time, such that the additional surface sites from chemisorption/desorption can be utilized. In this regard, static flow systems are comparable to a pulsed continuous flow system. Therefore, a higher GPC would be anticipated for a static flow system over a traditional continuous flow system,[312] particularly since EF and TBF are relatively bulky precursor molecules.

3.3.3 FeO_x Characterization

To confirm the conformal nature of the FeO_x ALD process, and to demonstrate the ALD temperature window, AFM was performed for depositions on Si at 50, 150, and 300 °C (Figure 3.4). Comparison of an uncoated Si(100) wafer and FeO_x deposition at 150 °C on Si(100) (Figures 3.4a and 3.4c, respectively) showcases ideal conformal growth, with no increase in RMS roughness. Operating at a substrate temperature of 150 °C was shown to produce ideal saturating behaviour in Figure 3.3 and the AFM results corroborate this. Furthermore, Figure 3.3 indicates that substrate temperatures of 50 °C and 300 °C are outside of the ALD temperature window and yield non-ideal growth, which should generate less conformal and rougher deposits. AFM images of 50 °C and 300 °C FeO_x depositions (Figures 3.4b and 3.4d, respectively) confirm this hypothesis, with more than a 10% increase in surface roughness. The absolute roughness between 150 °C and non-saturating temperatures of 50 °C and 300 °C is relatively low

because the deposited films are only 10 nm in thickness. However, the roughness values presented in Figure 3.4 are similar to other reports for FeO_x ALD.[213,224]

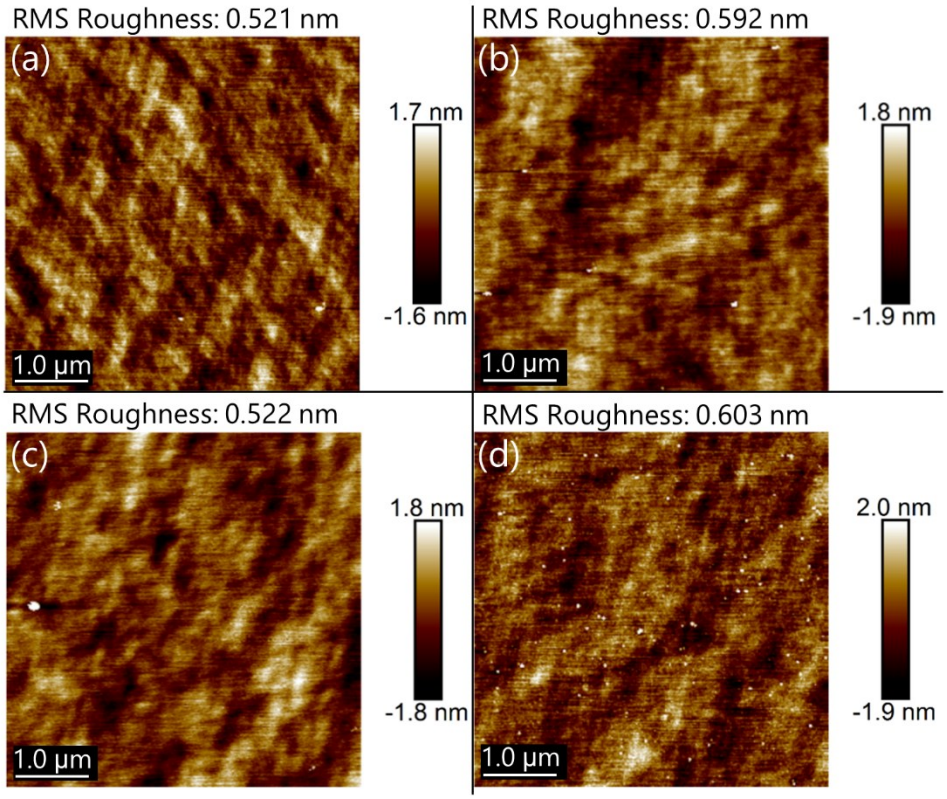

Figure 3.4. AFM images of FeO_x deposits on a Si(100) wafer. (a) Bare Si(100) without any deposition, (b) FeO_x at 50 °C, (c) FeO_x at 150 °C, and (d) FeO_x at 300 °C. All depositions followed the ALD timing scheme of 3/20/15/5.

SEM was used to image the FeO_x deposited on the carbon substrate (GDL). Figure S3.3 shows images of the 150 °C FeO_x film in the unannealed and annealed conditions (Figures S3.3b and 3.3c, respectively). Also included is the bare substrate without any ALD coating (Figure S3.3a). Overall, there is no appreciable difference in morphology after deposition of a 10 nm FeO_x coating, or after a 300 °C annealing treatment for 30 minutes. Since the GDL particles are on the order of 100 nm in size, a 10 nm coating is difficult to distinguish in the SEM.

To examine the penetration depth of ALD into the porous GDL, cross sectional SEM was performed with EDX line scans revealing the relative amounts of Fe from the surface of the substrate into the porosity (Figure 3.5). Linescans were done for FeO_x ALD at substrate temperatures of 50, 150, and 300 °C (Figures 3.5f, 3.5g, and 3.5h, respectively). The total

number of FeO_x ALD cycles was 243, 420, and 365 for 50, 150 and 300 °C, respectively, to account for the differences in growth rate (Figure 3.3e), so that similar film thicknesses were deposited. Figure 3.5b illustrates the morphology of the GDL in this work, comprised of a high surface area MPL and a high porosity backing layer (BL). Using N_2 physisorption analysis, the total pore volume and pore size distribution of the GDL substrate was determined (Figures S3.4a and S3.4b, respectively). The total pore volume is 0.009 $cm^3\ g^{-1}$ with a BET surface area of 50 $m^2\ g^{-1}$. Low-magnification images of Figures 3.5f, 3.5g and 3.5h (Figures 3.5c, 3.5d and 3.5e, respectively) demonstrate that linescans were taken from the MPL. This bilayer construction for the GDL facilitates transport of oxygen into the cell while still providing a support for catalyst loading and preventing leakage of the electrolyte.[32] In order to deposit films deep within the porosity of this substrate, precursors and reactants must diffuse through the porosity. For plasma-based ALD, surface recombination of plasma radicals often limits the deposition of high aspect ratio substrates. This phenomenon may be temperature dependent, with higher temperatures reducing the coverage of high aspect ratio structures.[166,307]

In line with previous work on ALD of porous GDL (MnO_x deposition), it was anticipated that the non-saturating deposition temperatures of 50 °C and 300 °C would result in a lower penetration depth of Fe.[54] However, EDX results do not support this behaviour (Figure 3.5a). At higher depths into the porosity (*e.g.*, 6 μm), the Fe signal is largest for the 50 °C sample, with the 150 °C and 300 °C samples exhibiting a lower Fe signal. This trend indicates that temperature contributes towards the penetration depth of FeO_x into the GDL. The pressure inside the reaction chamber is maintained at approximately 1 Torr during deposition; therefore, the mean-free-path of the precursor molecules is large relative to the porosity size and is not likely responsible for the variation in deposition coverage. Moreover, an increase in temperature would increase the mean-free-path of the precursor molecules, contrary to the observed behaviour (Figure 3.5a).[313] Thus, recombination losses of the plasma radicals is likely the major factor limiting deposition deep within a porous structure; the depth of deposition is not constrained by non-saturating ALD behaviour. Another potential reason why non-saturating behaviour does not impact penetration depth of the FeO_x in this work is that ALD coatings are only 10 nm thick, while previous work in our group on ALD of porous GDL used 40 nm thick films (MnO_x). In the latter case, non-saturating depositions were found to fuse GDL particles together and reduce overall porosity. This loss in porosity was likely a contributing factor to the reduction in penetration depth.[54,157]

As shown in Figure S3.3, the 10 nm coatings in this work do not fuse GDL particles together or modify the porosity. Overall, the penetration depth of ALD coatings in this work aligns with previous work in that the peak Fe signal is identified at ~2 μm from the surface and that the signal tapers off to a baseline values at around 10-15 μm.[54,157] This depth of catalyst loading is an improvement over other synthesis methods, such as electrodeposition or spray coating, and is proposed to improve cycling performance of the air electrode in a ZAB by limiting the effects of electrolyte flooding.[54,157]

Since the 10 nm films deposited in this work are indistinguishable in the SEM, TEM/STEM was required to resolve the FeO_x coating on the GDL particles. STEM analysis of the unannealed FeO_x is shown in Figure 3.6. The high angle annular dark field (HAADF) image (Figure 3.6a) shows the nano-sized features present in the MPL of the GDL. A thin coating surrounds the spherical particles, represented by bands of higher brightness in the HAADF image, due to the higher atomic numbers of Fe and O relative to carbon. EDX maps of Fe and O clearly illustrate the coating (Figures 3.6c and 3.6d, respectively). The elemental maps are convincing evidence of a conformal coating that encases the carbon particles. The overlap of Fe and O signals indicates the presence of an FeO_x, confirming the success of the ALD recipe. A selected area diffraction (SAD) pattern obtained from the unannealed FeO_x coating is provided in Figure 3.6b. Several rings were identified from this pattern and their d spacing values are presented in Table 3.1. Also shown in Table 3.1 are the d spacing values for α-Fe_2O_3 (Figure S3.5), which are a good match for those in Figure 3.6b. Therefore, SAD results indicate the FeO_x coating is deposited as α-Fe_2O_3. It is not surprising that a highly energetic O plasma reactant produces the most thermodynamically stable, oxygen-rich phase of FeO_x.[93]

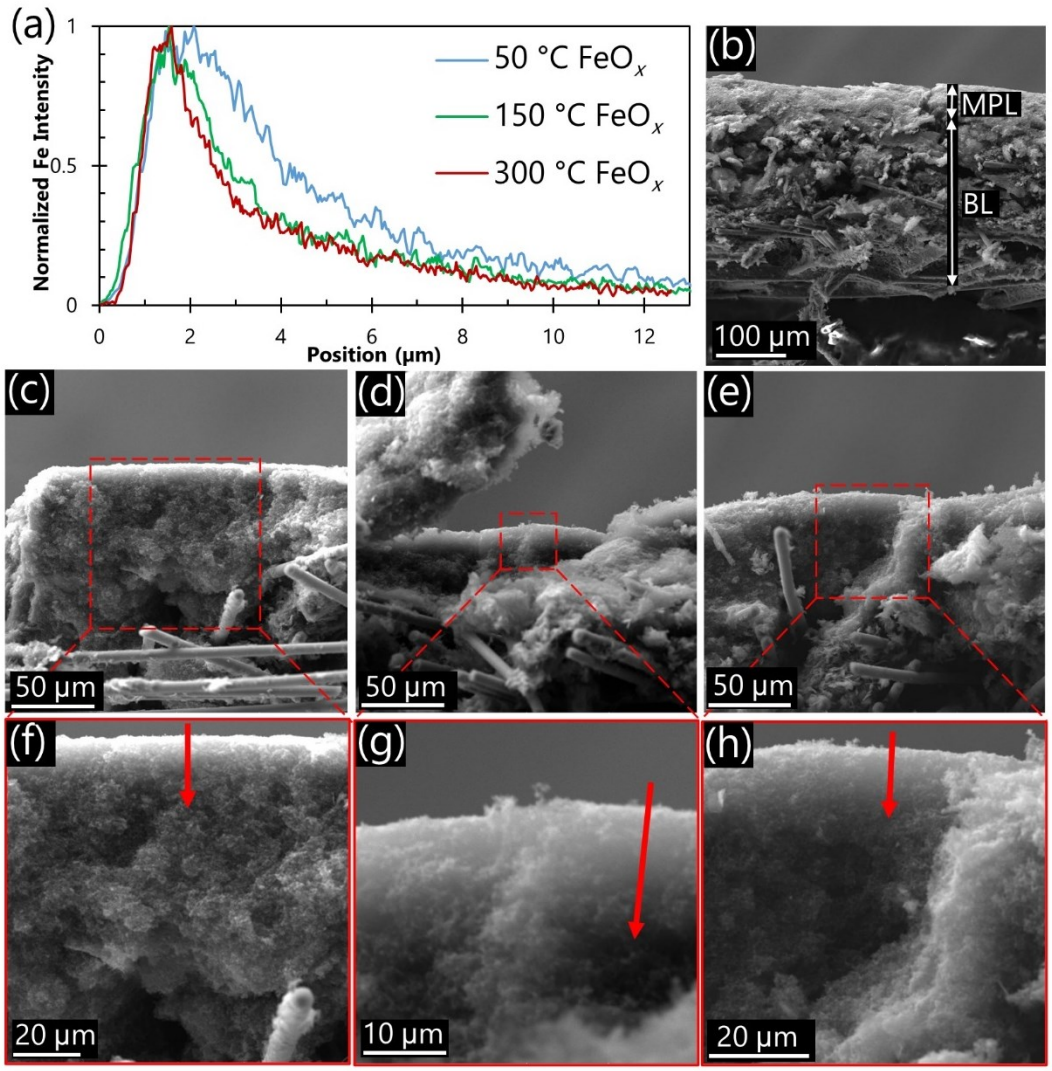

Figure 3.5. EDX linescans and secondary electron images from cross sections of unannealed ALD-coated GDL. (a) Fe EDX distributions for 50, 150, and 300 °C FeO_x depositions. The intensities are normalized with respect to the maximum number of Fe X-ray counts. (b) Low-magnification view of GDL cross section, illustrating the microporous layer (MPL) and backing layer (BL), (c, d, e) low-magnification view of panels f, g and h, respectively, with the red boxes showing the regions of higher magnification, and (f, g, h) SEM images of 50, 150 and 300 °C cross sections, respectively, with red arrows indicating the location of the linescans in panel (a).

A high resolution TEM (HRTEM) image, showing the FeO_x coating on the carbon substrate, is provided in Figure 3.6e. The thickness of the indicated particle is ~10 nm which correlates with the SE results. Additional thickness measurements were done on 25 particles using high

magnification HAADF images. The average thickness was 8.0 nm (standard deviation of 1.3 nm), which is slightly lower than the value determined using SE of deposits on Si substrates.

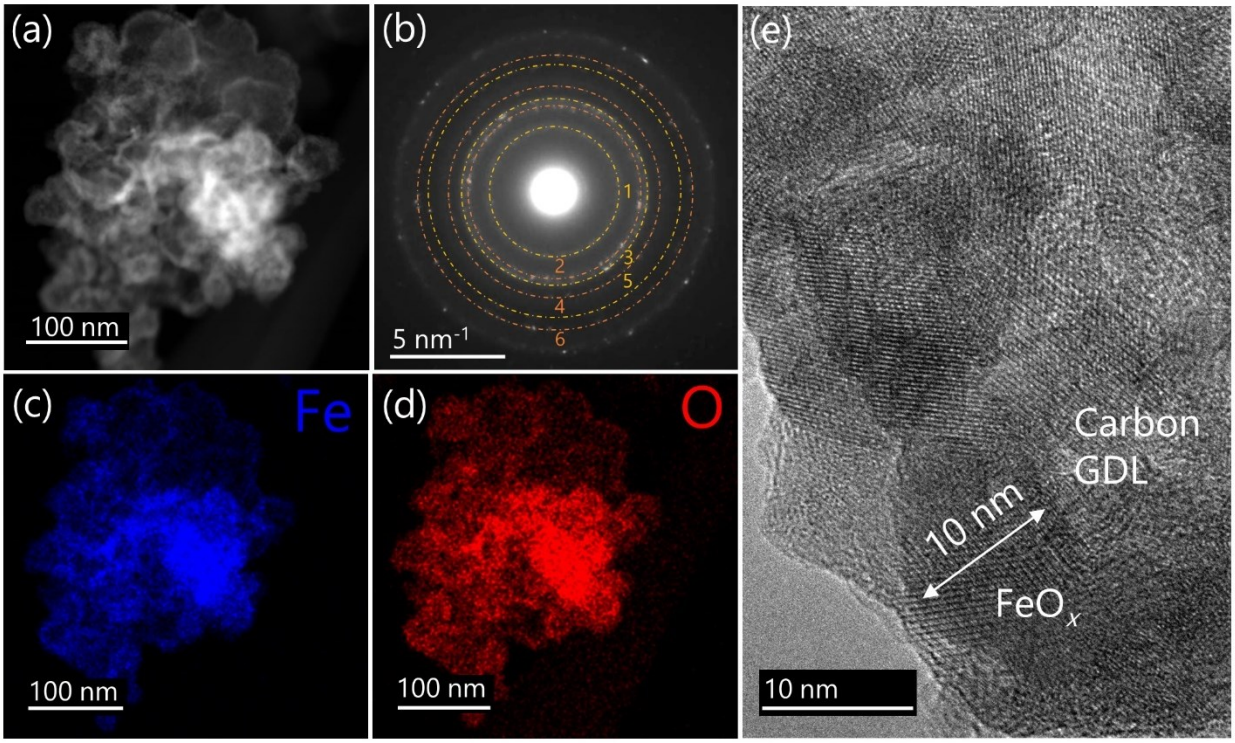

Figure 3.6. STEM analysis of unannealed 10 nm FeO_x coating on GDL. (a) HAADF image. (b) SAD pattern; indexing of the SAD pattern is presented in Table 3.1. EDX mapping of (c) Fe and (d) O. (e) HRTEM image.

STEM analysis after a 300 °C annealing treatment for 30 minutes is shown in Figure 3.7. Similar to Figure 3.6, a thin coating is present around the nano-featured carbon particles, manifesting as bright bands in the dark field image (Figure 3.7a). EDX mapping (Figures 3.7c and 3.7d) confirms the FeO_x coating is still present after annealing, with Fe and O signals overlapping as with the unannealed sample. SAD from annealed FeO_x produces a similar pattern to its unannealed counterpart; indexing of Figure 3.7b in Table 3.1 reveals that the crystal structure of hematite is maintained after annealing. FeO_x thicknesses were measured using HAADF images (15 particles) and the average thickness of 7.9 nm (with a standard deviation of 1.0 nm) is essentially the same as that for the unannealed sample. Furthermore, an HRTEM image (Figure 3.7e) indicates the same oxide thickness as the unannealed oxide layer (~10 nm).

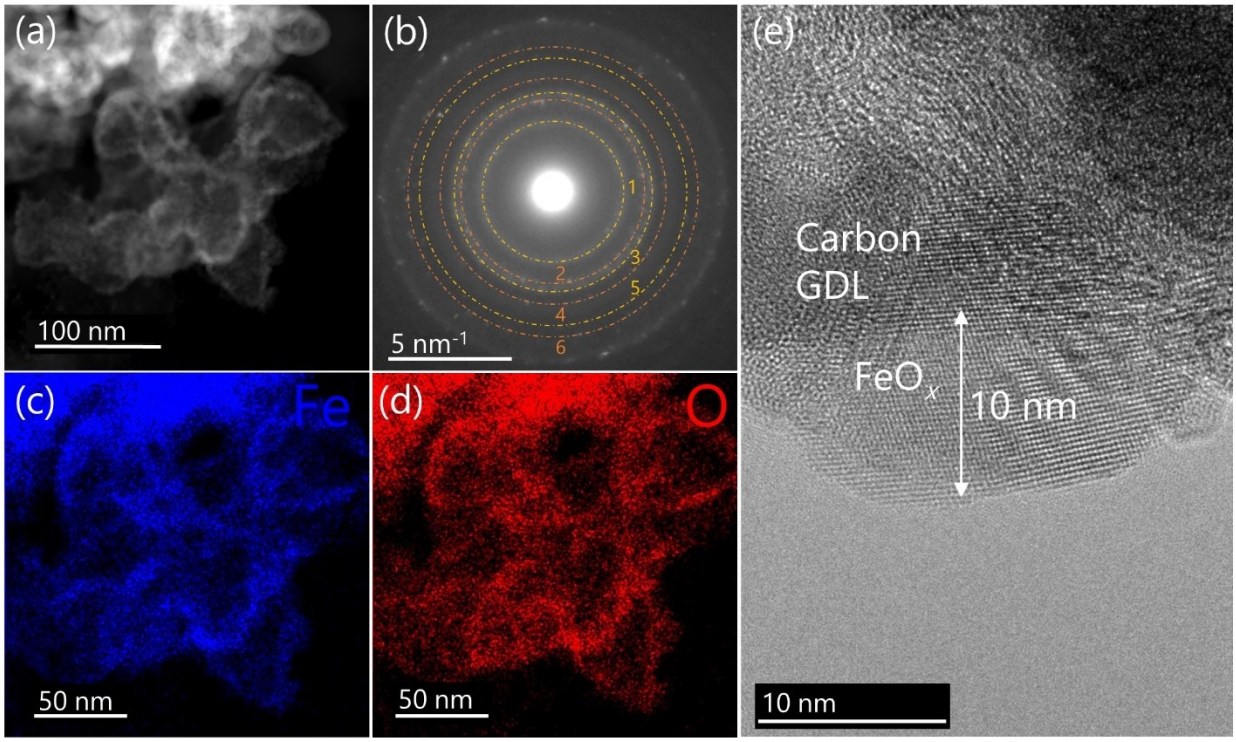

Figure 3.7. STEM analysis of annealed 10 nm FeO_x coating on GDL. (a) HAADF image. (b) SAD pattern; indexing of the SAD pattern is presented in Table 3.1. EDX mapping of (c) Fe and (d) O. (e) HRTEM image.

Table 3.1. SAD pattern d spacings for unannealed and annealed FeO_x compared with the d spacings, Miller indices and intensity values for α-Fe_2O_3 (hematite: PDF#33-0664).

	FeO_x – Un	FeO_x – An	α-Fe_2O_3		
Ring No.	d spacing (nm)	d spacing (nm)	d spacing (nm)	Rhombohedral (h k l)	Intensity (%)
1	0.361	0.365	0.3684	(0 1 2)	30.0
2	0.265	0.265	0.2700	(1 0 4)	100.0
3	0.248	0.246	0.2519	(1 1 0)	70.0
4	0.219	0.215	0.2207	(1 1 3)	20.0
5	0.180	0.181	0.1840	(0 2 4)	40.0
6	0.168	0.168	0.1694	(1 1 6)	45.0

The identity of the unannealed FeO_x was further probed through XPS analysis. Figure 3.8 presents the survey, C 1s, O 1s and Fe 2p spectra of the FeO_x deposit on GDL, with deconvolution results indicated by coloured curves and tabulated in Table S3.1. In Figure 3.8b, the main component of the C 1s spectrum (shown in red) is attributed to alkyl carbon (C-C, C-H),[270] and was set to a binding energy of 285.0 eV to calibrate all XPS spectra.[102] A shoulder peak at 286.2 eV (shown in green) was identified as ether and hydroxyl contributions (C-O-C and C-O-H, respectively).[157,270,314,315] A second peak at 288.9 eV (shown in blue) is due to carboxylate (O=C-O).[270,314–316] The presence of an F peak in the survey scan (Figure 3.8a) indicates that at least some of the GDL substrate (which contains PTFE) was also sampled by XPS and that some of the carbon signal may originate from the GDL. To discern how much carbon signal originated from the carbon-based substrate, XPS was also performed on the same ALD coating deposited on a Si substrate (Figure S3.6a). Comparison of the XPS results for FeO_x deposits on the GDL and Si substrates (Figure S3.6b) shows that the carbon levels for both substrates are similar, with slightly more carbon for the GDL sample. This indicates that only a minor amount of the carbon signal comes from the GDL itself. The remaining carbon signal may arise from impurities in the growing ALD film, adventitious carbon, or a combination of both. Unfortunately, sputter cleaning before XPS analysis to remove adventitious carbon is not feasible without also removing the thin ALD film, and thus adventitious carbon is inevitable. Therefore, the source of the carbon is not certain; however, both adventitious carbon and cyclopentadienyl ligand impurities contain alkyl carbon, which is the majority component in the C 1s curve (83% of the peak area). Ether, hydroxyl, and carboxylate contributions are likely a result of the highly oxidizing O plasma utilized in the ALD recipe.[317]

Deconvolution of the O 1s spectrum (Figure 3.8c) exhibits a large fraction (72.4% area) of lattice oxygen (M-O-M) at 529.8 eV (shown in red).[157,315,318,319] This is not surprising for a metal oxide surface. A shoulder at 531.4 eV (shown in green) matches well with hydroxide (M-O-H),[157,318,319] which is also expected in metal oxide samples. In agreement with the C 1s spectrum, a minor contribution from carboxylate (O=C-O) is located at 533.3 eV (shown in blue).[315,316]

For deconvolution of the Fe 2p spectrum (Figure 3.8d), three separate Shirley-type backgrounds were employed to better subtract the background signal. One background was utilized for the $2p_{3/2}$ multiplet-splitting, another was created for the $2p_{3/2}$ satellite at 717.8 eV, and the last one

covered the $2p_{1/2}$ and respective satellite peak.[320] The main Fe $2p_{3/2}$ peak requires multiplet splitting due to unpaired electrons in Fe's orbital structure. When photoionization creates an electron vacancy in a core-shell, the outer-shell's unpaired electron can couple with the inner-shell unpaired electron, yielding a series of final states that are presented in the photoelectron spectrum.[270,320] Deconvolution of the Fe $2p_{3/2}$ exposed four peaks at 709.8, 710.9, 712.2, and 713.7 eV (shown in red); the full-width half-maximum (FWHM) of these sub peaks was restricted to 1.6 eV as reported by Grosvenor *et al.*[320] This deconvolution of the Fe $2p_{3/2}$ is in agreement with literature for FeO_x in a 3+ oxidation state.[102,270,320] A so-called pre-peak was required to better fit the data at 707.9 eV (shown in green). This pre-peak has been reported to be caused by defects in the structure, likely a result of synthesis.[320] A clear satellite feature was found at 718.8 eV (shown in blue) for the Fe $2p_{3/2}$. This value is corroborated in the literature,[316,318,320,321] and the 8 eV difference between the main $2p_{3/2}$ peak and the satellite feature (Figure 3.8d) is evidence of α-Fe_2O_3.[321–323] This distinct satellite peak is well-known to be absent in Fe_3O_4 spectra, reinforcing the Fe_2O_3 identification.[321,322] The Fe $2p_{1/2}$ main peak is located at 724.3 eV (dashed red), further indicative of a 3+ Fe state.[305,321] An Fe $2p_{1/2}$ satellite feature at 732.4 eV was also fit to the spectrum (dashed blue). Excluding the satellite features, the area ratio (Table S3.1) between the Fe $2p_{1/2}$ peak and $2p_{3/2}$ peak is 0.5, as expected for 2p spectra.[268]

High resolution XPS scans of Mn 2p and 3s did not reveal any discernible signal, in line with the absence of Mn peaks in the survey scan (Figure 3.8a). This indicates that there is no contaminating Mn species on the surface layer. Thus, electrochemical testing was conducted on a pure FeO_x surface without any contributions from the MnO_x sublayer.

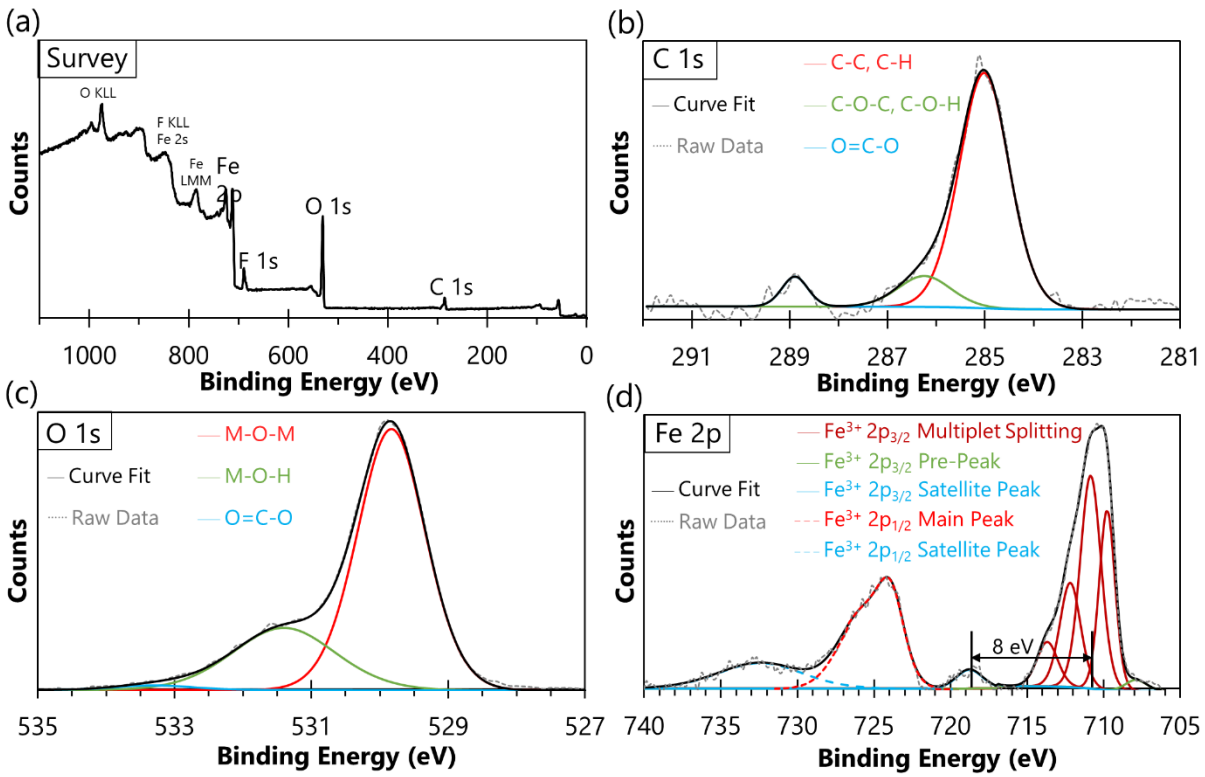

Figure 3.8. XPS results for unannealed FeO_x on the GDL substrate. (a) Survey scan, (b) deconvolution of the C 1s spectrum, (c) deconvolution of the O 1s spectrum, and (d) deconvolution of the Fe 2p spectrum. Both the Mn 2p and 3s spectra (not shown) presented only background noise, indicating no Mn is present at the surface of the oxide. The F signal in (a) originates from PTFE in the GDL substrate.

3.3.4 Electrochemical Performance

Preliminary electrochemical testing was done on the ALD FeO_x films to demonstrate their potential application as catalysts, primarily for OER. For completeness, however, both OER and ORR LSV tests were done in O_2-saturated 1 M KOH and the results are shown in Figure 3.9. Ar-saturated CV tests were also conducted on the FeO_x films in the ORR potential range. These show negligible current (Figure S3.7), confirming that the currents in Figure 3.9a are entirely due to ORR. For quantitative comparison, the ORR/OER onset potentials in this work are defined as the potentials at which |10| mA cm^{-2} is obtained. Onset values are summarized in Table S3.2. Figure 3.9a reveals an improvement in ORR performance upon coating the GDL with FeO_x. The onset potential is improved by 40 mV, and the maximum current density is nearly doubled. The

OER performance of the FeO_x samples is drastically superior to bare GDL, with the latter unable to reach 10 mA cm^{-2} at 1 V (Figure 3.9b). No difference is observed between the annealed and unannealed FeO_x in terms of ORR and OER. Previous work on MnO_x showed improvement in electrochemical activity after annealing, which was attributed to the removal of N and C contamination, as well as the oxidation of transition metal elements.[54] For the FeO_x in this work, the highly-reactive O plasma reactant likely eliminated any carbon contamination and the plasma fully oxidized the Fe species during deposition. TEM diffraction analysis (Table 3.1) indicated that there was no change in crystal structure after annealing. Thus, an annealing step resulted in no noticeable improvement. When compared to the Pt-Ru-C benchmark, the FeO_x-coated GDL is a poor ORR catalyst but shows promise as an OER catalyst. ORR and OER onset values for Pt-Ru-C are 130 mV and 170 mV better, respectively, than the values for FeO_x. On the other hand, the maximum current density of the FeO_x coating is superior to Pt-Ru-C at higher oxidizing potentials (Figure 3.9b).

One of the main hurdles associated with the FeO_x ALD process in this work is the slow growth rate of 0.1 Å $cycle^{-1}$. However, as shown in Figure S2, deposition of FeO_x on a MnO_x sublayer exhibits improved growth behavior, particularly for the substrate-enhanced growth regime. Therefore, the integration of multiple MnO_x layers into the FeO_x ALD process should boost the overall growth rate. This opens up the possibility of thicker coatings which are likely to improve the overall catalytic performance. However, the coating should not be too thick such that it blocks porosity in the air electrode. Porosity is necessary for oxygen and hydroxyl ion diffusion during ORR and OER, respectively. As an added benefit, the MnO_x film is catalytically active towards ORR.[157] Thus, the promising OER activity displayed by the FeO_x in this work could be combined with the ORR activity of the MnO_x layer to produce ALD coatings with bifunctional activity towards both ORR and OER. One approach is to use ALD supercycles, which involve depositing alternating layers of MnO_x and FeO_x. Bifunctional ALD coatings are the subject of on-going future work.

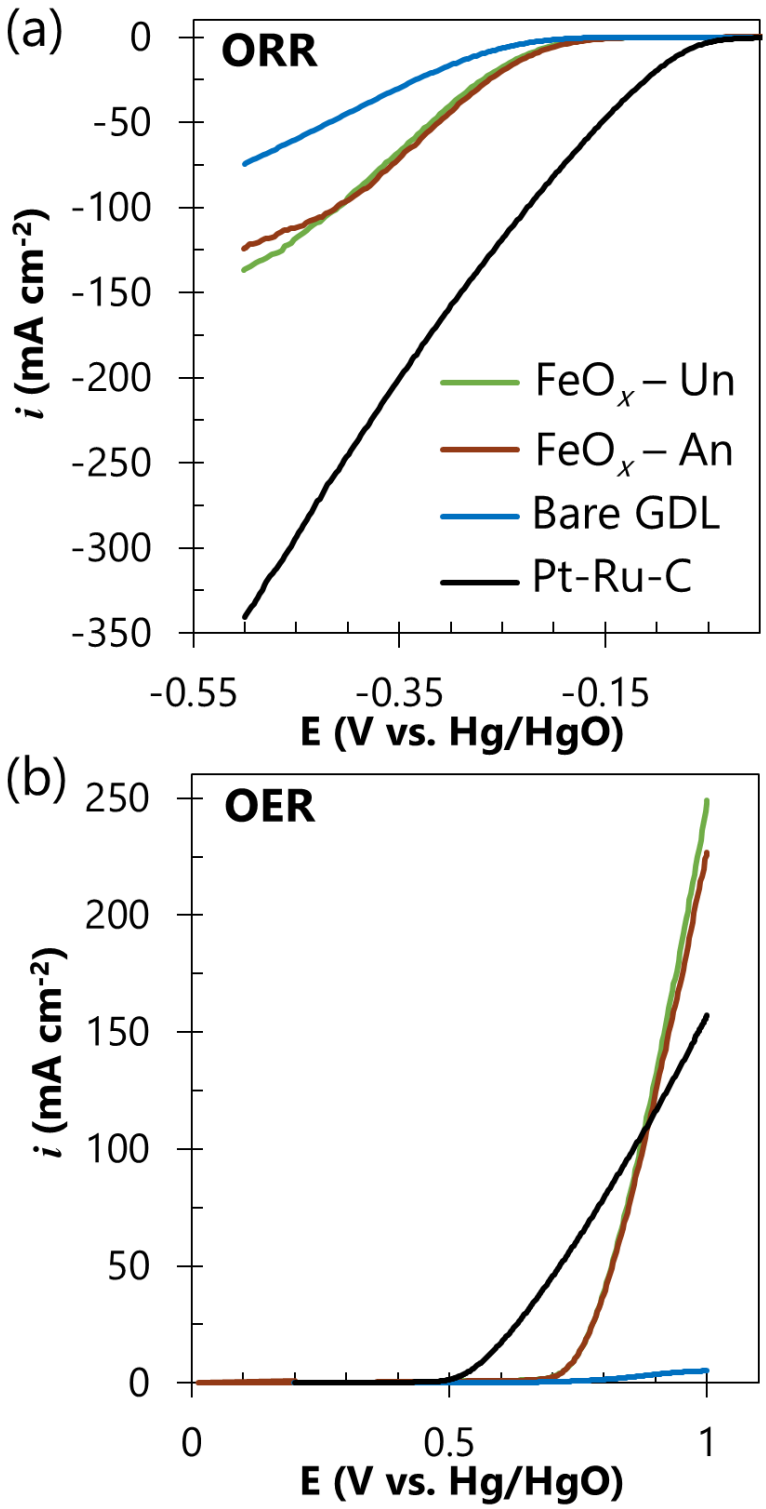

Figure 3.9. ORR and OER (a and b, respectively) LSV results for 10 nm thick unannealed (FeO_x-Un – green) and annealed (FeO_x-An – brown) FeO_x films, uncoated GDL (blue), and a Pt-Ru-C benchmark (black).

3.4 Conclusions

An FeO_x atomic layer deposition (ALD) process was developed using the novel precursor of ethylferrocene (EF) with an O plasma co-reactant. A relatively low saturating growth per cycle (GPC) of approximately 0.1 Å $cycle^{-1}$ was established over a wide temperature range of 150 °C to 250 °C. Thermal ALD reactants such as water were unsuccessful in achieving ALD growth with EF, while plasma reactants other than oxygen resulted in much lower GPC. The low reactivity of EF is a result of the inherent stability of the ferrocene molecule, which on the other hand enables EF to be air stable, reducing associated safety costs. Atomic force microscopy demonstrated that depositions at 150 °C yield ideally conformal coatings that do not increase surface roughness. At temperatures outside of this ALD window, increased surface roughness indicates non-ideal ALD behaviour.

The FeO_x coating was applied to porous carbon gas diffusion layers (GDL) for the application of ZABs. An ALD MnO_x layer was first deposited to protect the carbon-based substrate from the highly oxidizing O plasma co-reactant. Cross sectional X-ray microanalysis of ALD-coated GDL illustrated the high penetration depth of catalyst loading into the porosity. Substrate temperature was found to affect the extent of penetration, with non-ideal ALD growth having a minimal impact. Transmission electron microscopy analysis revealed a conformal FeO_x coating surrounds the GDL particles. Selected area diffraction patterns of this coating were indexed to α-Fe_2O_3; this was further corroborated by X-ray photoelectron spectroscopy.

The electrochemical half cell performance of GDL showed improvements in both the oxygen reduction and evolution reactions after deposition of the FeO_x, with promising activity for the oxygen evolution reaction displayed at higher oxidizing potentials. Annealing at 300 °C did not improve electrochemical performance of the FeO_x coating.

3.5 Supporting Information

Growth per cycle (GPC) is calculated from spectroscopic ellipsometry (SE) data from a Si(100) substrate during atomic layer deposition (ALD). Typical growth behaviour of the ALD process in this work is shown in Figure S3.1a. Film thickness increases linearly with cycle number for the first 100 cycles, then transitions to a new linear region with a lower slope. This substrate-enhanced growth may be the result of preferential precursor adsorption to a SiO_x surface as opposed to an FeO_x surface, or the result of a larger density of active surface sites on SiO_x.[154] As the film increases in thickness, the residual effect of the SiO_x substrate is lost. Therefore, the secondary linear region should continue indefinitely, since each ALD cycle refreshes a new FeO_x surface, presumably without any contribution from the original SiO_x substrate.[154] This secondary linear region was used as the GPC value in creating the plots in Figure 3.3.

Figure S3.1b illustrates the *in situ* SE data from growth of FeO_x on a sublayer of MnO_x. SE indicates the total film thickness is approximately 10 nm. While SE data is collected from a Si wafer, the carbon substrate (gas diffusion layer, GDL) was also placed in the deposition reactor. Scanning transmission electron microscopy results (Figures 3.6 and 3.7) confirm that the ALD coating is indeed approximately 10 nm in thickness on the GDL substrate. Figure S3.1b begins the first 10 cycles with a 1.4 nm MnO_x sublayer to protect the delicate carbon substrate from O plasma radicals. The remaining 420 cycles deposit an 8.3 nm FeO_x coating. One observation from Figure S3.1b is an increased growth rate for FeO_x as compared to ALD directly on the Si substrate (Figure S3.1a). Not only is the growth rate of the substrate-enhanced region increased (*i.e.*, the first 100 cycles), but also the secondary linear growth region experiences an increase in growth rate. An increase in the saturating GPC for different substrates has been observed for other ALD chemistries as well.[308,309]

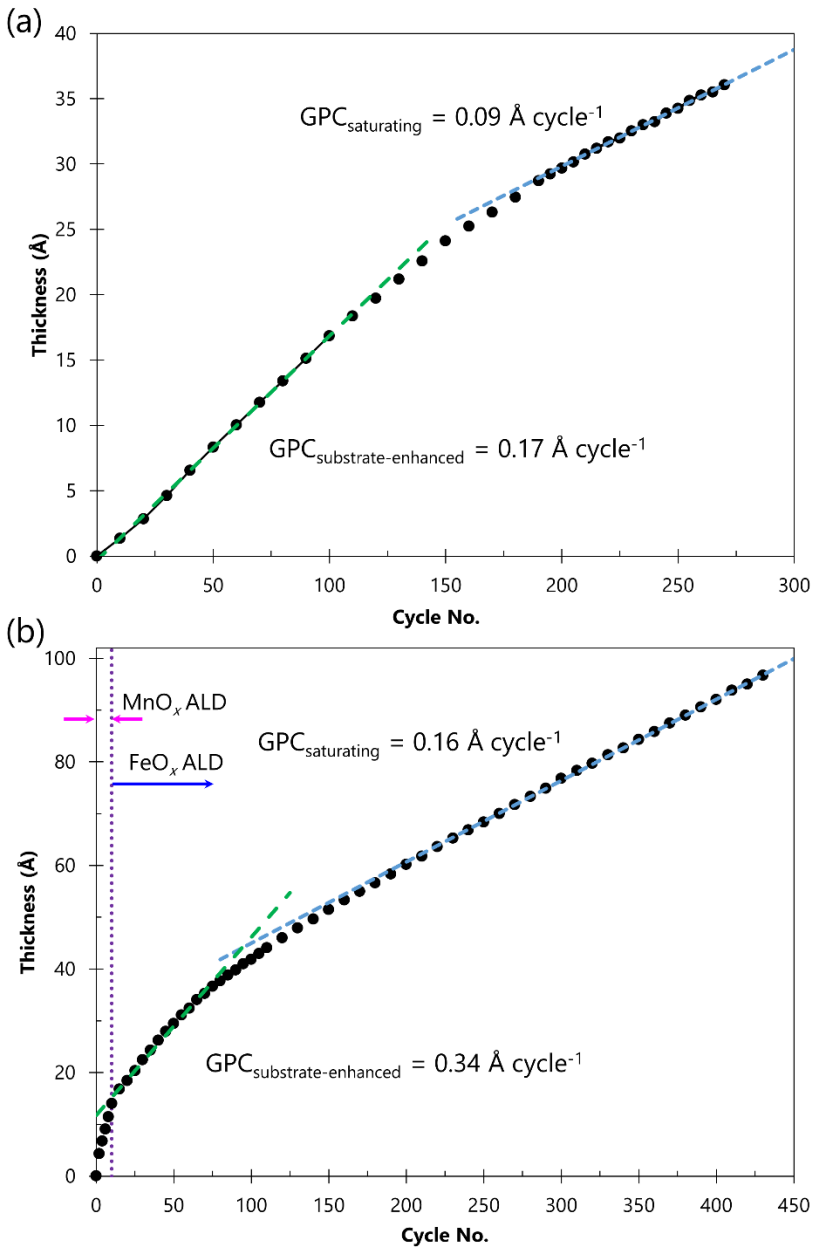

Figure S3.1. Thickness versus cycle number for FeO_x deposition at 150 °C using the optimized timing scheme (3/20/15/5). Thickness values extracted from *in situ* SE are represented by black dots. (a) Typical behaviour for ethylferrocene and an O plasma on a Si(100) wafer. Substrate-enhanced GPC is calculated from the slope of thickness values from cycle 0 to 100, while the saturating GPC is determined from cycle 200 to 270. (b) FeO_x deposition on a MnO_x sublayer. The first 10 cycles are deposition of Mn oxide (MnO_x), while the remaining 420 cycles are Fe oxide (FeO_x) growth. Substrate-enhanced GPC was calculated from cycle 10 to 75, while the saturating GPC was determined from the slope of the last 200 cycles.

Electrochemical characterization of the FeO_x films required direct deposition onto a carbon-based substrate. The highly reactive O plasma that successfully yields FeO_x growth is likely to etch the carbon surface and damage the functionality of the air electrode. Furthermore, polytetrafluoroethylene acts as a binder in the microporous region of the GDL and the highly oxidative environment of an O plasma may deteriorate the integrity of the GDL. Thus, alternative reactants for FeO_x ALD from ethylferrocene (EF) were investigated. Other highly active co-reactants available include a forming gas (FG: 5% H_2, 95% N_2) plasma or an H (5% H_2, 95% Ar) plasma. Furthermore, a previous report found that an FG plasma and water mixture served as an effective oxide reactant and was investigated.[157] The results of these investigations are showcased in Figure S3.2. A water reactant at substrate temperatures of both at 150 °C and 300 °C did not yield any ALD growth, despite this serving as a reliable oxide co-reactant for many other ALD studies.[176,224] Furthermore, a non-plasma O_2 gas reactant did not result in any detectible ALD growth at a substrate temperature of 300 °C. The plots in Figure S3.2 contain less than 100 ALD cycles since the alternative reactants were deemed inferior to an O plasma reactant (Figure S3.2a) based on the initial 50 cycles. Using the secondary linear regime, GPC values of 0.09, 0.05, 0.05, and 0.06 Å $cycle^{-1}$ were extracted for O plasma, FG plasma, FG plasma and water, and H plasma reactants, respectively.

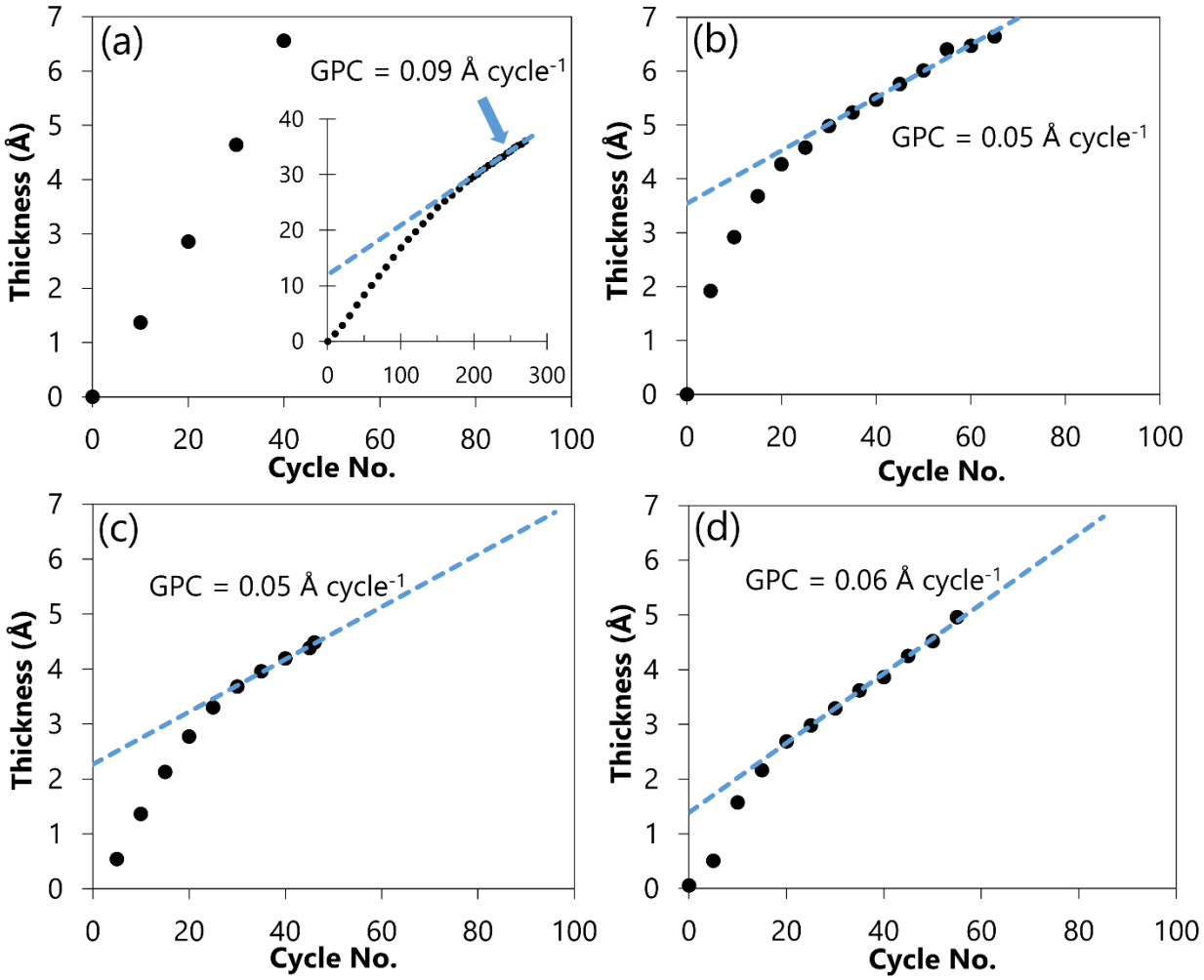

Figure S3.2. Thickness versus cycle number for FeO_x deposition at 150 °C using various reactants. Thickness values extracted from *in situ* SE are represented by black dots. (a) O plasma reactant, (b) FG plasma reactant, (c) FG plasma and water reactant, and (d) H plasma reactant. Tests were conducted at 150 °C and EF dose and purge times were always 3 s and 20 s, respectively. FG dose and purge times of 30 s and 5 s were employed in (b). FG dose and purge times, as well as water pulse and purge times, of 20, 3, 2 and 30 s were employed in (c). H plasma dose and purge time of 30 s and 5 s were employed in (d).

Field-emission scanning electron microscopy (FE-SEM) images of the FeO_x coating deposited on the GDL substrate are presented in Figure S3.3. Comparison of the bare substrate without deposition (Figure S3.3a) with the unannealed 10 nm FeO_x coating on GDL (Figure S3.3b) presents no noticeable difference in morphology; the porosity is maintained and no agglomeration of GDL particles is observed. This is most likely because the coating is merely 10 nm in thickness and the diameter of GDL particles is on the order of ~100 nm. Comparison of the unannealed and annealed coating (Figure S3.3b and c, respectively) demonstrates no morphology alterations as a result of the 300 °C annealing treatment.

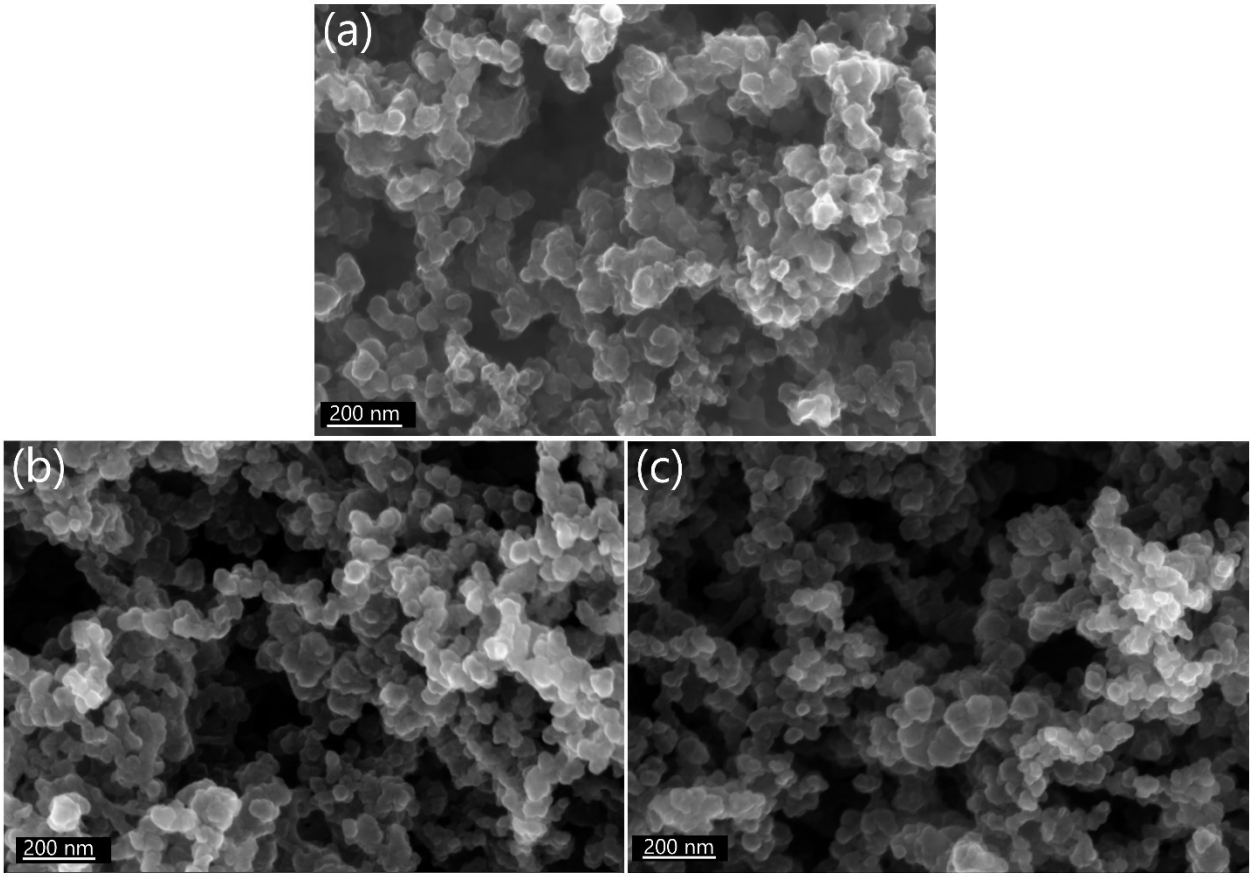

Figure S3.3. FE-SEM secondary electron images of ALD coatings on GDL. (a) Bare GDL without deposition, (b) unannealed FeO_x, and (c) annealed FeO_x. ALD coatings are approximately 10 nm in total thickness in all cases and were deposited at 150 °C using the optimized timing scheme (3/20/15/5).

An N_2 physisorption technique was used to analyze the porosity of the microporous layer (MPL) of the GDL substrate.

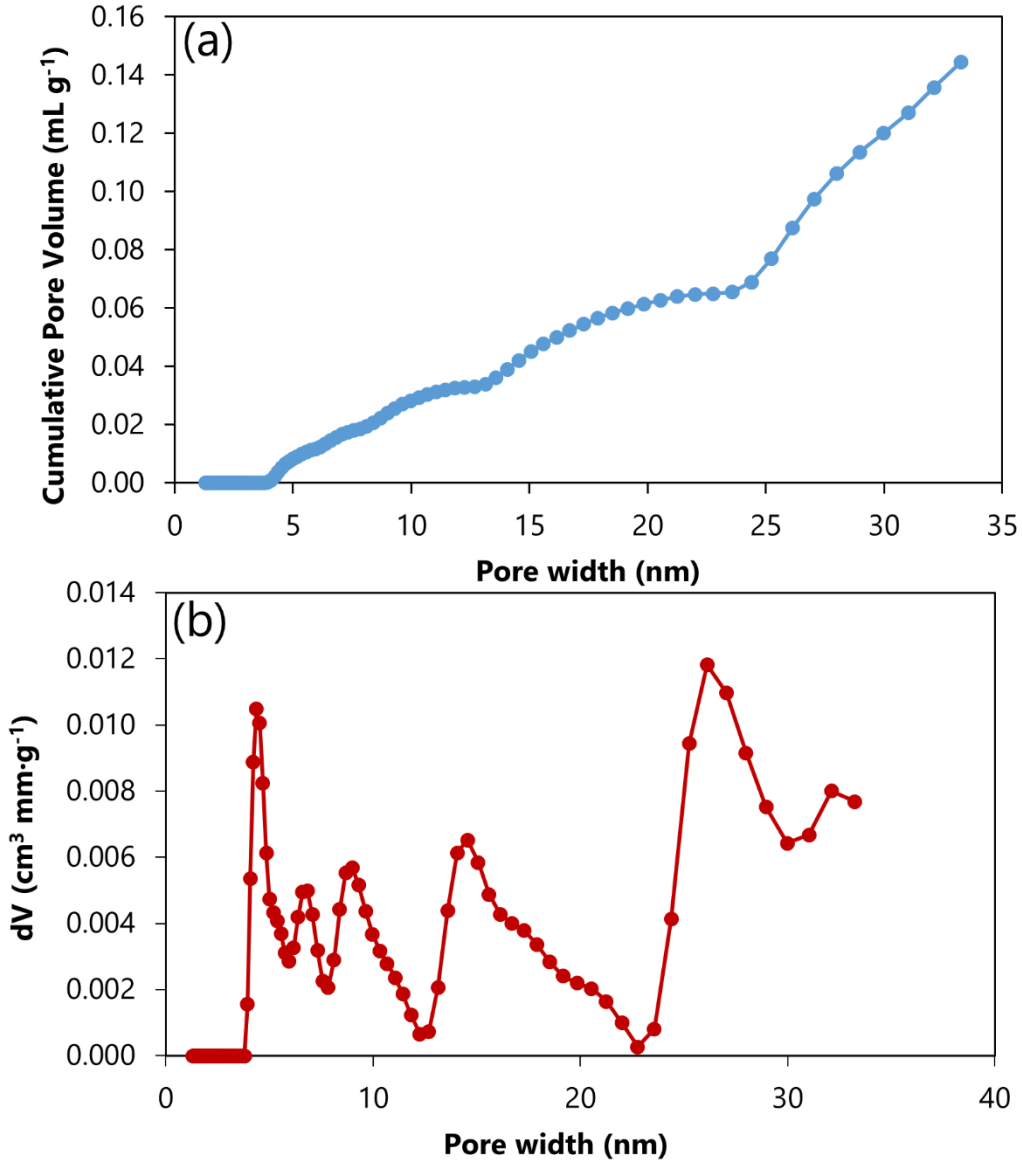

Figure S3.4. N_2 physisorption results for the MPL of the GDL. (a) Total pore volume and, (b) pore size distribution.

The diffraction patterns obtained in Figures 3.6 and 3.7 were indexed to hematite, based on its powder diffraction file (PDF) (Figure S3.5).

PDF#33-0664: QM=Star/Calculated; d=Other/Unknown; I=(Unknown)
Hematite, syn
Fe2O3
Radiation=CuKa1 Lambda=1.5406 Filter=
Calibration= d-Cutoff= I/Ic(RIR)=2.4
Ref= Level-1 PDF

Rhombohedral, R-3c(167) Z=6 mp=
Cell=5.036x5.036x13.749<90x90x120> Pearson=
Density(c)=5.26 Density(m)= Mwt= Vol=
Ref= Ibid.

Strong Line: 2.70/X 2.52/7 1.69/5 1.84/4 3.68/3 1.49/3 1.45/3
2.21/2

d(A)	I(f)	I(v)	h	k	l	n^2	2-Theta	Theta	1/(2d)	2pi/d
3.684	30.0	22.0	0	1	2		24.138	12.069	0.1357	1.7055
2.700	100.0	100.0	1	0	4		33.152	16.576	0.1852	2.3271
2.519	70.0	75.0	1	1	0		35.611	17.806	0.1985	2.4943
2.292	3.0	4.0	0	0	6		39.276	19.638	0.2182	2.7414
2.207	20.0	24.0	1	1	3		40.854	20.427	0.2266	2.8469
2.077	3.0	4.0	2	0	2		43.518	21.759	0.2406	3.0238
1.840	40.0	59.0	0	2	4		49.479	24.740	0.2717	3.4137
1.694	45.0	72.0	1	1	6		54.089	27.045	0.2951	3.7089
1.636	1.0	2.0	2	1	1		56.150	28.075	0.3055	3.8389
1.603	5.0	8.0	1	2	2		57.428	28.714	0.3119	3.9189
1.599	10.0	17.0	0	1	8		57.589	28.794	0.3127	3.9290
1.485	30.0	55.0	2	1	4		62.449	31.225	0.3365	4.2285
1.453	30.0	56.0	3	0	0		63.989	31.995	0.3439	4.3219
1.413	1.0	2.0	1	2	5		66.026	33.013	0.3537	4.4442
1.349	3.0	6.0	2	0	8		69.599	34.799	0.3705	4.6552
1.311	10.0	21.0	1	0	10		71.935	35.968	0.3812	4.7908
1.306	6.0	12.0	1	1	9		72.260	36.130	0.3827	4.8095
1.259	8.0	17.0	2	2	0		75.428	37.714	0.3971	4.9898
1.227	4.0	9.0	3	0	6		77.727	38.864	0.4073	5.1183
1.214	2.0	4.0	2	2	3		78.758	39.379	0.4118	5.1752
1.189	5.0	11.0	1	2	8		80.709	40.354	0.4203	5.2818
1.163	5.0	12.0	0	2	10		82.937	41.468	0.4298	5.4016
1.141	7.0	17.0	1	3	4		84.913	42.457	0.4382	5.5063
1.103	7.0	17.0	2	2	6		88.539	44.269	0.4531	5.6939
1.076	2.0	5.0	0	4	2		91.342	45.671	0.4643	5.8351
1.055	7.0	18.0	2	1	10		93.712	46.856	0.4736	5.9517
1.042	1.0	3.0	1	1	12		95.236	47.618	0.4795	6.0253
1.039	3.0	8.0	4	0	4		95.659	47.830	0.4811	6.0456
0.989	4.0	11.0	3	1	8		102.282	51.141	0.5055	6.3518
0.971	1.0	3.0	2	2	9		104.910	52.455	0.5147	6.4675
0.960	5.0	14.0	3	2	4		106.619	53.309	0.5205	6.5409
0.958	4.0	11.0	0	1	14		107.021	53.511	0.5219	6.5580
0.951	5.0	14.0	4	1	0		108.086	54.043	0.5254	6.6028
0.931	2.0	6.0	4	1	3		111.514	55.757	0.5366	6.7431

Figure S3.5. Hematite (α-Fe_2O_3) PDF.

X-ray photoelectron spectroscopy of the unannealed FeO_x coating on GDL exhibits significant C 1s, O 1s, and Fe 2p peaks. The deconvolution results from Figure 3.8 are presented in Table S3.1.

Table S3.1. Deconvolution of the C 1s, O 1s and Fe 2p spectra for unannealed FeO_x on GDL, illustrating the position (eV), full-width half-maximum (FWHM; eV), and % area for each component.

			Position (eV)	FWHM (eV)	% Area
C 1s		C-C, C-H	285.0	1.21	83.0
		C-O-C, C-O-H	286.2	1.27	11.5
		O=C-O	288.9	0.63	5.5
O 1s		M-O-M	529.8	1.17	72.4
		M-O-H	531.4	1.77	26.1
		O=C-O	533.3	1.34	1.5
Fe 2p	$2p_{3/2}$ (3+)	Peak Splitting #1	709.8	1.20	15.3
		Peak Splitting #2	710.9	1.60	23.8
		Peak Splitting #3	712.2	1.60	11.7
		Peak Splitting #4	713.7	1.60	5.0
		Pre-Peak	707.9	1.60	1.3
		Satellite	718.8	2.01	2.7
	$2p_{1/2}$ (3+)	Main Peak	724.3	---	28.5
		Satellite	732.4	6.50	11.7

XPS analysis was performed on the ALD film deposited on a Si substrate and the survey scan is shown in Figure S3.6a. The XPS quantification from this survey spectrum is presented in Figure S3.6b, along with quantification from the survey spectrum on GDL (Figure 3.8a).

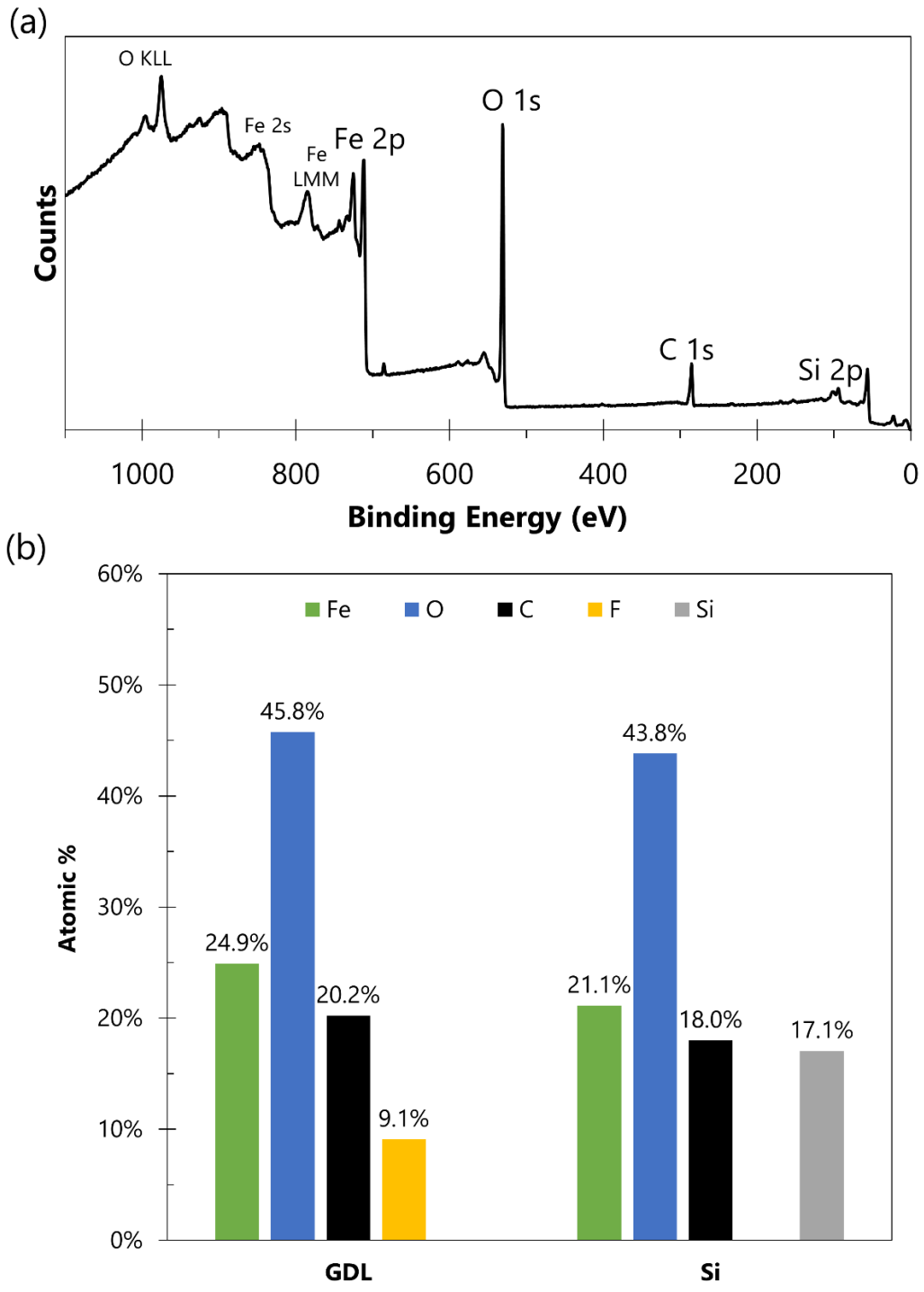

Figure S3.6. (a) XPS survey scan of unannealed FeO_x deposited on a Si substrate. (b) Quantification results from XPS of unannealed FeO_x on both substrates.

To confirm that the current obtained from FeO_x during linear sweep voltammetry (Figure 3.9) is due to the oxygen reduction reaction (ORR), an Ar-saturated environment was used in Figure S3.7 to obtain relatively flat cyclic voltammetry curves. Upon the addition of O_2 in the electrolyte in Figure S3.7, the current density increased in accordance with an oxygen reduction mechanism.

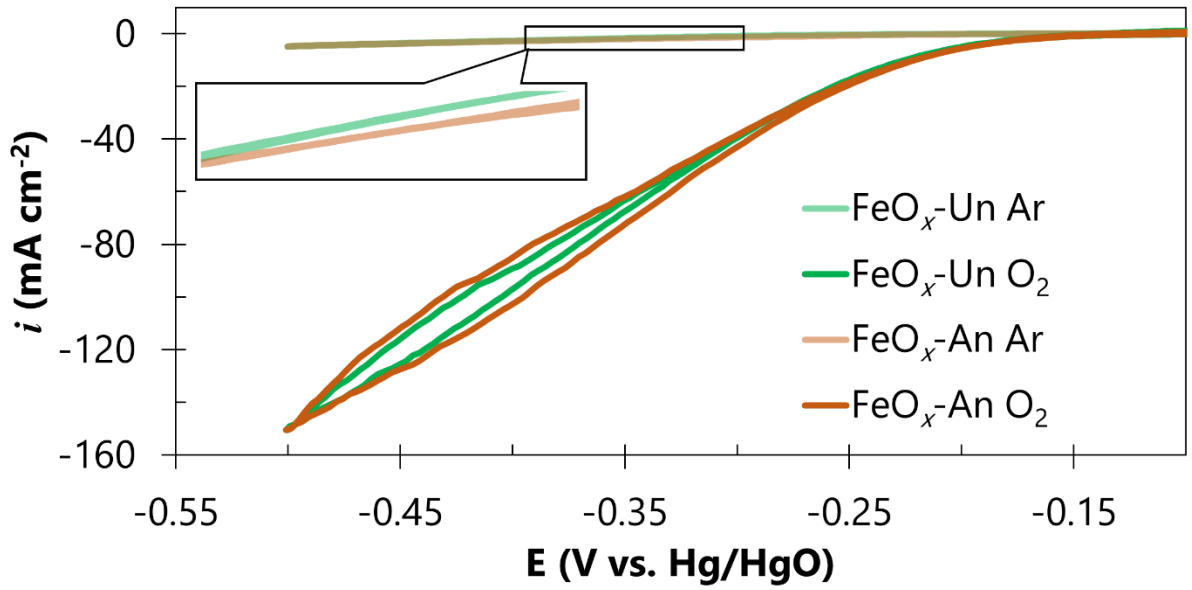

Figure S3.7. Ar-saturated and O_2-saturated cyclic voltammetry curves (20 mV s^{-1}) for FeO_x in 1 M KOH.

Figures of merit extracted from linear sweep voltammetry curves (Figure 3.9) are presented in Table S3.2. This includes the onset potential for ORR and the oxygen evolution reaction (OER), and the maximum current density obtained at the end of the potential window.

Table S3.2. Quantitative comparison of electrochemical ability of FeO_x films studied, an uncoated substrate, and a benchmark Pt-Ru-C catalyst. V_{ORR}/V_{OER} are the onset voltages (V vs. Hg/HgO) defined at a current density of 10 mA cm^{-2}; $i_{ORR, Max}/i_{OER, Max}$ is the maximum current density (mA cm^{-2}) obtained at -0.5V/1.0V vs. Hg/HgO; V_{OER}-V_{ORR} is the potential gap (V) between |10| mA cm^{-2} for ORR and OER.

Sample	ORR		OER		$V_{OER} - V_{ORR}$
	V_{ORR}	$i_{ORR, Max}$	V_{OER}	$i_{OER, Max}$	
FeO_x - Un	-0.23	-136.5	0.74	249.2	0.97
FeO_x - An	-0.22	-124.0	0.74	226.8	0.96
Bare GDL	-0.27	-74.1	>1.00	5.1	>1.27
Pt-Ru-C	-0.10	-206.5	0.57	157.3	0.67

4. Growth of Multiple Island Layers during Fe Oxide Atomic Layer Deposition: An Electron Microscopy and Spectroscopic Ellipsometry Investigation

A version of this chapter has been published in a peer-reviewed journal:

M. Labbe, K. Cadien, and D. G. Ivey, "Growth of Multiple Island Layers during Iron Oxide Atomic Layer Deposition: An Electron Microscopy and Spectroscopic Ellipsometry Investigation," *J. Phys. Chem. C*, vol. 126, issue 46, pp. 19883-19894, 2022.

4.1 Introduction

There has been recent interest in using atomic layer deposition (ALD), a fabrication method designed for the semiconductor industry,[53] for alternative areas such as corrosion,[324] catalysis,[50] and batteries.[48,325] Some of the advantages of ALD include digital control over film thickness, conformal growth over complex substrate geometry, and no line-of-sight restrictions for depositing thin films.[156] The benefits of ALD arise from the self-saturating nature of the deposition process. A gaseous precursor adsorbs to a substrate surface, where complementary physisorption and chemisorption effects limit no more than a monolayer of adsorbed species.[52] With the introduction of a compatible reactant, the adsorbed monolayer is converted into a single atomic layer of a desired material.[49] The process is then repeated, where a thin film is cyclically grown layer-by-layer. An ideal ALD process creates conformal, pinhole-free films on high aspect ratio substrates.[156]

Steric hindrance from bulky precursor molecules and a limited number of reactive surface sites lead to a full monolayer of material being rarely deposited.[154] Furthermore, as with other thin film techniques,[162] the deposition morphology during ALD is not necessarily layer-by-layer (Frank-van der Merwe) growth. Island (Volmer-Weber) growth has been identified for several ALD processes.[326–330] In addition, the growth mode is not necessarily static. For example, Stranski-Krastanov growth describes a situation where the deposition begins via layer-by-layer formation but changes into island growth due to the effects of stress in the film.[154,163,164]

The most common method of characterizing the growth of an ALD film is to plot the thickness increase, or amount of material deposited, as a function of the number of cycles. This growth plot may then be categorized into three main classes: linear growth, where the growth per cycle (GPC) is constant starting from the first cycle; substrate-enhanced growth, where the GPC is initially higher before eventually reaching linear growth; and substrate-inhibited growth, where the GPC is initially lower before establishing linear growth behaviour.[154] For the latter two cases, the competition of reactive site density between the substrate and growing material is often provided as an explanation for the behaviour.[154] Accordingly, as the substrate is completely covered by depositing material, the GPC should be constant as new material is deposited on itself.[154,331–334] To better distinguish between these three growth behaviours, a derivative of the growth plot is often created. This GPC plot then highlights changes in the GPC value during the deposition process to indicate the occurrence of a change in growth mode.

For the case of substrate-inhibited growth, there may also be two different types. Type 1 substrate-inhibited growth is characterized by a steady increase in GPC until linear behaviour is established. For Type 2 substrate-inhibited growth, a peak in GPC is developed prior to linear growth.[154] By studying ALD chemistries that exhibit Type 2 substrate-inhibited growth, such as oxide-based ALD on H-terminated Si surfaces,[327,328,335–339] several authors have developed models that explain the GPC behaviour in terms of an island growth mode.[334,338,340–343] In these models, the steady increase in GPC is attributed to the gradual increase in surface area of island particles. As the islands grow, they provide a greater number of active sites, increasing the GPC. The islands eventually coalesce and merge together; however, the total surface area for deposition is decreased, yielding a slight drop in GPC.[338,344]

One of the hallmarks of ALD is the development of a constant GPC when the effects of the substrate are eliminated and growth occurs on already deposited material. Termed linear growth, this regime occurs at the end of all three classes of GPC behaviour and is commonly observed by other researchers after sufficient ALD cycles.[331–334,339,340,345,346] While it is tempting to speculate that layer-by-layer growth is occurring during linear growth, there is insufficient evidence in the literature to confirm this.[154] For island growth, it might be suggested than an inverse of the Stranski-Krastanov growth mode occurs, where initial Volmer-Weber growth is followed by Frank-van der Merwe growth. Some authors do claim that layer-by-layer growth occurs after

island coalescence,[338,339,341,345] while other authors are careful not to speculate that layer-by-layer growth is occurring. Instead, most research concerning an island growth mode during the initial stages of ALD simply reports that continuous layers are developed after island coalescence, without specifying layer-by-layer growth.[329,347–349] There remains a lack of physical evidence that layer-by-layer growth is in fact occurring post island coalescence, save for one recent article by Perrotta *et al.*, who utilize atomic force microscopy (AFM), X-ray reflectivity and spectroscopic ellipsometry (SE) evidence to support layer-by-layer growth after island coalescence.[346] To the best of the authors' knowledge, no one has used plan view transmission electron microscopy (TEM) to directly confirm layer-by-layer growth after island coalescence.

In this work, scanning TEM (STEM) imaging is used to visually identify the surface fraction of growing ALD films, as opposed to indirect measurements, such as low energy ion scattering (LEIS)[226,327,337,350,351] or time-of-flight secondary ion-mass spectroscopy (TOFSIMS).[331,335,338,350] In both techniques, the number of ions originating from the surface serve as an indication of the relative surface coverage.[260,351] For TOFSIMS, the decay rate of the signal is an indicator of layer-by-layer growth, with a slower decay rate indicating non-two-dimensional growth.[335,350] For LEIS, an increase in signal is directly correlated to an increase in surface fraction.[226,350] On the other hand, scattering of electrons from a transmitted beam through the sample is used to generate images in STEM, with a high angle annular dark field (HAADF) image constructed from the scattered electrons. Complementary images using the unscattered electrons can also be obtained in bright field (BF) mode. Contrast arises from an increase in local scattering due to changes in film thickness or density.[260] Therefore, the visualization of island morphology in STEM is a direct observation as opposed to indirect measurements such as LEIS or TOFSIMS.

In the realm of catalysis, ALD is attractive for depositing nanoscale thin films of catalyst material on high surface area substrates.[49] For the application of air electrodes in metal-air batteries or fuel cells, direct deposition of catalyst material onto the air electrode can enhance catalytic performance and stability.[51,54] For rechargeable metal-air batteries or electrolyzers (fuel cells operating in reverse), the oxygen evolution reaction (OER) is a source of energy loss which benefits from the use of a catalyst.[352] A conventional platinum-group metal catalyst is RuO_2, which offers reduced overpotentials for OER but Ru is expensive and scarce. Several alternative catalyst materials have been reported in the literature; some are carbon-based and some are

transition metal-based.[42,353] Fe oxide (FeO_x) is one example of an OER catalyst replacement for RuO_2 in metal-air batteries and fuel cells.[354] With the rising demand for versatile and portable energy storage devices such as supercapacitors,[355,356] batteries,[357,358] and fuel cells,[359] replacing platinum-group metal components with lower cost, more abundant alternatives is important.

The end goal of this work is to study, through electron microscopy, the nucleation and growth behaviour of an FeO_x ALD process on carbon-based air electrodes for metal-air batteries. To simplify electron microscopy sample preparation, ALD films are grown directly on carbon-coated TEM grids. These substrates can accurately reflect the behaviour of the growth process on carbon-based materials. The ALD process explored in this work, which was recently published by the authors (Chapter 3), utilizes an O plasma to deposit FeO_x using the inexpensive and air stable precursor ethylferrocene (EF). Details of the process development can be found in Chapter 3.[360] However, previous investigations in our group found that an O plasma reactant during ALD can etch the carbon substrate.[54,360] Indeed, this was also the case in the current work, where TEM imaging of FeO_x deposited by ALD on a carbon-coated TEM grid revealed that the carbon substrate was severely damaged (Figure S4.1a). To minimize carbon etching, a thin layer of Mn oxide (MnO_x) was deposited prior to FeO_x ALD to act as a protective sublayer. The MnO_x layer is also grown through ALD, but does not damage the carbon substrate since no harmful O plasma is required.[157] The MnO_x sublayer protects the delicate carbon substrate from the O plasma step during prolonged FeO_x ALD (Figure S4.1b). An added benefit is that the MnO_x layer has been shown to enhance the GPC for the FeO_x ALD process (Figure S3.1 in Chapter 3).[360]

This work explores the dynamic growth behaviour of FeO_x ALD by characterizing films through electron microscopy and SE at various stages of growth. Both substrate-enhanced growth and substrate-inhibited growth are displayed during the ALD process, with an overall island growth mode revealed. There is no evidence to support layer-by-layer growth after island coalescence. Instead, multiple stages of island nucleation, growth, and coalescence occur. An appropriate SE model is devised for this behaviour and an explanation of the growth process is provided. This work challenges the assumption that ALD layer-by-layer growth always occurs during the linear growth regime after island coalescence.

4.2 Experimental Conditions

4.2.1 ALD

All ALD depositions were carried out in a hot-walled continuous flow ALD reactor (Kurt J. Lesker Company, ALD 150L) operating at ~1 Torr with ultra-high purity Ar (Linde Canada Inc., 99.999%) as the carrier gas.[361] O_2 (Linde Canada Inc., 99.993%) and forming gas (FG: 5% H_2, balance N_2; Linde Canada Inc.) lines were fed into an inductively coupled remote plasma system, operating at 600 W, which served as the source of O and FG plasma reactants, respectively. FeO_x ALD was accomplished using EF (STREM Chemicals, Inc., 98%) as the Fe precursor and O plasma as the reactant. EF was heated to 80 °C and the precursor valve and delivery lines were maintained at 100 °C and 110 °C, respectively. The ALD timing sequence employed for each cycle (in s) was 0.25/15/1/20/0.5/5 (EF dose/Ar purge/O_2 gas/O plasma dose/O_2 gas/Ar purge); the extra O_2 gas steps were required because of a delay in the plasma gas delivery line. Samples in this work are referred to by the number of FeO_x ALD cycles employed (*e.g.*, 650cy).

A MnO_x ALD layer was deposited prior to FeO_x ALD to protect the carbon-based substrate from the aggressive O plasma reactant during FeO_x ALD. The MnO_x ALD process employed bis(ethylcyclopentadienyl)manganese ($(EtCp)_2Mn$; STREM Chemicals, Inc., 98%) as the precursor, heated to 80 °C. The valve and delivery lines for $(EtCp)_2Mn$ were also maintained at 100 °C and 110 °C, respectively. A vapour boost method enabled delivery of $(EtCp)_2Mn$ without the use of a bubbler, as reported elsewhere.[157] An FG plasma, followed by a distilled water pulse, served as the reactant for the MnO_x ALD process; the distilled water was maintained at ~22 °C. The MnO_x ALD timing sequence (in s) was 3/5/20/20/2/30 ($(EtCp)_2Mn$ dose/$(EtCp)_2Mn$ charge/Ar purge/FG plasma dose/water dose/Ar purge); the $(EtCp_2)Mn$ charge step was a requirement of the vapour boost technique. Ten cycles of MnO_x ALD produced approximately 1.5 nm of MnO_x, as measured by SE, which served as the protective sublayer. Since the MnO_x sublayer enhanced the GPC of the FeO_x ALD process,[360] the protective MnO_x sublayer is hereafter referred to as the MnO_x seed layer.

To emulate the carbon-based air electrodes in ZABs, carbon-coated Cu TEM grids (Ted Pella, Inc., Prod #01881-F) were used as substrates in the ALD reactor. To enable *in situ* SE measurements of the ALD process, Si(100) witness wafers with the native oxide intact

(University Wafers, 525 μm P-type single side polished) were placed adjacent to the TEM grids in the reactor. For all depositions, a pretreatment of 60 s of O plasma was carried out to clean the substrate surface and provide active sites for ALD nucleation. All depositions were performed at a substrate temperature of 150 °C.

4.2.2 Electron Microscopy

ALD-coated TEM grids were placed directly from the ALD reactor into the TEM/STEM (JEOL, JEM-ARM200CF). All S/TEM images and energy dispersive X-ray (EDX) maps, as well as selected area diffraction (SAD) patterns, were done at an accelerating voltage of 200 kV. Select deposits on the Si witness wafers were also examined by TEM and scanning electron microscopy (SEM). TEM cross section samples were prepared using a plasma-focused ion beam (FIB)/SEM (Thermo Fisher Scientific Inc., Helios 5 Hydra DualBeam). The ALD film was capped with a 500 nm thick carbon layer, followed by 2 μm of Pt. A 10 pA Xe beam at 30 kV was used to section the sample. The FIB sample was then transferred to a Cu grid for viewing in the TEM. SEM imaging using a field-emission SEM (ZEISS, Sigma 300 VP) was done at an accelerating voltage of 1.5 kV and a 4.3 mm working distance.

Plan view HAADF STEM images were analyzed using ImageJ software.[348,362] An image filter was applied as needed to reduce pixel noise and then an automatic thresholding algorithm was applied to each image in order to separate different phases of the deposited material. Surface fraction was calculated based on the number of pixels for each phase as compared to the total number of pixels in the image. Quantification of the size and number of islands during initial FeO_x deposition was accomplished using the *Analyze Particles* built-in function. A full workflow of the image analysis is presented in Tables S4.1 and S4.2.

4.2.3 SE

Si witness wafers were characterized *in situ* by SE (J. A. Woollam Co., Inc., M-2000DI) during ALD growth,[303] and the acquired SE data were analyzed using CompleteEASE (J. A. Woollam Co., Inc., version 4.48). Layers of MnO_x and FeO_x were modelled using independent single Tauc-Lorentz oscillators,[170,363] while an effective medium approximation (EMA) model was used to incorporate void characteristics.[170] A Bruggeman EMA was employed using a depolarization factor of 0.333. All SE models accounted for the native Si oxide (SiO_x: ~15 Å).

Derivative values for the GPC plot were calculated by a central difference approximation, except for the first and last cycle, which were determined by a forward and backward approximation, respectively.[364] A five-point triangular smooth was applied to reduce noise in the raw derivative values.[365]

4.3 Results & Discussion

4.3.1 S/TEM on Carbon

STEM images of the FeO_x film, on a carbon substrate, after various ALD cycles are shown in Figure 4.1. A large number of small, equally spaced circular particles coat the surface of the carbon substrate after 10 cycles of MnO_x ALD (zero cycles of FeO_x ALD; 0cy). This is the seed layer deposited prior to FeO_x ALD (Figure 4.1a). When the seed layer is covered by 10 cycles of FeO_x ALD (Figure 4.1b), non-circular, worm-like islands are formed. Compared with the initial particles, the islands are larger and fewer in number. Quantitatively, the islands are over five times larger but there is a four-fold decrease in the number of particles (Figure S4.2). Therefore, it can be surmised that four original MnO_x particles are linked together in the worm-like islands after 10 cycles of FeO_x. A larger than four-fold increase in particle size is the result of FeO_x deposition on the bare substrate, which bridges neighbouring islands together. Probing the initial island formation further, the number of islands is halved after just one ALD cycle, while one third of the original amount is present after 3 ALD cycles (Figure S4.2).

Upon further FeO_x ALD, the islands continue to grow in size, connecting together to form a web of worm-like islands (Figure 4.1c). This worm-like island morphology has been observed by others, who also attribute this to the merging of neighbouring islands during coalescence.[366,367] After 30 FeO_x cycles, gaps (pinholes) remain in the web of islands but the layer is essentially continuous. After 50 cycles, the continuous FeO_x layer is partially covered by another layer of islands (Figure 4.1d), which is better shown after image processing (Figure 4.2d). The new islands also exhibit a worm-like morphology. After 100 ALD cycles, this second layer of worm-like islands has grown in coverage and size (Figure 4.1e). Note that the first layer of ALD material is still distinguishable in the STEM image and continues to have pinholes (Figure 4.2e). As well, comparing the worm-like islands of Figure 4.1e to a similar stage of growth for the first layer (Figure 4.1b), it is apparent that the islands are larger in size and fewer in number.

Therefore, it can be surmised that there are fewer nucleation events for the second layer of islands compared with the first layer, resulting in more growth per individual island and a longer time interval for island coalescence.[350]

After 200 cycles of FeO_x ALD, the outer layer of material contains fewer islands than at 100 cycles (Figure 4.1f), occupying a lower overall surface fraction (Figure 4.2f). The islands at 100 cycles have coalesced and yet another layer of islands has formed. At 420 cycles (Figure 4.1g), the STEM image shows a web of islands merging together, similar to that observed after 30 cycles (Figure 4.1c). Through appropriate modelling of SE data, it will be shown that an additional layer forms between 200 and 420 cycles (Section 4.3.2.1). After 650 ALD cycles, a complete layer (with pinholes) is visible with brighter regions corresponding to the formation of another layer of worm-like islands (Figure 4.1h). Later analysis reveals this to be the fifth layer and the start of the sixth layer, respectively.

This multi-staged nucleation and growth of worm-like islands is peculiar and does not reflect common ALD behaviour reported in the literature. In addition, relatively few ALD articles point to the existence of pinholes in continuous ALD films.[349] However, of those that do, an island growth mechanism is often cited.[335,348] Since multiple stages of island nucleation, growth, and coalescence are apparent in Figure 4.1, it is understandable that pinholes continue to exist throughout growth. Quantification of the amount of pinholes in the continuous layers is shown in Figure 4.2 and is generally on the order of 2-4%.

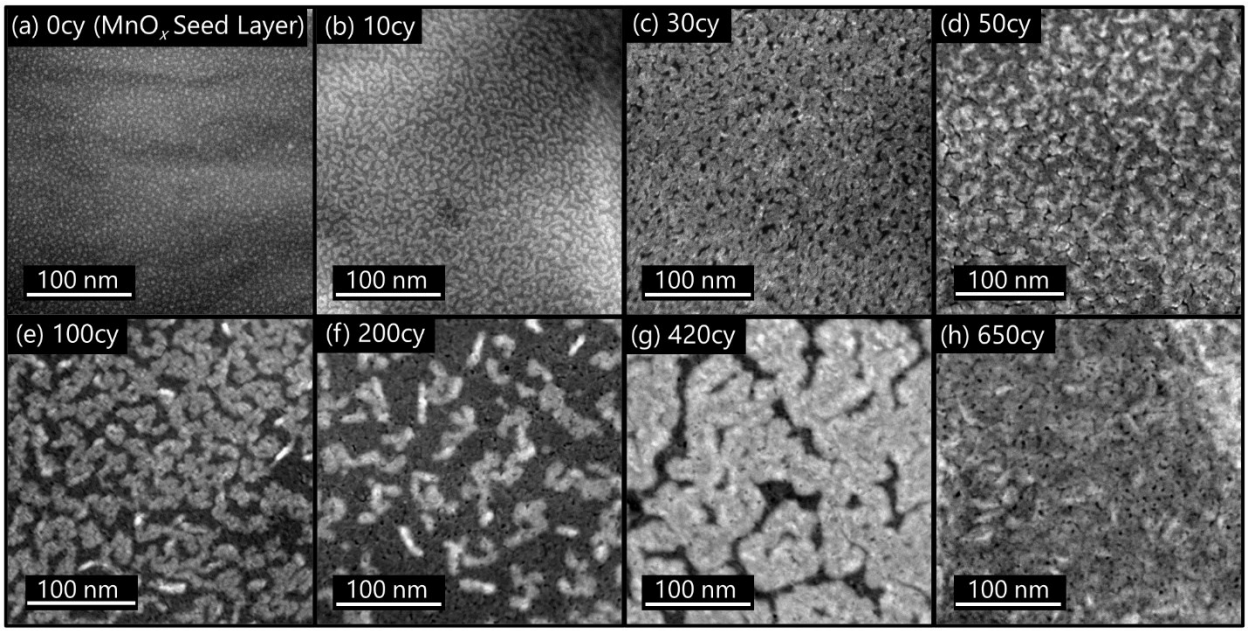

Figure 4.1. Plan view HAADF STEM images of the carbon substrate after (a) zero cycles, (b) 10 cycles, (c) 30 cycles, (d) 50 cycles, (e) 100 cycles, (f) 200 cycles, (g) 420 cycles, and (h) 650 cycles of FeO_x ALD.

Plan view STEM images of the ALD material (Figure 4.1) were analyzed using ImageJ to extract the quantitative surface fractions of each layer of islands. The full workflow of image processing is compiled in Table S4.2. New layers of islands are highlighted in Figure 4.2 through the use of different colours. Theot MnO_x seed layer, shown in pink, is coated by the first layer of FeO_x islands, represented in green, while some bare substrate surface is still observable in grey (Figures 4.2a and 4.2b). These islands merge together (Figure 4.2c), whereupon another layer of islands is nucleated on top (shown in blue in Figures 4.2d and 4.2e). This second layer coalesces and yet another layer of islands is nucleated in red (Figure 4.2f). This process is then repeated for the fourth (green), fifth (blue) and sixth (red) layers of islands (Figures 4.2g and 4.2h).

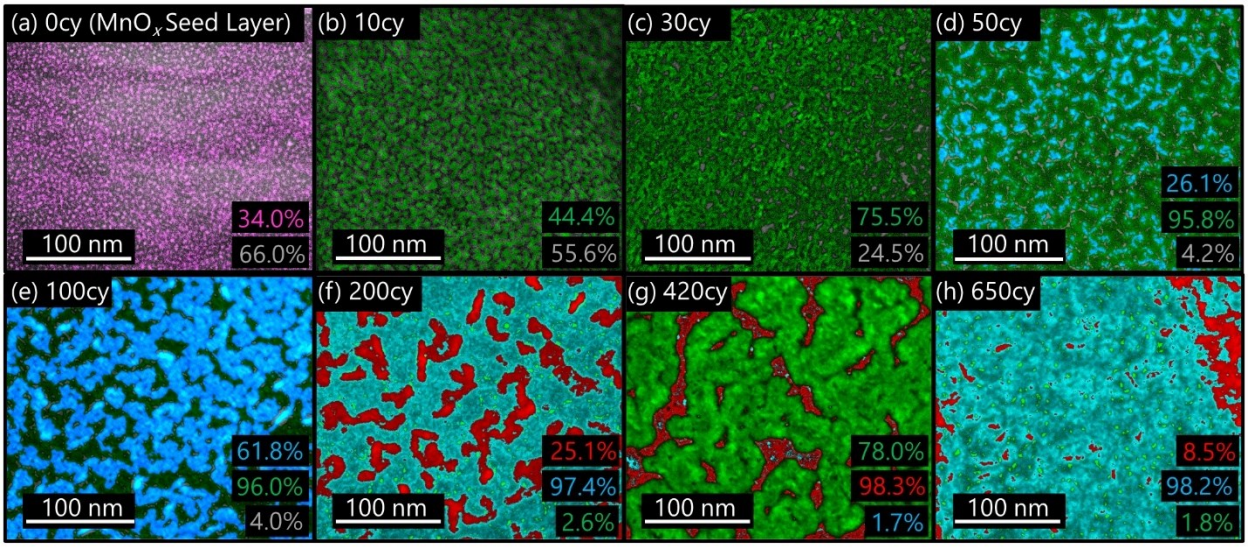

Figure 4.2. Colourized plan view HAADF STEM images of the carbon substrate after (a) zero cycles, (b) 10 cycles, (c) 30 cycles, (d) 50 cycles, (e) 100 cycles, (f) 200 cycles, (g) 420 cycles, and (h) 650 cycles of FeO_x ALD. The surface fraction of each observable layer is tabulated in the bottom-right corner of each image and represented by green, blue, and red colours in the image. These colours correspond to the first and fourth layer, second and fifth layer, and third and sixth layer, respectively. The grey values correspond to the original carbon substrate while pink is used to represent the MnO_x seed layer in (a).

EDX mapping was also conducted on several samples from Figures 4.1 and S4.2 and the results are compiled in Figure S4.3. Overall, the Fe signal increases in intensity with an increase in the number of FeO_x cycles. Furthermore, the Fe and O maps are consistent with the island formation in the STEM images (Figures 4.1 and S4.3), particularly for the later cycles. The O signal is present in more areas than Fe for cycles less than 30 since the substrate has adsorbed O-containing surface species.[368]

The Mn signal for the 0cy sample (Figure S4.3a) coincides with the seed layer morphology in the STEM image (Figure 4.1a), confirming the existence of the MnO_x seed layer. Mn appears to be detected for all samples, even those with multiple layers of FeO_x covering the MnO_x seed layer. This can be attributed to two effects. Firstly, there is considerable K-peak overlap for Mn and Fe in the EDX spectrum; the position of the Fe Kα peak at 6.40 keV overlaps the Mn Kβ peak at 6.49 keV.[369] Secondly, Mn X-rays from the seed layer can pass through the FeO_x layer and reach the detector.

SAD patterns were obtained for several samples from Figure 4.1 and are shown in Figure S4.4. The rings increase in intensity and become more spotty as the number of ALD cycles increases. This indicates that as more FeO_x is deposited, the crystallinity improves. The MnO_x seed layer pattern (Figure S4.4a), although faint, can be indexed to cubic Mn_3O_4. The FeO_x rings, for all ALD cycles, can be indexed to α-Fe_2O_3 (hematite). This is the same structure determined in our previous work on FeO_x ALD using the same precursor (Chapter 3).[360] Table S4.3 provides a more detailed indexing of the patterns, including the measured interplanar spacings and the corresponding PDF cards for both α-Fe_2O_3 and Mn_3O_4.

High resolution TEM (HRTEM) was performed for the samples; examples for 200, 420 and 650 cycles are shown in Figure S4.5. In all cases the deposits are nanocrystalline, with grains sizes less than 20 nm. Lattice planes for some of the grains are highlighted and these correspond to the (104) planes of hematite.

4.3.2 SE on Si

To assist in the understanding of the growth behaviour for the FeO_x ALD material, *in situ* SE was conduced for the samples in Figure 4.1. A Si witness wafer was placed adjacent to the carbon TEM substrates in the ALD reactor and ellipsometry readings were taken continuously throughout deposition. A uniform continuous layer of FeO_x was fit to the data (*i.e.*, assuming layer-by-layer growth) and the evolution of thickness was plotted as a function of cycle number. Figure 4.3 shows a representative growth plot that reflects the behaviour of all the samples from Figure 4.1. Inset (i) in Figure 4.3 shows the typical growth behaviour of the MnO_x seed layer, followed directly by the FeO_x process. Inset (ii) shows that, initially, a GPC of 0.43 Å cycle^{-1} is established for FeO_x ALD on the MnO_x seed layer. However, after roughly 50 ALD cycles, the GPC reduces to 0.17 Å cycle^{-1} and remains constant thereafter. The development of two distinct linear regions in the thickness versus cycle number plot is consistent with previous work on FeO_x ALD using a MnO_x seed layer.[360] This change in GPC indicates a modification in the growth mode of FeO_x in the vicinity of 50 ALD cycles. As shown in later analysis, this represents the development of the second layer of islands. It is also worth noting that the GPC values exhibited for FeO_x growth (0.43 Å cycle^{-1} and 0.17 Å cycle^{-1}) are much lower than for a theoretical monolayer (3.70 Å cycle^{-1} for Fe_2O_3).[370–372] This suggests incomplete coverage of the FeO_x film

on the substrate surface, possibly due to steric hindrance of the large EF molecule,[340] the low reactivity of EF,[360] and a low nucleation site density on the substrate.[329,335]

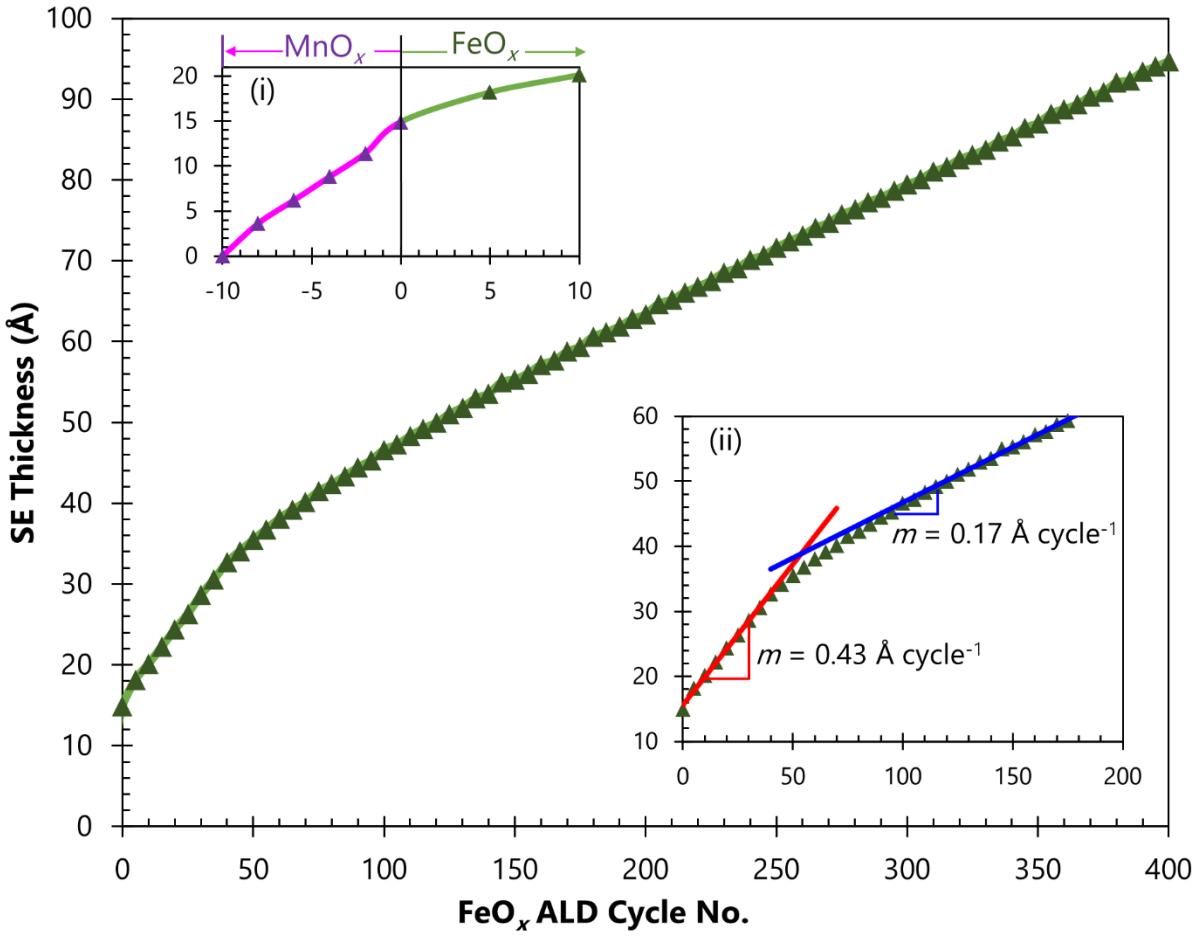

Figure 4.3. Thickness values obtained as a function of ALD cycles. Triangles on the plot represent a data point extracted every 5 ALD cycles. Inset (i) shows 10 cycles of the MnO_x seed layer followed by 10 cycles of FeO_x. Inset (ii) highlights the change in slope in the range of 50 FeO_x ALD cycles. Insets have the same units for the x-axis and y-axis as the main graph.

To better demonstrate the change in growth mode revealed by SE, the derivative of Figure 4.3 is plotted in Figure 4.4. For a thickness versus cycle number plot, the derivative is the GPC.[341] Thus, Figure 4.4 displays the GPC as a function of ALD cycle number. At first glance, Figure 4.4 appears to reflect the behaviour of substrate-enhanced growth, where the initial GPC is markedly higher than the GPC obtained after extended ALD cycles.[334] However, a steady-state GPC regime is maintained only until 35 ALD cycles. The GPC value of this brief plateau (~0.4 Å $cycle^{-1}$) aligns with the first linear region in Figure 4.3. After this initial plateau, a substantial

drop in GPC occurs in the range of ~30-70 ALD cycles. The GPC then begins to level off in the range of 100 cycles, to a value on the order of ~0.15 Å cycle^{-1}. This value correlates with the second linear region in Figure 4.3, which represents the long-term steady-state GPC for the FeO_x ALD process.

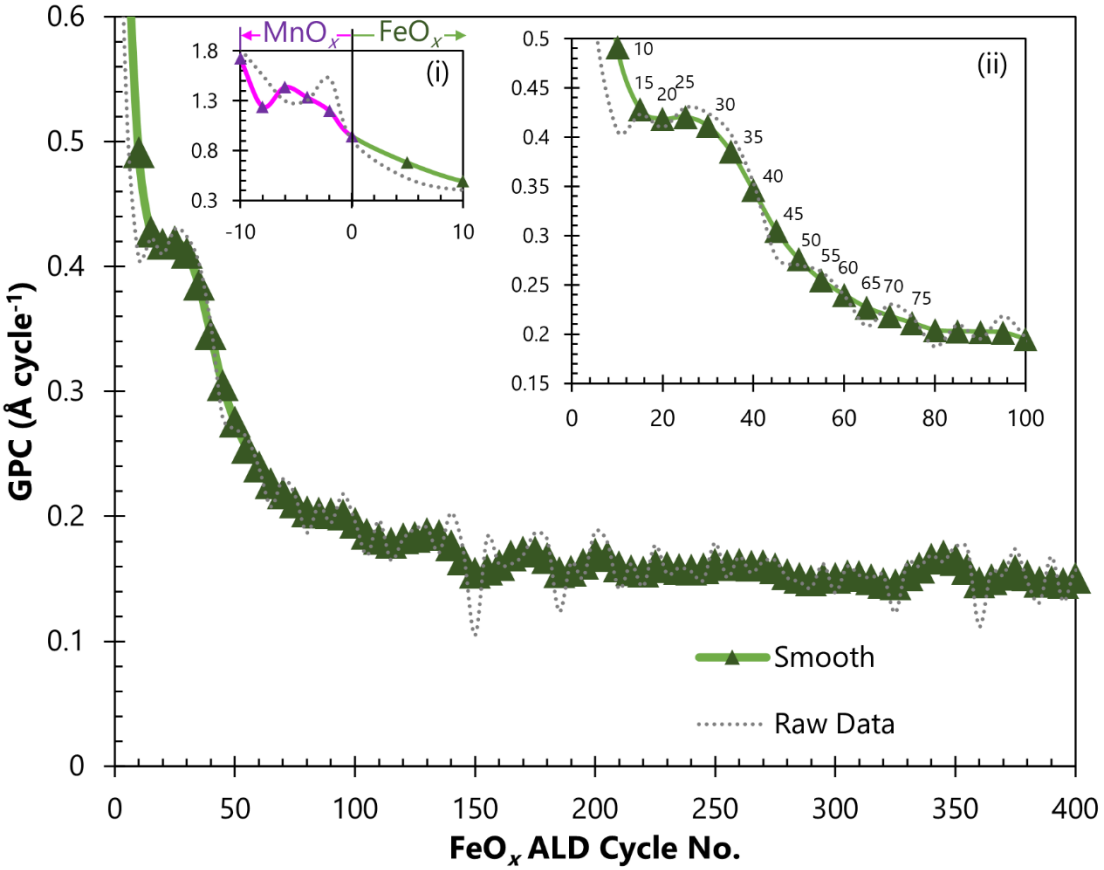

Figure 4.4. GPC plotted as a function of ALD cycles. Triangles on the plot represent a data point calculated every 5 ALD cycles, with the height of each triangle representing the error bars in the data. Inset (i) shows 10 cycles of a MnO_x seed layer, followed by 10 cycles of FeO_x. Inset (ii) focuses on the plateau region at around ~25 FeO_x ALD cycles. The raw derivative values are plotted as a dotted grey line, while the smoothed data are shown in green. Insets have the same units for x-axis and y-axis as the main graph.

Since the MnO_x seed layer provides nucleation sites for FeO_x growth (Figure S4.2), the seed layer is effectively the substrate surface when discussing substrate-enhanced growth of FeO_x ALD. Therefore, the initial substrate-enhanced growth is attributed to the MnO_x seed layer

present on the surface (inset (i) of Figure 4.4). It is difficult to say for certain when the depositing FeO_x completely covers the MnO_x seed layer since this is not a typical substrate-enhanced process. In conventional substrate-enhanced growth, the substrate surface is completely coated when the GPC is reduced to a lower steady-state value. At this point, ALD occurs on already deposited material and there are no longer contributions from the substrate.[332,334] Following this logic, the MnO_x seed layer is covered after ~15 ALD cycles, where the GPC reaches a plateau of ~0.4 Å cycle^{-1} (inset (ii) of Figure 4.4).

The impact of the seed layer on the GPC is not lost once the depositing FeO_x encapsulates the MnO_x. Because of the higher number density of islands created by the MnO_x seed layer as compared with subsequent island layers without the seed layer (Section 4.3.1), a larger surface area for deposition is created by the MnO_x seed layer. This translates into an enhanced GPC for the first layer of islands. A similar argument has been made in the literature regarding the effect of surface roughness on GPC; higher surface roughness translates into a larger surface area for deposition, resulting in a higher GPC.[329,332,340] Likewise, in this work, a higher number density of islands in the first layer provides more surface area and, thus, a higher GPC, which decreases for the second and subsequent layers. Figure 4.4 suggests that closure of the first layer of islands, and nucleation of the second layer, occurs in the range of ~30-70 ALD cycles, where the secondary drop in GPC occurs. This agrees with STEM imaging at 30 and 50 ALD cycles (Figures 4.1c and 4.1d, respectively).

The island growth mode exhibited in Figure 4.1 suggests that a maximum should be displayed in the GPC plot, in line with Type-2 substrate-inhibited growth. This peak occurs just before the islands coalesce and, based on Figure 4.1, is anticipated at ~30 ALD cycles.[334,338,341,342] However, the worm-like shape of the growing islands complicates the comparison with conventional Type 2 substrate-inhibited growth and is likely responsible for the development of a brief plateau in the GPC plot as opposed to a peak. The substrate-enhanced effects of the MnO_x seed layer are also expected to complicate the Type 2 substrate-inhibited growth behaviour displayed in Figure 4.4.

Slight oscillations in the GPC curve occur for the long-term linear growth region in Figure 4.4 (cycles >100). A similar phenomenon of oscillations in the GPC plot has been documented by Wind *et al.*, who claim the oscillations are the result of new island growth and subsequent

smoothing processes (film closure).[373] In the current work, the frequency of oscillations does not match the progress of island development in either the STEM images (Figure 4.1) or the EMA model (discussed in Section 4.3.2.1). Furthermore, the absence of any additional drops in GPC due to island coalescence events, like that seen in Type 2 substrate-inhibited growth, can be explained by the simultaneous nucleation of another island layer (Section 4.3.2.1), which provides an increase in GPC to offset the change. The oscillations featured in Figure 4.4 are likely the result of noise in the SE data.

4.3.2.1 Effective Medium Approximation (EMA) Model

The ellipsometry model used to construct Figures 4.3 and 4.4 assumes that a flat, planar layer of FeO_x is deposited through ideal layer-by-layer growth. As shown in Figure 4.1, this is not the case. Therefore, the ellipsometry model was modified to better reflect the island growth process. In SE, surface roughness or island growth can be simulated using an EMA model. In this model, the optical properties of the island layer are approximated by a secondary phase contained within a matrix. The secondary phase has the optical properties of the island material, while the matrix is given the optical properties of a vacuum to simulate voids.[170] In this work, a Bruggeman EMA with a depolarization factor of 0.333 was utilized to model the growing islands.[303,329] In order to fit the SE data to this model, the thickness of each island layer was maintained at a constant value and the volume fraction of the ALD material was the manipulated variable against cycle number. To calibrate the model, the surface fraction values from Figure 4.2 were fitted to the data at their respective cycle numbers. To bridge the gap between volume fraction in the EMA model and surface fraction determined from plan view STEM images, simple geometrical approximations were developed. Based on Figure 4.1a, the MnO_x seed layer forms as hemispheres on the surface, in line with other ALD reports of island growth.[338,345,374] Therefore, the relationship between volume fraction and surface fraction is calculated assuming a hemispherical geometry (Figure S4.6).[174] On the other hand, the morphology of the FeO_x islands is not hemispherical and the worm-like islands are instead approximated by hemicylinders (Figures S4.7 and S4.8). Since rounded objects are assumed in these geometric models, an EMA depolarization parameter of 0.333 is most appropriate because it is used to model spherical secondary particles.[171–173,375] Additional details regarding the geometric models employed can be

found in the Supporting Information. The EMA model produces a good fit to the SE data (Figure S4.9).

EMA modelling results for the SE data are shown in Figure 4.5, with black squares representing the measured surface fraction from STEM imaging (Figure 4.2) as a comparison. Overall, there is a good match between the surface fraction values from STEM images and the surface fraction values extracted from SE. Note that FeO_x surface fraction values from STEM imaging of the first layer of islands are inconclusive and are, therefore, not represented in the black squares in Figure 4.5. The slope of Figure 4.5 represents the rate of surface coverage increase per ALD cycle (coverage per cycle, or CPC). In terms of island growth, this value represents the rate of island closure. CPC values are displayed in Figure 4.5 and calculated using a linear fit from ~15% to ~95% surface fraction. The CPC is higher for the first layer of islands (1.8% $cycle^{-1}$) compared with subsequent island layers (0.71±0.06% $cycle^{-1}$). This correlates with Figure 4, which shows substrate-enhanced growth from the MnO_x seed layer. The seed layer directly increases the amount of FeO_x deposited by providing more active sites (conventional substrate-enhanced growth), but even after the depositing FeO_x envelops all the MnO_x seed layer, an indirect influence of the seed layer remains throughout the first layer because of the higher number density of islands. Nucleation of the second layer of islands erases any influence of the seed layer and a lower number density of islands then translates into a lower GPC and CPC for the second and subsequent layers, as shown in Figures 4.4 and 4.5, respectively. This effect is also demonstrated by the number of ALD cycles required to reach comparable surface fraction values in STEM for the first and second layer of islands (30 cycles and 100 cycles in Figures 4.2c and 4.2e, respectively). More than twice the amount of ALD cycles during formation of the second layer of islands yields a lower surface fraction than during formation of the first layer, which compares favorably with the CPC values extracted from Figure 4.5.

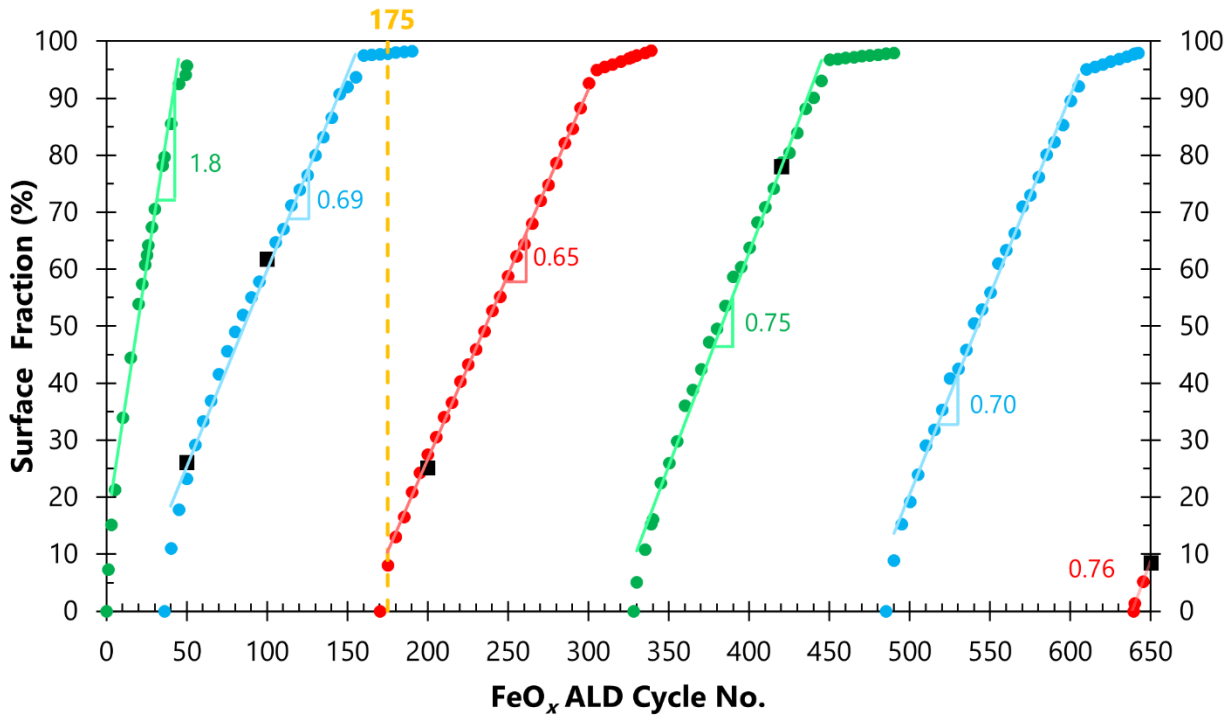

Figure 4.5. EMA modelling results for the SE data. Plot of surface fraction (%) against cycle number for 650 total FeO_x ALD cycles. Each circle represents a data point obtained from the EMA model, while the black boxes indicate the surface fraction values determined from the STEM images. Slope (CPC) values are also displayed. Colours are used to distinguish between layers following the convention in Figure 4.2. A yellow vertical line at ~175 cycles shows the onset of nucleation of the third layer prior to previous layer completion.

An interesting observation in Figure 4.5 is the overlap between the final stages of island coalescence for one layer and nucleation of the next island layer. For example, at ~175 ALD cycles (yellow line in Figure 4.5), the second layer of islands has not yet reached the final surface fraction value but nucleation of the third island layer has already begun (surface fraction of the third layer is >0%). Physically, this represents a situation where nuclei of another island layer are created before the current island layer has reached closure. In terms of pinholes acting as nucleation sites (Section 4.3.4), this represents the stage where material deposition on the pinhole defect sites is preferred over deposition on the curved surface of the already-deposited islands.

4.3.3 Materials Characterization on Si

So far, the nucleation and growth process of FeO_x ALD has been characterized by STEM imaging on carbon TEM grids and by SE on Si wafers with a native SiO_x. While the two techniques have been complementary in shedding light on the growth mode for ALD, it is important to confirm through other characterization methods that an island morphology is indeed occurring on the SiO_x/Si substrates. The Si witness wafers were placed in the ALD reactor alongside the carbon TEM grids so that both substrates experienced the same deposition conditions.

To confirm that the nucleation and growth behaviour on SiO_x/Si and carbon substrates is comparable, high magnification SEM micrographs for the 200cy sample were taken directly from the Si witness wafer used to obtain *in situ* SE data (Figure S4.10a). A worm-like island morphology is present on the SiO_x/Si substrate, confirming the similar growth behaviour for the two substrate materials. A STEM image of the 200cy sample, on the carbon substrate, is shown in Figure S4.10b. The FeO_x morphology for the two substrates are similar, although there is slightly better coverage on SiO_x/Si than on carbon. Nucleation of ALD films on carbon is notoriously difficult,[329,376,377] while Si, with the native oxide preserved, has more nucleation sites for ALD.[156,303] With a greater density of active sites, more islands will nucleate on SiO_x/Si compared with carbon and island coalescence will occur sooner.[350] Nevertheless, both substrates exhibit an island growth mode for FeO_x ALD, justifying the complementary use of both characterization techniques (STEM and SE).

Cross sectional S/TEM imaging of ALD FeO_x deposits on SiO_x/Si was done to visually confirm the existence of islands and to measure the thickness of deposited layers. One example, *i.e.*, the 200cy sample, is shown in Figure 4.6. The HRTEM image (Figure 4.6a) shows three distinct layers of material between the single crystal Si substrate and the protective carbon layer deposited on the ALD film during FIB preparation. These layers correspond to the Si native oxide (SiO_x), the MnO_x seed layer, and the FeO_x layer. The identity of the layers was confirmed through EDX mapping (Figures 4.6c-4.6g). The STEM BF image (Figure 4.6b) clearly shows the SiO_x layer and the ALD material. FeO_x islands are also visible in the STEM image (indicated by arrows in Figure 4.6b). The thickness of the native SiO_x layer in Figure 4.6a (~2.0 nm) aligns with the values determined from SE (~1.5 nm). The measured thickness of the MnO_x seed layer

in Figure 4.6a (~1.4 nm) is similar to the SE values (~1.7 nm). The FeO_x deposit is ~5.1 nm, which is close to the 5.4 nm value determined from the EMA model.

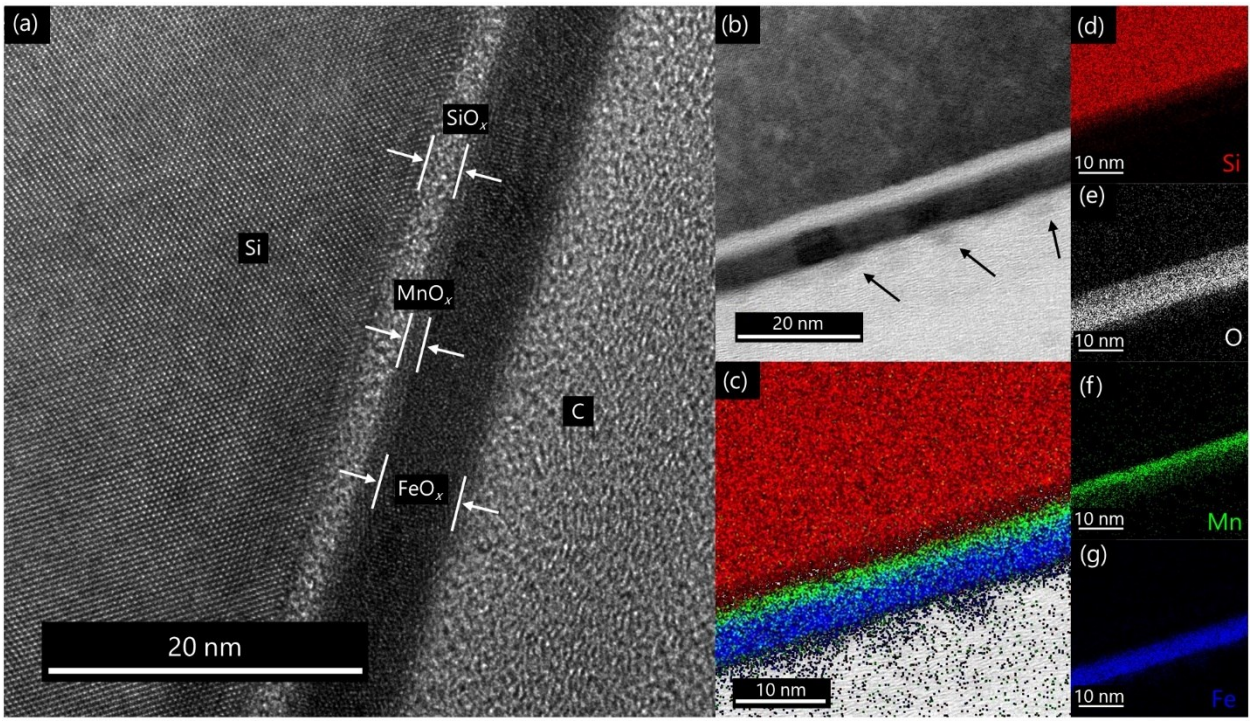

Figure 4.6. Cross sectional S/TEM imaging and EDX elemental mapping of the 200cy sample on the Si wafer substrate. (a) HRTEM image, (b) STEM BF, and (c) overlay of Si, Mn and Fe EDX maps, with (d), (e), (f) and (g) showing individual maps for Si, O, Mn, and Fe, respectively.

4.3.4 Multi-layer Island Growth

The overall nature of FeO_x growth through ALD demonstrated in this work – namely island nucleation, growth, coalescence, and re-nucleation – is quite unique in the ALD literature. Wind *et al.* speculated this could be occurring for ALD of W on Al_2O_3 surfaces, but they did not investigate this phenomenon to any extent.[373] A similar formation process to that displayed by the current work was recently published for the physical vapour deposition (not ALD) of metallic glasses.[367] Dubbed periodic island-layer-island growth, AFM images and roughness values revealed the establishment of typical island growth, smooth continuous layers, and then the development of island growth again thereafter. A reduction in free energy via the agglomeration of adatoms, facilitated by fast surface diffusion in metallic glasses, was cited as the reason for

island formation.[367] When the islands reach a critical size, the diffusion lengths required for maintaining an island morphology exceeds the deposition rate of the process and a continuous film develops.[367] Other reports on the formation of multi-layered islands during continuous deposition provide similar thermodynamic-based adatom migration explanations.[378–380] However, due to the discrete nature of ALD, and because chemisorption effects inhibit adatom migration, a similar rationale is unlikely to account for the present work.

The initial island growth mode exhibited by the ALD process indicates that the bare substrate, whether carbon or SiO_x/Si, is less active towards ALD than either MnO_x or FeO_x. The active species for ALD growth of an oxide is usually attributed to OH groups.[310,326,349,374,381–384,327,328,331,335,339–341,344] Therefore, the density of OH groups on either carbon or SiO_x/Si must be lower than that on MnO_x or FeO_x. This is supported by literature data, where the density of OH groups for MnO_x and FeO_x are similar, on the order of 10^{15} OH groups cm^{-2},[385] while for SiO_x/Si, this value is lower by up to an order of magnitude.[340,386] Although the density of OH groups could not be found for carbon, it is well documented that ALD films are more difficult to nucleate on carbon, which results in lower GPC values.[329,376,377]

The proposed growth mechanism for FeO_x ALD, based on complementary studies of electron microscopy and SE, is illustrated in Figure 4.7 and outlined as follows. The use of a 60 s O plasma preclean provides an artificially large number of active sites for MnO_x ALD[326,346,348,350,374,376,381,384,387] and, combined with the relatively large GPC for the MnO_x ALD process,[157] produces many small nuclei of MnO_x on the initial substrate (Figure 4.7a). Due to the aforementioned active site densities, FeO_x ALD begins primarily on the MnO_x seed layer (Figure 4.7b). Furthermore, the hemispherical islands produced by the seed layer have a curved surface, which is a higher energy conformation than a planar surface such as the substrate and promotes ALD growth.[329,383,388] At the same time, the interfacial region between the MnO_x islands and the substrate is an area of higher energy and facilitates heterogeneous nucleation. FeO_x ALD occurs on substrate areas adjacent to the MnO_x islands and the islands connect, forming the worm-like morphology (Figure 4.7c). With further FeO_x ALD, growth continues to occur along the sides of the islands for the same reasons as mentioned above, *i.e.*, more active sites as compared with the planar substrate surface.

With enough FeO_x cycles, the first layer of islands begins to coalesce (Figure 4.7d). However, in line with other reports for island growth in ALD, pinholes exist in the continuous layer created by island coalescence.[335,348] The pinholes in the continuous layer can then act as nucleation sites for a second layer of islands to grow. The pinholes between islands are likely rife with defects that act as preferred sites for ALD. Not all pinholes serve as nucleation sites, as some pinholes are visible in the lower continuous layer (Figure 4.2e). As such, there are fewer nucleation events in the second and subsequent layers of FeO_x compared with the MnO_x-initiated first layer of FeO_x (Figure 4.7e).

Additional ALD cycles result in the growth of the second layer of islands (Figure 4.7f) through the same mechanism as discussed previously; *i.e.*, more defect sites on curved surfaces compared with planar surfaces and the interfacial boundary between the first and second layer of material provide additional sites for FeO_x formation. The low reactivity of the EF precursor is likely responsible for deviation from ideal layer-by-layer growth. Only high energy defect sites enable growth of FeO_x from EF, favouring repeated island growth over layer-by-layer growth. Similar to the first layer, the second layer of islands coalesce into a continuous layer with pinholes (Figure 4.7g), and a third layer of FeO_x islands nucleate in the pinholes of the second layer (Figure 4.7h). The growth, coalescence, and re-nucleation of islands continues, ultimately resulting in the development of five continuous layers of FeO_x and a partial sixth layer (Figure 4.2h) after 650 ALD cycles.

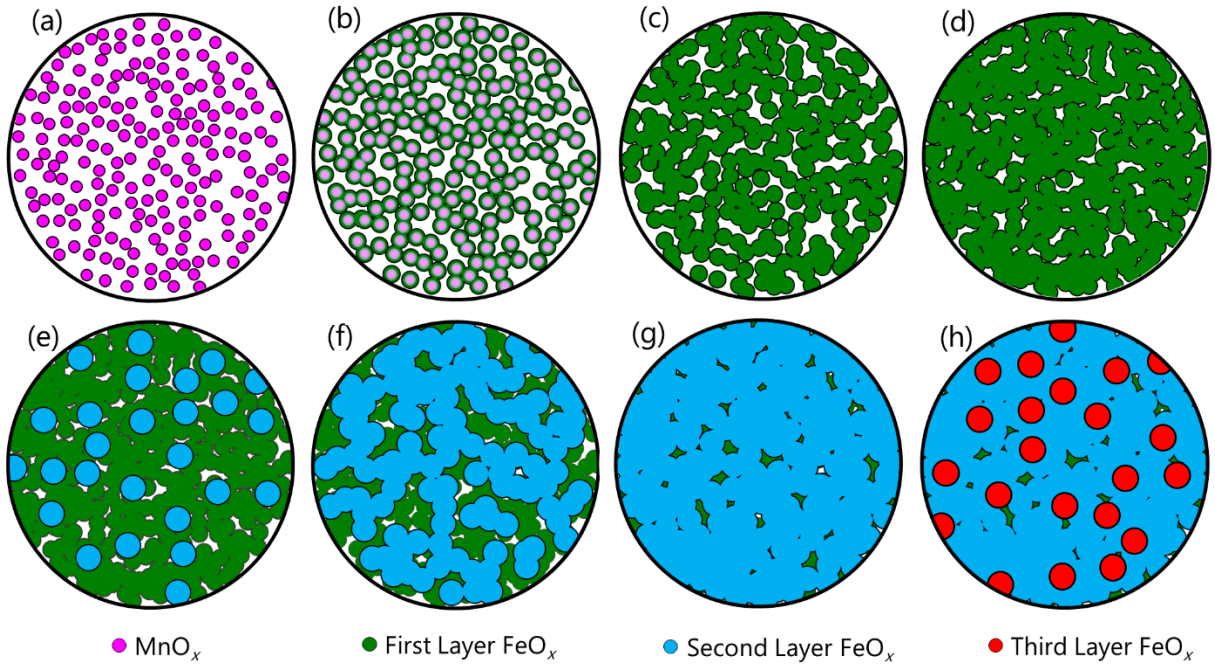

Figure 4.7. Schematic of the proposed FeO_x nucleation and growth process. (a) MnO_x seed layer; (b) FeO_x nucleates on the seed layer; (c) FeO_x islands grow in size; (d) FeO_x islands coalesce; (e) another layer of FeO_x islands nucleate in the pinholes of the continuous first layer; (f) the second layer of islands grow; (g) the second layer of islands coalesce, and (h) a third layer of islands is formed on top of the second layer and the process repeats.

It also interesting to note that the MnO_x seed layer does not hermetically protect the vulnerable carbon substrate from the O plasma reactant during FeO_x ALD. This is revealed by the non-continuous islands of MnO_x shown in Figure 4.1a, produced by only ten cycles of MnO_x ALD. Instead, the MnO_x seed layer indirectly reduces the exposure of the carbon substrate to the O plasma reactant by enhancing the growth per cycle (GPC) during FeO_x formation. Without a MnO_x seed layer, the FeO_x ALD GPC using EF and an O plasma is so low that the exposed carbon substrate is subject to excessive amounts of O plasma radicals, before a continuous layer of FeO_x can be developed, and the carbon substrate is etched. With a MnO_x seed layer, the GPC of the FeO_x process is enhanced, reducing the number of ALD cycles required to achieve a continuous (and thereby protective) layer of material and, thus, reduces the total exposure of the carbon substrate to the O plasma reactant.

4.4 Conclusions

The deposition characteristics of an FeO_x atomic layer deposition (ALD) process were studied using electron microscopy and *in situ* spectroscopic ellipsometry (SE). Carbon substrates were employed to mimic the growth behaviour on air electrodes in metal-air batteries and fuel cells, with a thin ALD coating of MnO_x serving as a protective seed layer. FeO_x deposition displayed a unique formation process where multiple layers of islands were successively nucleated and grown into a continuous film with pinholes. Initial FeO_x layer formation, through nucleation on MnO_x islands, was faster than subsequent FeO_x formation on underlying FeO_x layers. Conventional SE modelling displayed mixed substrate-enhanced and substrate-inhibited growth, with linear growth displayed after extended ALD cycles. The formation of six island layers during 650 ALD cycles were modelled through an effective medium approximation (EMA) approach to the SE data. Scanning electron microscopy and cross sectional TEM were used to confirm the same island growth mode on SiO_x/Si substrates used for SE.

4.5 Supporting Information

The necessity of a protective MnO_x sublayer is demonstrated in Figure S4.1. In the absence of a protective film (Figure S4.1a), etching of the carbon substrate occurs during atomic layer deposition (ALD) of FeO_x. The damaged carbon layer is unstable in the electron beam during transmission electron microscopy (TEM) imaging. With a protective MnO_x layer (Figure S4.1b), the carbon substrate remains intact.

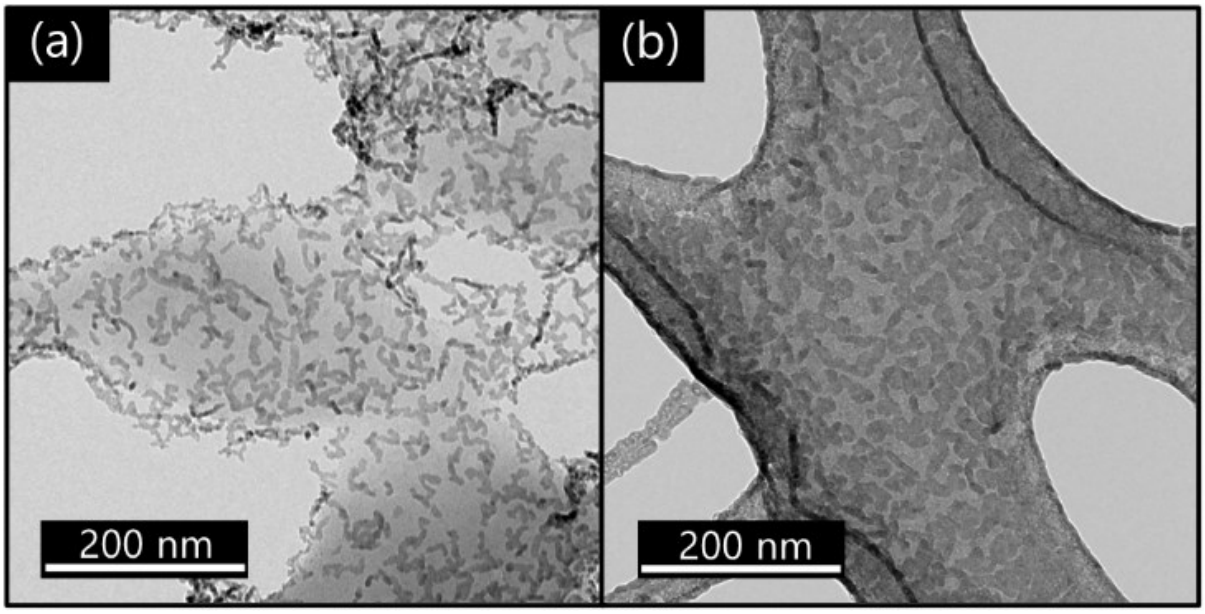

Figure S4.1. TEM bright field images of 200 cycles of FeO_x ALD (a) without and (b) with a protective MnO_x sublayer.

Processing of the scanning TEM (STEM) images during the first 10 cycles of FeO_x growth was conducted using ImageJ in order to differentiate between the growing islands and the substrate material. A workflow of the processing steps is shown in Table S4.1.

Table S4.1. Image processing parameters for early stage FeO_x growth STEM images on carbon substrates.

Sample	Image Filter			Auto Local Threshold	
	Type	Radius (pixels)	Background Subtraction Radius (pixels)	Algorithm	Radius (pixels)
0cy	Mean	1	200	Otsu	10
1cy	Median	1	20	Otsu	20
3cy	Median	1	250, 100	Otsu	15
10cy	Median	1	100	Otsu	30

Processing of plan view STEM images taken throughout 650 ALD cycles was conducted in ImageJ in order to differentiate between different layers of FeO_x growth. Separation of the different phases was achieved by selective thresholding of the image (Table S4.2). Quantification of surface fraction was calculated by counting the number of pixels for each phase identified.

Table S4.2. Image processing parameters for the plan view STEM images on the carbon substrate. Thresholding enabled quantification of the surface fractions for individual material layers. The indicated colours correspond to the colour scheme that is introduced in Figure 4.2.

Sample		0cy	10cy	30cy	50cy	100cy	200cy	420cy	650cy
Image Filter	Type	-	Mean	-	-	Mean	-	-	Mean
	Radius (pixels)	-	2	-	-	1	-	-	1
Top Layer Thresholding	Algorithm	Bernsen	Bernsen	Phansalkar	MaxEntropy	Minimum	IsoData	Minimum	MaxEntropy
	Radius (pixels)	22	10	20	-	-	-	-	-
Lower Layer Thresholding	Algorithm	-	-	-	Saulova	Sauvola	Sauvola	Sauvola	Sauvola
	Radius (pixels)	-	-	-	14	15	15	8	10
Quantative Surface Fraction	Carbon Substrate (grey)	66.0%	55.6%	24.5%	4.2%	4.0%	-	-	-
	MnO_x Seed Layer (pink)	34.0%	-	-	-	-	-	-	-
	First Layer (green)	-	44.4%	75.5%	95.8%	96.0%	2.6%	-	-
	Second Layer (blue)	-	-	-	26.1%	61.8%	97.4%	1.7%	-
	Third Layer (red)	-	-	-	-	-	25.1%	98.3%	-
	Fourth Layer (green)	-	-	-	-	-	-	78.0%	1.8%
	Fifth Layer (blue)	-	-	-	-	-	-	-	98.2%
	Sixth Layer (red)	-	-	-	-	-	-	-	8.5%

High angle annular dark field (HAADF) STEM images at zero, one, three, and ten cycles of FeO_x ALD were analyzed with ImageJ using the *Analyze Particles* function to extract the number density and average size of island particles. The full workflow of image processing is compiled in Table S4.1. Surface fraction is calculated based on the area occupied by the measured particles over the entire area investigated. A hypothesis on the formation of worm-like islands is also presented, based on FeO_x deposition that bridges together neighbouring islands.

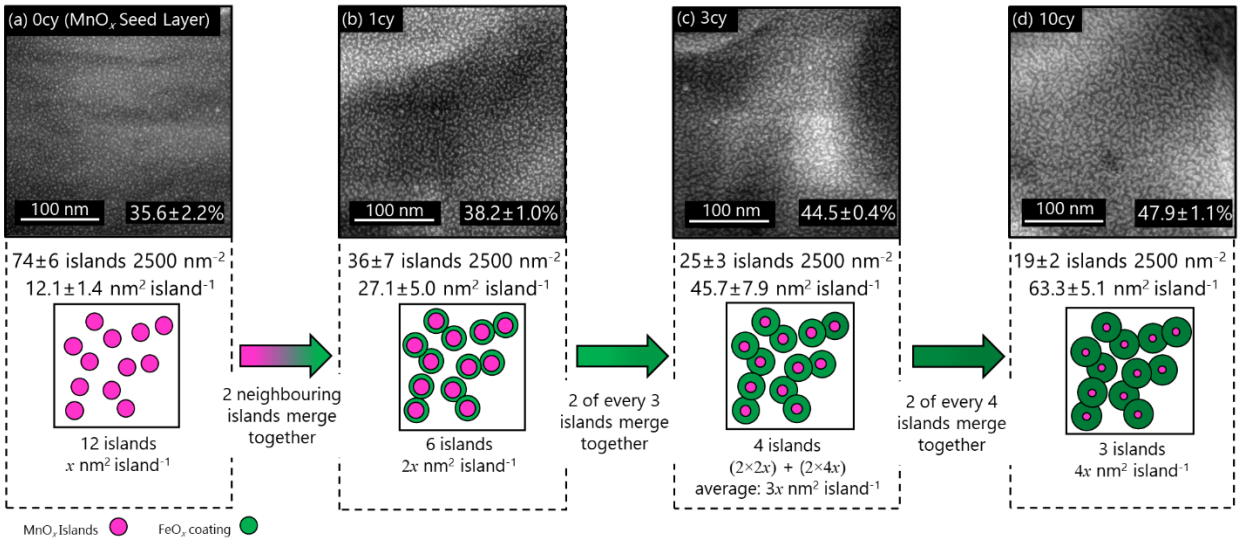

Figure S4.2. Progression of the ALD film from (a) initial MnO_x hemispherical islands to (b) one cycle, (c) three cycles, and (d) ten cycles of FeO_x ALD. HAADF STEM images are shown alongside measured characteristics of the surface particles, including the average number of islands in a 2500 nm^2 area, the average size of each island, and the surface fraction occupied by the islands. A model of coalescence into the worm-like islands is illustrated.

Energy dispersive X-ray (EDX) spectroscopy was conducted on select samples from Figures 4.1 and S4.2 to map out the distribution of O, Mn and Fe elements in the deposits. HAADF images are also included to show the island morphology of the films.

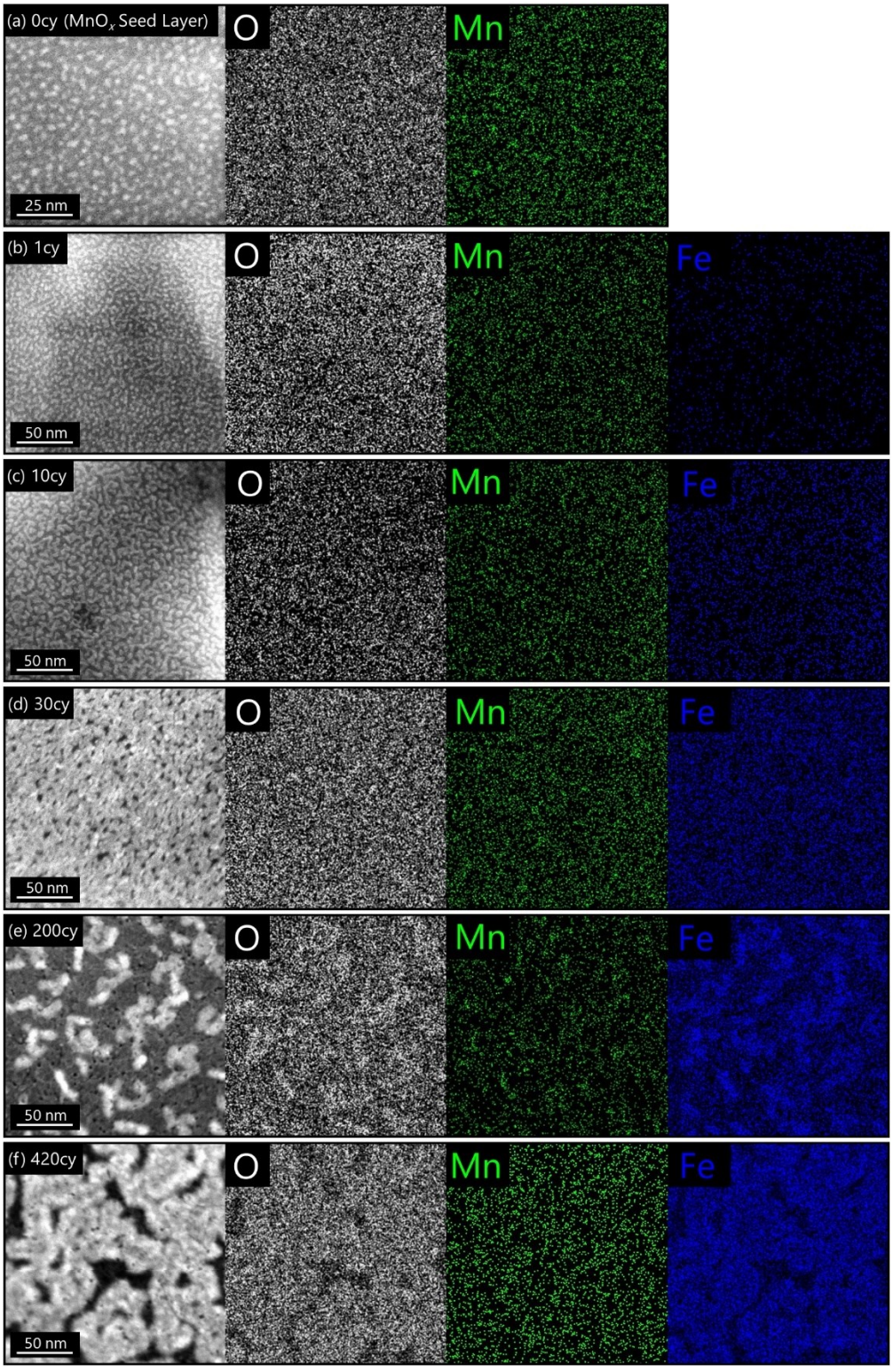

Figure S4.3. HAADF STEM images and EDX maps for (a) zero cycles, (b) one cycle (c) 10 cycles, (d) 30 cycles, (e) 200 cycles, and (f) 420 cycles of FeO_x ALD. O is shown in white, Mn in green, and Fe in blue.

Selected area diffraction (SAD) patterns were obtained during TEM analysis of the samples from Figure 4.1 and are presented in Figure S4.4. Indexing of the patterns to either Fe_2O_3 or Mn_3O_4 is represented by different line types and colours shown in Figure S4.4.

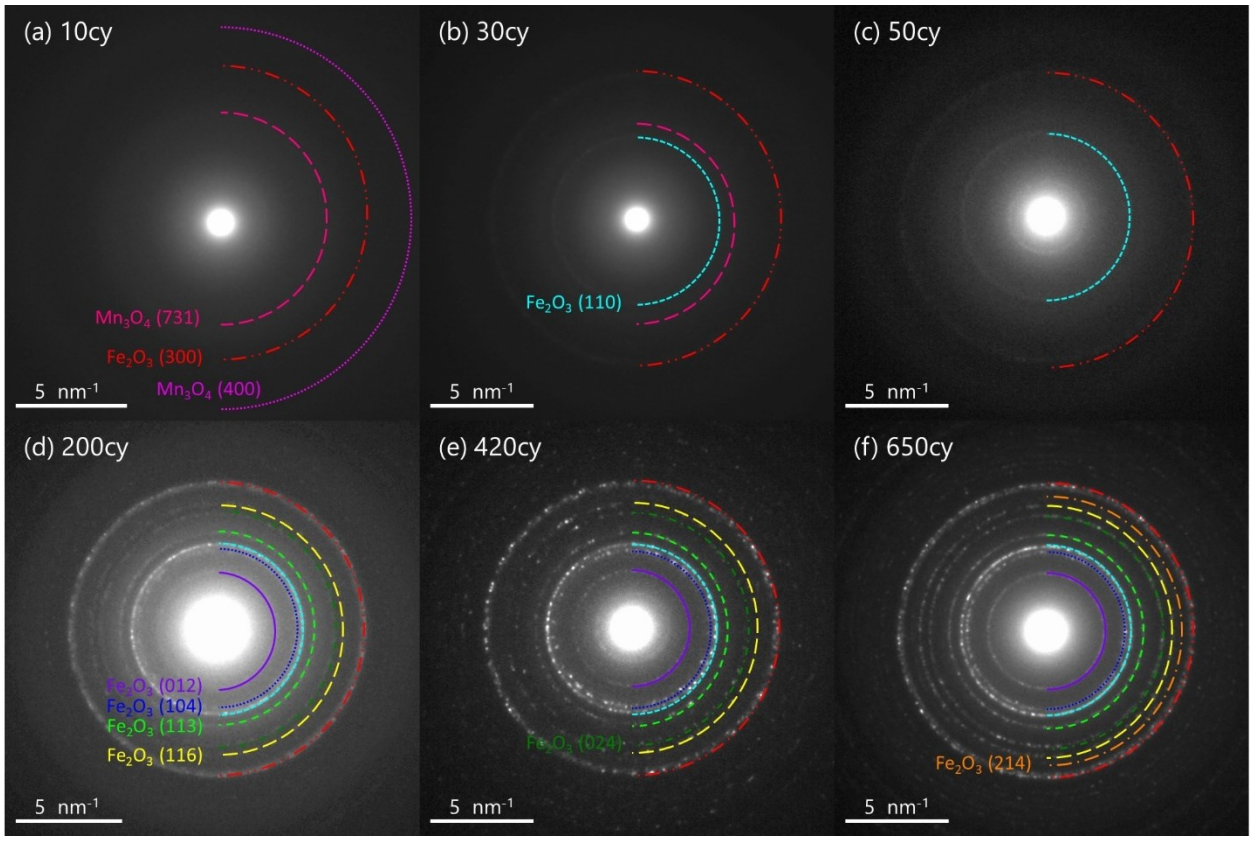

Figure S4.4. SAD patterns for several FeO_x ALD samples. (a) 10 cycles, (b) 30 cycles, (c) 50 cycles, (d) 200 cycles, (e) 420 cycles, and (f) 650 cycles of FeO_x ALD. Each ring identified is matched to a specific plane for either Fe_2O_3 or Mn_3O_4 and is distinguished through different colours and line types.

Rings from the selected area diffraction (SAD) patterns (Figure S4.4) were indexed to Fe_2O_3 or Mn_3O_4 according to the measured d-spacing. The colour and line type of each ring indicates a matching plane with either Fe_2O_3 or Mn_3O_4.

Table S4.3. Analysis of SAD patterns in Figure S4.4, with measured d-spacings matched to appropriate planes in either Fe_2O_3 or Mn_3O_4. The colour scheme of Figure S4.4 is maintained.

(h k l)	d (Å)	I (%)	Measured d (Å)					
α-Fe_2O_3 (PDF#33-0664)			**10cy**	**30cy**	**50cy**	**200cy**	**420cy**	**650cy**
(0 1 2)	3.684	30%	---	---	---	3.79	3.60	3.68
(1 0 4)	2.700	100%	---	---	---	2.75	2.62	2.59
(1 1 0)	2.519	70%	---	2.51	2.52	2.51	2.46	2.45
(1 1 3)	2.207	20%	---	---	---	2.21	2.15	2.15
(0 2 4)	1.840	40%	---	---	---	1.83	1.78	1.78
(1 1 6)	1.694	45%	---	---	---	1.67	1.67	1.66
(2 1 4)	1.485	30%	---	---	---	---	---	1.55
(3 0 0)	1.453	30%	1.45	1.43	1.44	1.45	1.44	1.42
Mn_3O_4 (PDF#13-0162)								
(4 0 0)	2.100	50%	2.05	2.09	---	---	---	---
(7 3 1)	1.126	40%	1.13	---	---	---	---	---

High resolution TEM (HRTEM) was conducted on ALD deposits to illustrate the nano-crystalline nature of the FeO_x films. The lattice fringes correspond to the (104) planes of Fe_2O_3; measured values were within 3% of the published 2.700 Å value [PDF #33-0664].

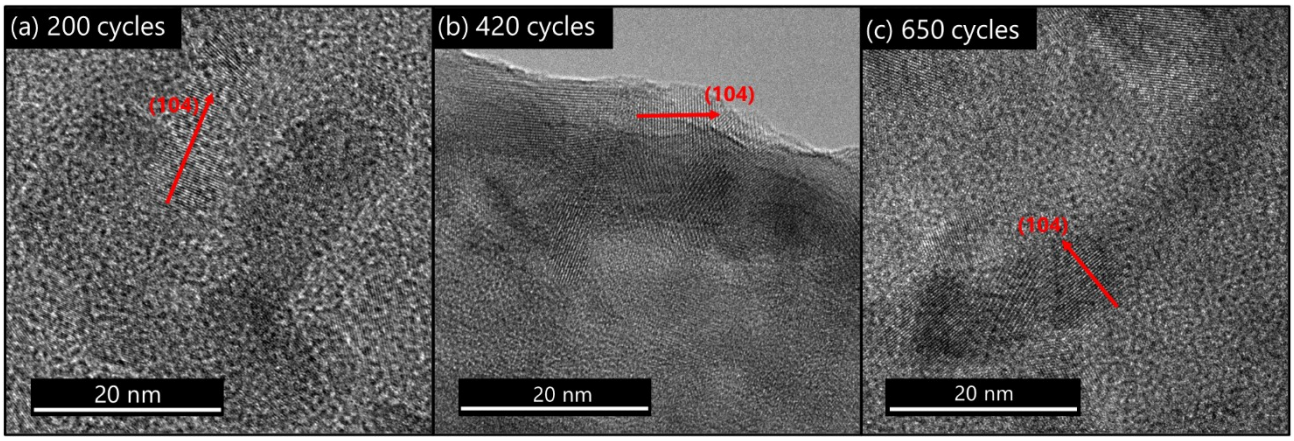

Figure S4.5. HRTEM images of the ALD coating on a carbon substrate with a MnO_x seed layer. (a) 200, (b) 420, and (c) 650 cycles of FeO_x ALD. The measured (104) planar d-spacings were ~2.75±0.01 Å.

The effective medium approximation (EMA) model used in this work approximates surface islands as a secondary phase contained within a matrix of voids.[170] The model calculates the effective electrical and optical properties of this mixed layer through a mathematical combination of the two phases with a defined volume fraction of each phase.[170–173] An EMA model is fit to the *in situ* spectroscopic ellipsometry (SE) data to extract volume fraction values for the secondary phase as the deposition process occurs. These values can then be interpreted to model the island growth process as a function of ALD cycle. To calibrate the EMA model with the plan view STEM images of the island growth process, a conversion factor is required to convert between surface fraction values calculated from STEM images and volume fraction values that can be used in the EMA model.

Based on plan view STEM images of the MnO_x seed layer (Figure 4.1a), the seed layer forms as hemispheres on the surface, in agreement with other ALD reports concerning an island growth mode.[338,345,374] Thus, the relationship between volume fraction and surface fraction is calculated assuming a hemispherical geometry (Figure S4.6).[174] In line with the EMA methodology, the height of the total EMA layer is equivalent to the height of the MnO_x seed layer, as determined by fitting the SE data.

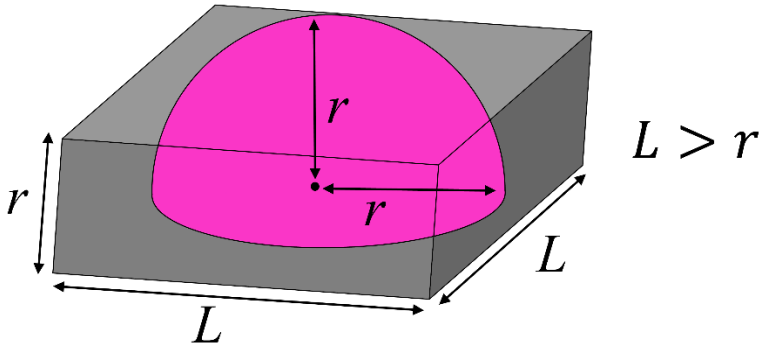

Figure S4.6. Hemispherical geometry approximation for the MnO_x seed layer (pink). The void space considered in the EMA model is represented by the grey rectangle.

The surface fraction (f_S) is the plan view areal projection of the MnO_x seed layer (A_{MnOx}) divided by the total area of interest (A_{total}).

$$f_S = \frac{A_{MnO_x}}{A_{total}} = \frac{\pi r^2}{L^2} \quad \text{(S4.1)}$$

The volume fraction (f_V) is the volume of the MnO_x seed layer (V_{MnOx}) divided by the total volume of interest (V_{total}).

$$f_V = \frac{V_{MnO_X}}{V_{total}} = \frac{\left(\frac{1}{2}\right)\frac{4}{3}\pi r^3}{L^2 r} = \frac{2\pi r^2}{3L^2} \tag{S4.2}$$

The ratio between f_V and f_S can then be used to remove common variables.

$$\frac{f_V}{f_S} = \frac{\frac{2\pi r^2}{3L^2}}{\frac{\pi r^2}{L^2}} = \frac{2\pi r^2}{3L^2} \times \frac{L^2}{\pi r^2} = \frac{2}{3} \tag{S4.3}$$

Lastly, f_V for the MnO_x seed layer can be determined in terms of f_S.

$$f_V = \left(\frac{2}{3}\right) f_S \tag{S4.4}$$

The result of this geometric approximation is that the volume fraction is 2/3 the value of the surface fraction (Equation S4.4). Note, this relationship only holds true for the MnO_x seed layer prior to FeO_x deposition (0cy sample). Since Figure 4.2a shows 34.0% surface coverage for the MnO_x seed layer, this is equivalent to a 22.7% volume fraction (Equation S4.5). This volume fraction is used in the EMA model to describe the contribution of the MnO_x seed layer.

$$f_V|_{0.340} = \frac{2}{3}(0.340) = 0.227 \Rightarrow 22.7\% \tag{S4.5}$$

When FeO_x deposition begins, FeO_x deposits on both the MnO_x surfaces and substrate surface, simultaneously. Deposition on the MnO_x surfaces occurs because MnO_x enhances the GPC of the ALD process and thus provides active sites for deposition. Furthermore, Figure S4.2 illustrates that the MnO_x seed layer acts as nucleation sites for FeO_x growth. At the same time, deposition of FeO_x on the substrate surface occurs because the total surface fraction of the ALD film, measured from the STEM images, increases during FeO_x ALD. As also shown in Figure S4.2, the depositing FeO_x bridges together neighbouring islands and, therefore, grows on the substrate at locations directly adjacent to the MnO_x seed layer. A geometric model of this process was originally devised in order to convert between surface fraction and volume fraction for FeO_x. However, the model was inadequate in that it could not provide surface fraction values for FeO_x that correlated with STEM images. Furthermore, the volume fraction values predicted were

unreasonably low. Therefore, no geometric model was applied to the data extracted between 0 and 50 ALD cycles. In this case, an EMA model was still used to fit the SE data (volume fraction), but the surface fraction values presented in Figure 4.5 are simply a best-fit line between the two data points of surface fraction measured from the STEM images at 30 and 50 cycles. Earlier analysis could not accurately predict when complete coverage of the MnO_x seed layer occurs, but it is highly likely that this occurs prior to the 30cy sample, when over 75% of the substrate surface is coated in ALD material. Thus, the 30cy and 50cy values were used to represent the surface fraction of FeO_x for the first layer of islands. The line of best fit was an $Ax^{2/3}$ curve, where x is the ALD cycle number and A is a fitting parameter; the exponent of 2/3 was chosen to mimic the behaviour of the latter layers of islands, as will be demonstrated later.

When the second layer of islands nucleates, the islands are 100% FeO_x (as opposed to the mixed MnO_x seed layer – FeO_x film first layer). This simplifies the required geometric model to bridge surface fraction and volume fraction. As illustrated by Figures 4.1e-g, the morphology of the FeO_x islands for the second and successive layers is not hemispherical like the MnO_x seed layer. Instead, the worm-like islands are approximated by hemicylinders (Figure S4.7). Also contrary to the MnO_x seed layer, the height of an EMA layer is not the same as the height of the hemicylinders. This is because, as FeO_x deposition occurs, the hemicylinders increase in size in both the lateral and vertical directions. Thus, according to the EMA methodology outlined previously, the height of an EMA layer was fixed at the highest point of hemicylindrical growth. This was found by fitting the SE data at a point corresponding to the maximum surface fraction for that layer (*e.g.*, 97.4% for the second layer according to Figure 4.2f). In this way, the thickness of the EMA layer remains constant (at the highest value) while volume fraction independently varies. As a result, the height of the growing hemicylinders is less than the ceiling value (Figure S4.7).

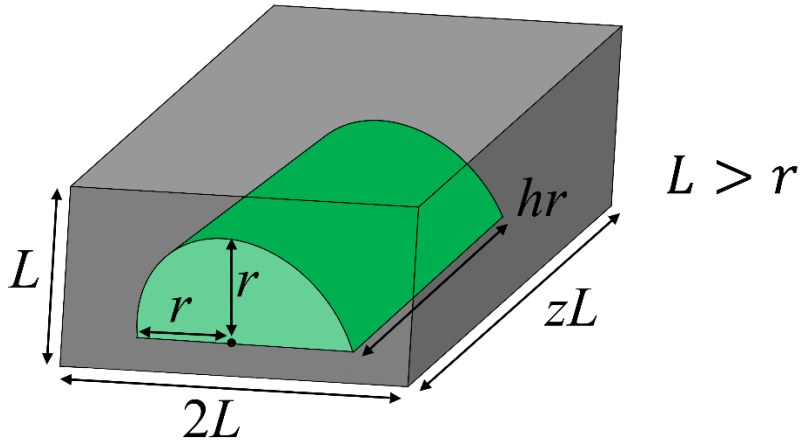

Figure S4.7. Hemicylindrical geometry for the worm-like FeO_x islands (green). The void space considered in the EMA model is represented by the grey rectangle. Proportionality factors of *h* and *z* define the aspect ratio of the hemicylinders and void space, respectively.

The surface fraction (f_S) is the plan view projection of the FeO_x islands (A_{FeOx}) divided by the total area of interest (A_{total}).

$$f_S = \frac{A_{FeO_x}}{A_{total}} = \frac{2r \cdot hr}{2L \cdot zL} = \left(\frac{h}{z}\right)\frac{r^2}{L^2} \tag{S4.6}$$

The volume fraction (f_V) is the volume of FeO_x islands (V_{FeOx}) divided by the total volume of interest (V_{total}).

$$f_V = \frac{V_{FeO_x}}{V_{total}} = \frac{\left(\frac{1}{2}\right)\pi r^2 hr}{2L \cdot zL \cdot L} = \left(\frac{h}{z}\right)\left(\frac{\pi}{4}\right)\frac{r^3}{L^3} \tag{S4.7}$$

The ratio between f_V and f_S can then be calculated.

$$\frac{f_V}{f_S} = \frac{\left(\frac{h}{z}\right)\left(\frac{\pi}{4}\right)\frac{r^3}{L^3}}{\left(\frac{h}{z}\right)\frac{r^2}{L^2}} = \left(\frac{\pi}{4}\right)\frac{r^3}{L^3} \times \frac{L^2}{r^2} = \left(\frac{\pi}{4}\right)\frac{r}{L} \tag{S4.8}$$

f_V for the FeO_x worm-like islands can be found in terms of f_S.

$$f_V = \left(\frac{\pi}{4}\right)\left(\frac{r}{L}\right) f_S \tag{S4.9}$$

Identifying that $\frac{r^2}{L^2}$ is a term in f_S, Equations S4.6 and S4.9 can be manipulated to remove common variables.

$$f_V{}^2 = \left(\frac{\pi}{4}\right)^2 \left(\frac{r^2}{L^2}\right) f_S{}^2 = \left(\frac{\pi}{4}\right)^2 \left(\left(\frac{z}{h}\right) f_S\right) f_S{}^2 = \left(\frac{\pi}{4}\right)^2 \left(\frac{z}{h}\right) f_S{}^3 \quad \text{(S4.10)}$$

Lastly, it is assumed that $h = z$ (*i.e.*, same aspect ratio for hemicylinders and total space) to find f_V exclusively in terms of f_S.

$$f_V = \left(\frac{\pi}{4}\right)\left(\frac{z}{h}\right)^{1/2} (f_S)^{3/2} = \frac{\pi}{4}(f_S)^{3/2} \quad \text{(S4.11)}$$

f_S for the FeO_x islands can then be determined in terms of f_V.

$$f_S = \left(\left(\frac{4}{\pi}\right) f_V\right)^{2/3} \quad \text{(S4.12)}$$

Since a ceiling value larger than the height of the growing hemicylinders is applied, a non-linear relationship between surface fraction and volume fraction is calculated for the growing FeO_x islands (Equation S4.12).

One special case of converting between surface and volume fraction for the FeO_x island layers is the 650cy sample. At this point, the thickness of the EMA layer is fit to the actual height of the islands (Figure S4.8) because this is the end of the deposition process (*i.e.*, maximum film height).

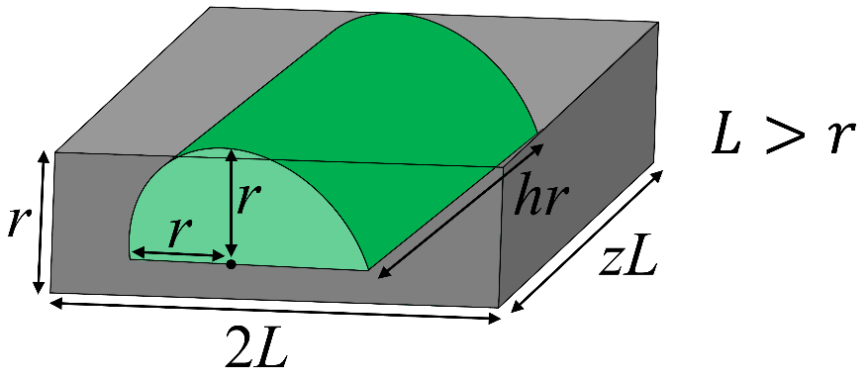

Figure S4.8. Hemicylindrical geometry for the 650cy FeO_x islands (green). The void space considered in the EMA model is represented by the grey rectangle. Proportionality factors of *h* and *z* define the aspect ratio of the hemicylinders and void space, respectively.

The surface fraction (f_S) and volume fraction (f_V) of the FeO_x islands is derived using the new geometry (Equations S4.13 and S4.14, respectively).

$$f_S = \frac{A_{FeO_x}}{A_{total}} = \frac{2r \cdot hr}{2L \cdot zL} = \left(\frac{h}{z}\right)\frac{r^2}{L^2} \tag{S4.13}$$

$$f_V = \frac{V_{FeO_x}}{V_{total}} = \frac{\left(\frac{1}{2}\right)\pi r^2 hr}{2L \cdot zL \cdot r} = \left(\frac{h}{z}\right)\left(\frac{\pi}{4}\right)\frac{r^2}{L^2} \tag{S4.14}$$

Again, the ratio between the two fractions can be used to eliminate common variables (Equation S4.15) and f_V can be determined exclusively in terms of f_S (Equation S4.16).

$$\frac{f_V}{f_S} = \frac{\left(\frac{h}{z}\right)\left(\frac{\pi}{4}\right)\frac{r^2}{L^2}}{\left(\frac{h}{z}\right)\frac{r^2}{L^2}} = \left(\frac{\pi}{4}\right)\frac{r^2}{L^2} \times \frac{L^2}{r^2} = \left(\frac{\pi}{4}\right) \tag{S4.15}$$

$$f_V = \left(\frac{\pi}{4}\right) f_S \tag{S4.16}$$

Like the MnO_x seed layer, there is a linear relationship between volume fraction and surface fraction when the ceiling height matches that of the island geometry. In this case, however, the constant of proportionality is π/4 (Equation S4.16). For the 650cy sample, the surface fraction from STEM imaging (Figure 4.2h) is 8.48%, translating into a volume fraction of 6.66% (Equation S4.17) that was used to calibrate the EMA model.

$$f_V|_{0.0848} = \frac{\pi}{4}(0.0848) = 0.0666 \Rightarrow 6.66\% \tag{S4.17}$$

A simplification in converting between surface fraction and volume fraction for the EMA model is required during island coalescence. When neighbouring islands contact each other during coalescence, the surface coverage approaches unity while the total volume fraction does not. This is a direct result of the hemicylindrical geometry utilized in this model. Essentially, even after the islands reach 100% surface coverage, there continues to be deposition of material between the hemicylinders to fill the volume gaps between mounds. In other words, the curvature of the hemicylinders is increased up to infinity during this post-coalescence growth period, where the surface fraction is maintained at 100%.[334,342] A similar phenomenon likely occurs during the actual coalescence of the FeO_x islands and so this behaviour is not necessarily non-physical. However, using the previously defined relationship between volume fraction and surface fraction, the EMA model would predict surface coverages in excess of 100%. Instead,

this stage of growth is approximated by linear interpolation between the point where the surface fraction reaches the value seen in STEM imaging and the cycle number where volume fraction is equal to this surface fraction. At this latter point, the film has filled in the gaps to the same amount as recorded by STEM and an essentially continuous layer is formed. The sharp changes in slope in Figure 4.5 at the late stages of growth for each layer (~95%) are a result of this linear interpolation.

It is assumed that the FeO_x islands visible in Figure 4.1, which are used to calibrate the model, include every stage of island nucleation and growth. In other words, it is assumed that no additional layers of FeO_x islands form between any of the cycles depicted in Figure 4.1.

Figure S4.9 shows the overlap between the psi and delta values from the SE measurement and the corresponding EMA model after 100 cycles of FeO_x ALD. With a mean-squared-error (MSE) of less than 7.3, there is a good fit to the data,[170,389] especially in light of the complex nature of the EMA model and the multi-layer island growth phenomenon.

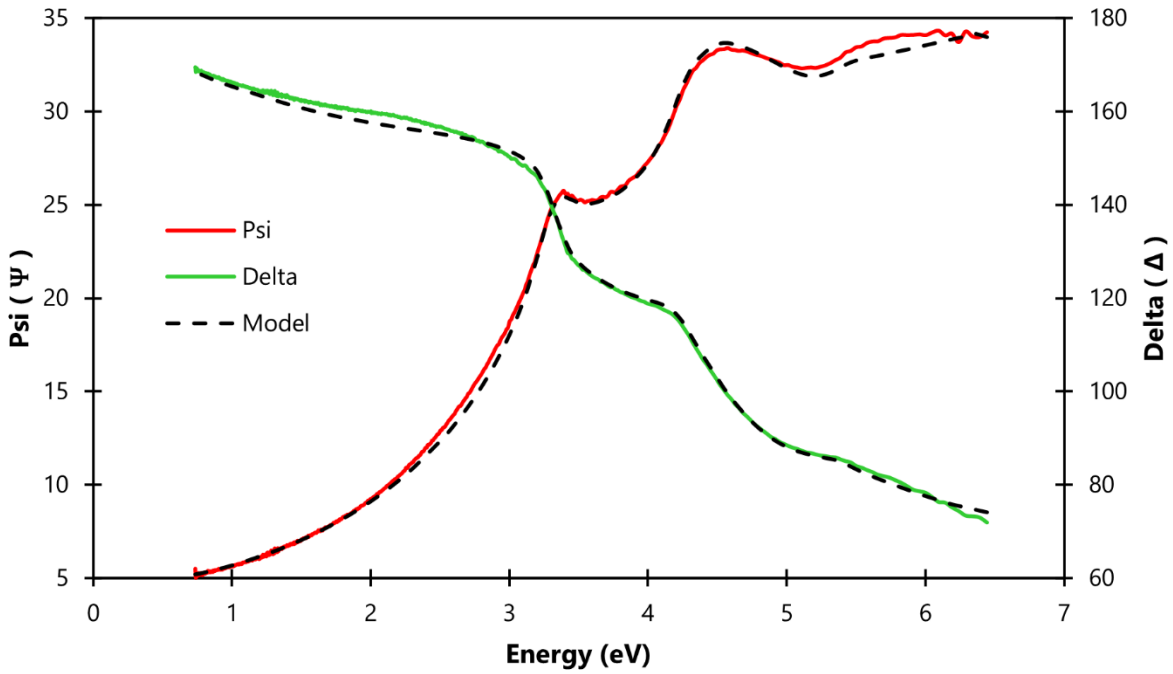

Figure S4.9. SE psi and delta plots after 100 cycles of FeO_x ALD and the corresponding EMA model, displaying a fit with an MSE less than 7.3.

The morphology of the ALD material after 200 cycles of FeO_x ALD on a SiO_x/Si substrate and on a carbon substrate are juxtaposed in Figure S4.10.

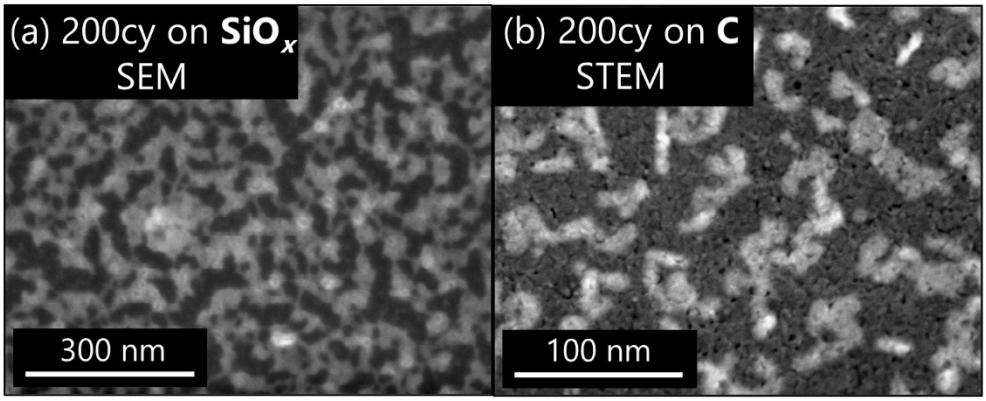

Figure S4.10. (a) Scanning electron microscopy (SEM) secondary electron image of the 200cy SiO_x/Si sample. (b) HAADF STEM image of the 200cy sample on a carbon TEM grid.

5. Bifunctional Mn-Fe Oxide Catalysts for Zn-Air Battery Air Electrodes Fabricated Through Atomic Layer Deposition

A version of this chapter has been accepted for publication in a peer-reviewed journal:

M. Labbe, M. P. Clark, K. Cadien, and D. G. Ivey, "Bifunctional Mn-Fe Oxide Catalysts for Zn-Air Battery Air Electrodes Fabricated Through Atomic Layer Deposition," *Batter. Supercaps*, in-press, e202400133, 2024.

5.1 Introduction

Primary Zn-air batteries (ZABs), while not a new technology, have only ever penetrated the market for hearing-aids due to low power outputs from inefficient reaction kinetics.[16,32] The main culprit is often identified as the oxygen reduction reaction (ORR) during battery discharge.[38] For secondary ZABs, the oxygen evolution reaction (OER) during recharge is also sluggish and reduces overall battery efficiency.[38] The use of an appropriate catalyst, however, can modify the reaction kinetics and improve the power yield of ZABs.[36,39] The traditional catalyst for ORR is Pt, while that for OER is RuO_2.[32] These precious metal catalysts impede the practicality of ZABs and increase their potential cost. On the other hand, earth-abundant materials such as transition metal oxides can also be applied as ORR and OER catalysts and have sparked a tremendous growth in research.[32,39,390] Furthermore, a bifunctional catalyst, active towards both ORR and OER, is highly desirable and can often be achieved using a combination of several transition metal oxides.[36,39] These bifunctional transition metal oxide catalysts are also more stable than their precious metal counterparts during prolonged battery cycling.[54,102,318] Mn oxides (MnO_x) are the most common candidates for ORR catalysis, while OER catalysts include the oxides of Co, Ni, and Fe.[39,58,391] Among these options, Mn and Fe are found in the greatest abundance in the earth[46] and at the lowest industrial cost.[392] Thus, mixed oxides of Mn and Fe have been well explored in the literature as OER,[393,394] ORR,[395] and bifunctional catalysts.[396,397] However, the application of these particular oxides in ZABs is rare.[101–103]

In ZABs, ORR and OER occur at the air electrode, a porous membrane that allows oxygen exchange between the battery cell and the ambient environment (Figure 5.1). This membrane, usually carbon-based, is often called the gas diffusion layer (GDL) and is composed of two

distinct layers. The air facing side, called the backing layer, features large porosity for oxygen flow and a hydrophobic treatment, often with polytetrafluoroethylene (PTFE), to prevent electrolyte loss. The electrolyte facing side, called the microporous layer, features much higher surface area but smaller porosity and is usually constructed of carbon particles bound together with a binder, such as PTFE, which also affords some hydrophobicity.[64] Moreover, the high surface area microporous layer serves as a substrate for ORR and OER catalyst loading.[39] Indirect catalyst loading, often via spray-coating, deposits catalyst particles on the outermost surface of the microporous layer only (Figure 5.1a). Direct catalyst loading techniques, on the other hand, can take advantage of the porosity in the microporous layer to increase the amount of catalyst loading. A gas-phase technique, atomic layer deposition (ALD) can deposit catalyst layers on GDL particles deep within the porosity since it does not require line-of-sight (Figure 5.1b). This leads to an improvement in the utilization of the catalyst on the GDL. Furthermore, the deep penetration of catalyst material into the substrate can increase the resiliency of the air electrode against electrolyte flooding during prolonged battery cycling, extending the battery's lifetime.[54]

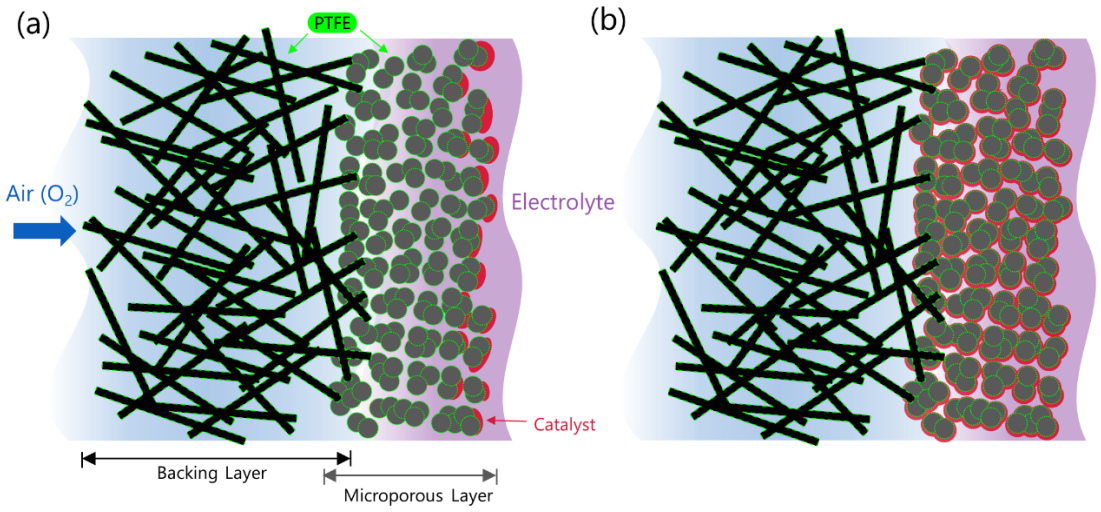

Figure 5.1. Schematic of the GDL structure and catalyst loading on the air electrode. The green outline around the backing layer and microporous layer particles represents PTFE in the GDL. The catalyst material is shown in red. (a) Representation of an indirect catalyst loading technique, which only coats the outermost surface of the air electrode. (b) Representation of loading catalyst material with ALD, which coats throughout the porosity of the microporous layer.

Often categorized as a special form of chemical vapour deposition (CVD), ALD differs from CVD in that chemical species are active only on a substrate surface, eliminating line-of-sight shortfalls and enabling extremely conformal coatings.[158] A chemical precursor and co-reactant are separated by inert gas purges to ensure that only surface adsorbed species contribute to material growth.[52] As a result, ALD coatings are deposited in cycles, with more cycles generally leading to thicker films. A binary ALD process, which often deposits monometallic oxides (*e.g.*, Fe_2O_3), has four steps within one cycle: precursor delivery, inert gas purge, reactant delivery, and inert gas purge.[52] An ALD supercycle is the combination of two or more binary processes to deposit a multi-element film, such as a bimetallic oxide (*e.g.*, $CoFe_2O_4$).[243] Within one supercycle, there can be several cycles of each binary ALD process, denoted as subcycles (*e.g.*, five cycles of Fe_2O_3 and five cycles of CoO). The number of subcycles for each material within a supercycle can be tailored for the desired film chemistry.[55] Like any ALD process, increasing the total number of supercycles results in increased film thickness.[158] While the ALD chemistry of transition metal single oxides has been extensively explored,[154] ALD of bimetallic and trimetallic oxides is not as common place.[55] In particular, there have been a handful of bimetallic oxides explored in the literature that include either Mn or Fe as components,[191,198,245,247,254,398,399] but to the authors' knowledge, this work is the first reporting Mn-Fe oxide ($MnFe_xO_y$) deposited via ALD.

Several reviews have explored the application of ALD towards energy conversion and storage, [48,50,325,400] citing specific examples towards the more established technologies of Li-ion batteries, fuel cells, and solar water splitting devices. For studies on ZABs in particular, ALD is generally focused on catalyst development at the air electrode. In some cases, ALD is applied to a high surface area substrate but the catalyst itself is applied to the air electrode indirectly.[401–404] Direct ALD onto the air electrode has been conducted for Co_9S_8,[51] NiS_x,[405] and MnO_x catalysts.[54] For the first two instances, carbon nanotube functional additives were added to air electrode, while the latter case was an ALD coating directly on the as-received GDL material. Herein, an ALD recipe to deposit a bimetallic $MnFe_xO_y$ catalyst directly on the air electrode is developed. The ALD supercycle process builds upon previous work in the research group on the binary depositions of MnO_x and Fe oxide (FeO_x; Chapter 3), which have demonstrated catalytic activity towards ORR and OER, respectively.[157,360] The optimized supercycle process deposits Fe substituted Mn_3O_4 (denoted as $(Mn,Fe)_3O_4$) and produces a uniform layer of the mixed oxide that

encases GDL particles. The electrochemical characteristics of the $MnFe_xO_y$ film are a mix of both MnO_x and FeO_x monometallic oxides and the mixed oxide proves to be a stable bifunctional ZAB catalyst, with over 600 h (1565 cycles) of discharge-charge cycling at 10 mA cm^{-2}.

The innovation of the current study is two-fold. Firstly, based on the research of the authors, the current study is the first report of mixed Mn-Fe oxide in the ALD literature. A supercycle process to deposit mixed Mn-Fe oxides is thoroughly investigated and optimized to maximize bifunctional activity towards ORR and OER. Secondly, this work is the first to apply a mixed transition metal oxide catalyst towards ZAB catalysis using ALD supercycles. Previous reports of ALD for ZAB catalysts use binary ALD processes that deposit only single metal oxides. In this work, a supercycle process to deposit a mixed oxide is developed and applied towards ZAB catalysis. One ALD report in the literature has developed a mixed Fe-Pt catalyst, which was deposited using binary processes and annealing post-deposition, as opposed to direct supercycle deposition performed in this study.[401] Furthermore, mixed Mn-Fe oxide catalysts are rarely reported in the ZAB literature, which also demonstrates the novelty of the present work. In addition to the innovation of the current study, the cycling stability of the ALD mixed Mn-Fe oxide catalyst is quite good, with over 600 h (1565 cycles) of stable cycling at 10 mA cm^{-2}.

5.2 Experimental

5.2.1 ALD

A hot-walled continuous flow ALD reactor (Kurt J. Lesker Company, ALD 150L) was used to deposit all ALD films at an operating pressure of ~1 Torr using ultra high purity Ar (Linde Canada Inc., 99.999%).[361] A substrate temperature of 150 °C was employed for all depositions, unless otherwise specified. A showerhead design supplied the precursor and reactant lines into the reactor.[160] The system was also equipped with a 600 W inductively coupled radiofrequency remote plasma system, operating with Ar and either O_2 (O plasma, Linde Canada Inc., 99.993%), forming gas (FG plasma: 5% H_2, balance N_2; Linde Canada Inc.), or H_2 (H plasma: 5% H_2, balance Ar, Linde Canada Inc.).[361] The Fe precursor (ethylferrocene, EF, STREM Chemicals, Inc., 98%) and Mn precursor (bis(ethylcyclopentadienyl)manganese, $(EtCp)_2Mn$), STREM Chemicals, Inc., 98%) were maintained at 80 °C, with precursor delivery lines and valves heated to 110 and 100 °C, respectively. An ampoule of distilled H_2O, serving as the H_2O reactant, was

kept at room temperature (~22 °C) with a delivery line and ALD valve at 100 °C. Various ALD reactants for the supercycle process were investigated (Figure S5.1). An O plasma reactant was selected for the FeO_x subcycle process, while a combined FG plasma and H_2O reactant was chosen for the MnO_x subcycle process. FeO_x ALD cycles followed the timing scheme of 0.25/5/1/20/5 (EF dose/Ar purge/pre-plasma O_2 flow/O plasma/Ar purge), while MnO_x ALD cycles followed a timing scheme of 3/5/20/20/2/30 ($(EtCp)_2Mn$ dose/ampoule charge/Ar purge/FG plasma/H_2O dose/Ar purge). A saturation study for each binary ALD process on their opposing supercycle surface (*e.g.*, FeO_x deposition on a MnO_x surface) revealed that both of these timing values yielded saturating growth during supercycle depositions (Figures S5.2 and S5.3).

For electrochemical characterization of ALD films, carbon paper-based GDL (SIGRACET© 39BB, SGL Carbon) substrates were placed in the ALD reactor with a 60 s O plasma pretreatment prior to deposition. Film growth was monitored *in situ* using spectroscopic ellipsometry (SE) on a Si(100) witness wafer piece (University Wafers, 525 μm p-type single side polished) placed adjacent to the GDL material in the reactor. The spectrometer (J.A. Woollam Co., Inc., M-2000DI) was directly connected to the ALD reactor and SE results were analyzed in CompleteEase (J.A. Woollam Co., Inc., ver. 4.48) using Tauc Lorentz oscillators to model the ALD films during growth.[303,406] Previous work (Chapter 3) has determined that the FeO_x ALD process deposits a homogenous, nano-crystalline phase of Fe_2O_3.[360] Nevertheless, the ALD process and resulting material deposited through the EF and O plasma process will be referred to as FeO_x in this work. Previous work on the MnO_x ALD process, on the other hand, could not completely identify the phase(s) present in the deposited material and, thus, the nomenclature of MnO_x employed in that work is utilized here.[54,157] Furthermore, a 30 min 300 °C *ex situ* annealing treatment was investigated for select ALD coated GDL samples, which are referred to as annealed. Samples without an annealing treatment are referred to as unannealed.

5.2.2 Electrochemical Characterization

The half cell setup featured ALD coated GDL as the working electrode, submerged in a 1 M KOH (Fisher Chemical, certified ACS) electrolyte saturated with ultra high purity O_2 (Linde Canada Inc., 99.993%) flowing at 40 standard cm^3 min^{-1}. The room temperature (~22 °C) electrolyte also contained a Pt coil counter electrode and Hg/HgO reference electrode (0.098 V

vs. SHE). A Biologic VSP potentiostat was used to conduct linear sweep voltammetry (LSV) at both ORR and OER potentials. The onset of ORR and OER was measured at a current density of 10 mA cm^{-2}. The full cell setup featured ALD coated GDL as the air electrode with a 0.5 mm thick strip of as-received Zn foil (McMaster-Carr, 99%) acting as the Zn electrode. The homemade vertical ZAB cell is described elsewhere.[318,407] Ambient air entered the cell through the GDL without mechanical assistance and the electrolyte was 6 M KOH and 0.25 M ZnO (Fisher Chemical, certified ACS). A Biologic VSP potentiostat was used to conduct galvanostatic discharge and charge tests at |2|, |5|, |10| and |20| mA cm^{-2}, with a hold period of 10 min each. Using the values at a current density of |20| mA cm^{-2}, the efficiency of a candidate catalyst was calculated as the discharge potential divided by the charge potential. Long-term cycling tests employed a similar battery cell to the full cell design but with additional provisions to reduce electrolyte loss.[408] An Arbin LBT20084 battery cycler was used to conduct galvanostatic cycling at |10| mA cm^{-2}, with 10 min charge and discharge periods. For the first 200 cycles (100 h), a 5 min rest period was added between charge and discharge. For cycles beyond 200, the rest period was reduced to 1 min.

Individual oxides of MnO_x and FeO_x were deposited on GDL using the binary ALD processes to electrochemically compare with the mixed oxide catalyst. As with previous work,[360] ALD of FeO_x on GDL was preceded by 10 cycles of MnO_x ALD to protect the carbon substrate. The FeO_x sample was only deposited to a thickness of 10 nm due to its slow growth rate. The MnO_x sample was deposited to a thickness of 40 nm. In addition, a Pt-Ru-C catalyst benchmark comparison was prepared via spray-coating an ink onto GDL substrates with a mass loading of ~1 mg cm^{-2}. The ink was a mixture of a commercial Pt-Ru-C powder (Alfa Aeser; 40 wt% Pt, 20 wt% Ru, balance carbon black), a 60 wt% PTFE dispersion (Chemours Teflon™ PTFE DISP 30), reagent alcohol (Fisher Chemical, histological grade), and H_2O. The FeO_x, MnO_x and Pt-Ru-C samples were also annealed at 300 °C for 30 min.

5.2.3 Materials Characterization

Scanning electron microscopy (SEM) imaging and energy dispersive X-ray (EDX) analysis were conducted at 20 kV and a working distance of 15 mm using a TESCAN Vega3 tabletop SEM equipped with an EDX detector. Transmission electron microscopy (TEM) samples were prepared by scraping off the microporous layer of ALD coated GDL, dispersing in reagent

alcohol, and drop casting onto carbon coated, Cu TEM grids (Ted Pella, Inc., Prod #01881-F). TEM/scanning TEM (STEM) was conducted at 200 kV using either a Tecnai Osiris TEM/STEM or a JEOL JEM-ARM 200CF TEM/STEM, both equipped with EDX detectors. Selected area diffraction (SAD) patterns were obtained for crystal structure analysis. X-ray photoelectron spectroscopy (XPS) of the ALD films on Si(100) wafers was conducted using a VersaProbe III instrument with monochromatic Al Kα (1486.6 eV) radiation. A 60 s Ar sputtering pretreatment was used to remove adventitious carbon. XPS spectra were analyzed in CasaXPS software (version 2.3.19), with Shirley type background subtraction for all spectra,[270,272,304,319,409] and a GL(30) curve shape for all peak fitting.[270,272,409,410] Glancing angle X-ray diffraction (XRD) was performed on a bare GDL substrate and a GDL sample with an ALD coating. The instrument (Rigaku Ultima IV) had a Co X-ray source (K_α = 1.789 Å) and reported 2θ values were converted to $Cu_{2\theta}$ values. Background subtraction was conducted using JADE MDI 6.5.26 software.

5.3 Results and Discussion

5.3.1 Supercycle Optimization

Due to the self-limiting nature of ALD, no more than one monolayer of material can be deposited per cycle. This affords precise control over the thickness of individual layers used to construct a ternary oxide film. As explained in a review by Mackus *et al.*, there are two main parameters that can be modified to tailor a supercycle process: the cycle ratio and the bilayer period.[55] The cycle ratio describes the compositional mix of the two individual ALD processes, while the bilayer period characterises the thickness of each layer used in the supercycle. In this work, the nomenclature adopted describes the number of MnO_x ALD cycles deposited followed by the number of FeO_x ALD cycles deposited, in one supercycle. For example, the sample labelled 30:10 indicates that 30 MnO_x ALD cycles were deposited, followed by 10 FeO_x ALD cycles, and this was then repeated until the desired thickness was reached (Figure 5.2). Following the nomenclature presented by Mackus *et al.*, 30:10 employs a cycle ratio of (30/40=) 0.75 for MnO_x and (10/40=) 0.25 for FeO_x, with a bilayer period of (30+10=) 40. During supercycle optimization, ALD films were deposited to a total thickness of approximately 10 nm to be comparable with the thickness of the binary ALD FeO_x films developed previously.[360]

However, due to the digital nature of supercycles, not all films were exactly 10 nm; the exact number of supercycles employed and the resulting thickness of each sample are reported in Table S5.1.

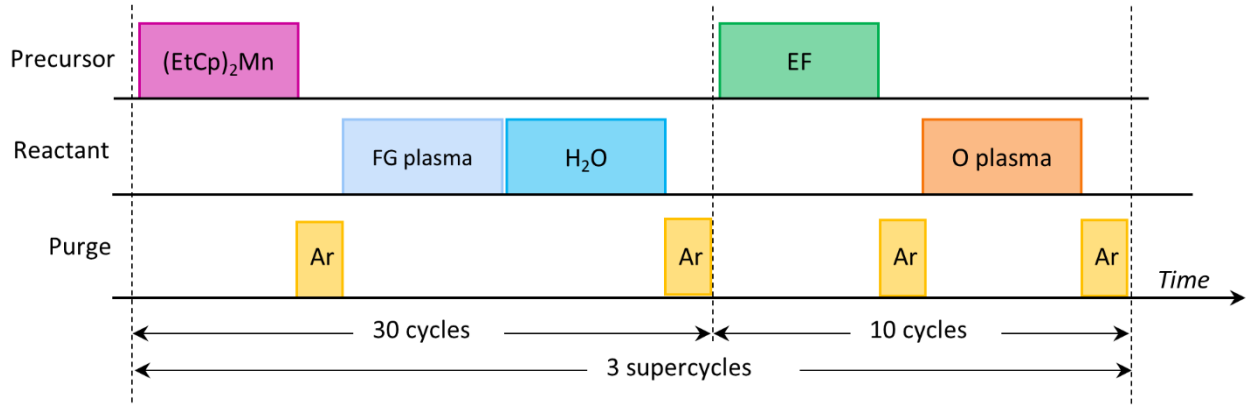

Figure 5.2. Schematic of the atomic layer deposition (ALD) supercycle process for a 10 nm thick 30:10 $MnFe_xO_y$ sample.

In a similar manner to other reports of ternary oxide catalysts for ZABs,[102] the composition of deposited films is systematically manipulated to optimize the catalytic performance. To evaluate bifunctional catalytic performance, two common electrochemical techniques employed in ZAB testing were used. Half cell tests submerge the ALD coated GDL into an electrochemical cell to study the oxygen half cell reactions (ORR and OER). Full cell tests employ the ALD coated GDL as the air electrode in a homemade ZAB cell, studying the rate performance of the air electrode. All samples were investigated via the half cell configuration, while only those showing promising results were examined further in the full cell configuration. Aside from the elemental composition of the ALD films, the application of an annealing treatment was also studied during the optimization process. Previous reports for ZAB catalysts have also explored an annealing treatment, with overall mixed results.[102,151,157,358] Complete performance metrics (extracted from half cell and full cell results) for all samples explored in this work are summarized in Table S5.2.

5.3.1.1 Casting a Wide Net

As an initial survey of cycle ratios and bilayer thicknesses, three different supercycle schemes were tested: 1:10, 5:30, and 10:20. In this way, the FeO_x cycle ratio varies from 0.91 to 0.67 and the bilayer period varies from 11 to 35, casting a wide net to uncover the optimal supercycle

scheme. Figure 5.3a shows the half cell performance of these films, in both unannealed and annealed conditions. The sample with the highest MnO_x cycle ratio (10:20) exhibits the lowest half cell ORR overpotential (η). This is not surprising considering MnO_x is the ORR-active species in the supercycle. Furthermore, annealing improves the half cell ORR onset for the MnO_x-rich sample, in-line with the results from other studies.[157] Conversely, the sample with the highest FeO_x cycle ratio (1:10) provides the best half cell OER onset since FeO_x is the OER-active species. Thus, overall, larger proportions of MnO_x provide better ORR performance, but at the expense of lower OER performance due to the reduced proportion of FeO_x. Quantifying the half cell results by calculating the voltage gap between charge and discharge (Table S5.2), the annealed 10:20 sample provides the best bifunctional performance in half cell. The full cell results in Figure 5.3b do not vary as much among samples compared with the half cell results, but annealing consistently improves discharge potentials at the expense of increasing the charge potential. Nevertheless, annealing typically results in an increased overall bifunctional efficiency. Based on the combined results of half cell and full cell testing, the 10:20 sample was considered for further optimization, in both unannealed and annealed states.

5.3.1.2 Cycle Ratio Optimization

To further optimize the composition of the $MnFe_xO_y$ catalyst, the cycle ratio of MnO_x was varied from 0.8 to 0.2, with a bilayer period restricted to factors of 10 (like that exhibited by the 10:20 sample). As shown in Figure 5.3c, generally, the half cell OER onset is reduced as the MnO_x cycle ratio is reduced (and the FeO_x cycle ratio is increased). At the same time, the half cell ORR onset is increased as the MnO_x cycle ratio is reduced. These effects are similar to the trend observed in Figure 5.3a, where more MnO_x content translates into improved ORR performance at the expense of OER performance. Referring to the voltage gap data (Table S5.2), the annealed 10:20 sample continues to provide the best bifunctional half cell performance. Not all samples were subsequently studied in full cell and, based on the onset potentials during half cell, the unannealed and annealed 20:10 and 10:40 samples were excluded from further analysis, in addition to the unannealed 40:10 and 30:10 samples. The remaining samples were studied in full cell and the results are shown in Figure 5.3d. The annealed 30:10 sample yields the highest bifunctional efficiency at 55.0% at 20 mA cm^{-2}. Therefore, this sample is the best $MnFe_xO_y$ catalyst thus far and was considered for further optimization. Note that the annealed 10:20

sample is a close second at 54.1% bifunctional efficiency. For almost all the samples in Figures 5.3c and 5.3d, annealing results in improved bifunctional efficiency and, therefore, all samples explored hereafter were subjected to annealing.

5.3.1.3 Bilayer Thickness Optimization

The 30:10 sample results in a MnO_x cycle ratio of 0.75 and the ratio was kept constant as the bilayer thickness was modified. Bilayer periods ranging from 11 to 80 were investigated and the electrochemical results of the annealed samples are shown in Figures 5.3e and 5.3f. Surveying the half cell results (Figure 5.3e), the annealed 60:20 sample provides the best overall bifunctional performance. This is mainly due to an improved OER onset, however, as the ORR onset is less sensitive to the bilayer period. The full cell results (Figure 5.3f) display the opposite effect. The discharge potential varies greatly with bilayer period, whereas the charging potential is relatively constant. In this case, the 60:20 sample is the worst bifunctional catalyst. While it was intended that all samples in Figures 5.3e and 5.3f have similar thicknesses, the 60:20 sample is 15-25% thicker than the other samples (Table S5.1). A 60:20 supercycle, with the largest bilayer period of 80, does not allow for precise thickness adjustments: two supercycles results in a 14 nm thick film, while only one supercycle yields a 7 nm film. The larger thickness for the 60:20 sample results in a lower half cell OER onset potential, a phenomenon that has also been observed when comparing 10 and 40 nm thick ALD MnO_x samples. The bifunctional efficiency of full cell testing is a more important criterion, since full cell testing better represents actual ZAB performance. Thus, the annealed 30:10 sample is considered the best $MnFe_xO_y$ supercycle composition. There is also a trend in the discharge potentials of Figure 5.3f based on the bilayer period. The 30:10 sample has a bilayer period of 40, whereas the 21:7 and 45:15 samples have bilayer periods of 28 and 60, respectively. With similar amounts of deviation from the optimal bilayer period of 40, both the 21:7 and 45:15 samples have reduced discharge potentials. This trend continues for the 9:3, 15:5, and 60:20 samples, which deviate even further from a bilayer period of 40 and, thus, have even more inferior discharge potentials. This trend reaffirms that 30:10, with a bilayer period of 40, is the best $MnFe_xO_y$ ALD supercycle composition.

5.3.1.4 Increasing Overall Thickness

Samples discussed thus far have been deposited to a thickness of roughly 10 nm in order to be comparable with the thickness of the FeO_x sample (which itself is limited to only 10 nm due to a

low ALD growth rate).[360] It is anticipated that improvements in catalytic performance can be achieved by depositing thicker films. As such, the best supercycle composition of 30:10 was deposited to a total thickness of 20, 30, and 40 nm. The half cell results in Figure S5.4a demonstrate that increasing thickness improves the OER onset. These results also support the explanation as to why the 60:20 sample yields the best half cell OER performance when manipulating the bilayer period. Not surprisingly, the thickest film also provides the best overall bifunctional half cell performance. However, full cell results in Figure S5.4b are less straight-forward. An increase in thickness does provide a benefit for the discharge potential, but the charging potential is more scattered, without any apparent trend. Nevertheless, based on bifunctional efficiency values in Figure S5.4b, the 40 nm thick 30:10 sample is still regarded as the best catalyst explored so far. The estimated mass loading on GDL for this sample is 50 μg cm^{-2}. Hereafter, unless otherwise specified, the nomenclature $MnFeO_x$ will refer to the annealed 40 nm thick 30:10 $MnFe_xO_y$ ALD sample.

5.3.2 Double Supercycle Air Electrode Coatings

For ZABs, OER typically occurs at the interface between the air electrode and electrolyte, while ORR occurs at the interface between the air electrode and outside air environment. Electrolyte is also required for ORR, but electrode flooding dictates where the three phases interact. Thus, an ORR active catalyst should be deposited deeper within the air electrode porosity, closer to the air environment, while an OER active catalyst should reside at the upper surface of the air electrode, in contact with the electrolyte. Referring to the half cell results shown in Figure 5.3c, the best OER performance is exhibited by the 10:20 sample, while the best ORR performance is demonstrated by the 30:10 sample. To maximize bifunctional activity, the ORR-active 30:10 supercycle was deposited to 30 nm and followed by 10 nm of the 10:20 supercycle process. In this way, the ORR active catalyst is deposited first, deep into the electrode porosity, while the OER active catalyst is deposited last, closer to the surface layer of the electrode. This process was repeated using binary FeO_x ALD instead of the 10:20 supercycle. The electrochemical performance of these two composite catalysts are shown in Figure 5.4. No improvements in the bifunctional activity is observed in both half cell (Figure 5.4a) or full cell (Figure 5.4b) for these composite catalysts. In fact, the 30:10+FeO_x sample is inferior to a 40 nm thick 10:20 or 30:10 sample (Figure 5.4). A potential explanation as to why these composite catalysts did not yield

enhanced bifunctional activity is related to the conformal nature of ALD. The second, OER active layer can hermetically coat the first, ORR active layer resulting in only an OER active layer as the electrochemically active catalyst. Therefore, another method of deposition, which does not penetrate as deep as ALD, is required to deposit the OER active catalyst at the surface layers only. One possibility could be the implementation of an unsaturating ALD recipe, which generally does not provide as conformal growth as true ALD. In one report, an unsaturating ALD recipe was shown to deposit on the surface layers only, while a standard ALD recipe, deposited on the same sample, was applied through the depth of the substrate.[54]

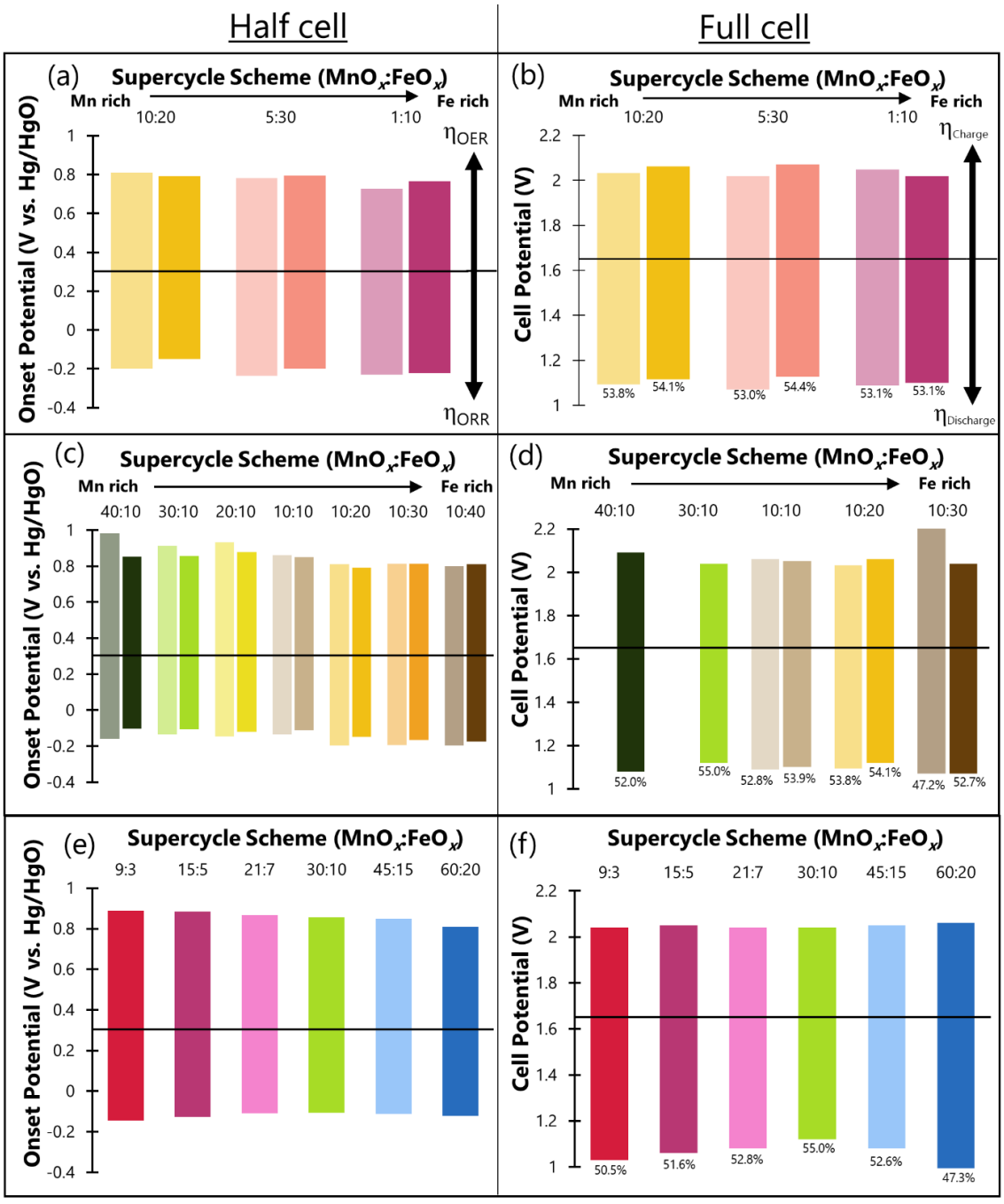

Figure 5.3. Stages of optimization for the $MnFe_xO_y$ supercycle recipe. (a, b) An initial survey of compositions, (c, d) optimization of the cycle ratio, and (e, f) optimization of the bilayer thickness. Boxes a, c, and e represent half cell performance, while boxes b, d, and f are full cell results. Lighter shade bars (on the left of each label) indicate an unannealed sample, while dark shaded bars (those on the right) represent annealed samples. In (e) and (f), only annealed sample results are presented.

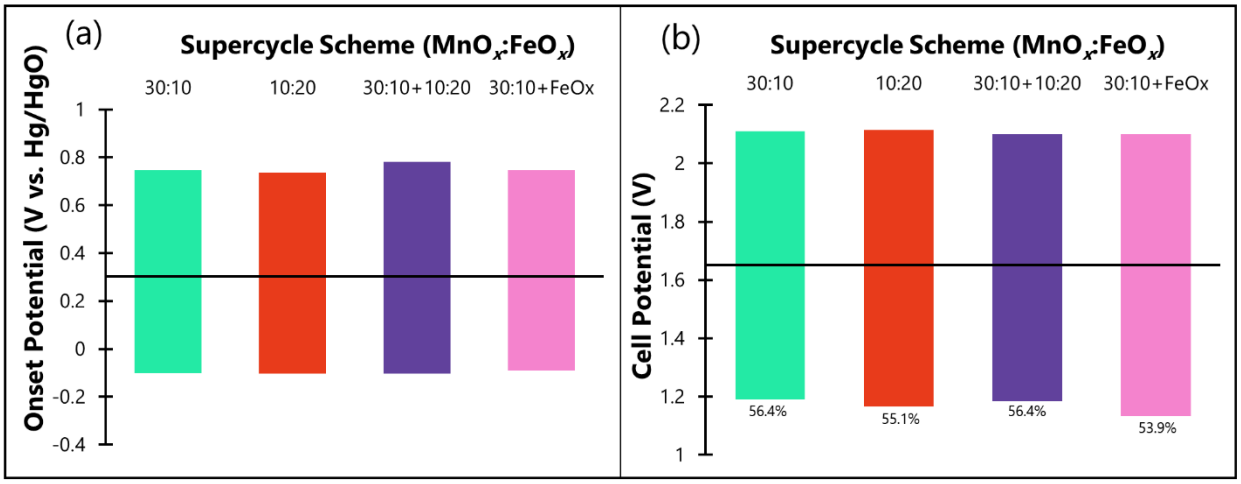

Figure 5.4. (a) Half cell and (b) full cell results for 40 nm thick ALD coatings on GDL. 30:10 and 10:20 describe 40 nm thick films that are grown using a single supercycle process. 30:10+10:20 describes a double supercycle combined process where 30 nm of a 30:10 supercycle film was first deposited, followed by 10 nm of a 10:20 supercycle film. 30:10+FeO_x is the same except that the 10 nm of a 10:20 film was replaced with 10 nm of FeO_x deposited using a binary ALD process.

5.3.3 Materials Characterization of $MnFeO_x$

5.3.3.1 SEM

Low magnification SEM images of the unannealed and annealed $MnFeO_x$ coating on GDL (Figures S5.5a-b and S5.6a-b) are essentially identical, revealing no apparent microscopic morphological changes after the annealing treatment. EDX spectra from both samples (Figures S5.5c and S5.6c) indicate a Mn/Fe atomic ratio of roughly 3, as anticipated by the 30:10 supercycle process. Elemental mapping (Figures S5.5d-g and S5.6d-g) shows complete surface coverage with Mn, Fe, and O species. Minor Mn and Fe enrichment occurs at edge features of the microporous surface. For the most part, edge effects from the electron beam interaction volume can account for this phenomenon.[260] However, it is also possible that the cavities surrounding the edge features in the microporous layer allow for increased diffusion of precursor species during ALD, leading to an increased amount of deposition on edge surfaces.[49]

5.3.3.2 TEM/STEM

TEM/STEM examination of the $MnFeO_x$ coating on GDL, in the unannealed state, is presented in Figure 5.5. The GDL material featured in the STEM bright field (BF) images (Figures 5.5a and 5.5b) displays a dark border encasing each carbon particle, representing the higher atomic number $MnFeO_x$ coating. A STEM high angle annular dark field (HAADF) image from another region (Figure 5.5c) displays an ALD coating thickness of ~25 nm. *In situ* SE during ALD growth indicated a film thickness of 40 nm. This discrepancy in thickness is attributed to sampling errors during preparation of the TEM sample. ALD coated particles of the air electrode are scraped off and affixed to a TEM grid, but the location of these particles can be from deep within the air electrode porosity, where there is lower ALD coverage.[54,157,360] The outer-most surface particles of the air electrode likely contain a 40 nm thick coating, but it is difficult to prepare a TEM sample of only these particles. EDX maps (Figure 5.5d-g) reveal overlapping signals of O, Mn and Fe. There are no discrete layers of Mn and Fe, but rather a homogenous mixture, demonstrating that the ALD supercycle process produces a mixed oxide and not separate films of each oxide. The EDX spectrum (Figure S5.7a) shows a Mn/Fe atomic ratio of ~1.5, which is lower than that from SEM analysis (Figure S5.5c). This may be a sampling phenomenon, as the volume of material analyzed using EDX spectroscopy in the STEM is significantly smaller than that in the SEM. As such, EDX analysis in the SEM is less localized and more representative of the overall composition. Based on the high resolution TEM (HRTEM) image in Figure 5.5h, the coating is nanocrystalline; the red circles in Figure 5.5h highlight crystalline grains. The nanocrystallinity is also reflected in the SAD pattern (Figure 5.5i) taken from the overall region shown in Figure 5.5a. There are several diffuse rings which can be indexed to several possible oxides of Mn and Fe. The best fit is to Fe_3O_4, Mn_3O_4, and $MnFe_2O_4$, which are all isostructural (cubic spinel); a comparison of d-spacings is provided in Table S5.3. The relatively strong diffraction ring at a d-spacing of 0.354 nm is attributed to graphitic GDL, while the diffraction rings at 0.125 nm and 0.211 nm can be matched to the carbon TEM grid as well as the ALD film (Figure S5.8 and Table S5.3).[54] Figure S5.9 shows TEM dark field (DF) images obtained from part of the (311) and (400) rings in Figure 5.5i. The bright spots in the images correspond to individual nanocrystals of the $MnFeO_x$ film.

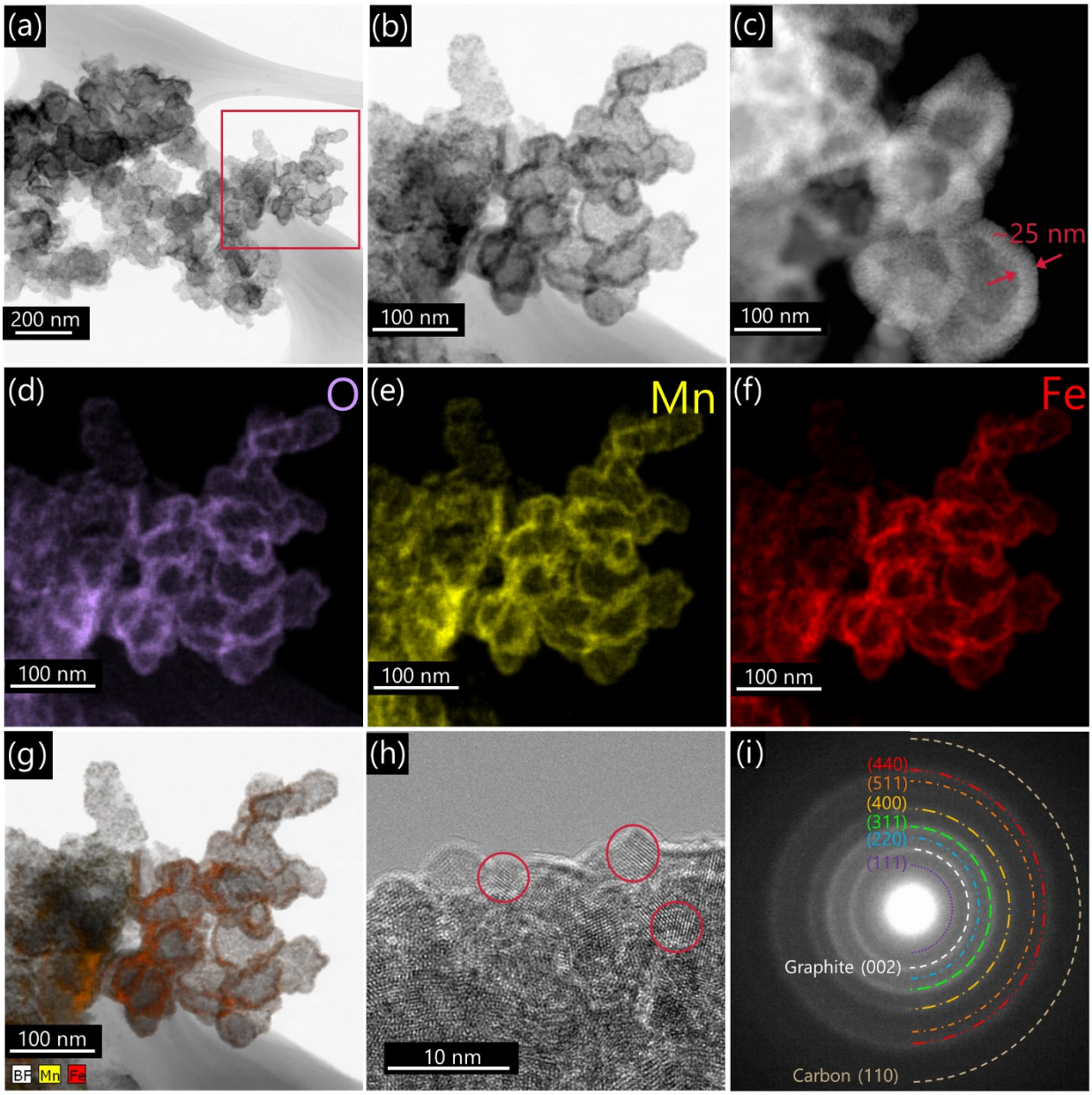

Figure 5.5. TEM/STEM characterization of an unannealed $MnFeO_x$ coating on GDL. (a) STEM BF image, (b) magnified image of the indicated area in (a). (c) Higher magnification STEM HAADF image from another region. EDX mapping (from region (b)) showing (d) O, (e) Mn, and (f) Fe. (g) Overlapping maps of Fe and Mn on the BF image. (h) HRTEM image, with red circles identifying a few individual grains. (i) SAD pattern from the region shown in (a).

STEM analysis of the $MnFeO_x$ coating on GDL in the annealed condition reveals that the ALD coating undergoes a slight nanoscopic morphology change upon annealing. Whereas before the ALD film was smooth and uniform, after annealing the coating breaks up into more discrete nanoparticles, as evident in the STEM BF images (Figures 5.6a and 5.6b). This likely increases the effective area for catalysis, resulting in the electrochemical improvements noted earlier for the annealed samples during supercycle optimization. The driving force for this phenomenon is unclear. One possibility is that there is residual stress in the ALD coating and annealing enables redistribution of atoms into nanoparticles to reduce interfacial stress, not unlike the Stranski-Krastanov growth model of thin films.[163] Another possibility is that the slight migration of atoms into discrete nanoparticles, enabled by annealing, leads to a more thermodynamically stable arrangement of discrete crystalline regions. However, the HRTEM image (Figure 5.6c) and electron diffraction pattern (Figure 5.6d) indicate no noticeable improvement in the crystallinity of the coating after annealing. The SAD pattern of the annealed sample (Figure 5.6d) is very similar to the unannealed sample (Figure 5.5i) and can be indexed to the same crystal structures (Table S5.3). Figure 5.6e shows a DF image from a different region where the ALD coating thickness is ~30 nm. EDX mapping (Figure 5.6f-i) again shows overlapping signals of Mn, Fe, and O, without any evidence of elemental segregation after annealing. The STEM EDX spectrum (Figure S5.7b) indicates a Mn/Fe atomic ratio of 3.1, which is in line with the 30:10 ALD supercycle used to produce the film and agrees with the SEM EDX results (Figure S5.6c).

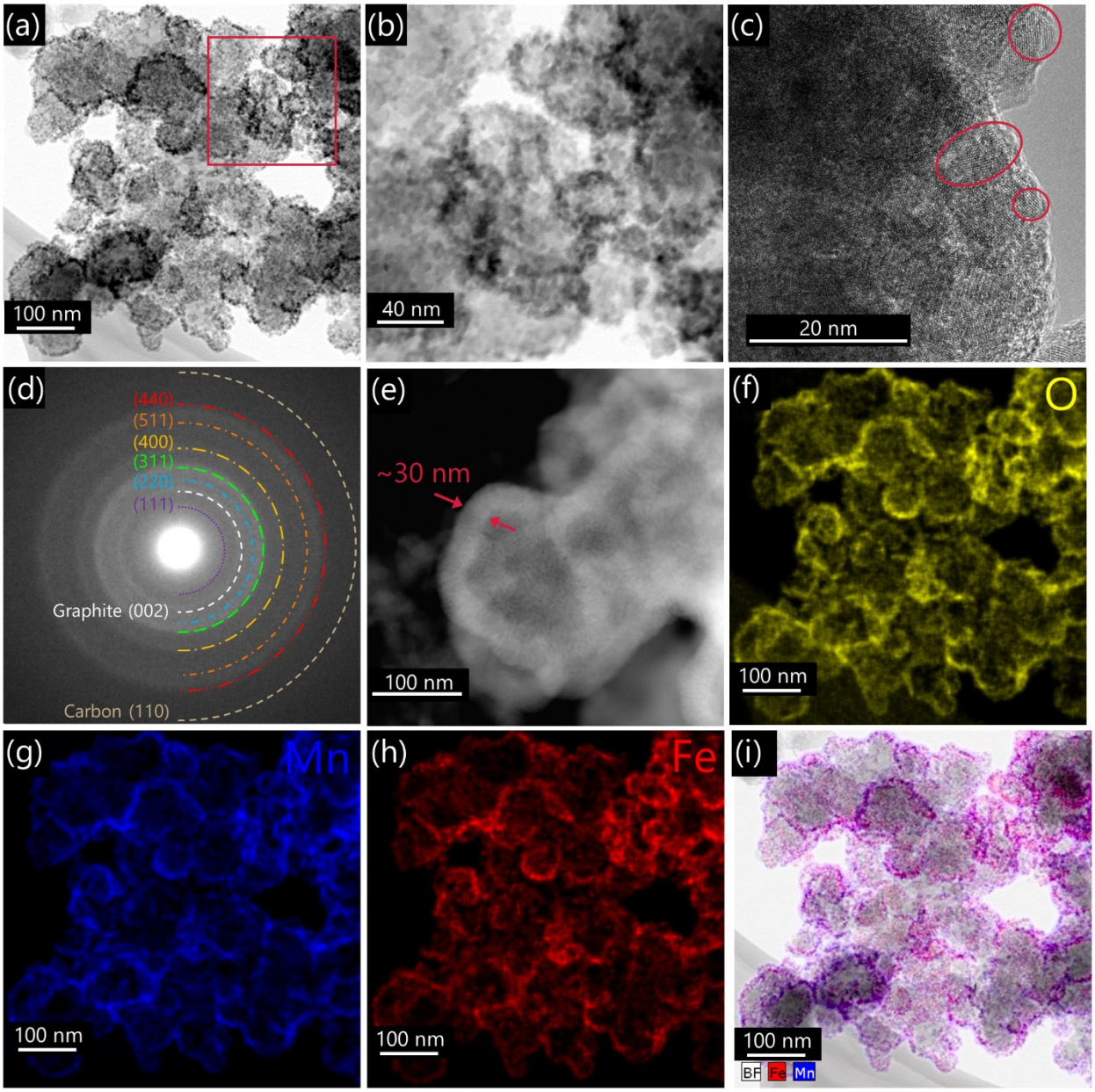

Figure 5.6. TEM/STEM characterization of an annealed $MnFeO_x$ coating on GDL. (a) STEM BF image, (b) magnified STEM BF image of the indicated area in (a). (c) HRTEM image, with red circles identifying a few individual grains. (d) SAD pattern from the region in (a). (e) High magnification STEM HAADF image from another region. EDX mapping (from region (a)) showing (f) O, (g) Mn, and (h) Fe. (i) Overlapping maps of Fe and Mn on the BF image.

5.3.3.3 XPS

XPS was conducted on both the unannealed and annealed $MnFeO_x$ deposits to further study the chemical state. The Si substrate samples were selected for analysis to obtain better XPS spectra. Figure 5.7a shows the overall survey spectra for the unannealed and annealed samples. Quantitative analysis was carried out for the regions highlighted in Figure 5.7a and is shown in the pie charts in Figure 5.7b. The unannealed spectrum features a small contribution from F and N, while both spectra exhibit significant Mn, Fe and O peaks. An Ar peak is identified in both spectra as a result of the sputter clean performed prior to XPS analysis. The N signal in the unannealed sample likely results from the FG plasma used during MnO_x ALD cycles and, similar to other reports, is reduced or eliminated entirely upon annealing.[54,157] The F peak in the unannealed sample is the result of volatile F species that deposit on the Si substrate during ALD growth. These volatile F species originate from plasma treatment of the GDL substrate (which contains PTFE) that is also present in the ALD reactor. Like N, the F contribution is removed with annealing.

The C 1s spectra (Figure S5.10) feature deconvolution results in line with previous investigations on carbon-based GDL substrates,[157] and the main peak was set to 284.8 eV to calibrate the rest of the XPS results.[157,270,315] Detailed deconvolution results for all XPS spectra are tabulated in Table S5.4. For the O 1s spectra (Figure 5.7c), the main peak (shown in blue) results from lattice oxygen and was fit to 529.5 and 529.6 eV for the unannealed and annealed sample, respectively.[315,319,411,412] Contributions from hydroxyl species (shown in orange) were fit to the shoulders featured at 531.2 and 531.0 eV for the unannealed and annealed samples, respectively.[102,315,319,411–413] The full-width at half-maximum of these peaks was constrained to values found in the literature.[315,411] The annealed sample has a smaller component of hydroxyl species in the O 1s spectrum, which is similar to the annealed C 1s spectrum (Figure S5.10).[102] Lastly, a peak at 531.8 eV was fit to both spectra (shown in green) to account for the ester and/or carbonyl contributions identified in the C 1s spectra.[157,314,315,414]

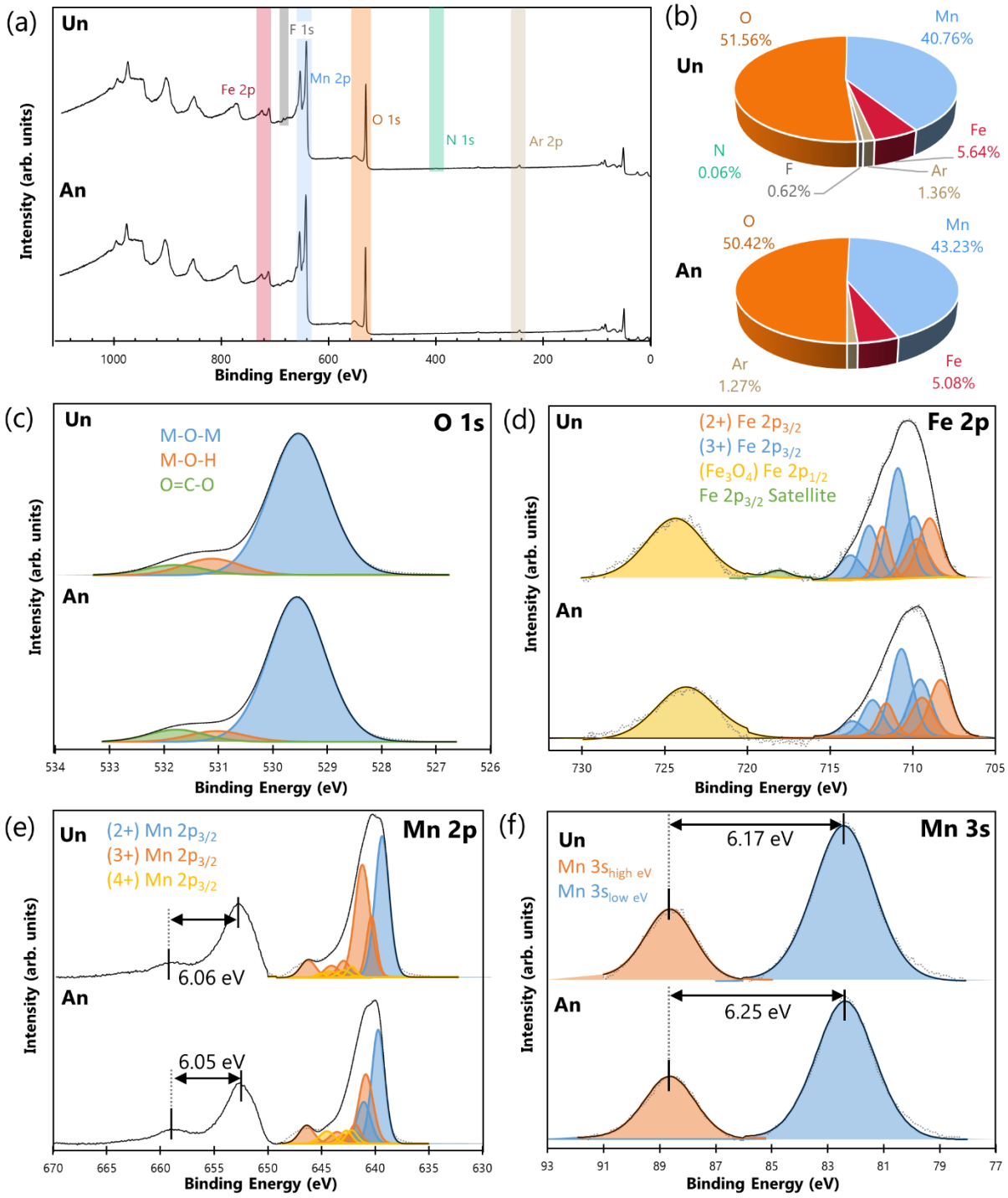

Figure 5.7. XPS results for unannealed (Un) and annealed (An) $MnFeO_x$ on Si. (a) Survey spectra, (b) quantitative analysis from the survey spectra, and (c-f) deconvolution of the O 1s, Fe 2p, Mn 2p, and Mn 3s spectra.

The Fe 2p spectra, shown in Figure 5.7d, exhibit separate $2p_{3/2}$ and $2p_{1/2}$ peaks because of spin-orbit coupling.[415] Multiplet splitting of the $2p_{3/2}$ curve was fit using both Fe^{2+} and Fe^{3+} contributions (shown in orange and blue, respectively),[270,320] and the relative area of the two oxidation states resulted in a calculated overall oxidation state for Fe of 2.6 for both the unannealed and annealed samples.[102,109] This agrees with the electron diffraction patterns which were indexed to a spinel structure (*e.g.*, Fe_3O_4), which has an oxidation state of 2.67. Furthermore, the position of the Fe $2p_{1/2}$ peak for the unannealed and annealed samples (shown in yellow) was fit to 724.3 and 723.8 eV, respectively, which both align with Fe_3O_4.[318,321] A small satellite feature around 718.0 eV (shown in green) was identified in the unannealed spectrum. This satellite feature is normally absent in Fe_3O_4 spectra and thus indicates the existence of a small amount of some other Fe structure in the unannealed sample.[321,322] This may be Fe_2O_3, as previous work by the authors (Chapter 3) demonstrated that the binary ALD FeO_x process deposits as Fe_2O_3.[360] Upon annealing, Fe and O species are able to fully diffuse into the mixed Mn-Fe oxide spinel structure, eliminating the satellite feature in the Fe 2p spectrum.

The Mn 2p spectra, shown in Figure 5.7e, also display spin-orbit coupling. Multiplet splitting was fit using Mn^{2+}, Mn^{3+}, and Mn^{4+} contributions (shown in blue, orange, and yellow, respectively),[102,270,416] and the overall oxidation state was calculated to be 2.7 and 2.6 for the unannealed and annealed samples, respectively. This result is in agreement with the electron diffraction results, where the SAD patterns were indexed to a mixed Mn-Fe oxide spinel structure, designated as $(Mn,Fe)_3O_4$. On the other hand, the position of the overall Mn $2p_{3/2}$ peak lies at 640.6 and 640.3 eV for the unannealed and annealed samples, respectively. Comparison of this peak position with the literature suggests that Mn in $MnFeO_x$ exists as MnO (*i.e.*, a Mn^{2+} oxidation state).[268,417,418] As well, the overall shape of the Mn 2p spectra, with pronounced satellite features for both $2p_{3/2}$ and $2p_{1/2}$, bares a striking resemblance to published spectra for MnO.[419] Another means of determining the oxidation state for Mn is by measuring the amount of peak splitting that occurs for the Mn 3s spectrum (Figure 5.7f).[102,157] For the unannealed sample, two peaks can be fit at 88.59 and 82.42 eV (orange and blue, respectively). For the annealed sample, these peaks are fit to 88.63 and 82.38 eV (Table S5.4). The result is peak splitting of 6.17 and 6.25 eV for the unannealed and annealed samples, respectively (Figure 5.7f). Literature values for Mn 3s peak splitting are generally lower than 6.0 eV, with an anticipated peak splitting for Mn_3O_4 anywhere from 5.5 to 5.8 eV.[272,319,418] Mn 3s peak splitting above 6 eV

indicates a Mn^{2+} oxidation state, as reported for MnO reference samples.[271,272,417,420–422] Yet another method of estimating the oxidation state of Mn is to measure the separation between the Mn $2p_{1/2}$ main peak and its satellite feature ($\Delta 2p_{1/2}$).[54] For the current work, $\Delta 2p_{1/2}$ values of 6.06 and 6.05 eV are measured for the unannealed and annealed samples, respectively (Figure 5.7e). This value also corroborates a Mn^{2+} oxidation state when compared with literature values.[272]

5.3.3.4 XRD

To further characterize the $MnFeO_x$ film deposited via ALD, XRD was conducted on a coated and unannealed GDL sample. The XRD pattern is shown in Figure 5.8 alongside a bare GDL pattern, as well as the major diffraction peaks for several power diffraction files (PDF) for comparison. Overall, the bare GDL and ALD coated GDL patterns look identical, aside from a minor shift to higher 2θ values for the two most intense peaks of the ALD coated sample. No additional peaks are identified in the ALD coated GDL pattern, indicating that the ALD film is undetected by XRD. Even though glancing angle XRD was employed, the thin nature of the ALD coating and the uneven, porous surface of GDL impaired detection of XRD signal from the coating. The most intense peak at ~27° for both patterns can be indexed to the most intense peak for carbon (either graphite (PDF#41-1487) or carbon (PDF#26-1080)). The lower intensity peaks at ~45°, ~56°, and ~79° can also be indexed to carbon. These peaks are undoubtedly from the GDL substrate, which is a carbon-based material. Also present in GDL is polytetrafluoroethylene (PTFE), which acts as a binder for the carbon particles. A survey of the literature found two independent reports for XRD of PTFE, which both display a strong peak at ~18°.[423,424] This matches with the second most intense peak in the GDL patterns at ~18°. A minor XRD peak at ~36° in the GDL patterns also correlate with the XRD patterns for PTFE.[423,424] In the report by Atta and Ali, the main peak for PTFE was found to shift to a slightly higher 2θ value after an O plasma treatment.[423] This likely explains the shift in the two most intense peaks for the ALD coated GDL pattern, since the ALD process employs an O plasma reactant. Also featured in Figure 5.8 is the diffraction data for a $MnFe_2O_4$ spinel (PDF#10-0319), which compared favourably with the SAD results for the unannealed ALD film in Figure 5.5i and Table S5.3. The (111) peak for $MnFe_2O_4$ at a 2θ ~18° matches with the ALD coated pattern, but it also matches with the bare GDL pattern. As such, the peak at ~18˚ is due to PTFE and not $MnFeO_x$. More importantly, the most intense peak for $MnFe_2O_4$ at ~35° ((311) plane) does not appear in the

ALD coated GDL XRD pattern, nor do any other peaks for $MnFe_2O_4$. Therefore, XRD is unable to corroborate the phase identification from electron diffraction and XPS.

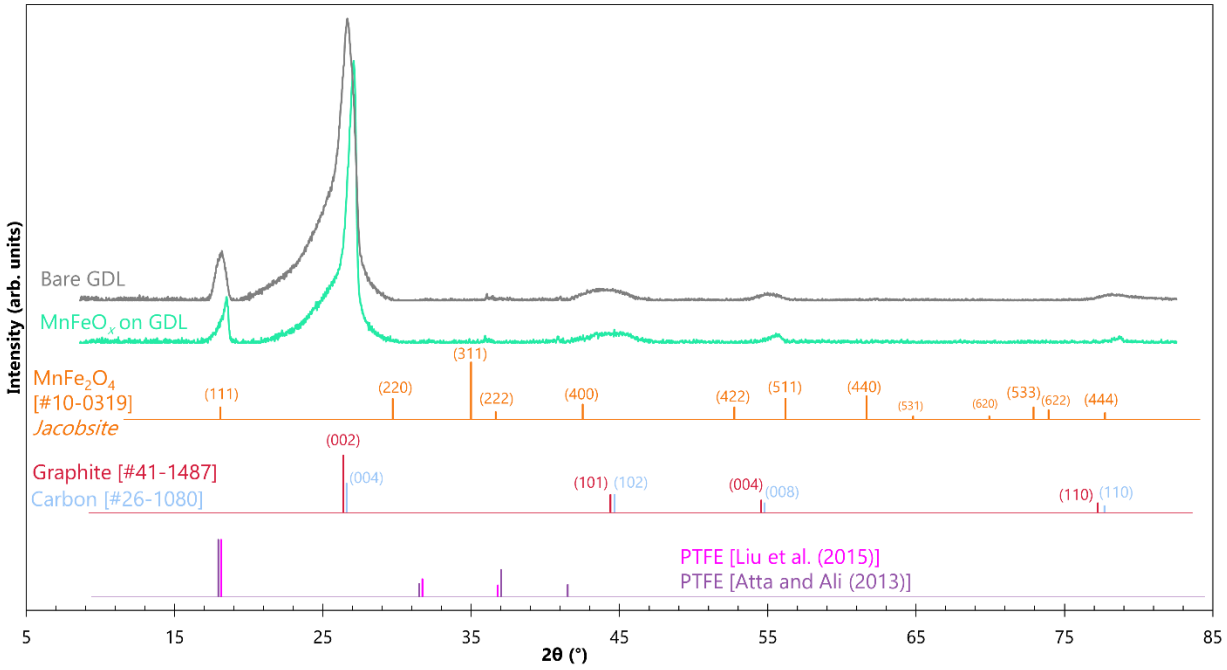

Figure 5.8. XRD patterns for bare GDL and ALD coated GDL compared with the main diffraction peaks for several PDF cards and data from the literature.

Quantitative analysis of the unannealed and annealed survey spectra (Figure 5.7b) yields a Mn/Fe atomic ratio of 7.2 and 8.5, respectively. These values are well above ~3, the value determined from SEM and STEM and anticipated by the 30:10 supercycle mix. Based on the thermodynamic potentials of Mn and Fe oxidation,[425] there is a greater driving force for the creation of MnO_x as opposed to FeO_x. As such, it is likely that the surface layer examined by XPS was enriched by Mn species preferentially oxidizing at the air interface. Furthermore, both XPS samples were exposed to 60 s of Ar sputtering to remove adventitious carbon. This Ar sputtering can also preferentially sputter oxygen species, inadvertently reducing the chemical species at the surface of the material.[426,427] Therefore, the Mn XPS analysis, which indicates an oxidation state of Mn^{2+}, does not represent the bulk oxidation state of the mixed Mn-Fe oxide. The Fe XPS analysis, on the other hand, which indicates a mixed oxidation state of $Fe^{2.6+}$ and supports the existence of Fe_3O_4, agrees with the electron diffraction results which can be matched to several different spinels of Mn, Fe, and O. Taken together with the Mn/Fe atomic

ratios from EDX analysis, the crystal structure of the mixed Mn-Fe oxide is most likely a mixed spinel oxide of the type $(Mn,Fe)_3O_4$, where Mn and Fe have mixed valences of 2+ and 3+ and the overall ratio of Mn:Fe is ~3.

5.3.4 ZAB Application of $MnFeO_x$

5.3.4.1 Electrocatalytic Activity

Figure 5.9 displays electrochemical performance values of the $MnFeO_x$ ALD coating on GDL towards the oxygen reactions involved at the air electrode in ZABs. Also featured in Figure 5.9 are several different benchmark catalysts to compare the performance of $MnFeO_x$. All samples were exposed to a 30 min 300 °C *ex situ* annealing treatment, except for bare GDL (a substrate sample without catalyst). When the mixed oxide ($MnFeO_x$) catalyst is compared with its monometallic constituents of MnO_x and FeO_x, both also deposited via ALD, the advantages of the mixed oxide become apparent. In half cell testing (Figure 5.9a), the poor OER performance of MnO_x is augmented by the addition of FeO_x and the resulting mixed film has an OER onset similar to that of FeO_x. The good ORR performance of MnO_x is not only retained, but actually improved when mixed with FeO_x and, therefore, the mixed oxide has an overall lower voltage gap than either monometallic oxide film. Full cell testing (Figure 5.9b) reveals similar charge potentials for both MnO_x and FeO_x and, thus, the charge potential of the mixed $MnFeO_x$ film is also similar. Like the half cell results, the full cell discharge performance of the mixed oxide catalyst is slightly superior to MnO_x and so, among the three catalysts, the overall bifunctional efficiency of $MnFeO_x$ is the highest at 52.5% at 20 mA cm^{-2}. Lastly, discharge polarization and power curves were obtained from full cell ZABs constructed with each catalyst (Figure 5.9c). The peak power delivered by MnO_x and FeO_x is almost the same at around 86 mW cm^{-2}, while the mixed oxide can deliver over 92 mW cm^{-2} of power, which is an improvement over the monometallic oxides. The mixed Mn-Fe oxide outperforms monometallic MnO_x for both ORR and OER due to several possible effects. Firstly, the electronic conductivity of FeO_x is higher than MnO_x and, thus, the mixed oxide has an increased electronic conductivity compared with MnO_x,[428] leading to improvements in the overall electron transfer process.[429] Secondly, the addition of Fe to MnO_x enables a cubic crystal structure (revealed by SAD) and a reduction of Jahn-Teller distortion in the crystal structure.[430] In other Mn-based mixed oxides, a reduction in Jahn-Teller distortion and the transformation from a tetragonal to cubic crystal structure led to

improvements in both ORR and OER performance.[431–433] Lastly, the addition of other transition metal elements to MnO_x modifies the oxidation state of Mn and alters the electronic structure of the oxide, resulting in improvements to both ORR and OER kinetics.[90,103,434–436]

As another comparison, Figure 5.9 also shows the electrochemical performance of a bare GDL sample and a spray-coated commercial Pt-Ru-C catalyst. The half cell onset potentials featured in Figure 5.9a show that ALD prepared $MnFeO_x$ is inferior to the commercial Pt-Ru-C catalyst, although the ORR onsets are close at -0.10 V and -0.07 V, respectively, and complete half cell curves (Figure S5.11) show that, at higher OER potentials, ALD $MnFeO_x$ is similar to Pt-Ru-C in terms of deliverable current density. The bare GDL substrate shows negligible OER activity but not an insignificant amount of ORR activity. The high surface area carbon structure featured in GDL has been reported to provide some inherent ORR activity.[32] When examined in full cell (Figure 5.9b), the bare GDL substrate is extremely ineffective at catalyzing either the discharge or charge reactions, resulting in an overall bifunctional efficiency of less than 25% at a current density of 20 mA cm^{-2}. In fact, the charge potential is beyond the scale of Figure 5.9b and the complete full cell figure (Figure S5.12) shows that bare GDL reaches the cut-off voltage of 3.5 V at 20 mA cm^{-2}. As with half cell results in Figure 5.9a, full cell values in Figure 5.9b show that Pt-Ru-C is a better ZAB catalyst than the ALD $MnFeO_x$ film, boasting a bifunctional efficiency of 61.2% at 20 mA cm^{-2} compared against only 52.5% efficiency for the ALD film. Nevertheless, compared with other bimetallic and bimetallic oxides catalysts in the ZAB literature, the ALD $MnFeO_x$ catalyst in this work is quite competitive (Table S5.5). For example, the complex hydrothermal and pyrolysis synthesis method for creating spinel $MnFe_2O_4$/metallic Fe hybrid nanoparticles encapsulated in N-doped mesoporous hollow carbon nanospheres (Fe/Mn-N-C), as reported by Wu *et al.*,[101] provides a bifunctional efficiency of 55.6% but at only 8 mA cm^{-2}. In comparison, the current ALD $MnFeO_x$ catalyst delivers 52.5% efficiency at a greater current density of 20 mA cm^{-2}. Another catalyst, an Fe-doped MnO_2 catalyst developed by Mathur and Halder,[103] provides only 30.2% bifunctional efficiency at 25 mA cm^{-2}.

The polarization and power curves of Figure 5.9c indicate a peak power density of 119 mW cm^{-2} for Pt-Ru-C and only 51 mW cm^{-2} for bare GDL. Compared with the peak power density of 92 mW cm^{-2} for ALD $MnFeO_x$, Pt-Ru-C is a better ZAB catalyst than ALD $MnFeO_x$, prior to cycling. While the electrochemical characterization tests demonstrate that Pt-Ru-C is more

catalytically active for ZABs than ALD $MnFeO_x$, long duration cycling tests (presented in the next section) show the benefit of ALD, which distributes the catalyst material within the porous GDL. Prolonged ZAB cycling can lead to electrolyte flooding into the air electrode, where the reaction sites for the oxygen reactions are shifted to regions deeper within the air electrode. If catalyst material is only deposited on the outermost surface of the electrode, then flooding results in a loss of catalytic reaction sites and a degradation in efficiency. For catalyst preparation techniques that can deposit material deep into the porosity of the air electrode, such as ALD, the migration of oxygen reaction sites during flooding does not necessarily result in the loss of catalytic reaction sites and the improved battery efficiency from the catalyst can be maintained.[54,318]

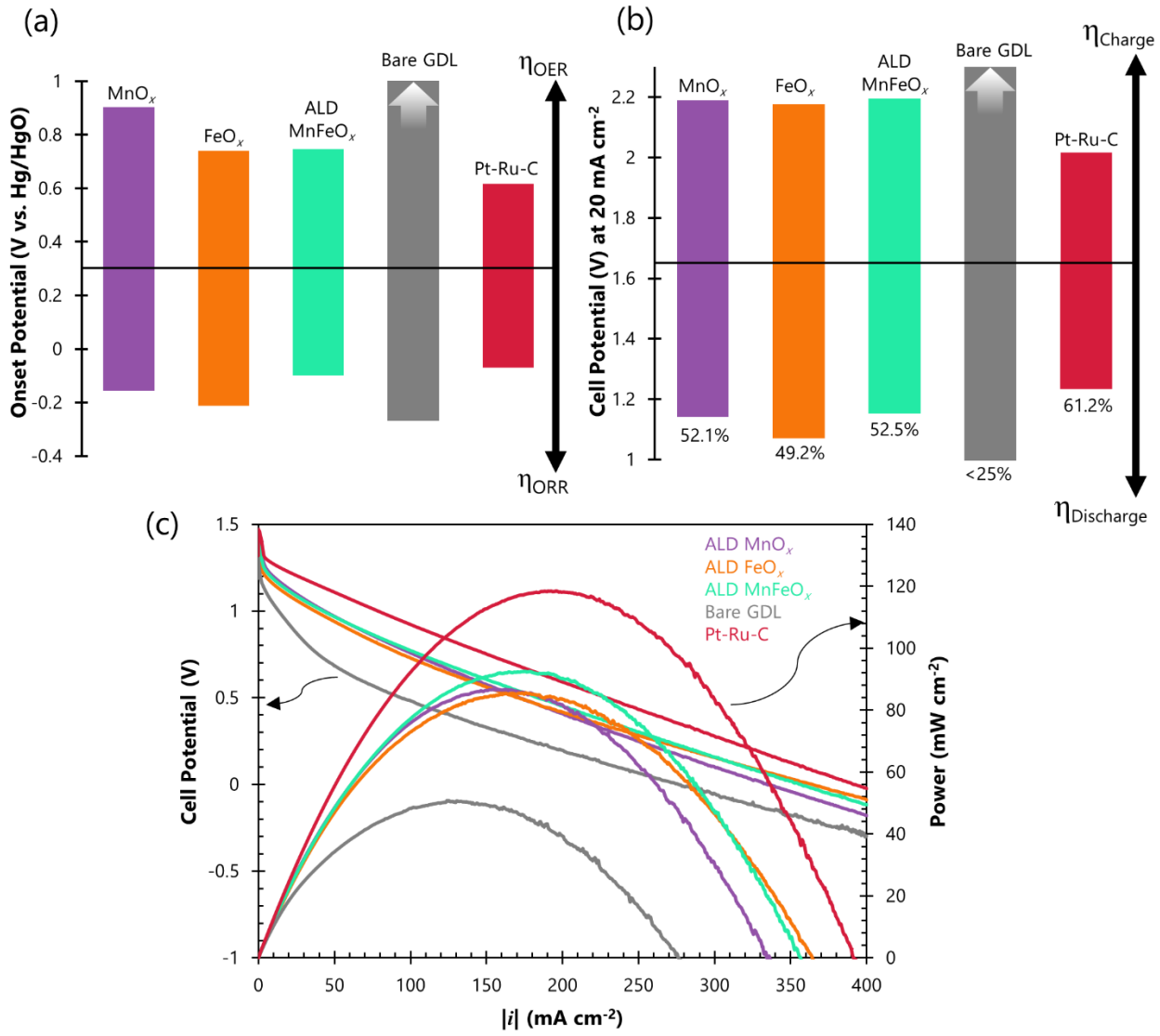

Figure 5.9. ZAB test results for ALD deposited MnO_x, FeO_x, and $MnFeO_x$, compared with bare GDL and a benchmark Pt-Ru-C catalyst. (a) Half cell onset potentials at |10| mA cm^{-2} . (b) Full cell discharge and charge operating voltages and bifunctional efficiencies at |20| mA cm^{-2}. The OER/charge performance of bare GDL in half cell/full cell is very poor and the values extend beyond the plot, as represented by arrows. (c) Full cell discharge polarization (left axis) and power density (right axis) curves.

Cycling Stability

Practical application of ZABs requires at least several hundred cycles of charge and discharge and, as such, candidate catalysts should be exposed to long-term cycling tests.[32,36] Figure 5.10a shows overlapping cycling curves for bare GDL, Pt-Ru-C, and ALD $MnFeO_x$ when cycled at 10 mA cm^{-2}. Individual cycling plots for these catalysts, as well as the other catalysts featured in Figure 5.9, are included in Figure S5.13. The bifunctional efficiencies of bare GDL, Pt-Ru-C, and $MnFeO_x$ at various intervals throughout the cycling test are displayed in Figure 5.10b; the bifunctional efficiencies of the remaining catalysts are included in Table S5.6. At the beginning of cycling, Pt-Ru-C demonstrates the lowest charge potential and highest discharge potential of all catalysts explored, resulting in the highest bifunctional efficiency of 61.9% at 10 mA cm^{-2}. However, the discharge potential and, especially, the charge potential of the Pt-Ru-C catalyst quickly deviates towards inferior values, resulting in a low bifunctional efficiency of 44.9% at 60 h of 10 mA cm^{-2} cycling. Some recovery in the charging potential is observed around 70 h, but nevertheless, the bifunctional efficiency of Pt-Ru-C remains at 45.3% or below for the remaining 530 h of cycling. The instantaneous improvement in charging potential for Pt-Ru-C at 70 h is likely due to the dislodging of one or more bubbles within the air electrode, freeing up catalyst sites that were blocked by an O_2 bubble formed during OER.[318]

At 54.3%, the initial bifunctional efficiency of the ALD $MnFeO_x$ catalyst is less than that for Pt-Ru-C, but the overall degradation in bifunctional efficiency is much less for ALD $MnFeO_x$. At 100 h (200 cycles) of bifunctional cycling at 10 mA cm^{-2}, the efficiency of ALD $MnFeO_x$ is 54.1%, yielding an efficiency retention of 99.6%, compared with only 73.2% efficiency retention for Pt-Ru-C. Furthermore, as cycling continues for another 500 h (1290 cycles), the efficiency of ALD $MnFeO_x$ is maintained at or above 46.0%, resulting in a final efficiency retention of 84.7% after 600 h (1565 cycles) of bifunctional cycling. Pt-Ru-C, on the other hand, has only 66.2% retention after the same period. The Pt-Ru-C catalyst, synthesized by spray-coating, suffers drastic losses in charge and discharge potential due to flooding because spray-coating only supplies the outer-most surface with catalyst material. The ALD $MnFeO_x$ catalyst, on the other hand, displays much more stable cycling potentials because catalyst material is embedded deeper within the air electrode thickness and maintains catalytic reaction sites even after electrolyte floods into the electrode. The sharp increase in charge potential, followed by a sudden decrease

in charge potential, and equivalent fluctuations in the discharge potential, for ALD $MnFeO_x$ at around 20 h and 50 h is attributed to leaking of the ZAB cell. Once more electrolyte was added to the cell, the performance recovered. As such, the potential fluctuations do not reflect air electrode performance but rather unresolved issues in ZAB cell design.[408] No other accounts of cycling a ZAB using a $MnFe_xO_y$ catalyst were found in the literature except for one report by Mathur and Halder.[103] A ZAB prepared, via drop-casting, with their Fe-doped MnO_2 catalyst only showed 200 min of stable discharge-charge cycling, and the voltage gap at 20 mA cm^{-2} was over 3 V. Comparatively, at 20 mA cm^{-2}, the ALD $MnFeO_x$ catalyst in this work showed only a 1.11 V voltage gap (Figure 5.9b). While cycling was conducted at a lower current density of 10 mA cm^{-2}, the ALD $MnFeO_x$ ZAB in this work was able to cycle for 600 h (1565 cycles).

Also shown in Figure 5.10 is the cycling of bare GDL, which features an immediate loss in bifunctional efficiency within the first 20 h of cycling. However, a gradual recovery in both charge and discharge potentials is observed over the course of several hundred hours of cycling. This behaviour is attributed to proper wetting of the air electrode by the electrolyte. Bare GDL is exceptionally hydrophobic compared with catalyst coated air electrodes and requires several cycles at high overpotential to oxidize the carbon material and improve the wettability of the electrode. This improvement in the wettability affords a larger effective surface area for the oxygen reactions and results in a lower effective current density at the electrode, improving the discharge and charge potentials. Still, the bifunctional efficiency of bare GDL is drastically inferior to any of the explored catalysts, with an initial efficiency of 38.9% and reaching only 40.7% at 400 h of cycling. At around 300 h of cycling, the charge potential of bare GDL reaches the same value as Pt-Ru-C, while the same is true for the discharge potentials at around 400 h. At this point, the Pt-Ru-C sample is no better than bare GDL and it is likely that the catalyst material has detached, oxidized, or agglomerated and is no longer effective.[32,437,438] The ALD $MnFeO_x$ sample, however, does not reach the same charge or discharge potential as bare GDL, demonstrating that ALD is a more robust synthesis method for long-term ZAB cycling. The bare GDL sample suddenly deteriorates and reaches the cut-off voltages of 0.5 and 3.0 V for discharge and charge, respectively, at around 550 h. The Pt-Ru-C sample, on the other hand, continues at the same potentials until 600 h.

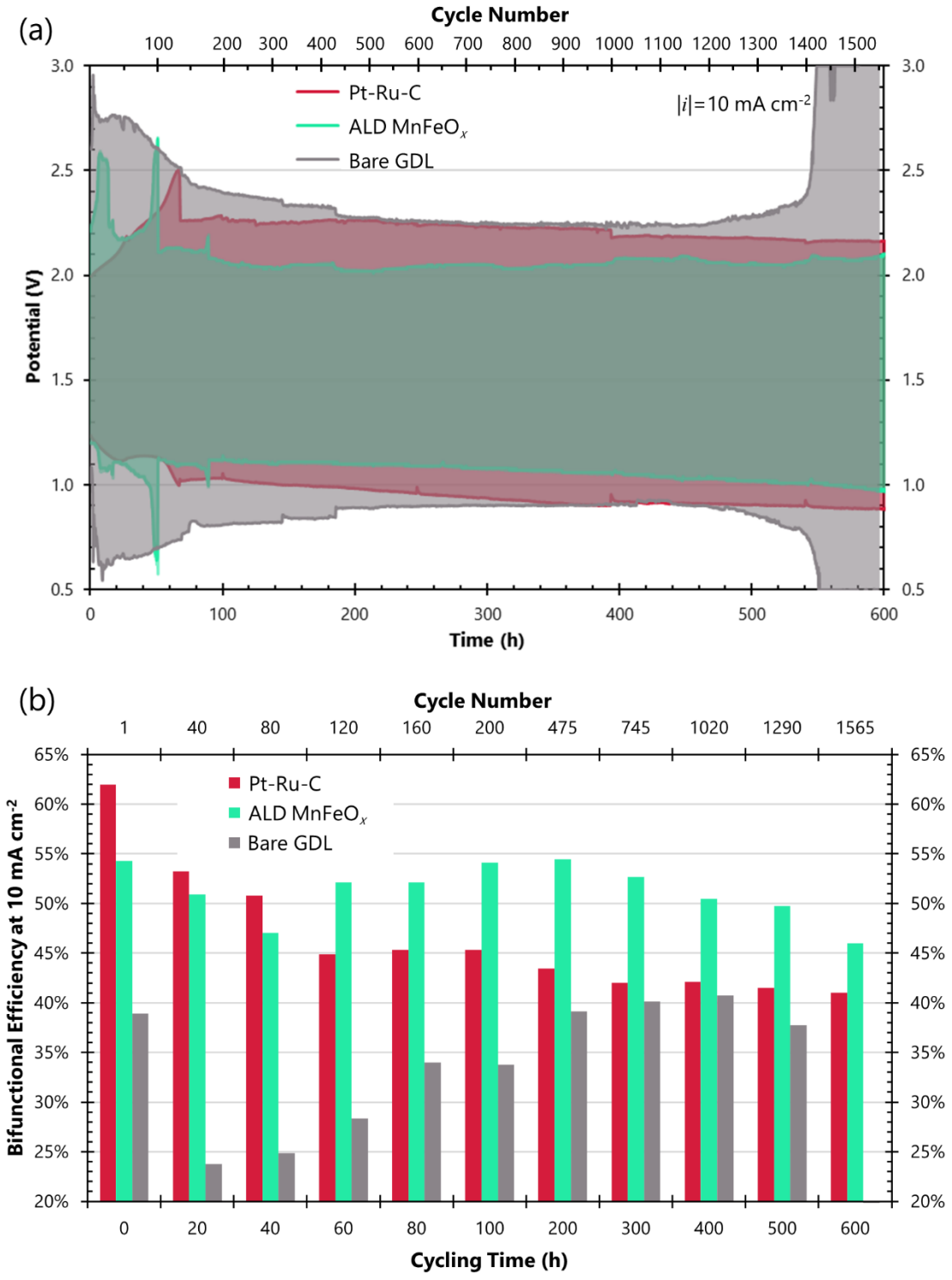

Figure 5.10. (a) Galvanostatic cycling of bare GDL, Pt-Ru-C, and ALD $MnFeO_x$. All samples are discharged and charged for 10 min at 10 mA cm^{-2} for each cycle. (b) Bifunctional efficiency at various cycling times for bare GDL, Pt-Ru-C, and ALD $MnFeO_x$.

Bifunctional cycling of the ALD FeO_x air electrode (Figure S5.13d) does not produce stable charge or discharge potentials and the discharge potential reaches the cut-off voltage of 0.5 V after only 135 h (300 cycles). Such poor cycling performance is due to the excessive amount of O plasma required to grow 10 nm of FeO_x. The GDL substrate for the FeO_x sample has little to no PTFE treatment remaining and a significant amount of carbon oxidation occurs. As a result, severe flooding of the air electrode takes place and eventual electrolyte loss through the air electrode occurs. As the electrolyte level reduces in the cell, a smaller area of the electrode is exposed to the electrolyte and the current density on the electrode increases, accelerating degradation of the electrode. With the ALD MnO_x sample (Figure S5.13e), relatively stable cycling performance is observed up to 630 h (1645 cycles). In this case, no O plasma reactant is required during deposition and the carbon substrate and PTFE treatment are preserved. Likewise, the ALD $MnFeO_x$ electrode is much more stable than the ALD FeO_x sample because the MnO_x layers within the mixed deposit act as a protective layer against the aggressive ALD FeO_x steps.[360] The occasional spike in charge or discharge potential for the ALD MnO_x sample is attributed to cell design flaws and electrolyte leaking similar to that experienced by the ALD $MnFeO_x$ sample, where replenishing the electrolyte level recovers the potentials values completely. The bifunctional efficiency of the ALD MnO_x electrode throughout cycling (Table S5.6) is, in most cases, lower than that for the ALD $MnFeO_x$ electrode, demonstrating the benefit of the mixed oxide process.

5.3.4.2 SEM of Catalyst Penetration into GDL

As a means to somewhat quantify the amount of catalyst material that penetrates into the depth of the GDL substrate during deposition, SEM and EDX analysis for the $MnFeO_x$ and Pt-Ru-C samples was done at three locations within the GDL structure: at the surface microporous layer and at the microporous-backing layer boundary, from both the microporous side and the backing layer side. These three regions are schematically shown at the top of Figure S5.14. The entire GDL structure is 315 μm thick,[64] with a microporous layer thickness of ~50 μm.[360] The largest component of the EDX signal for all spectra in Figure S5.14 is C, arising from the graphite-based GDL substrate used as the air electrode. Also contained within this GDL material is PTFE, which produces a large F signal for the surface microporous layer spectra (Figures S5.14a and

S5.14d). The F signal is less intense for the remaining spectra as these spectra are taken at the microporous-backing layer interface, where the backing layer has a lower PTFE loading.[64]

Figures S5.14a-c show the EDX spectra for ALD $MnFeO_x$. The surface microporous layer (Figure S5.14a) has an approximately 3:1 weight ratio for Mn and Fe, and, since Mn and Fe have similar atomic masses, this value aligns with the 30:10 supercycle ratio employed during ALD. At the microporous-backing layer interface (Figures S5.14b and S5.14c), the intensity of the Mn Kα peak at 5.9 keV is reduced and the Fe Kα peak at 6.4 keV is eliminated entirely. The semi-quantitative analysis displays only 0.5 and 0.3 wt% of Mn for Figures S5.14b and S5.14c, respectively, down from 6.1 wt% in Figure S5.14a. While this may indicate an inability of the current ALD technique to deposit material within the air electrode structure, it should be emphasized that the low mass loading of ALD makes Mn and Fe detection difficult with EDX spectroscopy. Since the Mn Kα peak is still visible in the spectra, it can be concluded that at least some of the precursor vapours can penetrate through the entire microporous layer of the GDL structure during ALD.

Figures S5.14d-f show the EDX spectra for the spray-coated Pt-Ru-C sample. Semi-quantitative analysis at the surface microporous layer (Figure S5.14d) shows an almost 2:1 ratio for Pt and Ru, as anticipated by the stoichiometry of the commercial powder (40 wt% Pt and 20 wt% Ru). Very weak Zn and S signals are suspected to be due to contamination of the sample but do not impact the analysis in any meaningful way. At the microporous and backing layer interface (Figures S5.14e and S5.14f), there is no detectable Pt or Ru signal, indicating that the spray-coating technique is unable to penetrate catalyst material into the depth of the GDL, accounting for the poor cycling stability of Pt-Ru-C in Figure 5.10. As the air electrode is flooded during prolonged cycling, the electroactive area for the oxygen reactions is shifted deeper into the GDL and towards the backing layer. Without any catalyst material present at this interface, the electrochemical activity of the spray-coated Pt-Ru-C sample becomes essentially bare GDL, as seen in Figure 5.10 for cycling times above 400 h.

5.3.5 Post-Cycling Characterization of $MnFeO_x$

5.3.5.1 SEM

SEM imaging of the annealed $MnFeO_x$ sample after cycling for 600 h (1565 cycles) (Figure 5.11) reveals that damage occurs to the ALD coated GDL. More cracks are featured on the GDL surface, with portions of the microporous layer absent (Figures 5.11a-c). EDX analysis indicates a loss in Mn species, with the Mn/Fe atomic ratio reduced to ~0.8 (Figure 5.11b). In previous work with MnO_x ALD, the addition of an O plasma to the deposition process resulted in an unstable MnO_x coating that dissolved during cycling.[54] A similar phenomenon likely occurs for the ALD $MnFeO_x$ coating in this work based on Figure 5.11b. Additional elements are found in the cycled sample that were not present in the uncycled annealed sample. K and Zn are most notable (Figures 5.11g and 5.11h) and can be traced back to the ZAB electrolyte. K_2CO_3 forms when the KOH electrolyte reacts with atmospheric CO_2 or during carbon corrosion of GDL,[39] while ZnO can precipitate from Zn containing electrolyte.[102] A Ni current collector featured in the cell design may account for the Ni species (Figure 5.11i), which, like Zn, can precipitate as an oxide on the surface.

5.3.5.2 STEM

STEM analysis of the annealed ALD $MnFeO_x$ sample after cycling for 600 h (1565 cycles) is displayed in Figure S5.15. As with the SEM analysis, Zn and Ni species appear in the EDX maps (Figures S5.15f-g). It is difficult to determine if the Zn and Ni are incorporated into the catalyst material, as opposed to simply surface films, since electron diffraction from post-cycling material is inconclusive and features a variety of spots/rings that correspond to both the uncycled material and a possible Zn-incorporated phase.[54]

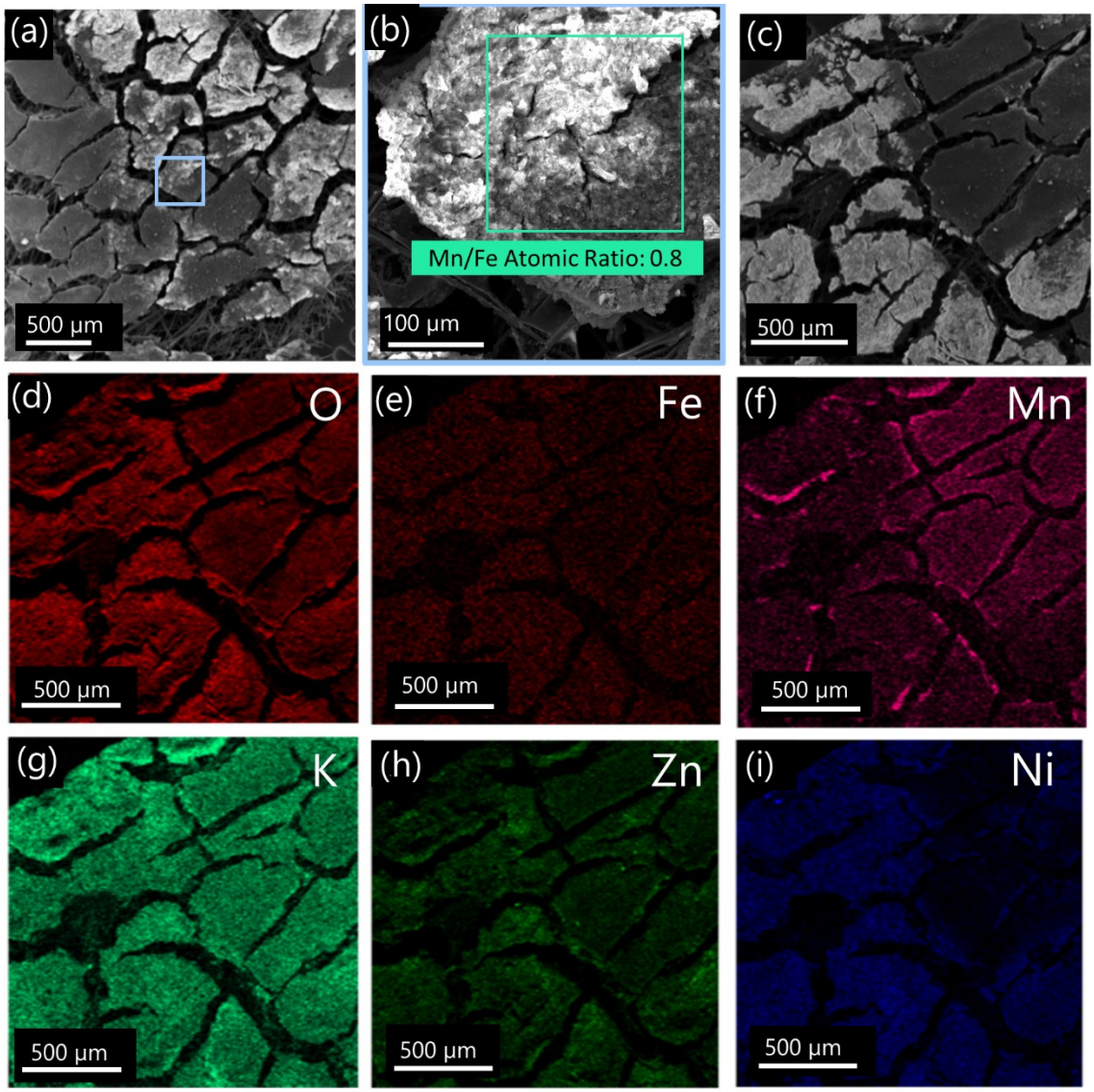

Figure 5.11. SEM/EDX analysis of the annealed and cycled ALD $MnFeO_x$ coating on GDL. (a) Low-magnification secondary electron image, (b) magnified image of the indicated area in (a), with EDX of the region indicated in green providing a Mn/Fe atomic ratio of 0.8. (c) Secondary electron image taken from another region with elemental mapping of (d) O, (e) Fe, (f) Mn, (g) K, (h) Zn, and (i) Ni.

5.4 Conclusions

An atomic layer deposition (ALD) supercycle process for $MnFe_xO_y$ was developed from previously established binary ALD processes for MnO_x and FeO_x. Optimization of the cycle ratio and bilayer thickness for the supercycle determined that a 30:10 mix of MnO_x and FeO_x ALD cycles provides the most catalytically active film for oxygen reduction and evolution in a Zn-air battery (ZAB). Electron microscopy analysis revealed that a homogenously mixed ALD film uniformly encased the carbon particles of the air electrode. Electron diffraction and X-ray photoelectron spectroscopy identified the coating as a $(Mn,Fe)_3O_4$ cubic spinel. The electrocatalytic activity of the bimetallic oxide ALD film in a ZAB exceeded the activity of either monometallic oxide ALD film. Long-term ZAB cycling of the ALD $MnFe_xO_y$ catalyst yielded an efficiency retention of over 84% after 600 h (1565 cycles) at 10 mA cm^{-2}. A precious metal Pt-Ru-C catalyst, under the same conditions, only provided 66% efficiency retention. Energy dispersive X-ray microanalysis of the bilayer air electrode structure revealed that ALD of $MnFe_xO_y$ delivered catalyst material to regions deep within the air electrode structure. The spray-coated precious metal catalyst, however, did not penetrate into the air electrode and thus did not cycle well.

5.5 Supporting Information

5.5.1 Experimental

5.5.1.1 ALD

The complexity of a supercycle process can be minimized by using a common reactant for both binary ALD cycles.[55] As shown in a previous report, the MnO_x ALD process has been developed for a combined FG plasma + H_2O reactant.[157] However, the Fe precursor of EF does not yield growth with a FG plasma + H_2O reactant; it only yields appreciable growth with an O plasma reactant.[360] On the other hand, it is possible for a non-saturating binary ALD process to become saturating when combined with another ALD cycle in a supercycle scheme.[439] Therefore, it is worthwhile to reinvestigate common ALD reactants in the development of a mixed Mn-Fe oxide supercycle.

Figure S5.1 showcases the ORR and OER onset values obtained for preliminary ALD supercycle films deposited using a common reactant. For this initial investigation, all supercycles were 1:10

in terms of MnO_x and FeO_x subcycles, respectively. The reasoning behind this was to attempt to achieve a 50:50 atomic ratio between MnO_x and FeO_x. As proposed by Mackus *et al.*, the atomic composition of a $MnFe_xO_y$ supercycle film can be approximated using the rule of mixtures (Equation S5.1), where ρ, g and CR represent density, growth rate, and cycle ratio, respectively.[55]

$$Atomic\ composition\ (\%\ of\ Mn) = \frac{\rho_{MnOx} g_{MnOx} CR_{MnOx}}{\rho_{MnOx} g_{MnOx} CR_{MnOx} + \rho_{FeOx} g_{FeOx} CR_{FeOx}} \quad \text{(S5.1)}$$

Since MnO_x exhibits a growth rate that is 10 times larger than that for FeO_x,[157,360] the number of MnO_x cycles should be 10 times less than that for FeO_x to achieve ternary oxide with a 50:50 Mn:Fe ratio. Using density values for Mn_3O_4 and Fe_2O_3,[370] the atomic composition for a 1:10 supercycle is calculated as 54 at% MnO_x and 46 at% FeO_x (Equations S5.2 and S5.3).

$$Atomic\ composition\ = \frac{\left(4.84\frac{g}{cm^3}\right)\left(1.15\frac{\dot{A}}{cy}\right)(1/11)}{\left(4.84\frac{g}{cm^3}\right)\left(1.15\frac{\dot{A}}{cy}\right)(1/11)+\left(5.25\frac{g}{cm^3}\right)\left(0.09\frac{\dot{A}}{cy}\right)(10/11)} = 54\ at\%\ Mn \quad \text{(S5.2)}$$

$$\Rightarrow 100 - 54 = 46\ at\%\ Fe \quad \text{(S5.3)}$$

Unfortunately, as is the case with binary FeO_x ALD growth, an FG plasma and an H plasma do not yield appreciable supercycle growth. After more than 15 supercycles, the films reached a thickness of ~1 nm. An O plasma, on the other hand, was able to generate sufficient ALD supercycle growth, producing a 13 nm film after 16 supercycles. The 1.5 nm thick FG plasma and H plasma supercycle films were nonetheless investigated using electrochemical techniques. Compared with the FG plasma and H plasma films, the O plasma supercycle process produced far superior catalytic films, as evident by the half cell results in Figure S5.1a. This is likely the result of the thickness differences between the samples and because of the ability of O plasma to oxidize the Fe and Mn precursors (EF and $(EtCp)_2Mn$, respectively).

Since a combined FG plasma + H_2O reactant was proposed as the best reactant for the MnO_x process,[157] two more supercycle schemes were explored. In both cases, the combined FG plasma + H_2O reactant was employed for the MnO_x cycles, while for the FeO_x cycles either an FG plasma or an O plasma was utilized. An H plasma could not be used in conjunction with the combined FG plasma + H_2O reactant because the ALD facility was unable to simultaneously use FG and H_2 gas. In the case of an FG plasma for the FeO_x process, the performance was slightly

worse than that for an O plasma for both FeO_x and MnO_x. In the case of an O plasma for FeO_x, combined with an FG plasma + H_2O reactant for the MnO_x process, the ORR and OER onsets are comparable to the shared O plasma reactant. Also featured in Figure S5.1b are full cell results from the same five combinations of ALD reactants. These results reinforce the conclusions drawn from half cell, particularly the benefit of using a combined FG plasma + H_2O reactant for the MnO_x process and an O plasma reactant for the FeO_x process. This combination outperforms the shared O plasma reactant more so than revealed by half cell. For this reason, and because using an O plasma for both processes would no doubt lead to issues with the delicate carbon-based substrate,[54,406] hereafter, an O plasma reactant was selected for the FeO_x process, while a combined FG plasma + H_2O reactant was chosen for the MnO_x process. It should also be noted that this combination of reactants required the fewest amount of supercycles to reach a thickness of 10 nm, permitting practical depositions of films beyond 10 nm in thickness.

The substrate temperature during ALD supercycle deposition was also investigated, in part to see if this would improve the growth or electrochemical performance when using an FG plasma in the FeO_x process. Based on the ALD window for the two binary ALD processes,[157,360] the maximum allowable temperature is 250 °C. At this temperature, however, no improvements were observed in the growth characteristics or electrochemical performance, for any of the investigated supercycle films. In addition, a post-deposition annealing treatment was conducted for all the investigated films. The light-shaded bars in Figure S5.1 represent as-deposited (unannealed) films, while the dark-shaded bars represent annealed samples. In all cases, the annealing treatment improves the ORR performance of the catalyst film. On the other hand, the OER performance is often inferior after annealing. Overall, annealing yields mixed results during the survey of ALD supercycle reactants.

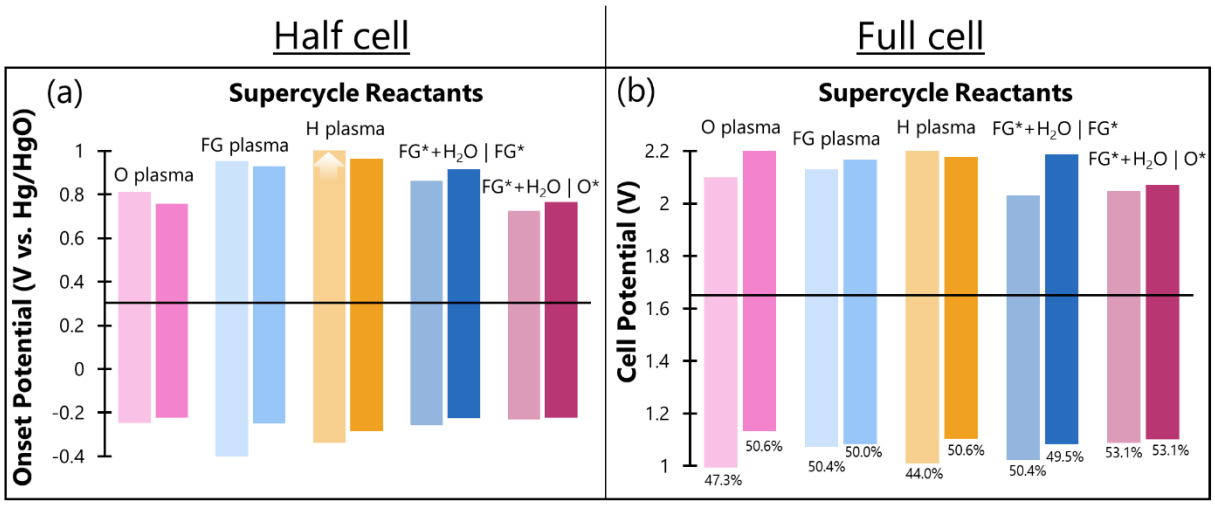

Figure S5.1. Half cell and full cell performance metrics for the reactants explored during 1:10 $MnFe_xO_y$ supercycles. FG*+H_2O denotes the combined FG plasma and H_2O reactant for the MnO_x process, while FG* and O* represent FG plasma and O plasma reactants, respectively, for the FeO_x process. FG plasma, H plasma, and FG*+H_2O|FG* films are only 1 nm thick, while the O plasma and FG*+H_2O|O* films are 10 nm thick. When using an H plasma for both the Mn and Fe reactant, without annealing, the resulting film is unable to yield 10 mA cm^{-2} at +1.0 V vs. Hg/HgO (the maximum potential in the half cell LSV technique employed). Therefore, the OER onset is provided a placeholder value that extends beyond the range of the plot.

The supercycle $MnFe_xO_y$ process alternates between MnO_x and FeO_x binary atomic layer deposition (ALD) steps. As a result, the MnO_x ALD step will deposit on the previous FeO_x surface and, likewise, the FeO_x ALD step will grow on the previous MnO_x surface. It is, therefore, of interest to examine the saturation behaviour of each ALD process on the opposite substrate. This was suggested by Mackus *et al.* in their review of ALD supercycles.[55] It is valuable to ensure saturation when depositing on the air electrode of a Zn-air battery (ZAB) because non-saturating depositions can clog porosity and impact battery performance.[157] In a similar manner to binary ALD saturation studies, the growth per cycle (GPC) of the ALD process is measured as a function of each ALD parameter within a cycle. In this case, however, the starting Si substrate also includes approximately 1 nm of either MnO_x or FeO_x deposited via ALD. GPC values in the saturation studies are the steady-state slope in the thickness vs. cycle number graphs after 70 cycles for the MnO_x on FeO_x depositions (Mn-Fe), and after 200 cycles for the FeO_x on MnO_x depositions (Fe-Mn). Substrates for the saturation studies were Si(100)

wafer pieces with a 30 s *in situ* O plasma pretreatment, followed by either 10 cycles of MnO_x ALD or 45 cycles of FeO_x ALD,[157,406] for Fe-Mn and Mn-Fe depositions, respectively. A 60 s *in situ* O plasma was performed between MnO_x and FeO_x depositions in either saturation study.

For the Fe-Mn process, there are six parameters of interest: ethylferrocene (EF) dose time, post-EF purge time, pre-plasma O_2 flow time, O plasma dose time, post-plasma purge time, and substrate temperature. The timing values from a previous saturation study of the same FeO_x process on a Si substrate (Fe-Si; Chapter 3) were used as starting values.[360] However, due to recent modifications to the ALD system, the starting dose time was reduced from 3 s to 1 s. Figure S5.2 shows the GPC behaviour when each parameter is independently varied. For the EF dose time (Figure S5.2a), surface saturation occurs for as little as 0.05 s. Nevertheless, a 0.25 s dose time was implemented to improve the deposition on the high surface area and porous gas diffusion layer (GDL) substrate, which requires longer diffusion times.[52,156,306] In addition, longer times are beneficial during a saturation study to reduce the interdependence of cycle parameters.[52,360] For the EF purge time (Figure S5.2b), as little as 2 s is sufficient to remove non-reacted EF molecules and by-products from the substrate surface. This may be due to the continuous flow setup of the ALD system, which ensures good mass transport of species within the ALD reactor.[155] Nonetheless, a 5 s EF purge time was chosen since excess purging is not harmful and, as mentioned previously, may also reduce the interdependence of the ALD parameters. For the ALD reactor in this work, there is a large physical distance between the mass flow controller for O_2 gas and the plasma tube. When the plasma strikes, it is an Ar-only plasma since the O_2 gas is still in transit to the plasma tube. This reduces the actual O plasma time recorded by the plasma controller. To compensate, O_2 gas flows in the lines for a predefined amount of time before the plasma strikes. This ensures that the gas mixture in the plasma tube is O_2 rich. The length of time for this pre-plasma O_2 gas flow is shown as a function of GPC in Figure S5.2c. At least 1 s of O_2 gas flow is required to ensure satisfactory plasma performance and to avoid a loss in GPC. The actual plasma time, with the pre-plasma O_2 flow in place, is shown in Figure S5.2d. In line with previous work on the FeO_x ALD process (Chapter 3),[360] the GPC steadily increases with O plasma time to saturation. Beyond saturation, all the precursor fragments adsorbed to the substrate are oxidized and any excess O plasma does not lead to added growth. For the Fe-Mn process, at least 20 s of O plasma is required to reach saturation. Interestingly, a pre-plasma O_2 time of less than 1 s in Figure S5.2c is equivalent to an O plasma

time of less than 20 s in Figure S5.2d, both of which yield a lower GPC. This exemplifies the delay in the O_2 delivery line. For the plasma purge time, shown in Figure S5.2e, essentially zero purge time is required to maintain saturation. However, a non-zero purge time is more appropriate to ensure that reaction by-products are removed from the substrate surface. Therefore, 5 s was selected as the post-plasma purge time. Lastly, Figure S5.2f shows the ALD temperature window for the Fe-Mn process. For a temperature range of 150 °C to 250 °C, the ALD process yields approximately the same GPC within experimental error. This temperature window is identical to that for the Fe-Si process reported previously (Figure 3.3 in Chapter 3).[360] At temperatures below and above this range, non-conformal chemical vapour deposition (CVD)-like mechanisms are responsible for the observed increase in GPC.[158,160] The optimized ALD timing scheme for the FeO_x process (0.25/5/1/20/5) was repeated three times to yield a saturating GPC of 0.17 ± 0.01 Å cycle^{-1}. The error value of GPC represents the error bars shown in Figure S5.2.

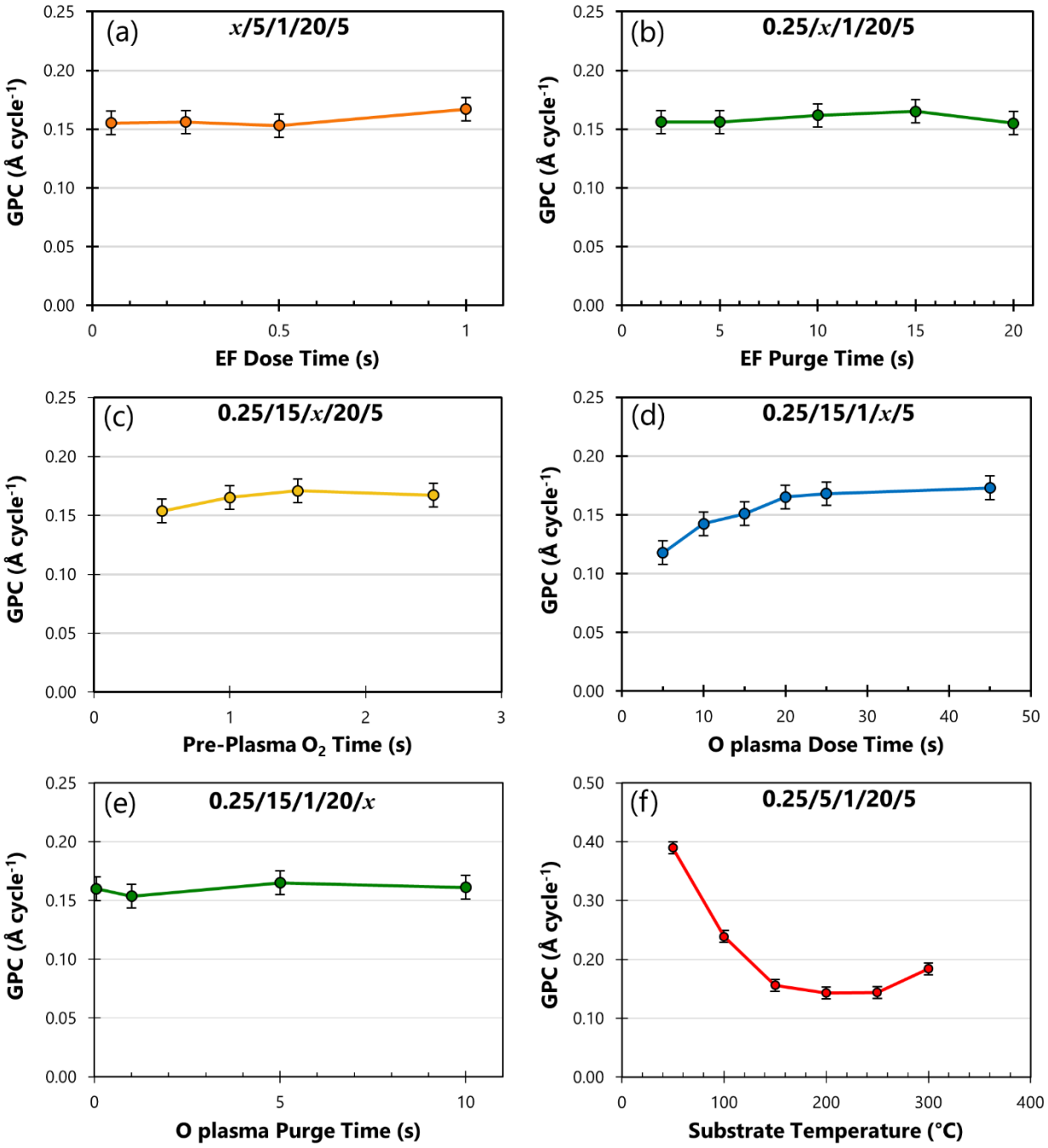

Figure S5.2. (a-e) Saturation curves for FeO_x ALD on a MnO_x surface at 150 °C. GPC vs. (a) EF dose time, (b) EF purge time, (c) pre-plasma O_2 flow, (d) O plasma time, and (e) post-plasma purge time. The label on each figure shows the ALD timing values ($t_1/t_2/t_3/t_4/t_5$), where t_1 is the EF dose time, t_2 is the EF purge time, t_3 is the pre-plasma O_2 time, t_4 is the O plasma time, and t_5 is the post-plasma purge time. (f) GPC as a function of substrate temperature for the optimized FeO_x ALD recipe on a MnO_x surface.

For the Mn-Fe process, there are seven parameters of interest: bis(ethylcyclopentadienyl)manganese ($(EtCp)_2Mn$) dose time, $(EtCp)_2Mn$ charge time, post-precursor purge time, FG plasma dose time, H_2O dose time, post-H_2O purge time, and substrate temperature. The timing values previously determined for the same MnO_x process on a Si substrate were used as starting values for the saturation study on a FeO_x surface.[157] There are two ALD timings for the precursor dose step (Figure S5.3a) since the low vapour pressure precursor requires an ampoule charging step. While a precursor dose and charge time of 3 and 5 s, respectively, were previously reported,[157] an equal amount of charging and dosing is preferred to avoid any unsafe pressurization. Figure S5.3a shows that a 4 s dose and 4 s charge provide an equivalent GPC to the standard 3 and 5 s timing values. Furthermore, a 5 s dose and charge do not yield a higher GPC, indicating that both a 4 s charge and dose, as well as the original 3 and 5 s charge and dose, result in saturating behaviour. Figure S5.3b illustrates the required amount of precursor purging to ensure saturating behaviour. For precursor purge times less than 10 s, precursor fragments or reaction by-products may remain on the surface during subsequent reactant steps and hinder the reaction process, thereby reducing the GPC.[160] Therefore, sufficient precursor purging is required and 15 s was adopted as the precursor purge time for the Mn-Fe process. For the original MnO_x ALD process devised by Clark *et al.*, an FG plasma was required prior to the H_2O reactant to achieve saturating growth.[157] This is also the case in the current work; however, only 5 s of FG plasma is required (Figure S5.3c), a considerable reduction from the 20 s reported in the original work. Conservatively, 10 s was selected as the ideal FG plasma time for the Mn-Fe process. Once the plasma is deactivated, H_2O is immediately pulsed, without the need for a post-plasma purge.[160] An investigation of the H_2O dose time is shown in Figure S5.3d, which reveals that 1 s is sufficient to reach a saturating GPC. Nonetheless, 1.5 s was chosen for the Mn-Fe process, down from 2 s from the original report.[157] The post-H_2O purge is shown in Figure S5.3e. Post-H_2O purges, unlike post-plasma purges, are relatively long. This is because polar H_2O molecules have strong interactions with oxide surfaces and reactor walls.[158,160] While there is an obvious decrease in GPC after 10 s of post-H_2O purge in Figure S5.3e, there is still a reduction in GPC observed when increasing the purge time to 30 s. Furthermore, the GPC at 30 s of post-H_2O purge is more in line with the saturating GPC in Figures S5.3a-d. Therefore, the post-H_2O purge time is maintained at 30 s. Figure S5.3f displays the ALD temperature window for the Mn-Fe process. For depositions at substrate temperatures

below 100 °C, there is a large increase in the GPC, attributed to CVD-like growth during precursor condensation.[156,158,160] However, depositions at 150 °C or higher exhibit a constant, saturating GPC. The optimized ALD timing scheme for the MnO_x process, (4/4/15/10/1.5/30), was repeated five times to yield a saturating GPC of 1.49 ± 0.13 Å cycle^{-1}. The error value in GPC represents the error bars shown in Figure S5.3.

To successfully integrate the Mn-Fe and Fe-Mn processes into one ALD supercycle, the deposition temperature should be within the temperature window of both binary ALD processes. Thus, 150 °C is the lowest acceptable deposition temperature and was selected for the ALD supercycle process. This temperature is also compatible with the GDL substrates used during electrochemical characterization. High temperatures, particularly those above 300 °C, can decompose polytetrafluoroethylene and damage the GDL substrate.[440,441]

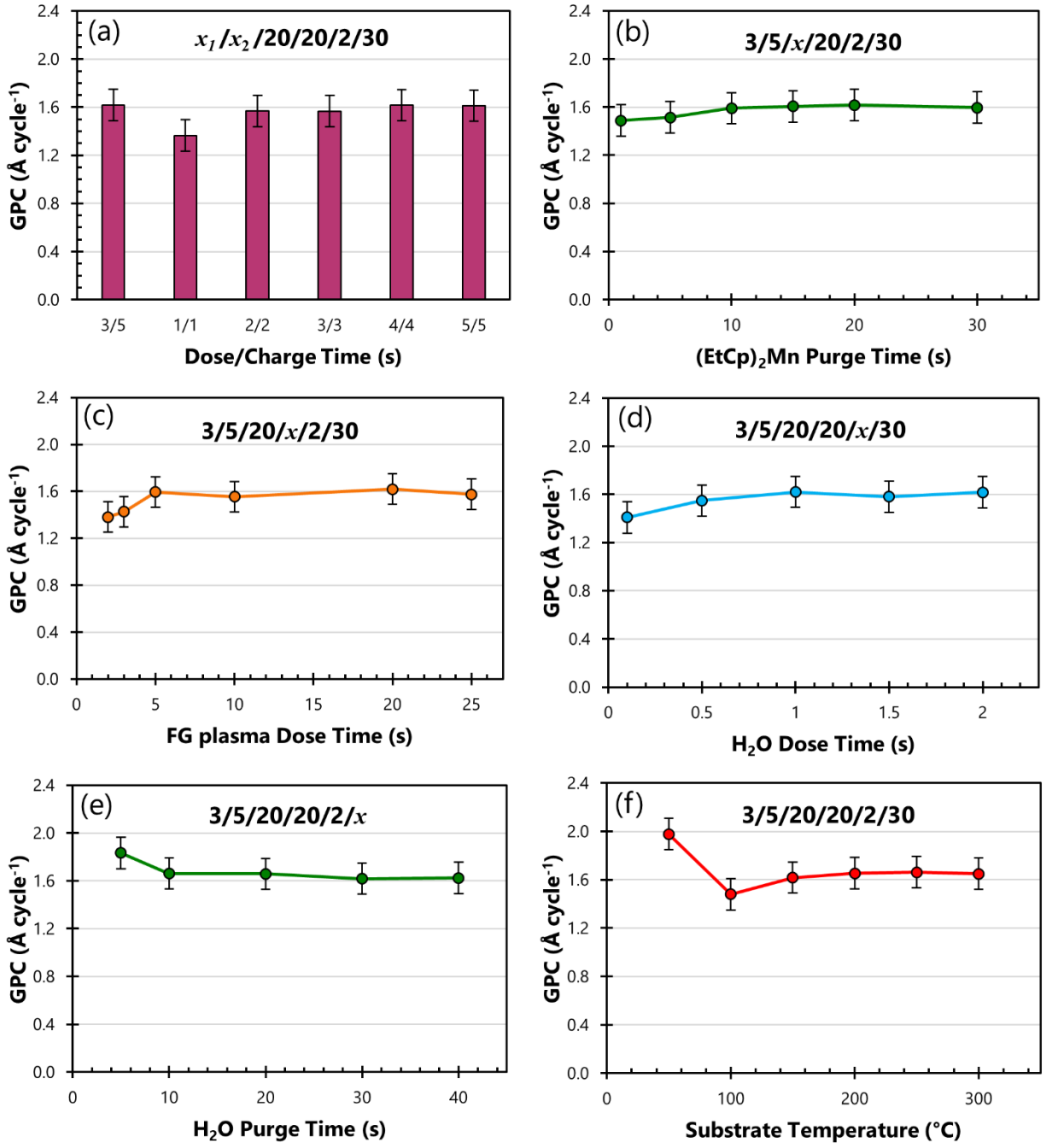

Figure S5.3. (a-e) Saturation curves for MnO_x ALD on an FeO_x surface at 150 °C. GPC vs. (a) dose and charge time, (b) $(EtCp)_2Mn$ purge time, (c) FG plasma dose time, (d) H_2O dose time, and (e) post-H_2O purge time. The label on each figure shows the ALD timing values ($t_1/t_2/t_3/t_4/t_5$), where t_1 is the $(EtCp)_2Mn$ dose time, t_2 is the $(EtCp)_2Mn$ charge time, t_3 is the FG plasma time, t_4 is the H_2O dose time, and t_5 is the post-H_2O purge time. (f) GPC as a function of substrate temperature for MnO_x ALD on an FeO_x surface.

5.5.2 Results and Discussion

5.5.2.1 Supercycle Optimization

Table S5.1. Deposition conditions for all ALD samples explored in this work. Thickness values are based on *in situ* spectroscopic ellipsometry (SE) analysis during ALD.

Supercycle Optimization Step	Sample Name	MnO_x Binary ALD Cycle Timing	FeO_x Binary ALD Cycle Timing	Supercycle Formula (MnO_x:FeO_x)	No. of Supercycles	Thickness (nm)
Supercycle Reactants (1:10)	O-plasma	3/5/20/1/15/5	3/20/1/15/5	1:10	16	13.0
	FG-plasma	3/5/20/1/20/5	3/20/1/20/5	1:10	18	1.5
	H-plasma	3/5/20/1/45/5	3/20/1/30/5	1:10	16	1.1
	FG*+H_2O|FG*	3/5/20/20/2/30	3/20/1/30/5	1:10	20	1.9
	FG*+H_2O|O*	3/5/20/20/2/30	3/20/1/15/5	1:10	13	10.0
Wide Net	1:10	3/5/20/20/2/30	3/20/1/15/5	1:10	13	10.0
	5:30	3/5/20/20/2/30	3/20/1/15/5	5:30	7	11.5
	10:20	3/5/20/20/2/30	3/20/1/15/5	10:20	5	9.2
Cycle Ratio {10's}	40:10	3/5/20/20/2/30	3/20/1/15/5	40:10	2	9.6
	30:10	3/5/20/20/2/30	3/20/1/15/5	30:10	3	11.5
	20:10	3/5/20/20/2/30	3/20/1/15/5	20:10	4	11.5
	10:10	3/5/20/20/2/30	3/20/1/15/5	10:10	6	11.0
	10:20	3/5/20/20/2/30	3/20/1/15/5	10:20	5	9.2
	10:30	3/5/20/20/2/30	3/20/1/15/5	10:30	4	9.2
	10:40	3/5/20/20/2/30	3/20/1/15/5	10:40	4	10.4
Bilayer Thickness {3:1}	9:3	3/5/20/20/2/30	3/20/1/15/5	9:3	8	12.6
	15:5	3/5/20/20/2/30	3/20/1/15/5	15:5	5	12.0
	21:7	3/5/20/20/2/30	3/20/1/15/5	21:7	4	12.8
	30:10	3/5/20/20/2/30	3/20/1/15/5	30:10	3	11.5
	45:15	3/5/20/20/2/30	3/20/1/15/5	45:15	2	11.5
	60:20	3/5/20/20/2/30	3/20/1/15/5	60:20	2	14.7
30:10 Thickness	30:10 | 10 nm	3/5/20/20/2/30	3/20/1/15/5	30:10	3	11.5
	30:10 | 20 nm	3/5/20/20/2/30	0.25/5/1/20/5	30:10	5	19.7
	30:10 | 30 nm	3/5/20/20/2/30	0.25/5/1/20/5	30:10	7	32.8
	30:10 | 40 nm	4/4/15/10/1.5/30	0.25/5/1/20/5	30:10	8	39.8
Double Supercycles	30:10	3/5/20/20/2/30	0.25/5/1/20/5	30:10	8	42.8
	10:20	3/5/20/20/2/30	0.25/5/1/20/5	10:20	14	41.8
	30:10+10:20	4/4/15/10/1.5/30	0.25/5/1/20/5	30:10	7	30.5
		4/4/15/10/1.5/30	0.25/5/1/20/5	10:20	4	12.8
	30:10+FeO_x	4/4/15/10/1.5/30	0.25/5/1/20/5	30:10	7	30.3
		-	0.25/5/1/20/5	:1	420	9.0
Benchmark Comparisons	MnO_x	4/4/15/10/1.5/30	---	1:	400	41.2
	FeO_x	4/4/15/10/1.5/30	---	1:	10	1.3
		---	0.25/5/1/20/5	:1	420	10.0
	Pt-Ru-C	---	---	---	---	---
	Bare GDL	---	---	---	---	---

Table S5.2. Quantified half cell and full cell performance metrics of all samples explored in this work.

Supercycle Optimization Step	Sample Name	Heat Treatment	Half Cell			Full Cell				
			LSV ORR (V @ -10 mA cm^{-2})	LSV OER (V @ 10 mA cm^{-2})	Voltage Gap (V @ |10mA cm^{-2}|)	GCPL Discharge (V @ -20 mA cm^{-2})	GCPL Charge (V @ 20 mA cm^{-2})	Efficiency (@ |20 mA cm^{-2}|)	Voltage Gap (V @ |20 mA cm^{-2}|)	Peak Power (mW cm^{-2})
Supercycle Reactants	O-plasma	Unannealed	-0.25	0.81	1.06	0.99	2.10	47.3%	1.11	
		Annealed	-0.22	0.76	0.98	1.13	2.24	50.6%	1.11	
	FG-plasma	Unannealed	-0.40	0.95	1.35	1.07	2.13	50.4%	1.06	
		Annealed	-0.25	0.93	1.18	1.08	2.17	50.0%	1.08	
	H-plasma	Unannealed	-0.34	---	---	1.01	2.29	44.0%	1.28	
		Annealed	-0.28	0.96	1.25	1.10	2.18	50.6%	1.08	
	FG*+H_2O|FG*	Unannealed	-0.26	0.86	1.12	1.02	2.03	50.4%	1.01	
		Annealed	-0.23	0.92	1.14	1.08	2.19	49.5%	1.10	
	FG*+H_2O|O*	Unannealed	-0.23	0.73	0.96	1.09	2.05	53.1%	0.96	
		Annealed	-0.22	0.77	0.99	1.10	2.07	53.1%	0.97	
Wide Net	1:10	Unannealed	-0.23	0.73	0.96	1.09	2.05	53.1%	0.96	
		Annealed	-0.22	0.77	0.99	1.10	2.02	54.5%	0.97	
	5:30	Unannealed	-0.24	0.78	1.02	1.07	2.02	53.1%	0.95	
		Annealed	-0.20	0.79	0.99	1.13	2.07	54.4%	0.94	
	10:20	Unannealed	-0.20	0.81	1.01	1.09	2.03	53.8%	0.94	
		Annealed	-0.15	0.79	0.94	1.12	2.06	54.1%	0.95	
Cycle Ratio {10's}	40:10	Unannealed	-0.16	0.98	1.14	---	---	---	---	
		Annealed	-0.10	0.85	0.96	1.08	2.09	52.0%	1.00	
	30:10	Unannealed	-0.14	0.91	1.05					
		Annealed	-0.11	0.86	0.96	1.12	2.04	55.0%	0.92	
	20:10	Unannealed	-0.15	0.93	1.08	---	---	---	---	
		Annealed	-0.12	0.88	1.00	---	---	---	---	
	10:10	Unannealed	-0.13	0.86	0.99	1.09	2.06	52.8%	0.97	
		Annealed	-0.11	0.85	0.96	1.10	2.05	53.9%	0.94	
	10:20	Unannealed	-0.20	0.81	1.01	1.09	2.03	53.8%	0.94	
		Annealed	-0.15	0.79	0.94	1.12	2.06	54.1%	0.95	
	10:30	Unannealed	-0.19	0.81	1.01	1.07	2.26	47.2%	1.19	
		Annealed	-0.17	0.81	0.98	1.07	2.04	52.7%	0.96	
	10:40	Unannealed	-0.20	0.80	1.00	---	---	---	---	
		Annealed	-0.18	0.81	0.99	---	---	---	---	
Bilayer Thickness {3:1}	9:3	Annealed	-0.14	0.89	1.03	1.03	2.04	50.5%	1.01	
	15:5	Annealed	-0.13	0.88	1.01	1.06	2.05	51.6%	0.99	
	21:7	Annealed	-0.11	0.87	0.98	1.08	2.04	52.7%	0.96	
	30:10	Annealed	-0.11	0.86	0.96	1.12	2.04	55.0%	0.92	
	45:15	Annealed	-0.11	0.85	0.96	1.08	2.05	52.6%	0.97	
	60:20	Annealed	-0.12	0.81	0.93	0.97	2.06	47.3%	1.09	
30:10 Thickness	30:10 | 10 nm	Annealed	-0.11	0.86	0.96	1.12	2.04	55.0%	0.92	
	30:10 | 20 nm	Annealed	-0.11	0.86	0.98	1.13	2.17	52.4%	1.04	
	30:10 | 30 nm	Annealed	-0.09	0.80	0.89	1.15	2.13	54.1%	0.98	
	30:10 | 40 nm	Annealed	-0.10	0.75	0.85	1.19	2.11	56.3%	0.92	
Double Supercycles	30:10	Annealed	-0.10	0.75	0.85	1.19	2.11	56.4%	0.92	
	10:20	Annealed	-0.10	0.74	0.84	1.16	2.11	55.1%	0.95	
	30:10+10:20	Annealed	-0.10	0.78	0.88	1.18	2.10	56.4%	0.92	
	30:10+FeO_x	Annealed	-0.09	0.75	0.84	1.13	2.10	53.9%	0.97	
Benchmark Comparisons	30:10 | 40 nm	Annealed	-0.10	0.75	0.85	1.15	2.20	52.5%	1.04	93
	MnO_x	Annealed	-0.16	0.90	1.06	1.14	2.19	52.1%	1.05	87
	FeO_x	Annealed	-0.21	0.74	0.95	1.07	2.18	49.2%	1.11	86
	Pt-Ru-C	Annealed	-0.07	0.62	0.69	1.23	2.02	61.2%	0.78	119
	Bare GDL	Unannealed	-0.27	---	---	0.96	>4	<25%	---	51

LSV: linear sweep voltammetry; **ORR**: oxygen reduction reaction; **OER**: oxygen evolution reaction; **GCPL**: galvanostatic cycling with potential limitation.

5.5.2.2 Increasing Overall Thickness

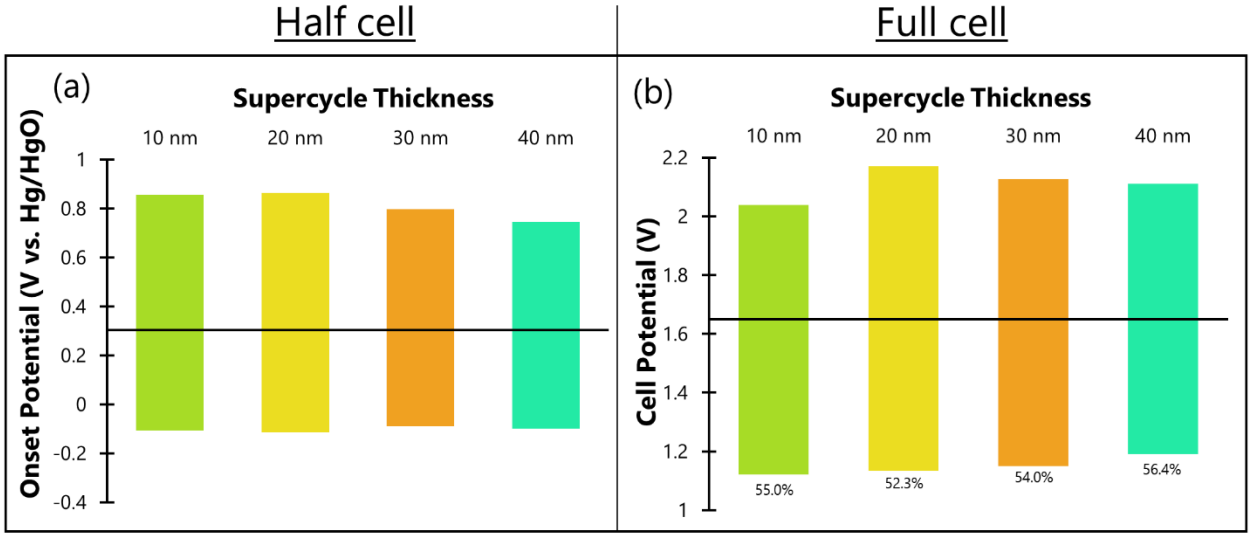

Figure S5.4. (a) Half cell and (b) full cell performance metrics for annealed $MnFe_xO_y$ 30:10 films with thicknesses ranging from 10 to 40 nm.

5.5.3 Materials Characterization of $MnFeO_x$

5.5.3.1 SEM

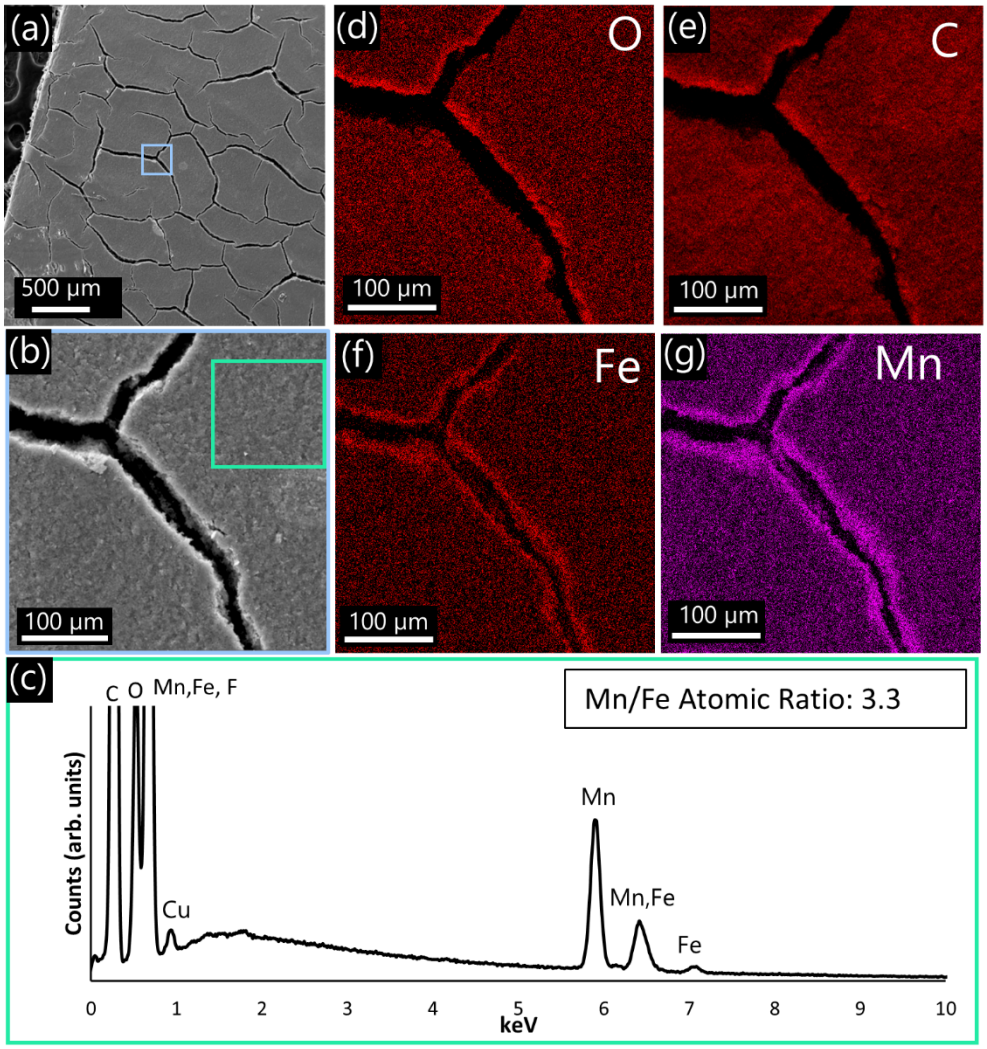

Figure S5.5. Scanning electron microscopy (SEM) analysis of the unannealed $MnFeO_x$ coating on GDL. (a) Low-magnification secondary electron image, (b) magnified image of the indicated area in (a), (c) energy dispersive X-ray (EDX) spectrum from the green area in (b). A Mn/Fe atomic ratio of 3.3 was calculated from semi-quantification of the spectrum. (d-g) Elemental mapping of O, C, Fe and Mn, respectively, for the overall area in (b).

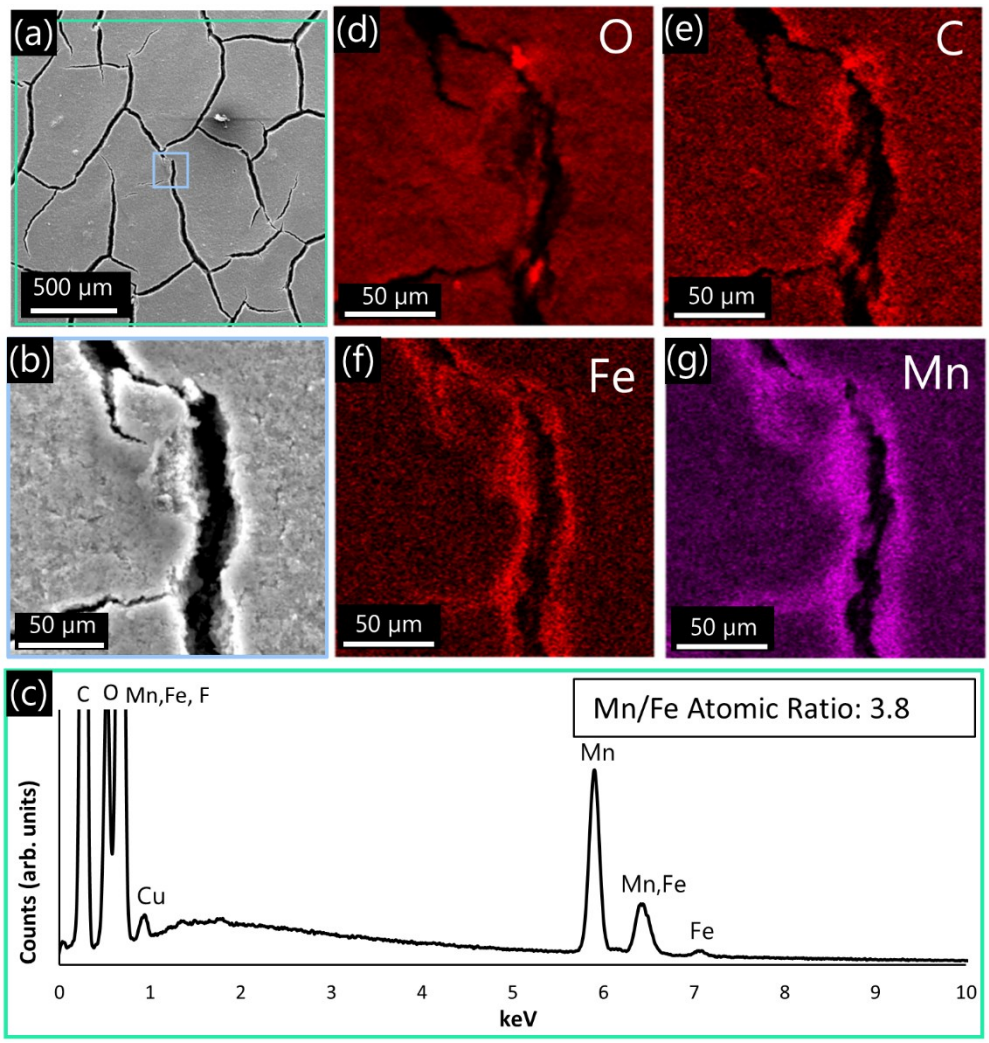

Figure S5.6. SEM/EDX analysis of the annealed $MnFeO_x$ on GDL. (a) Low-magnification secondary electron image, (b) magnified image of the blue indicated area in (a), (c) EDX spectrum from the green area in (a). A Mn/Fe atomic ratio of 3.8 was calculated from semi-quantification of the spectrum. (d-g) Elemental mapping of O, C, Fe and Mn, respectively, for the overall area in (b).

5.5.3.2 TEM/STEM

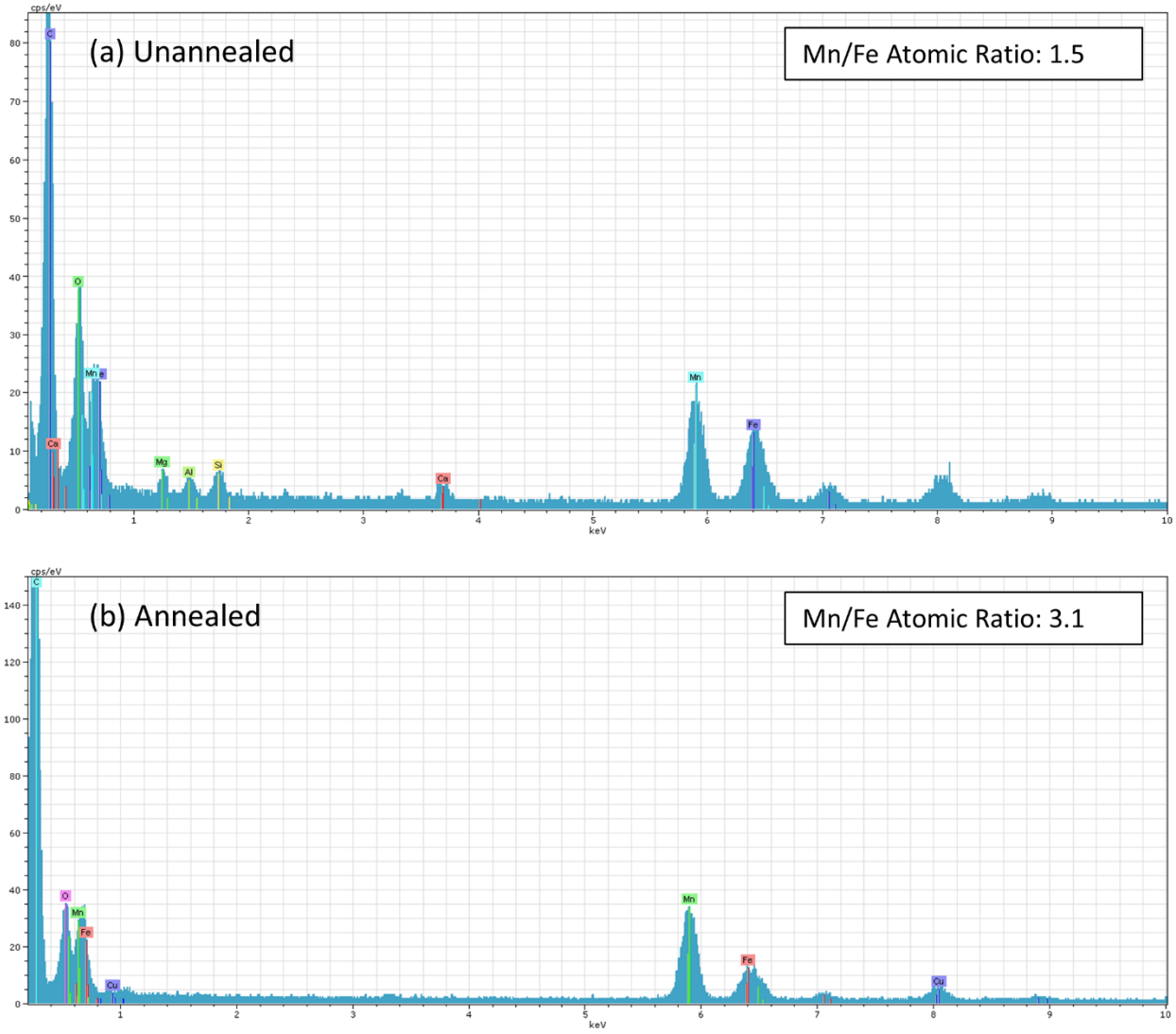

Figure S5.7. Scanning transmission electron microscopy (STEM) EDX spectrua and Mn/Fe atomic ratio calculated from semi-quantification of the spectrua. (a) Unannealed $MnFeO_x$ coating on GDL, (b) annealed $MnFeO_x$ coating on GDL.

Table S5.3. Measured d-spacings for the SAD patterns of unannealed (Un) and annealed (An) $MnFeO_x$ in Figures 5.5i and 5.6d alongside the reported d-spacings for cubic oxide spinels of Mn and Fe. Contributions from the amorphous carbon TEM grid and graphitic carbon GDL are also identified.

ALD $MnFeO_x$		$MnFe_2O_4$ (Jacobsite)			Mn_3O_4 (cubic)			Fe_3O_4 (Magnetite)			Graphite			Carbon		
Un	**An**	PDF #10-0319			PDF #13-0162			PDF #19-0629			PDF #41-1487			PDF #26-1081		
d spacing (nm)	**d spacing (nm)**	d spacing (nm)	(h k l)	Intensity (%)	d spacing (nm)	(h k l)	Intensity (%)	d spacing (nm)	(h k l)	Intensity (%)	d spacing (nm)	(h k l)	Intensity (%)	d spacing (nm)	(h k l)	Intensity (%)
0.125	**0.119**	0.1296	(5 3 3)	20	0.1284	(5 3 3)	20	0.1281	(5 3 3)	10	0.1234	(1 1 0)	3	0.1261	(1 1 0)	48
0.154	**0.149**	0.1503	(4 4 0)	40	0.1488	(4 4 0)	60	0.1485	(4 4 0)	40	0.1548	(1 0 3)	1	0.1580	(1 0 9)	2
0.168	**0.170**	0.1636	(5 1 1)	35	0.1620	(5 1 1)	50	0.1616	(5 1 1)	30	0.1681	(0 0 4)	4	0.1665	(1 0 6)	2
0.211	**0.206**	0.2124	(4 0 0)	25	0.2100	(4 0 0)	50	0.2099	(4 0 0)	20	0.2139	(1 0 0)	2	0.2081	(1 0 3)	100
0.262	**0.253**	0.2563	(3 1 1)	100	0.2540	(3 1 1)	100	0.2532	(3 1 1)	100						
0.301	**0.304**	0.3005	(2 2 0)	35	0.2980	(2 2 0)	50	0.2967	(2 2 0)	30						
0.354	**0.342**										0.3376	(0 0 2)	100			
0.503	**0.517**	0.4906	(1 1 1)	20	0.4860	(1 1 1)	50	0.4852	(1 1 1)	8						

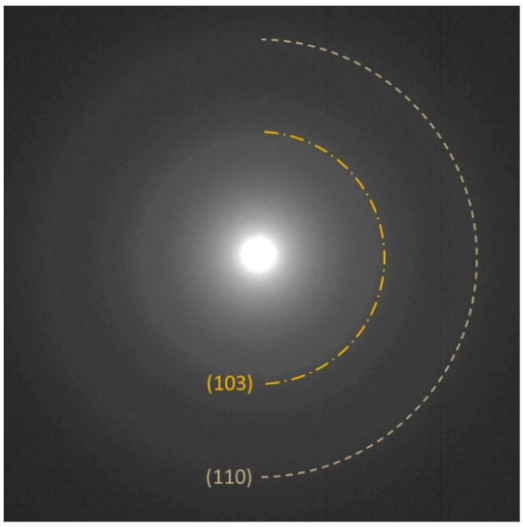

Figure S5.8. SAD pattern from the amorphous carbon TEM support used to examine the ALD coated GDL particles in TEM/STEM. Two diffuse rings are visible and indexed to the (103) and (110) planes using the same colour convention as Table S5.3.

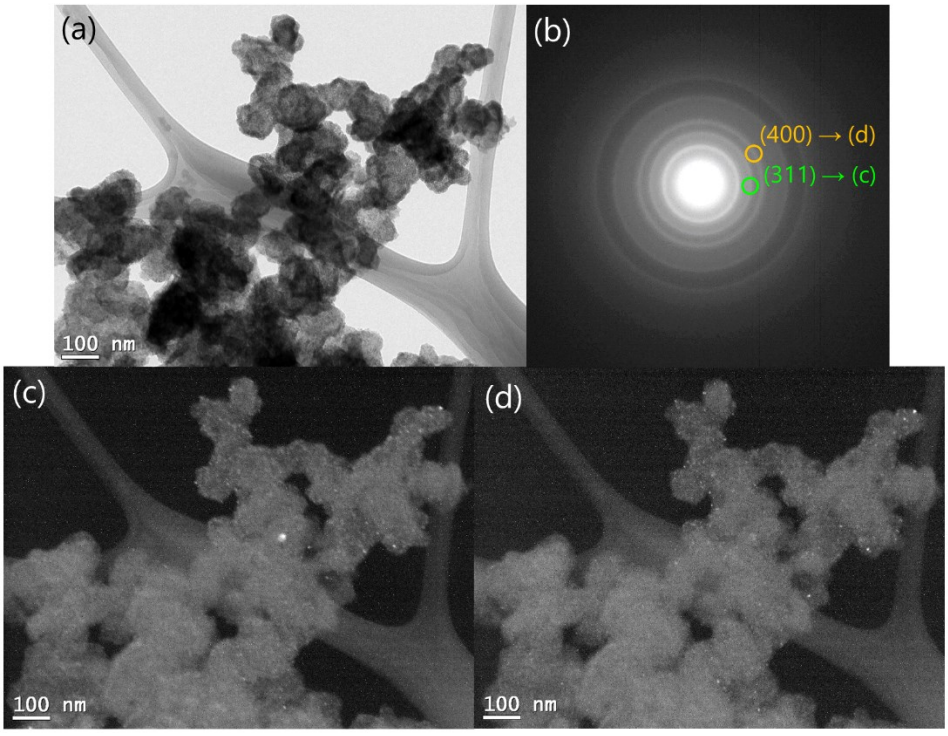

Figure S5.9. TEM of the $MnFeO_x$ ALD film. (a) BF image, (b) SAD pattern from the overall area of (a) with rings matching those found in Figure 5.6d, (c) DF image from part of the (311) ring of $MnFeO_x$, and (d) DF image from part of the (400) ring of $MnFeO_x$. Small bright contrast features in the DF images are nanocrystalline grains of $MnFeO_x$.

5.5.3.3 XPS

The C 1s spectra for the unannealed and annealed $MnFeO_x$ samples are shown in Figure S5.10, with deconvoluted peaks demonstrated by different colors. The full results of deconvolution are included in Table S5.4. The alkyl C peak (shown in blue) was set to a binding energy of 284.8 eV to calibrate all other spectra.[157,270,315] This peak, usually the largest component of the C 1s spectrum, is relatively small because of a sputter clean conducted on the X-ray photoelectron spectroscopy (XPS) samples, designed to remove adventitious carbon. In accordance with the procedure outlined by Biesinger *et al.*, the full-width at half-maximum (FWHM) of the remaining C peaks are restricted to the same value as the alkyl C peak.[270] A shoulder peak, attributed to ether and hydroxyl contributions (shown in orange), was fit to 1.5 eV above the alkyl peak.[268,270,315] A lower contribution of the spectrum is occupied by this shoulder peak for the annealed sample because the annealing process can remove hydroxyl species.[407] The largest peak of the spectra, fit to 4.9 eV above the alkyl peak, was assigned to ester and/or carbonyl contributions (shown in green).[268,270,314] In line with the survey spectra, an additional contribution for N-bound C (shown in yellow) was found for the unannealed sample at 288.0 eV,[268,442,443] but was not present for the annealed sample.

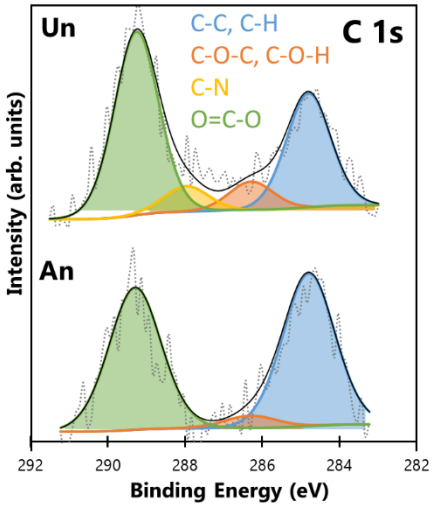

Figure S5.10. C1s spectra for unannealed (Un) and annealed (An) samples of ALD $MnFeO_x$ on Si substrates.

Table S5.4. Deconvolution of the C 1s, O 1s, Fe 2p, Mn 2p, and Mn 3s XPS spectra for unannealed and annealed $MnFeO_x$. The position (eV), FWHM (eV), and % area for each identified component are included.

				Unannealed			Annealed		
				Position (eV)	FWHM (eV)	% Area	Position (eV)	FWHM (eV)	% Area
C 1s			C-C, C-H	284.8	1.37	32.6	284.8	1.59	49.8
			C-O-C, C-O-H	286.3	1.37	8.15	286.3	1.59	3.90
			C-N	288.0	1.37	7.22			
			O=C-O	289.3	1.37	52.1	289.3	1.59	46.3
O 1s			M-O-M	529.5	1.26	84.0	529.6	1.25	86.5
			M-O-H	531.1	1.26	9.94	531.0	1.22	6.33
			O=C-O	531.8	1.26	6.03	531.8	1.22	7.20
Fe 2p	$2p_{3/2}$	2+	Peak #1	708.9	1.60	11.3	708.3	1.60	12.8
			Peak #2	709.7	1.60	7.41	709.4	1.60	8.84
			Peak #3	711.8	1.03	6.47	711.6	1.18	5.53
		3+	Peak #1	709.9	1.47	10.9	709.6	1.60	12.9
			Peak #2	710.8	1.45	19.2	710.7	1.57	19.3
			Peak #3	712.6	1.36	8.76	712.4	1.49	7.63
			Peak #4	713.7	1.60	4.71	713.7	1.60	3.40
			Satellite	718.0	1.43	1.17			
	$2p_{1/2}$		Main Peak	724.3	4.16	30.0	723.8	4.20	29.55
Mn 2p	$2p_{3/2}$		Main Peak	640.6	-	-	640.3	-	-
		2+	Peak #1	639.8	1.49	36.5	639.7	1.43	33.1
			Peak #2		-		641.1	1.51	12.8
			Peak #3	642.3	1.00	0.46	642.0	1.25	3.03
			Peak #4	642.8	1.17	1.68	642.9	1.34	1.14
			Peak #5	643.9	1.38	0.41		-	
		3+	Peak #1	640.7	1.04	11.0	640.9	1.60	22.6
			Peak #2	641.6	1.60	31.2	641.9	1.19	4.68
			Peak #3	643.2	1.34	3.92	642.9	1.38	2.42
			Peak #4	644.3	1.60	3.32	643.6	1.60	3.79
			Peak #5	646.4	0.60	4.89	646.4	1.60	5.85
		4+	Peak #1	642.2	1.00	0.31	642.2	1.26	3.44
			Peak #2	642.5	1.00	1.94	642.7	1.21	3.19
			Peak #3	643.2	1.35	1.76			
			Peak #4	644.5	1.60	1.78	644.5	1.60	4.01
			Peak #5	645.3	1.00	0.76			
	$2p_{1/2}$		Main Peak	652.6	-	-	652.6	-	-
			Satellite	658.6	-	-	658.7	-	-
Mn 3s			High eV	88.59	2.54	73.0	88.63	2.47	71.6
			Low eV	82.42	2.08	27.0	82.38	2.16	28.4

5.5.4 ZAB Application of $MnFeO_x$

5.5.4.1 Electrocatalytic Activity

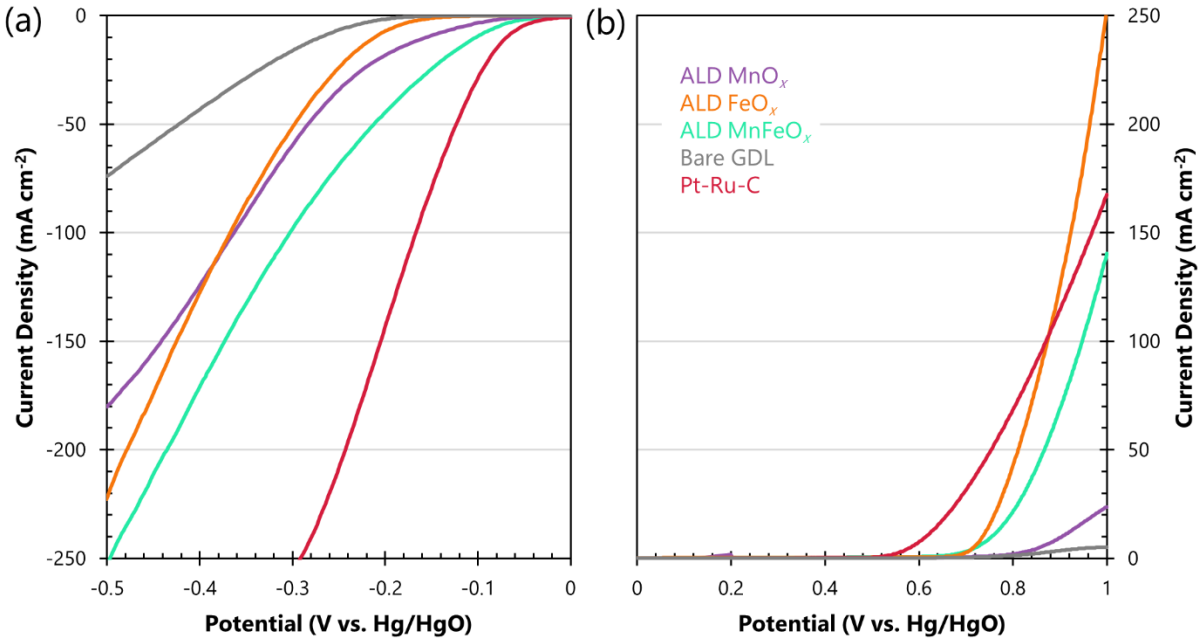

Figure S5.11. Half cell LSV curves for ALD MnO_x, ALD FeO_x, ALD $MnFeO_x$, bare GDL, and a Pt-Ru-C benchmark. (a) ORR potential range, (b) OER potential range. The colour-coded legend is the same for both plots.

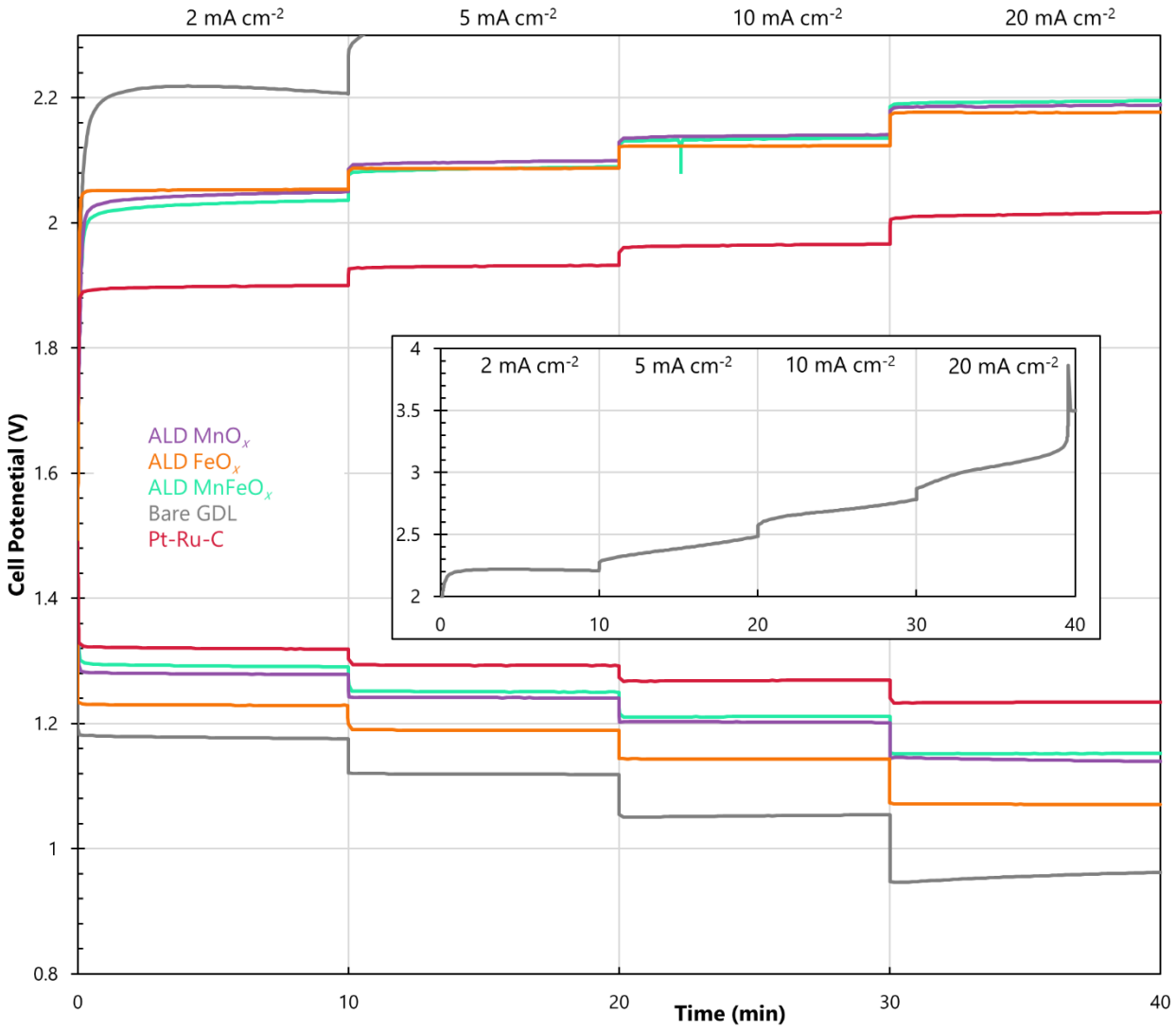

Figure S5.12. Full cell rate test curves for ALD MnO_x, ALD FeO_x, ALD $MnFeO_x$, bare GDL, and a Pt-Ru-C benchmark. The inset shows the extent of the charge potential range for bare GDL and the inset uses the same axes (cell potential (V) vs. time (min)) as the full plot.

Table S5.5. Comparison of bifunctional energy efficiency for various bimetallic and bimetallic oxide ZAB air electrode catalysts in the literature.

Ref.	Catalyst Material	Preparation Method	Current Density (mA cm^{-2})	Discharge Potential (V)	Charge Potential (V)	Bifunctional Efficiency
This Work	$(Mn,Fe)_3O_4$	Direct ALD supercycle	20	1.15	2.20	52.5%
[54]	$MnO_x + CoO_x$	Direct ALD (two binary steps)	10	1.23	2.06	59.7%
[101]	Fe/Mn-N-C	Indirect hydrothermal/pyrolysis + ink	8	1.24	2.23	55.6%
[103]	Fe-doped MnO_2	Indirect hydrothermal + ink	25	0.81	2.68	30.2%
[102]	$MnFeO_x$/N-CNT	Direct sonication & impregnation	20	1.20	2.05	58.5%
[444]	FeCo-NGS	Indirect solution/pyrolysis + ink	10	1.15	1.94	59.4%
[445]	Co-MnO_2	Indirect molten salt/solution + ink	5	1.27	2.02	62.9%

CNT: carbon nanotube; N-CNT: nitrogen-doped CNT; NGS: nanoarray graphene sponge

5.5.4.2 Cycling Stability

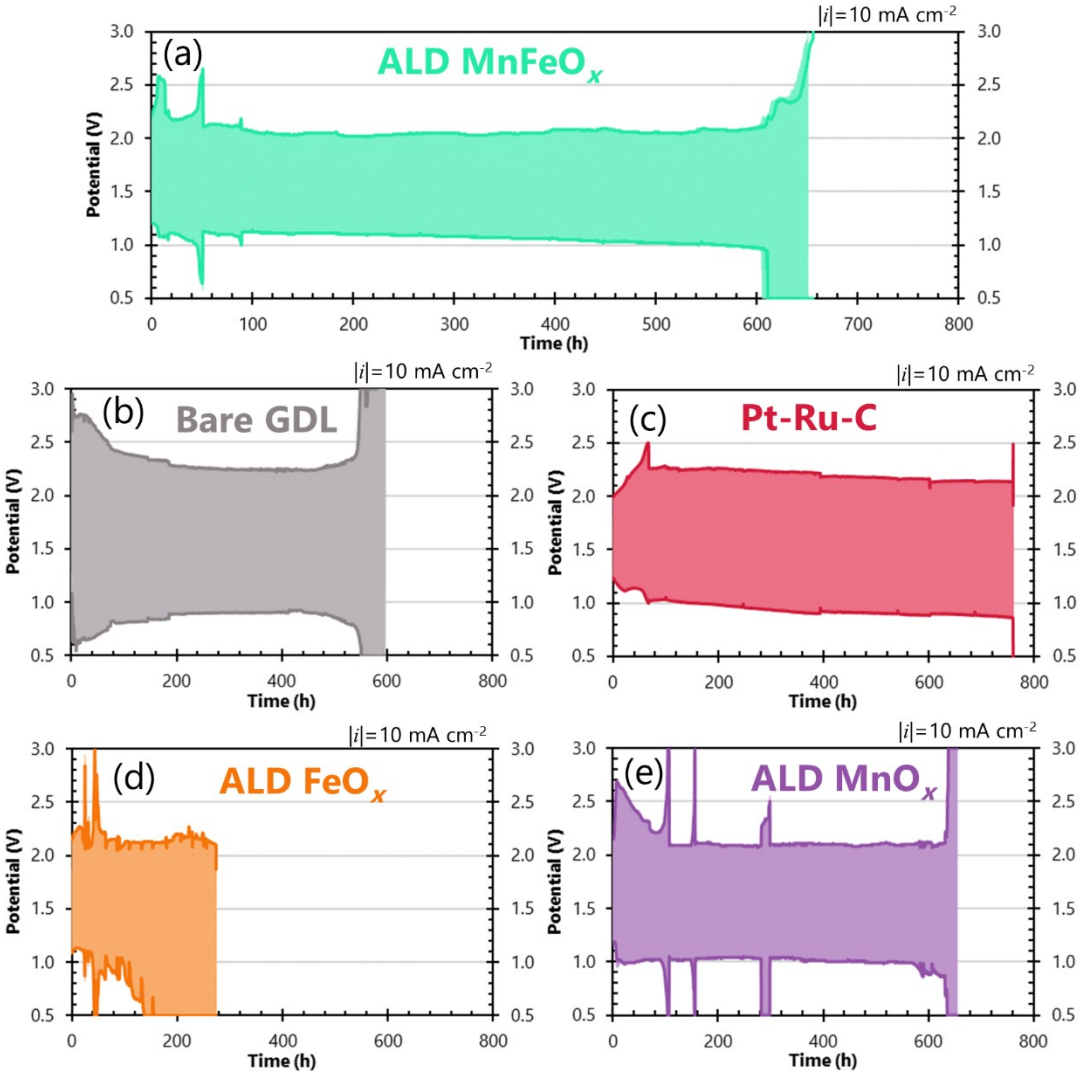

Figure S5.13. Bifunctional ZAB cycling of (a) ALD $MnFeO_x$, (b) bare GDL, (c) Pt-Ru-C, (d) ALD FeO_x, and (e) ALD MnO_x air electrodes. Charge and discharge at 10 mA cm^{-2} was conducted for 10 min periods with a rest period between charge and discharge.

Table S5.6. Bifunctional efficiency values calculated from charge and discharge potentials in Figure S5.13. The time values for column headings are rounded to the nearest 5 h, while cycle number values are exact. The last column features the percent retention of bifunctional efficiency, calculated as the efficiency at cycle 200 or 1565, divided by the initial efficiency at cycle 1.

Time (h)	**0**	**20**	**40**	**60**	**80**	**100**	**%Ret**
Cycle No.	**1**	**40**	**80**	**120**	**160**	**200**	**1st to 200th**
Bare GDL	38.9%	23.8%	24.9%	28.4%	34.0%	33.8%	86.8%
Pt-Ru-C	61.9%	53.2%	50.8%	44.9%	45.3%	45.3%	73.2%
ALD $MnFeO_x$	54.3%	50.9%	47.1%	52.1%	52.1%	54.1%	99.6%
ALD FeO_x	51.2%	49.3%	44.1%	39.8%	42.3%	45.0%	88.0%
ALD MnO_x	54.4%	37.9%	40.6%	44.0%	46.2%	34.6%	63.6%
Time (h)	**0**	**200**	**300**	**400**	**500**	**600**	**%Ret**
Cycle No.	**1**	**475**	**745**	**1020**	**1290**	**1565**	**1st to 1565th**
Bare GDL	38.9%	39.1%	40.1%	40.7%	37.7%	-	-
Pt-Ru-C	61.9%	43.4%	42.0%	42.1%	41.5%	41.0%	66.2%
ALD $MnFeO_x$	54.3%	54.5%	52.7%	50.5%	49.8%	46.0%	84.7%
ALD FeO_x	51.2%	22.7%	-	-	-	-	-
ALD MnO_x	54.4%	49.5%	49.5%	48.1%	47.1%	41.5%	76.3%

5.5.4.3 SEM of Catalyst Penetration into GDL

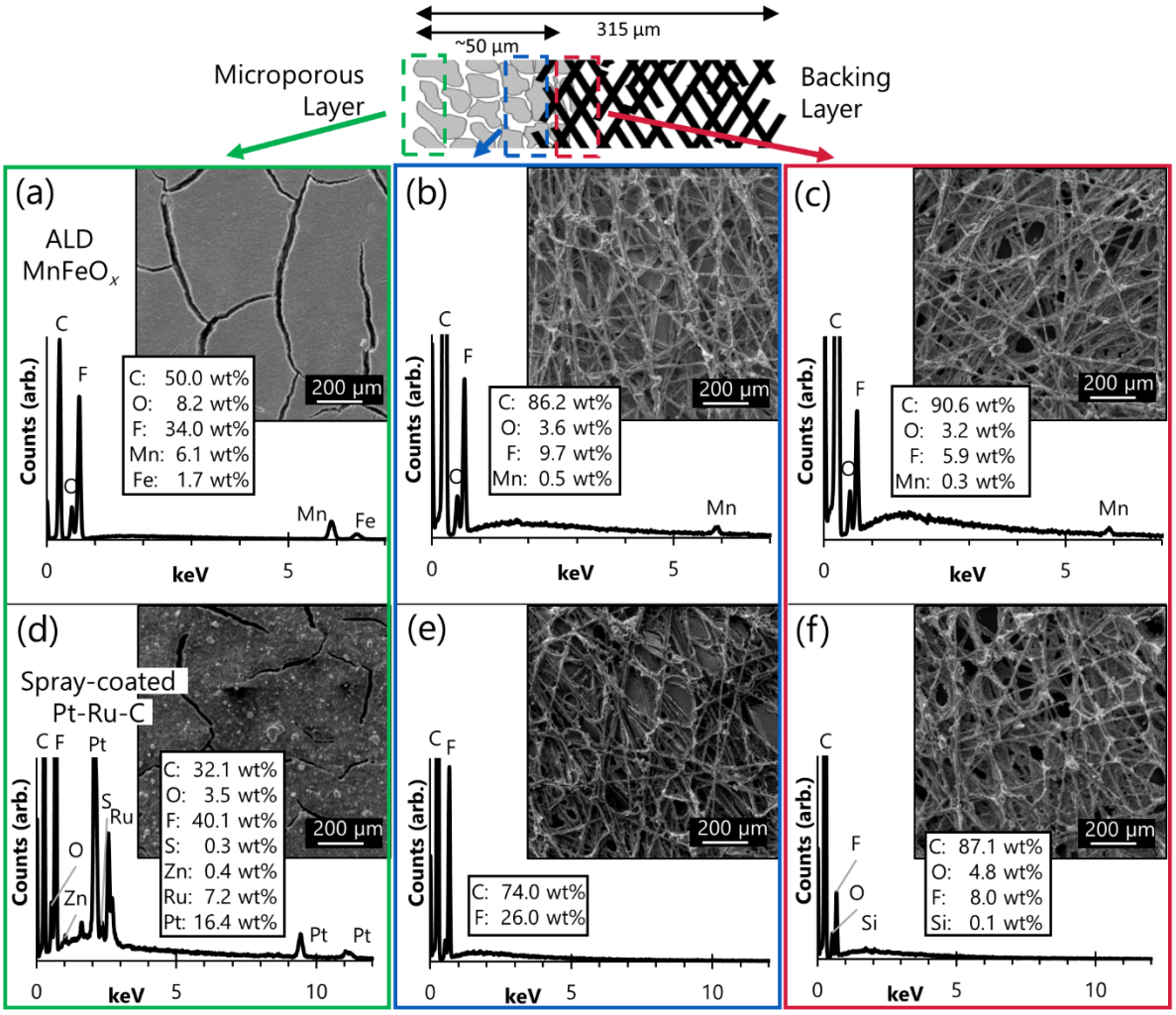

Figure S5.14. SEM and EDX analysis of the microporous and backing layer (areas shown by the upper figure) for (a-c) ALD MnFeO$_x$, and (d-f) spray-coated Pt-Ru-C.

5.5.5 Post-Cycling Characterization of $MnFeO_x$

5.5.5.1 STEM

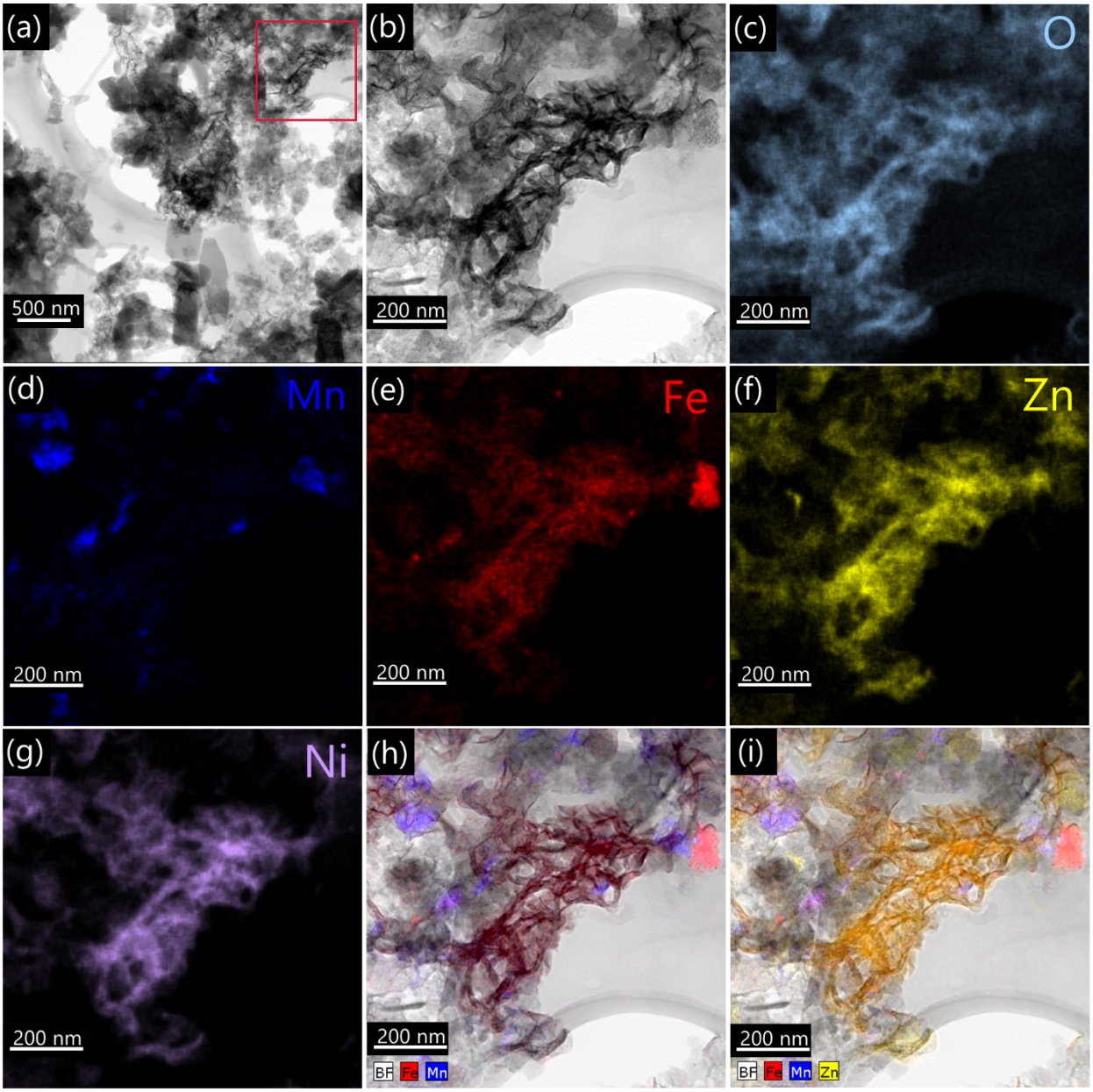

Figure S5.15. STEM characterization of an annealed $MnFeO_x$ coating on GDL after cycling. (a) BF image, (b) magnified BF image of the indicated area in (a), EDX mapping of (c) O, (d) Mn, (e) Fe, (f) Zn, and (g) Ni. Overlapping maps of (h) Fe and Mn, and (i) Fe, Mn, and Zn overlain on the BF image from (b).

6. Atomic Layer Deposition of Zn-Based Transition Metal Oxides Catalysts for Zn-Air Batteries

6.1 Introduction

Large scale energy storage technologies, such as pumped hydro or flywheels, are required to integrate intermittent renewable energy sources (such as wind or solar) into the consistent and on-demand electrical energy grid.[11] Another energy storage technology that can be used for this application are electrochemical batteries. These are versatile, easily scalable, and do not require large land use. The landscape of rechargeable electrochemical batteries has been dominated by Li-ion batteries for the past decade. Yet, Li-ion batteries have several key drawbacks, notably high cost and high safety risks, limiting their application.[446,447] An alternative battery chemistry with great potential for grid-scale energy storage is Zn-air. Using the much more abundant components of Zn and O_2, these batteries boast higher theoretical energy density, lower cost, and safer operation compared with Li-ion cells.[41] However, their implementation has been limited by low cycle life, poor efficiency, and low power outputs.[58] A major culprit to these factors is the slow kinetics of the oxygen reactions at the air electrode. A large overpotential is required to drive the oxygen reduction reaction (ORR) during battery discharge and a similar overpotential is required for the oxygen evolution reaction (OER) during recharge. Various catalytic materials have been investigated to reduce the overpotentials at the air electrode, with precious metals and their oxides, such as Pt or RuO_2, demonstrating some of the best improvements. Of course, these precious metal catalysts reduce the practicality of the Zn-air batteries (ZABs) and also do not have satisfactory stability during battery cycling.[32]

A popular class of alternative catalysts include earth-abundant transition metal oxides, such as MnO_x or FeO_x. Resources for these materials are much greater, their cost is much lower, and they often provide improved cycling performance over precious metal catalysts.[42] Yet, the longevity of rechargeable ZABs using these catalyst is still insufficient for practical use. One strategy to improve the efficiency and lifetime of transition metal oxide catalysts is to combine multiple single metal oxides together into bimetallic or trimetallic oxides.[42] While ZnO_x does not show very much inherent catalytic ability towards the oxygen reactions, the incorporation of Zn into

the catalyst material during ZAB cycling has been speculated by several researchers.[54,108,358] During discharge, the metallic Zn electrode dissolves into the battery electrolyte and these dissolved Zn ions can diffuse to the air electrode side. Furthermore, Zn ions are often intentionally added to ZAB electrolytes to help facilitate the recharge reaction at the Zn electrode.[32] As a result, Zn incorporation into the air electrode and the catalyst material within is quite possible. In fact, this integration of Zn into the oxide catalyst during cycling could possibly be responsible for the long-term stability at the air electrode documented by some researchers.[108,109,358] Therefore, the investigation of Zn-based transition metal oxide catalysts may unlock highly stable air electrode catalysts.

Zn-based catalysts are not commonly found in the ZAB literature, except for the relatively common $ZnCo_2O_4$. This catalyst has been explored for OER,[110–112] ORR,[107,448] and bifunctional ZABs.[105,106] Metal organic frameworks have also been explored, which frequently feature Zn doping in the N-doped carbon structure.[449,450] In a couple reports, multiple different transition metal oxide catalysts were simultaneously developed and tested, but the Zn-based catalysts were the least catalytically active contenders.[451,452] Nevertheless, Aasen *et al.* used a simple sonication method to synthesize several Zn-based oxides using Mn, Fe, Co, and/or Ni. They found that $ZnCo_xO_y$, $ZnMn_xO_y$, and $ZnMn_xCo_yO_z$ catalysts performed better in half cell ORR than their non-Zn counterparts of Co_3O_4, Mn_3O_4, and $MnCo_xO_y$, with the $ZnMn_xO_y$ and $ZnCo_xO_y$ providing improved OER performance as well. The last two bimetallic oxides also showed improvements in cycling behaviour over their non-Zn equivalents.[109] As well, McDougall *et al.* investigated the addition of Zn to a Ni-Mn-Co oxide with the aim of improving the cycling performance in a ZAB. This Zn addition improved the stability and OER potentials during bifunctional cycling.[358] Lastly, Costa *et al.* inadvertently formed a $ZnCo_2O_4$ catalyst when they electrodeposited W-Co and cycled the material in a KOH and ZnO electrolyte. The W-Co catalyst immediately oxidized when exposed to the air, forming a W-Co oxide. The W oxide was unstable in the electrolyte and was instead replaced with Zn, forming the $ZnCo_2O_4$ material responsible for the bifunctional activity displayed, which was more stable during cycling than a Pt-Ru-C benchmark catalyst.[108]

Originally developed for depositing ZnS films for electroluminescent flat-panel displays,[53] atomic layer deposition (ALD) is a bottom-up synthesis method that deposits coatings layer by layer at the atomic level. While it has many similarities to chemical vapour deposition, the

precursor and reactant steps in ALD are separated by inert gas purges, which allow ALD to avoid gas phase reactions and improve the step coverage during film growth.[52] This benefits the application of ALD towards depositing catalytic films on the air electrode of ZABs. The conformal ALD film does not plug porosity at the air electrode and can be deposited on high surface area substrates to increase the area for catalysis.[49] As well, the nature of gas-based delivery allows ALD to coat deep within the air electrode substrate, reducing efficiency losses at the air electrode during extended ZAB cycling.[54] The deposition of ZnO_x is a well behaved ALD process and can easily be incorporated into existing ALD processes for transition metal oxide catalysts.[157,227,360,453] Intertwining two or more ALD processes together, with alternating layers of each ALD process, is known as an ALD supercycle, which is repeated like any other ALD cycle to deposit films of a desired thickness.[158] The number of subcycles of process A deposited before process B begins, and the number of subcycles for process B before repeating process A, define the bilayer thickness and cycle ratio of a supercycle process.[55] These parameters can be adjusted to modify the chemistry of the deposited film.

The deposition of bimetallic Zn-based oxides via ALD in the literature includes Zn oxides of Al, Co, Fe, Ga, Mg, Mn, Sn, Ta, Ti, Zr, Cd, and Hf.[55] Furthermore, trimetallic oxides of $InGa_xZn_yO_z$, $InZn_xSn_yO_z$, $ZnAl_xZr_yO_z$, $ZnMg_xAl_yO_z$, and $ZnTi_xZr_yO_z$ have also been deposited.[55,454,455] Most of these oxides, however, are deposited for semiconductor applications. For $ZnMn_xO_y$ and $ZnFe_xO_y$ chemistries, only one case of ALD has been recorded for either material. For $ZnMn_xO_y$, doping of ZnO with Mn was investigated, but a thorough investigation of the film properties was not performed.[399] For $ZnFe_xO_y$, binary ALD processes for Fe_2O_3 and ZnO were performed sequentially and then the deposit was annealed to produce a homogenous film. The authors attempted a supercycle process, but ultimately could not yield the desired $ZnFe_2O_4$ film in this way.[254] To the best of the author's knowledge, no work in the literature has investigated $ZnMn_xFe_yO_z$ depositions.

In this work, a ZnO_x ALD process is appended to three previously developed ALD processes for air electrode catalysts. An optimization process is performed for each Zn-based oxide to fine tune the ALD chemistry for the most catalytically active film. The optimized $ZnFe_xO_y$, $ZnMn_xO_y$, and $ZnMn_xFe_yO_z$ coatings are then examined in scanning electron microscopy (SEM) to probe the elemental composition of the deposits. Further analysis of the $ZnMn_xFe_yO_z$ coating

includes SEM cross sectional analysis and transmission electron microscopy (TEM) characterization. The Zn-Fe, Zn-Mn and Zn-Mn-Fe oxides are then electrochemically tested as air electrode catalysts in ZABs and are directly compared with their Fe, Mn and Mn-Fe oxide counterparts to investigate whether the addition of Zn provides any bifunctional activity increase or improvement in cycling stability.

6.2 Experimental

6.2.1 ALD

All ALD films were deposited in a commercial hot-walled reactor (Kurt J. Lesker Company, ALD 150L) at a substrate temperature of 150 °C. Inert gas (Ar, Linde Canada Inc., 99.999%) continuously flowed through the system at ~1 Torr and a showerhead system delivered precursor reactants to the substrate surface. A 600 W inductively coupled radiofrequency remote plasma system provided plasma reactants using either O_2 (Linde Canada Inc., 99.993%) or forming gas (FG: 5% H_2, balance N_2; Linde Canada Inc.). An ampoule of distilled water, kept at room temperature (~22 °C) with 100 °C delivery line and ALD valve temperatures, served as the H_2O reactant. The Fe precursor (ethylferrocene, EF, STREM Chemicals, Inc., 98%) was heated to 80 °C with ALD valve and delivery line temperatures of 100 and 110 °C, respectively. The Mn precursor (bis(ethylcyclopentadienyl)manganese, $(EtCp)_2Mn$), STREM Chemicals, Inc., 98%) was also maintained at 80 °C with 100 and 110 °C ALD valve and delivery line temperatures, respectively. The Zn precursor (diethylzinc, DEZ, Sigma-Aldrich) was kept at ~50 °C with ALD valve and delivery lines temperatures of 70 and 110 °C, respectively. The ALD timing sequence for the EF and O plasma binary process (denoted as FeO_x) was 0.25/5/1/20/5 (EF dose/Ar purge/pre-plasma O_2 flow/O plasma/Ar purge).[453] The ALD timing sequence for the $(EtCp)_2Mn$ and FG plasma/H_2O binary process (denoted as MnO_x) was 4/4/15/10/1.5/30 ($(EtCp)_2Mn$ dose/ampoule charge/Ar purge/FG plasma/H_2O dose/Ar purge).[453] The ALD timing sequence for the DEZ and H_2O binary process (denoted as ZnO_x) was 0.04/8/0.5/10 (DEZ dose/Ar purge/H_2O dose/Ar purge).[456,457] The substrates for ALD were pieces of a carbon paper gas diffusion layer (GDL, SIGRACET© 39BB, SGL Carbon) and a Si(100) wafer (University Wafers, 525 μm p-type single side polished). A 60 s O plasma treatment preceded all depositions to prepare the surface for ALD.[346,374,456] The GDL material was used for electrochemical investigation of the deposited films, while the Si(100) substrate enabled *in situ* spectroscopic ellipsometry (SE) of

the growing ALD films. SE results from the spectrometer (J.A. Woollam Co., Inc., M-2000DI) were analyzed in CompleteEase (J.A. Woollam Co., Inc., ver. 4.48) using Tauc Lorentz oscillators to model the ALD films.

6.2.2 Electrochemical Characterization

Half cell linear sweep voltammetry was employed at room temperature (~22 °C) to study the ORR and OER overpotentials at the air electrode. In this setup, the GDL substrate, coated with catalyst material, was submerged in a 1 M KOH (Fisher Chemical, certified ACS) electrolyte, purged with O_2 gas (Linde Canada Inc., 99.993%) flowing at a rate of 40 standard cubic cm^3 min^{-1}. This three-electrode setup featured a Pt coil counter electrode, a Hg/HgO reference electrode (0.098 V vs. SHE), and the GDL material as the working electrode. The onset potential in half cell was defined as the working electrode potential required to obtain |10| mA cm^{-2} of current flow. Onset potential values above the equilibrium value (0.303 V vs. Hg/HgO) represent an OER overpotential while potentials values below the equilibrium represent an ORR overpotential. Full cell galvanostatic rate testing was also employed at room temperature (~22 °C), but with the ALD coated GDL acting as the air electrode in a homemade ZAB cell. This two-electrode setup had ambient O_2 from the atmosphere enter the cell naturally through the GDL air electrode, which also acted as the working electrode. The combined counter and reference electrode was a 0.5 mm thick strip of as-received Zn foil (McMaster-Carr, 99%). A 3D printed, homemade ZAB cell was used to secure the air electrode and Zn electrode with a reservoir of a 6 M KOH and 0.25 M ZnO (Fisher Chemical, certified ACS) electrolyte (see Appendix B).[408] Rate testing was conducted at |2|, |5|, |10|, and |20| mA cm^{-2} for 10 min each. Potential values above the equilibrium value (1.650 V vs. $Zn/Zn^{++}_{pH=14}$) represent ZAB charging, while potentials below the equilibrium represent discharge. The operating voltages at |20| mA cm^{-2} were used as criteria to evaluate the bifunctional efficiency for each sample, which was calculated as the discharge potential divided by the charge potential (at current densities of -20 mA cm^{-2} and +20 mA cm^{-2}, respectively). Both half cell and full cell tests were conducted using a Biologic VSP potentiostat, while an Arbin Instruments (LBT20084) battery cycler was used to conduct long-term cycling tests. The long-term cycling tests featured the full cell setup with additional provisions to facilitate electrolyte management. One cycle featured 10 min of galvanostatic discharge at -10 mA cm^{-2}, an open-circuit rest period, 10 min of galvanostatic

charge at +10 mA cm^{-2}, and one more open-circuit rest period before repeating the cycle. For the first 200 cycles, a 5 min rest period was employed, while the remaining cycles after 200 had only a 1 min rest period.

Individual coatings of ZnO_x, FeO_x, and MnO_x, as well as a bimetallic $MnFe_xO_y$ film (referred to as $MnFeO_x$), were also deposited on GDL as comparison samples using their respective ALD processes.[157,360,453,458] The FeO_x process featured a 1 nm MnO_x buffer layer to protect the GDL substrate during deposition and the FeO_x film was only deposited to 10 nm in thickness.[360] The ZnO_x, MnO_x, and $MnFeO_x$ films were 40 nm in thickness. Additionally, a precious metal comparison was created by spray-coating GDL substrates with a mixture of Pt-Ru-C catalyst (Alfa Aeser; 40 wt% Pt, 20 wt% Ru, balance carbon black), reagent alcohol (Fisher Chemical, histological grade), H_2O, and polytetrafluoroethylene (PTFE) binder (Chemours Teflon™ PTFE DISP 30). The mass loading of the Pt-Ru-C catalyst was ~1 mg cm^{-2} while the mass loading for all ALD samples was ~50 μg cm^{-2}. An annealing treatment at 300 °C for 30 min was performed for all samples except for bare GDL. During the optimization process for the Zn-based oxides, samples without the annealing treatment (referred to as unannealed) were also electrochemically characterized to study the benefit of the annealing process.

6.2.3 Materials Characterization

SEM and energy dispersive X-ray (EDX) analysis were conducted using a TESCAN Vega3 tabletop SEM operating at 20 kV and a 15 mm working distance. Plan view semi-quantitative EDX results were the average of three different areas while the cross sectional EDX linescan was a representative example of analysis from three different areas. A TEM sample was prepared by drop-casting a suspension of ALD coated GDL particles in reagent alcohol onto a carbon coated, Cu TEM grid (Ted Pella, Inc., Prod #01881-F). TEM/scanning TEM (STEM) and EDX mapping were performed using a Tecnai Osiris TEM/STEM operating at 200 kV. A selected area diffraction (SAD) pattern was obtained in TEM mode for crystal structure analysis.

6.3 Results and Discussion

6.3.1 Optimization of $ZnFe_xO_y$ Supercycle Films

Previous work on ALD supercycle films (Chapter 5) revealed that bilayer periods in multiples of 10 are a good starting point in the optimization of mixed element film chemistry.[453] Accordingly, bimetallic oxides of $ZnFe_xO_y$ were initially deposited using supercycle schemes of 30:10, 20:10, 10:10, 10:20, and 10:30, which span Zn:Fe atomic ratios of 75% to 25%. The first number in this nomenclature represents the number of ZnO_x cycles, while the second number represents the number of FeO_x cycles, all within one supercycle. Supercycles were repeated as required to reach approximately 10 nm in total thickness. Plots of the half cell and full cell performance for each of the initial $ZnFe_xO_y$ films are featured in Figure 6.1a and Figure 6.1b, respectively. Half cell metrics (Figure 6.1a) reveal that 30:10 and 20:10 films, whether annealed or unannealed, are inferior to 10:10, 10:20, or 10:30 films. The OER potentials (above the x-axis) for the former two films are higher than the latter three films, representing larger overpotentials to reach the same current density and thus inferior catalysts. The 30:10 and 20:10 films have a larger proportion of ZnO_x, which is not very catalytically active towards OER as compared with FeO_x. The annealing treatment (darker shaded bars) yields slightly higher OER potentials for the 10:10, 10:20, and 10:30 films, while the ORR potentials (below the x-axis) are also slightly higher for the annealed films. In this case, higher ORR potential represents a lower overpotential and thus a better catalyst. Overall, annealing appears to improve ORR performance at the expense of OER performance. Based on having the smallest voltage gap in half cell, the unannealed 10:30 $ZnFe_xO_y$ film is the most bifunctionally active towards OER/ORR. Full cell results (Figure 6.1b) for the above films were very similar to each other but, generally, the annealing treatment again improved discharge (below the x-axis) performance while negatively impacting the charge (above the x-axis) performance. To evaluate the best bifunctional catalyst in this grouping, bifunctional efficiency values were calculated as the discharge potential divided by the charge potential. Echoing the conclusion from half cell, the unannealed 10:30 film shows the highest catalytic activity.

The next stage of $ZnFe_xO_y$ optimization kept the ratio of ZnO_x:FeO_x at 10:30 but modified the bilayer thickness from 20:60 to 1:3 (Figure 6.1c). Half cell results for the films in Figure 6.1c are somewhat mixed, with the annealed film of 1:3 far superior to its unannealed counterpart, while

the unannealed film of 3:9 has a smaller voltage gap than the annealed 3:9 film. The annealed versions of 20:60 and 5:15 have the best OER performance, while the annealed 1:3 film is the best ORR catalyst. The full cell results (Figure 6.1d), featuring efficiency values, provide a quantitative measure to compare films. In this case, the annealed 1:3 film is the most bifunctionally active of all the $ZnFe_xO_y$ films. A new full cell configuration was employed for Figures 6.1d and 6.1f (refer to Appendix B). Since the annealed version of 10:30 $ZnFe_xO_y$ provided the best performance in Figure 6.1b, only it was retested in the new cell configuration and is shown in Figure 6.1d. As a last step to the $ZnFe_xO_y$ optimization process, the thickness of the 1:3 $ZnFe_xO_y$ film was increased from 10 nm to 30 nm. A 40 nm thick sample was prepared but the excessive amount of O plasma required to deposit a 40 nm thick FeO_x-based film deteriorated the air electrode to such an extent that electrolyte completely flooded the air electrode, making the 40 nm film impractical for a ZAB. Regardless, the 20 nm and 30 nm 1:3 $ZnFe_xO_y$ films are inferior to the 10 nm $ZnFe_xO_y$ film in both half cell (Figure 6.1e) and full cell (Figure 6.1f). Ultimately, the annealed 10 nm thick 1:3 $ZnFe_xO_y$ film was selected for further analysis in SEM and long-term cycling and this representative $ZnFe_xO_y$ sample is simply referred to, hereafter, as $ZnFeO_x$.

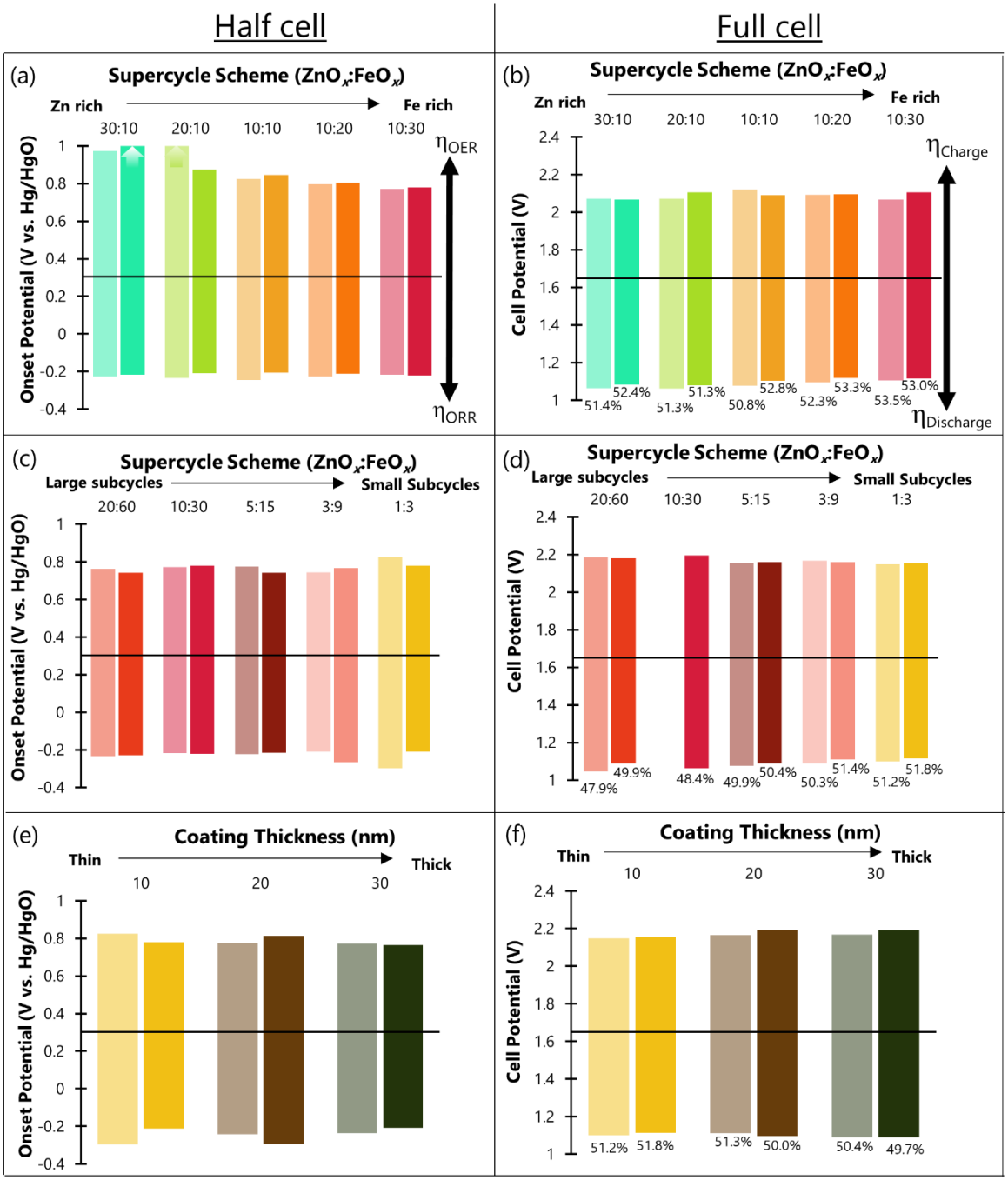

Figure 6.1. Optimization process flow for the $ZnFe_xO_y$ supercycle recipe. (a) Half cell and (b) full cell electrochemical results for various ZnO_x:FeO_x ratios using subcycles that are multiples of 10. (c) Half cell and (d) full cell electrochemical results for a constant 1:3 ZnO_x:FeO_x ratio at different subcycle values. (e) Half cell and (f) full cell electrochemical results for 1:3 ZnO_x:FeO_x supercycle films at different coating thicknesses. All films were approximately 10 nm in thickness unless otherwise indicated. Percentages in (b), (d), and (f) are bifunctional efficiencies.

6.3.2 Optimization of $ZnMn_xO_y$ Supercycle Films

Similar to the initial depositions for the $ZnFe_xO_y$ films, bilayer periods in multiples of 10 were explored for $ZnMn_xO_y$ films, each approximately 10 nm in thickness. In addition to the initial supercycle ratios, a $ZnMn_xO_y$ supercycle of 3:27 was also explored, influenced by the work of Aasen *et al.* in which the most active $ZnMn_xO_y$ catalyst in their work was revealed to exhibit a 1:9 Zn:Mn ratio according to SEM EDX analysis.[109] A 3:27 supercycle scheme was selected to obtain a bilayer period of 30, which is also a multiple of 10. Figure 6.2a displays the half cell results of the preliminary films, while Figure 6.2b includes the full cell results. Surveying Figure 6.2a, the sample with the lowest onset potential for ORR is the annealed 3:27 film. For OER, the annealed 3:27 film is the most active with the lowest onset potential. The full cell results of Figure 6.2b show that the annealed 3:27 film has the lowest discharge potential, but unlike the half cell, full cell results indicate that the 3:27 film does not have the smallest charge overpotential and instead the annealed 20:10 sample is the best sample for charge. Using the bifunctional efficiency values calculated in Figure 6.2b, both the 20:10 and 3:27 samples, in the annealed state, provide the highest efficiency at 54.1%. However, half cell results (Figure 6.2a) for the annealed 20:10 sample are much worse than for the annealed 3:27 film. Thus, taking both half cell (Figure 6.2a) and full cell (Figure 6.2b) results together, the annealed 3:27 film is the best $ZnMn_xO_y$ catalyst and was selected as the basis for further optimization.

Maintaining the same ratio between ZnO_x and MnO_x cycles, $ZnMn_xO_y$ films of 6:54, 2:18, and 1:9 were deposited, and all were ~10 nm in thickness. The half cell and full cell results of the films, compared against the 3:27 sample, are shown in Figures 6.2c and 6.2d, respectively. Similar to the second set of $ZnFeO_x$ samples in Figure 6.1d, only the annealed 3:27 film is shown in Figure 6.2d due to a change in full cell design (refer to Appendix B). Based on the half cell results (Figure 6.2c), the annealed film of 1:9 provides the lowest ORR and OER onset values, demonstrating the smallest bifunctional voltage gap. As the subcycle values are increased in Figure 6.2c (from right to left), the ORR and OER potential gap widens slightly. This trend suggests that the annealed 1:9 sample, with the smallest subcycles and smallest possible bilayer thickness for a cycle ratio of 1:9, is the optimal supercycle for the $ZnMn_xO_y$ process. A similar conclusion was reached for the $ZnFeO_x$ process, where the smallest subcycle values of 1:3 results in the best catalyst. The full cell results for the second set of $ZnMn_xO_y$ films (Figure 6.2d) are in

agreement with the half cell results, with the annealed 1:9 sample providing the highest bifunctional efficiency at 46.9%. Thicker ALD films (up to 40 nm) were also explored for the 1:9 $ZnMn_xO_y$ sample, but the results (not shown) did not provide any improvement in the electrochemical performance. The 10 nm thick annealed 1:9 $ZnMn_xO_y$ sample was selected for further study in long duration ZAB cycling and is simply referred to, hereafter, as $ZnMnO_x$.

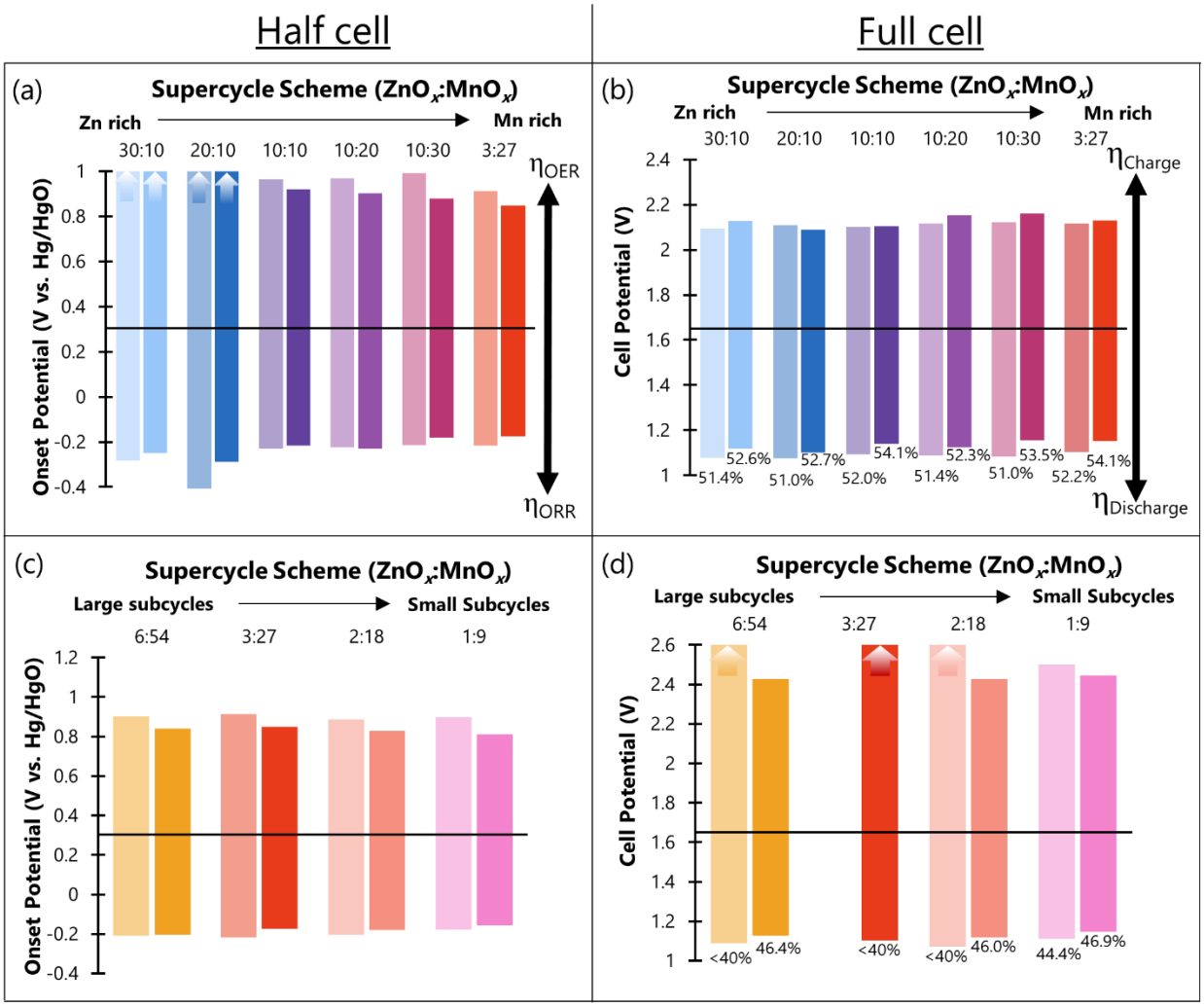

Figure 6.2. Optimization process flow for the $ZnMn_xO_y$ supercycle recipe. (a) Half cell and (b) full cell electrochemical results for various ZnO_x:MnO_x ratios using subcycles that are multiples of 10, with an additional 3:27 supercycle format. (c) Half cell and (d) full cell electrochemical results for a constant 1:9 ZnO_x:MnO_x ratio at different subcycles values. All coatings were approximately 10 nm thick. Percentages in (b) and (d) are bifunctional efficiencies.

6.3.3 Optimization of $ZnMn_xFe_yO_z$ Supercycle Films

The ALD facility used to deposit binary oxide films of $ZnMn_xO_y$ and $ZnFe_xO_y$ was easily adapted to deposit ternary oxide films of $ZnMn_xFe_yO_z$. The challenge with ternary oxide films, however, is optimizing the exponentially larger number of permutations for the chemistry of the ALD film. Subcycles that are multiples of 10 were initially employed and based upon the successes of a 30:10 mixture for $MnFeO_x$ and 10:30 for $ZnFeO_x$, five initial stoichiometries of 10:10:10, 30:10:10, 10:30:10, 10:10:30, and 10:30:30 were devised for $ZnMn_xFe_yO_z$ supercycle development, with all deposited to ~10 nm in thickness. The half cell and full cell results of the initial five $ZnMn_xFe_yO_z$ samples are shown in Figures 6.3a and 6.3b, respectively. Half cell performance (Figure 6.3a) indicates that the most ORR active ternary oxide catalyst is the annealed 10:30:10 film, with the annealed 10:30:30 and 30:10:10 a close second and third, respectively. For OER, on the other hand, the unannealed 10:10:30 and 10:30:30 films have the lowest onset potentials. Considering the combined ORR-OER voltage gap, the best bifunctional film is the unannealed 10:30:30 sample, with the annealed 10:10:30 sample a close second. Full cell results (Figure 6.3b) provide a different ranking among the initial $ZnMn_xFe_yO_z$ films. The annealed 30:10:10, 10:30:10, and 10:30:30 films, as well as the unannealed 10:30:10 and 10:30:30 films, all reached a 2.5 V cutoff value set during charge testing at 20 mA cm^{-2}. Thus, while the true bifunctional efficiency of these samples cannot be ascertained, they are likely less than 40%. Of the remaining samples that did not reach the 2.5 V cutoff, both the unannealed and annealed 10:10:30 samples provide the best full cell performance, with bifunctional efficiency values of 48.3% and 48.4%, respectively.

Further optimization of the trimetallic oxide supercycle chemistry was realized through three additional samples. Since the $ZnMnO_x$ 3:27 film was among the best initial ALD cycle ratios explored, the subcycles for ZnO_x were maintained at a value of 3 for the last three supercycle schemes. During previous optimization of the bimetallic $MnFeO_x$ process (Chapter 5),[453] a cycle ratio of 30:10 for MnO_x:FeO_x resulted in the best overall bifunctional catalyst. Therefore, a 3:30:10 cycle ratio was explored for the $ZnMn_xFe_yO_z$ process. Based only on the half cell results of the initial set of $ZnMn_xFe_yO_z$ samples (Figure 6.3a), the lowest voltage gap was associated with the unannealed 10:30:30 sample and, therefore, a 3:30:30 $ZnMn_xFe_yO_z$ sample was also explored. Lastly, the full cell results from the initial set of $ZnMn_xFe_yO_z$ samples (Figure 6.3b)

indicate that a cycle ratio of 10:10:30 produces a film with the highest bifunctional efficiency. The aforementioned $MnFeO_x$ optimization process also showed that a MnO_x:FeO_x cycle ratio of 10:20 produces films almost as efficient as the 30:10 ratio, with the 10:20 films yielding the second highest bifunctional efficiency in that study (Figure 5.3 in Chapter 5).[453] Taking these last two points together, a 3:10:20 $ZnMn_xFe_yO_z$ sample was also investigated. The half cell and full cell results of the final three $ZnMn_xFe_yO_z$ films, all ~10 nm in thickness, are displayed in Figures 6.3c and 6.3d, respectively. The half cell ORR onsets of the three film chemistries, in both the unannealed and annealed states, are all fairly similar at ~0.2 V vs. Hg/HgO (Figure 6.3c). For the unannealed 3:30:30 sample, the OER onset is much higher than the other films investigated. Based on bifunctional voltage gap in half cell, the unannealed 3:30:10 sample is the best sample in Figure 6.3c. However, full cell results in Figure 6.3d show that the unannealed 3:30:10 sample reaches the 2.5 V charge cut off value and is not as bifunctionally active in a full ZAB cell. The annealed 3:10:20 sample is instead the best bifunctional catalyst at 48.9% efficiency. Comparing this to the previous set of $ZnMn_xFe_yO_z$ samples (Figure 6.3b), the annealed 3:10:20 sample is slightly superior to the annealed 10:10:30 sample at 48.4% efficiency. The results of the bimetallic Zn oxide optimizations for $ZnFeO_x$ and $ZnMnO_x$ indicate that thicker films do not translate into performance upgrades. Therefore, thicker films were not investigated for the $ZnMn_xFe_yO_z$ process and for final performance evaluation during ZAB cycling, the 10 nm thick annealed 3:10:20 film was chosen as the representative $ZnMn_xFe_yO_z$ sample, and is referred to, hereafter, as $ZnMnFeO_x$.

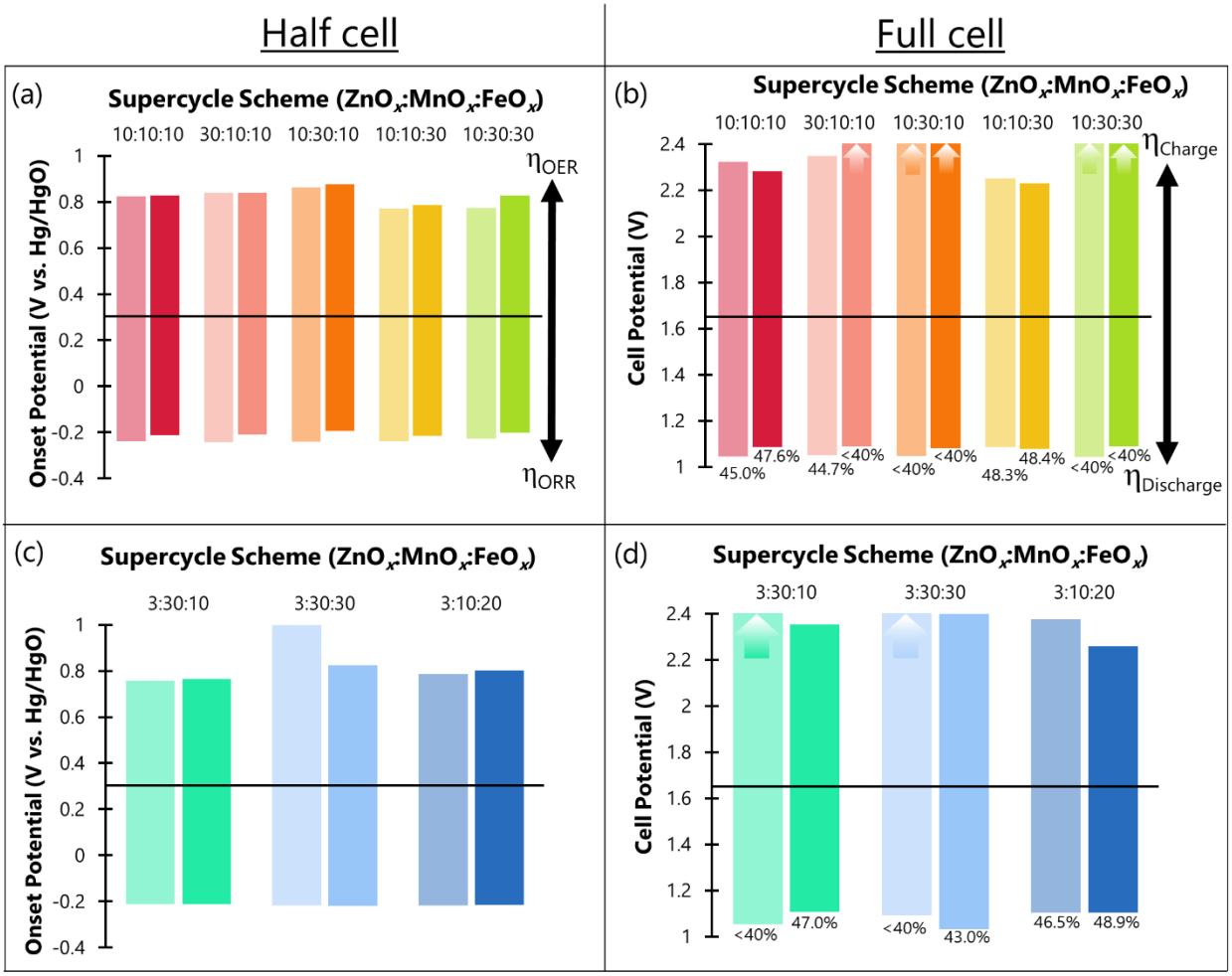

Figure 6.3. Optimization process flow for the $ZnMn_xFe_yO_z$ supercycle recipe. (a) Half cell and (b) full cell electrochemical results for various ZnO_x:MnO_x:FeO_x ratios using subcycles of either 10 or 30. (c) Half cell and (d) full cell electrochemical results for three additional $ZnMn_xFe_yO_z$ supercycle formats. All coatings were approximately 10 nm in thickness. Percentages in (b) and (d) are bifunctional efficiencies.

6.3.4 SEM, EDX, and Compositional Analysis of $ZnFeO_x$, $ZnMnO_x$, and $ZnMnFeO_x$

Since a supercycle process is comprised of two or more binary ALD processes repeated at fixed intervals, a simple estimate of the final film composition can be predicted with the rule of mixtures using the characteristics of the individual binary ALD processes. For example, a supercycle process is comprised of *v* cycles of ALD process *I* and *w* cycles of ALD process *II*. The coating material deposited via only process *I* is known as material A, while the film deposited by via only process *II* is known as material B. The rule of mixtures, applied to ALD

supercycles, predicts that the final film composition is a weighted average of materials A and B, with the weighting parameters being the growth rates (g) of processes *I* and *II*, the densities (ρ) of materials A and B, and the overall cycle ratio of the supercycle process (Equation 6.1).[55]

$$Atomic\ composition\ (\%\ of\ A) = \frac{\rho_A g_I (v/(v+w))}{\rho_A g_I (v/(v+w)) + \rho_B g_{II} (w/(v+w))} \times 100\% \quad (6.1)$$

In this work, both binary films are oxides (MO_x) which share a common non-metallic element. Equation 6.1 can be modified to provide the relative amounts of metallic components only, ignoring the contribution from oxygen. The metal fractions (f) for the binary oxide materials are added to Equation 6.1 to yield Equation 6.2.

$$Atomic\ composition\ (\%\ of\ M_A) = \frac{\rho_A g_I (v/(v+w)) f_A}{\rho_A g_I (v/(v+w)) f_A + \rho_B g_{II} (w/(v+w)) f_B} \times 100\% \quad (6.2)$$

The growth rates of the FeO_x and MnO_x binary processes are published in previous literature (also in Chapter 3),[157,360] while the growth rate for ZnO_x was measured in this work as 1.78 Å cycle^{-1}. Density values for Fe_2O_3, Mn_3O_4, and ZnO were employed based on the phase identification from previous reports for these binary ALD processes.[54,360,370,456] An example calculation of the amount of Fe in $ZnFeO_x$ is shown in Equation 6.3. The rule of mixtures (Equation 6.2) can easily be extended to a three part supercycle and was also used to predict the metallic composition of the trimetallic $ZnMnFeO_x$ film. The predicted metallic compositions for the $ZnFeO_x$, $ZnMnO_x$, and $ZnMnFeO_x$ films are shown in Table 6.1.

$$at\%\ Fe\ in\ ZnFeO_x = \frac{\left(5.25\frac{g}{cm^3}\right)\left(0.09\frac{\text{Å}}{cy}\right)(3/4)(2/5)}{\left(5.25\frac{g}{cm^3}\right)\left(0.09\frac{\text{Å}}{cy}\right)(3/4)(2/5) + \left(5.6\frac{g}{cm^3}\right)\left(1.78\frac{\text{Å}}{cy}\right)(1/4)(3/7)} \times 100\% = 10.2\ at\%\ Fe \quad (6.3)$$

Table 6.1. Predicted atomic compositions of Zn, Mn, and Fe in $ZnFeO_x$, $ZnMnO_x$, and $ZnMnFeO_x$ based on the rule of mixtures.

Supercycle Scheme						Composition (at%)		
Zn	**:**	**Mn**	**:**	**Fe**		**Zn**	**Mn**	**Fe**
1			:	3		89.8	-	10.2
1	:	9				18.8	81.2	-
3	:	10	:	20		35.1	56.0	8.9

SEM of the GDL material with the three Zn-based ALD oxides is shown in Figures 6.4a-c. Similar to previous work with ALD on GDL substrates, the overall surface appearance of GDL at low magnification is not modified by ALD.[360] EDX analysis of the three ALD coatings from Figures 6.4a-c is displayed in Figure 6.4d. The $ZnFeO_x$ coating, deposited with a ZnO_x:FeO_x cycle ratio of 1:3, is predicted as 89.8 at% Zn and 10.2 at% Fe (Table 6.1). While the cycle ratio is FeO_x rich, the order of magnitude difference in growth rates for FeO_x and ZnO_x ALD results in a much more Zn rich predicted composition. Comparing the calculated values in Table 6.1 with the experimental semi-quantitative results in Figure 6.4d, the rule of mixtures provides a very good match to the experimental values, which were measured as 87.7 at% Zn and 12.3 at% Fe. The predicted metallic composition for the $ZnMnO_x$ film, with a ZnO_x:MnO_x cycle ratio of 1:9, is 18.8 at% Zn and 81.2 at% Mn (Table 6.1). In this case, with comparable ALD growth rates, the MnO_x rich supercycle scheme is calculated to produce a Mn rich coating. The experimental EDX values show good agreement with this calculation, with 22.7 at% Zn and 77.3 at% Mn (Figure 6.4d). For the $ZnMnFeO_x$ film, on the other hand, the predicted metallic composition values in Table 6.1 do not match those determined experimentally. The rule of mixtures, using the saturating growth rates for the binary ALD processes on a Si surface, predicts a metallic composition of 35.1 at% Zn, 56.0 at% Mn and 8.9 at% Fe. The experimental EDX results, however, are 41.7 at% Zn, 22.1 at% Mn, and 36.3 at% Fe. Clearly, within the $ZnMnFeO_x$ supercycle, the growth rate for the MnO_x step is slower than in the binary process, while the FeO_x step has a faster growth rate than the binary process.

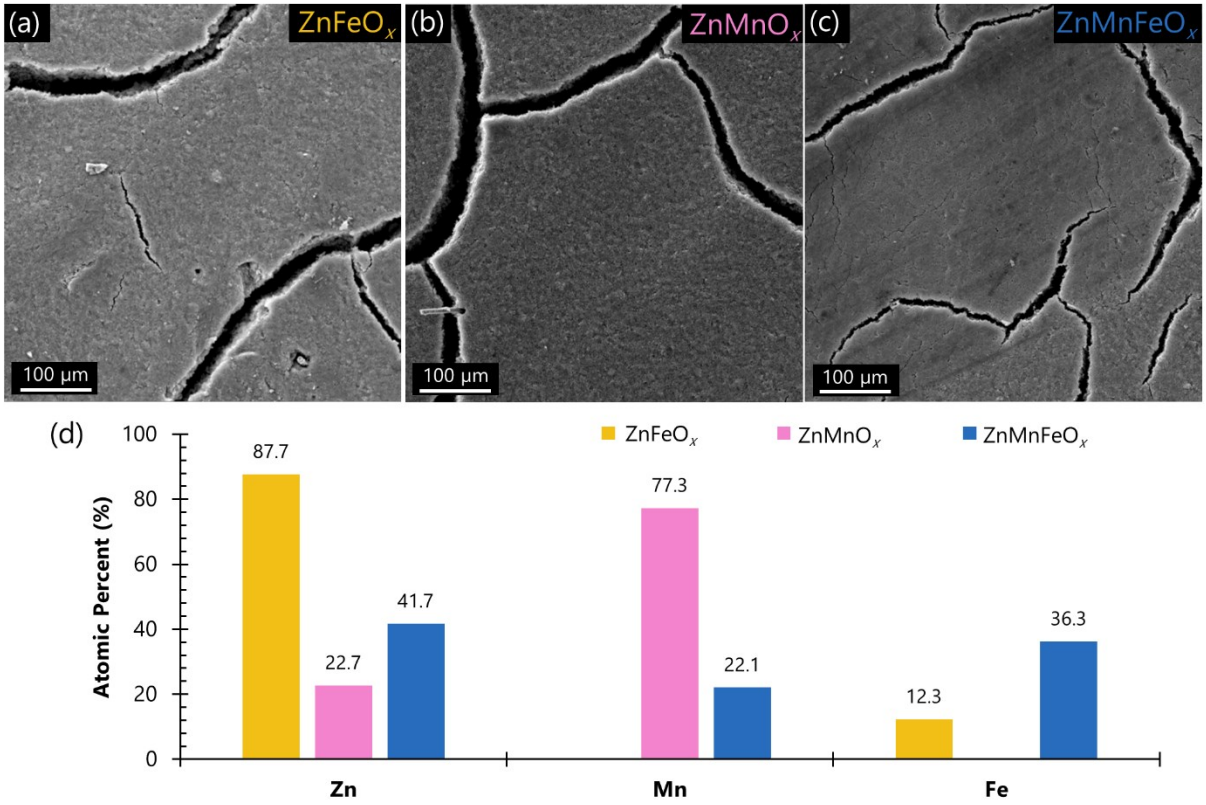

Figure 6.4. Plan view SEM images of GDL with (a) $ZnFeO_x$, (b) $ZnMnO_x$, and (c) $ZnMnFeO_x$ coatings. (d) Semi-quantitative EDX analysis of the three metal oxide coatings on GDL.

The rule of mixtures (Equation 6.2) assumes that the growth rate from a binary process can be translated to a supercycle deposition. While this assumption generally holds for the $ZnFeO_x$ and $ZnMnO_x$ processes, the $ZnMnFeO_x$ process is more complicated, with MnO_x deposition steps occurring on a ZnO_x surface and FeO_x deposition on a MnO_x surface. If the prediction is updated with growth rates for the FeO_x and MnO_x ALD processes on non-Si surfaces (from the saturation studies in Chapter 5),[453] then the predicted metallic composition becomes 28.2 at% Zn, 58.3 at% Mn, and 13.5 at% Fe. Comparing these values with the experimental values in Figure 6.4d shows that the modified growth rates are still not enough to account for the discrepancy. It is important to note that with a 3:10:20 supercycle scheme (ZnO_x:MnO_x:FeO_x), none of the binary ALD steps have a chance to enter the saturating growth regime and it is likely that substrate enhanced or substrate inhibited growth is occurring at every step in the supercycle deposition. To match the experimental composition shown in Figure 6.4d, the growth rates for ZnO_x, MnO_x, and FeO_x are calculated as 1.61, 0.35, and 0.28 Å cycle^{-1}, respectively, assuming the same densities as before.

When compared with the original growth rates of 1.78, 1.15, and 0.09 Å cycle^{-1} for ZnO_x, MnO_x and FeO_x, respectively, the ZnO_x process is slightly substrate inhibited, the MnO_x process is severely substrate inhibited, and the FeO_x process is substrate enhanced. The growth rates calculated to match the experimental composition should not be taken as actual ALD growth rates, since that requires a more rigorous procedure, but these values nonetheless provide an indication of the complexity of an ALD supercycle deposition. Additionally, the density values employed when calculating atomic compositions may not be representative of true film densities. For example, the FeO_x binary ALD process (Chapter 3) deposits as rhombohedral α-Fe_2O_3,[360] but an investigation into a $MnFe_xO_y$ supercycle (Chapter 5) found that the crystal structure was a cubic spinel analogous to Fe_3O_4.[453] Diffraction patterns (discussed below) obtained from the $ZnMnFeO_x$ coating also suggest a cubic spinel crystal structure, which would change the density values for the ZnO_x and FeO_x steps of the ALD process (the MnO_x process forms Mn_3O_4).[54]

6.3.5 Cross Sectional EDX Analysis of $ZnMnFeO_x$

A GDL sample, coated with the $ZnMnFeO_x$ film, was cleaved and examined in cross section to investigate the depth of catalyst deposition into the air electrode substrate. Figure 6.5a shows the cross sectional profile of GDL, with the microporous layer the main area of interest. This portion of the GDL is comprised of carbon particles bound together with a PTFE binder,[64] creating a high surface area for catalyst loading and a hydrophobic barrier to seal off the air side of a ZAB.[32,39] The microporous region of GDL is the area within the air electrode where the electrolyte and oxygen react and, thus, a sufficient amount of catalyst should be deposited throughout this layer to ensure all possible reaction sites are catalyzed.[54,459] Figure 6.5b shows the region of the microporous layer that was sampled during an EDX linescan (Figure 6.5c). The results in Figure 6.5 are for the trimetallic $ZnMnFeO_x$ coating but they can also be used to illustrate the bimetallic $ZnFeO_x$ and $ZnMnO_x$ distributions since the same binary ALD processes are employed in all three coatings.

Plan view SEM and EDX analysis in Figure 6.4d shows that the normalized Zn:Mn:Fe atomic ratio for $ZnMnFeO_x$ is 1:0.52:0.86. This ratio is also reflected in the linescan data of Figure 6.5c, with maximum normalized counts of 1, 0.46, and 0.87 for Zn, Mn, and Fe, respectively. In line with previous investigations of ALD coatings on GDL,[54,157,360] the overall penetration depth of the $ZnMnFeO_x$ deposition is around 15 μm, after which a baseline value is established. For Zn,

the baseline amount of counts is more than for Mn or Fe because the ZnO_x step is deposited using thermal ALD. Conversely, the MnO_x and FeO_x steps employ plasma enhanced ALD with plasma-based reactants as opposed to solely H_2O in the case of ZnO_x. Plasma radicals have a short lifetime and are prone to recombination on surfaces in high aspect ratio structures,[156,166] reducing the depth coverage of ALD in high aspect ratio structures such as the microporous layer in GDL. In addition, the Zn precursor of DEZ is an ideal ALD precursor, with high volatility and reactivity.[154,160,227] The Mn and Fe precursors, on the other hand, are large, bulky cyclopentadienyl compounds with lower volatility and reactivity. In fact, the necessity of an O plasma reactant is due to the low reactivity of the Fe precursor.[360] For the Mn precursor, the volatility is so low that an inert gas boost is required to deliver the precursor vapours.[157] As such, both the plasma reactants and the cyclopentadienyl precursors are responsible for the lower depth penetration of Mn and Fe in Figure 6.5c. To improve the penetration depth of Mn and Fe loading, the precursor and plasma dose times for the MnO_x and FeO_x ALD steps can be increased, improving the chances of precursor molecules and plasma reactant radicals reaching deeper regions of the microporous layer.[157,166,306]

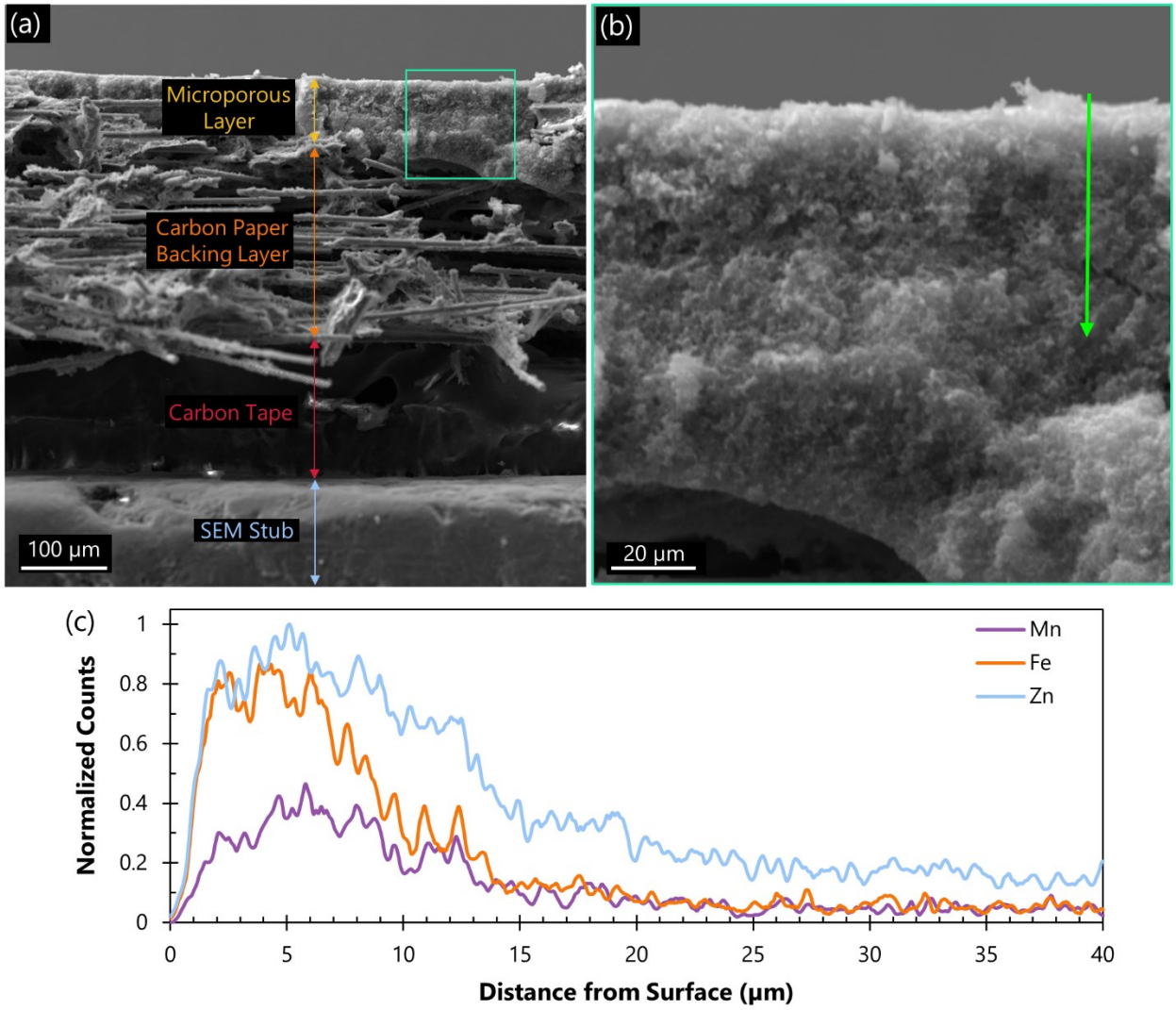

Figure 6.5. SEM analysis of a cross sectional sample of $ZnMnFeO_x$ on GDL. (a) Overview of a GDL cross section with different layers labelled. (b) Magnified image of the microporous layer indicated in (a). (c) EDX linescan results for Mn, Fe, and Zn as a function of distance from the GDL surface as shown by the green arrow in (b). Counts are normalized to the maximum Zn intensity.

6.3.6 TEM/STEM Analysis of $ZnMnFeO_x$

TEM samples were prepared by scraping off the surface of the $ZnMnFeO_x$ coated GDL and drop casting the material onto a TEM grid. STEM bright field (BF) and high angle annular dark field (HAADF) images of the ALD coated carbon particles are shown in Figures 6.6a and 6.6b,

respectively. The dark bands surrounding the particles in the BF image, or the bright white borders around the particles in the HAADF image, represent the transition metal oxide coating on the carbon particles. An SAD pattern from the area shown in Figure 6.6a is shown in Figure 6.6c. Several diffuse rings are visible, with the most intense central ring of 0.360 nm attributable to the graphitic GDL particles (Table 6.2). The as-received TEM grid is coated with a layer of amorphous carbon and this can be matched with the ring at 0.212 nm (Table 6.2). This carbon layer on the TEM grid is also visible in the EDX mapping of the sample in Figure 6.6d. EDX maps for Zn, Mn, Fe and O are also featured in Figures 6.6e-h. The ALD coating identified in the BF and HAADF images (Figures 6.6a and 6.6b, respectively) also lines up with the EDX maps of Zn, Mn, Fe, and O. The signal intensity for Mn (Figure 6.6f) is noticeably lower than that for Zn (Figure 6.6e) and Fe (Figure 6.6g) because the metallic composition of Mn in the film is lower (22.1 at% Mn, Figure 6.6.4d). An overlap of all the EDX maps onto the STEM BF image is shown in Figure 6.6i. The orange coloured coating on the GDL particles indicates that all four elements (Zn, Mn, Fe, and O) overlap, demonstrating a fully homogenous, trimetallic oxide coating. The EDX spectrum from the whole area is displayed in Figure 6.6j along with the semi-quantitative analysis for Zn, Mn, and Fe. The composition obtained from STEM EDX analysis agrees reasonably well with the composition from SEM EDX analysis, with Zn, Mn, and Fe atomic percentages of 33%, 26%, and 41%, respectively, for STEM EDX analysis and 41.7%, 22.1%, and 36.3%, respectively, for SEM EDX analysis. Note that smaller volumes of material are examined in STEM relative to SEM, which could account for the minor discrepancy between EDX values. In addition, preparation of the TEM sample is somewhat random and could yield GDL particles from areas deeper in the microporous layer, generating a slightly different composition than the coating at the outer surface as examined by SEM. Referring back to the diffraction pattern (Figure 6.6c), the remaining rings not accounted for by carbonaceous materials can be matched to several different oxides of Zn, Mn, and/or Fe. However, characterization of a $MnFe_xO_y$ supercycle process (Chapter 5), using the same binary MnO_x and FeO_x processes, identified the mixed oxide film as a cubic spinel ($(Mn,Fe)_3O_4$).[453] In the present work, cubic spinels featuring Zn, Mn and/or Fe can also be matched to the diffraction pattern (Table 6.2). Tetragonal spinels for Mn oxides also match the diffraction rings in Figure 6.6c since these structures are very similar to cubic spinels and differ only in stretching of the c axis due to the presence of Mn.[430,460] Ultimately, it is more likely that the $ZnMnFeO_x$ coating is a

cubic structure because the addition of Fe was found to reduce the tetragonal distortion in hausmannite (Mn_3O_4),[430] and because franklinite ($ZnFe_2O_4$) is cubic and the Zn:Mn:Fe ratio is 33:26:41 (*i.e.*, Mn is only ~1/4 of the metal composition in the oxide).

6.3.7 Analysis of Catalytic Activity

The half cell and full cell performance of the optimized $ZnFeO_x$, $ZnMnO_x$, and $ZnMnFeO_x$ films are shown in Figures 6.7a and 6.7b, respectively, alongside the non-Zn oxides of FeO_x, MnO_x, and $MnFeO_x$. For the OER onset, the Zn-based oxides are all inferior to their non-Zn counterparts. This is not surprising considering the pure ZnO_x film displays an OER onset beyond that of the plot and is just as poor an OER catalyst as bare GDL (Figure 6.7a). For the $ZnFeO_x$ and FeO_x samples, the ORR onset is the same, while for the $ZnMnO_x$, $ZnMnFeO_x$, MnO_x and $MnFeO_x$ samples, the ORR onset of the Zn-based films is also inferior. Therefore, based on half cell results, the addition of Zn to transition metal oxides of Mn and Fe has a negative impact on the ORR/OER activity. Surveying the full cell results for these same films in Figure 6.7b, the addition of Zn to FeO_x, MnO_x, and $MnFeO_x$ is only beneficial for FeO_x. In this case, the discharge and charge voltages are both slightly better for $ZnFeO_x$ than for FeO_x, leading to an increase of 2.6% in bifunctional efficiency. For $ZnMnO_x$ and MnO_x, the operating voltage during charge is much worse for the Zn-based film, while the discharge values are comparable. As a result, the efficiency of $ZnMnO_x$ is 5.2% less than that for MnO_x. For the $MnFeO_x$ and $ZnMnFeO_x$ films, both discharge and charge are negatively impacted by Zn addition, with an overall loss of 3.6 % efficiency. The discharge polarization behaviour and peak power densities of the same set of transition metal oxides films is displayed in Figure 6.7c. Consistent with the poor performance displayed in Figures 6.7a and 6.7b, the monometallic ZnO_x film produces a maximum power density that is on par with bare GDL at around 55 mW cm^{-2}. The Zn-based oxides of $ZnFeO_x$ and $ZnMnO_x$ both perform worse in terms of polarization and power than their non-Zn counterparts. For FeO_x and $ZnFeO_x$, peak power densities of ~85 and ~65 mW cm^{-2} are obtained, respectively, while MnO_x and $ZnMnO_x$ deliver peak power densities of ~85 and ~75 mW cm^{-2}, respectively. Even for the trimetallic $ZnMnFeO_x$ film, the addition of Zn results in a lower peak power density of ~80 mW cm^{-2}, compared with ~90 mW cm^{-2} for the non-Zn $MnFeO_x$ film.

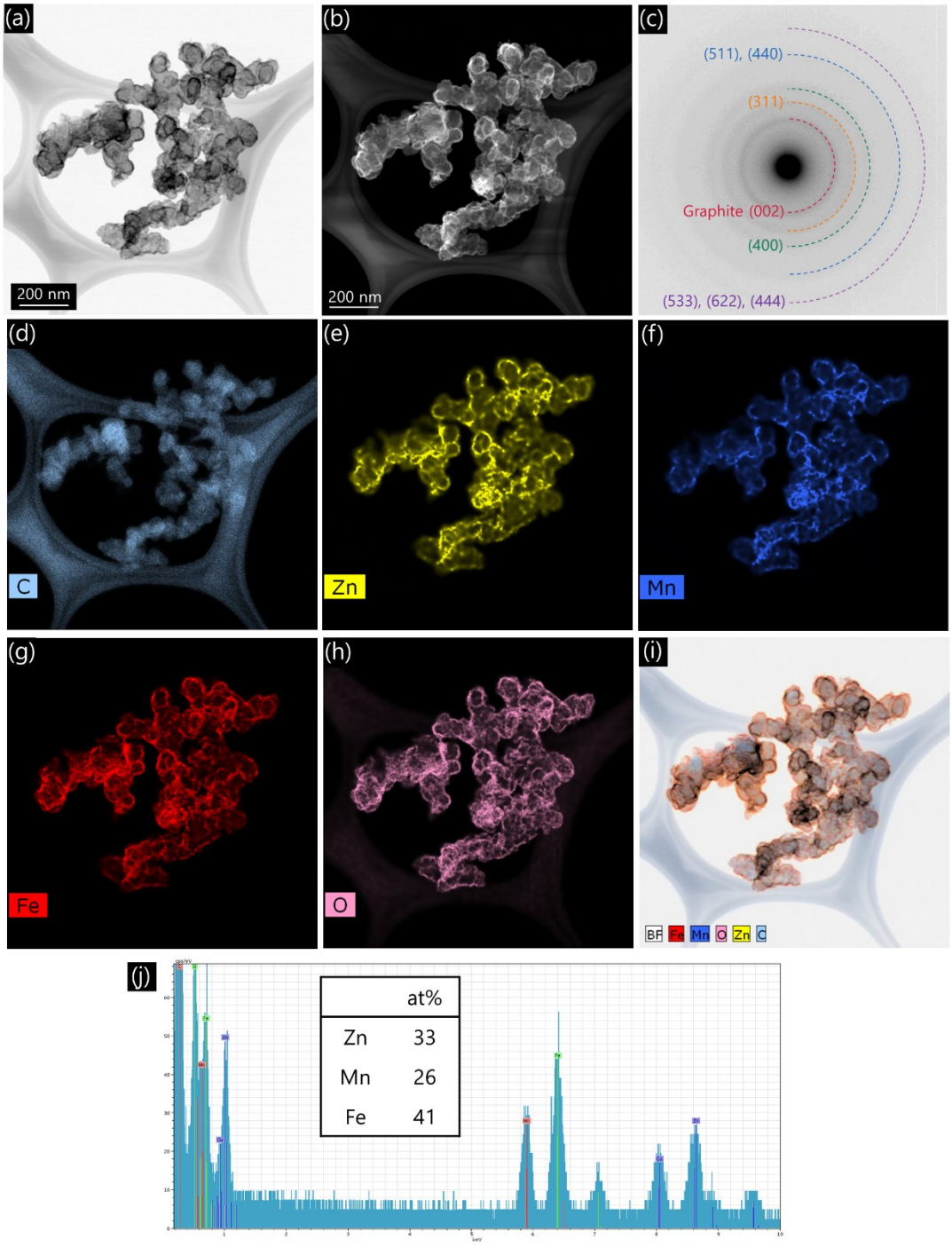

Figure 6.6. TEM/STEM characterization of the $ZnMnFeO_x$ coating on GDL. (a) STEM BF image and (b) STEM HAADF image. (c) SAD pattern with diffraction rings indexed to a cubic spinel oxide. EDX mapping of (d) C, (e) Zn, (f) Mn, (g) Fe, and (h) O. (i) EDX maps of Fe, Mn, O, Zn, and C overlapped on the STEM BF image. (j) EDX spectrum and semi-quantitative analysis of Zn, Mn and Fe concentrations.

Table 6.2. Measured d spacings for the diffraction pattern of $ZnMnFeO_x$ on GDL (Figure 6.6c) compared with the reported d spacings for several different transition metal oxides. Contributions from the graphitic carbon GDL and the amorphous carbon TEM grid are also identified.

Crystal Name - Formula	Jacobsite - $MnFe_2O_4$			Franklinite - $ZnFe_2O_4$			Magnetite - Fe_3O_4			Mn_3O_4		
PDF# / Crystal Structure / Space Group	10-0319	Cubic	Fd-3m(227)	22-1012	Cubic	Fd-3m(227)	19-0629	Cubic	Fd-3m(227)	13-0162	Cubic	Fd-3m(227)
Cell Dimensions (Å)	8.50 x 8.50 x 8.50			8.44 x 8.44 x 8.44			8.40 x 8.40 x 8.40			8.42 x 8.42 x 8.42		
SAD d spacing (nm)	d spacing (nm)	Intensity (%)	(h k l)	d spacing (nm)	Intensity (%)	(h k l)	d spacing (nm)	Intensity (%)	(h k l)	d spacing (nm)	Intensity (%)	(h k l)
0.360												
0.265	0.2563	100	(311)	0.2543	100	(311)	0.2532	100	(311)	0.2540	100	(311)
0.212	0.2124	25	(400)	0.2109	17	(400)	0.2099	20	(400)	0.2100	50	(400)
0.152	0.1636	35	(511)	0.1624	30	(511)	0.1616	30	(511)	0.1620	50	(511)
	0.1503	40	(440)	0.1491	35	(440)	0.1485	40	(440)	0.1488	60	(440)
0.123	0.1296	20	(533)	0.1287	9	(533)	0.1281	10	(533)	0.1284	20	(533)
	0.1281	15	(622)	0.1272	4	(622)	0.1266	4	(622)			
	0.1228	10	(444)	0.1218	2	(444)	0.1212	2	(444)	0.1215	10	(444)

Crystal Name - Formula	Hetaerolite - $ZnMn_2O_4$			Hausmannite - Mn_3O_4			Graphite -2H			Carbon		
PDF# / Crystal Structure / Space Group	24-1133	Tetragonal	$I4_1/amd(141)$	24-0734	Tetragonal	$I4_1/amd(141)$	41-1487	Hexagonal	$P6_3/mmc(194)$	26-1081	Trigonal	P3m1(156)
Cell Dimensions (Å)	5.72 x 5.72 x 9.24			5.76 x 5.76 x 9.47			2.47 x 2.47 x 6.72			2.52 x 2.52 x 20.59		
SAD d spacing (nm)	d spacing (nm)	Intensity (%)	(h k l)	d spacing (nm)	Intensity (%)	(h k l)	d spacing (nm)	Intensity (%)	(h k l)	d spacing (nm)	Intensity (%)	(h k l)
0.360							0.3376	100	(002)			
0.265	0.2466	100	(211)	0.2487	100	(211)						
0.212	0.2022	16	(220)	0.2037	20	(220)	0.2139	2	(100)	0.2081	100	(103)
0.152	0.1564	25	(321)	0.1576	25	(321)	0.1684	4	(004)	0.1580	2	(109)
	0.1522	40	(224)	0.1544	50	(224)	0.1548	1	(103)			
0.123	0.1265	9	(413)	0.1278	10	(413)	0.1234	3	(110)	0.1261	48	(110)
	0.1233	4	(422)	0.1243	6	(422)				0.1259	5	(111)
	0.1216	3	(404)	0.1231	5	(404)						

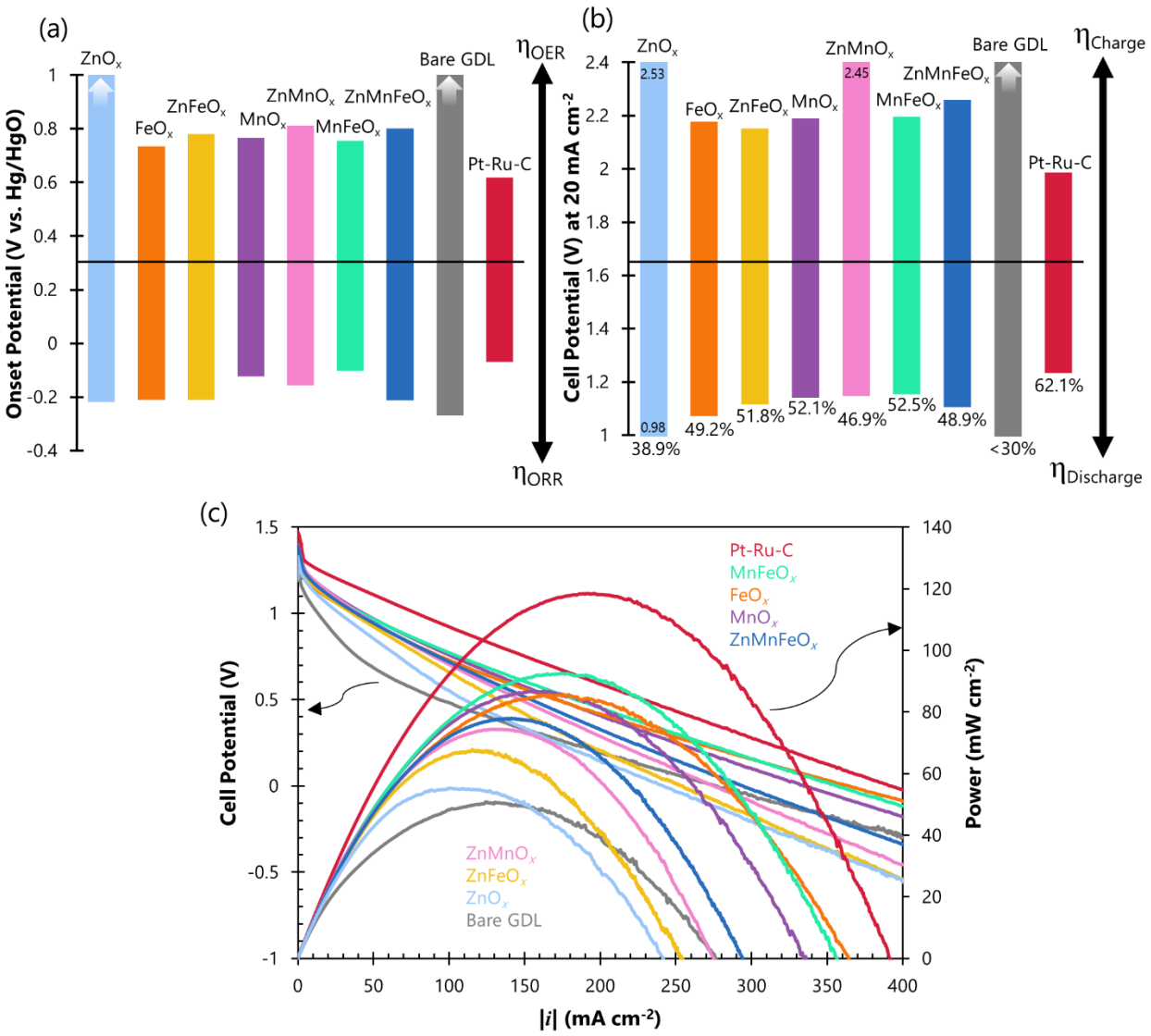

Figure 6.7. ZAB test results for GDL air electrodes deposited with ALD coatings of ZnO_x, FeO_x, $ZnFeO_x$, MnO_x, $ZnMnO_x$, $MnFeO_x$, and $ZnMnFeO_x$, compared with a spray-coated Pt-Ru-C catalyst and an uncoated, bare GDL electrode. (a) Half cell onset potentials at |10| mA cm^{-2}. (b) Full cell discharge and charge operating voltages and bifunctional efficiencies at |20| mA cm^{-2}. The half cell OER potentials for bare GDL and ZnO_x are beyond the range of the plot and this is represented by arrows on the bars. The same is true for the full cell bare GDL charge potential. (c) Full cell discharge polarization (left axis) and power density (right axis) curves.

6.3.8 Analysis of Cycling Stability

Among all the ALD films in Figure 6.7, $MnFeO_x$ developed previously in Chapter 5 displays the best overall catalytic activity for ZAB air electrodes, but is still not as efficient as the Pt-Ru-C benchmark. However, the $MnFeO_x$ catalyst showed improved stability over the precious metal comparison when tested in long-term cycling.[453] The intention behind deliberately mixing ZnO_x with other transition metal oxide catalysts was to further improve the stability of the catalyst during cycling. Therefore, the same ALD films from Figure 6.7 were cycled in a ZAB over several hundred cycles and the results are shown in Figure 6.8. The $ZnFeO_x$ film is directly compared with the ZnO_x and FeO_x catalysts in Figure 6.8a, with the bifunctional efficiency of these films at select cycles displayed in the bar graph in Figure 6.8b. The cycling behaviour of the ALD FeO_x film is unstable for the majority of the test, with the discharge potential reaching the cutoff voltage of 0.5 V after ~140 h of cycling (Figure 6.8a). This poor cycling performance is attributed to the O plasma reactant involved in the direct deposition of FeO_x on the GDL substrate. Without any buffer steps in the ALD process, the repetitive exposure of the carbon GDL to an O plasma results in oxidation of the carbon material as well as degradation of the PTFE wet proofing within the GDL air electrode. The electrolyte penetrates completely through the GDL membrane, blocking active sites for reaction and leading to electrolyte loss and eventual failure of the ZAB. The addition of ZnO_x to the FeO_x ALD process acts like a buffer, protecting the carbon substrate from the O plasma reactant. This same effect was also found during the development of the $MnFeO_x$ process, where the MnO_x ALD steps shielded the substrate from the oxidizing reactant.[453] The cycling behaviour of the $ZnFeO_x$ sample is thus superior to the FeO_x comparison, with relatively stable voltages displayed for over 300 h. The bifunctional efficiency of the $ZnFeO_x$ sample is higher than either FeO_x or ZnO_x on their own at almost every cycle displayed (Figure 6.8b). Therefore, the addition of ZnO_x to an FeO_x ALD process is, in this case, beneficial in terms of long-term cycling stability for an air electrode catalyst.

The cycling performance of ZnO_x, MnO_x, and $ZnMnO_x$ is displayed in Figure 6.8c. The MnO_x sample shows some instability at the beginning of the test, but is mostly stable after 200 h of cycling and, provides a bifunctional efficiency on par with, or better than, the $ZnMnO_x$ sample (Figure 6.8d). At around 420 h of cycling, the $ZnMnO_x$ sample reaches the potential cutoff value

during discharge and the ZAB fails. The Zn electrode remained intact and replacing the electrolyte did not result in recovery of discharge performance (not shown); therefore, the air electrode was responsible for battery failure. Regardless, the addition of ZnO_x to the ALD MnO_x process did not result in any appreciable improvement in cycling behaviour based on Figures 6.8c and 6.8d. In general, the MnO_x sample was also superior to the ZnO_x sample during cycling, as expected from the initial electrochemical tests shown in Figure 6.7. Lastly, the cycling performance of the $MnFeO_x$ film is compared with that of the $ZnMnFeO_x$ film in Figures 6.8e and 6.8f. For every cycle plotted in Figure 6.8f, the $MnFeO_x$ film outperforms both the ZnO_x and $ZnMnFeO_x$ films in terms of bifunctional efficiency. This is also observed in Figure 6.8e since the green curve ($MnFeO_x$) represents the highest discharge potential and lowest charge potential for the entire 600 h of cycling, aside from the brief instability at around 50 h (100 cycles). The brief instability in the $MnFeO_x$ curve is attributed to other factors in the ZAB cell and the cycling performance is otherwise completely recoverable.[453] Like the binary MnO_x ALD process, the addition of ZnO_x to the $MnFeO_x$ supercycle process does not afford any benefit in terms of catalytic activity (Figure 6.7) or cycling stability (Figure 6.8).

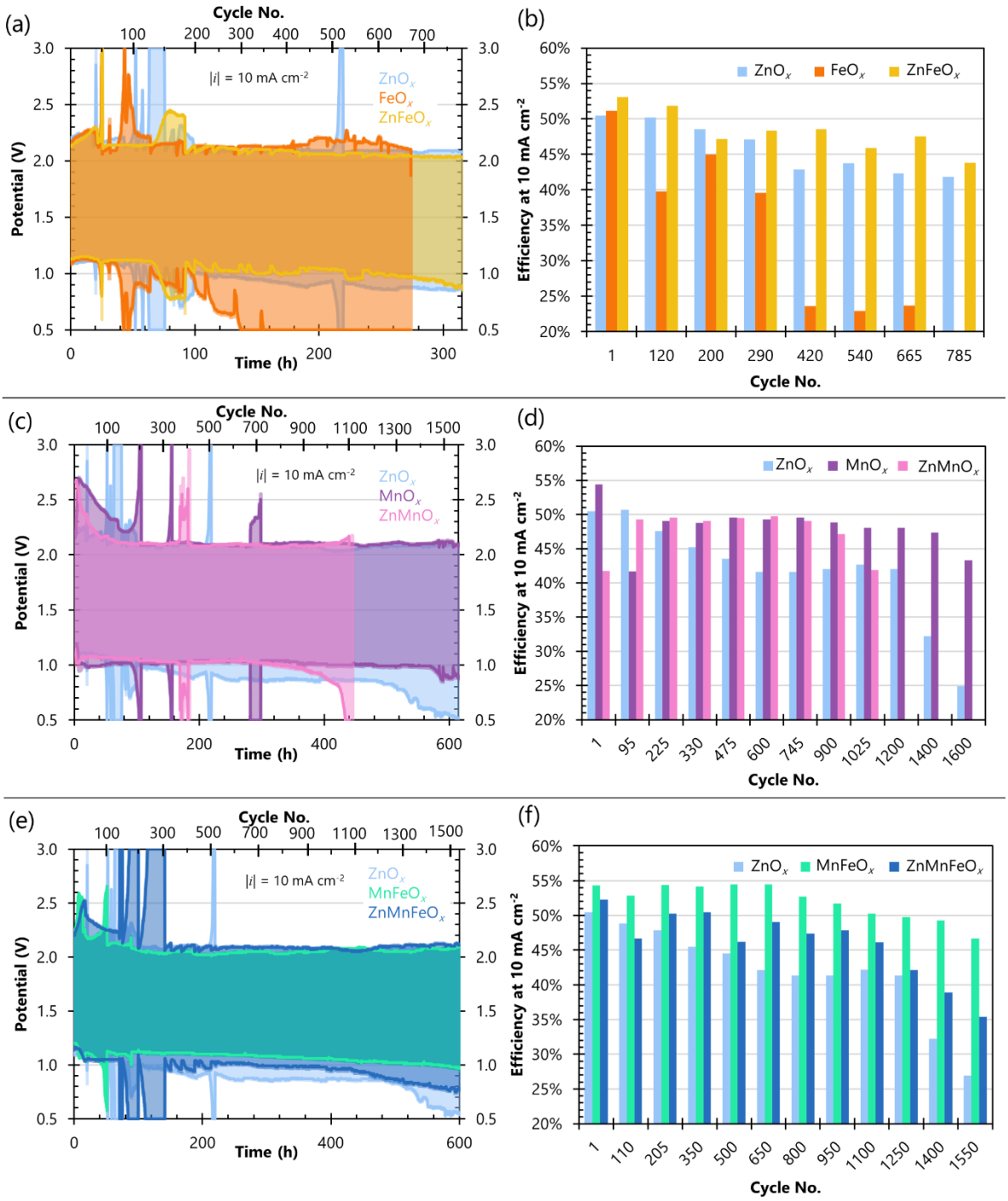

Figure 6.8. ZAB cycling at |10| mA cm^{-2} for 10 min discharge and charge periods. (a) Cycling plots of ZnO_x, FeO_x, and $ZnFeO_x$ and (b) bifunctional efficiency values calculated at select cycles. (c) Cycling plots of ZnO_x, MnO_x, and $ZnMnO_x$ and (d) bifunctional efficiency values calculated at select cycles. (e) Cycling plots of ZnO_x, $MnFeO_x$, and $ZnMnFeO_x$ and (f) bifunctional efficiency values calculated at select cycles.

6.3.9 Comparison with Literature

The motivation for this work stemmed from observations in previous research on ZAB electrocatalysts. In most cases, SEM and/or STEM EDX analysis of transition metal oxide catalysts after ZAB cycling showed evidence of Zn species. The electrolyte employed in ZABs is concentrated KOH with small amounts of a Zn salt deliberated added to improve the rechargeability of the cell.[32] When a ZAB is cycled, the catalyst and support material are completely submerged in the electrolyte and after removing from the cell, even after washing, residual KOH salt is usually present. Similar precipitation of ZnO from the electrolyte on the air electrode surface can account for the Zn detected in EDX. Nevertheless, researchers have speculated that Zn incorporation into the catalyst material could occur during cycling,[54,358] possibly indicating the most stable configuration of the oxide material.[108] In fact, deliberate addition of Zn to transition metal oxide catalysts was studied by Aasen *et al.* and McDougall *et al.* In both studies, the authors concluded that Zn promotes higher oxidation states for the other transition metals, leading to improvements in ORR and OER activity, as well as enhanced cycling stability.[109,358] However, Aasen *et al.* also noted that one exception is the addition of Zn to their $(Co,Fe)_3O_4$ catalyst, which led to a decrease in ZAB performance. For this particular case, a mixed oxidation state of both +2 and +3 for Co and Fe was the key to high bifunctional activity for the $(Co,Fe)_3O_4$ catalyst. The addition of Zn, which induced higher oxidation states for Co and Fe, disrupted this mixed valence.[109]

The Mn:Fe:Zn ratio, based on an average from EDX in both STEM (Figure 6.6j) and SEM (Figure 6.4c), is 37:24:39 for $ZnMnFeO_x$. With this Mn:Fe:Zn ratio, and based on a spinel AB_2O_4 structure, the Mn and Fe species in the $ZnMnFeO_x$ coating are likely only present with a valence of 3+ (*i.e.*, $Zn(Mn,Fe)_2O_4$) given that Zn can only be in a 2+ oxidation state. Another possibility is that Fe is also in a 2+ oxidation state and Mn has a 4+ oxidation state (*i.e.*, $Mn(Zn,Fe)_2O_4$), but considering there is roughly 1.5 times more Fe than Mn in $ZnMnFeO_x$ this is unlikely the case. The electrochemical activity of transition metal oxides as catalysts for oxygen reduction and evolution in ZABs is reportedly dependent on the oxidation state.[42] In the ternary oxide of $MnFeO_x$, identified as $(Mn,Fe)_3O_4$, the Mn and Fe species are found in a mixed oxidation state of both +2 and +3.[453] Thus, the loss of +2 valence species for Mn and Fe in $ZnMnFeO_x$ could explain the decrease in ORR and OER activity seen in Figures 6.7 and 6.8

between $MnFeO_x$ and $ZnMnFeO_x$, not unlike the aforementioned mechanism proposed by Aasen *et al.* regarding $(Co,Fe)_3O_4$.[109] A similar argument can be made for the loss of +2 Mn in the $ZnMnO_x$ sample if the crystal structure of $ZnMnO_x$ is also a spinel, since the Zn:Mn ratio is ~1:3 (Figure 6.4c) and would force a larger proportion of Mn species into a 3+ oxidation state. Furthermore, ZnO_x on its own does not show catalytic activity (Figure 6.7) and so replacing MnO_x with ZnO_x in $ZnMnO_x$, and replacing both MnO_x and FeO_x with ZnO_x in $ZnMnFeO_x$, leads to a decrease in average catalytic activity for the mixed oxides. Lastly, both the MnO_x and $MnFeO_x$ films are 40 nm thick, while the $ZnMnO_x$ and $ZnMnFeO_x$ films are only 10 nm in thickness. Despite the 40 nm thick $ZnMnO_x$ film not showing any improvement in performance over the 10 nm $ZnMnO_x$ film, the larger thickness for the MnO_x and $MnFeO_x$ samples may enhance their air electrode performance compared with the 10 nm thick $ZnMnO_x$ and $ZnMnFeO_x$ samples.

For the addition of Zn to binary FeO_x in this work, unlike with MnO_x or $MnFeO_x$, an increase in catalytic activity and cycling stability is observed. Yet, the oxidation state of Fe in FeO_x is undoubtedly already 3+.[360] SEM EDX results (Figure 6.4d) indicate only 12.3 at% Fe in the $ZnFeO_x$ film. Crystal structure analysis for the $ZnFeO_x$ film is beyond the scope of the present work, but it can be speculated that the hexagonal wurtzite structure, the most common Zn oxide structure, is likely formed with substitution of Fe for Zn. Rather than promoting the 3+ oxidation state for Fe by the addition of Zn, it is more likely that the reverse is true, where the Fe added to ZnO is forced into a 2+ oxidation state. Since the modification of oxidation states changes the electrochemistry for Mn and Co oxides,[42,78,110,461] it is possible this forced 2+ oxidation state for Fe explains the higher catalytic performance for the $ZnFeO_x$ sample compared with the FeO_x sample. Regardless, the catalytic activity of ZnO_x by itself is very poor, but 12.3 at% doping by Fe is sufficient to substantially enhance the ORR and OER activity (Figure 6.7).

6.4 Conclusions

Zn-based transition metal oxides of $ZnFeO_x$, $ZnMnO_x$, and $ZnMnFeO_x$ were deposited using atomic layer deposition (ALD) onto gas diffusion layer (GDL) substrates for air electrodes in ZABs. The deposition chemistry for each oxide film was optimized in terms of oxygen reduction and evolution (ORR/OER) activity. Energy dispersive X-ray (EDX) analysis during scanning electron microscopy (SEM) revealed a Zn rich $ZnFeO_x$ film and a Mn rich $ZnMnO_x$ film, with a more equal distribution of atomic elements for the $ZnMnFeO_x$ film. Cross sectional SEM and EDX analysis of the $ZnMnFeO_x$ coating displayed a good penetration depth for the ALD catalyst into the GDL porosity, in line with previous ALD investigations. Lower amounts of Mn and Fe were found in deep regions of the GDL substrate compared with Zn, because of both the plasma-based reactants and large organometallic precursors utilized in the MnO_x and FeO_x ALD steps. Scanning transmission electron microscopy (STEM) analysis of the $ZnMnFeO_x$ sample demonstrated the conformal nature of the ALD coating and overlapping EDX maps showed a homogenous mix of Zn, Mn, Fe, and O. Electron diffraction analysis of the $ZnMnFeO_x$ film indicated a cubic spinel crystal structure so that the coating was likely in the form of $Zn(Mn,Fe)_2O_4$. The electrochemical activity, as well as the cycling stability, of the $ZnFeO_x$ catalyst was superior to the original FeO_x catalyst. However, the $ZnMnO_x$ and $ZnMnFeO_x$ catalysts were both inferior to their non-Zn counterparts (MnO_x and $MnFeO_x$) during half cell, full cell, and long-term cycling testing. A modification to the oxidation state for the Mn and Fe species after Zn addition is likely responsible for the changes in catalytic activity observed in the Zn-based transition metal oxide catalysts.

7. Conclusions and Recommendations

7.1 Conclusions

Using atomic layer deposition (ALD), transition metal oxide coatings were applied to the air electrode in Zn-air batteries (ZABs) to enhance the oxygen reactions during charge and discharge. This study began in Chapter 3 with a novel Fe precursor for ALD which is inexpensive and commercially available. Reasonable oxide growth from this precursor required an aggressive O plasma reactant, which deteriorated the carbon air electrode substrate during deposition. The implementation of a forming gas plasma Mn oxide (MnO_x) ALD recipe prior to the O plasma ALD process proved to protect the carbon substrate from significant damage. The Fe oxide (FeO_x) coating demonstrated catalytic activity towards the oxygen evolution reaction (OER) required during ZAB charging.

Initial characterization of the FeO_x ALD coating in Chapter 3 revealed deep penetration of the catalyst material into the porosity of a ZAB air electrode. Several techniques confirmed that both the as-deposited and post-annealed coatings were present as hematite, or α-Fe_2O_3. Atomic force microscopy confirmed the saturating growth of the FeO_x ALD recipe and indicated a relatively smooth coating. However, electron microscopy performed in Chapter 4 discovered that the morphology of the FeO_x ALD coating does not follow traditional layer-by-layer growth as anticipated for ALD, but rather that the FeO_x coating grows in successive layers of island growth. While the FeO_x ALD process overall experienced substrate enhanced growth due to the MnO_x ALD pretreatment, *in situ* spectroscopic ellipsometry (SE) also identified substrate inhibited growth during deposition on the low energy carbon substrate. This substrate inhibited growth led to the initial development of islands and the relatively poor reactivity of the Fe precursor forced successive layers of FeO_x to grow on the high energy defect sites between previous islands, overall generating a coating comprised of multiple layers of islands. The growth of multiple island layers during ALD was replicated in the SE data by employing an effective medium approximation model, which indicated six distinct layers of island growth occurred over a period of 650 FeO_x ALD cycles.

The protective MnO_x ALD layer deposited prior to FeO_x ALD was developed previously in our research group as an oxygen reduction reaction (ORR) catalyst for the discharge reaction in ZABs.[54,157] In Chapter 5, the ORR active MnO_x coating and the OER active FeO_x coating from

Chapter 3 were deposited together in an ALD supercycle, with the aim of depositing a bifunctionally active mixed oxide film. Several supercycle parameters were systematically optimized in order to maximize the bifunctional catalytic activity of the ALD film towards the discharge and charge reactions in ZABs. The optimal supercycle chemistry was a 30:10 mixture of MnO_x:FeO_x ALD cycles, which deposited as a nanocrystalline spinel structure of the type $(Mn,Fe)_3O_4$. Transmission electron microscopy showed that the ALD coating conformally coated the carbon particles of the air electrode's microporous layer, with a homogeneous mixture of Mn and Fe and, thus, a fully mixed oxide layer. The advantage of using ALD to apply catalytic coatings to the air electrode of ZABs was demonstrated by the high retention of bifunctional efficiency after prolonged discharge-charge cycling for the $(Mn,Fe)_3O_4$ coating. After 600 h (1565 cycles) of bifunctional cycling at 10 mA cm^{-2}, the ALD $(Mn,Fe)_3O_4$ coating retained 84.7% of its initial energy efficiency, while a spray-coated precious metal benchmark catalyst of Pt-Ru-C retained only 66.2% of its initial energy efficiency for the same cycling conditions.

The addition of Zn to transition metal oxide catalysts for ZABs had been suggested by prior research in our group to enhance the stability of a ZAB during cycling.[109,358] Since ALD of Zn oxide (ZnO_x) is a well understood process, the addition of Zn to the mixed Mn-Fe oxide catalyst from Chapter 5 was undertaken in Chapter 6. Zn was also added to the binary ALD process for both FeO_x and MnO_x. An optimization process similar to that in Chapter 5 was conducted for each of the three Zn-based oxide films. The optimized supercycle ratios were 1:3 ZnO_x:FeO_x for $ZnFeO_x$, 1:9 ZnO_x:MnO_x for $ZnMnO_x$, and 3:10:20 ZnO_x:MnO_x:FeO_x for $ZnMnFeO_x$. Compositional analysis indicated that the $ZnFeO_x$ film was Zn rich, the $ZnMnO_x$ film was Mn rich, and the $ZnMnFeO_x$ film was an approximately equal mixture of the three transition metal elements. Further analysis of the $ZnMnFeO_x$ film suggested the spinel crystal structure of $(MnFe)_3O_4$ was maintained after Zn addition, forming $Zn(Mn,Fe)_2O_4$. Electrochemical testing of the $ZnFeO_x$ film displayed slightly improved catalytic activity over its non-Zn FeO_x counterpart, but both $ZnMnO_x$ and $ZnMnFeO_x$ films displayed inferior catalytic activity compared with their non-Zn counterparts. When exposed to ZAB cycling, the $ZnFeO_x$ coating was superior in terms of cycling stability than its non-Zn counterpart. The $ZnMnO_x$ and $ZnMnFeO_x$ oxides, however, were inferior to their non-Zn counterparts. Overall, the addition of Zn to transition metal oxide coatings, prepared via ALD, does not afford similar benefits as reported by other researchers.

7.2 Recommended Future Work

7.2.1 Improving ALD Penetration Depth

Based on the cross sectional composition analysis in Chapters 3 and 6, it is evident that the plasma-based ALD reactants have some difficulty penetrating deep into the pores of the air electrode material. Therefore, replacing the plasma reactants with non-plasma reactants could enhance the deposition characteristics of the ALD processes in this work. This could be achieved by using other energy enhanced reactants such as ozone, or by changing the precursor compounds to ones that are reactive with thermal ALD reactants such as water. Another strategy to improve the deposition of coatings deep into the pores of the air electrode is to utilize a static-pulsing ALD system as opposed to the currently employed continuous-flow system. Static-pulsing systems deliver the precursor or reactant vapours without a continuously running vacuum pump such that the chemical vapours have a long residence time in the reactor. This increases the chances of precursor or reactant molecules reaching deeper regions within the substrate material. As an additional means to improve deposition in deep regions of porous substrates, the pressure in the ALD reactor can be increased during precursor or reactant delivery.[462] In this way, the vapours are propelled with greater force into the deep recesses of a substrate's topography. Furthermore, utilizing multiple short precursor bursts as opposed to a single long precursor dose can improve utilization and penetration of precursor vapours into complex substrate architectures.[311,463]

7.2.2 Duplex Air Electrode Catalyst Structure

Section 5.3.2 in Chapter 5 featured an attempt at creating a two layered catalyst in the air electrode of a ZAB battery. In this design, an ORR active catalyst is deposited closer to the air side of the air electrode, while an OER active catalyst is deposited closer to the electrolyte side of the air electrode. This duplex structure would enable highly active monofunctional ORR or OER catalysts to be used at the air electrode without requiring separate charge and discharge electrodes, such as that employed in decoupled electrode setups.[151] Unfortunately, the work in Chapter 5 did not yield any improvement in electrochemical performance. However, this could be due to the conformal nature of ALD, which hermetically coated the first, ORR active layer with the second, OER active layer. Therefore, a more surface concentrated technique should

instead be used to apply the second, OER active layer on the air electrode. For example, an ORR active coating of MnO_x could be deposited via ALD to reach the air side of the air electrode substrate. This could then be followed by electrodeposition or chemical vapour deposition of an OER active coating, such as Ni oxide, which would only deposit on the outer surface of the air electrode substrate, at the electrolyte facing side.[54] Low penetration depth coating techniques would not cover the initially deposited ORR active layer and potentially enable two distinctly different catalysts to operate simultaneously in one air electrode. This process was somewhat already conducted by a previous researcher in our group, however, only electrodeposition was employed and was used to deposit both the ORR and OER active coatings.[67] Combining the high penetration depth of ALD with a low penetration depth coating method is essential to enable the full functionality of both catalysts.

7.2.3 Air Electrode Substrate Material

A reoccurring theme in this thesis is the damaging properties of the O plasma reactant on the carbon-based air electrode substrate during ALD. The carbon material is oxidized and the polytetrafluoroethylene wet proofing treatment is damaged when exposed to the aggressive O plasma reactant. A possible solution to this issue is to exchange the carbon-based air electrode with a metal-based air electrode substrate.[32,36,63] Alternatives such as Ni foam or stainless steel mesh would be completely stable under O plasma exposure and still provide the conductivity and high surface area requirements of the air electrode. Furthermore, ALD, as a direct synthesis method, would avoid binders and conductive additives necessary for other catalyst integration methods used on metallic air electrode substrates.[32] Combined with the high penetration depth of ALD, metallic air electrodes could deliver extremely stable ZAB performance. A wet proofing treatment would be required after ALD on the metallic substrate to prevent electrolyte loss at the air electrode, facilitate proper wetting, and maintain an adequate three phase boundary area with gaseous oxygen.

7.2.4 ALD at the Zn Electrode

This thesis has concentrated its efforts on depositing catalytic layers at the air electrode of a ZAB. However, ALD can also be used to improve the performance at the Zn electrode. This can be accomplished either as a functional interlayer between the Zn electrode and the electrolyte

(similar to the solid-electrolyte interface in Li-ion batteries),[464] or as an engineered Zn electrode, where a high surface area support is coated with a thick layer of ZnO through ALD.[32,465,466]

References

1. Canadian Interagency Forest Fire Centre Inc., “Wildfire Graphs,” 2024. [Online]. Available: https://ciffc.net/statistics. [Accessed: 23-Apr-2024].

2. World Meteorological Organization, “Provisional State of the Global Climate 2023,” 2023, https://wmo.int/files/provisional-state-of-global-climate-2023.

3. S. Perkins-Kirkpatrick, D. Barriopedro, R. Jha, L. Wang, A. Mondal, R. Libonati, and K. Kornhuber, “Extreme terrestrial heat in 2023,” *Nat. Rev. Earth Environ.*, vol. 5, pp. 244–246, 2024.

4. NOAA National Centers for Environmental Information, “Monthly Global Climate Report for Annual 2023,” 2024. [Online]. Available: https://www.ncei.noaa.gov/access/monitoring/monthly-report/global/202313. [Accessed: 23-Apr-2024].

5. IPCC, “Summary for Policymakers,” in *Climate Change 2023: Synthesis Report. Contribution of Working Groups I, II and III to the Sixth Assessment Report of the Intergovernmental Panel on Climate Change*, H. Lee and J. Romero, Eds. Geneva, Switzerland: IPCC, 2023, pp. 1–34.

6. IEA, “Global CO2 emissions by sector, 2019-2022,” Paris, 2023, https://www.iea.org/data-and-statistics/charts/global-co2-emissions-by-sector-2019-2022.

7. M. S. Javed, T. Ma, J. Jurasz, and M. Y. Amin, “Solar and wind power generation systems with pumped hydro storage: Review and future perspectives,” *Renew. Energy*, vol. 148, pp. 176–192, 2020.

8. Z. Zhu, T. Jiang, M. Ali, Y. Meng, Y. Jin, Y. Cui, and W. Chen, “Rechargeable Batteries for Grid Scale Energy Storage,” *Chem. Rev.*, vol. 122, no. 22, pp. 16610–16751, 2022.

9. X. Luo, J. Wang, M. Dooner, and J. Clarke, “Overview of current development in electrical energy storage technologies and the application potential in power system operation,” *Appl. Energy*, vol. 137, pp. 511–536, 2015.

10. S. Koohi-Fayegh and M. A. Rosen, “A review of energy storage types, applications and

recent developments," *J. Energy Storage*, vol. 27, no. February 2020, p. 101047, 2020.

11. M. A. Rahman, J. H. Kim, and S. Hossain, "Recent advances of energy storage technologies for grid: A comprehensive review," *Energy Storage*, vol. 4, no. 6, pp. 1–28, 2022.

12. B. Dunn, H. Kamath, and J. M. Tarascon, "Electrical energy storage for the grid: A battery of choices," *Science*, vol. 334, no. 6058, pp. 928–935, 2011.

13. A. A. Kebede, T. Kalogiannis, J. Van Mierlo, and M. Berecibar, "A comprehensive review of stationary energy storage devices for large scale renewable energy sources grid integration," *Renew. Sustain. Energy Rev.*, vol. 159, p. 112213, 2022.

14. V. Etacheri, R. Marom, R. Elazari, G. Salitra, and D. Aurbach, "Challenges in the development of advanced Li-ion batteries: A review," *Energy Environ. Sci.*, vol. 4, no. 9, pp. 3243–3262, 2011.

15. V. J. Reddy, N. P. Hariram, R. Maity, M. F. Ghazali, and S. Kumarasamy, "Sustainable Vehicles for Decarbonizing the Transport Sector: A Comparison of Biofuel, Electric, Fuel Cell and Solar-Powered Vehicles," *World Electr. Veh. J.*, vol. 15, no. 3, p. 93, 2024.

16. K. W. Beard and T. B. Reddy, Eds., *Linden's Handbook of Batteries*, 5th Ed. New York, NY: McGraw-Hill, 2019.

17. T. B. Clarke, M. W. Glasscott, and J. E. Dick, "The Role of Oxygen in the Voltaic Pile," *J. Chem. Educ.*, vol. 98, no. 9, pp. 2927–2936, 2021.

18. A. Volta, "On the electricity excited by the mere contact of conducting substances of different kinds. In a letter from Mr. Alexander Volta, F. R. S. Professor of Natural Philosophy in the University of Pavia, to the Rt. Hon. Sir Joseph Banks, Bart. K.B. P. R. S.," *Phil. Trans. R. Soc.*, vol. 90, pp. 403–431, 1800.

19. D. Linden and T. B. Reddy, Eds., *Handbook of Batteries*, 3rd Ed. New York, NY: McGraw-Hill, 2002.

20. T. M. I. Mahlia, T. J. Saktisahdan, A. Jannifar, M. H. Hasan, and H. S. C. Matseelar, "A review of available methods and development on energy storage; Technology update,"

Renew. Sustain. Energy Rev., vol. 33, pp. 532–545, 2014.

21. H. Chen, T. N. Cong, W. Yang, C. Tan, Y. Li, and Y. Ding, “Progress in electrical energy storage system : A critical review,” *Prog. Nat. Sci.*, vol. 19, no. 3, pp. 291–312, 2009.

22. Y. Liang, C. Z. Zhao, H. Yuan, Y. Chen, W. Zhang, J. Q. Huang, D. Yu, Y. Liu, M. M. Titirici, Y. L. Chueh, H. Yu, and Q. Zhang, “A review of rechargeable batteries for portable electronic devices,” *InfoMat*, vol. 1, no. 1, pp. 6–32, 2019.

23. L. Wang, J. Wang, L. Wang, M. Zhang, R. Wang, and C. Zhan, “A critical review on nickel-based cathodes in rechargeable batteries,” *Int. J. Miner. Metall. Mater.*, vol. 29, no. 5, pp. 925–941, 2022.

24. G. E. Blomgren, “The development and future of lithium ion batteries,” *J. Electrochem. Soc.*, vol. 164, no. 1, pp. A5019–A5025, 2017.

25. M. Armand and J.-M. Tarascon, “Building better batteries,” *Nature*, vol. 451, pp. 652–657, 2008.

26. J. M. Tarascon, “The li-ion battery: 25 years of exciting and enriching experiences,” *Electrochem. Soc. Interface*, vol. 25, no. 3, pp. 79–83, 2016.

27. G. Crabtree, E. Kócs, and L. Trahey, “The energy-storage frontier: Lithium-ion batteries and beyond,” *MRS Bull.*, vol. 40, no. 12, pp. 1067–1076, 2015.

28. J. B. Goodenough and Y. Kim, “Challenges for rechargeable Li batteries,” *Chem. Mater.*, vol. 22, no. 3, pp. 587–603, 2010.

29. A. G. Olabi, Q. Abbas, P. A. Shinde, and M. A. Abdelkareem, “Rechargeable batteries: Technological advancement, challenges, current and emerging applications,” *Energy*, vol. 266, no. October 2022, p. 126408, 2023.

30. Y. Ding, Z. P. Cano, A. Yu, J. Lu, and Z. Chen, “Automotive Li-Ion Batteries: Current Status and Future Perspectives,” *Electrochem. Energy Rev.*, vol. 2, no. 1, pp. 1–28, 2019.

31. E. A. Olivetti, G. Ceder, G. G. Gaustad, and X. Fu, “Lithium-Ion Battery Supply Chain Considerations: Analysis of Potential Bottlenecks in Critical Metals,” *Joule*, vol. 1, no. 2, pp. 229–243, 2017.

32. J. Fu, Z. P. Cano, M. G. Park, A. Yu, M. Fowler, and Z. Chen, “Electrically Rechargeable Zinc-Air Batteries: Progress, Challenges, and Perspectives,” *Adv. Mater.*, vol. 29, no. 7, p. 1604685, 2017.

33. G. J. May, A. Davidson, and B. Monahov, “Lead batteries for utility energy storage: A review,” *J. Energy Storage*, vol. 15, pp. 145–157, 2018.

34. M. A. Hannan, M. M. Hoque, A. Mohamed, and A. Ayob, “Review of energy storage systems for electric vehicle applications: Issues and challenges,” *Renew. Sustain. Energy Rev.*, vol. 69, no. December 2016, pp. 771–789, 2017.

35. S. Vazquez, S. M. Lukic, E. Galvan, L. G. Franquelo, and J. M. Carrasco, “Energy storage systems for transport and grid applications,” *IEEE Trans. Ind. Electron.*, vol. 57, no. 12, pp. 3881–3895, 2010.

36. X. Chen, Z. Zhou, H. E. Karahan, Q. Shao, L. Wei, and Y. Chen, “Recent Advances in Materials and Design of Electrochemically Rechargeable Zinc–Air Batteries,” *Small*, vol. 14, no. 44, pp. 1–29, 2018.

37. F. Cheng and J. Chen, “Metal-air batteries: From oxygen reduction electrochemistry to cathode catalysts,” *Chem. Soc. Rev.*, vol. 41, no. 6, pp. 2172–2192, 2012.

38. J.-S. Lee, S. T. Kim, R. Cao, N. S. Choi, M. Liu, K. T. Lee, and J. Cho, “Metal – Air Batteries with High Energy Density : Li – Air versus Zn – Air,” *Adv. Energy Mater.*, vol. 1, no. 1, pp. 34–50, 2011.

39. E. Davari and D. G. Ivey, “Bifunctional electrocatalysts for Zn–air batteries,” *Sustain. Energy Fuels*, vol. 2, no. 1, pp. 39–67, 2018.

40. V. Neburchilov, H. Wang, J. J. Martin, and W. Qu, “A review on air cathodes for zinc-air fuel cells,” *J. Power Sources*, vol. 195, no. 5, pp. 1271–1291, 2010.

41. P. Gu, M. Zheng, Q. Zhao, X. Xiao, H. Xue, and H. Pang, “Rechargeable zinc-air batteries: A promising way to green energy,” *J. Mater. Chem. A*, vol. 5, no. 17, pp. 7651–7666, 2017.

42. H. Osgood, S. V. Devaguptapu, H. Xu, J. Cho, and G. Wu, “Transition metal (Fe, Co, Ni,

and Mn) oxides for oxygen reduction and evolution bifunctional catalysts in alkaline media," *Nano Today*, vol. 11, no. 5, pp. 601–625, 2016.

43. S. M. Ewing, "Cobalt Mineral Commodity Summary - 2024," *National Minerals Information Center, USGS*. 2024.

44. C. Tuck, "Iron Mineral Commodity Summary - 2024," *National Minerals Information Center, USGS*. 2024.

45. J.-E. Kim, "Manganese Mineral Commodity Summary - 2024," *National Minerals Information Center, USGS*. 2024.

46. J. R. Rumble, Ed., "Abundance of Elements in the Earth's Crust and in the Seas," in *CRC Handbook of Chemistry and Physics*, Boca Raton, FL: CRC Press/Taylor & Francis, 2023.

47. Z. W. She, J. Kibsgaard, C. F. Dickens, I. Chorkendorff, J. K. Nørskov, and T. F. Jaramillo, "Combining theory and experiment in electrocatalysis: Insights into materials design," *Science*, vol. 355, no. 6321, 2017.

48. C. Marichy, M. Bechelany, and N. Pinna, "Atomic layer deposition of nanostructured materials for energy and environmental applications," *Adv. Mater.*, vol. 24, no. 8, pp. 1017–1032, 2012.

49. C. Detavernier, J. Dendooven, S. Pulinthanathu Sree, K. F. Ludwig, and J. A. Martens, "Tailoring nanoporous materials by atomic layer deposition," *Chem. Soc. Rev.*, vol. 40, no. 11, pp. 5242–5253, 2011.

50. B. J. Oneill, D. H. K. Jackson, J. Lee, C. Canlas, P. C. Stair, C. L. Marshall, J. W. Elam, T. F. Kuech, J. A. Dumesic, and G. W. Huber, "Catalyst design with atomic layer deposition," *ACS Catal.*, vol. 5, no. 3, pp. 1804–1825, 2015.

51. H. Li, Z. Guo, and X. Wang, "Atomic-layer-deposited ultrathin Co9S8 on carbon nanotubes: An efficient bifunctional electrocatalyst for oxygen evolution/reduction reactions and rechargeable Zn-air batteries," *J. Mater. Chem. A*, vol. 5, no. 40, pp. 21353–21361, 2017.

52. T. Muneshwar, M. Miao, E. R. Borujeny, and K. Cadien, "Atomic Layer Deposition:

Fundamentals, Practice, and Challenges," in *Handbook of Thin Film Deposition*, 4th Ed., K. Seshan and D. Schepis, Eds. Cambridge, MA: Elsevier Inc., 2018, pp. 359–377.

53. T. Suntola, "Atomic layer epitaxy," *Mater. Sci. Reports*, vol. 4, no. 5, pp. 261–312, 1989.

54. M. P. Clark, M. Xiong, K. Cadien, and D. G. Ivey, "High Performance Oxygen Reduction/Evolution Electrodes for Zinc-Air Batteries Prepared by Atomic Layer Deposition of MnOx," *ACS Appl. Energy Mater.*, vol. 3, no. 1, pp. 603–613, 2020.

55. A. J. M. Mackus, J. R. Schneider, C. MacIsaac, J. G. Baker, and S. F. Bent, "Synthesis of Doped, Ternary, and Quaternary Materials by Atomic Layer Deposition: A Review," *Chem. Mater.*, vol. 31, no. 4, pp. 1142–1183, 2019.

56. G. Girishkumar, B. McCloskey, A. C. Luntz, S. Swanson, and W. Wilcke, "Lithium-air battery: Promise and challenges," *J. Phys. Chem. Lett.*, vol. 1, no. 14, pp. 2193–2203, 2010.

57. Y. A. Çengel and M. A. Boles, *THERMODYNAMICS: An Engineering Approach*, 8th Ed. New York, NY: McGraw-Hill Education, 2015.

58. Y. Li and H. Dai, "Recent advances in zinc-air batteries," *Chem. Soc. Rev.*, vol. 43, no. 15, pp. 5257–5275, 2014.

59. D. Sieminski, "Recent advances in rechargeable zinc-air battery technology," in *The Twelfth Annual Battery Conference on Applications and Advances*, 1997, pp. 171–180.

60. F. L. Meng, K. H. Liu, Y. Zhang, M. M. Shi, X. B. Zhang, J. M. Yan, and Q. Jiang, "Recent Advances toward the Rational Design of Efficient Bifunctional Air Electrodes for Rechargeable Zn–Air Batteries," *Small*, vol. 14, no. 32, pp. 1–20, 2018.

61. J. Fu, R. Liang, G. Liu, A. Yu, Z. Bai, L. Yang, and Z. Chen, "Recent Progress in Electrically Rechargeable Zinc – Air Batteries," *Adv. Mater.*, vol. 31, no. 31, p. 1805230, 2019.

62. L. Jörissen, J. Ludwig, and L. Jörissen, "Bifunctional oxygen/air electrodes," *J. Power Sources*, vol. 155, no. 1, pp. 23–32, 2006.

63. S. Park, J. W. Lee, and B. N. Popov, "A review of gas diffusion layer in PEM fuel cells:

Materials and designs," *Int. J. Hydrogen Energy*, vol. 37, no. 7, pp. 5850–5865, 2012.

64. R. Schweiss, S. Hofmeister, C. Meiser, D. Dan, A. Baumann, T. Kuster, N. Haak, and S. Bacher, "Powering up fuel cells: Our gas diffusion layer [White Paper]." SGL Carbon, Meitingen, Germany, pp. 1–8, 2021.

65. A. J. Bard, R. Parson, and J. Jordan, Eds., *Standard Potetials in Aqueous Solution*. Boca Raton, FL: CRC Press, 1985.

66. A. C. Jones and M. L. Hitchman, "Overview of Chemical Vapour Deposition," in *Chemical Vapour Deposition*, A. C. Jones and M. L. Hitchman, Eds. Cambridge, UK: Royal Society of Chemistry, 2009, pp. 1–36.

67. M. Xiong and D. G. Ivey, "Sequentially Electrodeposited MnOX/Co-Fe as Bifunctional Electrocatalysts for Rechargeable Zinc-Air Batteries," *J. Electrochem. Soc.*, vol. 164, no. 6, pp. A1012–A1021, 2017.

68. X. Ge, A. Sumboja, D. Wuu, T. An, B. Li, F. W. T. Goh, T. S. A. Hor, Y. Zong, and Z. Liu, "Oxygen Reduction in Alkaline Media: From Mechanisms to Recent Advances of Catalysts," *ACS Catal.*, vol. 5, no. 8, pp. 4643–4667, 2015.

69. E. Yeager, "Dioxygen Electrocatalysis: Mechanisms in Relation to Catalyst Structure," *J. Mol. Catal.*, vol. 38, no. 1–2, pp. 5–25, 1986.

70. J. R. Rumble, Ed., "Dissociation Constants of Inorganic Acids and Bases," in *CRC handbook of chemistry and physics*, 100th ed., Boca Raton, FL: CRC Press/Taylor & Francis.

71. D. C. Harris, *Quantitative Chemical Analysis*, 7th Ed. New York: W. H. Freeman and Company, 2007.

72. P. H. Rieger, *Electrochemistry*, 2nd Ed. Dordrecht, NL: Springer Science+Business Media, 1994.

73. J. R. Rumble, Ed., "Electrochemical Series," in *CRC handbook of chemistry and physics*, 102nd ed., Boca Raton, FL: CRC Press/Taylor & Francis.

74. W. T. Hong, M. Risch, K. A. Stoerzinger, A. Grimaud, J. Suntivich, and Y. Shao-Horn,

"Toward the rational design of non-precious transition metal oxides for oxygen electrocatalysis," *Energy Environ. Sci.*, vol. 8, no. 5, pp. 1404–1427, 2015.

75. Y. Wang and P. B. Balbuena, "Design of oxygen reduction bimetallic catalysts: Ab-initio-derived thermodynamic guidelines," *J. Phys. Chem. B*, vol. 109, no. 40, pp. 18902–18906, 2005.

76. A. A. Gewirth and M. S. Thorum, "Electroreduction of dioxygen for fuel-cell applications: Materials and challenges," *Inorg. Chem.*, vol. 49, no. 8, pp. 3557–3566, 2010.

77. D. U. Lee, P. Xu, Z. P. Cano, A. G. Kashkooli, M. G. Park, and Z. Chen, "Recent progress and perspectives on bi-functional oxygen electrocatalysts for advanced rechargeable metal–air batteries," *J. Mater. Chem. A*, vol. 4, no. 19, pp. 7107–7134, 2016.

78. S. Ghosh and R. N. Basu, "Multifunctional nanostructured electrocatalysts for energy conversion and storage: current status and perspectives," *Nanoscale*, vol. 10, no. 24, pp. 11241–11280, 2018.

79. M. G. Park, D. U. Lee, M. H. Seo, Z. P. Cano, and Z. Chen, "3D Ordered Mesoporous Bifunctional Oxygen Catalyst for Electrically Rechargeable Zinc-Air Batteries," *Small*, vol. 12, no. 20, pp. 2707–2714, 2016.

80. S. L. Gojković, S. Gupta, and R. F. Savinell, "Heat-treated iron(III) tetramethoxyphenyl porphyrin chloride supported on high-area carbon as an electrocatalyst for oxygen reduction: Part III. Detection of hydrogen-peroxide during oxygen reduction," *J. Electroanal. Chem.*, vol. 462, pp. 63–72, 1999.

81. L. Hadidi, E. Davari, D. G. Ivey, and J. G. C. Veinot, "Microwave-assisted synthesis and prototype oxygen reduction electrocatalyst application of N-doped carbon-coated Fe3O4 nanorods," *Nanotechnology*, vol. 28, no. 9, 2017.

82. J. M. Ang, Y. Du, B. Y. Tay, C. Zhao, J. Kong, L. P. Stubbs, and X. Lu, "One-Pot Synthesis of Fe(III)-Polydopamine Complex Nanospheres: Morphological Evolution, Mechanism, and Application of the Carbonized Hybrid Nanospheres in Catalysis and Zn-Air Battery," *Langmuir*, vol. 32, no. 36, pp. 9265–9275, 2016.

83. C. Shu, X. Yang, Y. Chen, Y. Fang, Y. Zhou, and Y. Liu, “Nano-Fe3O4 grown on porous carbon and its effect on the oxygen reduction reaction for DMFCs with a polymer fiber membrane,” *RSC Adv.*, vol. 6, no. 43, pp. 37012–37017, 2016.

84. D. Zhou, L. Yang, L. Yu, J. Kong, X. Yao, W. Liu, Z. Xu, and X. Lu, “Fe/N/C hollow nanospheres by Fe(iii)-dopamine complexation-assisted one-pot doping as nonprecious-metal electrocatalysts for oxygen reduction,” *Nanoscale*, vol. 7, no. 4, pp. 1501–1509, 2015.

85. B. J. Kim, D. U. Lee, J. Wu, D. Higgins, A. Yu, and Z. Chen, “Iron- and nitrogen-functionalized graphene nanosheet and nanoshell composites as a highly active electrocatalyst for oxygen reduction reaction,” *J. Phys. Chem. C*, vol. 117, no. 50, pp. 26501–26508, 2013.

86. Y. Li, M. Gong, Y. Liang, J. Feng, J.-E. E. Kim, H. Wang, G. Hong, B. Zhang, and H. Dai, “Advanced zinc-air batteries based on high-performance hybrid electrocatalysts,” *Nat. Commun.*, vol. 4, no. May, p. 1805, 2013.

87. M. Gong and H. Dai, “A mini review of NiFe-based materials as highly active oxygen evolution reaction electrocatalysts,” *Nano Res.*, vol. 8, no. 1, pp. 23–39, 2014.

88. D. Kubo, K. Tadanaga, A. Hayashi, and M. Tatsumisago, “Multifunctional inorganic electrode materials for high-performance rechargeable metal-air batteries,” *J. Mater. Chem. A*, vol. 1, no. 23, pp. 6804–6809, 2013.

89. L. Gong, J. Koh, B. Siang, and B. S. Yeo, “Mechanistic Study of the Synergy between Iron and Transition Metals for the Catalysis of the Oxygen Evolution Reaction,” *ChemSusChem*, vol. 11, no. 21, pp. 3790–3795, 2018.

90. R. D. L. L. Smith, M. S. Prévot, R. D. Fagan, S. Trudel, C. P. Berlinguette, M. S. Pre, R. D. Fagan, and S. Trudel, “Water oxidation catalysis: Electrocatalytic response to metal stoichiometry in amorphous metal oxide films containing iron, cobalt, and nickel,” *J. Am. Chem. Soc.*, vol. 135, no. 31, pp. 11580–11586, 2013.

91. R. F. Scarr, “The Mechanism of Oxygen Evolution on Nickel, Platinum, and Other Metals and Alloys,” *J. Electrochem. Soc.*, vol. 116, no. 11, p. 1526, 1969.

92. M. E. G. G. Lyons and M. P. Brandon, “The oxygen evolution reaction on passive oxide covered transition metal electrodes in alkaline solution. Part III-Iron.,” *Int. J. Electrochem. Sci.*, vol. 3, pp. 1463–1503, 2008.

93. L. MacHala, J. Tuček, and R. Zbořil, “Polymorphous transformations of nanometric iron(III) oxide: A review,” *Chem. Mater.*, vol. 23, no. 14, pp. 3255–3272, 2011.

94. B. Iandolo, B. Wickman, I. Zorić, and A. Hellman, “The rise of hematite: origin and strategies to reduce the high onset potential for the oxygen evolution reaction,” *J. Mater. Chem. A*, vol. 3, no. 33, pp. 16896–16912, 2015.

95. W. L. Kwong, C. C. Lee, A. Shchukarev, E. Björn, and J. Messinger, “High-performance iron (III) oxide electrocatalyst for water oxidation in strongly acidic media,” *J. Catal.*, vol. 365, pp. 29–35, 2018.

96. R. Karunagaran, C. Coghlan, T. T. Tung, S. Kabiri, D. N. H. Tran, C. J. Doonan, and D. Losic, “Study of iron oxide nanoparticle phases in graphene aerogels for oxygen reduction reaction,” *New J. Chem.*, vol. 41, no. 24, pp. 15180–15186, 2017.

97. H. Wan, M. Lv, X. Liu, G. Chen, N. Zhang, Y. Cao, H. Wang, R. Ma, and G. Qiu, “Activating Hematite Nanoplates via Partial Reduction for Electrocatalytic Oxygen Reduction Reaction,” *ACS Sustain. Chem. Eng.*, vol. 7, no. 13, pp. 11841–11849, 2019.

98. H. Zhu, S. Zhang, Y. Huang, L. Wu, and S. Sun, “Monodisperse MxFe3−xO4 (M = Fe, Cu, Co, Mn) Nanoparticles and Their Electrocatalysis for Oxygen Reduction Reaction,” *Nano Lett.*, vol. 13, pp. 2947–2951, 2013.

99. Y. Zhan, C. Xu, M. Lu, Z. Liu, and J. Y. Lee, “Mn and Co co-substituted Fe3O4 nanoparticles on nitrogen-doped reduced graphene oxide for oxygen electrocatalysis in alkaline solution,” *J. Mater. Chem. A*, vol. 2, no. 38, pp. 16217–16223, 2014.

100. S. Luo and D. B. Zhou, “Preparation and Electrochemical Performance of Co-Fe/C for Bi-Functional Air Electrode,” *J. Electrochem. Soc.*, vol. 161, no. 1, pp. A23–A27, 2014.

101. X. Wu, Y. Niu, B. Feng, Y. Yu, X. Huang, C. Zhong, W. Hu, and C. M. Li, “Mesoporous Hollow Nitrogen-Doped Carbon Nanospheres with Embedded MnFe 2O4/Fe Hybrid Nanoparticles as Efficient Bifunctional Oxygen Electrocatalysts in Alkaline Media,” *ACS*

Appl. Mater. Interfaces, vol. 10, pp. 20440–20447, 2018.

102. D. Aasen, M. P. Clark, and D. G. Ivey, "Investigation of Transition Metal-Based (Mn, Co, Ni, Fe) Trimetallic Oxide Nanoparticles on N-doped Carbon Nanotubes as Bifunctional Catalysts for Zn-Air Batteries," *J. Electrochem. Soc.*, vol. 167, no. 4, p. 040503, 2020.

103. A. Mathur and A. Halder, "One-step synthesis of bifunctional iron-doped manganese oxide nanorods for rechargeable zinc-air batteries," *Catal. Sci. Technol.*, vol. 9, no. 5, pp. 1245–1254, 2019.

104. W. B. Jensen, "The place of zinc, cadmium, and mercury in the periodic table," *J. Chem. Educ.*, vol. 80, no. 8, pp. 952–961, 2003.

105. Z. Q. Liu, H. Cheng, N. Li, T. Y. Ma, and Y. Z. Su, "ZnCo2O4 Quantum Dots Anchored on Nitrogen-Doped Carbon Nanotubes as Reversible Oxygen Reduction/Evolution Electrocatalysts," *Adv. Mater.*, vol. 28, no. 19, pp. 3777–3784, 2016.

106. S. Chakrabarty, A. Mukherjee, W. N. Su, and S. Basu, "Improved bi-functional ORR and OER catalytic activity of reduced graphene oxide supported ZnCo2O4 microsphere," *Int. J. Hydrogen Energy*, vol. 44, no. 3, pp. 1565–1578, 2019.

107. H. Wang, X. Song, H. Wang, K. Bi, C. Liang, S. Lin, R. Zhang, Y. Du, J. Liu, D. Fan, Y. Wang, and M. Lei, "Synthesis of hollow porous ZnCo2O4 microspheres as high-performance oxygen reduction reaction electrocatalyst," *Int. J. Hydrogen Energy*, vol. 41, no. 30, pp. 13024–13031, 2016.

108. J. M. Costa, M. P. Clark, A. F. de Almeida Neto, and D. G. Ivey, "In-situ transformation of electrodeposited W–Co oxide to ZnCo2O4 nanoparticles as an effective bifunctional catalysts in Zn-air batteries," *Int. J. Hydrogen Energy*, vol. 45, no. 32, pp. 16122–16132, 2020.

109. D. A. Aasen, Y. Shen, and D. G. Ivey, "Zn-Based Oxides Anchored to Nitrogen-Doped Carbon Nanotubes as Efficient Bifunctional Catalysts for Zn-Air Batteries," *ChemElectroChem*, vol. 7, no. 10, pp. 2283–2296, 2020.

110. T. W. Kim, M. A. Woo, M. Regis, and K. S. Choi, "Electrochemical synthesis of spinel type ZnCo2O4 electrodes for use as oxygen evolution reaction catalysts," *J. Phys. Chem.*

Lett., vol. 5, no. 13, pp. 2370–2374, 2014.

111. B. Chi, J. Li, X. Yang, H. Lin, and N. Wang, "Electrophoretic deposition of ZnCo2O4 spinel and its electrocatalytic properties for oxygen evolution reaction," *Electrochim. Acta*, vol. 50, no. 10, pp. 2059–2064, 2005.

112. X. Liu, Z. Chang, L. Luo, T. Xu, X. Lei, J. Liu, and X. Sun, "Hierarchical Zn x Co3-xO4 nanoarrays with high activity for electrocatalytic oxygen evolution," *Chem. Mater.*, vol. 26, no. 5, pp. 1889–1895, 2014.

113. F. R. McLarnon and E. J. Cairns, "The Secondary Alkaline Zinc Electrode," *J. Electrochem. Soc.*, vol. 138, no. 2, pp. 645–664, 1991.

114. S. Hosseini, A. Abbasi, L. Uginet, N. Haustraete, S. Praserthdam, T. Yonezawa, and S. Kheawhom, "The Influence of Dimethyl Sulfoxide as Electrolyte Additive on Anodic Dissolution of Alkaline Zinc-Air Flow Battery," *Sci. Rep.*, vol. 9, no. 14958, pp. 1–12, 2019.

115. Z. Zhao, X. Fan, J. Ding, W. Hu, C. Zhong, J. Lu, X. Fan, J. Ding, W. Hu, C. Zhong, and J. Lu, "Challenges in Zinc Electrodes for Alkaline Zinc–Air Batteries: Obstacles to Commercialization," *ACS Energy Lett.*, vol. 4, no. 9, pp. 2259–2270, 2019.

116. M. Xu, D. G. Ivey, E. Dy, W. Qu, and Z. Xie, "Exploration of Electrolytes for Zn-Anode Rechargeable Batteries: Room Temperature Ionic Liquids as Major or Suporting Components," in *Ionic Liquids: Synthesis, Characterization and Applications*, A. Brooks, Ed. Nova Science Publishers, Inc., 2014, pp. 99–123.

117. K. Wang, P. Pei, Z. Ma, H. Chen, H. Xu, D. Chen, and X. Wang, "Dendrite growth in the recharging process of zinc – air batteries," *J. Mater. Chem. A*, vol. 3, no. 45, pp. 22648–22655, 2015.

118. A. N. Moskvichev, Y. L. Gunko, M. G. Mikhalenko, A. A. Sletov, V. A. Kozyrin, and O. L. Kozina, "Zinc Oxidation in Limited Volume of Alkaline Electrolyte," *Russ. J. Electrochem.*, vol. 55, no. 4, pp. 322–332, 2019.

119. M. Bockelmann, M. Becker, L. Reining, U. Kunz, and T. Turek, "Passivation of zinc anodes in alkaline electrolyte: Part I. Determination of the starting point of passive film

formation," *J. Electrochem. Soc.*, vol. 165, no. 13, pp. A3048–A3055, 2018.

120. T. P. Dirkse, "Electrolytic Oxidation of Zinc in Alkaline Solutions," *J. Electrochem. Soc.*, vol. 102, no. 9, pp. 497–501, 1955.

121. T. P. Dirkse, "The Behavior of the Zinc Electrode in Alkaline Solutions: V. Supersaturated Zincate Solutions," *J. Electrochem. Soc.*, vol. 128, no. 7, pp. 1412–1415, 1981.

122. H. Gerischer, "Kinetik der Entladung einfacher und komplexer Zink-Ionen," *Zeitschrift für Phys. Chemie*, vol. 202, no. 1, pp. 302–317, 1953.

123. N. A. Hampson and G. A. Herdman, "Some Kinetic and Thermodynamic Studies of the System Zn/Zn(II), OH-," *Electroanal. Chem. Interfacial Electrochem.*, vol. 25, pp. 9–18, 1970.

124. V. S. Bagotsky, A. M. Skundin, and Y. M. Volfkovich, "Main Battery Types," in *Electrochemical Power Sources: Batteries, Fuel Cells, and Supercapacitors*, Hoboken, New Jersey: John Wiley & Sons, Inc, 2015, pp. 11–25.

125. C. Debiemme-chouvy and J. Vedel, "Supersaturated Zincate Solutions: A Study of the Decomposition Kinetics," *J. Electrochem. Soc.*, vol. 138, no. 9, pp. 2538–2542, 1991.

126. C. Debiemme-Chouvy, J. Vedel, M.-C. Bellissent-Funel, and R. Cortes, "Supersaturated Zincate Solutions: A Structural Study," *J. Electrochem. Soc.*, vol. 142, no. 5, pp. 1359–1364, 1995.

127. T. P. Dirkse, "Aqueous Potassium Hydroxide as Electrolyte for the Zinc Electrode," *J. Electrochem. Soc.*, vol. 134, no. 1, pp. 11–13, 1987.

128. J. P. G. Farr and N. A. Hampson, "Evaluation of the Characteristics of Exchange Reactions: I. Exchange Reaction at a Solid Zinc Electrode in Alkali," *Electroanal. Chem. Interfacial Electrochem.*, vol. 13, no. 4, pp. 433–441, 1967.

129. T. P. Dirkse and N. A. Hampson, "The Zn (II)/Zn Exchange Reaction in KOH Solutions: III. Exchange Current Measurements Using the Potentiostatic Method," *Electrochim. Acta*, vol. 17, no. 6, pp. 1113–1119, 1972.

130. J. O. Bockris, Z. Nagy, and A. Damjanovic, “On the Deposition and Dissolution of Zinc in Alkaline Solutions,” *J. Electrochem. Soc.*, vol. 119, no. 3, pp. 285–295, 1972.

131. Y. C. Chang and G. Prentice, “A Model for the Anodic Dissolution of Zinc in Alkaline Electrolyte: Kinetics of Initial Dissolution,” *J. Electrochem. Soc.*, vol. 131, no. 7, pp. 129–132, 1984.

132. D. A. Payne and A. J. Bard, “Mechanism of the Zinc(II)-Zinc Amalgam Electrode Reaction in Alkaline Media As Studied By Chronocoulometric and Voltammetric Techniques,” *J. Electrochem. Soc.*, vol. 119, no. 12, pp. 1665–1674, 1972.

133. R. Khezri, K. Jirasattayaporn, A. Abbasi, T. Maiyalagan, A. A. Mohamad, and S. Kheawhom, “Three-Dimensional Fibrous Iron as Anode Current Collector for Rechargeable Zinc – Air Batteries,” *Energies*, vol. 13, no. 6, p. 1429, 2020.

134. P. Pei, K. Wang, and Z. Ma, “Technologies for extending zinc – air battery’s cyclelife : A review,” *Appl. Energy*, vol. 128, pp. 315–324, 2014.

135. A. R. Mainar, E. Iruin, L. C. Colmenares, A. Kvasha, I. De Meatza, M. Bengoechea, O. Leonet, I. Boyano, Z. Zhang, and J. A. Blazquez, “An overview of progress in electrolytes for secondary zinc-air batteries and other storage systems based on zinc,” *J. Energy Storage*, vol. 15, pp. 304–328, 2018.

136. M. Xu, D. G. Ivey, Z. Xie, and W. Qu, “Rechargeable Zn-air batteries: Progress in electrolyte development and cell configuration advancement,” *J. Power Sources*, vol. 283, pp. 358–371, 2015.

137. D. Schröder, N. N. S. Borker, M. König, and U. Krewer, “Performance of zinc air batteries with added K2CO3 in the alkaline electrolyte,” *J. Appl. Electrochem.*, vol. 45, no. 5, pp. 427–437, 2015.

138. V. Caramia and B. Bozzini, “Materials science aspects of zinc-air batteries: A review,” *Mater. Renew. Sustain. Energy*, vol. 3, no. 2, 2014.

139. J. F. Drillet, F. Holzer, T. Kallis, S. Müller, and V. M. Schmidt, “Influence of CO2 on the stability of bifunctional oxygen electrodes for rechargeable zinc/air batteries and study of different CO2 filter materials,” *Phys. Chem. Chem. Phys.*, vol. 3, no. 3, pp. 368–371,

2001.

140. C. C. Yang and S. J. Lin, “Alkaline composite PEO-PVA-glass-fibre-mat polymer electrolyte for Zn-air battery,” *J. Power Sources*, vol. 112, no. 2, pp. 497–503, 2002.

141. T. N. T. Tran, H. J. Chung, and D. G. Ivey, “A study of alkaline gel polymer electrolytes for rechargeable zinc–air batteries,” *Electrochim. Acta*, vol. 327, p. 135021, 2019.

142. Z. Zhang, C. Zuo, Z. Liu, Y. Yu, Y. Zuo, and Y. Song, “All-solid-state Al-air batteries with polymer alkaline gel electrolyte,” *J. Power Sources*, vol. 251, pp. 470–475, 2014.

143. A. Guerfi, J. Trottier, I. Boyano, I. De Meatza, J. A. Blazquez, S. Brewer, K. S. Ryder, A. Vijh, and K. Zaghib, “High cycling stability of zinc-anode/conducting polymer rechargeable battery with non-aqueous electrolyte,” *J. Power Sources*, vol. 248, pp. 1099–1104, 2014.

144. M. Kar, T. J. Simons, M. Forsyth, and D. R. MacFarlane, “Ionic liquid electrolytes as a platform for rechargeable metal-air batteries: A perspective,” *Phys. Chem. Chem. Phys.*, vol. 16, no. 35, pp. 18658–18674, 2014.

145. H. Zhao, G. A. Baker, and S. Holmes, “New eutectic ionic liquids for lipase activation and enzymatic preparation of biodiesel,” *Org. Biomol. Chem.*, vol. 9, no. 6, pp. 1908–1916, 2011.

146. Q. Zhang, K. De Oliveira Vigier, S. Royer, and F. Jérôme, “Deep eutectic solvents: Syntheses, properties and applications,” *Chem. Soc. Rev.*, vol. 41, no. 21, pp. 7108–7146, 2012.

147. S. Liu, W. Han, B. Cui, X. Liu, H. Sun, J. Zhang, M. Lefler, and S. Licht, “Rechargeable Zinc Air Batteries and Highly Improved Performance through Potassium Hydroxide Addition to the Molten Carbonate Eutectic Electrolyte,” *J. Electrochem. Soc.*, vol. 165, no. 2, pp. A149–A154, 2018.

148. E. L. Dewi, K. Oyaizu, H. Nishide, and E. Tsuchida, “Cationic polysulfonium membrane as separator in zinc-air cell,” *J. Power Sources*, vol. 115, no. 1, pp. 149–152, 2003.

149. P. Arora and Z. Zhang, “Battery separators,” *Chem. Rev.*, vol. 104, no. 10, pp. 4419–4462,

2004.

150. H. J. Hwang, W. S. Chi, O. Kwon, J. G. Lee, J. H. Kim, and Y. G. Shul, “Selective Ion Transporting Polymerized Ionic Liquid Membrane Separator for Enhancing Cycle Stability and Durability in Secondary Zinc-Air Battery Systems,” *ACS Appl. Mater. Interfaces*, vol. 8, no. 39, pp. 26298–26308, 2016.

151. M. Xiong, M. P. Clark, M. Labbe, and D. G. Ivey, “A horizontal zinc-air battery with physically decoupled oxygen evolution/reduction reaction electrodes,” *J. Power Sources*, vol. 393, pp. 108–118, 2018.

152. J. Zhang, Z. Zhao, Z. Xia, and L. Dai, “A metal-free bifunctional electrocatalyst for oxygen reduction and oxygen evolution reactions,” *Nat. Nanotechnol.*, vol. 10, no. 5, pp. 444–452, 2015.

153. W. Hong, H. Li, and B. Wang, “A horizontal three-electrode structure for zinc-air batteries with long-term cycle life and high performance,” *Int. J. Electrochem. Sci.*, vol. 11, no. 5, pp. 3843–3851, 2016.

154. R. L. Puurunen, “Surface chemistry of atomic layer deposition : A case study for the trimethylaluminum/water process,” *J. Appl. Phys.*, vol. 97, no. 12, p. 121301, Jun. 2005.

155. M. Ritala and M. Leskela, “Atomic Layer Deposition,” in *Handbook of Thin Film Materials*, vol. 1, H. S. Nalwa, Ed. San Diego, CA: Academic Press, 2002, pp. 103–159.

156. S. M. George, “Atomic Layer Deposition : An Overview,” *Chem. Rev.*, vol. 110, no. 1, pp. 111–131, 2010.

157. M. P. Clark, T. Muneshwar, M. Xiong, K. Cadien, and D. G. Ivey, “Saturation Behavior of Atomic Layer Deposition MnOx from Bis(Ethylcyclopentadienyl) Manganese and Water: Saturation Effect on Coverage of Porous Oxygen Reduction Electrodes for Metal-Air Batteries,” *ACS Appl. Nano Mater.*, vol. 2, no. 1, pp. 267–277, 2019.

158. H. C. M. M. Knoops, S. E. Potts, A. A. Bol, and W. M. M. M. Kessels, “Atomic Layer Deposition,” in *Handbook of Crystal Growth: Thin Films and Epitaxy*, 2nd Ed., T. F. Kuech, Ed. Elsevier B.V., 2015, pp. 1101–1134.

159. H. Van Bui, F. Grillo, and J. R. van Ommen, “Atomic and molecular layer deposition : off the beaten track,” *Chem. Commun.*, vol. 53, no. 1, pp. 45–71, 2017.

160. M. Ritala and J. Niinistö, “Atomic Layer Deposition,” in *Chemical Vapour Deposition*, A. C. Jones and M. L. Hitchman, Eds. Cambridge, UK: Royal Society of Chemistry, 2009, pp. 158–206.

161. T. Suntola, “Atomic layer epitaxy,” *Thin Solid Films*, vol. 216, no. 1, pp. 84–89, 1992.

162. G. Cao, *Nanostructures and Nanomaterials*. World Scientific Publishing Company, 2004.

163. Z. Guo and L. Tan, *Fundamentals and Applications of Nanomaterials*. Norwood, MA: Artech House, 2009.

164. G. H. Gilmer and M. H. Grabow, “Models of Thin Film Growth Modes,” *Jom*, vol. 39, no. 6, pp. 19–23, 1987.

165. R. W. Johnson, A. Hultqvist, and S. F. Bent, “A brief review of atomic layer deposition: from fundamentals to applications,” *Mater. Today*, vol. 17, no. 5, pp. 236–246, 2014.

166. H. B. Profijt, S. E. Potts, M. C. M. van de Sanden, and W. M. M. Kessels, “Plasma-Assisted Atomic Layer Deposition: Basics, Opportunities, and Challenges,” *J. Vac. Sci. Technol. A Vacuum, Surfaces, Film.*, vol. 29, no. 5, p. 050801, 2011.

167. E. Langereis, S. B. S. Heil, H. C. M. Knoops, W. Keuning, M. C. M. Van De Sanden, and W. M. M. Kessels, “In situ spectroscopic ellipsometry as a versatile tool for studying atomic layer deposition,” *J. Phys. D. Appl. Phys.*, vol. 42, no. 7, 2009.

168. A. Roth, *Vacuum Technology*, 3rd Ed. Amsterdam, The Netherlands: Elsevier Science B.V., 1990.

169. G. Liu, A. Bertuch, E. W. Deguns, M. J. Dalberth, G. M. Sundaram, and J. Svenja Becker, “METHOD AND APPARATUS FOR PRECURSOR DELIVERY,” US20110311726A1, 2011.

170. J.A. Woollam, *CompleteEASE Software Manual*, 6.54. Lincoln, NE: J. A. Woollam Co., Inc., 2020.

171. H. Fujiwara, J. Koh, P. I. Rovira, and R. W. Collins, “Assessment of effective-medium

theories in the analysis of nucleation and microscopic surface roughness evolution for semiconductor thin films," *Phys. Rev. B - Condens. Matter Mater. Phys.*, vol. 61, no. 16, pp. 10832–10844, 2000.

172. M. Scheller, C. Jansen, and M. Koch, "Applications of Effective Medium Theories in the Terahertz Regime," in *Recent Optical and Photonic Technologies*, K. Y. Kim, Ed. London, United Kingdom: IntechOpen, 2010, pp. 231–250.

173. J. Humlicek, "Data Analysis for Nanomaterials: Effective Medium Approximation, Its Limits and Implementations," in *Ellipsometry at the Nanoscale*, M. Losurdo and K. Hingerl, Eds. Springer-Verlag Berlin Heidelberg, 2013, pp. 225–256.

174. D. E. Aspnes, J. B. Theeten, and F. Hottier, "Investigation of effective-medium models of microscopic surface roughness by spectroscopic ellipsometry," *Phys. Rev. B*, vol. 20, no. 8, pp. 3292–3302, 1979.

175. R. Landauer, "Electrical conductivity in inhomogeneous media," *AIP Conf. Proc.*, vol. 40, no. 1, pp. 2–45, 1978.

176. J. R. Avila, D. W. Kim, M. Rimoldi, O. K. Farha, and J. T. Hupp, "Fabrication of Thin Films of α-Fe2O3 via Atomic Layer Deposition Using Iron Bisamidinate and Water under Mild Growth Conditions," *ACS Appl. Mater. Interfaces*, vol. 7, no. 30, pp. 16138–16142, 2015.

177. B. B. Burton, F. H. Fabreguette, and S. M. George, "Atomic layer deposition of MnO using Bis(ethylcyclopentadienyl)manganese and H2O," *Thin Solid Films*, vol. 517, no. 19, pp. 5658–5665, 2009.

178. K. L. Pickrahn, S. W. Park, Y. Gorlin, H. B. R. Lee, T. F. Jaramillo, and S. F. Bent, "Active MnOx Electrocatalysts Prepared by Atomic Layer Deposition for Oxygen Evolution and Oxygen Reduction Reactions," *Adv. Energy Mater.*, vol. 2, no. 10, pp. 1269–1277, 2012.

179. K. L. Pickrahn, Y. Gorlin, L. C. Seitz, A. Garg, D. Nordlund, T. F. Jaramillo, and S. F. Bent, "Applications of ALD MnO to electrochemical water splitting," *Phys. Chem. Chem. Phys.*, vol. 17, no. 21, pp. 14003–14011, 2015.

180. N. Yang, J. S. Yoo, J. Schumann, P. Bothra, J. A. Singh, E. Valle, F. Abild-Pedersen, J. K. Nørskov, and S. F. Bent, “Rh-MnO Interface Sites Formed by Atomic Layer Deposition Promote Syngas Conversion to Higher Oxygenates,” *ACS Catal.*, vol. 7, no. 9, pp. 5746–5757, 2017.

181. M. J. Young, M. Neuber, A. C. Cavanagh, H. Sun, C. B. Musgrave, and S. M. George, “ Sodium Charge Storage in Thin Films of MnO 2 Derived by Electrochemical Oxidation of MnO Atomic Layer Deposition Films ,” *J. Electrochem. Soc.*, vol. 162, no. 14, pp. A2753–A2761, 2015.

182. A. L. Lipson, K. Puntambekar, D. J. Comstock, X. Meng, M. L. Geier, J. W. Elam, and M. C. Hersam, “Nanoscale investigation of solid electrolyte interphase inhibition on li-ion battery MnO electrodes via atomic layer deposition of Al 2O3,” *Chem. Mater.*, vol. 26, no. 2, pp. 935–940, 2014.

183. N. C. Strandwitz, D. J. Comstock, R. L. Grimm, A. C. Nichols-Nielander, J. Elam, and N. S. Lewis, “Photoelectrochemical behavior of n-type Si(100) electrodes coated with thin films of manganese oxide grown by atomic layer deposition,” *J. Phys. Chem. C*, vol. 117, no. 10, pp. 4931–4936, 2013.

184. K. Matsumoto, K. Maekawa, H. Nagai, and J. Koike, “Deposition behavior and substrate dependency of ALD MnOx diffusion barrier layer,” *Proc. 2013 IEEE Int. Interconnect Technol. Conf. IITC 2013*, pp. 9–11, 2013.

185. X. Yang, C. Du, R. Liu, J. Xie, and D. Wang, “Balancing photovoltage generation and charge-transfer enhancement for catalyst-decorated photoelectrochemical water splitting: A case study of the hematite/MnOx combination,” *J. Catal.*, vol. 304, pp. 86–91, 2013.

186. M. J. Young, C. D. Hare, A. S. Cavanagh, C. B. Musgrave, and S. M. George, “Rapid Growth of Crystalline Mn5O8 by Self-Limited Multilayer Deposition using Mn(EtCp)2 and O3,” *ACS Appl. Mater. Interfaces*, vol. 8, no. 28, pp. 18560–18569, 2016.

187. H. L. Ã. Lu, G. Scarel, X. L. Li, and M. Fanciulli, “Thin MnO and NiO films grown using atomic layer deposition from ethylcyclopentadienyl type of precursors,” *J. Cryst. Growth*, vol. 310, no. 24, pp. 5464–5468, 2008.

188. J. W. Linnett, “The electronic structure of ferrocene and related compounds,” *Trans. Faraday Soc.*, vol. 52, pp. 904–912, 1956.

189. R. H. Crabtree, *The Organometallic Chemistry of the Transition Metals*, 4th ed. Hoboken, New Jersey: John Wiley & Sons, Inc, 2005.

190. D. Astruc, “Why is Ferrocene so Exceptional?,” *Eur. J. Inorg. Chem.*, vol. 2017, no. 1, pp. 6–29, 2017.

191. Y. T. Chong, E. M. Y. Yau, K. Nielsch, and J. Bachmann, “Direct atomic layer deposition of ternary ferrites with various magnetic properties,” *Chem. Mater.*, vol. 22, no. 24, pp. 6506–6508, 2010.

192. J. Liu, B. Xiao, M. N. Banis, R. Li, T. K. Sham, and X. Sun, “Atomic layer deposition of amorphous iron phosphates on carbon nanotubes as cathode materials for lithium-ion batteries,” *Electrochim. Acta*, vol. 162, pp. 275–281, 2015.

193. A. B. F. Martinson, M. J. Devries, J. A. Libera, S. T. Christensen, J. T. Hupp, M. J. Pellin, and J. W. Elam, “Atomic Layer Deposition of Fe2O3 Using Ferrocene and Ozone,” *J. Phys. Chem. C*, vol. 115, no. 10, pp. 4333–4339, 2011.

194. B. M. Klahr, A. B. F. F. Martinson, and T. W. Hamann, “Photoelectrochemical Investigation of Ultrathin Film Iron Oxide Solar Cells Prepared by Atomic Layer Deposition,” *Langmuir*, vol. 27, no. 1, pp. 461–468, 2011.

195. C. Gong, L. Zhao, S. Li, H. Wang, Y. Gong, R. Wang, and B. He, “Atomic layered deposition iron oxide on perovskite LaNiO3 as an efficient and robust bi-functional catalyst for lithium oxygen batteries,” *Electrochim. Acta*, vol. 281, pp. 338–347, 2018.

196. Y. Wen, J. Cai, J. Zhang, J. Yang, L. Shi, K. Cao, R. Chen, and B. Shan, “Edge-Selective Growth of MCp2 (M = Fe, Co, and Ni) Precursors on Pt Nanoparticles in Atomic Layer Deposition: A Combined Theoretical and Experimental Study,” *Chem. Mater.*, vol. 31, no. 1, pp. 101–111, 2019.

197. S. Porro, K. Bejtka, A. Jasmin, M. Fontana, G. Milano, A. Chiolerio, C. F. Pirri, and C. Ricciardi, “A multi-level memristor based on atomic layer deposition of iron oxide,” *Nanotechnology*, vol. 29, no. 49, p. 495201, 2018.

198. X. Li, N. C. Fan, and H. J. Fan, “A Micro-pulse Process of Atomic Layer Deposition of Iron Oxide Using Ferrocene and Ozone Precursors and Ti-Doping,” *Chem. Vap. Depos.*, vol. 19, no. 4–6, pp. 104–110, 2013.

199. M. Li and H. He, “Study on electrochemical performance of multi-wall carbon nanotubes coated by iron oxide nanoparticles as advanced electrode materials for supercapacitors,” *Vacuum*, vol. 143, pp. 371–379, 2017.

200. C. Guan, J. Liu, Y. Wang, L. Mao, Z. Fan, Z. Shen, H. Zhang, and J. Wang, “Iron Oxide-Decorated Carbon for Supercapacitor Anodes with Ultrahigh Energy Density and Outstanding Cycling Stability,” *ACS Nano*, vol. 9, no. 5, pp. 5198–5207, 2015.

201. A. Tamm, M. C. Dimri, J. Kozlova, A. Aidla, T. Tätte, T. Arroval, U. Mäeorg, H. Mändar, R. Stern, and K. Kukli, “Atomic layer deposition of ferromagnetic iron oxide films on three-dimensional substrates with tin oxide nanoparticles,” *J. Cryst. Growth*, vol. 343, no. 1, pp. 21–27, 2012.

202. Q. Hu, S. Wang, Z. Gao, Y. Li, Q. Zhang, Q. Xiang, and Y. Qin, “The precise decoration of Pt nanoparticles with Fe oxide by atomic layer deposition for the selective hydrogenation of cinnamaldehyde,” *Appl. Catal. B Environ.*, vol. 218, pp. 591–599, 2017.

203. J. R. Scheffe, A. Francés, D. M. King, X. Liang, B. A. Branch, A. S. Cavanagh, S. M. George, and A. W. Weimer, “Atomic layer deposition of iron(III) oxide on zirconia nanoparticles in a fluidized bed reactor using ferrocene and oxygen,” *Thin Solid Films*, vol. 517, no. 6, pp. 1874–1879, 2009.

204. J. R. Scheffe, M. D. Allendorf, E. N. Coker, B. W. Jacobs, A. H. McDaniel, and A. W. Weimer, “Hydrogen Production via Chemical Looping Redox Cycles Using Atomic Layer Deposition-Synthesized Iron Oxide and Cobalt Ferrites,” *Chem. Mater.*, vol. 23, no. 8, pp. 2030–2038, 2011.

205. N. Yan, L. Qin, J. Li, F. Zhao, and H. Feng, “Atomic layer deposition of iron oxide on reduced graphene oxide and its catalytic activity in the thermal decomposition of ammonium perchlorate,” *Appl. Surf. Sci.*, vol. 451, pp. 155–161, 2018.

206. M. Rooth, A. Johansson, K. Kukli, J. Aarik, M. Boman, and A. Hårsta, “Atomic layer

deposition of iron oxide thin films and nanotubes using ferrocene and oxygen as precursors," *Chem. Vap. Depos.*, vol. 14, no. 3–4, pp. 67–70, 2008.

207. T. M. Onn, M. Monai, S. Dai, L. Arroyo-Ramirez, S. Zhang, X. Pan, G. W. Graham, P. Fornasiero, and R. J. Gorte, "High-surface-area, iron-oxide films prepared by atomic layer deposition on γ-Al2O3," *Appl. Catal. A Gen.*, vol. 534, pp. 70–77, 2017.

208. Strem Chemicals, "Product Catalog 26-0700: t-Butylferrocene, min. 98%," *Strem Chemicals, Inc.*, 2020. [Online]. Available: https://www.strem.com/catalog/v/26-0700/32/iron_1316-98-9. [Accessed: 16-Jun-2020].

209. Strem Chemicals, "Product Catalog 26-1600: Ethylferrocene, 98%," *Strem Chemicals, Inc.*, 2020. [Online]. Available: https://www.strem.com/catalog/v/26-1600/32/iron_1273-89-8. [Accessed: 16-Jun-2020].

210. L. Steier, J. Luo, M. Schreier, M. T. Mayer, T. Sajavaara, and M. Grätzel, "Low-Temperature Atomic Layer Deposition of Crystalline and Photoactive Ultrathin Hematite Films for Solar Water Splitting," *ACS Nano*, vol. 9, no. 12, pp. 11775–11783, 2015.

211. M. K. Singh, Y. Yang, and C. G. Takoudis, "Low-pressure metallorganic chemical vapor deposition of Fe 2O3 thin films on Si(100) using n-butylferrocene and oxygen," *J. Electrochem. Soc.*, vol. 155, no. 9, pp. 618–623, 2008.

212. N. F. W. Thissen, M. A. Verheijen, R. G. Houben, C. van der Marel, W. M. M. Kessels, and A. A. Bol, "Synthesis of single-walled carbon nanotubes from atomic-layer-deposited Co3O4 and Co3O4/Fe2O3 catalyst films," *Carbon*, vol. 121, pp. 389–398, 2017.

213. R. K. Ramachandran, J. Dendooven, and C. Detavernier, "Plasma enhanced atomic layer deposition of Fe2O3 thin films," *J. Mater. Chem. A*, vol. 2, no. 27, pp. 10662–10667, 2014.

214. T. Dobbelaere, F. Mattelaer, J. Dendooven, P. Vereecken, and C. Detavernier, "Plasma-Enhanced Atomic Layer Deposition of Iron Phosphate as a Positive Electrode for 3D Lithium-Ion Microbatteries," *Chem. Mater.*, vol. 28, no. 10, pp. 3435–3445, 2016.

215. L. Pasin, J. Meyer, E. Eiche, and G. Kasper, "On the Activity Enhancing Role of Iron Oxide for Noble Metal Oxidation Catalysts: A CVD-Based Study with Differently

Structured Combinations of Pt and FeOx Coatings on Al2O3," *Coatings*, vol. 8, no. 6, pp. 1–13, 2018.

216. G. Charpak, V. Peskov, F. Sauli, and D. Scigocki, "Ethyl Feorrocene in gas, condensed, or adsorbed phases: three types of photosensitive elements for use in gaseous detectors," *Nucl. Instruments Methods Phys. Res. A*, vol. 277, no. 2–3, pp. 537–546, 1989.

217. G. Charpak, P. Benaben, P. Breuil, P. Martinengo, E. Nappi, and V. Peskov, "Progress in the development of a S-RETGEM-based detector for an early forest fire warning system," *J. Instrum.*, vol. 4, no. December, pp. 1–16, 2009.

218. P. Miné, "Photoemissive materials and their application to gaseous detectors," *Nucl. Inst. Methods Phys. Res. A*, vol. 343, no. 1, pp. 99–108, 1994.

219. G. Vasileiadis, G. Malamud, P. Miné, and D. Vartsky, "Solid and vapour phase UV photocathodes for gaseous detectors," *Nucl. Instruments Methods Phys. Res. A*, vol. 372, no. 1–2, pp. 31–34, 1996.

220. K. Kukli, M. C. Dimri, A. Tamm, M. Kemell, T. Käämbre, M. Vehkamäki, M. Puttaswamy, R. Stern, I. Kuusik, A. Kikas, M. Tallarida, D. Schmeißer, M. Ritala, and M. Leskelä, "Structural and magnetic studies on iron oxide and iron-magnesium oxide thin films deposited using ferrocene and (Dimethylaminomethyl)ferrocene precursors," *ECS J. Solid State Sci. Technol.*, vol. 2, no. 3, pp. 45–54, 2013.

221. M. Daub, J. Bachmann, J. Jing, M. Knez, U. Gösele, S. Barth, S. Mathur, J. Escrig, D. Altbir, and K. Nielsch, "Ferromagnetic nanostructures by atomic layer deposition: From thin films towards core-shell nanotubes," *ECS Trans.*, vol. 11, no. 7, pp. 139–148, 2007.

222. J. Bachmann, J. Jing, M. Knez, S. Barth, H. Shen, S. Mathur, M. Planck, M. Physics, A. Weinberg, U. Gösele, and K. Nielsch, "Ordered Iron Oxide Nanotube Arrays of Controlled Geometry and Tunable Magnetism by Atomic Layer Deposition," *J. Am. Chem. Soc.*, vol. 5, no. 31, pp. 9554–9555, 2007.

223. J. R. Schneider, J. G. Baker, and S. F. Bent, "The Influence of Ozone: Superstoichiometric Oxygen in Atomic Layer Deposition of Fe2O3 Using tert-Butylferrocene and O3," *Adv. Mater. Interfaces*, vol. 7, no. 11, pp. 1–10, 2020.

224. J. A. Klug, N. G. Becker, S. C. Riha, A. B. F. Martinson, J. W. Elam, M. J. Pellin, and T. Proslier, “Low temperature atomic layer deposition of highly photoactive hematite using iron(III) chloride and water,” *J. Mater. Chem. A*, vol. 1, no. 38, pp. 11607–11613, 2013.

225. M. Lie, H. Fjellvåg, and A. Kjekshus, “Growth of Fe2O3 thin films by atomic layer deposition,” *Thin Solid Films*, vol. 488, no. 1–2, pp. 74–81, 2005.

226. M. de Ridder, P. C. van de Ven, R. G. van Welzenis, H. H. Brongersma, S. Helfensteyn, C. Creemers, P. Van Der Voort, M. Baltes, M. Mathieu, and E. F. Vansant, “Growth of iron oxide on yttria-stabilized zirconia by atomic layer deposition,” *J. Phys. Chem. B*, vol. 106, no. 51, pp. 13146–13153, 2002.

227. T. Tynell and M. Karppinen, “Atomic layer deposition of ZnO: A review,” *Semicond. Sci. Technol.*, vol. 29, no. 4, 2014.

228. M. Tammenmaa, T. Koskinen, L. Hiltunen, L. Niinistö, and M. Leskelä, “Zinc chalcogenide thin films grown by the atomic layer epitaxy technique using zinc acetate as source material,” *Thin Solid Films*, vol. 124, no. 2, pp. 125–128, 1985.

229. M. Puttaswamy, M. Vehkamäki, K. Kukli, M. C. Dimri, M. Kemell, T. Hatanpää, M. J. Heikkilä, K. Mizohata, R. Stern, M. Ritala, and M. Leskelä, “Bismuth iron oxide thin films using atomic layer deposition of alternating bismuth oxide and iron oxide layers,” *Thin Solid Films*, vol. 611, pp. 78–87, 2016.

230. C. Hägglund, T. Grehl, J. T. Tanskanen, Y. S. Yee, M. N. Mullings, A. J. M. Mackus, C. MacIsaac, B. M. Clemens, H. H. Brongersma, and S. F. Bent, “Growth, intermixing, and surface phase formation for zinc tin oxide nanolaminates produced by atomic layer deposition,” *J. Vac. Sci. Technol. A*, vol. 34, no. 2, p. 021516, 2016.

231. P. Myllymäki, M. Nieminen, J. Niinistö, M. Putkonen, K. Kukli, and L. Niinistö, “High-permittivity YScO3 thin films by atomic layer deposition using two precursor approaches,” *J. Mater. Chem.*, vol. 16, no. 6, pp. 563–569, 2006.

232. A. Del Vitto, R. Piagge, E. Ravizza, S. Spadoni, A. Sebastiani, C. Scozzari, C. Wiemer, G. Ghidini, M. Alessandri, M. Fanciulli, J. W. Maes, and M. Verghese, “ Evaluation of HfLaO x as Blocking Layer for Innovative Nonvolatile Memory Applications ,” *ECS*

Trans., vol. 33, no. 3, pp. 417–424, 2010.

233. M. Popovici, A. Delabie, S. Van Elshocht, S. Clima, G. Pourtois, L. Nyns, K. Tomida, N. Menou, K. Opsomer, J. Swerts, C. Detavernier, D. Wouters, and J. A. Kittl, "Growth and Material Characterization of Hafnium Titanates Deposited by Atomic Layer Deposition," *J. Electrochem. Soc.*, vol. 156, no. 10, p. G145, 2009.

234. C. Adelmann, D. Lin, L. Nyns, B. Schepers, A. Delabie, S. Van Elshocht, and M. Caymax, "Atomic-layer-deposited tantalum silicate as a gate dielectric for III-V MOS devices," *Microelectron. Eng.*, vol. 88, no. 7, pp. 1098–1100, 2011.

235. S. Song, E. Kim, K. Kim, J. Bae, J. Lee, C. H. Jung, H. Lim, and H. Jeon, "Crystallinity-Controlled Atomic Layer Deposition of Ti-Doped ZrO2 Thin Films," *ECS Adv.*, vol. 3, no. 1, p. 012002, 2024.

236. E. B. Yousfi, T. Asikainen, V. Pietu, P. Cowache, M. Powalla, and D. Lincot, "Cadmium-free buffer layers deposited by atomic layer epitaxy for copper indium diselenide solar cells," *Thin Solid Films*, vol. 361–362, pp. 183–186, 2000.

237. P. Genevée, F. Donsanti, N. Schneider, and D. Lincot, "Atomic layer deposition of zinc indium sulfide films: Mechanistic studies and evidence of surface exchange reactions and diffusion processes," *J. Vac. Sci. Technol. A*, vol. 31, no. 1, p. 01A131, 2013.

238. J. Harjuoja, S. Väyrynen, M. Putkonen, L. Niinistö, and E. Rauhala, "Crystallization of bismuth titanate and bismuth silicate grown as thin films by atomic layer deposition," *J. Cryst. Growth*, vol. 286, no. 2, pp. 376–383, 2006.

239. T. Cheon, S. H. Choi, S. H. Kim, and D. H. Kang, "Atomic layer deposition of RuAlO thin films as a diffusion barrier for seedless Cu interconnects," *Electrochem. Solid-State Lett.*, vol. 14, no. 5, pp. D57–D61, 2011.

240. T. K. Eom, S. H. Kim, K. S. Park, S. Kim, and H. Kim, "Formation of nano-crystalline ru-based ternary thin films by plasma-enhanced atomic layer deposition," *Electrochem. Solid-State Lett.*, vol. 14, no. 1, pp. D10–D12, 2011.

241. Y. R. Shin, W. S. Kwack, Y. C. Park, J. H. Kim, S. Y. Shin, K. Il Moon, H. W. Lee, and S. H. Kwon, "Structural and electrical properties of ternary Ru-AlN thin films prepared by

plasma-enhanced atomic layer deposition," *Mater. Res. Bull.*, vol. 47, no. 3, pp. 790–793, 2012.

242. W. Besling, A. Satta, J. Schuhmacher, T. Abell, V. Sutcliffe, A.-M. Hoyas, G. Beyer, D. Gravesteijn, and K. Maex, "Atomic layer deposition of barriers for interconnect," in *Proceedings of the IEEE 2002 International Interconnect Technology Conference (Cat. No.02EX519)*, 2002, pp. 288–291.

243. C. D. Pham, J. P. J. Chang, M. A. Zurbuchen, and J. P. J. Chang, "Magnetic Properties of CoFe2O4 Thin Films Synthesized by Radical-Enhanced Atomic Layer Deposition," *ACS Appl. Mater. Interfaces*, vol. 9, no. 42, pp. 36980–36988, 2017.

244. M. Lie, K. B. Klepper, O. Nilsen, H. Fjellvåg, and A. Kjekshus, "Growth of iron cobalt oxides by atomic layer deposition," *Dalt. Trans.*, no. 2, pp. 253–259, 2008.

245. K. Uusi-Esko, E. L. Rautama, M. Laitinen, T. Sajavaara, and M. Karppinen, "Control of oxygen nonstoichiometry and magnetic property of MnCo2O4 thin films grown by atomic layer deposition," *Chem. Mater.*, vol. 22, no. 23, pp. 6297–6300, 2010.

246. M. Mäntymäki, M. Ritala, and M. Leskelä, "Metal fluorides as lithium-ion battery materials: An atomic layer deposition perspective," *Coatings*, vol. 8, no. 8, 2018.

247. V. Miikkulainen, A. Ruud, E. Østreng, O. Nilsen, M. Laitinen, T. Sajavaara, and H. Fjellvaìšg, "Atomic layer deposition of spinel lithium manganese oxide by film-body-controlled lithium incorporation for thin-film lithium-ion batteries," *J. Phys. Chem. C*, vol. 118, no. 2, pp. 1258–1268, 2014.

248. J. Liu, M. N. Banis, Q. Sun, A. Lushington, R. Li, T. K. Sham, and X. Sun, "Rational Design of Atomic-Layer-Deposited LiFePO4 as a High-Performance Cathode for Lithium-Ion Batteries," *Adv. Mater.*, vol. 26, no. 37, pp. 6472–6477, 2014.

249. J. Hämäläinen, J. Holopainen, F. Munnik, T. Hatanpää, M. Heikkilä, M. Ritala, and M. Leskelä, "Lithium Phosphate Thin Films Grown by Atomic Layer Deposition," *J. Electrochem. Soc.*, vol. 159, no. 3, pp. A259–A263, 2012.

250. A. C. Kozen, A. J. Pearse, C. F. Lin, M. Noked, and G. W. Rubloff, "Atomic Layer Deposition of the Solid Electrolyte LiPON," *Chem. Mater.*, vol. 27, no. 15, pp. 5324–

5331, 2015.

251. B. Xiao, B. Wang, J. Liu, K. Kaliyappan, Q. Sun, Y. Liu, G. Dadheech, M. P. Balogh, L. Yang, T. K. Sham, R. Li, M. Cai, and X. Sun, "Highly stable Li1.2Mn0.54Co0.13Ni0.13O2 enabled by novel atomic layer deposited AlPO4 coating," *Nano Energy*, vol. 34, pp. 120–130, 2017.

252. T. Aaltonen, O. Nilsen, A. Magrasó, and H. Fjellvåg, "Atomic Layer Deposition of Li2O–Al2O3 Thin Films," *Chem. Mater.*, vol. 23, no. 21, pp. 4669–4675, 2011.

253. J. R. Scheffe, J. Li, and A. W. Weimer, "A spinel ferrite/hercynite water-splitting redox cycle," *Int. J. Hydrogen Energy*, vol. 35, no. 8, pp. 3333–3340, 2010.

254. A. G. Hufnagel, K. Peters, A. Müller, C. Scheu, D. Fattakhova-Rohlfing, and T. Bein, "Zinc Ferrite Photoanode Nanomorphologies with Favorable Kinetics for Water-Splitting," *Adv. Funct. Mater.*, vol. 26, no. 25, pp. 4435–4443, 2016.

255. A. G. Hufnagel, H. Hajiyani, S. Zhang, T. Li, O. Kasian, B. Gault, B. Breitbach, T. Bein, D. Fattakhova-Rohlfing, C. Scheu, and R. Pentcheva, "Why Tin-Doping Enhances the Efficiency of Hematite Photoanodes for Water Splitting—The Full Picture," *Adv. Funct. Mater.*, vol. 28, no. 52, pp. 1–10, 2018.

256. R. T. M. van Limpt, M. Lavorenti, M. A. Verheijen, M. N. Tsampas, and M. Creatore, "Control by atomic layer deposition over the chemical composition of nickel cobalt oxide for the oxygen evolution reaction," *J. Vac. Sci. Technol. A*, vol. 41, no. 3, 2023.

257. J. G. Baker, J. R. Schneider, J. A. Garrido Torres, J. A. Singh, A. J. M. Mackus, M. Bajdich, and S. F. Bent, "The Role of Aluminum in Promoting Ni-Fe-OOH Electrocatalysts for the Oxygen Evolution Reaction," *ACS Appl. Energy Mater.*, vol. 2, no. 5, pp. 3488–3499, 2019.

258. K. L. Pickrahn, A. Garg, and S. F. Bent, "ALD of ultrathin ternary oxide electrocatalysts for water splitting," *ACS Catal.*, vol. 5, no. 3, pp. 1609–1616, 2015.

259. J. I. Goldstein, D. E. Newbury, P. Echlin, D. C. Joy, C. Fiori, and E. Lifshin, *Scanning Electron Microscopy and X-Ray Microanalysis*, 2nd Ed. New York, NY: Plenum Press, 1984.

260. Y. Leng, *Materials Characterization*, 2nd Ed. Weinheim, Germany: Wiley-VCH, 2013.

261. J. I. Goldstein, D. E. Newbury, J. R. Michael, N. W. M. Ritchie, J. H. J. Scott, and D. C. Joy, *Scanning Electron Microscopy and X-Ray Microanalysis*, 4th Ed. New York, NY: Springer Science+Business Media, 2018.

262. D. B. Williams and C. B. Carter, *Transmission Electron Microscopy*, 2nd Ed. New York, NY: Springer Science+Business Media, 2009.

263. R. J. Keyse, A. J. Garratt-Reed, and P. J. Goodhew, *Introduction to Scanning Transmission Electron Microscopy*. New York: Taylor & Francis, 1998.

264. G. F. Harrington and J. Santiso, "Back-to-Basics tutorial: X-ray diffraction of thin films," *J. Electroceramics*, vol. 47, no. 4, pp. 141–163, 2021.

265. B. A. van Brussel and J. T. M. De Hosson, "Glancing angle x-ray diffraction: A different approach," *Appl. Phys. Lett.*, vol. 64, no. 12, pp. 1585–1587, 1994.

266. H. D. Young, R. A. Freedman, and A. Lewis Ford, *Sears and Zemansky's University Physics: with modern physics*, 13th Ed. San Francisco, CA: Pearson Education, Inc., 2014.

267. G. B. Arfken, D. F. Griffing, D. C. Kelly, and J. Priest, *University Physics*. Orlando, FL: Academic Press, Inc., 1984.

268. J. F. Moulder, W. F. Stickle, P. E. Sobol, and K. D. Bomben, *Handbook of X-ray Photoelectron Spectroscopy*, 2nd Ed. Eden Prairie, MN: Perkin-Elmer Coporation, 1992.

269. D. R. Baer, K. Artyushkova, C. R. Brundle, J. E. Castle, M. H. Engelhard, K. J. Gaskell, J. T. Grant, R. T. Haasch, M. R. Linford, C. J. Powell, A. G. Shard, P. M. A. Sherwood, and V. S. Smentkowski, "Practical guides for x-ray photoelectron spectroscopy: First steps in planning, conducting, and reporting XPS measurements," *J. Vac. Sci. Technol. A*, vol. 37, no. 3, p. 031401, 2019.

270. M. C. Biesinger, B. P. Payne, A. P. Grosvenor, L. W. M. Lau, A. R. Gerson, and R. S. C. Smart, "Resolving surface chemical states in XPS analysis of first row transition metals, oxides and hydroxides: Cr, Mn, Fe, Co and Ni," *Appl. Surf. Sci.*, vol. 257, no. 7, pp. 2717–2730, 2011.

271. V. R. Galakhov, M. Demeter, S. Bartkowski, M. Neumann, N. A. Ovechkina, E. Z. Kurmaev, N. I. Lobachevskaya, Y. M. Mukovskii, J. Mitchell, and D. L. Ederer, "Mn 3s exchange splitting in mixed-valence manganites," *Phys. Rev. B - Condens. Matter Mater. Phys.*, vol. 65, no. 11, pp. 1–4, 2002.

272. Y. Gorlin, B. Lassalle-Kaiser, J. D. Benck, S. Gul, S. M. Webb, V. K. Yachandra, J. Yano, and T. F. Jaramillo, "In situ X-ray absorption spectroscopy investigation of a bifunctional manganese oxide catalyst with high activity for electrochemical water oxidation and oxygen reduction," *J. Am. Chem. Soc.*, vol. 135, no. 23, pp. 8525–8534, 2013.

273. J. R. Shallenberger, N. J. Smith, and J. Banerjee, "Derivation of empirical XPS relative sensitivity factors from silicate glasses," *Surf. Interface Anal.*, vol. 53, no. 6, pp. 569–579, 2021.

274. M. Thommes, K. Kaneko, A. V. Neimark, J. P. Olivier, F. Rodriguez-Reinoso, J. Rouquerol, and K. S. W. Sing, "Physisorption of gases, with special reference to the evaluation of surface area and pore size distribution (IUPAC Technical Report)," *Pure Appl. Chem.*, vol. 87, no. 9–10, pp. 1051–1069, 2015.

275. S. Brunauer, P. H. Emmett, and E. Teller, "Adsorption of Gases in Multimolecular Layers," *J. Am. Chem. Soc.*, vol. 60, no. 2, pp. 309–319, 1938.

276. A. J. Bard and L. A. Faulkner, *Electrochemical Methods*, 2nd Ed. New York, NY: John Wiley & Sons, Inc, 2001.

277. N. Elgrishi, K. J. Rountree, B. D. McCarthy, E. S. Rountree, T. T. Eisenhart, and J. L. Dempsey, "A Practical Beginner's Guide to Cyclic Voltammetry," *J. Chem. Educ.*, vol. 95, no. 2, pp. 197–206, 2018.

278. R. A. Cottis, "Electrochemical Methods," in *Shreir's Corrosion*, vol. 2, B. Cottis, M. Graham, R. Lindsay, S. Lyon, T. Richardson, D. Scantlebury, and H. Stott, Eds. Elsevier, 2010, pp. 1341–1373.

279. M. Ciobanu, J. P. Wilburn, M. L. Krim, and D. E. Cliffel, "Fundamentals," in *Handbook of Electrochemistry*, C. G. Zoski, Ed. Elsevier, 2007, pp. 3–29.

280. R. W. Ramette, “Textbook forum: Outmoded terminology: The normal hydrogen electrode,” *J. Chem. Educ.*, vol. 64, no. 10, p. 885, 1987.

281. J. Harrison, “CHEM 512.” University of Alberta, Edmonton, AB, 2018.

282. “CHI152 Alkaline/Mercury Oxide Reference Electrode,” CH Instruments, Inc., Austin, TX, 2024.

283. W. Xing, M. Yin, Q. Lv, Y. Hu, C. Liu, and J. Zhang, “Oxygen Solubility, Diffusion Coefficient, and Solution Viscosity,” in *Rotating Electrode Methods and Oxygen Reduction Electrocatalysts*, W. Xing, G. Yin, and J. Zhang, Eds. Amsterdam, The Netherlands: Elsevier, 2014, pp. 1–31.

284. A. Peroff, “What is iR drop?,” *Pine Research Instrumentation*, 2023. [Online]. Available: https://pineresearch.com/shop/kb/theory/general-electrochemistry/ir-compensation/. [Accessed: 09-Apr-2024].

285. B. Inglis, J. Ullrich, and M. J. T. Milton, “The International System of Units (SI) - 9th Edition,” Bureau International des Poids et Mesures, Paris, France, 2019.

286. M. Xiong, “Electrodeposited Electrocatalysts For Rechargeable Zinc-air Batteries,” Doctoral Thesis, University of Alberta, 2018.

287. Gamry Instruments, “The Basics of Electrochemical Impedance Spectroscopy,” Warminster, PA, https://www.gamry.com/application-notes/EIS/basics-of-electrochemical-impedance-spectroscopy/.

288. T. Han, H. Sun, J. Hu, N. Sun, Y. Liu, J. Chen, M. Chen, and D. Cao, “Self-assembly of porous curly graphene film as an efficient gas diffusion layer for high-performance Zn-air batteries,” *Carbon*, vol. 223, p. 119025, 2024.

289. K. F. Blurton and A. F. Sammells, “Metal/air batteries: Their status and potential - a review,” *J. Power Sources*, vol. 4, no. 4, pp. 263–279, 1979.

290. T. N. T. Tran, M. P. Clark, H. J. Chung, and D. G. Ivey, “Effects of Crosslinker Concentration in Poly(Acrylic Acid)-KOH Gel Electrolyte on Performance of Zinc-Air Batteries,” *Batter. Supercaps*, vol. 3, no. 5, pp. 409–416, 2020.

291. W. Choi, H.-C. Shin, J. M. Kim, J.-Y. Choi, and W.-S. Yoon, “Modeling and Applications of Electrochemical Impedance Spectroscopy (EIS) for Lithium-Ion Batteries,” *J. Electrochem. Sci. Technol.*, vol. 11, no. 1, pp. 1–13, 2020.

292. S. C. Riha, J. M. Racowski, M. P. Lanci, A. Klug, A. S. Hock, A. B. F. F. Martinson, J. A. Klug, A. S. Hock, and A. B. F. F. Martinson, “Phase Discrimination through Oxidant Selection in Low-Temperature Atomic Layer Deposition of Crystalline Iron Oxides,” *Langmuir*, vol. 29, no. 10, pp. 3439–3445, 2013.

293. X. Wan, F. Gao, X. Lian, X. Ji, E. Hu, L. He, Y. Tong, and Y. Guo, “Bio-mimicked atomic-layer-deposited iron oxide-based memristor with synaptic potentiation and depression functions,” *Jpn. J. Appl. Phys.*, vol. 57, no. 6, p. 060303, 2018.

294. Y. Lin, Y. Xu, M. T. Mayer, Z. I. Simpson, G. Mcmahon, S. Zhou, and D. Wang, “Growth of p-Type Hematite by Atomic Layer Deposition and Its Utilization for Improved Solar Water Splitting,” *J. Am. Chem. Soc.*, vol. 134, no. 12, pp. 5508–5511, 2012.

295. K. B. Gandrud, A. Pettersen, O. Nilsen, and H. Fjellvåg, “High-performing iron phosphate for enhanced lithium ion solid state batteries as grown by atomic layer deposition,” *J. Mater. Chem. A*, vol. 1, no. 32, pp. 9054–9059, 2013.

296. Strem Chemicals, “Product Catalog 26-0145: Bis(N,N’-di-t-butylacetamidinato)iron(II), min. 98%,” *Strem Chemicals, Inc.*, 2020. [Online]. Available: https://www.strem.com/catalog/v/26-0145/32/iron_635680-56-7. [Accessed: 20-Apr-2020].

297. Strem Chemicals, “Product Catalog 26-3910: Tris(2,2,6,6-tetramethyl-3,5-heptanedionato)iron(III), 99% (99.9%-Fe) [Fe(TMHD)3],” *Strem Chemicals, Inc.*, 2020. [Online]. Available: https://www.strem.com/catalog/v/26-3910/32/iron_14876-47-2. [Accessed: 20-Apr-2020].

298. S. Mathur, M. Veith, V. Sivakov, H. Shen, V. Huch, U. Hartmann, and H. Bin Gao, “Phase Selective Deposition and Microstructure Control in Iron Oxide Films Obtained by Single-Source CVD,” *Chem. Vap. Depos.*, vol. 8, no. 6, pp. 277–283, 2002.

299. B. S. Lim, A. Rahtu, and R. G. Gordon, “Atomic layer deposition of transition metals,” *Nat. Mater.*, vol. 2, no. 11, pp. 749–754, 2003.

300. M. Aronniemi, J. Saino, and J. Lahtinen, “Characterization and gas-sensing behavior of an iron oxide thin film prepared by atomic layer deposition,” *Thin Solid Films*, vol. 516, no. 18, pp. 6110–6115, 2008.

301. Strem Chemicals, “Product Catalog 26-1400: N,N-Dimethylaminomethylferrocene, min. 95%,” *Strem Chemicals, Inc.*, 2020. [Online]. Available: https://www.strem.com/catalog/v/26-1400/32/iron_1271-86-9. [Accessed: 20-Apr-2020].

302. A. J. Bard and M. A. Fox, “Artificial Photosynthesis: Solar Splitting of Water to Hydrogen and Oxygen,” *Acc. Chem. Res.*, vol. 28, no. 3, pp. 141–145, 1995.

303. T. Muneshwar and K. Cadien, “Probing initial-stages of ALD growth with dynamic in situ spectroscopic ellipsometry,” *Appl. Surf. Sci.*, vol. 328, pp. 344–348, 2015.

304. D. A. Shirley, “High-Resolution X-Ray Photoemission Spectrum of the Valence Bands of Gold,” *Phys. Rev. B*, vol. 5, no. 12, pp. 4709–4714, 1972.

305. W. Bian, Z. Yang, P. Strasser, and R. Yang, “A CoFe2O4/graphene nanohybrid as an efficient bi-functional electrocatalyst for oxygen reduction and oxygen evolution,” *J. Power Sources*, vol. 250, pp. 196–203, 2014.

306. J. W. Elam, D. Routkevitch, P. P. Mardilovich, and S. M. George, “Conformal Coating on Ultrahigh-Aspect-Ratio Nanopores of Anodic Alumina by Atomic Layer Deposition,” *Chem. Mater.*, vol. 15, no. 18, pp. 3507–3517, 2003.

307. H. C. M. Knoops, E. Langereis, M. C. M. van de Sanden, and W. M. M. Kessels, “Conformality of Plasma-Assisted ALD: Physical Processes and Modeling,” *J. Electrochem. Soc.*, vol. 157, no. 12, p. G241, 2010.

308. S. W. Lee, B. J. Choi, T. Eom, J. H. Han, S. K. Kim, S. J. Song, W. Lee, and C. S. Hwang, “Influences of metal, non-metal precursors, and substrates on atomic layer deposition processes for the growth of selected functional electronic materials,” *Coord. Chem. Rev.*, vol. 257, no. 23–24, pp. 3154–3176, 2013.

309. H. H. Sønsteby, A. Yanguas-Gil, and J. W. Elam, “Consistency and reproducibility in atomic layer deposition,” *J. Vac. Sci. Technol. A*, vol. 38, no. 2, p. 020804, 2020.

310. S. J. Song, S. W. Lee, G. H. Kim, J. Y. Seok, K. J. Yoon, J. H. Yoon, C. S. Hwang, J. Gatineau, and C. Ko, “Substrate dependent growth behaviors of plasma-enhanced atomic layer deposited nickel oxide films for resistive switching application,” *Chem. Mater.*, vol. 24, no. 24, pp. 4675–4685, 2012.

311. T. Muneshwar and K. Cadien, “AxBAxB ... pulsed atomic layer deposition: Numerical growth model and experiments,” *J. Appl. Phys.*, vol. 119, no. 8, 2016.

312. S. C. Riha, J. A. Libera, J. W. Elam, and A. B. F. Martinson, “Design and implementation of an integral wall-mounted quartz crystal microbalance for atomic layer deposition,” *Rev. Sci. Instrum.*, vol. 83, no. 9, 2012.

313. S. A. Campbell, *Fabrication Engineering at the Micro- and Nanoscale*, 3rd ed. New York, NY, NY: Oxford University Press, Inc., 2008.

314. J. L. Hueso, J. P. Espinós, A. Caballero, J. Cotrino, and A. R. González-Elipe, “XPS investigation of the reaction of carbon with NO, O2, N2 and H2O plasmas,” *Carbon*, vol. 45, no. 1, pp. 89–96, 2007.

315. B. P. Payne, M. C. Biesinger, and N. S. McIntyre, “Use of oxygen/nickel ratios in the XPS characterisation of oxide phases on nickel metal and nickel alloy surfaces,” *J. Electron Spectros. Relat. Phenomena*, vol. 185, no. 5–7, pp. 159–166, 2012.

316. D. Wilson and M. A. Langell, “XPS analysis of oleylamine/oleic acid capped Fe3O4 nanoparticles as a function of temperature,” *Appl. Surf. Sci.*, vol. 303, pp. 6–13, 2014.

317. T. J. Park, P. Sivasubramani, R. M. Wallace, and J. Kim, “Effects of growth temperature and oxidant feeding time on residual C- and N-related impurities and Si diffusion behavior in atomic-layer-deposited La 2O3 thin films,” *Appl. Surf. Sci.*, vol. 292, pp. 880–885, 2014.

318. D. Aasen, M. P. Clark, and D. G. Ivey, “(Co,Fe)3O4 Decorated Nitrogen-Doped Carbon Nanotubes in Nano-Composite Gas Diffusion Layers as Highly Stable Bifunctional Catalysts for Rechargeable Zinc-Air Batteries,” *Batter. Supercaps*, vol. 3, no. 2, pp. 174–

184, 2020.

319. M. Chigane and M. Ishikawa, “Manganese Oxide Thin Film Preparation by Potentiostatic Electrolyses and Electrochromism,” *J. Electrochem. Soc.*, vol. 147, no. 6, p. 2246, 2000.

320. A. P. Grosvenor, B. A. Kobe, M. C. Biesinger, and N. S. McIntyre, “Investigation of multiplet splitting of Fe 2p XPS spectra and bonding in iron compounds,” *Surf. Interface Anal.*, vol. 36, no. 12, pp. 1564–1574, 2004.

321. T. Yamashita and P. Hayes, “Analysis of XPS spectra of Fe 2+ and Fe 3+ ions in oxide materials,” *Appl. Surf. Sci.*, vol. 254, no. 8, pp. 2441–2449, 2008.

322. D. D. Hawn and B. M. DeKoven, “Deconvolution as a Correction for Photoelectron Inelastic Energy Losses in the Core Level XPS Spectra of Iron Oxides,” *Surf. Interface Anal.*, vol. 10, no. 2–3, pp. 63–74, 1987.

323. P. Mills and J. L. Sullivan, “A study of the core level electrons in iron and its three oxides by means of x-ray photoelectron spectroscopy,” *J. Phys. D. Appl. Phys.*, vol. 16, no. 5, pp. 723–732, 1983.

324. E. Marin, A. Lanzutti, L. Paussa, L. Guzman, and L. Fedrizzi, “Long term performance of atomic layer deposition coatings for corrosion protection of stainless steel,” *Mater. Corros.*, vol. 66, no. 9, pp. 907–914, 2015.

325. X. Meng, X. Wang, D. Geng, C. Ozgit-Akgun, N. Schneider, and J. W. Elam, “Atomic layer deposition for nanomaterial synthesis and functionalization in energy technology,” *Mater. Horizons*, vol. 4, no. 2, pp. 133–154, 2017.

326. A. M. Hoyas, J. Schuhmacher, D. Shamiryan, J. Waeterloos, W. Besling, J. P. Celis, and K. Maex, “Growth and characterization of atomic layer deposited WC0.7N0.3 on polymer films,” *J. Appl. Phys.*, vol. 95, no. 1, pp. 381–388, 2004.

327. R. L. Puurunen, W. Vandervorst, W. F. A. A. Besling, O. Richard, H. Bender, T. Conard, C. Zhao, A. Delabie, M. Caymax, S. De Gendt, M. Heyns, M. M. Viitanen, M. De Ridder, H. H. Brongersma, Y. Tamminga, T. Dao, T. de Win, M. Verheijen, M. Kaiser, and M. Tuominen, “Island growth in the atomic layer deposition of zirconium oxide and aluminum oxide on hydrogen-terminated silicon: Growth mode modeling and

transmission electron microscopy," *J. Appl. Phys.*, vol. 96, no. 9, pp. 4878–4889, 2004.

328. W. F. A. Besling, E. Young, T. Conard, C. Zhao, R. Carter, W. Vandervorst, M. Caymax, S. De Gendt, M. Heyns, J. Maes, M. Tuominen, and S. Haukka, "Characterisation of ALCVD Al2O3-ZrO2 nanolaminates, link between electrical and structural properties," *J. Non. Cryst. Solids*, vol. 303, no. 1, pp. 123–133, 2002.

329. Z. Baji, Z. Lábadi, Z. E. Horváth, G. Molnár, J. Volk, I. Bársony, and P. Barna, "Nucleation and growth modes of ALD ZnO," *Cryst. Growth Des.*, vol. 12, no. 11, pp. 5615–5620, 2012.

330. M. Cassir, F. Goubin, C. Bernay, P. Vernoux, and D. Lincot, "Synthesis of ZrO2 thin films by atomic layer deposition: growth kinetics , structural and electrical properties," *Appl. Surf. Sci.*, vol. 193, no. 1–4, pp. 120–128, 2002.

331. L. Lamagna, C. Wiemer, M. Perego, S. Spiga, J. Rodríguez, D. Santiago Coll, M. E. Grillo, S. Klejna, and S. D. Elliott, "Mechanisms for substrate-enhanced growth during the early stages of atomic layer deposition of alumina onto silicon nitride surfaces," *Chem. Mater.*, vol. 24, no. 6, pp. 1080–1090, 2012.

332. T. Gougousi, J. C. Hackley, J. D. Demaree, and J. W. Lacis, "Growth and Interface Evolution of HfO2 Films on GaAs(100) Surfaces," *J. Electrochem. Soc.*, vol. 157, no. 5, p. H551, 2010.

333. H. Kim and S. M. Rossnagel, "Growth kinetics and initial stage growth during plasma-enhanced Ti atomic layer deposition," *J. Vac. Sci. Technol. A Vacuum, Surfaces, Film.*, vol. 20, no. 3, pp. 802–808, 2002.

334. R. L. Puurunen and W. Vandervorst, "Island growth as a growth mode in atomic layer deposition: A phenomenological model," *J. Appl. Phys.*, vol. 96, no. 12, pp. 7686–7695, Dec. 2004.

335. M. L. Green, M. Y. Ho, B. Busch, G. D. Wilk, T. Sorsch, T. Conard, B. Brijs, W. Vandervorst, P. I. Räisänen, D. Muller, M. Bude, and J. Grazul, "Nucleation and growth of atomic layer deposited HfO2 gate dielectric layers on chemical oxide (Si-O-H) and thermal oxide (SiO2 or Si-O-N) underlayers," *J. Appl. Phys.*, vol. 92, no. 12, pp. 7168–

7174, 2002.

336. E. P. Gusev, C. Cabral, M. Copel, C. D'Emic, and M. Gribelyuk, "Ultrathin HfO2 films grown on silicon by atomic layer deposition for advanced gate dielectrics applications," *Microelectron. Eng.*, vol. 69, no. 2–4, pp. 145–151, 2003.

337. M. Copel, M. Gribelyuk, and E. Gusev, "Structure and stability of ultrathin zirconium oxide layers on Si(001)," *Appl. Phys. Lett.*, vol. 76, no. 4, pp. 436–438, 2000.

338. G. P. Gakis, C. Vahlas, H. Vergnes, S. Dourdain, Y. Tison, H. Martinez, J. Bour, D. Ruch, A. G. Boudouvis, B. Caussat, and E. Scheid, "Investigation of the initial deposition steps and the interfacial layer of Atomic Layer Deposited (ALD) Al2O3 on Si," *Appl. Surf. Sci.*, vol. 492, no. April, pp. 245–254, 2019.

339. J. Dendooven, S. Pulinthanathu Sree, K. De Keyser, D. Deduytsche, J. A. Martens, K. F. Ludwig, and C. Detavernier, "In situ X-ray fluorescence measurements during atomic layer deposition: Nucleation and growth of TiO2 on planar substrates and in nanoporous films," *J. Phys. Chem. C*, vol. 115, no. 14, pp. 6605–6610, 2011.

340. M. A. Alam and M. L. Green, "Mathematical description of atomic layer deposition and its application to the nucleation and growth of HfO2 gate dielectric layers," *J. Appl. Phys.*, vol. 94, no. 5, pp. 3403–3413, 2003.

341. E. V. Skopin, L. Rapenne, H. Roussel, J. L. Deschanvres, E. Blanquet, G. Ciatto, D. D. Fong, M. I. Richard, and H. Renevier, "The initial stages of ZnO atomic layer deposition on atomically flat In0.53Ga0.47As substrates," *Nanoscale*, vol. 10, no. 24, pp. 11585–11596, 2018.

342. O. Nilsen, C. E. Mohn, A. Kjekshus, and H. Fjellvåg, "Analytical model for island growth in atomic layer deposition using geometrical principles," *J. Appl. Phys.*, vol. 102, no. 2, p. 024906, 2007.

343. R. L. Puurunen, "Analysis of hydroxyl group controlled atomic layer deposition of hafnium dioxide from hafnium tetrachloride and water," *J. Appl. Phys.*, vol. 95, no. 9, pp. 4777–4786, 2004.

344. E. V. Skopin, K. Abdukayumov, P. Abi Younes, M. Anikin, H. Roussel, J. L.

Deschanvres, and H. Renevier, “In situ ellipsometry monitoring of TiO2 atomic layer deposition from Tetrakis(dimethylamido)titanium(IV) and H2O precursors on Si and In0.53Ga0.47As substrates,” *Thin Solid Films*, vol. 723, no. February, pp. 1–8, 2021.

345. J. R. Avila, J. D. Emery, M. J. Pellin, A. B. F. Martinson, O. K. Farha, and J. T. Hupp, “Porphyrins as Templates for Site-Selective Atomic Layer Deposition: Vapor Metalation and in Situ Monitoring of Island Growth,” *ACS Appl. Mater. Interfaces*, vol. 8, no. 31, pp. 19853–19859, 2016.

346. A. Perrotta, J. Pilz, R. Resel, O. Werzer, and A. M. Coclite, “Initial growth and crystallization onset of plasma enhanced-atomic layer deposited ZnO,” *Crystals*, vol. 10, no. 4, pp. 11–16, 2020.

347. J. Ihanus, M. Ritala, M. Leskelä, T. Prohaska, R. Resch, G. Friedbacher, and M. Grasserbauer, “AFM studies on ZnS thin films grown by atomic layer epitaxy,” *Appl. Surf. Sci.*, vol. 120, no. 1–2, pp. 43–50, 1997.

348. C. de Paula, N. E. Richey, L. Zeng, and S. F. Bent, “Mechanistic Study of Nucleation Enhancement in Atomic Layer Deposition by Pretreatment with Small Organometallic Molecules,” *Chem. Mater.*, vol. 32, no. 1, pp. 315–325, 2020.

349. W. J. Lee, Z. Wan, C. M. Kim, I. K. Oh, R. Harada, K. Suzuki, E. A. Choi, and S. H. Kwon, “Atomic Layer Deposition of Pt Thin Films Using Dimethyl (N, N-Dimethyl-3-Butene-1-Amine- N) Platinum and O2 Reactant,” *Chem. Mater.*, vol. 31, no. 14, pp. 5056–5064, 2019.

350. A. Delabie, R. L. Puurunen, B. Brijs, M. Caymax, T. Conard, B. Onsia, O. Richard, W. Vandervorst, C. Zhao, M. M. Heyns, M. Meuris, M. M. Viitanen, H. H. Brongersma, M. De Ridder, L. V. Goncharova, E. Garfunkel, T. Gustafsson, and W. Tsai, “Atomic layer deposition of hafnium oxide on germanium substrates,” *J. Appl. Phys.*, vol. 97, no. 6, p. 064104, 2005.

351. J. P. Jacobs, L. P. Lindfors, J. G. H. H. Reintjes, O. Jylhä, H. H. Brongersma, and O. Jylh, “The growth mechanism of nickel in the preparation of Ni/Al2O3 catalysts studied by LEIS, XPS and catalytic activity,” *Catal. Letters*, vol. 25, no. 3–4, pp. 315–324, 1994.

352. N.-T. Suen, S.-F. Hung, Q. Quna, N. Zhang, Y.-J. Xu, and H. M. Chen, “Electrocatalysis for the oxygen evolution reaction: recent development and future perspectives,” *Chem. Soc. Rev.*, vol. 46, no. 2, pp. 337–365, 2017.

353. C. Hu and L. Dai, “Carbon-Based Metal-Free Catalysts for Electrocatalysis beyond the ORR,” *Angew. Chemie - Int. Ed.*, vol. 55, no. 39, pp. 11736–11758, 2016.

354. C. Feng, M. B. Faheem, J. Fu, Y. Xiao, C. Li, and Y. Li, “Fe-Based Electrocatalysts for Oxygen Evolution Reaction: Progress and Perspectives,” *ACS Catal.*, vol. 10, no. 7, pp. 4019–4047, 2020.

355. Z. Abedi, D. Leistenschneider, W. Chen, and D. G. Ivey, “Superior Performance of Electrochemical Double Layer Supercapacitor Made with Asphaltene Derived Activated Carbon Fibers,” *Energy Technol.*, vol. 8, no. 12, pp. 1–11, 2020.

356. Z. Abedi, D. Leistenschneider, W. Chen, and D. G. Ivey, “Improved Capacitive Behavior of Birnessite Type Mn Oxide Coated on Activated Carbon Fibers,” *J. Electrochem. Soc.*, vol. 169, no. 1, p. 010507, 2022.

357. Z. Abedi, D. Leistenschneider, W. Chen, and D. G. Ivey, “Spinel Type Mn-Co Oxide Coated Carbon Fibers as Efficient Bifunctional Electrocatalysts for Zinc-air Batteries,” *Batter. Supercaps*, vol. 5, no. 2, p. e202100339, 2022.

358. A. McDougall, Z. Abedi, and D. G. Ivey, “Tri- and tetra-metallic oxides anchored to nitrogen-doped carbon nanotubes as bifunctional electrocatalysts for rechargeable zinc-air batteries,” *J. Appl. Electrochem.*, vol. 52, no. 3, pp. 437–459, 2022.

359. D. G. Ivey, E. Brightman, and N. Brandon, “Structural modifications to nickel cermet anodes in fuel cell environments,” *J. Power Sources*, vol. 195, no. 19, pp. 6301–6311, 2010.

360. M. Labbe, M. P. Clark, Z. Abedi, A. He, K. Cadien, and D. G. Ivey, “Atomic layer deposition of iron oxide on a porous carbon substrate via ethylferrocene and an oxygen plasma,” *Surf. Coatings Technol.*, vol. 421, p. 127390, 2021.

361. T. Muneshwar and K. Cadien, “Low temperature plasma enhanced atomic layer deposition of conducting zirconium nitride films using tetrakis (dimethylamido) zirconium

and forming gas (5% H2 + 95% N2) plasma," *J. Vac. Sci. Technol. A Vacuum, Surfaces, Film.*, vol. 33, no. 3, p. 031502, 2015.

362. C. A. Schneider, W. S. Rasband, and K. W. Eliceiri, "NIH Image to ImageJ: 25 years of image analysis," *Nat. Methods*, vol. 9, no. 7, pp. 671–675, 2012.

363. G. E. Jellison and F. A. Modine, "Parameterization of the optical functions of amorphous materials in the interband region," *Appl. Phys. Lett.*, vol. 69, no. 3, pp. 371–373, 1996.

364. J. P. Mmbaga, K. Nandakumar, and R. E. Hayes, *Computational Methods for Process Engineers*. Edmonton, AB: ALPHA Education Press, 2014.

365. T. C. O'Haver, "An introduction to signal processing in chemical measurement," *J. Chem. Educ.*, vol. 68, no. 6, p. A147, Jun. 1991.

366. D. J. Hagen, J. Connolly, I. M. Povey, S. Rushworth, and M. E. Pemble, "Island Coalescence during Film Growth: An Underestimated Limitation of Cu ALD," *Adv. Mater. Interfaces*, vol. 4, no. 18, pp. 1–6, 2017.

367. F. Yang, C. Wang, H. Bai, W. Wang, and Y. Liu, "Periodic island-layer-island growth during deposition of ultrastable metallic glasses," *Commun. Mater.*, vol. 2, no. 1, pp. 1–7, 2021.

368. R. C. Seymour and J. C. Wood, "Paramagnetic gas adsorption," *Surf. Sci.*, vol. 27, no. 3, pp. 605–610, 1971.

369. A. Thompson, D. Attwood, E. Gullikson, M. Howells, K.-J. Kim, J. Kirz, J. Kortright, I. Lindau, Y. Liu, P. Pianetta, A. Robinson, J. Scofield, J. Underwood, G. Williams, and H. Winick, *X-Ray Data Booklet*, Third Ed. Berkeley, CA: Lawrence Berkeley National Laboratory, University of California, 2009.

370. J. R. Rumble, Ed., "Physical Constants of Inorganic Compounds," in *CRC Handbook of Chemistry and Physics*, 102nd ed., Boca Raton, FL: CRC Press/Taylor & Francis, 2021.

371. R. L. Puurunen, "Random deposition as a growth mode in atomic layer deposition," *Chem. Vap. Depos.*, vol. 10, no. 3, pp. 159–170, 2004.

372. T. Arroval, L. Aarik, R. Rammula, V. Kruusla, and J. Aarik, "Effect of substrate-enhanced

and inhibited growth on atomic layer deposition and properties of aluminum-titanium oxide films," *Thin Solid Films*, vol. 600, pp. 119–125, 2016.

373. R. W. Wind, F. H. Fabreguette, Z. A. Sechrist, and S. M. George, "Nucleation period, surface roughness, and oscillations in mass gain per cycle during W atomic layer deposition on Al2 O3," *J. Appl. Phys.*, vol. 105, no. 7, 2009.

374. Y. Zhang, C. Guerra-Nuñez, I. Utke, J. Michler, M. D. Rossell, and R. Erni, "Understanding and controlling nucleation and growth of TiO2 deposited on multiwalled carbon nanotubes by atomic layer deposition," *J. Phys. Chem. C*, vol. 119, no. 6, pp. 3379–3387, 2015.

375. D. Polder and J. H. Van Santen, "The Effective Permeability of Mixtures of Solids," *Physica*, vol. 12, no. 5, pp. 257–271, 1946.

376. A. Dameron, J. Bult, S. Pylypenko, C. Engtrakul, C. Bochert, L. Chen, J. Leong, S. Frisco, L. Simpson, H. Dinh, and B. Pivovar, "Atomic layer deposition for aligned growth of and conformal deposition onto double and triple walled carbon nanotubes," in *SPIE 7761, Carbon Nanotubes, Graphene, and Associated Devices III*, p. 776108 (24 August 2010).

377. M. J. Young, C. B. Musgrave, and S. M. George, "Growth and Characterization of Al2O3 Atomic Layer Deposition Films on sp2-Graphitic Carbon Substrates Using NO2/Trimethylaluminum Pretreatment," *ACS Appl. Mater. Interfaces*, vol. 7, no. 22, pp. 12030–12037, 2015.

378. C. M. Zhang, M. C. Bartelt, J. M. Wen, C. J. Jenks, J. W. Evans, and P. A. Thiel, "Submonolayer island formation and the onset of multilayer growth during Ag/Ag(100) homoepitaxy," *Surf. Sci.*, vol. 406, no. 1–3, pp. 178–193, 1998.

379. J. W. Evans, P. A. Thiel, and M. Li, "Kinetic Monte Carlo simulation of epitaxial thin film growth: Formation of submonolayer islands and multilayer mounds," *AIP Conf. Proc.*, vol. 916, pp. 191–211, 2007.

380. F. F. Leal, S. C. Ferreira, and S. O. Ferreira, "Modelling of epitaxial film growth with an Ehrlich-Schwoebel barrier dependent on the step height," *J. Phys. Condens. Matter*, vol. 23, no. 29, 2011.

381. J. W. Elam, C. A. Wilson, M. Schuisky, Z. A. Sechrist, and S. M. George, “Improved nucleation of TiN atomic layer deposition films on SiLK low-k polymer dielectric using an Al2O3 atomic layer deposition adhesion layer,” *J. Vac. Sci. Technol. B Microelectron. Nanom. Struct.*, vol. 21, no. 3, p. 1099, 2003.

382. M. D. Sampson, J. D. Emery, M. J. Pellin, and A. B. F. Martinson, “Inhibiting metal oxide atomic layer deposition: Beyond zinc oxide,” *ACS Appl. Mater. Interfaces*, vol. 9, no. 39, pp. 33429–33436, 2017.

383. E. Stevens, Y. Tomczak, B. T. Chan, E. Altamirano Sanchez, G. N. Parsons, and A. Delabie, “Area-Selective Atomic Layer Deposition of TiN, TiO2, and HfO2 on Silicon Nitride with inhibition on Amorphous Carbon,” *Chem. Mater.*, vol. 30, no. 10, pp. 3223–3232, 2018.

384. L. Ye, J. A. Kropp, and T. Gougousi, “In situ infrared spectroscopy study of the surface reactions during the atomic layer deposition of TiO 2 on GaAs (100) surfaces,” *Appl. Surf. Sci.*, vol. 422, pp. 666–674, 2017.

385. H. Tamura, K. Mita, A. Tanaka, and M. Ito, “Mechanism of hydroxylation of metal oxide surfaces,” *J. Colloid Interface Sci.*, vol. 243, no. 1, pp. 202–207, 2001.

386. S. Haukka and A. Root, “The reaction of hexamethyldisilazane and subsequent oxidation of trimethylsilyl groups on silica studied by solid-state NMR and FTIR,” *J. Physial Chem.*, vol. 98, no. 6, pp. 1695–1703, 1994.

387. S. Y. Liao, Y. C. Yang, S. H. Huang, and J. Y. Gan, “Synthesis of Pt@TiO2@CNTs hierarchical structure catalyst by atomic layer deposition and their photocatalytic and photoelectrochemical activity,” *Nanomaterials*, vol. 7, no. 5, p. 97, 2017.

388. L. Liu, K. Ye, Q. Zhan, T. Xue, K. Zhai, Y. Cheng, Z. Jia, A. Nie, J. Y. Xiang, C. P. Mu, B. Wang, F. Wen, Z. Zhao, Y. Gong, Y. Tian, and Z. Liu, “Ultrasensitive biochemical sensors based on controllably grown films of high-density edge-rich multilayer WS2 islands,” *Sensors Actuators B Chem.*, vol. 353, no. July 2021, p. 131081, 2022.

389. J. A. Woollam, “Data Analysis - CompleteEASE Training Series - Video 1/11,” 2015. [Online]. Available: https://www.youtube.com/watch?v=ykoDk9zbeao. [Accessed: 18-

Apr-2022].

390. H. Wang, Y. Pei, K. Wang, Y. Zuo, M. Wei, J. Xiong, P. Zhang, Z. Chen, N. Shang, D. Zhong, and P. Pei, “First-Row Transition Metals for Catalyzing Oxygen Redox,” *Small*, vol. 19, no. 46, p. 2304863, 2023.

391. L. Han, S. Dong, and E. Wang, “Transition-Metal (Co, Ni, and Fe)-Based Electrocatalysts for the Water Oxidation Reaction,” *Adv. Mater.*, vol. 28, no. 42, pp. 9266–9291, 2016.

392. S. Ahmed, P. A. Nelson, K. G. Gallagher, N. Susarla, and D. W. Dees, “Cost and energy demand of producing nickel manganese cobalt cathode material for lithium ion batteries,” *J. Power Sources*, vol. 342, pp. 733–740, 2017.

393. C. Broicher, F. Zeng, N. Pfänder, M. Frisch, T. Bisswanger, J. Radnik, J. M. Stockmann, S. Palkovits, A. K. Beine, and R. Palkovits, “Iron and Manganese Containing Multi-Walled Carbon Nanotubes as Electrocatalysts for the Oxygen Evolution Reaction - Unravelling Influences on Activity and Stability,” *ChemCatChem*, vol. 12, no. 21, pp. 5378–5384, 2020.

394. J. Luo, W. H. Guo, Q. Zhang, X. H. Wang, L. Shen, H. C. Fu, L. L. Wu, X. H. Chen, H. Q. Luo, and N. B. Li, “One-pot synthesis of Mn-Fe bimetallic oxide heterostructures as bifunctional electrodes for efficient overall water splitting,” *Nanoscale*, vol. 12, no. 38, pp. 19992–20001, 2020.

395. Q. Zhou, Z. Su, Y. Tang, L. Ai, G. Fu, Z. Wu, D. Sun, and Y. Tang, “Pt-Like Oxygen Reduction Activity Induced by Cost-Effective MnFeO 2 /N-Carbon,” *Chem. Eur. J.*, vol. 25, no. 24, pp. 6226–6232, 2019.

396. N. I. Villanueva-Martínez, C. Alegre, I. Martínez-Visús, and M. J. Lázaro, “Bifunctional oxygen electrocatalysts based on non-critical raw materials: Carbon nanostructures and iron-doped manganese oxide nanowires,” *Catal. Today*, vol. 420, no. November 2022, p. 114083, 2023.

397. N. Bhandary, P. P. Ingole, and S. Basu, “Electrosynthesis of Mn-Fe oxide nanopetals on carbon paper as bi-functional electrocatalyst for oxygen reduction and oxygen evolution reaction,” *Int. J. Hydrogen Energy*, vol. 43, no. 6, pp. 3165–3171, 2018.

398. C. D. Pham, J. Chang, M. A. Zurbuchen, and J. P. Chang, “Synthesis and Characterization of BiFeO3 Thin Films for Multiferroic Applications by Radical Enhanced Atomic Layer Deposition,” *Chem. Mater.*, vol. 27, no. 21, pp. 7282–7288, 2015.

399. K. Kopalko, A. Wójcik, M. Godlewski, E. Łusakowska, W. Paszkowicz, J. Z. Domagała, M. M. Godlewski, A. Szezerbakow, K. Świątek, and K. Dybko, “Growth by atomic layer epitaxy and characterization of thin films of ZnO,” *Phys. Status Solidi C Conf.*, vol. 2, no. 3, pp. 1125–1130, 2005.

400. T. M. Onn, R. Küngas, P. Fornasiero, K. Huang, and R. J. Gorte, “Atomic layer deposition on porous materials: Problems with conventional approaches to catalyst and fuel cell electrode preparation,” *Inorganics*, vol. 6, no. 1, p. 34, 2018.

401. Q. Wang, H. Liang, J. Zhou, J. Wang, Z. Ye, M. Zhao, H. Yang, Y. Song, and J. Guo, “Boosting oxygen reduction catalysis by introducing Fe bridging atoms between Pt nanoparticles and N-doped graphene,” *Chem. Eng. J.*, vol. 467, no. April, p. 143482, 2023.

402. X. Shi, B. He, L. Zhao, Y. Gong, R. Wang, and H. Wang, “FeS2–CoS2 incorporated into nitrogen-doped carbon nanofibers to boost oxygen electrocatalysis for durable rechargeable Zn-air batteries,” *J. Power Sources*, vol. 482, no. August 2020, p. 228955, 2021.

403. P. Chu, Y. Zhang, J. He, J. Chen, J. Zhuang, Y. Li, X. Ren, P. Zhang, L. Sun, B. Yu, and S. Chen, “Defective Fe3O4-x Few-Atom Clusters Anchored on Nitrogen-Doped Carbon as Efficient Oxygen Reduction Electrocatalysts for High-Performance Zinc–Air Batteries,” *Small Methods*, vol. 6, no. 7, pp. 4–11, 2022.

404. A. Seong, J. Kim, O. Kwon, H. Y. Jeong, R. J. Gorte, J. M. Vohs, and G. Kim, “Self-reconstructed interlayer derived by in-situ Mn diffusion from La0.5Sr0.5MnO3 via atomic layer deposition for an efficient bi-functional electrocatalyst,” *Nano Energy*, vol. 71, no. January, p. 104564, 2020.

405. S. Yan, H. Li, J. Zhu, W. Xiong, R. Lei, and X. Wang, “Atomic layer deposited nickel sulfide for bifunctional oxygen evolution/reduction electrocatalysis and zinc–air

batteries," *Nanotechnology*, vol. 32, no. 27, p. 275402, 2021.

406. M. Labbe, K. Cadien, and D. G. Ivey, "Growth of Multiple Island Layers during Iron Oxide Atomic Layer Deposition: An Electron Microscopy and Spectroscopic Ellipsometry Investigation," *J. Phys. Chem. C*, vol. 126, no. 46, pp. 19883–19894, 2022.

407. D. Aasen, M. Clark, and D. G. Ivey, "A Gas Diffusion Layer Impregnated with Mn3O4 - Decorated N-Doped Carbon Nanotubes for the Oxygen Reduction Reaction in Zinc-Air Batteries," *Batter. Supercaps*, vol. 2, no. 10, pp. 882–893, 2019.

408. M. Labbe and D. G. Ivey, "Experimental Concerns of Current Collector Interference and Electrolyte Creep During Zinc-Air Battery Testing," *J. Electrochem. Soc.*, vol. 170, no. 9, p. 090515, 2023.

409. F. Visentin, R. Gerbasi, G. Rossetto, C. De Zorzi, N. El Habra, D. Barreca, and A. Gasparotto, " Fe 2 O 3 -TiO 2 systems grown by MOCVD: an XPS study ," *Surf. Sci. Spectra*, vol. 18, no. 1, pp. 29–35, 2011.

410. Y. Meng, W. Song, H. Huang, Z. Ren, S. Y. Chen, and S. L. Suib, "Structure-property relationship of bifunctional MnO2 nanostructures: Highly efficient, ultra-stable electrochemical water oxidation and oxygen reduction reaction catalysts identified in alkaline media," *J. Am. Chem. Soc.*, vol. 136, no. 32, pp. 11452–11464, 2014.

411. M. Chigane, M. Ishikawa, and M. Izaki, "Preparation of Manganese Oxide Thin Films by Electrolysis/Chemical Deposition and Electrochromism," *J. Electrochem. Soc.*, vol. 148, no. 7, p. D96, 2001.

412. B. P. Payne, M. C. Biesinger, and N. S. McIntyre, "The study of polycrystalline nickel metal oxidation by water vapour," *J. Electron Spectros. Relat. Phenomena*, vol. 175, no. 1–3, pp. 55–65, 2009.

413. J. Jia, P. Zhang, and L. Chen, "Catalytic decomposition of gaseous ozone over manganese dioxides with different crystal structures," *Appl. Catal. B Environ.*, vol. 189, pp. 210–218, 2016.

414. T. Zhang, Z. Li, L. Wang, Z. Zhang, and S. Wang, "Spinel CoFe2O4 supported by three dimensional graphene as high-performance bi-functional electrocatalysts for oxygen

reduction and evolution reaction," *Int. J. Hydrogen Energy*, vol. 44, no. 3, pp. 1610–1619, 2019.

415. F. A. Stevie and C. L. Donley, "Introduction to x-ray photoelectron spectroscopy," *J. Vac. Sci. Technol. A*, vol. 38, no. 6, p. 063204, 2020.

416. E. S. Ilton, J. E. Post, P. J. Heaney, F. T. Ling, and S. N. Kerisit, "XPS determination of Mn oxidation states in Mn (hydr)oxides," *Appl. Surf. Sci.*, vol. 366, pp. 475–485, 2016.

417. S. Ardizzone, C. L. Bianchi, and D. Tirelli, "Mn3O4 and γ-MnOOH powders, preparation, phase composition and XPS characterisation," *Colloids Surfaces A Physicochem. Eng. Asp.*, vol. 134, no. 3, pp. 305–312, 1998.

418. M. Oku, K. Hirokawa, and S. Ikeda, "X-ray photoelectron spectroscopy of manganese-oxygen systems," *J. Electron Spectros. Relat. Phenomena*, vol. 7, no. 5, pp. 465–473, 1975.

419. M. Oku, K. Wagatsuma, and T. Konishi, "Relation between 2p X-ray photoelectron and Kα X-ray emission spectra of manganese and iron oxides," *J. Electron Spectros. Relat. Phenomena*, vol. 98–99, pp. 277–285, 1999.

420. J. Gao, C. Jia, L. Zhang, H. Wang, Y. Yang, S. F. Hung, Y. Y. Hsu, and B. Liu, "Tuning chemical bonding of MnO2 through transition-metal doping for enhanced CO oxidation," *J. Catal.*, vol. 341, pp. 82–90, 2016.

421. V. Di Castro and G. Polzonetti, "XPS study of MnO oxidation," *J. Electron Spectros. Relat. Phenomena*, vol. 48, no. 1, pp. 117–123, 1989.

422. J. S. Foord, R. B. Jackman, and G. C. Allen, "An X-ray photoelectron spectroscopic investigation of the oxidation of manganese," *Philos. Mag. A Phys. Condens. Matter, Struct. Defects Mech. Prop.*, vol. 49, no. 5, pp. 657–663, 1984.

423. A. Atta and H. E. Ali, "Structural and Thermal Properties of PTFE Films by Argon and Oxygen Plasma," *Arab J. Nucl. Sci. Appl.*, vol. 46, no. 5, pp. 106–114, 2013.

424. S. Liu, C. Fu, A. Gu, and Z. Yu, "Structural changes of polytetrafluoroethylene during irradiation in oxygen," *Radiat. Phys. Chem.*, vol. 109, pp. 1–5, 2015.

425. H. J. T. Ellingham, “Reducibility of Oxides and Sulphides in Metallurgical Processes,” *J. Soc. Chem. Ind.*, vol. 63, no. 5, pp. 125–144, 1944.

426. S. Pétigny, H. Mostéfa-Sba, B. Domenichini, E. Lesniewska, A. Steinbrunn, and S. Bourgeois, “Superficial defects induced by argon and oxygen bombardments on (110) TiO2 surfaces,” *Surf. Sci.*, vol. 410, no. 2–3, pp. 250–257, 1998.

427. S. Hashimoto, K. Hirokawa, Y. Fukuda, K. Suzuki, T. Suzuki, N. Usuki, N. Gennai, S. Yoshida, M. Koda, H. Sezaki, H. Horie, A. Tanaka, and T. Ohtsubo, “Correction of Peak Shift and Classification of Change of X-ray Photoelectron Spectra of Oxides as a Result of Ion Sputtering,” *Surf. Interface Anal.*, vol. 18, no. 12, pp. 799–806, 1992.

428. T. Battault, R. Legros, and A. Rousset, “Structural and electrical properties of iron manganite spinels in relation with cationic distribution,” *J. Eur. Ceram. Soc.*, vol. 15, no. 11, pp. 1141–1147, 1995.

429. Y. Zhan, C. Xu, M. Lu, Z. Liu, and J. Y. Lee, “Mn and Co co-substituted Fe3O4nanoparticles on nitrogen-doped reduced graphene oxide for oxygen electrocatalysis in alkaline solution,” *J. Mater. Chem. A*, vol. 2, no. 38, pp. 16217–16223, 2014.

430. V. Baron, J. Gutzmer, H. Rundlöf, and R. Tellgren, “The influence of iron substitution on the magnetic properties of hausmannite, Mn2+(Fe,Mn)3+2O4,” *Am. Mineral.*, vol. 83, no. 7–8, pp. 786–793, 1998.

431. Q. Zhao, Z. Yan, C. Chen, and J. Chen, “Spinels: Controlled Preparation, Oxygen Reduction/Evolution Reaction Application, and beyond,” *Chem. Rev.*, vol. 117, no. 15, pp. 10121–10211, 2017.

432. C. Li, X. Han, F. Cheng, Y. Hu, C. Chen, and J. Chen, “Phase and composition controllable synthesis of cobalt manganese spinel nanoparticles towards efficient oxygen electrocatalysis,” *Nat. Commun.*, vol. 6, pp. 4–11, 2015.

433. S. Hirai, S. Yagi, A. Seno, M. Fujioka, T. Ohno, and T. Matsuda, “Enhancement of the oxygen evolution reaction in Mn3+-based electrocatalysts: Correlation between Jahn-Teller distortion and catalytic activity,” *RSC Adv.*, vol. 6, no. 3, pp. 2019–2023, 2016.

434. I. Roche, E. Chaînet, M. Chatenet, and J. Vondrák, “Durability of carbon-supported manganese oxide nanoparticles for the oxygen reduction reaction (ORR) in alkaline medium,” *J. Appl. Electrochem.*, vol. 38, no. 9, pp. 1195–1201, 2008.

435. I. Roche, E. Chaînet, M. Chatenet, and J. Vondrák, “Carbon-supported manganese oxide nanoparticles as electrocatalysts for the Oxygen Reduction Reaction (ORR) in alkaline medium: Physical characterizations and ORR mechanism,” *J. Phys. Chem. C*, vol. 111, no. 3, pp. 1434–1443, 2007.

436. J. Vondrák, B. Klápště J, Velická, M. Sedlaříková, J. Reiter, I. Roche, E. Chainet, J. F. Fauvarque, and M. Chatenet, “Electrochemical activity of manganese oxide/carbon-based electrocatalysts,” *J. New Mater. Electrochem. Syst.*, vol. 8, no. 3, pp. 209–212, 2005.

437. S. Guo, S. Zhang, and S. Sun, “Tuning nanoparticle catalysis for the oxygen reduction reaction,” *Angew. Chemie - Int. Ed.*, vol. 52, no. 33, pp. 8526–8544, 2013.

438. N. Zamel, “The catalyst layer and its dimensionality - A look into its ingredients and how to characterize their effects,” *J. Power Sources*, vol. 309, pp. 141–159, 2016.

439. O. Nilsen, E. Rauwel, H. Fjellvåg, and A. Kjekshus, “Growth of La1-xCaxMnO3 thin films by atomic layer deposition,” *J. Mater. Chem.*, vol. 17, no. 15, pp. 1466–1475, 2007.

440. M. Xiong and D. G. Ivey, “Synthesis of Bifunctional Catalysts for Metal-Air Batteries Through Direct Deposition Methods,” *Batter. Supercaps*, vol. 2, no. 4, pp. 326–335, 2019.

441. J. A. Conesa and R. Font, “Polytetrafluoroethylene Decomposition in Air and Nitrogen,” *Polym. Eng. Sci.*, vol. 41, no. 12, pp. 2137–2147, 2001.

442. J. T. Titantah and D. Lamoen, “Carbon and nitrogen 1s energy levels in amorphous carbon nitride systems: XPS interpretation using first-principles,” *Diam. Relat. Mater.*, vol. 16, no. 3, pp. 581–588, 2007.

443. A. P. Dementjev, A. De Graaf, M. C. M. Van de Sanden, K. I. Maslakov, A. V. Naumkin, and A. A. Serov, “X-ray photoelectron spectroscopy reference data for identification of the C3N4 phase in carbon-nitrogen films,” *Diam. Relat. Mater.*, vol. 9, no. 11, pp. 1904–1907, 2000.

444. C. Chen, Y. Li, D. Cheng, H. He, and K. Zhou, “Graphite Nanoarrays-Confined Fe and Co Single-Atoms within Graphene Sponges as Bifunctional Oxygen Electrocatalyst for Ultralong Lasting Zinc-Air Battery,” *ACS Appl. Mater. Interfaces*, vol. 12, no. 36, pp. 40415–40425, 2020.

445. Y. Zhong, J. Dai, X. Xu, C. Su, and Z. Shao, “Facilitating Oxygen Redox on Manganese Oxide Nanosheets by Tuning Active Species and Oxygen Defects for Zinc-Air Batteries,” *ChemElectroChem*, vol. 7, no. 24, pp. 4949–4955, 2020.

446. L. Trahey, F. R. Brushett, N. P. Balsara, G. Ceder, L. Cheng, Y. M. Chiang, N. T. Hahn, B. J. Ingram, S. D. Minteer, J. S. Moore, K. T. Mueller, L. F. Nazar, K. A. Persson, D. J. Siegel, K. Xu, K. R. Zavadil, V. Srinivasan, and G. W. Crabtree, “Energy storage emerging: A perspective from the Joint Center for Energy Storage Research,” *Proc. Natl. Acad. Sci. U. S. A.*, vol. 117, no. 23, pp. 12550–12557, 2020.

447. K. Liu, Y. Liu, D. Lin, A. Pei, and Y. Cui, “Materials for lithium-ion battery safety,” *Sci. Adv.*, vol. 4, no. 6, p. eaas9820, 2018.

448. Z. Pu, Q. Liu, C. Tang, A. M. Asiri, A. H. Qusti, A. O. Al-Youbi, and X. Sun, “Spinel ZnCo2O4/N-doped carbon nanotube composite: A high active oxygen reduction reaction electrocatalyst,” *J. Power Sources*, vol. 257, pp. 170–173, 2014.

449. T. F. Hung, S. G. Mohamed, C. C. Shen, Y. Q. Tsai, W. S. Chang, and R. S. Liu, “Mesoporous ZnCo2O4 nanoflakes with bifunctional electrocatalytic activities toward efficiencies of rechargeable lithium-oxygen batteries in aprotic media,” *Nanoscale*, vol. 5, no. 24, pp. 12115–12119, 2013.

450. Z. Zhu, P. Liu, P. Du, B. Yu, X. Li, Y. Wang, and L. P. Lv, “Fe, Zn Co-Doped Porous Carbon Nanofiber-Based Rechargeable Zinc Air Batteries with Stable Operation over 1600 h,” *Ind. Eng. Chem. Res.*, vol. 62, no. 1, pp. 169–179, 2023.

451. Y. T. Lu, Y. J. Chien, C. F. Liu, T. H. You, and C. C. Hu, “Active site-engineered bifunctional electrocatalysts of ternary spinel oxides, M0.1Ni0.9Co2O4 (M: Mn, Fe, Cu, Zn) for the air electrode of rechargeable zinc-air batteries,” *J. Mater. Chem. A*, vol. 5, no. 39, pp. 21016–21026, 2017.

452. R. J. Toh, A. Y. S. Eng, Z. Sofer, D. Sedmidubsky, and M. Pumera, “Ternary Transition Metal Oxide Nanoparticles with Spinel Structure for the Oxygen Reduction Reaction,” *ChemElectroChem*, vol. 2, no. 7, pp. 982–987, 2015.

453. M. Labbe, M. P. Clark, K. Cadien, and D. G. Ivey, “Bifunctional Mn-Fe Oxide Catalysts for Zn-Air Battery Air Electrodes Fabricated Through Atomic Layer Deposition,” *Batter. Supercaps*, in-press, e202400133, 2024.

454. I. H. Baek, J. J. Pyeon, S. H. Han, G. Y. Lee, B. J. Choi, J. H. Han, T. M. Chung, C. S. Hwang, and S. K. Kim, “High-Performance Thin-Film Transistors of Quaternary Indium-Zinc-Tin Oxide Films Grown by Atomic Layer Deposition,” *ACS Appl. Mater. Interfaces*, vol. 11, no. 16, pp. 14892–14901, 2019.

455. Z. Wang, H. Xu, Y. Zhang, H. C. Cho, J. K. Jeong, and C. Choi, “Low temperature (<150 °C) annealed amorphous indium-gallium-tin oxide (IGTO) thin-film for flash memory application,” *Appl. Surf. Sci.*, vol. 605, p. 154614, 2022.

456. M. Shen, A. Afshar, Y. Y. Tsui, K. C. Cadien, and D. W. Barlage, “Performance of Nanocrystal ZnO Thin-Film Schottky Contacts on Cu by Atomic Layer Deposition,” *IEEE Trans. Nanotechnol.*, vol. 16, no. 1, pp. 135–139, 2017.

457. M. Shen, T. P. Muneshwar, K. C. Cadien, Y. Y. Tsui, and D. W. Barlage, “ZnO Schottky Nanodiodes Processed From Plasma-Enhanced Atomic Layer Deposition at Near Room Temperature,” *IEEE Trans. Electron Devices*, vol. 65, no. 10, pp. 4513–4519, 2018.

458. A. M. Ma, M. Gupta, A. Afshar, G. Shoute, Y. Y. Tsui, K. C. Cadien, and D. W. Barlage, “Schottky barrier source-gated ZnO thin film transistors by low temperature atomic layer deposition,” *Appl. Phys. Lett.*, vol. 103, no. 25, p. 253503, 2013.

459. M. Labbe and D. G. Ivey, “Catalyst Integration within the Air Electrode in Secondary Zn-air Batteries,” *J. Phys. Energy*, vol. 6, no. 3, p. 032002, 2024.

460. S. K. Ghosh, “Diversity in the Family of Manganese Oxides at the Nanoscale: From Fundamentals to Applications,” *ACS Omega*, vol. 5, no. 40, pp. 25493–25504, Oct. 2020.

461. J. Melder, S. Mebs, F. Lessing, H. Dau, and P. Kurz, “Tuning electrocatalytic water oxidation by MnOx through the incorporation of abundant metal cations,” *Sustain. Energy*

Fuels, vol. 7, no. 1, pp. 92–105, 2022.

462. M.-Y. Li, Y.-Y. Chang, H.-C. Wu, C.-S. Huang, J.-C. Chen, J.-L. Lue, and S.-M. Chang, "Effect of Process Pressure on Atomic Layer Deposition of Al2O3," *J. Electrochem. Soc.*, vol. 154, no. 11, p. H967, 2007.

463. A. J. Gayle, Z. J. Berquist, Y. Chen, A. J. Hill, J. Y. Hoffman, A. R. Bielinski, A. Lenert, and N. P. Dasgupta, "Tunable Atomic Layer Deposition into Ultra-High-Aspect-Ratio (>60000:1) Aerogel Monoliths Enabled by Transport Modeling," *Chem. Mater.*, vol. 33, no. 14, pp. 5572–5583, 2021.

464. S. Sun, Y. Wen, A. Billings, R. Rajabi, B. Wang, K. Zhang, and K. Huang, "Protecting Zn anodes by atomic layer deposition of ZrO2 to extend the lifetime of aqueous Zn-ion batteries," *Energy Adv.*, vol. 3, no. 1, pp. 299–306, 2024.

465. S. Sinha, P. N. Didwal, D. K. Nandi, J. Y. Cho, S. H. Kim, C. J. Park, and J. Heo, "Atomic layer deposited-ZnO@3D-Ni-foam composite for Na-ion battery anode: A novel route for easy and efficient electrode preparation," *Ceram. Int.*, vol. 45, no. 1, pp. 1084–1092, 2019.

466. J. Liu, C. Guan, C. Zhou, Z. Fan, Q. Ke, G. Zhang, C. Liu, and J. Wang, "A Flexible Quasi-Solid-State Nickel – Zinc Battery with High Energy and Power Densities Based on 3D Electrode Design," *Adv. Mater.*, vol. 28, no. 39, pp. 8732–8739, 2016.

Appendix A. Catalyst Integration within the Air Electrode in Secondary Zn-air Batteries

A version of this appendix has been published in a peer-reviewed journal:

M. Labbe and D. G. Ivey, "Catalyst Integration within the Air Electrode in Secondary Zn-air Batteries," *J. Phys. Energy*, vol. 6, no. 3, p. 032002, 2024.

Abstract

The air electrode of a Zn-air battery (ZAB) facilitates the O_2 reduction and evolution reactions during battery discharge and charge, respectively. These reactions are kinetically sluggish and appropriate catalysts are essential at the air electrode to increase battery efficiency. Precious metals are traditionally used, but increasingly attention has shifted towards non-precious metal catalysts to decrease the cost and increase the practicality of ZABs. However, loading of the catalyst onto the air electrode is equally as important as catalyst selection. Several methods can be used to deposit catalysts, each with their own advantages and disadvantages. Example methods include spray-coating, electrodeposition, and impregnation. These can be categorized as indirect, direct, and hybrid catalyst loading techniques, respectively. Direct and hybrid loading methods generally provide better depth of loading than indirect methods, which is an important consideration for the porous, air-breathing electrode of a ZAB. Furthermore, direct methods are free from ancillary materials such as a binder, required by indirect and hybrid methods, which translates into better cycling stability. This review examines the various techniques for fabricating catalyst-enhanced air electrodes with an emphasis on their contributions to battery performance and durability. More durable ZAB air electrodes directly translate to longer operational lifetimes for practical ZABs, which is an important consideration for the future implementation of electrochemical energy storage in energy systems and technologies. Generally, direct catalyst loading techniques, which integrate catalyst material directly onto the air electrode structure, provide superior cycling performance to indirect catalyst loading techniques, which distribute an *ex situ* synthesized material onto the top layer of the air electrode. Hybrid catalyst loading techniques, which grow catalyst material directly onto

nanostructured supports and then integrate them throughout the air electrode architecture, offer a compromise between direct and indirect methods.

A.1. Introduction

Strategies for achieving a carbon neutral energy landscape often involve renewable energy sources, such as wind and solar, which are inherently intermittent. As a means to capture excess renewable energy and release the stored energy on-demand, energy storage is perceived as the key to widespread adoption of renewable energy.[1–3] Of the various energy storage technologies available, electrochemical batteries are favoured for their versatility, scalability, and ease of use.[4] Currently, Li-ion batteries (LIBs) dominate the rechargeable (or secondary) battery market, replacing the aging technology of Pb-acid batteries.[1,5] However, several key drawbacks of LIBs include high cost,[3] limited material reserves, and safety concerns.[6] As a possible future replacement for LIBs, Zn-air batteries (ZABs) boast far higher energy density (1086 Wh kg^{-1} vs. 296 Wh kg^{-1} for LIB),[7–9] lower cost and highly abundant materials (mineral reserves of Zn are nearly twenty-times greater than for Li),[10,11] and safe operation (non-flammable components, especially the electrolyte).[6] However, challenges remain in the commercialization of ZABs due to Zn rechargeability issues, atmospheric complications (humidity, CO_2, *etc.*), and, most critically, poor air electrode kinetics.[6]

ZABs, and more generally any metal-air battery, combine a metallic electrode with an air-breathing electrode to establish an electrochemical cell.[12] An alkaline electrolyte is often chosen to reduce the overpotential for the air electrode reactions.[12] Of the various metallic electrodes stable in an alkaline solution, Zn provides the largest electrochemical potential and thus highest cell voltage.[13] During battery discharge, the Zn electrode undergoes oxidation in an alkaline environment according to Equation A.1.[7] At the air electrode, O_2 is reduced according to Equation A.2.[14] It is important to note that the O_2 reduction reaction (ORR, Equation A.2) requires chemical species in three different phases: gaseous O_2, liquid water, and solid electrons.[12] Thus, ORR can only proceed at three-phase boundary regions where all three phases coexist. In practical ZABs, this three-phase boundary area lies within the gas-permeable membrane that makes up the air-breathing electrode.[12]

$$\mathrm{Zn} + 4\mathrm{OH}^- \rightleftharpoons \mathrm{Zn(OH)_4}^{2-} + 2\mathrm{e}^- \qquad E^0 = -1.25\ \mathrm{V\ vs.\ SHE} \qquad \text{(A.1)}$$

$$O_2 + 2H_2O + 4e^- \rightleftharpoons 4OH^- \qquad E^0 = +0.401\ \text{V vs. SHE} \quad \text{(A.2)}$$

The air electrode of a metal-air battery has three requirements to facilitate ORR: (1) Electronic conductivity for supplying electrons, (2) gas permittivity to enable O_2 diffusion into the cell, and (3) hydrophilicity to provide access to water molecules.[6] However, the maximum concentration and mobility of O_2 species is much higher in a gaseous environment than a liquid one (*e.g.*, dissolved O_2 in water).[7,15] Therefore, a careful balance of hydrophobicity is crafted by applying a gradient of hydrophobic agents, the most common choice being polytetrafluoroethylene (PTFE).[6] The outside air-facing surface is highly hydrophobic to enable gaseous O_2 flow into the electrode, while the interior electrolyte-facing surface is more hydrophilic to improve the interface between the air electrode and electrolyte and thereby reduce the interfacial resistance.[12,16] This electrode structure, often called the gas diffusion layer (GDL),[14] is frequently made of carbon materials to satisfy electronic conductivity.[6,7,17] Another improvement made to the GDL is the development of a so-called microporous layer, where the interior electrolyte-facing side of the GDL contains a high surface area structure of carbon particles bound together,[6,14] forming pores on the order of 20 to 50 nm.[18] It should be noted that this pore structure size is actually classified as mesoporous in traditional chemistry,[19] but the nomenclature of a microporous layer persists nonetheless. This high surface area construction improves the solid-electrolyte interface and additionally provides a support for catalyst loading.[6,14,20] This is important since ORR is a notoriously sluggish electrochemical reaction and benefits greatly from electrochemical catalysts.[7,14,15]

A Zn electrode features the most active metal that can be electrodeposited in an aqueous electrolyte,[13] permitting reversal of the discharge reaction (reverse direction of Equation A.1) and recharging of the ZAB. At the air electrode, ORR is reversed in what is known as the O_2 evolution reaction (OER, reverse direction of Equation A.2), since O_2 is formed.[14,21] While the Zn electrode has its fair share of complexities and rechargeability issues,[6,22] the O_2 reduction and evolution reactions are sluggish and require significant activation overpotentials.[15] Therefore, the investigation of ORR and OER catalysts is a key focus of ZAB research.[14,23] It is possible to physically separate the discharge and charge processes of the air electrode,[24] but this adds to the size of the battery and reduces the effective energy and power density.[7,16] Thus, if both charge (OER) and discharge (ORR) occur at a single electrode, a bifunctional catalyst is required.[14] The

list of contenders for bifunctional ORR/OER catalysts is extensive, but generally lower cost and highly abundant materials are selected for practical ZAB application.[14,23] Commonly studied catalysts that meet this criteria are transition metal oxides, in particular oxides of metals that lie in the 4th period of the Periodic Table (*e.g.*, Mn, Fe, Co, Ni).[23] When experimentally evaluating the electrochemical performance of a bifunctional catalyst, it is common practice to compare results with a Pt and RuO_2 mixture as a benchmark catalyst.[6,7,12,14,25–27]

The GDL microporous layer serves as a scaffolding for catalyst loading and, thus, catalysts are usually applied at the interior electrolyte-facing side of the GDL.[14] The three-phase boundary area, where ORR can occur, is generally dictated by the hydrophobicity of the GDL and where liquid electrolyte penetration meets air flow.[7] The recharge reaction, OER, only requires two chemical phases (liquid hydroxide ions and solid electrons) and can occur anywhere the electrolyte is in contact with the electronically conductive GDL material. It is ideal to have catalyst material distributed throughout the GDL such that ORR and OER can always be catalyzed and activation overpotentials minimized. As such, catalyst material at the interior face (*i.e.*, where the electrolyte meets the electronic conductor) is favourable for OER, while catalyst material deeper within the GDL is desirable for catalyzing ORR, since this is where the three-phase boundary region exists.[28,29] With the right hydrophobic treatment, ORR occurs primarily close to the microporous layer such that any occurrence of ORR is enhanced by the catalyst (Figure A.1a). However, extensive charge and discharge cycling of a ZAB can deteriorate the PTFE treatment of the GDL and can lead to a phenomenon known as flooding.[6] During flooding, the electrolyte is able to penetrate deeper into the pores of GDL and pushes the three-phase boundary area (where liquid electrolyte meets gaseous O_2) to regions further away from the interior electrolyte facing side. This migration of the three-phase boundary area forces ORR to occur at areas deeper within the air electrode, where catalyst material may not have been deposited (Figure A.1b).[28,30] As a result, the activation overpotential of ORR increases and the overall efficiency of the ZAB is reduced. This phenomenon commonly appears as a loss in battery performance and efficiency over the course of many cycles. To reduce this effect, several different catalyst loading techniques can be used to apply catalyst material throughout the entire depth of the GDL, so that ORR catalyst is present at any region where the three-phase boundary area migrates.[30] ZABs that have less performance loss over the course of many charge and discharge cycles are often described as being highly durable or exhibiting stable performance.[21]

The deposition of catalysts onto/into the GDL can generally be classified as either indirect or direct.[17] Indirect methods synthesize the catalyst material *ex situ* (such as hydrothermal methods) and apply the catalyst through a traditional deposition technique, such as drop-casting or spray-coating.[21] Direct methods create the catalyst material using the GDL as a substrate (*i.e.*, *in situ* synthesis).[31] This results in strong adhesion and generally better distribution of catalyst. However, a hybrid method of catalyst development has also been identified, where catalyst particles are synthesized on conductive nanomaterials and subsequently introduced into the GDL. While the method is technically indirect, since the GDL is not the catalyst substrate, the integration of the catalyst loaded nanomaterial into the GDL is effective and thorough for hybrid methods, leading to similar benefits as direct deposition methods such as good adhesion and excellent catalyst distribution throughout the thickness of the GDL.

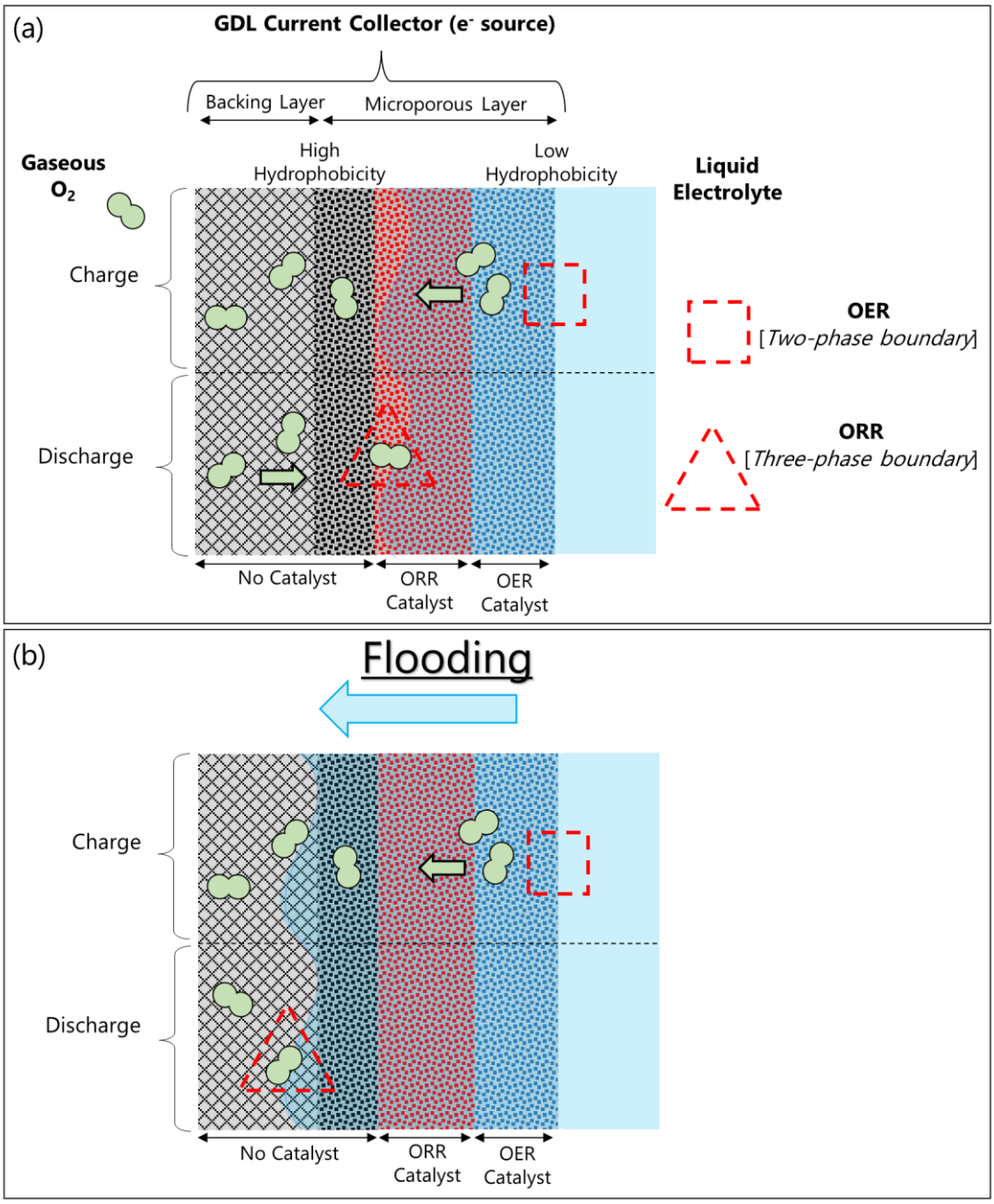

Figure A.1. Depiction of an idealized air electrode during charge and discharge. (a) A careful balance of hydrophobicity, ORR catalyst distribution, and OER catalyst distribution ensures that the two-phase boundary area between liquid electrolyte and the solid current collector during OER is catalyzed by OER catalyst particles, and the three-phase boundary area between liquid electrolyte, the solid current collector, and gaseous O_2 during ORR is catalyzed by ORR catalyst particles. (b) During flooding, the electrolyte penetrates deeper into the air electrode, shifting the three-phase ORR process into the un-catalyzed region, reducing battery performance.

A.2. Indirect Methods

The classical method of depositing a catalyst material onto the air electrode substrate is via an ink suspension (Figure A.2).[21,26] The catalyst powder is dispersed in a solvent along with a conductive filler and binder agent.[17,32] The conductive filler, often a carbon material,[33–36] compensates for catalysts that are inherently nonconductive, such as metal oxides,[14,23] to reduce the contact resistance between the catalyst surface and substrate material.[37] The binder agent enables the formation of a homogenous suspension and also works to reduce the contact resistance between the catalyst particles and the conductive filler.[38] Both PTFE and Nafion are used as binders;[38,39] the latter material is favored for polymer electrolyte membrane fuel cell electrodes.[40,41] Typical solvents include water,[42] glycerol,[41] ethanol,[33,43] isopropanol,[20,36] or any mixture of these.[44–46] Ultrasonication is a common step in synthesis to uniformly disperse the catalyst, binder, and filler and create a homogenous suspension.[41,44,47–49] The ink is then applied to the air electrode substrate either using drop-casting,[35,46,49,50] where the suspension is deposited onto the surface drop-wise, or spray-coating,[36,51] where the suspension is sprayed with an airbrush and painted onto the substrate.[44,52] After coating, the solvent evaporates and a residue of catalyst, filler, and binder remains on the surface to act as the catalyst layer.[20,40] Since the catalyst material is synthesized *ex situ* and applied to the air electrode substrate afterwards, the ink-based method is considered as an indirect method of catalyst loading.[17] Related to this is the paste method, which creates a more viscous slurry using the same components, which is then rolled or pressed onto the air electrode substrate.[29,33,34,38,53,54]

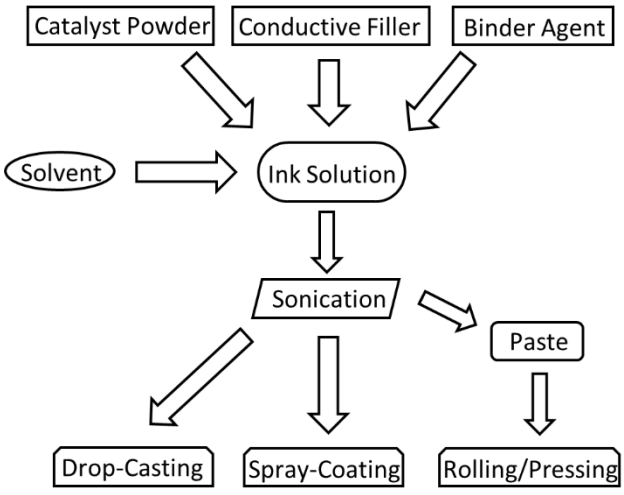

Figure A.2. Process flow of indirect catalyst loading techniques.

A beneficial aspect of indirect methods for ZAB catalyst loading is the freedom to synthesize the catalyst material using a variety of methods. Since catalyst formation occurs independent of the final air electrode substrate,[17] high temperatures[55] or aggressive solvents[42,45] can be utilized. Any number of synthesis methods are available, but common solution-based ones include sol-gel techniques,[56] hydrothermal formation,[53,54,57] and chemical reduction.[34] As well, most researchers prepare benchmark precious metal catalyst air electrodes via an indirect ink and spray-coating method. [58–61]

The additional materials required during indirect loading of catalysts (*i.e.*, binder and filler) can negatively impact overall battery performance.[6,16,58] Binders can block catalytic active sites[16,21,41] and degrade during ORR,[6,16,32,38] while carbon-based filler materials increase the overall mass of the air electrode[16,32] and corrode during OER.[6,14] For example, Wang *et al.* prepared a bifunctional $La_{0.8}Sr_{0.2}Co_{0.4}Mn_{0.6}O_3$ perovskite catalyst using a sol-gel method.[56] They subsequently used an indirect paste method to create a ZAB air electrode.[62] Over the course of 100 cycles, the OER potential increased by 150 mV when cycled at 10 mA cm^{-2} in 6 M KOH. The authors attributed this performance degradation to the oxidation of the carbon support used during preparation of the catalyst slurry.[56,62] More critically, however, indirect methods generally only deposit catalyst material on the top-most surface of the air electrode.[30,63] This results in severe performance loss during extended cycling, when electrolyte flooding migrates the three-phase boundary past the catalyst layer.[30] This is illustrated in a report by Prabu *et al.*, who deposited a graphene-supported $CoMn_2O_4$ (CMO) catalyst on GDL via an airbrush (Figure A.3). The efficiency of the assembled ZAB at the beginning of the cycling test is shown in Figure A.3a and is calculated as the discharge potential divided by the charge potential. For this example, the efficiency is 65% when cycled at 20 mA cm^{-2} in 6 M KOH (Figure A.3a). As the cycling test continues, with alternating periods of charge and discharge, the charge and discharge potentials deviate from the standard potential by greater and greater amounts. This is understood as the overpotential of the battery cell and is also denoted as the C-D potential gap in Figure A.3b. The battery efficiency calculated at the 200^{th} cycle is only 47% (Figure A.3b).[51] This represents a 28% loss in efficiency over the period of 200 cycles, or 14% per 100 cycles. The indirect catalyst loading technique experiences a large degradation in battery performance during cycling, as the three-phase boundary migrates past the spray-coated surface layer and into the uncatalyzed GDL substrate.

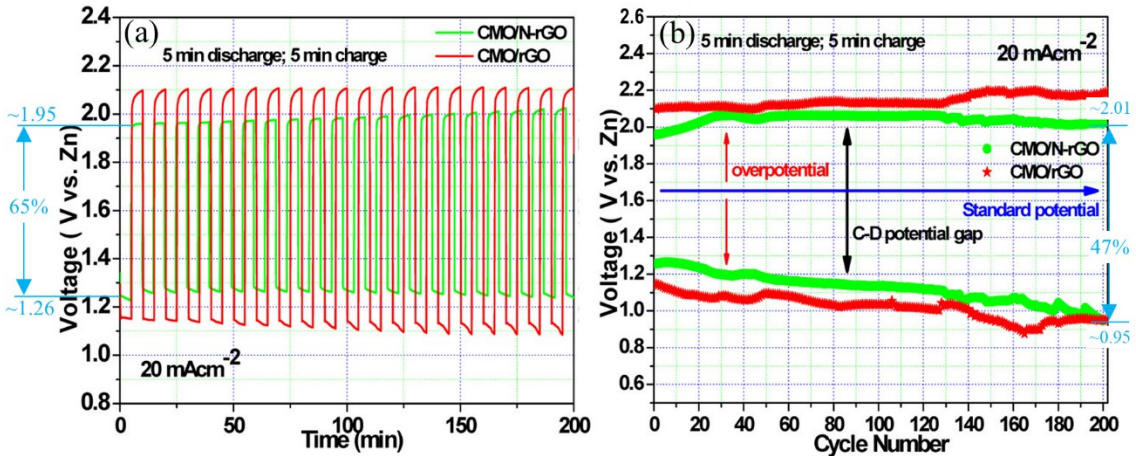

Figure A.3. ZAB cycling for an indirectly loaded catalytic air electrode. (a) The first 200 min of charge and discharge potentials and (b) the total charge and discharge potential curves after 200 cycles (33 h). Adapted with permission from Ref.[51]. Copyright 2014 Royal Society of Chemistry.

A.3. Direct Methods

In contrast to indirect methods, direct loading of ZAB catalysts involves synthesizing an electrocatalyst directly onto or even within the final air electrode substrate. This can be accomplished by an array of techniques including electrodeposition, electroless deposition, chemical vapour deposition (CVD), or physical vapour deposition (PVD).[17] The air electrode substrate is often a carbon-based GDL as described previously; however, other candidate substrates include metal foams or meshes using alkaline-stable metals such as Ni, Ti, or stainless steel.[6,21,24,64] A hydrophobic treatment or barrier layer is applied after catalyst synthesis to provide the necessary wet-proofing of the air electrode.[21,65] An obvious advantage of direct catalyst loading is the avoidance of additional materials such as binders or conductive fillers. These materials, susceptible to degradation during battery operation, are excluded so that the lifetime of the air electrode is extended.[58] Another advantage of direct catalyst synthesis is the improved interface between the current collector and catalyst material.[32] Electron flow from catalyst particles to the current collector is not impeded by any binders or secondary materials,[64,66] reducing the resistance of the air electrode.[6,58] As well, direct catalyst loading methods are generally faster and can simplify electrode design,[58,66] which is advantageous for commercializing and scaling up ZABs.[6,17,32,64] More importantly, however, direct deposit methods can deposit catalyst material throughout the air electrode structure, as opposed to only

surface-level deposition, increasing the catalytically-active surface area and improving the stability of the air electrode against flooding.[6,32,64,66] The main drawback of direct catalyst synthesis on the air electrode substrate is the sensitivity of the air electrode material. Aggressive deposition techniques, such as those involving high temperatures or oxidizing chemicals, can damage carbon-based GDLs and hydrophobic agents (*e.g.*, PTFE).[17,67] The use of non-carbon GDLs and *ex situ* hydrophobic treatments is a potential workaround to these limitations.

Depositing ZAB catalysts directly on the air electrode substrate can be achieved by either electrodeposition or electroless deposition. Used extensively in industry for applying coatings,[68,69] these techniques operate in the liquid phase by converting dissolved chemical species into a solid material. In electrodeposition, the voltage difference and current flow between electrodes are manipulated, resulting in deposition of material on the working electrode.[17] In electroless deposition, reducing agents in solution cause spontaneous deposition of material on the working electrode.[69] In either case, if GDL is used as the working electrode, ZAB catalysts can be directly coated onto the GDL. Electrically conductive substrates are required for electrodeposition, but not for electroless deposition.[17,69] GDLs are usually conductive to act as a current collector for the air reactions and are thus suitable substrates for either process. Xiong and Ivey published work on a Co-Fe catalyst for OER, electrodeposited directly on carbon GDL (Figures A.4a and A.4b).[37] Co-based catalysts benefit greatly from Fe doping, but synthesis procedures are often complex and involve additives such as carbon black or PTFE. In their work, Xiong and Ivey achieved ZAB cycling results comparable to a Pt-C commercial catalyst using a simple one-step electrodeposition process.[37] Improving upon their work, an ORR-active catalyst (MnO_x) was also directly electrodeposited onto GDL (Figures A.4c and A.4d), in addition to the OER Co-Fe catalyst.[70] By distributing the MnO_x catalyst on the GDL first, followed by the Co-Fe catalyst (Figures A.4e and A.4f), regions of ORR activity are catalysed by MnO_x while regions of OER activity benefit from the Co-Fe catalyst, similar to the depiction in Figure A.1. This double-layered catalyst air electrode provided superior ORR and OER performance than either catalyst layer alone based on cyclic voltammetry testing. Furthermore, ZAB rate testing in 6 M KOH revealed that the double-layered catalyst provides superior bifunctional efficiencies than a commercial Pt-C catalyst, with 62% and 60% bifunctional efficiencies at 10 mA cm^{-2} for the electrodeposited catalyst and Pt-C catalyst, respectively.[70] When cycled at 5 mA cm^{-2}, a ZAB constructed with the MnO_x/Co-Fe catalyst had

similar bifunctional efficiencies to one with a commercial Pt-C catalyst. The average discharge potential for the MnO_x/Co-Fe ZAB was 1.18 V, compared with 1.21 V for the Pt-C ZAB, while the average charge potential was 1.98 V for the MnO_x/Co-Fe ZAB compared with 2.03 V for the Pt-C ZAB. After 13 h of cycling, the ZAB with MnO_x/Co-Fe performed better than the ZAB with Pt-C in discharge-charge polarization testing.[70] Thus, the electrodeposition technique for the MnO_x/Co-Fe catalyst resulted in a more stable ZAB than the indirect spray-coated Pt-C electrode.

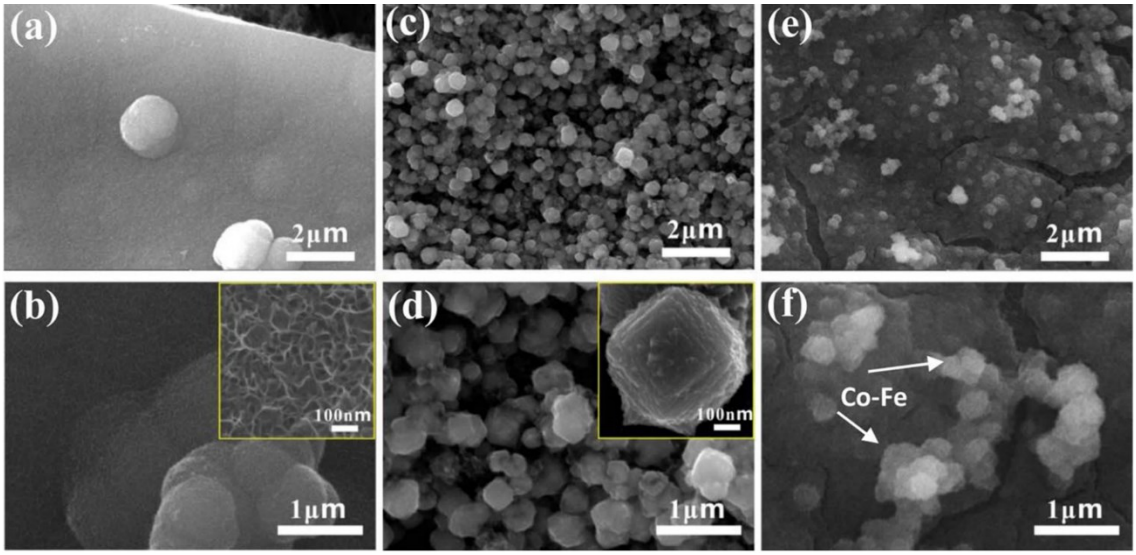

Figure A.4. SEM images of (a, b) MnO_x on GDL, (c,d) Co-Fe on GDL and (e,f) MnO_x/Co-Fe on GDL. Adapted with permission from Ref.[70]. Copyright 2017 The Electrochemical Society.

A double-layer electrodeposition process was also explored by Kim *et al.*, where they used a gel-mediated electrodeposition process to deposit ORR-active MnO_2 and OER-active Co_3O_4 directly onto Ni foam. A ZAB constructed with this catalyst showed only 0.05 V of degradation during either charge or discharge at 1 mA cm^{-2} over 400 h in 6 M KOH, maintaining approximately 60% bifunctional efficiency.[71] The direct electrodeposition process provided a strong connection between the catalyst and Ni foam substrate, resulting in stable cycling performance. Some researchers have applied a bifunctional catalyst directly onto a carbon substrate via a single-step electrodeposition process,[59,72,73] while others have used electrodeposition to add a second catalyst to a previously synthesized catalyst material.[74,75] Electroless deposition was used by Karajagi *et al.* to create a Ni interlayer on carbon air electrodes, protecting the electrodes from carbon corrosion and also providing OER activity.[76] In a different study, Lee *et al.* used an electroless

process to grow Co_3O_4 nanowire arrays directly on a stainless steel mesh. When applied as an air electrode, the directly grown catalyst was stable for 600 h, exhibiting 97% charge and 94% discharge retention over nearly one month of cycling in 6 M KOH at 18 mA cm^{-2}. Comparatively, a spray-coated Pt-C electrode failed after only 25 h, when the charging potential exceeded 3.0 V.[58] The excellent longevity of the electrodeposited catalyst exemplifies the benefit of a direct catalyst loading technique, while the poor cycling performance of the spray-coated Pt-C electrode highlights the inferiority of indirect catalyst loading techniques.

Since the GDL must be gas permeable for O_2 exchange between the cell and exterior environment, a gas-based deposition technique would be suitable for loading catalyst material throughout the GDL structure. Chemical vapour deposition (CVD) is a method of depositing thin film coatings on a substrate by employing gaseous reactants. Both surface-based and gas-based chemical reactions occur in CVD which lead to film growth as precursors are supplied to the surface.[77] A few examples of catalysts synthesized via CVD are found in the literature, but rather than use CVD to coat the GDL substrate, CVD is used as a method of synthesis for ZAB catalysts. Sometimes the catalysts are developed directly with the air electrode material[78,79] and other times they are deposited indirectly after *ex situ* synthesis.[80–83] A specialized form of CVD known as atomic layer deposition (ALD) isolates only surface-based chemical reactions to grow coatings, eliminating gas-phase reactions or thermal decomposition of precursors. As a result, the conformality or step-coverage of coatings via ALD is superior to traditional CVD.[77] Thus, ALD is ideally suited for high aspect ratio substrates, such as the high surface area microporous layer of GDL. Direct coating of the GDL substrate with an ALD film was studied by Clark *et al.* in their publication of a MnO_x catalyst active towards ORR. They found that a forming gas (5% H_2 in N_2) plasma pre-treatment was required to maintain saturating growth from the water-based MnO_x ALD process. Without the plasma pre-treatment, MnO_x ALD coatings on GDL were found to agglomerate carbon particles and reduce the porosity and surface area of the air electrode. The optimized ALD process instead uniformly coated the air electrode, maintaining the porosity and also enabling deeper penetration of catalyst material into the air electrode depth.[84] When assembled into a ZAB, the MnO_x ALD coated air electrode displayed superior polarization behaviour compared with a Pt-Ru-C benchmark catalyst at current densities above 200 mA cm^{-2}. High current densities consume O_2 quickly and battery performance relies on O_2 availability. The benchmark Pt-Ru-C air electrode was prepared via spray-coating and does not

provide as much O_2 access to catalyst material as the ALD coated electrode, with deep catalyst loading into the electrode porosity. Thus, the ALD MnO_x air electrode provided a superior peak power density of 170 mW cm^{-2} compared with 158 mW cm^{-2} for Pt-Ru-C.[30] To further improve the performance of the air electrode, CoO_x was added to the ALD process. Overall, the ALD coated electrode, with direct catalyst loading, was resilient to flooding, maintaining a stable discharge potential of ~1.25 V at 10 mA cm^{-2} for 20 h in 6 M KOH and only decreasing to ~1.17 V after 50 h of cycling. In comparison, a spray-coated Pt-Ru-C benchmark catalyst, with poor distribution of catalyst material from indirect loading, suffered greatly from flooding during cycling. The initial discharge potential of ~1.25 V quickly dropped to 1.1 V after only 20 h at 10 mA cm^{-2}.[30]

Direct deposition of ZAB catalysts using ALD was also studied by Labbe *et al.* by directly depositing an OER-active Fe_2O_3 catalyst on GDL. However, their ALD process utilized an O plasma which etched the carbon-based GDL substrate. To overcome this, a protective sublayer of ALD MnO_x was deposited prior to FeO_x ALD.[85] The MnO_x sublayer also enhanced the growth characteristics of the FeO_x process and it was found that the FeO_x ALD process experienced multiple stages of island growth, a phenomenon not typical in ALD.[67] By mixing the ORR-active MnO_x ALD layer developed by Clark *et al.* [84] with the OER-active FeO_x ALD layer, a bifunctional catalyst was developed via direct ALD. Optimization of the mixed MnO_x-FeO_x ALD process yielded a 30:10 mixture of MnO_x cycles to FeO_x cycles. Electron diffraction analysis in the transmission electron microscope (TEM) indicated that the mixed oxide is a Mn spinel structure with Fe substitution ($(Mn,Fe)_3O_4$). Energy dispersive x-ray (EDX) analysis in the scanning transmission electron microscope (STEM) (Figures A.5a-d) revealed a thin, uniform distribution of the ALD coating on the carbon particles of the GDL. Cycling results of a ZAB with the $(Mn,Fe)_3O_4$ catalyst indicate a long lifetime for the directly grown catalyst, with stable cycling results even after 600 h (1540 cycles) of 10 mA cm^{-2} cycling in 6 M KOH (Figure A.5e).[86] A Pt-Ru-C benchmark catalyst, on the other hand, deposited by indirect spray coating experienced performance loss and reached similar charge and discharge potentials as an uncoated electrode after 300 h of cycling.

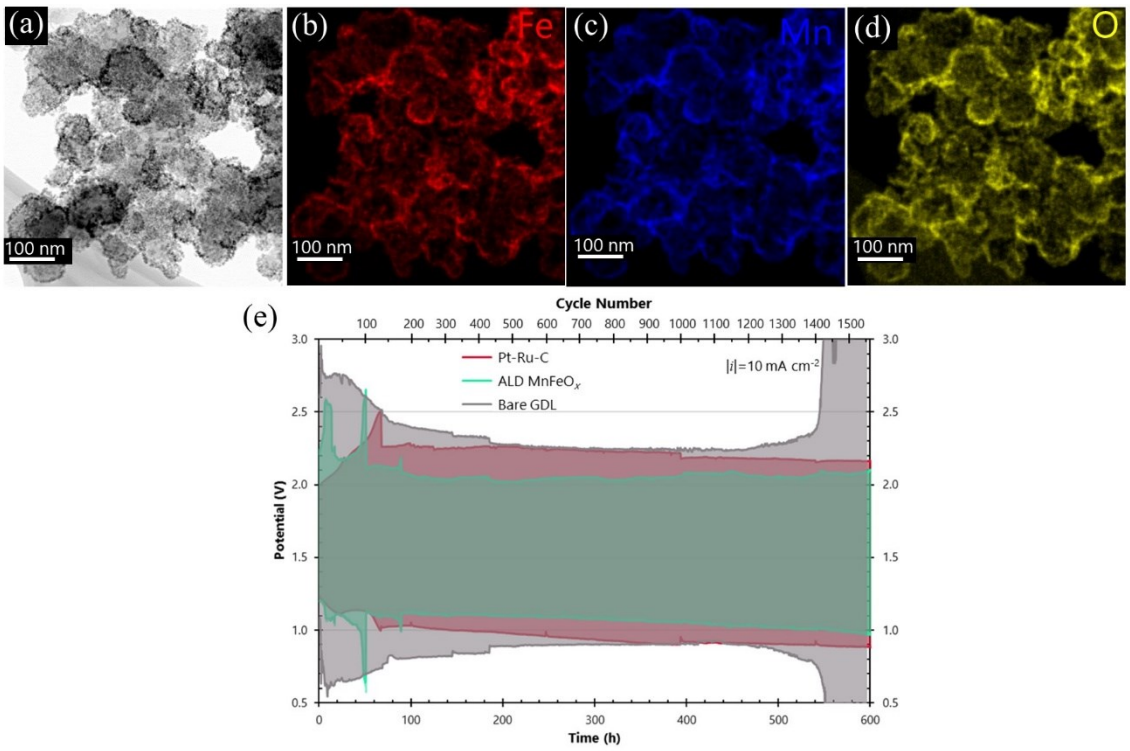

Figure A.5. Direct ALD of a $(Mn,Fe)_3O_4$ catalyst on GDL carbon particles. (a) STEM image of the GDL particles with the ALD coating represented by dark bands around the particles, (b-d) EDX mapping of Fe, Mn, and O, respectively, showing the coverage of the carbon particles with the thin ALD coating. (e) Cycling performance of ZABs with $(Mn,Fe)_3O_4$, Pt-Ru-C, and uncoated GDL air electrodes.[86]

Other ALD researchers preloaded a ZAB air electrode with carbon nanotubes (CNT) to provide a high surface area scaffolding. Both Co_9S_8 and NiS_x were deposited in this way,[87,88] yielding stable bifunctional performance in 6 M KOH and, in the case of Co_9S_8, very competitive peak power and efficiency values of 197.6 mW cm^{-2} and 62.5% at 10 mA cm^{-2}, respectively.[87] While ALD is classified as a direct catalyst loading method, some researchers have employed ALD more as an indirect catalyst synthesis method, where the catalyst is grown via ALD *ex situ* and deposited on the air electrode by an indirect method, such as drop-casting.[89–92] One reason to use ALD as an indirect method of synthesis is because of aggressive O-based reactants employed in ALD. Carbon-based organometallic ALD precursors, chosen because of their volatility and lack of contaminating Cl or N species,[93,94] often require the use of ozone or O plasma reactants to combust the carbon ligands of the precursor molecule and avoid carbon inclusion in the growing

ALD film.[93–96] While effective for this purpose, these highly reactive O-based reactants can also oxidize carbon substrates, such as GDL, during deposition.[30,67] Likewise, the PTFE in GDL can be damaged by ozone or O plasma reactants.[30,97,98] Both of these effects reduce the efficacy of the air electrode during ZAB cycling.[30,67]

In contrast to CVD, which involves chemical reactions to directly grow a film, physical vapour deposition (PVD) involves the physical redistribution of atoms from a target source onto a substrate. This vacuum deposition technique operates by vaporizing the target atoms through either heating (thermal evaporation), high energy lasers (pulsed laser deposition, PLD), or a beam of high energy electrons. Alternatively, target atoms can be removed via sputtering, where high energy ions impart kinetic energy to the target atoms.[99] Often metallic or alloy targets are used in PVD and the application of this deposition technique towards ZAB catalysts reflects this. Several papers by Chen *et al.* explored the direct deposition of an Ag-Cu nanoalloy onto Ni foam air electrodes using PLD.[100,101] They report ZAB performance values comparable to a Pt-C benchmark catalyst but with better stability, maintaining stable battery performance over 1200 cycles of charge and discharge in 6 M KOH, while noticeable deterioration of the Pt-C sample occurred after only four cycles.[102] Pham *et al.* also employed PLD, depositing a Ni_3Pt alloy directly onto Ni foam for the air electrode of a ZAB which ran for over 450 cycles.[103]

The terms “free standing,”[104,105] “self supporting,”[105] or “binder free”[32,74,103] are frequently used in the literature to describe a direct deposition catalyst, where the substrate material is often synthesized *in situ* during catalyst development.[106,107] Metal-organic frameworks (MOFs), which are porous crystalline structures comprised of metal nodes and organic linkers, are sometimes employed in these studies.[108,109] They provide high surface area and catalytic activity from both functional groups on the organic linkers and the uncoordinated metal centers. In particular, zeolitic imidazolate frameworks are frequently employed for their nitrogen functional groups on the organic components. Furthermore, metal or metal oxide nanoparticles can be attached within or on the surface of the framework structure to provide additional catalytic activity.[108] Synthesis routes for MOFs are generally hydrothermal/solvothermal,[108] with electroless deposition reagents added for anchoring metal oxide nanoparticles.[104,105,109,110]

A.4. Hybrid Methods

As the name suggests, hybrid catalyst loading techniques are a combination of both indirect and direct catalyst loading techniques. Hybrid methods directly grow catalyst material onto nanostructured supports (*e.g.*, CNTs, carbon fibers) and then distribute the catalyst coated nanostructure into the air electrode. The *ex situ* distribution into the air electrode provides the ability to manufacture the catalyst loaded nanostructures in a variety of environments and conditions, regardless of air electrode substrate material. When coupled with an effective distribution technique, competitive performance to direct deposition methods can be achieved because the catalyst material is integrated into the bulk of the air electrode and not surface level only. The nanostructured support is typically conductive (*e.g.*, carbon-based) and thus conductive additives can be omitted from the electrode integration process.[61] In addition, the direct growth of catalyst material onto the nanostructured support improves the interfacial contact between the catalyst and electronic conductor similar to direct catalyst loading methods. The main downside of hybrid catalyst loading is the continued necessity of polymeric binders, which can degrade during battery cycling, as occurs with indirect catalyst loading techniques.[6,16,32,38]

One hybrid method, reported by Aasen *et al.*, begins by growing metal oxide nanoparticles on N-CNTs via a simple ultrasonication method. The suspension of nanoparticle coated N-CNTs is then passed through a porous carbon GDL via vacuum filtration, essentially using GDL as filter paper (Figure A.6a). By doing so, the nanoparticle coated N-CNTs are distributed deep into the bulk of the GDL, up to 100 μm into the microporous layer.[61] Additionally, the GDL samples are presoaked in the catalyst suspension, increasing the loading of material within the GDL (Figure A.6b).[61] The researchers found that defect sites, created by doping CNTs with N, are a requirement for anchoring metal oxide nanoparticles onto the nanostructured support (Figure A.6c).[61] This hybrid deposition method provides a large catalyst surface area, improving overall catalytic performance, and maintains the three-phase boundary during extended battery cycling, leading to highly stable cycling performance.[111] For example, an ORR-active Mn_3O_4 catalyst on N-CNTs was cycled in a trielectrode configuration in 6 M KOH, where OER and ORR occur on independent electrodes, and showed only a 30 mV decrease in discharge potentials over 200 cycles at 20 mA cm^{-2}. This hybrid catalyst loading technique was further explored by Aasen *et*

al. in their investigation of a bifunctional $(Co,Fe)_3O_4$ catalyst decorated onto N-CNTs (Figures A.6d-g). Bifunctional cycling showed negligible discharge loss and less than 0.1 V of charge degradation after 500 cycles, maintaining ~58% efficiency at 10 mA cm^{-2} in 6 M KOH (Figure A.6h).[111] In addition to its high durability, the simplicity and low cost of this hybrid preparation method facilitates quick assessment of a wide variety of catalyst chemistries. Two additional reports by Aasen *et al.* and one by McDougall *et al.* explored metal oxide nanoparticle chemistries of $NiMnO_x$, $NiFeO_x$, $NiCoFeO_x$, $NiMnFeO_x$, $NiMnCoO_x$, $MnCoFeO_x$, $ZnCoO_x$, $ZnMnO_x$, $ZnMnCoO_x$, $ZnCoFeO_x$, and $ZnNiMnCoO_x$.[25,60,112] In all reports, the bifunctional cycling stability of the hybrid synthesized catalyst was superior to a spray-coated Pt-Ru-C comparison.

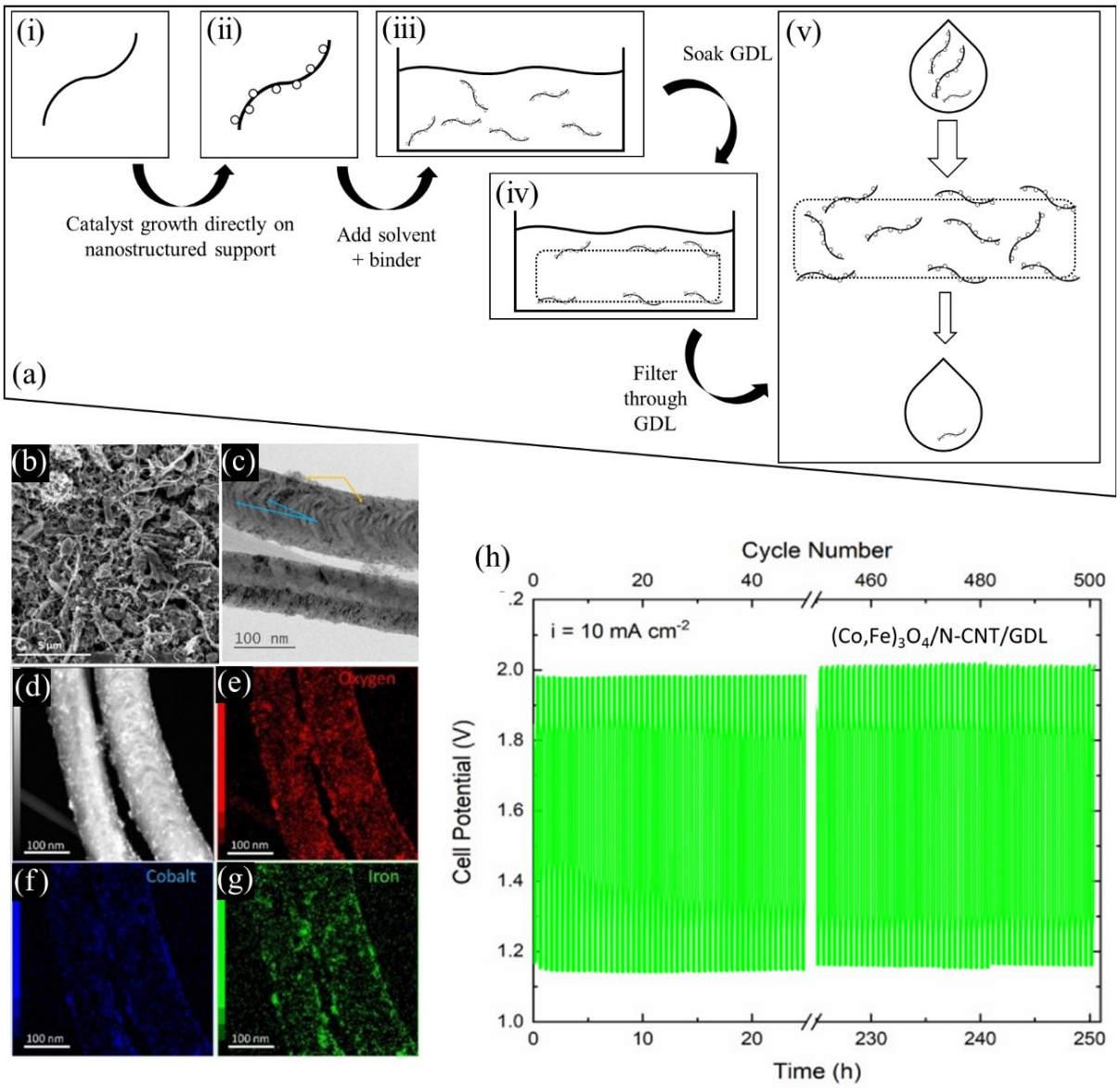

Figure A.6. (a) Process flow of soaking and filtering hybrid loading technique devised by Aasen *et al.*.[61] (i) Nanostructured support, (ii) direct growth of catalyst particles anchored onto nanostructured support, (iii) suspension of nanoparticle loaded nanostructures, (iv) soaking GDL in the suspension, and (v) filtration of the suspension through GDL. (b) Scanning electron microscopy (SEM) image of the GDL surface after soaking and filtering, (c) TEM image of $(Co,Fe)_3O_4$/N-CNTs, with yellow arrows indicating nanoparticles and blue arrows indicating nitrogen defects in the CNT wall. (d) STEM image and (e-g) O, Co, and Fe EDX mapping, respectively, of $(Co,Fe)_3O_4$/N-CNTs. (h) ZAB cycling of the hybrid loaded $(Co,Fe)_3O_4$/N-CNT catalyst. Adapted with permission from Ref.[111]. Copyright 2020 John Wiley & Sons, Inc.

The above soaking and filtering impregnation technique was also extended to nanoparticle-decorated hollow carbon structures in several reports by He *et al.* Instead of using commercially obtained N-CNTs as nanostructured supports, He *et al.* synthesized hollow mesoporous carbon spheres (HMCs) and hollow carbon cubes (HCCs, Figures A.7a and A.7b).[113–115] Reactive chemicals (such as HF) were used in combination with high temperatures (as high as 915 °C). These reaction conditions are generally not compatible with direct catalyst deposition methods on GDL. Yet, the hybrid impregnation technique ensured good distribution of the catalyst loaded nanostructures throughout the GDL and resulted in stable cycling performance. For a Mn_3O_4 catalyst on HMCs, trielectrode ZAB cycling at 20 mA cm^{-2} in 6 M KOH revealed a 3.3% loss in discharge potential (1.21 V to 1.17 V) after 235 cycles (Figure A.7c). A spray-coated Pt-Ru-C comparison, however, experienced 4.2% loss (1.19 V to 1.14 V) during the same cycling conditions (Figure A.7d).[113] For a Co_3O_4-decorated HMC catalyst, bifunctional ZAB cycling at 10 mA cm^{-2} revealed an initial efficiency of 63% with a final efficiency of 57% after 200 cycles (Figure A.7e). A spray-coated Pt-Ru-C comparison displayed initial and final efficiencies of 62% and 50%, respectively, after only 100 cycles at 10 mA cm^{-2} (Figure A.7f).[114] Lastly, a CoNi nanoparticle decorated HCC catalyst, impregnated into the GDL via the soaking and filtering hybrid loading technique, displayed an initial bifunctional efficiency of 59% during 10 mA cm^{-2} ZAB cycling in 6 M KOH. This was reduced to 55% after 90 h of cycling, yielding an overall 3.4% drop in efficiency (Figure A.7g). A spray-coated Pt-Ru-C electrode, on the other hand, had a 14.5% drop in efficiency (from 56% to 42%) after only 60 h of cycling (Figure A.7h).[115] These studies all reveal the ability of hybrid loading to provide the best of both worlds between indirect and direct catalyst loading techniques. Synthesis conditions not directly compatible with GDL material can be employed *ex situ* to develop state-of-the-art catalysts, while the hybrid loading method is effective in delivering the catalyst material deep into the GDL to provide stable long term cycling performance.

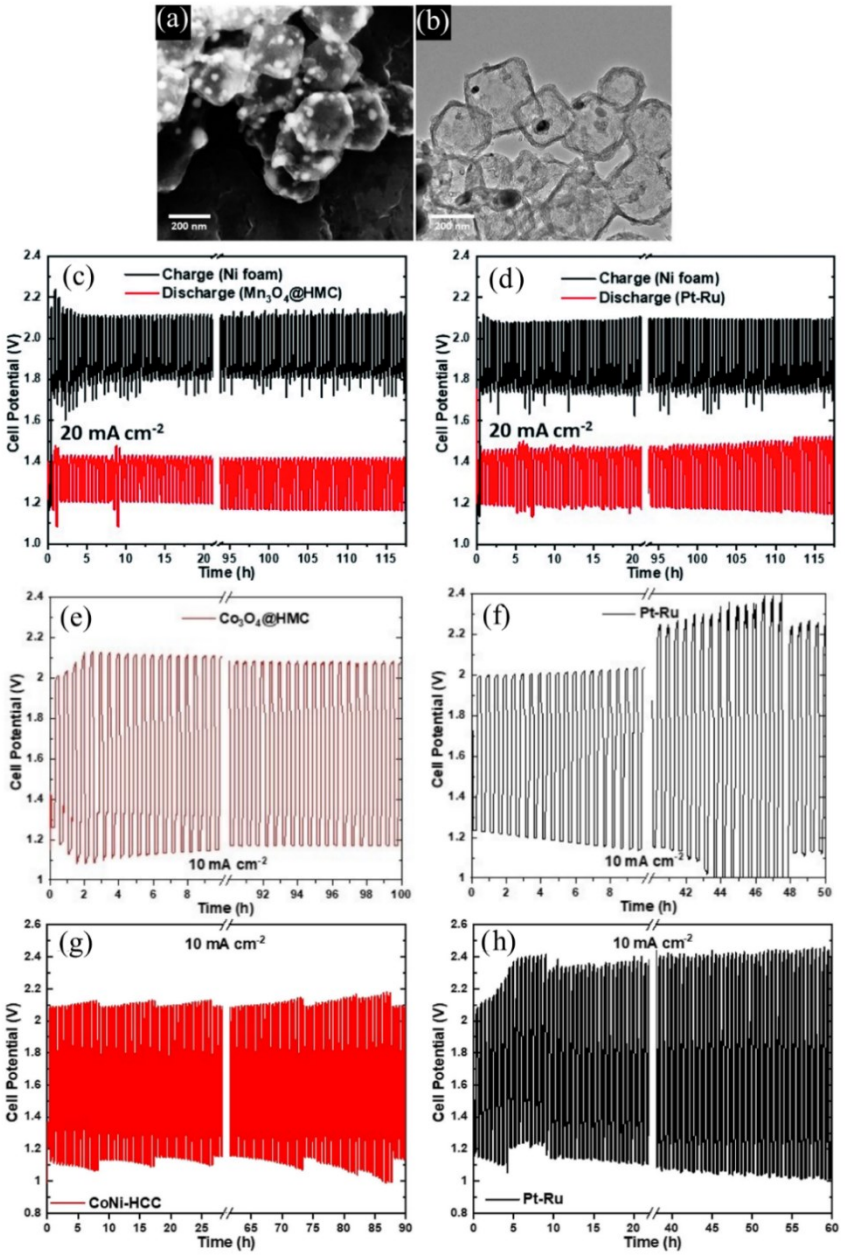

Figure A.7. Air electrodes made with impregnated nanoparticle-decorated hollow carbon nanostructure catalysts. (a) SEM and (b) TEM images of HCCs. (c) Trielectrode ZAB cycling at 20 mA cm^{-2} for Mn_3O_4-decorated HMCs and (d) spray-coated Pt-Ru-C. The lower set of curves are the discharge potentials during trielectrode cycling. (e) Bifunctional ZAB cycling at 10 mA cm^{-2} for Co_3O_4-decorated HMCs and (f) spray-coated Pt-Ru-C. (g) Bifunctional ZAB cycling at 10 mA cm^{-2} for CoNi decorated HCCs and (h) spray-coated Pt-Ru-C. Adapted with permission from Refs.[113–115]. Copyright 2020 Royal Society of Chemistry, Copyright 2021 John Wiley & Sons, Inc., Copyright 2022 American Chemical Society.

Another hybrid method was recently explored by Abedi *et al.* wherein metal oxide nanoparticles were grown on activated carbon fibers (CFs) via a sonication method (Figures A.8a-d),[116] which was similar to the processes reported by Aasen *et al.*[61] or Li *et al.*[117] No sonication in the synthesis procedure produced a discontinuous coating of catalyst material on the CF substrates, while too much sonication resulted in partial delamination of the coating. The optimized sonication time and Mn:Co salt ratio created a uniform, thick coating of $MnCo_2O_4$ material on the CF supports. It was proposed that the Mn species exist exclusively in the 2+ oxidization state, while Co species were only in the 3+ state. This combination resulted in high bifunctional activity, outperforming the Pt-Ru-C catalyst.[116] For this particular hybrid catalyst loading technique, Abedi et. al. transformed the catalyst loaded CFs into a paste with a small amount of carbon black filler and PTFE binder. It should be emphasized the nanoparticle coated carbon fibers are already conductive, so that the carbon black filler is largely for mechanical purposes as opposed to a conductive aid. The paste was then rolled onto a hydrophobic carbon paper backing layer to produce a ZAB air electrode with catalyst material distributed throughout the thickness of the GDL.[116] The homemade GDL showed good bifunctional activity and excellent cycling performance, far superior to a spray-coated Pt-Ru-C benchmark.[116] After a minor efficiency loss during the first few cycles, the hybrid paste $MnCo_2O_4$/CF exhibited almost identical charge and discharge potentials throughout 200 cycles at 10 mA cm^{-2} in 6 M KOH (Figure A.8e), while a Pt-Ru-C benchmark, prepared via spray-coating, experienced severe performance loss and an efficiency reduction from 57% to only 41% after 200 cycles at 10 mA cm^{-2} (Figure A.8f).[116] This GDL was even compatible with a gel electrolyte (polyacrylic acid with KOH) to yield a solid state ZAB, which displayed stable cycling behaviour for 130 cycles at 10 mA cm^{-2}, after which some degradation in performance is observed (Figure A.8g). A similar solid state ZAB with a spray-coated Pt-Ru-C catalyst on the air electrode, however, was not stable during cycling at 10 mA cm^{-2}, where degradation began after only 20 cycles and eventual failure occurred at 110 cycles (Figure A.8h).[118] The use of a gel electrolyte was also found to increase the power density of the ZAB, with the gel $MnCo_2O_4$ cell exhibiting a peak power density of 240 mW cm^{-2} compared with only 127 mW cm^{-2} for the aqueous version, and only 165 mW cm^{-2} for the solid state Pt-Ru-C cell. As an additional benefit, the gel electrolyte was tolerant to low temperatures, enabling stable cycling performance at temperatures as low as -25 °C (Figure A.8i). In this case, after 200 cycles of 2 mA cm^{-2} bifunctional cycling, the starting and final efficiencies were 53%

and 49%, respectively. At -45 °C (Figure A.8j), the ZAB was less stable and less efficient, but was able to withstand 200 cycles at 2 mA cm^{-2} without reaching the charge and discharge cutoff voltages of 3.0 V and 0.5 V, respectively.[119] Similar hybrid paste methods have been employed by other researchers, who developed their catalyst loaded nanostructures via microwave,[43] hydrothermal,[120] solvothermal,[27,121] and sol-gel[122] methods. The hybrid paste methods differ from traditional indirect paste methods because catalyst particles are directly anchored onto nanostructured (often conductive) supports, which are then transformed into the microporous layer of the GDL. Indirect paste methods, which disperse the catalyst (often non-conductive) in a mixture of a conductive filler and an insulating binder,[33,34,53] do not possess the synergy between the catalyst and nanostructured support and may only coat the outermost surface layers of the microporous layer.[53]

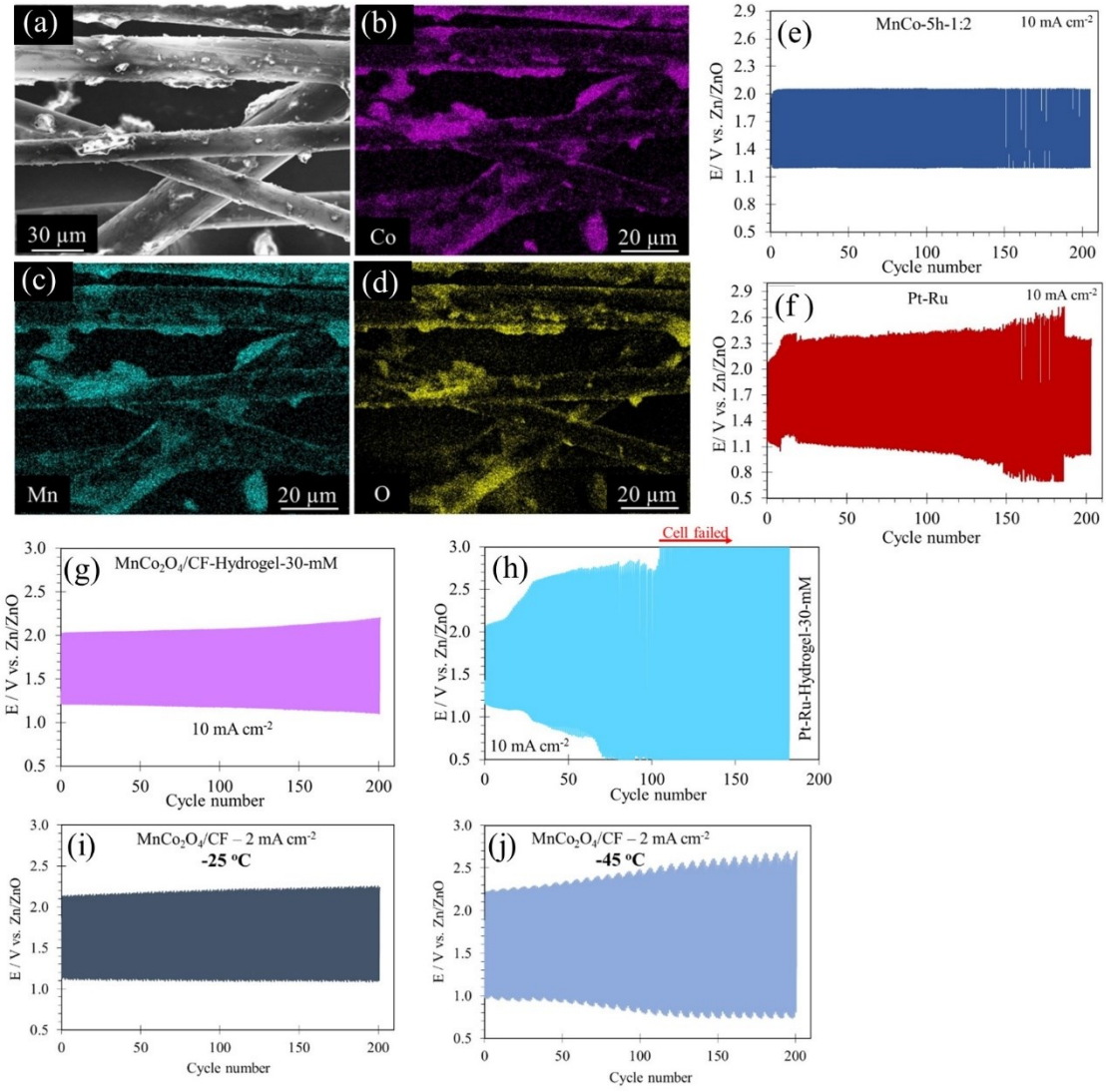

Figure A.8. $MnCo_2O_4$/CF hybrid synthesized air electrode. (a) SEM image of catalyst coated fibers, (b-d) EDX mapping of Co, Mn and O, respectively, (e) liquid electrolyte ZAB performance of the $MnCo_2O_4$/CF electrode, (f) liquid electrolyte ZAB performance of a spray-coated Pt-Ru-C electrode, (g) gel electrolyte ZAB performance of the $MnCo_2O_4$/CF electrode at room temperature, (h) gel electrolyte ZAB performance of a spray-coated Pt-Ru-C electrode, (i-j) gel electrolyte ZAB performance at -25 °C and -45 °C. Adapted with permission from Refs.[116,118,119]. Copyright 2022 John Wiley & Sons, Inc., Copyright 2023 American Chemical Society, Copyright 2022 John Wiley & Sons, Inc.

A.5. Battery Performance Comparison

A comparison of reported cycling performances for various air electrode catalysts explored in the literature is provided in Table A.1. Catalyst loading onto the air electrode is categorized as either indirect, direct, or hybrid, based on the methodology reported in the article. The testing conditions for ZAB cycling are not standardized and, as such, various different current densities and cycle lengths are employed.[6] For example, Lee *et al.* cycled their ZAB for 100 cycles at 6 h per cycle, yielding an overall cycling time of 600 h.[58] Clark *et al.* also cycled their ZAB for 100 cycles, but at 0.5 h per cycle, totalling only 200 h.[30] Another variable among the studies, in addition to the deposition method and cycle parameters, is the chemistry of the catalyst employed. Some catalysts are more electrocatalytically active than others and provide higher bifunctional efficiency. Therefore, Table A.1 features a calculation of the efficiency loss per 100 cycles. This normalizes the data for each catalyst such that the stability of the air electrode is emphasized. For indirect deposition methods, the efficiency loss per 100 cycles is on the order of 5 to 10%, representing poor stability where the efficiency of the battery decreases to ~50% of the initial value after only 500 cycles. Direct deposition methods, on the other hand, have efficiency loss per 100 cycles values on the order of 0.5% to 5%. This represents much higher ZAB stability, where the efficiency value drops to ~90% of the original value after 1000 or more cycles. For hybrid deposition methods, the efficiency loss per 100 cycles is on the order of 1% to 5%, which is on par with direct deposition methods. Thus, in terms of cycling stability, hybrid catalyst loading techniques are competitive with direct loading methods, both of which are far superior to indirect loading methods. This can also be seen in Figure A.9, which plots the efficiency retention against the total number of cycles tested. In this case, a higher value is desirable and represents an air electrode which can maintain its original bifunctional efficiency. The indirect air electrodes (shown as empty circles) populate the lower-left corner, which corresponds to low efficiency retention at low cycle numbers. The direct air electrodes (shown as black squares) are primarily found in the top portion of the graph, representing highly stable ZABs. The hybrid catalyst loaded air electrodes (shown as triangles) are also in the upper section of the plot, but are also at the far right edges, demonstrating long battery lifetimes.

Table A.1. Compilation of reported cycling performance for different ZAB air electrode catalysts, categorized based on the deposition method employed. Values in square brackets are indirectly obtained based on reported cycling details but are not explicitly stated. If efficiency values are not directly reported in an article, an estimate is provided based on the published figures, similar to the method shown in Figure A.3. All studies utilize a liquid 6 M KOH electrolyte.

Ref	Catalyst	Deposition Method	Current Density (mA cm^{-2})	Starting Efficiency	Battery Lifetime (h or cycles)	Final Efficiency	Efficiency Loss Per 100 Cycles
51	$CoMn_2O_4$/N-rGO	**Indirect** spray-coating	20	65%	[33 h] 200 cycles	47%	14%
36	Porous N-C	**Indirect** spray-coating	5	65%	120 h [360 cycles]	57%	3.4%
42	Fe/Fe_3C@N-MC	**Indirect** drop-casting	1	63%	[58 h] 350 cycles	55%	3.6%
46	Fe-Co @NSDC	**Indirect** drop-casting	1	89%	120 h [720 cycles]	64%	3.9%
56	$La_{0.8}Sr_{0.2}Co_{0.4}Mn_{0.6}O_3$	**Indirect** paste	10	66%	16 h 100 cycles	60%	9.1%
54	$NiMoO_4 \cdot xH_2O$ NRs	**Indirect** paste	5	64%	[18 h] 60 cycles	46%	47%
70	MnO_x/Co-Fe	**Direct** electrodeposition	5	60%	40 h 20 cycles	56%	33%
71	MnO_2-Co_3O_4	**Direct** electrodeposition	1	60%	400 h 96 cycles	59%	1.7%
59	$NiMn_2O_4$	**Direct** electrodeposition	10	56%	10 h 300 cycles	54%	1.2%
73	La-CO_3O_4	**Direct** electrodeposition	2	57%	100 h 300 cycles	56%	0.58%
58	Co_3O_4	**Direct** electroless deposition	[18]	50%	600 h 100 cycles	48%	4.0%
78	CoFe@CNT/MnO	**Direct** hydrothermal + CVD	10	56%	100h [300 cycles]	53%	1.8%
79	CoFe@NO-CNT	**Direct** electroless + CVD	5	64%	125h [720 cycles]	62%	0.43%

Ref	Catalyst	Deposition Method	Current Density (mA cm^{-2})	Starting Efficiency	Battery Lifetime (h or cycles)	Final Efficiency	Efficiency Loss Per 100 Cycles
[30]	MnO_x+CoO_x	**Direct** ALD	10	60%	50 h 100 cycles	53%	12%
[87]	Co_9S_8/CNT	**Direct** ALD	10	63%	96 h [576 cycles]	62%	0.28%
[86]	$(Mn,Fe)_3O_4$	**Direct** ALD	10	54%	600h 1540 cycles	46%	0.96%
[102]	AgCu-MG	**Direct** PLD	20	55%	[236 h] [1180 cycles]	50%	0.77%
[104]	Co_4N/CNW/CC	**Direct** electrodeposition + immersion + calcination	10	58%	136 h 408 cycles	57%	0.42%
[114]	Co_3O_4@N-HMC	**Hybrid** soaking & impregnation	10	63%	100h 200 cycles	57%	4.8%
[111]	$(Co,Fe)_3O_4$/N-CNT/GDL	**Hybrid** soaking & impregnation	10	59%	250 h 500 cycles	58%	0.34%
[116]	$MnCo_2O_4$/CF	**Hybrid** paste	10	64%	100 h 200 cycles	59%	3.9%
[43]	Co-Fe/C	**Hybrid** paste	50	46%	118 h [59 cycles]	45%	3.7%
[121]	A-SAC(Fe, Ni, Fe)/N-C	**Hybrid** paste	10	64%	358 h 2150 cycles	50%	1.0%
[27]	CNT-Co-Fe/N-C + CNT-CoS_2-Fe/N-C	**Hybrid** paste	10	67%	300 h 1800 cycles	64%	0.25%

rGO: reduced graphene oxide; **MC**: mesoporous carbon; **NSDC**: nitrogen/sulfur co-doped carbon; **NRs**: nanorods; **CNT**: carbon nanotube; **MG**: metallic glass; **CNW**: carbon fiber network; **CC**: carbon cloth; **N-HMC**: nitrogen-doped hollow MC nanosphere; **CF**: carbon fiber; **A-SAC**: ammonia-treated single-atom catalyst.

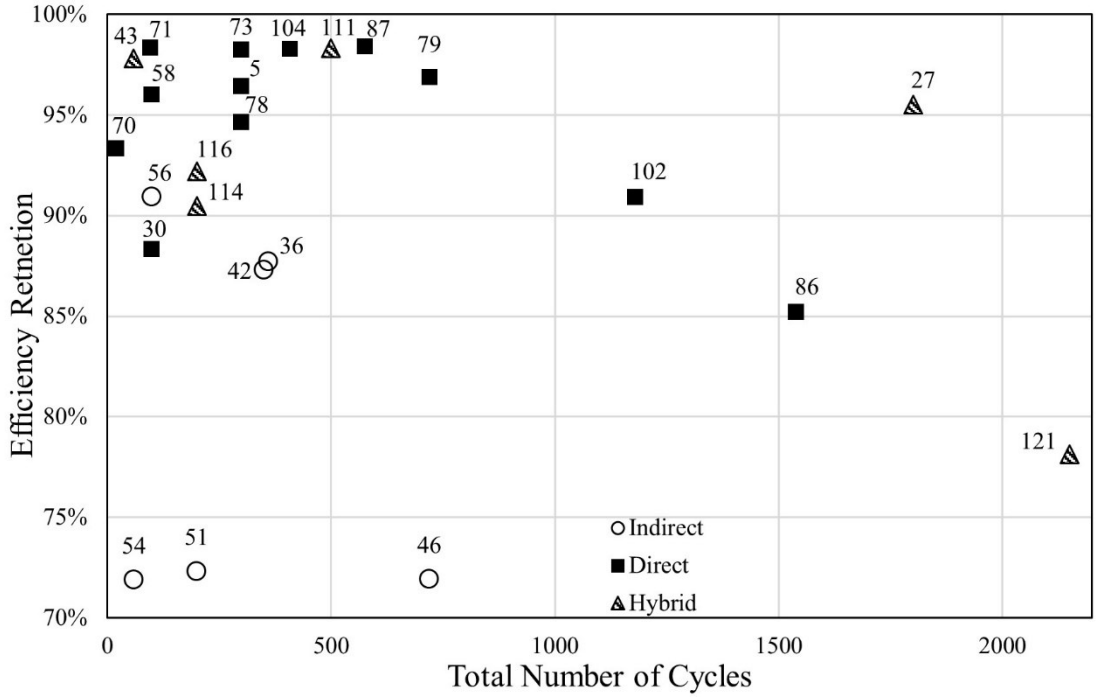

Figure A.9. Plot of bifunctional efficiency retention after cycling against the total number of charge-discharge cycles. Indirect catalyst loading data are shown as empty circles, direct loading as black squares, and hybrid methods as triangles. The numbers beside data points refer to the reference number for that work.

The benefits afforded by directly loading catalyst material onto the air electrode, as opposed to indirect loading methods, are best illustrated by comparative studies. In one such study, Lee *et al.* scraped off their directly grown Co_3O_4 nanowires on Ni foam, prepared an ink with the catalyst particles, isopropyl alcohol, and Nafion, and spray-coated the mixture onto carbon GDL. For both pulse cycling (with 5 min charge-discharge periods) and extended cycling (with 3 h charge-discharge periods), the spray-coated catalyst exhibited severe degradation in cycling performance while, at the same time, the directly-grown catalyst was extremely stable, retaining over 90% of the initial performance after 600 h of extended cycling at 18 mA cm^{-2} in 6 M KOH.[58] In another comparative study, Sumboja *et al.* grew MnO_x directly on GDL via electroless deposition. They also prepared MnO_x powder using the same electroless technique and applied it to GDL *ex situ* by drop-casting a Nafion and ethanol ink.[123] Again, both pulse cycling and extended cycling (15 mA cm^{-2} discharge and 7.5 mA cm^{-2} charge, both in 6 M KOH) showed that the directly loaded MnO_x was far superior in terms of stability than the indirect

MnO_x counterpart. In particular, the directly loaded MnO_x catalyst had no more than a 5% change in charging or discharging potential after 350 pulse cycles, while the drop-casted MnO_x experienced a 15% reduction in discharge potential after only 170 pulse cycles, with the charging potential reaching the 2.5 V cut-off potential within 110 pulse cycles. In the extended cycling, the directly deposited MnO_x electrode showed less than 7% change in the charge and discharge potentials over 15 extended cycles, while the indirect MnO_x electrode reached the charging cut-off value before the end of the first cycle.[123] It should be emphasized that the above two comparative studies carefully controlled the mass loading between the direct and indirect methodologies to ensure fairness. In another comparative study, Meng *et al.* utilized electrodeposition, calcination, and an immersion method to synthesize a bifunctional Co_4N decorated carbon fiber network catalyst directly on carbon cloth. The catalyst coated carbon cloth was shredded, formed into a paste with Nafion in alcohol, and applied to a separate carbon cloth substrate to represent an indirect deposition catalyst. The cycling behaviour of the paste method was remarkably worse than the case where the directly synthesized carbon cloth electrode was used. After 83 h of cycling at 10 mA cm^{-2} in 6 M KOH, the indirect paste electrode provided only 33% bifunctional efficiency, while the direct catalyst electrode retained a stable ~60% efficiency for 136 h at 10 mA cm^{-2}.[104] In essence, these studies reveal the benefit of directly deposited catalysts compared with chemically equivalent indirectly loaded catalysts.

A key feature of direct deposition methods that translates into stable cycling performance is the integration of catalyst material deeper within the air electrode structure compared with only surface bound catalyst particles deposited by indirect methods. When flooding occurs during prolonged cycling, the architecture of catalyst loading enables the continued catalysis of the three-phase boundary area and an overall stable cycling performance.[30] This concept guided the work of Yu *et al.* in their investigation of asymmetric air electrodes for ZABs.[63] They employed a NiFe layered double hydroxide (LDH) electrocatalyst directly grown on a carbon paper substrate via a liquid phase chemical process. The asymmetric electrode was developed by growing NiFe LDH inward from the hydrophilic face of the carbon paper, achieving a 3-dimensional (3D) interface of catalyst material (the third dimension being the thickness of the electrode; Figure A.10b). For comparison, a conventional air electrode (with a 2-dimensional (2D) interface) was prepared via drop-casting of NiFe LDH particles (Figure A.10a). Polarization tests in a ZAB with a 6 M KOH electrolyte revealed that the asymmetric electrode

had more active sites and better mass transfer than the conventional electrode, with max power densities of 93.9 and 42.1 mW cm^{-2} for the asymmetric and conventional electrodes, respectively.[63] ZAB cycling results reinforced the importance of catalyst architecture in the air electrode in achieving long-term stability. For the conventional drop-casted air electrode, the charge and discharge potentials were only stable for 650, 200, 80, and 25 cycles when cycled at 5, 10, 25, and 50 mA cm^{-2}, respectively. The asymmetric electrode, on the other hand, exhibited stable charge and discharge potentials for more than 2000, 600, 300, and 100 cycles, respectively, at the same current densities. The indirect catalyst loading method of the conventional electrode resulted in performance loss due to exfoliation and destruction of the electrocatalyst, while the direct catalyst loading process of the asymmetric electrode enabled high current and long cycle life in ZABs.[63]

Hybrid catalyst loading techniques also develop these 3D catalyst architectures and provide similar benefits to the direct catalyst loading methods. For example, Aasen *et al.* compared the ZAB rate performance of indirect spray-coating versus their hybrid soaking and filtering process for Mn_3O_4 coated N-CNTs. At all current densities investigated (2 to 10 mA cm^{-2}), the soaked and filtered air electrode showed a 0.1 V lower ORR overpotential than the spray-coated comparison.[61] It was revealed that their soaked and filtered electrode had abundant catalyst material up to 35 μm away from the surface of the GDL substrate, illustrating a 3D catalyst architecture using a hybrid deposition technique. Thus, hybrid catalyst loading is competitive with direct loading and both produce a tailored electrode architecture that is resistant to flooding and improves catalyst access in the air electrode.[61,63,111]

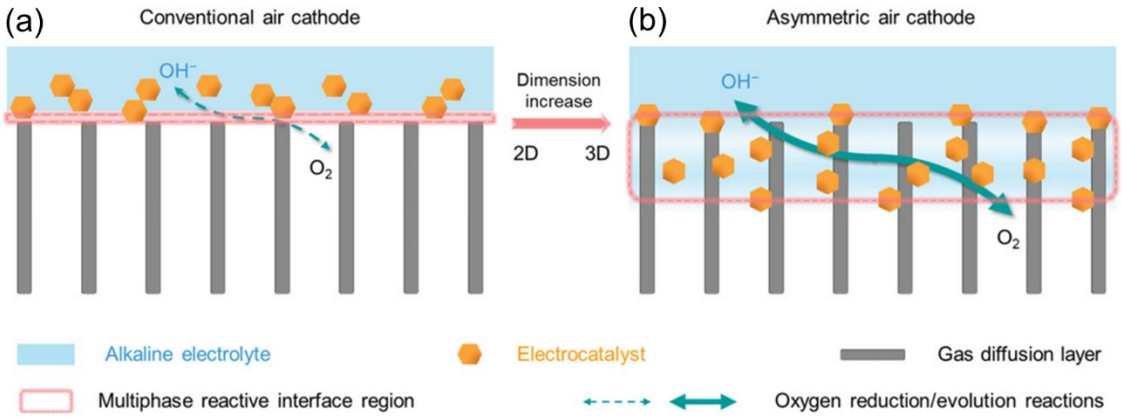

Figure A.10. Schematic illustrations of (a) conventional and (b) asymmetric air cathodes, which possess 2D and 3D multiphase reactive interfaces, respectively. The asymmetric air cathode exhibits an increased amount of active sties, accelerated mass transfer, and a dynamically stabilized reactive interface. Adapted with permission from Ref.[63]. Copyright 2020 John Wiley & Sons, Inc.

Using direct or hybrid methods for catalyst loading at the air electrode of a ZAB is far superior to indirect loading methods. Not only is catalyst material distributed more uniformly and deeper within the electrode substrate, enhancing long-term cycling behaviour, but the improved interface between the catalyst and current collector affords reduced Ohmic losses during battery operation.[32] However, the choice between direct or hybrid loading should be evaluated based on the available synthesis method (or methods) for a particular catalyst and the compatibility of the substrate material with that synthesis method. For example, Co-Fe oxide particles were anchored onto N-CNTs and integrated into a carbon-based GDL using the hybrid soaking and impregnation technique. This technique employed mild solvents and low temperatures which did not damage the carbon material or PTFE treatment of the air electrode. As a result, a ZAB using the Co-Fe oxide air electrode in 6 M KOH was able to successfully cycle for over 250 h at 10 mA cm^{-2}.[111] It is also feasible that an ALD process could deposit a Co-Fe oxide catalyst directly onto a GDL substrate, possibly preloaded with N-CNTs to increase the area for deposition.[87] However, the ALD process would require the use of an O plasma reactant for both FeO_x and CoO_x subcycles.[30,85] The use of an O plasma reactant, without any buffer layer integrated into the ALD process, has been demonstrated to be very damaging to a carbon substrate.[67] Thus, the direct loading of a Co-Fe oxide catalyst onto carbon GDL using an O plasma ALD process

would result in a poor performing air electrode. In this case, the hybrid soaking and impregnation technique is a better choice than a direct ALD process. Electrodeposition can also be used to directly deposit a Co-Fe catalyst (with a surface layer of Co-Fe oxide), which was shown to be compatible with a carbon GDL. A ZAB assembled with 6 M KOH and the electrodeposited Co-Fe GDL showed stable bifunctional cycling for over 20 h at 5 mA cm^{-2}.[37] In this case, the decision between a hybrid soaking and impregnation technique and a direct electrodeposition process comes down to the amount of deposited material, the penetration depth of catalyst loading, and whether a binder-free process is preferred. Rather than change the synthesis process, the substrate material can also be varied. For example, an ALD process for a Co-Fe oxide catalyst could easily be applied to a metal foam substrate.[124,125] In this case, the O plasma reactant is not detrimental to the substrate and the direct loading technique, with all its benefits, could be applied to the air electrode. Thus, the future of catalyst integration into the air electrode of ZABs will depend both on the synthesis method for state-of-the-art catalysts and the best practices for air electrode materials.

A.6. Conclusions

The loading of catalyst material on the air electrode of a ZAB is as critical as the choice of catalyst chemistry. Indirect catalyst loading methods, such as an ink and spray-coating techniques, are associated with poor stability due to binder decomposition, carbon corrosion, and a 2D catalyst interface with the electrolyte. Direct catalyst loading methods, such as electrodeposition or ALD, provide improved stability over indirect methods due to binder-free integration, enhanced conductivity pathways, and a 3D interface with the electrolyte that is less susceptible to flooding. Additionally, hybrid catalyst integration methods, such as a reported soaking and impregnation technique, can deliver performance on par with direct methods due to the synergy with nanostructured substrates and deep penetration of catalyst material within the air electrode structure. ZABs with either direct or hybrid catalyst loading exhibit superior cycling stability to indirect loading counterparts and are the key to long lifetime, stable ZABs.

References

1. M. A. Rahman, J. H. Kim, and S. Hossain, “Recent advances of energy storage technologies for grid: A comprehensive review,” *Energy Storage*, vol. 4, no. 6, pp. 1–28, 2022.

2. V. Etacheri, R. Marom, R. Elazari, G. Salitra, and D. Aurbach, “Challenges in the development of advanced Li-ion batteries: A review,” *Energy Environ. Sci.*, vol. 4, no. 9, pp. 3243–3262, 2011.

3. H. Chen, T. N. Cong, W. Yang, C. Tan, Y. Li, and Y. Ding, “Progress in electrical energy storage system : A critical review,” *Prog. Nat. Sci.*, vol. 19, no. 3, pp. 291–312, 2009.

4. C. Liu, F. Li, L.-P. Ma, and H.-M. Cheng, “Advanced Materials for Energy Storage,” *Adv. Energy Mater.*, vol. 22, no. 8, pp. E28–E62, 2010.

5. Y. Liang, C. Z. Zhao, H. Yuan, Y. Chen, W. Zhang, J. Q. Huang, D. Yu, Y. Liu, M. M. Titirici, Y. L. Chueh, H. Yu, and Q. Zhang, “A review of rechargeable batteries for portable electronic devices,” *InfoMat*, vol. 1, no. 1, pp. 6–32, 2019.

6. J. Fu, Z. P. Cano, M. G. Park, A. Yu, M. Fowler, and Z. Chen, “Electrically Rechargeable Zinc-Air Batteries: Progress, Challenges, and Perspectives,” *Adv. Mater.*, vol. 29, no. 7, p. 1604685, 2017.

7. Y. Li and H. Dai, “Recent advances in zinc-air batteries,” *Chem. Soc. Rev.*, vol. 43, no. 15, pp. 5257–5275, 2014.

8. T. Placke, R. Kloepsch, S. Dühnen, and M. Winter, “Lithium ion, lithium metal, and alternative rechargeable battery technologies: the odyssey for high energy density,” *J. Solid State Electrochem.*, vol. 21, no. 7, pp. 1939–1964, 2017.

9. M. Kane, “Tesla’s 4680-Type Battery Cell Teardown : Specs Revealed,” *InsideEVs*, 2022. [Online]. Available: https://insideevs.com/news/598656/tesla-4680-battery-cell-specs/. [Accessed: 27-Sep-2023].

10. A. C. Tolcin, “Zinc Mineral Commodity Summary - 2023,” *National Minerals Information Center, USGS*. 2023.

11. B. W. Jaskula, “Lithium Mineral Commodity Summary - 2023,” *National Minerals Information Center, USGS*. 2023.

12. F. Cheng and J. Chen, “Metal-air batteries: From oxygen reduction electrochemistry to cathode catalysts,” *Chem. Soc. Rev.*, vol. 41, no. 6, pp. 2172–2192, 2012.

13. K. W. Beard and T. B. . Reddy, Eds., *Linden’s Handbook of Batteries*, 5th Ed. New York, NY: McGraw-Hill, 2019.

14. E. Davari and D. G. Ivey, “Bifunctional electrocatalysts for Zn–air batteries,” *Sustain. Energy Fuels*, vol. 2, no. 1, pp. 39–67, 2018.

15. J.-S. Lee, S. T. Kim, R. Cao, N. S. Choi, M. Liu, K. T. Lee, and J. Cho, “Metal – Air Batteries with High Energy Density : Li – Air versus Zn – Air,” *Adv. Energy Mater.*, vol. 1, no. 1, pp. 34–50, 2011.

16. J. Pan, Y. Y. Xu, H. Yang, Z. Dong, H. Liu, and B. Y. Xia, “Advanced Architectures and Relatives of Air Electrodes in Zn–Air Batteries,” *Adv. Sci.*, vol. 5, no. 4, p. 1700691, 2018.

17. M. Xiong and D. G. Ivey, “Synthesis of Bifunctional Catalysts for Metal-Air Batteries Through Direct Deposition Methods,” *Batter. Supercaps*, vol. 2, no. 4, pp. 326–335, 2019.

18. R. Schweiss, S. Hofmeister, C. Meiser, D. Dan, A. Baumann, T. Kuster, N. Haak, and S. Bacher, “Powering up fuel cells: Our gas diffusion layer [White Paper].” SGL Carbon, Meitingen, Germany, pp. 1–8, 2021.

19. J. Rouquerol, D. Avnir, C. W. Fairbridge, D. H. Everett, J. M. Haynes, N. Pernicone, J. D. F. Ramsay, K. S. W. Sing, and K. K. Unger, “Recommendations for the characterization of porous solids (Technical Report),” *Pure Appl. Chem.*, vol. 66, no. 8, pp. 1739–1758, 1994.

20. B. Millington, S. Du, and B. G. Pollet, “The effect of materials on proton exchange membrane fuel cell electrode performance,” *J. Power Sources*, vol. 196, no. 21, pp. 9013–9017, 2011.

21. X. Chen, Z. Zhou, H. E. Karahan, Q. Shao, L. Wei, and Y. Chen, “Recent Advances in

Materials and Design of Electrochemically Rechargeable Zinc–Air Batteries," *Small*, vol. 14, no. 44, pp. 1–29, 2018.

22. F. R. McLarnon and E. J. Cairns, "The Secondary Alkaline Zinc Electrode," *J. Electrochem. Soc.*, vol. 138, no. 2, pp. 645–664, 1991.

23. H. Osgood, S. V. Devaguptapu, H. Xu, J. Cho, and G. Wu, "Transition metal (Fe, Co, Ni, and Mn) oxides for oxygen reduction and evolution bifunctional catalysts in alkaline media," *Nano Today*, vol. 11, no. 5, pp. 601–625, 2016.

24. M. Xiong, M. P. Clark, M. Labbe, and D. G. Ivey, "A horizontal zinc-air battery with physically decoupled oxygen evolution/reduction reaction electrodes," *J. Power Sources*, vol. 393, pp. 108–118, 2018.

25. D. Aasen, M. P. Clark, and D. G. Ivey, "Investigation of Transition Metal-Based (Mn, Co, Ni, Fe) Trimetallic Oxide Nanoparticles on N-doped Carbon Nanotubes as Bifunctional Catalysts for Zn-Air Batteries," *J. Electrochem. Soc.*, vol. 167, no. 4, p. 040503, 2020.

26. Y. Zang, H. Zhang, X. Zhang, R. Liu, S. Liu, G. Wang, Y. Zhang, and H. Zhao, "Fe/Fe2O3 nanoparticles anchored on Fe-N-doped carbon nanosheets as bifunctional oxygen electrocatalysts for rechargeable zinc-air batteries," *Nano Res.*, vol. 9, no. 7, pp. 2123–2137, 2016.

27. K. Y. Hung, S. Hosseini, T. E. Ko, C. M. Tseng, and Y. Y. Li, "Highly efficient rechargeable Zn-air batteries based on hybrid CNT-grafted, Co/CoS2-Fe embedded, Nitrogen-doped porous carbon Nano-frameworks," *Fuel*, vol. 316, p. 123328, 2022.

28. V. Neburchilov, H. Wang, J. J. Martin, and W. Qu, "A review on air cathodes for zinc-air fuel cells," *J. Power Sources*, vol. 195, no. 5, pp. 1271–1291, 2010.

29. V. R. J. Shepard, Y. G. Smalley, and D. R. Bentz, "Bifunctional metal-air electrode," U.S. Patent 5,306,579, 1994.

30. M. P. Clark, M. Xiong, K. Cadien, and D. G. Ivey, "High Performance Oxygen Reduction/Evolution Electrodes for Zinc-Air Batteries Prepared by Atomic Layer Deposition of MnOx," *ACS Appl. Energy Mater.*, vol. 3, no. 1, pp. 603–613, 2020.

31. T. Y. Ma, S. Dai, and S. Z. Qiao, “Self-supported electrocatalysts for advanced energy conversion processes,” *Mater. Today*, vol. 19, no. 5, pp. 265–273, 2016.

32. X. Yan, Y. Ha, and R. Wu, “Binder-Free Air Electrodes for Rechargeable Zinc-Air Batteries: Recent Progress and Future Perspectives,” *Small Methods*, vol. 5, no. 4, pp. 1–24, 2021.

33. J. Meng, F. Liu, Z. Yan, F. Cheng, F. Li, and J. Chen, “Spent alkaline battery-derived manganese oxides as efficient oxygen electrocatalysts for Zn-air batteries,” *Inorg. Chem. Front.*, vol. 5, no. 9, pp. 2167–2173, 2018.

34. C. S. Rao and G. Gunasekaran, “Cobalt-Lead-Manganese oxides combined cathode catalyst for air electrode in Zinc -air battery,” *Electrochim. Acta*, vol. 176, pp. 649–656, 2015.

35. D. Wang, H. Xu, P. Yang, X. Lu, J. Ma, R. Li, L. Xiao, J. Zhang, and M. An, “Fe-N4and Co-N4dual sites for boosting oxygen electroreduction in Zn-air batteries,” *J. Mater. Chem. A*, vol. 9, no. 23, pp. 13678–13687, 2021.

36. F. Gui, Q. Jin, D. Xiao, X. Xu, Q. Tan, D. Yang, B. Li, P. Ming, C. Zhang, Z. Chen, S. Siahrostami, and Q. Xiao, “High-Performance Zinc-Air Batteries Based on Bifunctional Hierarchically Porous Nitrogen-Doped Carbon,” *Small*, vol. 18, no. 8, p. 2105928, 2022.

37. M. Xiong and D. G. Ivey, “Electrodeposited Co-Fe as an oxygen evolution catalyst for rechargeable zinc-air batteries,” *Electrochem. commun.*, vol. 75, pp. 73–77, 2017.

38. N. Zamel, “The catalyst layer and its dimensionality - A look into its ingredients and how to characterize their effects,” *J. Power Sources*, vol. 309, pp. 141–159, 2016.

39. L. W. Niedrach, “Electrode Structure and Fuel Cell Incorporating the Same,” U.S. Patent 3,297,484, 1967.

40. M. R. Khan and S. D. Lin, “Using Pt sols to prepare low Pt-loading electrodes for polymer electrolyte fuel cells,” *J. Power Sources*, vol. 162, no. 1, pp. 186–191, 2006.

41. M. S. Wilson and S. Gottesfeld, “Thin-film catalyst layers for polymer electrolyte fuel cell electrodes,” *J. Appl. Electrochem.*, vol. 22, no. 1, pp. 1–7, 1992.

42. F. Zhang, Y. Chen, Y. Liu, X. Liu, and S. Gao, “Template-assisted polymerization-pyrolysis derived mesoporous carbon anchored with Fe/Fe3C and Fe−NX species as efficient oxygen reduction catalysts for Zn-air battery,” *Int. J. Hydrogen Energy*, vol. 46, no. 76, pp. 37895–37906, 2021.

43. S. Luo and D. B. Zhou, “Preparation and Electrochemical Performance of Co-Fe/C for Bi-Functional Air Electrode,” *J. Electrochem. Soc.*, vol. 161, no. 1, pp. A23–A27, 2014.

44. Y. Guo, F. Pan, W. Chen, Z. Ding, D. Yang, B. Li, P. Ming, and C. Zhang, *The Controllable Design of Catalyst Inks to Enhance PEMFC Performance: A Review*, vol. 4, no. 1. Springer Singapore, 2021.

45. X. Lyu, G. Li, X. Chen, B. Shi, J. Liu, L. Zhuang, and Y. Jia, “Atomic Cobalt on Defective Bimodal Mesoporous Carbon toward Efficient Oxygen Reduction for Zinc–Air Batteries,” *Small Methods*, vol. 3, no. 9, pp. 1–7, 2019.

46. Z. Li, L. Zhang, Q. Zhu, Z. Ke, and G. Hu, “Spatial separation strategy to construct N/S co-doped carbon nanobox embedded with asymmetrically coupled Fe-Co pair-site for boosted reversible oxygen electrocatalysis,” *J. Colloid Interface Sci.*, vol. 653, no. PB, pp. 1577–1587, 2024.

47. S. Litster and G. McLean, “PEM fuel cell electrodes,” *J. Power Sources*, vol. 130, no. 1–2, pp. 61–76, 2004.

48. Y. Guo, C. Wang, Y. Xiao, X. Tan, W. He, J. Chen, Y. Li, H. Cui, and C. Wang, “Stabilizing Fe single atom catalysts by implanting Cr atomic clusters to boost oxygen reduction reaction,” *Appl. Catal. B Environ.*, vol. 344, no. December 2023, p. 123679, 2024.

49. X. Lin, X. Zhang, D. Liu, L. Shi, L. Zhao, Y. Long, and L. Dai, “Asymmetric Atomic Tin Catalysts with Tailored p-Orbital Electron Structure for Ultra-Efficient Oxygen Reduction,” *Adv. Energy Mater.*, vol. 2303740, pp. 1–11, 2024.

50. Y. Li, M. Gong, Y. Liang, J. Feng, J.-E. E. Kim, H. Wang, G. Hong, B. Zhang, and H. Dai, “Advanced zinc-air batteries based on high-performance hybrid electrocatalysts,” *Nat. Commun.*, vol. 4, no. May, p. 1805, 2013.

51. M. Prabu, P. Ramakrishnan, H. Nara, T. Momma, T. Osaka, and S. Shanmugam, “Zinc-air battery: Understanding the structure and morphology changes of graphene-supported CoMn2O4 Bifunctional catalysts under practical rechargeable conditions,” *ACS Appl. Mater. Interfaces*, vol. 6, no. 19, pp. 16545–16555, 2014.

52. B. Ricciardi, W. da Silva Freitas, B. Mecheri, K. U. Nisa, J. Montero, V. C. A. Ficca, E. Placidi, C. Alegre, and A. D’Epifanio, “Hierarchical porous Fe/Ni-based bifunctional oxygen electrocatalysts for rechargeable zinc-air batteries,” *Carbon*, vol. 219, no. December 2023, p. 118781, 2024.

53. Y. T. Lu, Y. J. Chien, C. F. Liu, T. H. You, and C. C. Hu, “Active site-engineered bifunctional electrocatalysts of ternary spinel oxides, M0.1Ni0.9Co2O4 (M: Mn, Fe, Cu, Zn) for the air electrode of rechargeable zinc-air batteries,” *J. Mater. Chem. A*, vol. 5, no. 39, pp. 21016–21026, 2017.

54. R. R. Ayyaluri, B. N. V. Krishna, O. R. Ankinapalli, and J. S. Yu, “Facile hydrothermal synthesis of NiMoO4·xH2O nanorods-like structures as bifunctional oxygen electrocatalysts for rechargeable zinc-air batteries,” *J. Energy Storage*, vol. 78, no. November 2023, p. 110171, 2024.

55. C. Hu, Q. Liang, Y. Yang, Q. Peng, Z. Luo, J. Dong, T. T. Isimjan, and X. Yang, “Conductivity-enhanced porous N/P co-doped metal-free carbon significantly enhances oxygen reduction kinetics for aqueous/flexible zinc-air batteries,” *J. Colloid Interface Sci.*, vol. 633, pp. 500–510, 2023.

56. Q. Wang, Y. Xue, S. Sun, S. Li, H. Miao, and Z. Liu, “La0.8Sr0.2Co1-xMnxO3 perovskites as efficient bi-functional cathode catalysts for rechargeable zinc-air batteries,” *Electrochim. Acta*, vol. 254, pp. 14–24, 2017.

57. M. Prabu, P. Ramakrishnan, and S. Shanmugam, “CoMn2O4 nanoparticles anchored on nitrogen-doped graphene nanosheets as bifunctional electrocatalyst for rechargeable zinc-air battery,” *Electrochem. commun.*, vol. 41, no. 2014, pp. 59–63, 2014.

58. D. U. Lee, J. Y. Choi, K. Feng, H. W. Park, and Z. Chen, “Advanced extremely durable 3D bifunctional air electrodes for rechargeable zinc-air batteries,” *Adv. Energy Mater.*,

vol. 4, no. 6, pp. 1–5, 2014.

59. J. Béjar, A. D. Delgado, F. Espinosa-Magaña, A. Aguilar-Elguezabal, M. Guerra-Balcázar, N. Arjona, and L. Álvarez-Contreras, "Electrodeposition of small–sized NiM2O4 spinels (M: Co, Mn) as bifunctional nanomaterials for rechargeable zinc–air batteries," *J. Alloys Compd.*, vol. 929, p. 167266, 2022.

60. A. McDougall, Z. Abedi, and D. G. Ivey, "Tri- and tetra-metallic oxides anchored to nitrogen-doped carbon nanotubes as bifunctional electrocatalysts for rechargeable zinc-air batteries," *J. Appl. Electrochem.*, vol. 52, no. 3, pp. 437–459, 2022.

61. D. Aasen, M. Clark, and D. G. Ivey, "A Gas Diffusion Layer Impregnated with Mn3O4 - Decorated N-Doped Carbon Nanotubes for the Oxygen Reduction Reaction in Zinc-Air Batteries," *Batter. Supercaps*, vol. 2, no. 10, pp. 882–893, 2019.

62. S. Sun, H. Miao, Y. Xue, Q. Wang, S. Li, and Z. Liu, "Oxygen reduction reaction catalysts of manganese oxide decorated by silver nanoparticles for aluminum-air batteries," *Electrochim. Acta*, vol. 214, pp. 49–55, 2016.

63. J. Yu, B. Q. Li, C. X. Zhao, J. N. Liu, and Q. Zhang, "Asymmetric Air Cathode Design for Enhanced Interfacial Electrocatalytic Reactions in High-Performance Zinc–Air Batteries," *Adv. Mater.*, vol. 32, no. 12, pp. 1–7, 2020.

64. M. Wu, G. Zhang, M. Wu, J. Prakash, and S. Sun, "Rational design of multifunctional air electrodes for rechargeable Zn–Air batteries: Recent progress and future perspectives," *Energy Storage Mater.*, vol. 21, no. April, pp. 253–286, 2019.

65. S. Park, J. W. Lee, and B. N. Popov, "A review of gas diffusion layer in PEM fuel cells: Materials and designs," *Int. J. Hydrogen Energy*, vol. 37, no. 7, pp. 5850–5865, 2012.

66. H. Sun, Z. Yan, F. Liu, W. Xu, F. Cheng, and J. Chen, "Self-Supported Transition-Metal-Based Electrocatalysts for Hydrogen and Oxygen Evolution," *Adv. Mater.*, vol. 32, no. 3, pp. 1–18, 2020.

67. M. Labbe, K. Cadien, and D. G. Ivey, "Growth of Multiple Island Layers during Iron Oxide Atomic Layer Deposition: An Electron Microscopy and Spectroscopic Ellipsometry Investigation," *J. Phys. Chem. C*, vol. 126, no. 46, pp. 19883–19894, 2022.

68. M. Schlesinger, “Electroplating,” in *Kirk-Othmer Encyclopedia of Chemical Technology*, John Wiley & Sons, Inc, 2004, pp. 759–838.

69. B. Durkin, “Electroless Deposition,” in *Kirk-Othmer Encyclopedia of Chemical Technology*, John Wiley & Sons, Inc, 2016, pp. 1–59.

70. M. Xiong and D. G. Ivey, “Sequentially Electrodeposited MnOX/Co-Fe as Bifunctional Electrocatalysts for Rechargeable Zinc-Air Batteries,” *J. Electrochem. Soc.*, vol. 164, no. 6, pp. A1012–A1021, 2017.

71. G. P. Kim, H. H. Sun, and A. Manthiram, “Design of a sectionalized MnO2-Co3O4 electrode via selective electrodeposition of metal ions in hydrogel for enhanced electrocatalytic activity in metal-air batteries,” *Nano Energy*, vol. 30, no. October, pp. 130–137, 2016.

72. N. S. Gultom, M. Z. Silitonga, K. X. Hu, Y. C. Zhou, and D. H. Kuo, “Electrodeposition of bimetal Ni-Co oxide as a bifunctional electrocatalyst for rechargeable zinc air battery,” *J. Alloys Compd.*, vol. 955, p. 170232, 2023.

73. N. S. Gultom, Y. C. Zhou, and D. H. Kuo, “A facile and efficient method for preparing La-doped Co3O4 by electrodeposition as an efficient air cathode in rechargeable zinc-air batteries: Role of oxygen vacancies,” *J. Colloid Interface Sci.*, vol. 655, no. 43, pp. 394–406, 2024.

74. L. Wan, Z. Zhao, X. Chen, P. F. Liu, P. Wang, Z. Xu, Y. Lin, and B. Wang, “Controlled Synthesis of Bifunctional NiCo2O4@FeNi LDH Core-Shell Nanoarray Air Electrodes for Rechargeable Zinc-Air Batteries,” *ACS Sustain. Chem. Eng.*, vol. 8, no. 30, pp. 11079–11087, 2020.

75. J. L. Ma, L. L. Liu, R. H. Zhao, D. Yuan, and X. Ning, “MOF-derived Porous Carbon Nanofiber Assembly as High Efficiency ORR Electrocatalysts for Zinc-air Batteries,” *Chinese J. Polym. Sci.*, vol. 41, pp. 1889–1901, 2023.

76. I. Karajagi, R. K., P. C. Ghosh, A. Sarkar, and N. Rajalakshmi, “Nickel Integrated Carbon Electrodes for Improved Stability,” *J. Electrochem. Soc.*, vol. 167, no. 13, p. 130510, 2020.

77. A. C. Jones and M. L. Hitchman, “Overview of Chemical Vapour Deposition,” in *Chemical Vapour Deposition*, A. C. Jones and M. L. Hitchman, Eds. Cambridge, UK: Royal Society of Chemistry, 2009, pp. 1–36.

78. S. Chen, Y. Huang, M. Li, P. Sun, X. Lv, B. Li, L. Fang, and X. Sun, “MnOx anchored on N and O co-doped carbon nanotubes encapsulated with FeCo alloy as highly efficient bifunctional electrocatalyst for rechargeable Zinc–Air batteries,” *J. Electroanal. Chem.*, vol. 895, no. March, p. 115513, 2021.

79. M. Li, S. Chen, B. Li, Y. Huang, X. Lv, P. Sun, L. Fang, and X. Sun, “In situ growing N and O co-doped helical carbon nanotubes encapsulated with CoFe alloy as tri-functional electrocatalyst applied in Zn–Air Batteries driving Water Splitting,” *Electrochim. Acta*, vol. 388, p. 138587, 2021.

80. Y. Cheng, H. Wu, J. Han, S. Zhong, S. Huang, S. Chu, S. Song, K. M. Reddy, X. Wang, S. Wu, X. Zhuang, I. Johnson, P. Liu, and M. Chen, “Atomic Ni and Cu co-anchored 3D nanoporous graphene as an efficient oxygen reduction electrocatalyst for zinc-air batteries,” *Nanoscale*, vol. 13, no. 24, pp. 10862–10870, 2021.

81. K. Ma, R. Guo, J. Wang, X. Li, M. Ma, and M. Sheng, “Ni2P nanoparticles encapsulated in carbon nanotubes as high-performance electrocatalyst for rechargeable zinc-air battery,” *Mater. Lett.*, vol. 333, no. November 2022, p. 133665, 2023.

82. W. Ding, A. Saad, Y. Wu, Z. Wang, and X. Li, “CNTs/CNF-supported multi-active components as highly efficient bifunctional oxygen electrocatalysts and their applications in zinc-air batteries,” *Nano Res.*, vol. 16, no. 4, pp. 4793–4802, 2023.

83. M. Zhu and C. Zhang, “FeCo nanoalloys encapsulated in pod-like N-doped carbon nanotubes as efficient oxygen reduction reaction electrocatalysts for zinc-air batteries,” *J. Alloys Compd.*, vol. 921, p. 166122, 2022.

84. M. P. Clark, T. Muneshwar, M. Xiong, K. Cadien, and D. G. Ivey, “Saturation Behavior of Atomic Layer Deposition MnOx from Bis(Ethylcyclopentadienyl) Manganese and Water: Saturation Effect on Coverage of Porous Oxygen Reduction Electrodes for Metal-Air Batteries,” *ACS Appl. Nano Mater.*, vol. 2, no. 1, pp. 267–277, 2019.

85. M. Labbe, M. P. Clark, Z. Abedi, A. He, K. Cadien, and D. G. Ivey, “Atomic layer deposition of iron oxide on a porous carbon substrate via ethylferrocene and an oxygen plasma,” *Surf. Coatings Technol.*, vol. 421, p. 127390, 2021.

86. M. Labbe, M. P. Clark, K. Cadien, and D. G. Ivey, “Bifunctional Mn-Fe Oxide Catalysts for Zn-Air Battery Air Electrodes Through Atomic Layer Deposition,” *Batter. Supercaps*, e202400133, 2024.

87. H. Li, Z. Guo, and X. Wang, “Atomic-layer-deposited ultrathin Co9S8 on carbon nanotubes: An efficient bifunctional electrocatalyst for oxygen evolution/reduction reactions and rechargeable Zn-air batteries,” *J. Mater. Chem. A*, vol. 5, no. 40, pp. 21353–21361, 2017.

88. S. Yan, H. Li, J. Zhu, W. Xiong, R. Lei, and X. Wang, “Atomic layer deposited nickel sulfide for bifunctional oxygen evolution/reduction electrocatalysis and zinc–air batteries,” *Nanotechnology*, vol. 32, no. 27, p. 275402, 2021.

89. Q. Wang, H. Liang, J. Zhou, J. Wang, Z. Ye, M. Zhao, H. Yang, Y. Song, and J. Guo, “Boosting oxygen reduction catalysis by introducing Fe bridging atoms between Pt nanoparticles and N-doped graphene,” *Chem. Eng. J.*, vol. 467, no. April, p. 143482, 2023.

90. X. Shi, B. He, L. Zhao, Y. Gong, R. Wang, and H. Wang, “FeS2–CoS2 incorporated into nitrogen-doped carbon nanofibers to boost oxygen electrocatalysis for durable rechargeable Zn-air batteries,” *J. Power Sources*, vol. 482, no. August 2020, p. 228955, 2021.

91. P. Chu, Y. Zhang, J. He, J. Chen, J. Zhuang, Y. Li, X. Ren, P. Zhang, L. Sun, B. Yu, and S. Chen, “Defective Fe3O4-x Few-Atom Clusters Anchored on Nitrogen-Doped Carbon as Efficient Oxygen Reduction Electrocatalysts for High-Performance Zinc–Air Batteries,” *Small Methods*, vol. 6, no. 7, pp. 4–11, 2022.

92. A. Seong, J. Kim, O. Kwon, H. Y. Jeong, R. J. Gorte, J. M. Vohs, and G. Kim, “Self-reconstructed interlayer derived by in-situ Mn diffusion from La0.5Sr0.5MnO3 via atomic layer deposition for an efficient bi-functional electrocatalyst,” *Nano Energy*, vol. 71, no.

February, p. 104564, 2020.

93. M. Ritala and J. Niinistö, “Atomic Layer Deposition,” in *Chemical Vapour Deposition*, A. C. Jones and M. L. Hitchman, Eds. Cambridge, UK: Royal Society of Chemistry, 2009, pp. 158–206.

94. H. C. M. M. Knoops, S. E. Potts, A. A. Bol, and W. M. M. M. Kessels, “Atomic Layer Deposition,” in *Handbook of Crystal Growth: Thin Films and Epitaxy*, 2nd Ed., T. F. Kuech, Ed. Elsevier B.V., 2015, pp. 1101–1134.

95. H. B. Profijt, S. E. Potts, M. C. M. van de Sanden, and W. M. M. Kessels, “Plasma-Assisted Atomic Layer Deposition: Basics, Opportunities, and Challenges,” *J. Vac. Sci. Technol. A Vacuum, Surfaces, Film.*, vol. 29, no. 5, p. 050801, 2011.

96. S. M. George, “Atomic Layer Deposition : An Overview,” *Chem. Rev.*, vol. 110, no. 1, pp. 111–131, 2010.

97. A. Vesel and T. Semenič, “Etching rates of different polymers in oxygen plasma,” *Mater. Technol.*, vol. 46, no. 3, pp. 227–231, 2012.

98. E. A. D. Carbone, M. W. G. M. Verhoeven, W. Keuning, and J. J. A. M. Van Der Mullen, “PTFE treatment by remote atmospheric Ar/O2 plasmas: A simple reaction scheme model proposal,” *J. Phys. Conf. Ser.*, vol. 715, no. 1, p. 012011, 2016.

99. Z. Guo and L. Tan, *Fundamentals and Applications of Nanomaterials*. Norwood, MA: Artech House, 2009.

100. X. Wu, F. Chen, Y. Jin, N. Zhang, and R. L. Johnston, “Silver-Copper Nanoalloy Catalyst Layer for Bifunctional Air Electrodes in Alkaline Media,” *ACS Appl. Mater. Interfaces*, vol. 7, no. 32, pp. 17782–17791, 2015.

101. Y. Lei, F. Chen, Y. Jin, and Z. Liu, “Ag-Cu nanoalloyed film as a high-performance cathode electrocatalytic material for zinc-air battery,” *Nanoscale Res. Lett.*, vol. 10, no. 1, pp. 0–7, 2015.

102. X. Wu, F. Chen, N. Zhang, A. Qaseem, and R. L. Johnston, “A silver-copper metallic glass electrocatalyst with high activity and stability comparable to Pt/C for zinc-air

batteries," *J. Mater. Chem. A*, vol. 4, no. 9, pp. 3527–3537, 2016.

103. T. V. Pham, Y. Li, W. Luo, H. Guo, X. Gao, J. Wang, and H. Liu, "Binder-Free 3D Integrated Ni@Ni 3 Pt Air Electrode for Zn–Air Batteries," *Glob. Challenges*, vol. 3, no. 9, p. 1900027, 2019.

104. F. Meng, H. Zhong, D. Bao, J. Yan, and X. Zhang, "In Situ Coupling of Strung Co4N and Intertwined N-C Fibers toward Free-Standing Bifunctional Cathode for Robust, Efficient, and Flexible Zn-Air Batteries," *J. Am. Chem. Soc.*, vol. 138, no. 32, pp. 10226–10231, 2016.

105. D. Ji, L. Fan, L. Li, S. Peng, D. Yu, J. Song, S. Ramakrishna, and S. Guo, "Atomically Transition Metals on Self-Supported Porous Carbon Flake Arrays as Binder-Free Air Cathode for Wearable Zinc−Air Batteries," *Adv. Mater.*, vol. 31, no. 16, pp. 1–8, 2019.

106. Y. Niu, X. Teng, S. Gong, and Z. Chen, "A bimetallic alloy anchored on biomass-derived porous N-doped carbon fibers as a self-supporting bifunctional oxygen electrocatalyst for flexible Zn-air batteries," *J. Mater. Chem. A*, vol. 8, no. 27, pp. 13725–13734, 2020.

107. D. Ji, L. Fan, L. Li, N. Mao, X. Qin, S. Peng, and S. Ramakrishna, "Hierarchical catalytic electrodes of cobalt-embedded carbon nanotube/carbon flakes array for flexible solid-state zinc-air batteries," *Carbon*, vol. 142, pp. 379–387, 2019.

108. H. Konnerth, B. M. Matsagar, S. S. Chen, M. H. G. Prechtl, F. K. Shieh, and K. C. W. Wu, "Metal-organic framework (MOF)-derived catalysts for fine chemical production," *Coord. Chem. Rev.*, vol. 416, no. 1, p. 213319, 2020.

109. X. Wang, J. Zhou, H. Fu, W. Li, X. Fan, G. Xin, J. Zheng, and X. Li, "MOF derived catalysts for electrochemical oxygen reduction," *J. Mater. Chem. A*, vol. 2, no. 34, pp. 14064–14070, 2014.

110. Z. Wang, H. Jin, T. Meng, K. Liao, W. Meng, J. Yang, D. He, Y. Xiong, and S. Mu, "Fe, Cu-Coordinated ZIF-Derived Carbon Framework for Efficient Oxygen Reduction Reaction and Zinc–Air Batteries," *Adv. Funct. Mater.*, vol. 28, no. 39, p. 1802596, 2018.

111. D. Aasen, M. P. Clark, and D. G. Ivey, "(Co,Fe)3O4 Decorated Nitrogen-Doped Carbon Nanotubes in Nano-Composite Gas Diffusion Layers as Highly Stable Bifunctional

Catalysts for Rechargeable Zinc-Air Batteries," *Batter. Supercaps*, vol. 3, no. 2, pp. 174–184, 2020.

112. D. A. Aasen, Y. Shen, and D. G. Ivey, "Zn-Based Oxides Anchored to Nitrogen-Doped Carbon Nanotubes as Efficient Bifunctional Catalysts for Zn-Air Batteries," *ChemElectroChem*, vol. 7, no. 10, pp. 2283–2296, 2020.

113. Y. He, D. Aasen, H. Yu, M. Labbe, D. G. Ivey, and J. G. C. Veinot, "Mn3O4 nanoparticle-decorated hollow mesoporous carbon spheres as an efficient catalyst for oxygen reduction reaction in Zn–air batteries," *Nanoscale Adv.*, vol. 2, no. 8, pp. 3367–3374, 2020.

114. Y. He, D. Aasen, A. McDougall, H. Yu, M. Labbe, C. Ni, S. Milliken, D. G. Ivey, and J. G. C. Veinot, "Hollow Mesoporous Carbon Nanospheres Decorated with Metal Oxide Nanoparticles as Efficient Earth-Abundant Zinc-Air Battery Catalysts," *ChemElectroChem*, vol. 8, no. 8, pp. 1455–1463, Apr. 2021.

115. Y. He, Z. Abedi, C. Ni, S. Milliken, K. M. O'Connor, D. G. Ivey, and J. G. C. Veinot, "CoNi Nanoparticle-Decorated ZIF-67-Derived Hollow Carbon Cubes as a Bifunctional Electrocatalyst for Zn-Air Batteries," *ACS Appl. Nano Mater.*, vol. 5, no. 9, pp. 12496–12505, 2022.

116. Z. Abedi, D. Leistenschneider, W. Chen, and D. G. Ivey, "Spinel Type Mn-Co Oxide Coated Carbon Fibers as Efficient Bifunctional Electrocatalysts for Zinc-air Batteries," *Batter. Supercaps*, vol. 5, no. 2, p. e202100339, 2022.

117. L. Li, J. Yang, H. Yang, L. Zhang, J. Shao, W. Huang, B. Liu, and X. Dong, "Anchoring Mn 3 O 4 Nanoparticles on Oxygen Functionalized Carbon Nanotubes as Bifunctional Catalyst for Rechargeable Zinc-Air Battery," *ACS Appl. Energy Mater.*, vol. 1, no. 3, pp. 963–969, 2018.

118. Z. Abedi, J. Cui, W. Chen, and D. G. Ivey, "Zinc-Air Batteries with an Efficient and Stable MnCo2O4/Carbon Fiber Bifunctional Electrocatalyst and a Poly(acrylic Acid)-Based Gel Electrolyte," *ACS Appl. Energy Mater.*, vol. 5, no. 11, pp. 14164–14174, 2022.

119. Z. Abedi, J. Cui, W. Chen, and D. G. Ivey, "Efficient Low Temperature Performance of

All Solid-State Zinc-Air Batteries with MnCo2O4/Carbon Fiber Bifunctional Electrocatalyst and Poly(Acrylic Acid) (PAA) Gel Polymer Electrolyte," *Batter. Supercaps*, p. e202200526, Feb. 2023.

120. X. Zhong, W. Yi, Y. Qu, L. Zhang, H. Bai, Y. Zhu, J. Wan, S. Chen, M. Yang, L. Huang, M. Gu, H. Pan, and B. Xu, "Co single-atom anchored on Co3O4 and nitrogen-doped active carbon toward bifunctional catalyst for zinc-air batteries," *Appl. Catal. B Environ.*, vol. 260, no. September 2019, p. 118188, 2020.

121. J. E. Tsai, W. X. Hong, H. Pourzolfaghar, W. H. Wang, and Y. Y. Li, "A Fe-Ni-Zn triple single-atom catalyst for efficient oxygen reduction and oxygen evolution reaction in rechargeable Zn-air batteries," *Chem. Eng. J.*, vol. 460, no. February, p. 141868, 2023.

122. Z. Yan, H. Sun, X. Chen, X. Fu, C. Chen, F. Cheng, and J. Chen, "Rapid low-temperature synthesis of perovskite/carbon nanocomposites as superior electrocatalysts for oxygen reduction in Zn-air batteries," *Nano Res.*, vol. 11, no. 6, pp. 3282–3293, 2018.

123. A. Sumboja, X. Ge, F. W. T. Goh, B. Li, D. Geng, T. S. A. Hor, Y. Zong, and Z. Liu, "Manganese Oxide Catalyst Grown on Carbon Paper as an Air Cathode for High-Performance Rechargeable Zinc-Air Batteries," *Chempluschem*, vol. 80, no. 8, pp. 1341–1346, 2015.

124. S. Sinha, P. N. Didwal, D. K. Nandi, J. Y. Cho, S. H. Kim, C. J. Park, and J. Heo, "Atomic layer deposited-ZnO@3D-Ni-foam composite for Na-ion battery anode: A novel route for easy and efficient electrode preparation," *Ceram. Int.*, vol. 45, no. 1, pp. 1084–1092, 2019.

125. D. Xiong, Q. Zhang, W. Li, J. Li, X. Fu, M. F. Cerqueira, P. Alpuim, and L. Liu, "Atomic-layer-deposited ultrafine MoS2 nanocrystals on cobalt foam for efficient and stable electrochemical oxygen evolution," *Nanoscale*, vol. 9, no. 8, pp. 2711–2717, 2017.

Appendix B: Experimental Concerns of Current Collector Interference and Electrolyte Creep During Zn-Air Battery Testing

A version of this appendix has been published in a peer-reviewed journal:

M. Labbe and D. G. Ivey, "Experimental Concerns of Current Collector Interference and Electrolyte Creep During Zinc-Air Battery Testing," *J. Electrochem. Soc.*, vol. 170, no. 9, p. 090515, 2023.

Abstract

Evaluating the electrochemical performance of catalysts towards the oxygen reduction and evolution reactions in Zn-air batteries is a routine process often conducted using a two-electrode cell. At the air electrode, a current collector is necessary if a carbon paper-based gas diffusion layer (GDL) is employed. The catalytic properties of the current collector may interfere with the studied catalyst on the GDL if flaws in cell design allow electrolyte contact to be made with the current collector. At the Zn electrode, highly alkaline electrolytes (*e.g.*, KOH), with high surface tension, can easily climb up the electrode and accumulate at the interface between the cell and the surrounding atmosphere. An oxygen concentration cell is then enabled by the deposited electrolyte and the Zn electrode is rapidly corroded until failure, prematurely ending a long-term cycling test.

B.1. Introduction

With the electrification of the transport sector and the rampant integration of intermittent renewable energy into the power grid, the demand for energy storage technologies has never been higher. While Li-ion batteries (LIBs) have penetrated every market for energy storage, alternative technologies are beginning to be applied in more nuanced areas. Research into these alternative battery technologies is an important part of the chain to practical implementation and replacement of LIBs. Due to the widespread use and research into LIBs, battery testing for Li-ion technology is well established and standardized.[1,2] Unfortunately, the novel battery technologies set to replace Li-ion rarely have standard methods of testing and inconsistences between and within research groups is largely unavoidable.[3] The current report highlights two challenges encountered by the authors during testing of Zn-air batteries (ZABs): 1) Interference of the Ni current collector at the air electrode during the charge performance measurement and 2) aggressive corrosion of the Zn electrode resulting in battery failure. Mitigation strategies are also presented to assist other researchers in avoiding similar pitfalls.

B.2. Interference of the Current Collector on the Charging Potential

In ZABs, the cathodic air-breathing electrode is often fabricated from PTFE-coated carbon paper. Pores in the carbon paper enable oxygen exchange between the external environment and the cell, while the PTFE treatment renders the electrode hydrophobic to prevent electrolyte loss through the pores.[4] This porous carbon paper is known as the gas diffusion layer (GDL) and acts as a substrate for oxygen reaction catalysts deposited through a variety of methods.[5] Unfortunately, battery testers and potentiostats commonly feature metallic alligator clips and rigid cables that, due to the fragile nature of carbon paper,[4] lead to broken air electrodes if connected directly. Therefore, a common practice in ZAB fabrication is the use of a current collector (CC) at the air electrode. Made of Ni, stainless steel, or another conductive metal that is stable in the highly alkaline electrolyte, the role of the CC is to facilitate the transfer of charge between the air electrode and the power source, load, or battery tester.[6] By connecting to a CC, the brittle nature of the carbon paper air electrode is circumvented.

The CC should be placed on the air side of the electrode assembly to prevent electrolyte contact with the CC. Otherwise, if the CC is in contact with the electrolyte, it joins the electrochemical

cell of the battery and enables the surface of the CC to potentially act as a catalyst for the oxygen evolution reaction (OER) during ZAB charge (Figure B.1a). OER is a two-phase reaction, which only requires contact between the electrolyte and an electron conductor. Thus, the intended catalyst material deposited on the GDL competes with the surface of the CC during OER. As a result, the researcher may be inadvertently evaluating the catalytic performance of the CC instead of the intended OER catalyst. When the CC is, instead, placed on the air side of the electrode, the hydrophobic GDL prevents electrolyte contact with the CC, chemically isolating the CC from the cell reactions (Figure B.1b).

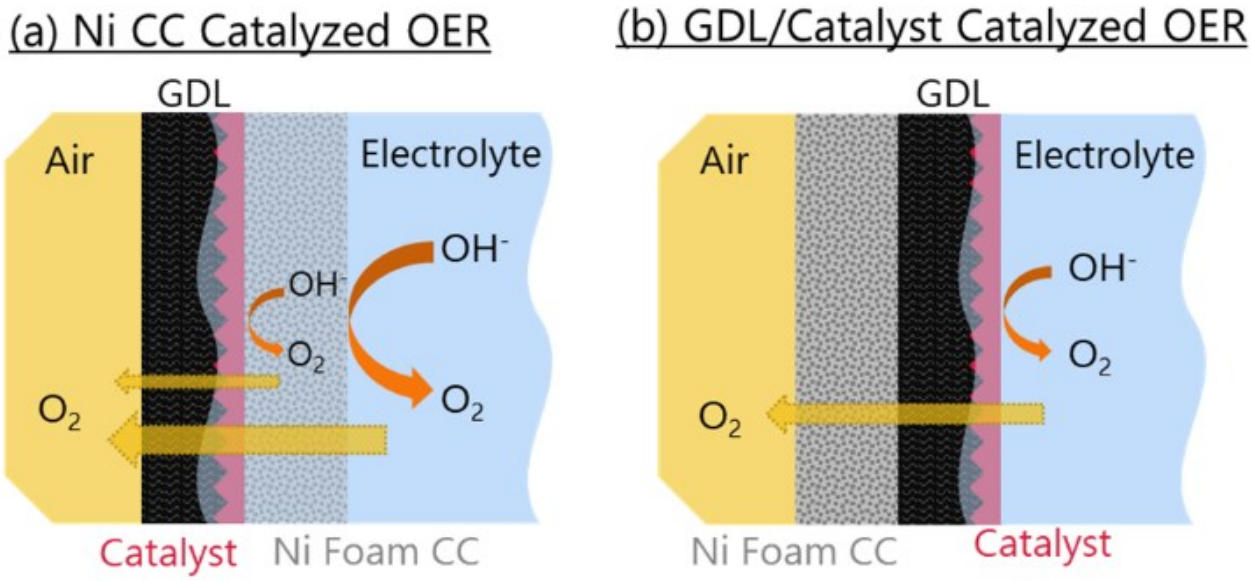

Figure B.1. Schematic of air electrode assembly when the CC (*e.g.*, Ni foam) is placed (a) on the electrolyte side and (b) on the air side.

Since rechargeable ZABs have yet to be commercialized, there is no universal cell for experimental testing. As such, difference research groups throughout the literature each have their own homemade prototype ZAB cells. A key component of ZABs is the air-breathing electrode, requiring cell designs to incorporate a window allowing O_2 flow into and out of the cell. The ZAB cell developed by the authors and colleagues is an acrylic box with a 1 cm x 1 cm window cut out (shown schematically in Figure B.2a).[7,8] A thin (0.5 mm) Ni sheet serves as the CC and is placed in contact with the catalyst-coated GDL sample (SIGRACET© 39BB, SGL Carbon) on the air side of the electrode assembly, as shown in Figure B.1b. Both the GDL sample and the CC measure 2 cm x 2 cm, while the CC has a 1 cm wide stem to connect to a

testing device (Figure B.2b). Furthermore, the Ni CC has a 1 cm x 1 cm window that aligns with the acrylic box to enable passive oxygen exchange with the ambient atmosphere through the GDL. The GDL and Ni CC are then sandwiched by another acrylic plate with four sets of nuts and bolts securing them to the cell wall (Figure B.2b).[9] The addition of O-rings at each bolt prevents electrolyte leakage from the bolt holes. A strip of Zn foil (~6 g) is placed in the center of the cell and the volume is filled with approximately 30 mL of a 6 M KOH plus 0.25 M ZnO electrolyte. Since there is an excessive amount of electrolyte in the cell and a relatively large separation distance between electrodes, there is no need for a separator in this design.

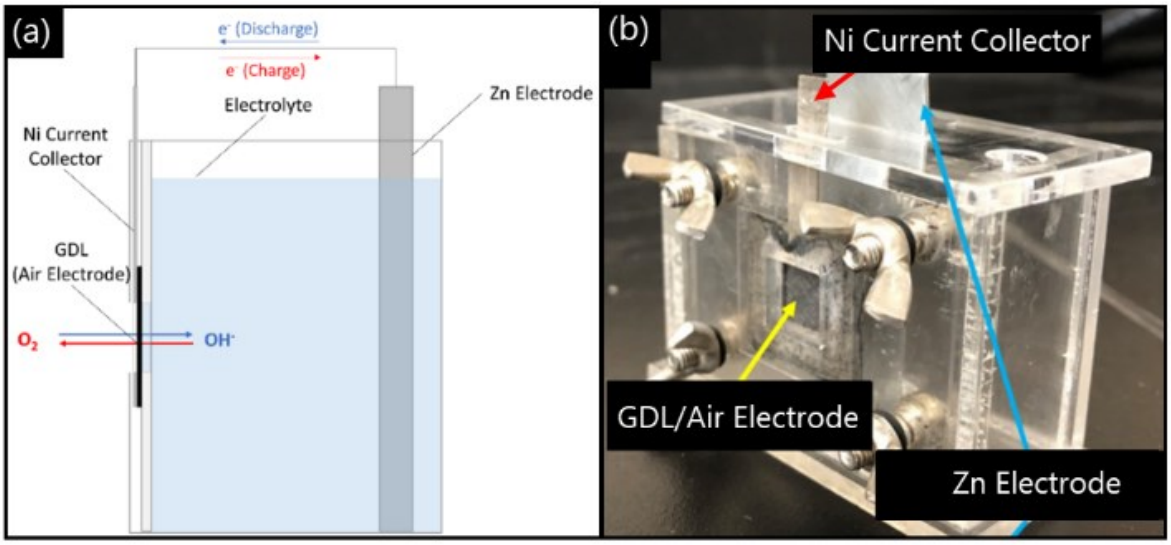

Figure B.2. (a) Diagram of a vertical two-electrode ZAB cell and (b) picture of the acrylic two-electrode cell. Adapted from refs.[8,9].

This acrylic two-electrode ZAB design was, initially, an effective means of investigating and comparing different air electrode catalysts attached to the GDL, with little to no electrolyte loss from the cell. However, at some point, electrolyte began to leak out of the window in the cell wall, particularly during long term cycling. At the time, the researchers simply periodically refilled the cell to compensate for electrolyte loss.

During investigation of a (Mn,Fe)O_x catalyst on GDL using the acrylic two-electrode cell (Chapter 5), the authors noticed that the potential during ZAB charging was not improved compared with GDL without any catalyst (bare GDL; Figure B.3a). In fact, bare GDL had slightly better charging behaviour. While the high surface area microporous carbon layer of bare

GDL does exhibit some inherent oxygen reduction reaction (ORR) activity,[4] it does not enhance OER capabilities. On the other hand, FeO_x-based catalysts should provide improvements in OER activity over bare GDL.[10,11] If bare GDL and GDL with the $(Mn,Fe)O_x$ catalyst are instead tested in a three-electrode half cell configuration, bare GDL provides little to no OER activity, while the $(Mn,Fe)O_x$ catalyst introduces substantial OER current (Figure B.4). In the case of the two-electrode design (Figure B.2), the GDL is placed in between ambient air and a reservoir of KOH, where electrode wetting and oxygen transport occur through unassisted natural phenomenon. In the three-electrode configuration, however, the GDL sample is suspended in 1 M KOH and O_2 gas is bubbled into the electrolyte. With a Hg/HgO reference electrode and a Pt wire counter electrode, the ORR and OER kinetics of the GDL working electrode can be studied through cyclic voltammetry, while avoiding complications from the two-electrode setup (electrode wetting, electrolyte flooding, porosity, oxygen diffusion, *etc.*).

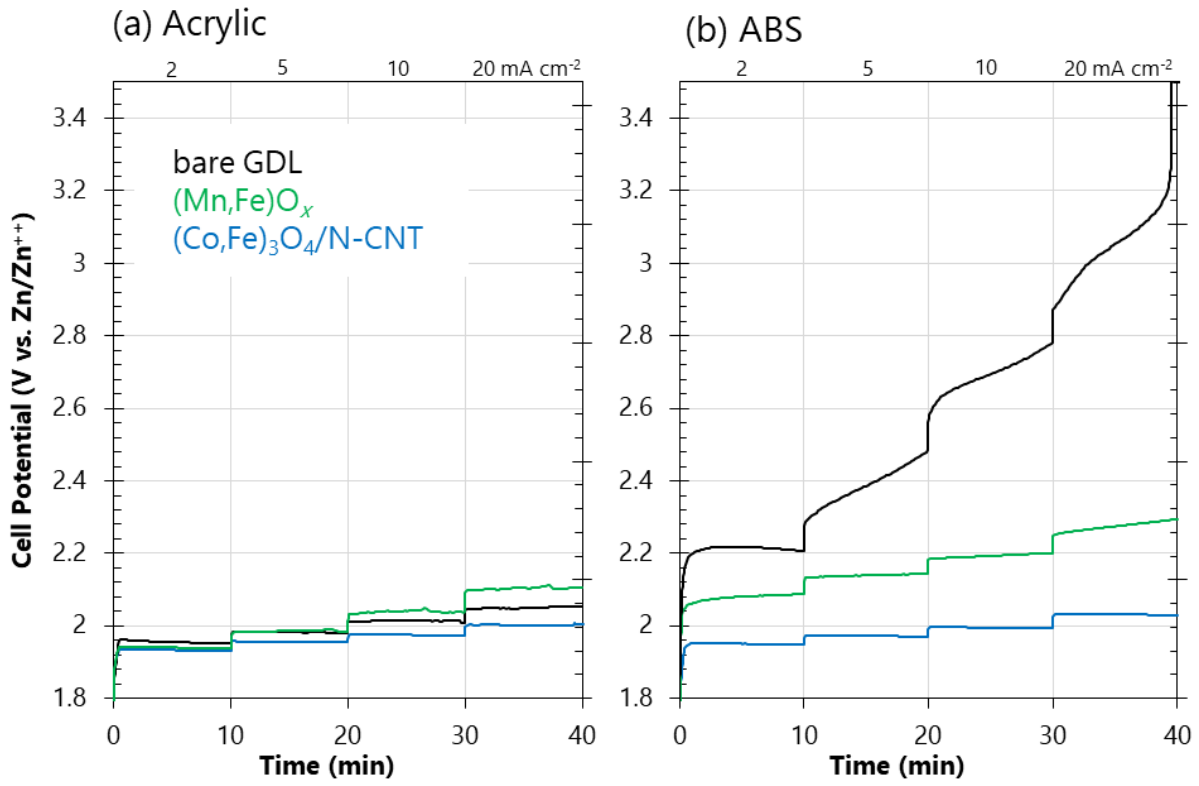

Figure B.3. Two-electrode rate testing at different charging current densities for bare GDL, a $(Mn,Fe)O_x$ catalyst, and a $(Co,Fe)_3O_4$/N-CNT catalyst in (a) acrylic and (b) ABS cells.

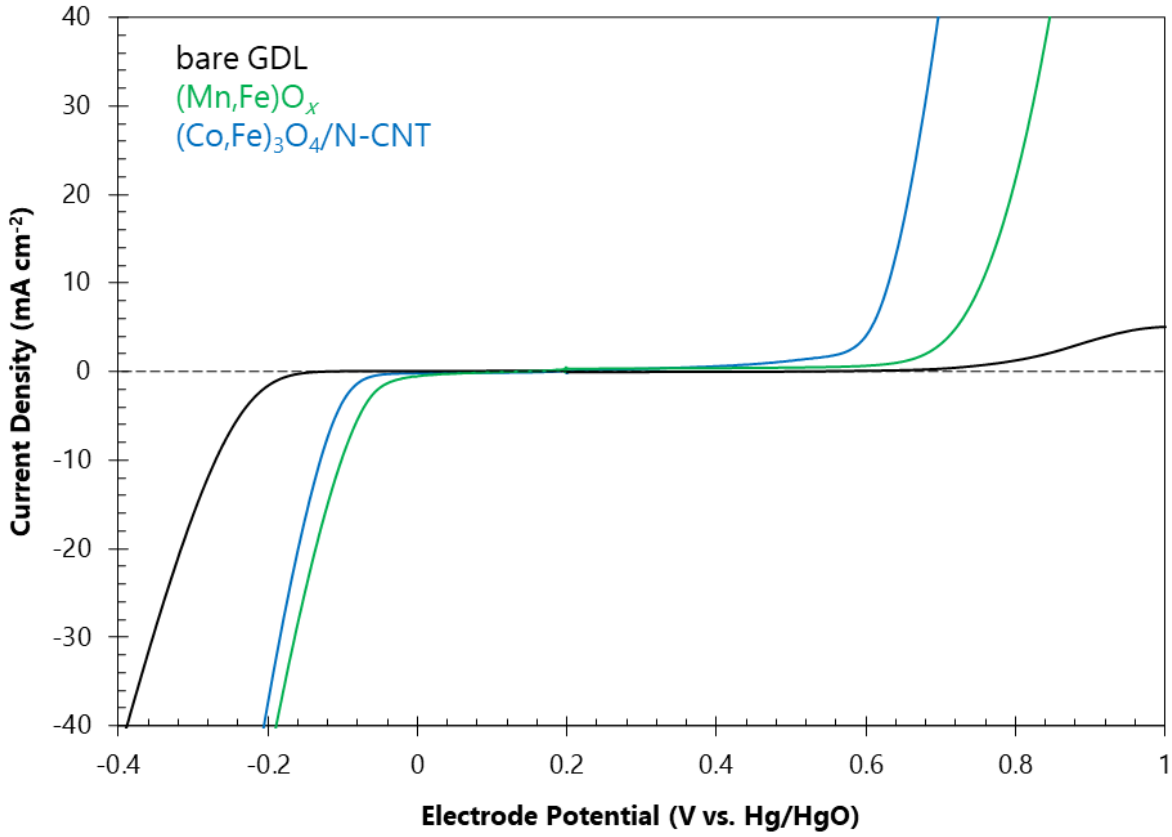

Figure B.4. Three-electrode linear sweep voltammetry testing of the air electrode half cell in O_2 saturated 1 M KOH for bare GDL, a $(Mn,Fe)O_x$ catalyst, and a $(Co,Fe)_3O_4$/N-CNT catalyst. OER is studied at potentials greater than 0.3 V vs. Hg/HgO, while ORR is studied at potentials less than 0.3 V vs. Hg/HgO.

The contradictory results can be attributed to deficiencies in the two-electrode cell design. It is proposed that the seal between the GDL, CC, and acrylic wall became compromised and electrolyte crept around the back of the GDL, around the edges of the carbon paper, and out through the bottom edge of the window in the cell wall. While electrolyte loss is not concerning in terms of evaluating catalyst behavior (as long as it is replenished as required), electrolyte creep allowed the CC on the air side of the GDL to become wet with electrolyte. With the CC in contact with electrolyte, the surface of the Ni CC became a component of the electrochemical cell and provided catalyzed OER active sites. NiO_x is a well-established OER catalyst, reducing the overpotential required during ZAB charging.[12] Ultimately, during charging tests of the acrylic cell, the investigated catalyst deposited onto the GDL was a secondary catalytic surface to the NiO_x surface of the CC. Furthermore, the geometric surface area of the CC is 3 cm^2,

compared with the exposed 1 cm^2 geometric surface area of the GDL. This effectively reduced the current density on the CC, enabling it to outperform the catalyst on the GDL.

Aware of the interference of the CC on OER performance, the authors set out to redesign the two-electrode cell to eliminate the effect of the Ni CC on OER behaviour. Since the development of the acrylic cell, the authors have gained access to a 3D printer. The faster production time and lower material waste from 3D printing compared with acrylic laser cutting facilitated more iterations of design optimization for the new cell. Acrylonitrile butadiene styrene (ABS) was selected as the filament material due to its availability, ease of use, and resistance to KOH.[13,14] The final version of the two-electrode cell (Figure B.5a) uses an O-ring between the GDL and the ABS wall to prevent electrolyte creep around the GDL which had resulted in wetting of the CC for the acrylic cell. A commonly employed polymer for O-rings, nitrile rubber, was selected as the O-ring material due to its availability, low cost, and acceptable resistance to KOH.[15] Another modification was to replace the Ni CC with a 0.5 mm thick Ni foam CC, which is more flexible and can be more easily shaped. Furthermore, the compressibility of the Ni foam is exploited in the new design to improve the seal between the GDL and the cell wall, and to reduce the amount of compression experienced by the porous GDL air electrode. This new ABS cell employs spring-loaded clamps (Anvil^{TM} 2 inch Spring Clamp) on the exterior to seal the GDL and CC to the ABS wall, eliminating bolts and bolt holes and simplifying the assembly process (Figure B.5b). Lastly, a tight-fitting lid reduces evaporation of the electrolyte and provides consistent placement of the Zn electrode. A hole is present in the lid to add electrolyte lost by evaporation or electrolyte creep and to maintain a consistent electrolyte water level; this hole is plugged when not required. The 3D object files for the ABS two-electrode cell are included as Supporting Information.

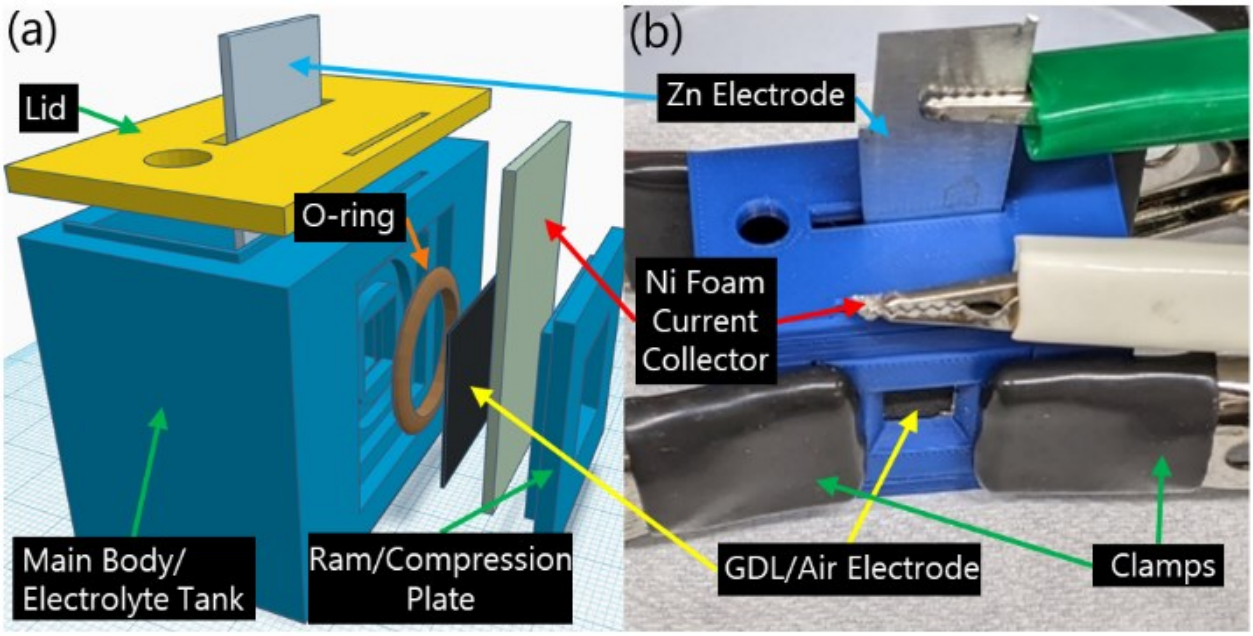

Figure B.5. (a) Exploded-view drawing and (b) picture of the ABS two-electrode cell.

Using the new ABS two-electrode cell, the charging performance of bare GDL was quite poor (Figure B.3b) as expected based on the three-electrode half cell testing. This confirms that the new ABS cell does not incorporate the Ni CC into the electrochemical reactions and can reliably test the performance of a catalyst-loaded GDL. In fact, the charging potential for the $(Mn,Fe)O_x$ catalyst was slightly worse in the ABS cell, implying that the Ni CC was a superior OER catalyst to the $(Mn,Fe)O_x$ catalyst and interfered with the rate testing results (Figure B.3b). It should be noted that catalysts with OER activity superior to the Ni CC do not suffer from an interference effect in the acrylic two-electrode cell. One such catalyst, a $(Co,Fe)_3O_4$/nitrogen-doped carbon nanotube (N-CNT) material,[9] does not exhibit noticeable differences in charging performance with either the acrylic or the ABS two-electrode cell (Figures B.3a and B.3b). In this case, the $(Co,Fe)_3O_4$/N-CNT catalyst is able to outperform the Ni CC and prevails as the catalyzing species in both the acrylic and ABS cell. Ultimately, the ABS cell provides a similar picture in terms of relative performance between bare GDL, $(Mn,Fe)O_x$, and $(Co,Fe)_3O_4$/N-CNT compared with that demonstrated by the three-electrode results (Figure B.4).

B.3. Zn Corrosion from Electrolyte Creep

At the Zn electrode in a ZAB, multiple phenomena can impact performance. Shape change, dendrite formation, passivation, and hydrogen evolution are all commonly investigated behaviour of the Zn electrode.[6] When specifically evaluating air electrode catalysts, it is important to avoid any effects of the Zn electrode on battery performance. The aforementioned Zn phenomena are largely avoided in practice by (i) employing a relatively thick and large Zn foil as the Zn electrode, (ii) increasing the separation distance between electrodes, and (iii) having a large reservoir of electrolyte in the cell. When testing candidate air electrodes, as long as the cell setup is maintained between tests, the effect of the Zn electrode on battery performance remains consistent and is accounted for when comparing results. For short-term tests (< 24 h), the Zn electrode does not interfere with testing. Another aspect of air electrode evaluation is the stability of the catalyst over an extended period of battery cycling.[6] An issue that can arise during long-term ZAB tests is the corrosion of the Zn electrode and eventual loss of electrical connectivity. It should be emphasized that this Zn corrosion is not considered self-discharge, since the area undergoing corrosion is not intended to be electrochemically active and serves only as the current collector for the lower, active portion of the Zn electrode.

Compared with the air electrode, the Zn electrode in the two-electrode cell setup is quite simple. A 0.5 mm thick piece of Zn foil, measuring 6.5 cm by 2.3 cm, is placed, as received, in the electrolyte reservoir and directly connected to the potentiostat/battery cycler as a combined counter and reference electrode. Unlike the carbon paper air electrode, the Zn electrode is strong enough to serve as its own current collector. Since the air electrode (and its catalyst) is the subject of interest, there is no requirement to control the active surface area of the Zn electrode, and generally, the entire submerged portion of the Zn electrode is electrochemical active. In fact, the exposed area of the counter (Zn) electrode should be larger than that of the working (air) electrode to avoid limiting the current density at the working (air) electrode. Based on the configuration of the ABS two-electrode cell (Figure B.5), approximately 8 cm^2 of the Zn electrode is submerged in the electrolyte. The lid design for the two-electrode cell includes a slot to position the Zn foil at a fixed distance from the air electrode, yielding a reproducible ohmic resistance in the cell.

After a couple days of testing the same ZAB cell, a white precipitate is observed on the Zn electrode at the lid line (Figure B.6a). More of this precipitate is grown over subsequent days and eventually, a large mass of this white precipitate encases the entire air-exposed Zn electrode (and even the alligator clip of the battery tester) (Figure B.6b). The electrical connection for the cell is, at first, unaffected and the battery continues to operate for several more days. At some point, however, the Zn electrode breaks at the lid line, terminating electrical contact with the counter electrode and stopping the ZAB test (Figure B.6c). The identity of this white precipitate is undoubtedly KOH, which is able to climb up the Zn electrode due to its high surface tension and the well-documented salt solution creep effect.[16,17] Post-mortem examination of the Zn electrode reveals that a low amount of corrosion occurs on the Zn foil above or below the lid line. Instead, the corrosion is concentrated to the area where the Zn just protrudes from the lid (Figure B.6d).

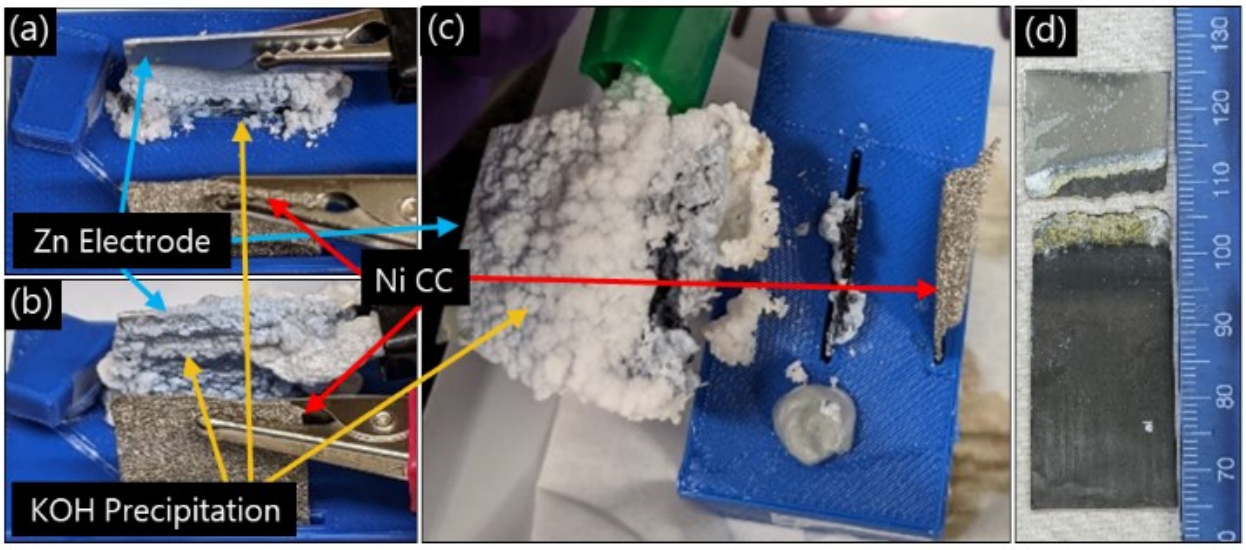

Figure B.6. Illustration of KOH creep and Zn electrode failure during long-term cycling in the two-electrode ABS cell. (a) Initial creep of KOH after two days, (b) KOH encapsulation of the Zn electrode and alligator clip after four days, (c) fracture of the Zn electrode after seven days, and (d) post-mortem image of the Zn foil electrode.

The lid in the two-electrode cell effectively creates a boundary between an area of high oxygen concentration (the atmosphere above) and an area of lower oxygen concentration (the air gap of the cell below the lid). This then gives rise to an oxygen concentration cell at the lid line, where the Zn electrode serves as the electron conductor and the electrolyte that has crept up the Zn as the ionic conductor. The electrolyte above the lid is infused with oxygen from the atmosphere,

making it more cathodic than the area below the lid. Thus, Zn metal is dissolved just below the lid line (anode) as oxygen reduction occurs on the Zn just above the lid line (cathode).[18,19] This waterline corrosion occurs until enough Zn is consumed to cause electrode failure. To make matters worse, a similar oxygen concentration cell is already established at the waterline below the lid where the electrolyte level meets the air gap in the cell (Figure B.7a). The consumption of oxygen in the air gap from corrosion at the water level further reduces the oxygen concentration of the anode at the lid line corrosion, exacerbating the corrosion at the lid line (Figure B.7b). Even with thick Zn foil, the severe corrosion at the lid line rapidly removes Zn material from the electrode and ultimately breaks the entire Zn electrode into two pieces, cutting off electrical contact with the remainder of the cell and causing an open-circuit failure. Since the manipulated variable between tests is the air electrode catalyst, it may be incorrectly concluded that the ZAB cell failed due to the air electrode. In any case, the failure of the Zn electrode prematurely ends a long-term cycling test and interrupts data collection.

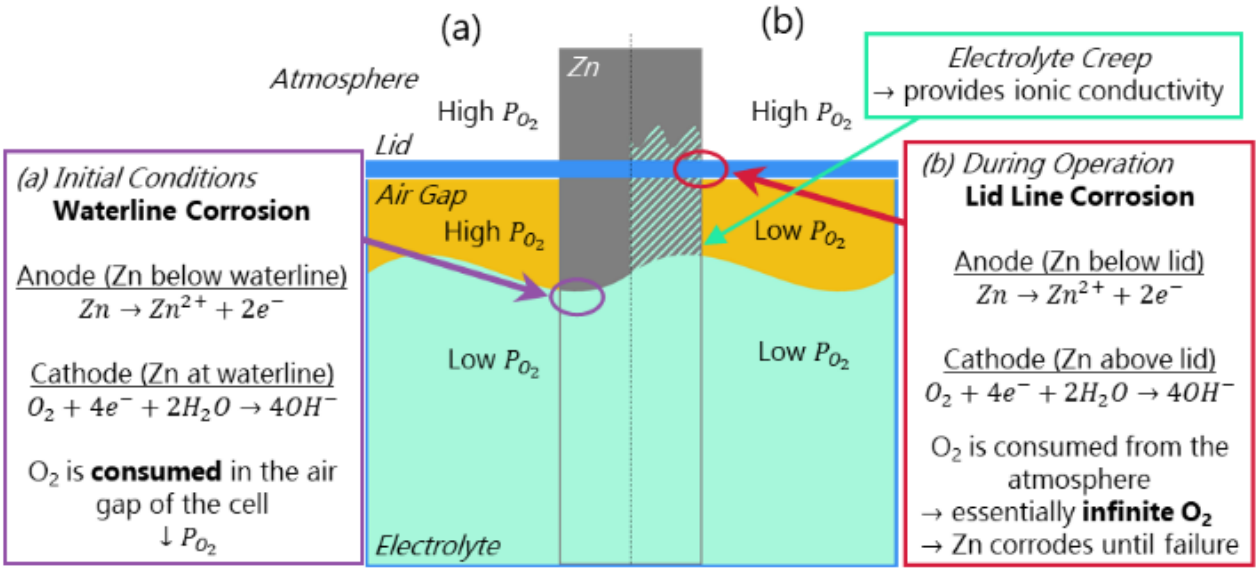

Figure B.7. Schematic of the oxygen concentration cell (a) that forms initially at the waterline and (b) that is established at the lid line as the electrolyte creeps along the Zn electrode.

One strategy to mitigate the corrosion of the Zn electrode at the lid line is to mask off an area around the location of the lid. For the authors, an epoxy resin (EpoThin™ 2, Buehler) was readily available as a masking compound and successfully extended the lifetime of the Zn electrode compared with no epoxy coating. However, long term cycling tests (> 3 weeks)

continued to result in failure due to Zn electrode corrosion. It was determined that the epoxy coating is not non-wetting towards the KOH solution and the salt creep effect was able to continue on the outside surface of the epoxy coating. While the area protected by the epoxy coating did not corrode, the corrosion cell simply shifted upwards to the unprotected portion of Zn electrode connected to the alligator clip, causing electrode failure at this location instead.

In a report published nearly a century ago, Washburn proposed that the application of an oily coating could stop electrolyte creep.[20] KOH creep testing in an open atmosphere revealed that a siloxane-based vacuum grease (Dow Corning® high vacuum grease) does indeed hamper the progress of electrolyte creep relative to no treatment, but does not stop it entirely (Figures B.8a and B.8b). Somewhat unexpectedly, a perfluoroniated-grease (Fomblin® per fluorinated grease), which may have superior non-wetting qualities, yields inferior results to a traditional siloxane-based vacuum grease (Figure B.8c). Instead, a PTFE-infused lubricant (WD-40 Specialist® Dry Lube - with PTFE) showed the most promising results in the KOH creep test, halting the progress of creep entirely (Figure B.8d).

A combined approach will likely provide the best longevity for the Zn foil electrode in the two-electrode setup. Firstly, an epoxy coating at the waterline in the cell will eliminate corrosion at this location, thus reducing the oxygen concentration gradient that arises at the cell lid. In addition, the application of a greasy, hydrophobic coating over the remaining length of the air-exposed Zn foil, including the electrode connection, will prevent creep of the KOH electrolyte. This will eliminate the ionic conductor necessary for the development of an oxygen concentration cell at the lid line.

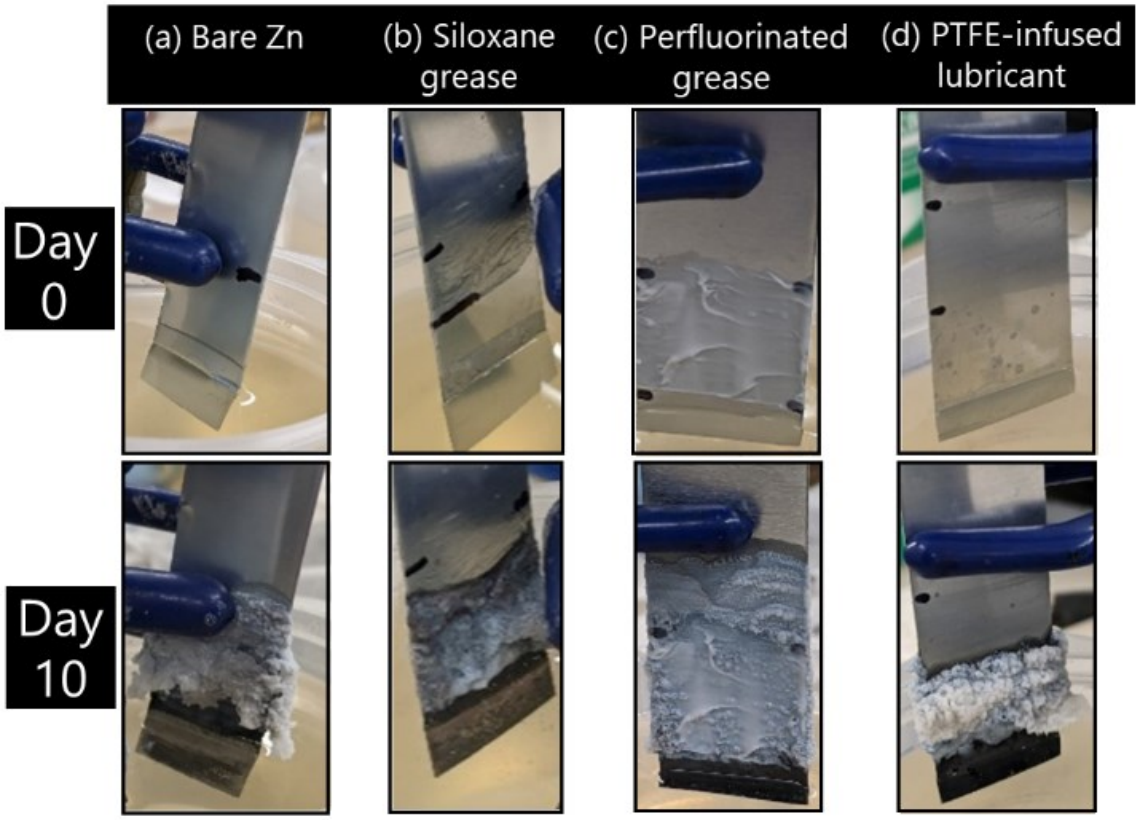

Figure B.8. Timelapse of KOH creep on Zn foil (a) with no coating, (b) coated with a siloxane-based vacuum grease, (c) coated with a perfluorinated vacuum grease, and (d) coated with a PTFE-infused lubricant. The coatings were applied between the two black marks shown in the Day 0 photos.

B.4. Conclusions

The design of an experimental cell in ZAB research is an important consideration that may influence electrochemical testing. When investigating air electrode catalysts, the influence of a Ni current collector on charging potentials can be significant if there is reason to believe the electrolyte is in contact with the current collector. The addition of an O-ring to the cell, to prevent electrolyte leaking during operation, has been shown to mitigate this effect. In open-to-air designs, electrolyte creep and corrosion of the Zn electrode will impact the lifetime of a battery. Efforts to protect the Zn electrode at the corrosion location may not eliminate electrolyte creep and simply move the corrosion location instead. Alternatively, hydrophobic, greasy coatings show promising results at preventing electrolyte creep altogether and extending the lifetime of a ZAB.

References

1. T. Marks, S. Trussler, A. J. Smith, D. Xiong, and J. R. Dahn, "A Guide to Li-Ion Coin-Cell Electrode Making for Academic Researchers," *J. Electrochem. Soc.*, vol. 158, no. 1, pp. A51–A57, 2011.

2. J. E. Harlow, X. Ma, J. Li, E. Logan, Y. Liu, N. Zhang, L. Ma, S. L. Glazier, M. M. E. Cormier, M. Genovese, S. Buteau, A. Cameron, J. E. Stark, and J. R. Dahn, "A Wide Range of Testing Results on an Excellent Lithium-Ion Cell Chemistry to be used as Benchmarks for New Battery Technologies," *J. Electrochem. Soc.*, vol. 166, no. 13, pp. A3031–A3044, 2019.

3. B. J. Hopkins, C. N. Chervin, J. F. Parker, J. W. Long, and D. R. Rolison, "An Areal-Energy Standard to Validate Air-Breathing Electrodes for Rechargeable Zinc–Air Batteries," *Adv. Energy Mater.*, vol. 10, no. 30, pp. 1–6, 2020.

4. J. Fu, Z. P. Cano, M. G. Park, A. Yu, M. Fowler, and Z. Chen, "Electrically Rechargeable Zinc-Air Batteries: Progress, Challenges, and Perspectives," *Adv. Mater.*, vol. 29, no. 7, p. 1604685, 2017.

5. M. Xiong and D. G. Ivey, "Synthesis of Bifunctional Catalysts for Metal-Air Batteries Through Direct Deposition Methods," *Batter. Supercaps*, vol. 2, no. 4, pp. 326–335, 2019.

6. X. Chen, Z. Zhou, H. E. Karahan, Q. Shao, L. Wei, and Y. Chen, "Recent Advances in Materials and Design of Electrochemically Rechargeable Zinc–Air Batteries," *Small*, vol. 14, no. 44, pp. 1–29, 2018.

7. T. N. T. Tran, M. P. Clark, H. J. Chung, and D. G. Ivey, "Effects of Crosslinker Concentration in Poly(Acrylic Acid)-KOH Gel Electrolyte on Performance of Zinc-Air Batteries," *Batter. Supercaps*, vol. 3, no. 5, pp. 409–416, 2020.

8. D. Aasen, M. Clark, and D. G. Ivey, "A Gas Diffusion Layer Impregnated with Mn3O4 - Decorated N-Doped Carbon Nanotubes for the Oxygen Reduction Reaction in Zinc-Air Batteries," *Batter. Supercaps*, vol. 2, no. 10, pp. 882–893, 2019.

9. D. Aasen, M. P. Clark, and D. G. Ivey, "(Co,Fe)3O4 Decorated Nitrogen-Doped Carbon Nanotubes in Nano-Composite Gas Diffusion Layers as Highly Stable Bifunctional

Catalysts for Rechargeable Zinc-Air Batteries," *Batter. Supercaps*, vol. 3, no. 2, pp. 174–184, 2020.

10. M. Labbe, M. P. Clark, Z. Abedi, A. He, K. Cadien, and D. G. Ivey, "Atomic layer deposition of iron oxide on a porous carbon substrate via ethylferrocene and an oxygen plasma," *Surf. Coatings Technol.*, vol. 421, p. 127390, 2021.

11. L. Gong, J. Koh, B. Siang, and B. S. Yeo, "Mechanistic Study of the Synergy between Iron and Transition Metals for the Catalysis of the Oxygen Evolution Reaction," *ChemSusChem*, vol. 11, no. 21, pp. 3790–3795, 2018.

12. H. Osgood, S. V. Devaguptapu, H. Xu, J. Cho, and G. Wu, "Transition metal (Fe, Co, Ni, and Mn) oxides for oxygen reduction and evolution bifunctional catalysts in alkaline media," *Nano Today*, vol. 11, no. 5, pp. 601–625, 2016.

13. J. D. Moore, "Acrylonitrile-butadiene-styrene (ABS) - a review," *Composites*, vol. 4, no. 3, pp. 118–130, 1973.

14. H. Zhang, L. Cai, M. Golub, Y. Zhang, X. Yang, K. Schlarman, and J. Zhang, "Tensile, Creep, and Fatigue Behaviors of 3D-Printed Acrylonitrile Butadiene Styrene," *J. Mater. Eng. Perform.*, vol. 27, no. 1, pp. 57–62, 2018.

15. Parker O-Ring and Engineered Seals Division, *Parker O-Ring Handbook ORD 5700*, vol. ORD 5700. Cleveland, OH: Parker Hannifin Corporation, 2021.

16. R. I. Slavchov and J. K. Novev, "Surface tension of concentrated electrolyte solutions," *J. Colloid Interface Sci.*, vol. 387, no. 1, pp. 234–243, 2012.

17. M. J. Qazi, H. Salim, C. A. W. W. Doorman, E. Jambon-Puillet, and N. Shahidzadeh, "Salt creeping as a self-amplifying crystallization process," *Sci. Adv.*, vol. 5, no. 12, p. eaax1853, Sep. 2019.

18. S. A. Bradford, *Corrosion Control*. New York, NY: Van Nostrand Reinhold, 1993.

19. M. Pourbaix, *Atlas of Electrochemical Equilibria in Aqueous Solutions*, Second Ed. Houston, TX: National Association of Corrosion Engineers, 1974.

20. E. R. Washburn, "The Creeping of Solutions," *J. Phys. Chem.*, vol. 31, no. 8, pp. 1246–1248, 1927.